

University of Strathclyde
Department of Mechanical and Aerospace Engineering

A numerical and experimental study
on cavitation in positive displacement
pumps and its application in valve
design optimization

Aldo Iannetti

A thesis presented in fulfilment of the requirements for the degree of
Doctor of Philosophy

2015

Declaration of Authenticity and Author's Rights

This thesis is the result of the author's original research. It has been composed by the author and has not been previously submitted for examination which has led to the award of a degree.

The copyright of this thesis belongs to the author under the terms of the United Kingdom Copyright Acts as qualified by University of Strathclyde Regulation 3.50. Due acknowledgement must always be made of the use of any material contained in, or derived from, this thesis.

Aldo Iannetti

July 2015

Abstract

A comprehensive and transient Computational Fluid Dynamic model of a Positive Displacement reciprocating pump in cavitating condition was developed in order to study the main features and the causes of cavitation in this kind of device. Several sensitivity analyses were also carried out in order to identify the most influential parameters on cavitation; the design of the inlet valve as well as the operating conditions were found to be the main parameters playing an important role in cavitation. To complete the numerical study, a sensitivity analysis on the air content in the water was carried out. This highlighted the importance of the physical properties of the working liquid in influencing the vapour generation during cavitation. The second part of the project was dedicated to the experimental analysis; a test rig replicating the numerical model was designed and built. The experimental tests were carried out and the results were compared to the numerical data obtained in the previous part. The comparison revealed a reasonable accuracy as well as good consistency although numerical problems were found in the way the cavitation model accounted for the influence of the air dissolved in the water which was overestimated. The validated numerical model was utilised to modify the design of the inlet valve. A new model of the valve was presented and described, it was demonstrated capable of minimising the vapour generation under the same operating condition with respect to the initial valve design. The modification proposed was implemented in the design of new valves which are already being manufactured and tested in the field, they will be introduced into the market afterwards. The project is the demonstration that numerical tools based on CFD are nowadays ready to effectively support designers and industries in bringing down the cost of the engineering process of new and more efficient products.

Contents

Declaration of Authenticity and Author’s Rights	i
Abstract.....	ii
Contents	iii
List of figures.....	vii
List of tables.....	xviii
Nomenclature.....	xxi
Acronyms	xxiii
1 Introduction.....	1
1.1 Overview.....	1
1.2 Scope of the project	2
1.3 Why CFD?	3
1.4 Dissertation summary	8
2 PD pump use.....	11
2.1 Introduction.....	11
2.2 PD pump Vs Centrifugal pumps	12
2.3 PD pump applications in industry	15
2.3.1 Hydraulics	15
2.3.2 Sea water desalination.....	16
2.3.3 Water jet cutting technology	16
2.4 Hydraulic fracturing.....	17
3 Positive displacement reciprocating pumps.....	19
3.1 Introduction.....	19
3.2 PD pump components	21
3.3 Kinematics	26
3.4 Theory.....	29
3.5 Reciprocating pump efficiency	31
3.6 NPSH	32
3.7 Introduction to CFD modelling of PD pumps.....	34
4 Cavitation Models.....	39
4.1 Introduction.....	39

4.2	Rayleigh-Plesset equation	41
4.3	Singhal et al. Cavitation model	44
4.3.1	Vapour and air in the Singhal et al. cavitation model	48
4.4	Zwart-Gerber-Belamri cavitation model.....	48
4.5	Schnerr and Sauer cavitation model.....	49
5	Comprehensive CFD model.....	52
5.1	Introduction.....	52
5.2	Boundary and initialization conditions	52
5.3	Water compressibility model	55
5.4	Moving mesh	57
5.5	Valve Dynamics UDF.....	59
5.6	CFD model settings.....	61
5.7	Mesh sensitivity test.....	62
5.8	Conclusion	67
6	Cavitation in PD pumps	69
6.1	Introduction.....	69
6.2	Cavitation Regimes	69
6.3	Cavitation Causes.....	70
6.3.1	Cavitation due to expansion	71
6.3.2	Cavitation due to pseudo-adhesion	71
6.3.3	Flow induced cavitation	71
6.4	Cavitation in PD pumps	72
7	CFD Simulation of cavitation in PD pumps	76
7.1	Introduction.....	76
7.2	Test Cases	76
7.3	Results discussion	77
7.3.1	Case 1.....	77
7.3.2	Case 2.....	79
7.3.3	Case 3.....	81
7.3.4	Case 4.....	82
7.4	Conclusion	82
8	CFD Sensitivity test on the non-condensable gas mass fraction.....	85
8.1	Introduction.....	85

8.2	Test cases	85
8.3	Numerical results and discussion	87
8.4	Conclusion	94
9	CFD Sensitivity tests on the parameters acting on cavitation in PD pumps	98
9.1	Introduction.....	98
9.2	Valve/seat design sensitivity test	99
9.2.1	Valve/seat designs description	99
9.2.2	Valve/seat design sensitivity test results	106
9.2.3	Valve-seat angle sensitivity test	110
9.2.4	Valve-seat angle sensitivity test results.....	112
9.3	Shaft angular speed sensitivity test	114
9.4	Spring preload sensitivity test.....	118
9.4.1	Valve spring preload test results	118
9.5	Valve mass sensitivity test	120
9.6	Conclusion	122
10	Optimised valve geometry	125
10.1	Introduction.....	125
10.2	Effect of the urethane ring shape	127
10.3	Optimised valve configuration.....	132
10.4	Optimised valve design results	137
10.5	Conclusion	143
11	Experimental test rig set-up	145
11.1	Introduction.....	145
11.2	Test rig specifications	145
11.3	Test rig layout	146
11.3.1	Single chamber pump.....	148
11.3.2	Linear motor.....	152
11.3.3	Rig frame	160
11.3.4	Inlet pipe	163
11.3.5	Venturi pipe	164
11.3.6	Outlet pipe.....	165
11.3.7	Water vessel	166
11.3.8	High speed camera	168

11.3.9	Data acquisition and driving system	170
11.4	Motor use issues.....	175
12	Experimental tests and CFD model validation.....	178
12.1	Introduction.....	178
12.2	Experimental tests.....	178
12.3	CFD model modification	179
12.4	CFD-Experiments results comparison	181
12.4.1	Test 1: Incipient cavitation.....	181
12.4.2	Test 2: Partial cavitation	183
12.4.3	Test 3: Full Cavitation.....	186
12.5	Conclusion	189
12.6	Experimental tests repeatability	191
12.7	Remarks on CFD-Experiments comparison.....	195
13	Conclusion and future improvements	202
13.1	Brief summary of the project	202
13.2	Conclusion	204
13.3	Future improvements	205
13.4	Legacy.....	206
	Bibliography	209
	Appendix.....	213
	Valve dynamics model UDF.....	213
	Water compressibility model UDF	217
	Technical sheets and Drawings.....	218

List of figures

Figure 1-1: Project tasks, the three parts are strongly related to each other.	9
Figure 2-1: Pump classification according to the specific speed N_s (Karassik et al. 2001) ...	12
Figure 2-2: PD Vs Centrifugal pumps: Head-flow qualitative curve.	13
Figure 2-3: Centrifugal pumps. The mass flow rate is defined by the pipeline pressure resistance curve.....	13
Figure 2-4: Centrifugal Vs PD pumps. Efficiency-head qualitative trend.....	14
Figure 2-5: Centrifugal Vs PD pumps, the qualitative dependence of the flow rate to the liquid kinematic viscosity is shown.	14
Figure 2-6: Centrifugal Vs PD pumps, the qualitative dependence of the efficiency to the liquid kinematic viscosity is shown.	15
Figure 2-7: Axial piston pump schematic (Manring 2003).....	16
Figure 3-1: Perpendicular sections of a single chamber PD reciprocating pump. Component legend.....	20
Figure 3-2: Plunger stroke, Top Dead Centre (TDC) and Bottom Dead Centre (BDC), the displacement volume is swept.....	20
Figure 3-3: Triplex PD reciprocating pump, WEIR SPM Destiny TWS 2500.....	21
Figure 3-4: Inlet valve spring. On the left the initial (preloaded) configuration, on the right the released configuration. Dimensions are in [mm].	22
Figure 3-5: Inlet valve spring retainer.....	22
Figure 3-6: Side closing cap, It also hooks the spring retainer to keep it in the correct position.....	23
Figure 3-7: The top cap closes on the upper part the pump case and also maintains the outlet valve spring initial compression.	23
Figure 3-8: Outlet valve spring. On the left the initial (pre-loaded) configuration, on the right the released configuration. Dimensions are in [mm]	23
Figure 3-9: Plunger section.....	23
Figure 3-10: (On the left) plunger threaded cap. (On the right) seals pack. The cap tightens the seals.....	24
Figure 3-11: (left) Side threaded cylinder. (Right) Top threaded cylinder.	24
Figure 3-12: inlet (and outlet) valve and seat assembly. The step between the valve main body and the urethane ring prevents the metal-metal contact.....	25
Figure 3-13: Spring stress-strain characteristic curve.....	25

Figure 3-14: urethane deformation when the pressure difference across the valves approaches the operating delivery pressure.	26
Figure 3-15: Reciprocating motion, parameters for the WEIR SPM Destiny TWS 2500 pump. Dimensions are expressed in [mm].	26
Figure 3-16: Plunger displacement law, $s(\theta)$	28
Figure 3-17: Plunger velocity law, $v(\theta)$	28
Figure 3-18: Plunger acceleration law, $a(\theta)$	29
Figure 3-19: Volume flow rate throughout the pumping cycle.	30
Figure 3-20: Theoretical mass flow rate @ standard condition ($\rho=998.2 \text{ kg/m}^3$).	30
Figure 3-21: Theoretical inlet mass flow rate Vs crank rotation for a triplex PD pump.	31
Figure 3-22: Mass flow inlet throughout the inlet stroke, comparison of the theoretical curve with the real behaviour simulated via a one phase CFD model without cavitation effects. ..	35
Figure 3-23: Mass flow outlet throughout the outlet stroke, comparison of the theoretical curve with the real behaviour simulated via a one phase CFD model without cavitation effects.	36
Figure 3-24: Numerical Vs Experimental data, comparison of the inlet stroke chamber pressure. Experiments by Wilson (Wilson et al. 2011).	36
Figure 3-25: Detail of the negative pressure spikes occurred in the CFD simulations. Experiments by Wilson (Wilson et al. 2011).	37
Figure 4-1: Qualitative phase diagram for water (Franc & Michel 2004).	39
Figure 4-2: Number of nuclei activated in a measurement rig based on a Venturi (Franc & Michel 2004).	40
Figure 4-3: Bubble radius stability. Water at room temperature and initial pressure was considered as well as a 0.01 mm initial bubbles radius.	43
Figure 5-1: Fluid end of the pump utilised.	52
Figure 5-2: Schematic of the chamber section of a triplex pump including the nomenclature.	53
Figure 5-3: Solid to fluid volumes: the plunger is located in the TDC position and the valves are both closed, just the parts of the inlet and outlet pipes close to the pump were modelled.	54
Figure 5-4: Pressure loss-mass flow characteristics of the inlet and outlet pipes. The values were calculated via independent CFD simulations carried out by fixing the geometry of the pipes at 4 different mass flow rates.	55
Figure 5-5: Plunger displacement Vs crank rotation angle.	55

Figure 5-6: decomposition pattern of the fluid volumes in the vicinity of the inlet valve and plunger essential to handle the moving mesh algorithms. The numbered items are listed in Table 5-2.	57
Figure 5-7: Valve motion UDF: the diagram shows how the UDF interacts with the RANS solver to achieve the self-actuating valve model (Aldo Iannetti, M. Stickland, et al. 2014), the C++ code can be viewed in the appendix.....	60
Figure 5-8: (left) 2.5 M cells mesh, (right) 3.7 M cells mesh.	63
Figure 5-9: Chamber pressure time history.....	64
Figure 5-10: Plunger vicinity 2 nd phase volume fraction	64
Figure 5-11: 2 nd phase valve-seat gap volume mean fraction	65
Figure 5-12: Inlet mass flow.	65
Figure 5-13: Inlet valve lift.	65
Figure 5-14: 2 nd phase chamber volume integral.	66
Figure 5-15: Valve-seat gap volume integral of the 2 nd phase.....	66
Figure 7-1: Chamber Pressure –time history, case 1 to 4. The pressure is monitored at a fixed point near the TDC position of the plunger	78
Figure 7-2: Inlet valve-seat gap volume mean 2 nd phase fraction time history, case 1 to 4... ..	78
Figure 7-3: Plunger surface mean 2 nd phase fraction, case 1 to 4.	79
Figure 7-4: Inlet valve-seat gap volume mean flow velocity, case 1 to 4.....	80
Figure 7-5: Inlet mass flow-time history, case 1 to 4. The theoretical curve is calculated as the positive displacement volume times the density of water at standard conditions.....	80
Figure 7-6: outlet mass flow-time history, case 1 to 4. The theoretical curve is calculated as the positive displacement volume times the density of water at standard conditions.....	80
Figure 7-7: Inlet valve lift-time histories. Case 1 to 4.	81
Figure 7-8: Outlet valve lift-time histories. Case 1 to 4.....	81
Figure 8-1: Pump chamber pressure history. A liquid with lower air mass fraction is affected by a higher pressure drop.	88
Figure 8-2: 2nd phase (water + air) volume fraction in the valve-seat lift volume when the air mass fraction is 15 and 1.5 ppm.....	88
Figure 8-3: Vapour volume fraction in the valve-seat lift volume when the air mass fraction is 15 and 1.5 ppm.	88
Figure 8-4: Air volume fraction in the valve-seat lift volume when the air mass fraction is 15 and 1.5 ppm.....	89
Figure 8-5: 2nd phase (water + air) volume fraction in the vicinity of the plunger when the air mass fraction is 15 and 1.5 ppm.	89

Figure 8-6: Vapour volume fraction in the vicinity of the plunger when the air mass fraction is 15 and 1.5 ppm.	89
Figure 8-7: Air volume fraction in the vicinity of the plunger when the air mass fraction is 15 and 1.5 ppm.	90
Figure 8-8: Chamber volume integral of the 2nd phase (vapour + air), when air mass fraction is 15 ppm (case 1) and 1.5 ppm (case 2).	91
Figure 8-9: Chamber volume integral of the vapour when air mass fraction is 15 ppm (case 1) and 1.5 ppm (case 2).	91
Figure 8-10: Chamber volume integral of the air when air mass fraction is 15 ppm (case 1) and 1.5 ppm (case 2).	91
Figure 8-11: Chamber volume integral of the second phase components Case number 1, air mass fraction 15 ppm.	92
Figure 8-12: Chamber volume integral of the second phase components Case number 2, air mass fraction 1.5 ppm.	92
Figure 8-13: (left) mass flow rate throughout the inlet stroke when the air mass fraction is 15 and 1.5 ppm. (right) valve lift history.	93
Figure 8-14. Case 1 (15 ppm air mass fraction) at 120° of crank rotation . (left) total second phase volume fraction. (middle) air volume fraction. (right) vapour volume fraction.	93
Figure 8-15. Case 2 (1.5 ppm air mass fraction) at 120° of crank rotation . (left) total second phase volume fraction. (middle) air volume fraction. (right) vapour volume fraction.	94
Figure 9-1: Original valve shape: the four legs slide inside the inner bore of the seat to allow a 1-DOF motion.	99
Figure 9-2: Modified geometry number 1: a stem slides in a bore drilled in the spring retainer replaced the legs, the inner diameter of the seat is smaller.	99
Figure 9-3: Modified geometry number 2: as the geometry number 1 a stem drives the valve motion, the inner diameter of the seat was reduced further, the valve/seat angle was reduced to 10°.	100
Figure 9-4: Modified geometry number 3, three additional opening areas were cut in the valve body, an additional body inside the seat was added to seal them.	100
Figure 9-5: Modified geometry number 4: an additional opening area was cut in the stem, an additional body inside the seat was needed to seal it.	101
Figure 9-6: Modified geometry number 5: a little modification on the detail B and the additional seat contact body makes it different from the geometry number 4.	101
Figure 9-7: Fluid volumes in the vicinity of the valve, the cylindrical flow area is shown.	104

Figure 9-8: The pushing area is the area where the integral of pressure forces acts and determines the maximum valve lift.....	104
Figure 9-9: Pressure drop across a flat pushing area valve at different valve-seat angles, one-phase steady-state simulations.	105
Figure 9-10: Valve-seat gap volume maximum velocity for a flat valve at different valve-seat angles, one-phase steady-state simulations. The maximum velocity affects the minimum pressure and thus cavitation.	106
Figure 9-11: Chamber pressure throughout the inlet stroke.....	107
Figure 9-12: Valve-seat gap 2 nd phase (vapour+air) mean vapour fraction.....	107
Figure 9-13: Plunger top surface mean vapour fraction.....	108
Figure 9-14: Inlet Mass flow rate.....	108
Figure 9-15: Inlet Valve lift.	109
Figure 9-16: Total flow area, sum of the main flow area and the additional one where present.....	109
Figure 9-17: Valve-seat gap volume vapour integral.....	109
Figure 9-18: Chamber volume vapour integral.....	110
Figure 9-19: Stem valve, urethane ring step neglected, 10° valve-seat angle.....	111
Figure 9-20: Stem valve, urethane ring step neglected, 20° valve-seat angle.....	111
Figure 9-21: Stem valve, urethane ring step neglected, 30° valve-seat angle.....	111
Figure 9-22: Valve-seat angle sensitivity test, chamber pressure for the 10°,20° and 30°..	112
Figure 9-23: Valve-seat angle sensitivity test, Valve-seat gap volume 2 nd phase fraction for the 10°,20° and 30°.....	112
Figure 9-24: Valve-seat angle sensitivity test, 2 nd phase volume fraction in the vicinity of the plunger for the 10°,20° and 30°.....	113
Figure 9-25: Inlet mass flow for the 10°,20° and 30° configurations.....	113
Figure 9-26: Chamber 2 nd phase integral for the 10°,20° and 30° configurations.....	113
Figure 9-27: Valve-seat gap volume 2 nd phase integral for the 10°,20° and 30° configurations.....	114
Figure 9-28: Mod2 and 5 at 260 rpm of shaft angular speed, chamber pressure during the inlet stroke.....	115
Figure 9-29: Mod2 and 5 geometry at 260 rpm, plunger top surface vapour fraction.....	115
Figure 9-30: Mod2 and 5 geometry at 260 rpm, valve-seat gap volume vapour fraction....	116
Figure 9-31: Mod2 and 5 geometry at 260 rpm, chamber vapour volume integral	116
Figure 9-32: Mod2 and 5 geometry at 260 rpm, mass flow rate compared with theory.....	116
Figure 9-33: Mod2 and 5 geometry at 260 rpm, valve-seat gap volume vapour integral....	117

Figure 9-34: Mod2 and 5 geometry at 260 rpm, valve lift history	117
Figure 9-35: Valve stiffness characteristic and chosen preload for the two cases discussed	118
Figure 9-36: Chamber pressure history, original and lower spring preloads cases n the original valve-seat geometry	119
Figure 9-37: Valve lift-time histories. Case 2 shows a higher maximum lift and as a consequence, a wider flow area.	119
Figure 9-38: Pump chamber vapour integral throughout the inlet stroke, Case 2 showed a significant reduction in vapour generation.....	119
Figure 9-39: Chamber pressure of the original valve and valve seat geometry when halving the valve mass	120
Figure 9-40: Vapour generated in the valve-seat gap volume, case of original valve mass compared to the lighter valve case	121
Figure 9-41: mass flow rate during the inlet stroke, original valve mass and shape compared to the lighter valve mass case and the theory valve	121
Figure 9-42: Valve lift history, original valve mass case and lighter valve case	121
Figure 10-1: Effect of the urethane ring section on the 2 nd phase integral (vapour + air) in the pump chamber throughout the inlet stroke, the configuration without the step in the urethane ring (Mod1) shows lower content.	126
Figure 10-2: (Left) original valve equipped with the urethane ring step, (right) mod 11 without step in the ring and a perfect valve-seat contact. Dimensions are expressed in [mm].	127
Figure 10-3: Fixed valve lift of 2 mm, (left) urethane step configuration can have a wider minimum passage area than the configuration without step (right). In this second case the minimum area is always the inner annulus highlighted in green colour in the figure on the right.....	128
Figure 10-4: No-step urethane ring configuration, how the radial distribution of flow area changes with the valve lift	129
Figure 10-5: Original (left of the axis) Vs No-step configuration valve geometry (right). .	130
Figure 10-6: Radial distribution of flow area when the lift is 2 mm. Original Vs no-step configuration comparison.	130
Figure 10-7: Original valve shape, how the radial distribution of flow area changes with the valve lift.	130
Figure 10-8: Original valve shape, how the radial distribution of flow area changes with the step thickness at fixed (2mm) lift.....	131

Figure 10-9: Original valve shape, how the radial distribution of flow area changes with the urethane ring inner radius at fixed (2mm) lift.....	131
Figure 10-10: How the valve lift history changes with/without the step in the urethane ring.	132
Figure 10-11: Flow velocity in the vicinity of the urethane-steel interface between the ring and the valve main body. A high erosion rate is expected.....	133
Figure 10-12: Original (left) Vs proposed Optimized valve geometry (right).....	134
Figure 10-13: Original, no-step and new proposed valve comparison. Fixes valve lift of 2 mm and fixed urethane inner radius of 51 mm	135
Figure 10-14: Proposed valve geometry, how the radial distribution of flow area varies with the urethane –seat angle at fixed (2mm) lift and fixed urethane inner radius (51 mm).	135
Figure 10-15: Proposed valve geometry, how the radial distribution of flow area varies with the urethane inner radius at fixed (2mm) lift and fixed urethane-seat angle (10°).	136
Figure 10-16: Proposed valve geometry, how the radial distribution of flow area varies with the valve lift at fixed urethane-seat angle (10°) and fixed urethane inner radius (51 mm)..	136
Figure 10-17: Chamber pressure, Original valve Vs new proposed modification with 10° urethane-seat angle.....	137
Figure 10-18: Valve-seat gap volume, original Vs modified valve comparison of vapour volume fraction.	138
Figure 10-19: Valve-seat gap volume, original Vs modified valve comparison of air volume fraction.	138
Figure 10-20: Valve-seat gap volume, original Vs modified valve comparison of 2 nd phase volume fraction (water + vapour)	139
Figure 10-21: Plunger vicinity, original Vs modified valve comparison of vapour volume fraction.	139
Figure 10-22: Plunger vicinity, original Vs modified valve comparison dissolved air volume fraction.	139
Figure 10-23: Plunger vicinity, original Vs modified valve comparison of 2 nd phase volume fraction (water + vapour).	140
Figure 10-24: Original valve Vs new geometry. (a) Inlet mass flow, the theory curve is also included.....	140
Figure 10-25: Original valve Vs new geometry. Inlet valve lift history.	140
Figure 10-26: Original valve Vs new geometry. Flow velocity through the valve-seat gap volume.	141
Figure 10-27: Original valve Vs new geometry. Chamber vapour integral.....	142

Figure 10-28: Original valve Vs new geometry. Chamber air volume integral.....	142
Figure 10-29: Original valve Vs new geometry. Valve-seat gap vapour integral.....	142
Figure 10-30: Original valve Vs new geometry. Valve-seat gap air volume integral.	143
Figure 11-1: Test rig schematic with legend. The pumping system is shown, the pressure sensors on the pump are not shown	146
Figure 11-2: Test rig in the laboratory room where the tests were carried out.	147
Figure 11-3: Von Mises stresses [MPa] of a 10 mm thick polycarbonate window under 20 bar of pressure.....	148
Figure 11-4: Chamber pressure, the maximum value can be estimated as 4 bar (1 barG inlet case).	149
Figure 11-5: Mean pressure in the valve-seat gap volume (0 barG inlet case).....	150
Figure 11-6: (left) Details of the modification carried out on the sealing system compared to the original design (right).....	151
Figure 11-7: Moog high performance linear servomotor.....	153
Figure 11-8: linear motor performance of maximum axial force Vs piston velocity	153
Figure 11-9: Inlet stroke, total axial force needed Vs axial force available. Test cases 0, 0.25, 0.5, 1 barG inlet pressure.	154
Figure 11-10: Outlet stroke, total axial force needed Vs axial force available. Test cases 0, 0.25, 0.5, 1 barG inlet pressure.	154
Figure 11-11: Total axial force needed throughout the pumping cycle.	155
Figure 11-12: MOOG linear motor Servo Drive MSD G392-045-020-001	156
Figure 11-13: Moog Drive Administrator: Linear motor parameters	157
Figure 11-14: Moog drive Administrator: Encoder parameters.....	157
Figure 11-15: Moog Drive Administrator: Limits	158
Figure 11-16: Automatic control: Setpoint table	158
Figure 11-17: Moog drive Administrator: Manual mode	159
Figure 11-18: Example of shaft displacement compared to the crankshaft motion @ 130rpm. There is a combination of parameters which makes the two functions matching closely. ..	160
Figure 11-19: Contour plot of the Von Mises Stress on the frame, Outlet stroke (left), Inlet stroke (right).....	162
Figure 11-20: Contour plot of the maximum displacements, Outlet stroke (left), Inlet stroke (right).	162
Figure 11-21: Inlet line pressure loss calculated by means of four steady state CFD simulations.	164

Figure 11-22: Venturi pipe ΔP Vs mass flow rate calculated by means of the Bernoulli's equation.....	164
Figure 11-23: Outlet line pressure loss calculated by means of four steady state CFD simulations.....	166
Figure 11-24: Plunger power throughout the pumping cycle estimated by the CFD analysis discussed in chapter 7.	167
Figure 11-25: High speed camera placed 1 m from the side inspection window	168
Figure 11-26: view of the inspection window	168
Figure 11-27: NI9205 Analog input module.....	171
Figure 11-28: NI9401 Digital input module	171
Figure 11-29: NI-CRIO-9076 integrated controller and Chassis System	171
Figure 11-30: Calibration line of the Venturi Upstream and Valve-seat sensors. The coefficients of linearity are provided.	172
Figure 11-31: Calibration line of the Venturi Downstream, pump chamber and outlet sensors. The coefficients of linearity are provided.....	173
Figure 11-32: Calibration line of the tank pressure sensors. The coefficients of linearity are provided.	173
Figure 11-33: LabView front panel of the calibration programme, the time histories and the mean value of the voltage were acquired to create the calibration line.	173
Figure 11-34: LabView acquisition main programme: how the calibration coefficients were utilised to transform the voltage signal to pressure.....	174
Figure 11-35: Labview acquisition main programme. How the signals are manipulated, visualised and stored.....	174
Figure 11-36: Motor shaft-Plunger coupling, detail of the items utilised.....	175
Figure 12-1: Plunger displacements and velocities created by means of the motor drive administrator (Aldo Iannetti et al. 2015).....	178
Figure 12-2: Pump chamber static pressure. Experiments Vs CFD (test 1).	181
Figure 12-3: Valve-seat static pressure. Experiments Vs CFD (test 1).	181
Figure 12-4: Second phase fraction composition according to CFD (test1).....	182
Figure 12-5: Valve lift, Experiment Vs CFD (test1).....	182
Figure 12-6: Null/incipient cavitation, only three frames show second phase presence which never obscures the view of the valve.	183
Figure 12-7: Pump chamber static pressure (Log scale). Experiments Vs CFD (test 2).	183
Figure 12-8: Valve-seat static pressure (Log scale). Experiments Vs CFD (test 2).	184

Figure 12-9: Test 2, Chamber pressure Vs valve velocity, the pressure peaks occur in the same time of the valve minimum velocity.	184
Figure 12-10: Second phase fraction composition according to CFD (test 2).	185
Figure 12-11: Valve lift, experiment Vs CFD (test2)	185
Figure 12-12: Partial cavitation. Four frames show a vapour cloud around the valve-lift gap, in two of them the view of the valve was obscured almost completely.	185
Figure 12-13: Pump chamber static pressure (Log scale). Experiments Vs CFD (test 3), the sensitivity to the air mass fraction is shown.	186
Figure 12-14: Valve-seat static pressure (Log scale). Experiments Vs CFD (test 3). The sensitivity to the air mass fraction is shown.	186
Figure 12-15: Vapour volume fraction in the valve-seat lift volume according to CFD (test 3).	187
Figure 12-16: Air volume fraction in the valve-seat lift volume according to CFD (test 3)	187
Figure 12-17: Test 3 valve lift, experiment Vs CFD, the sensitivity of the CFD solution to the air mass fraction is also shown.	188
Figure 12-18: Full cavitation, five frames show a vapour cloud around the valve-lift gap, in four of them the view of the valve is completely obscured.	189
Figure 12-19: Test 3, FFT of the chamber pressure signals, CFD VS Experiment.	189
Figure 12-20: Repeatability analysis on Test 1: lower plunger velocity. The Chamber pressure comparison is shown.	191
Figure 12-21: Repeatability analysis on Test 1: lower plunger velocity. The valve-seat pressure comparison is shown.	192
Figure 12-22: Repeatability analysis on Test 2: middle plunger velocity. The Chamber pressure comparison is shown.	192
Figure 12-23: Repeatability analysis on Test 2: middle plunger velocity. The valve-seat pressure comparison is shown.	193
Figure 12-24: Repeatability analysis on Test 3: high plunger velocity. The Chamber pressure (Log scale) comparison is shown.	193
Figure 12-25: Repeatability analysis on Test 3: high plunger velocity. The valve-seat pressure comparison is shown.	194
Figure 12-26: Test 1 mass flow rate, experiment Vs CFD, the Venturi pipe absolute pressure sensors output a not reliable signals.	195
Figure 12-27: Test 2 mass flow rate, experiment Vs CFD, the Venturi pipe absolute pressure sensors output a not reliable signals.	196

Figure 12-28: Test 3 mass flow rate, experiment Vs CFDs, the Venturi pipe absolute pressure sensors output a not reliable signals.	196
Figure 12-29: Crankshaft @130rpm Vs Linear motor (test 3), comparison of the displacement-time histories.	197
Figure 12-30: Test 1 mass flow rate, experiment Vs CFD, the Venturi pipe differential pressure sensor outputs not reliable signals.	198
Figure 12-31: Test 2 mass flow rate, experiment Vs CFD, the Venturi pipe differential pressure sensor outputs not reliable signals	198
Figure 12-32: mass flow rate, experiment Vs CFD, the Venturi pipe differential pressure sensor outputs not reliable signals	199
Figure 12-33: Test 3, full cavitation. The water vessel pressure sensor reading close to the inlet pipe is shown.	200

List of tables

Table 3-1: Valuation of k and C coefficients to estimate the acceleration head (Tackett et al. 2008).....	33
Table 5-1: Mesh sensitivity test, three mesh sizes were tested.....	59
Table 5-2: Mesh 2 details summary.....	59
Table 5-3: Solver Settings summary.....	61
Table 5-4: Quantitative comparison of the performance of the grids tested.....	66
Table 6-1: Full/developed cavitation cases, causes types and locations.....	73
Table 7-1: Test cases boundary conditions summary, ΔP trends were shown by figure 5.3.....	77
Table 7-2: Summary of the quantitative results, the volumetric efficiency related to the inlet valve closing time.....	78
Table 8-1: Solver settings summary.....	86
Table 8-2: Inlet pressure boundary and initial conditions for both cases under investigation.....	86
Table 8-3: Pump performance estimation summary, comparison of the two fluid properties 15 ppm vs 1.5 ppm air mass fraction.....	93
Table 9-1: Summary of the advantages and disadvantages of the design configuration from Original to Mod5.....	102
Table 9-2: Summary and comparison of the six configurations.....	110
Table 9-3: Summary and comparison of the three valve-seat angle configurations.....	114
Table 9-4: Mod2 and 5 at 260 rpm, volumetric efficiencies and their relation with vapour generation and valve delays.....	117
Table 9-5: Summary of the spring preload sensitivity test. Case 2 shows a lower valve opening and closing delay and higher efficiency.....	120
Table 10-1: Summary of the parameters defining the flow area distribution of Figure 10-6.....	129
Table 10-2: Original-New generation valve geometry detail comparison.....	134
Table 10-3: Summary and integration of Figure 10-14, Figure 10-15 and Figure 10-16. How the minimum flow area changes with respect to the valve lift and urethane-seat angle with fixed urethane inner radius of 51 mm. The table shows the extension of the area and the location: inner= close to the urethane/steel interface, outer= urethane exit edge.....	137
Table 10-4: Summary and integration of Figure 10-14, Figure 10-15 and Figure 10-16. How the minimum flow area changes with respect to the valve lift and urethane-seat angle with	

fixed urethane inner radius of 45 mm. The table shows the extension of the area and the location: inner= close to the urethane/steel interface, outer= urethane exit edge.	137
Table 10-5: Original valve Vs new geometry. Summary of the performance data.	141
Table 11-1: Technical specifications of the pump chamber pressure transmitter GEM 220SAB1001F3EA.	149
Table 11-2: Modal analysis results, the first structural frequency is significantly lower than the external force frequency.....	161
Table 11-3: Safety factor against yield.	162
Table 11-4: Venturi tube pressure sensors, characteristics summary. GEMS 2200SAA2501F3EA (upstream and downstream) and a Model z Wet/Wet RDP differential pressure transducer (Venturi differential).....	165
Table 11-5: Tank pressure sensor (Gefran TSAN1FBV25GTV) characteristics summary.	167
Table 12-1: Solver settings summary.....	179
Table 12-2: Volumetric efficiency estimation: CFD Vs Experiments.....	197
Table 12-3: The volumetric efficiency calculated by means of the differential pressure sensor gives different results every time the test is performed.	199

Nomenclature

B	<i>Compressibility modulus of liquid</i>
F_P	<i>Pressure force integral acting on the valve</i>
F_S	<i>Spring force acting on the valve</i>
F_{TOT}	<i>Total force acting on the valve</i>
g	<i>Acceleration due to gravity</i>
$[i]$	<i>Actual time step</i>
$[i - 1]$	<i>Previous time step</i>
k	<i>Turbulent kinetic energy</i>
$k(x)$	<i>Stiffness function of displacement (in x axis)</i>
m	<i>Valve mass</i>
P	<i>Flow RANS mean pressure</i>
p_{REF}	<i>Reference pressure (e.g. pressure at room condition)</i>
t	<i>Time</i>
$U_{i,j,k}$	<i>Flow RANS mean velocity respectively in x, y and z directions</i>
$x_{i,j,k}$	<i>x, y and z coordinates</i>
\ddot{x}	<i>Valve acceleration in x direction</i>
y^+	<i>Wall function unit</i>
δ_{ij}	<i>Kronecker symbol</i>
ε	<i>Turbulence dissipation rate</i>
μ	<i>Viscosity</i>
μ_T	<i>Turbulent viscosity</i>
ρ	<i>Density of the mixture (water and vapour)</i>
ρ_{REF}	<i>Reference density (e.g. density at room condition)</i>
τ_{ij}	<i>Reynolds stress tensor</i>
$\begin{cases} C_\mu = 0.09 \\ C_{S1} = 1.44 \\ C_{S2} = 1.92 \\ \sigma_k = 1.0 \\ \sigma_\varepsilon = 1.3 \end{cases}$	<i>Closure coefficients for the standard k-epsilon turbulence model</i>
α_v	<i>Vapour volume fraction</i>
α_g	<i>Gas volume fraction</i>
α_{nuc}	<i>Vapour volume fraction in the nucleation site</i>
γ	<i>Specific heats ratio</i>
μ	<i>Dynamic viscosity of the liquid phase</i>

ρ_l	<i>Density of the liquid phase</i>
ρ_v	<i>Density of the vapour phase</i>
σ	<i>Surface tension force</i>
C_e	<i>Evaporation constant of the Singhal et al. cavitation model</i>
C_c	<i>Condensation constant of the Singhal et al. cavitation model</i>
$\frac{D}{Dt}$	<i>Lagrangian derivative</i>
f_v	<i>Vapour mass fraction</i>
f_g	<i>Gas mass fraction</i>
F_{vap}	<i>Evaporation constant of the Zwart-Geber-Belamri cavitation model</i>
F_{cond}	<i>Condensation constant of the Zwart-Geber-Belamri cavitation model</i>
k	<i>Turbulent kinetic energy</i>
n	<i>Number of nuclei per volume unit</i>
p_{sat}	<i>Saturation pressure according to the phase diagram</i>
P	<i>Pressure in the bubble vicinity</i>
P_∞	<i>Pressure at bubble infinity distance</i>
P_C	<i>Bubble external critic pressure</i>
P_B	<i>Bubble internal pressure</i>
P_v	<i>Corrected saturation pressure</i>
p_g	<i>Bubble interior partial gas pressure</i>
p_{g0}	<i>Initial bubble interior partial gas pressure</i>
r	<i>Radial distance from the bubble centre</i>
R	<i>Interphase change rate generic</i>
R	<i>Ideal gas constant (equation 4.25 only)</i>
R_c	<i>Interphase change rate, vapour to liquid</i>
R_e	<i>Interphase change rate, liquid to vapour</i>
\mathfrak{R}_B	<i>Bubble radius</i>
\mathfrak{R}_{BC}	<i>Critic bubble radius</i>
\mathfrak{R}_{B0}	<i>Initial bubble radius</i>
t	<i>Time</i>
v	<i>Flow velocity</i>
v_{rel}	<i>Relative velocity (bubble-liquid)</i>
W	<i>Gas molecular weight</i>
We	<i>Weber number</i>

Acronyms

<i>API</i>	<i>American Petroleum Institute (American standards)</i>
<i>BDC</i>	<i>Bottom Dead Centre</i>
<i>CFD</i>	<i>Computational Fluid Dynamics</i>
<i>DIN</i>	<i>Deutsches Institut fur Normung (European standards)</i>
<i>DOF</i>	<i>Degrees Of Freedom</i>
<i>FEM</i>	<i>Finite Elements Method</i>
<i>FFT</i>	<i>Fast Fourier Transform</i>
<i>HPC</i>	<i>High Performance Computing</i>
<i>LAN</i>	<i>Local Area Network</i>
<i>NPSH</i>	<i>Net Positive Suction Head</i>
<i>PD</i>	<i>Positive Displacement</i>
<i>RANS</i>	<i>Reynolds Averaged Navier Stokes equations</i>
<i>SPM</i>	<i>Strokes Per Minute</i>
<i>TDC</i>	<i>Top Dead Centre</i>
<i>UDF</i>	<i>User Defined Function</i>

1 Introduction

1.1 Overview

The project being discussed in this thesis work deals with the numerical analysis of Positive Displacement (PD) reciprocating plunger pumps. The author leaves the full and detailed description of the device to the following chapters, it is important first to provide the reader with a general overview on the applications and the technology the device is utilised for, the background and the scope of the project. The pump introduced in the following chapter is widely utilised in the hydraulic fracturing (or fracking) industry. This technology is very new and has become, in recent years, widely utilised to exploit shale rock oil and gas reservoirs from which the extraction of oil and gas was not economical until a few years ago. Although the fracking technique is beyond the scope of this thesis, a brief description on this technology will be provided chapter 2.

Because of the operating condition to which they are subjected, fracturing pumps are affected by a significant amount of problems which usually act at the same time. Slurries, which are pumped together with water and chemicals, generate erosion which combines with corrosion, together with the high pressure forces they generates fatigue cracks in the pump because of which pump failures are not rare. Cavitation is a problem that overlaps all the mentioned issues and worsen the situation because it enhances the crack generation and propagation before failures occur. In particular, the cavitation phenomenon occurs when the pump acts in operating conditions where the local pressure in the pumped fluid falls below the saturation pressure for the local temperature. When this happens the liquid flashes to vapour as localised boiling occurs. This creates a large number of vapour bubbles within the flow field which are carried downstream with the flow. If the bubbles pass into an area where the pressure within the flow field increases above the fluid saturation pressure the bubbles will collapse as the vapour turns back into the liquid phase. When the bubbles collapse they create a very high localised pressure. If this happens in the middle of the flow field then the only effect that may be observed is a fizzing or hissing sound. However, if the bubble collapse occurs next to the device walls, surface damage in the form of localised pitting will result. This pitting will not only cause localised material erosion but, the stress concentrations created, may lead to the development and enhancement of corrosion and fatigue cracks as stated earlier.

The project will be focused on the study of cavitation only and will leave erosion, corrosion and fatigue out of the dissertation.

1.2 Scope of the project

The project aims at studying the phenomenon of cavitation in PD pumps mainly by means of numerical analysis based on Reynolds Averaged Navier Stokes (RANS) numerical solvers which belong to the widely known Computational Fluid Dynamics (CFD) solvers. The results achieved will be utilised in the optimization of the design of the device in order to mitigate the amount of damage due to cavitation. In more detail, the numerical part of the project will be composed of the following steps:

- 1) Creation and improvement of a comprehensive numerical model capable of simulating the real behaviour of the device during the pumping cycle at the operating conditions which lead to cavitation. The improvement of the model will be carried out by means of a step by step overlapping of sub-models of increasing complexity each of which will take care of a particular physical aspect of the fluid dynamics of pumping.
- 2) Step 1) could not be performed properly without an investigation of the numerical algorithms present in the literature capable of simulating cavitation in PD pumps. A study of the mathematical core, hypothesis and limits of these algorithms will be carried out as well.
- 3) Step 2) needs a detailed study supported by a literature review of the phenomenon of cavitation in PD pumps. In this kind of device, in fact, cavitation appears to have different causes with respect to other devices such as centrifugal pumps on which a great amount of data is present in literature.
- 4) The CFD model obtained will be utilised to test new designs of valves different from the original in order to come up with an optimised device capable of mitigating the phenomenon of cavitation and thus the damage.

A further and very important part of the project, ran parallel to the previous list, was the design and manufacture of a test rig to estimate the accuracy of the CFD model validating the work done from the numerical counterpart. The experimental work was not the main part of the project but the importance of it for data validation required a significant amount of money and time investment.

The author needs to point out that no numerical based analysis tools to test a PD pump in cavitating conditions have been developed so far and discussed in the free technical literature. This demonstrates the great contribution that this project provides to the scientific knowledge. It is important to highlight that the developed numerical model of PD pumps should be considered a numerical methodology with a wide field of applicability rather than

a process designed for the particular pump model that will be discussed in the following chapters. Indeed, the high potential of the methodology does not expire with the optimization of the device under investigation but is applicable to any kind of PD pump and any time an analyst is interested in investigating the performance variation of a PD pump under any operating condition. The reason for a numerical approach will be clear later on in this chapter but the author may anticipate the significant money saving that numerical techniques are capable of bringing especially when it is applied from the very first part of the engineering process resulting in a more competitive product available on the market.

1.3 Why CFD?

In the past, many tools have been designed to analyse PD pump behaviour. They range from experimental rigs to analytical 1-D procedures in which all parts making up the set of the components involved in the moving of the fluid (inlet manifold, inlet and outlet valves, cross bore, plunger, outlet pipe), sometimes referred to as the fluid end, are treated either as distributed parameters or 1D finite elements. Analytical models usually do not account for the real shape of the pump as they treat the geometry of the part they are dealing with (e. g. inlet pipe, valve or cross bore etc.) as a parameter summarizing the overall dimensions (e.g. length, diameter etc..). Also, a large amount of them account for mutual interaction among the parts by means of the iterative coupling of their analytical models.

Johnston (Johnston 1991) developed a mathematical model to simulate the pumping dynamics of positive displacement reciprocating pumps based on a lumped parameter and one-dimensional technique. The model was composed “of a number of inter-linked mathematical models representing the pump components”. Although Johnston’s work was based on a simplified approach his analysis was equipped with sub-models accounting for the cavitation occurring both through the valve and in the plunger vicinity. According to the experimental validation he carried out, Johnston achieved good accuracy but he also pointed out the limitation of the assumption made of constant inlet pressure. In the model, in fact, the inlet pipe was absent and therefore it did not account for the interaction between the pump and the pipeline which in many application results the further cause of cavitation. In this case the “complexity of the interaction between cavitation, air release and wave propagation..” makes the lumped parameter model not suitable for a complete simulation.

Edge and Shu (Shu et al. 1997; Edge et al. 1997) presented a distributed parameter model of pipeline transmission and an analytic model of the pump showing a time-domain simulation of pipeline pressure pulsation in pumping dynamics. Edge and Shu’s work improved what was earlier carried out by Johnston as the importance of the interaction between the pump

and the pipeline was demonstrated. Their model was based on a Galerkin finite element method which makes use of a uniformly spaced grid (1D) system with two degrees of freedom (flow rate and pressure). The results presented demonstrated the good accuracy of the model in terms of pumping dynamics mainly due to the real complexity of it which accounted for the pipeline-pump interaction and fluid inertia. On the other hand, it is to be pointed out again that the main limitation of a 1D approach lies in the treatment of each part of the pump as a distributed parameter; therefore, these methods cannot be applied in cases when topological optimization procedures need to be carried out.

Where geometry optimization is required, experimental tests appear to be the sole choice. Price et al., (Price et al. 1995), have been involved in valve shape optimization work that was carried out by means of experimental tests. Their work relied on the assumption that under-pressure and over-pressure spikes strongly depend on pumping dynamics that, in turn, are affected by valve shape and mass. Therefore an accurate model accounting for valve dynamics and geometry was essential and the method that the authors found appropriate was experimental. According to them, pressure spikes are the result of several combined effects including:

- Plunger side/line side dynamic pressures
- Differential area (unbalanced valve area)
- Acceleration of valve disc (due to change in running speed)
- Spring preload and stiffness
- Valve mass

Experimental tests revealed an important effect which influences valve dynamics: sticktion. It is also known as the pseudo-adhesion effect (Opitz et al. 2011) and will be discussed in chapter 6 which is dedicated to the discussion of cavitation causes in PD pumps. Sticktion is mainly due to valve and seat geometry, flow properties, fluid properties and the valve lift velocity. Price's experimental tests dealt with a series of different designs of valve and valve seat aiming at minimizing Bernoulli's effect and the consequent "valve lag" which is considered a cause of cavitation. Thus, the complexity of the valve and seat design tested implied that an analytical 1D approach would have been insensitive to geometric features.

The increasing computational resources that researchers and engineers can rely on have made advanced CFD techniques affordable. Furthermore, High Performance Computing (HPC) systems give to the analyst sufficient computational resources to analyse complete CFD models of the pumps. Nowadays, techniques such as dynamic meshes and customized

CFD solvers via User Defined Functions (UDF) are commonly used (ANSYS 2011b; ANSYS 2011c). The potential of CFD techniques have developed in recent years becoming capable of creating models as detailed as experimental tests and, sometimes, analysts can even replace experimental tests by CFD models.

Ragoth (Ragoth & Nataraj 2012), carried out a study on the performance of a plunger pump by means of CFD. Their model accounted for the geometry of the pump chamber and the initial part of the inlet and outlet pipes, the valve design was absent in the fluid volumes as their effect on the flow was modelled via a UDF. Their model did not take into account the compressibility of the working fluid.

The work being presented tried to overcome the fore mentioned limitations of both the analytic methodologies and the CFD studies mentioned so far. It succeeded in setting up a CFD model more comprehensive, i.e. more accurate, than the ones presented in the technical literature. It aimed at achieving the accuracy of experimental tests in order to provide engineers with a cheaper tool in the design of PD pumps capable of bringing to their attention more and reliable information than that available from experimental tests.

This dissertation will present a detailed transient CFD model of a PD pump accounting for:

1. The 180° crank rotation of the inlet stroke (half pumping cycle)
2. The complete model of the middle chamber of the pump, composed of: the inlet pipe, the inlet valve and seat, the chamber and the plunger, all parts modelled by means of the executive CAD model, accurate in all their geometric features.
3. A self-actuated inlet valve lift model governing the valve movement and its mutual interaction with the pressure field.
4. The compressibility of the working fluid
5. Cavitation by means of an appropriate model

The action of slurries, which are usually pumped by this device, was not considered.

An important method chosen to evaluate the interaction occurring in the fluid end and focusing on the fluid dynamics of pumping will be presented. As demonstrated by Edge (Edge et al. 1997) and Shu (Shu et al. 1997) as well as Price (Price et al. 1995), the pressure field in the pump chamber affects the dynamics of the valve and the latter has an effect on the former that is non-negligible in most cases. Therefore a two-way coupling between the pressure fields and the valve dynamics is crucial to achieve good accuracy. Edge and Shu succeeded in linking the dynamic model of the valve with a 1D model of the system pipeline-pump while the method exposed in this thesis linked the dynamic model of the

valve to a 3D transient CFD model of the pump which relied on good accuracy in terms of geometric details. The correlation between the two models was managed via a User Defined Function (UDF).

The resulting technique does not have the limitations of the analytic models and provided more detailed post-processing results which showed low pressure zones where cavitation takes place. On the other hand, the method may be used as an initial stage of a topological optimization procedure which results difficult to be performed by means of a distributed parameter method.

There are more technical reasons why analysts should also make use of the numerical approach. In recent years in fact, PD pumps issues such as erosion and cavitation are becoming a debated topic in technical literature and new methodologies of analysis will be soon needed. The reason for it is the lack of studies on the topic which depends on the following reasons:

- Over the last decades PD pumps have become gradually obsolete with respect to centrifugal pumps on which great effort has been spent by researchers both in experimental and numerical analysis. This was recalled by Tackett (Tackett et al. 2008) who identifies the cause of the great popularity of centrifugal pumps due to the technological improvement made in the last decades on them. He also pointed out that, as a consequence, PD pumps nowadays may be considered a technically “old” device.
- Despite their appearance PD pumps are a complex device to model and study particularly by means of CFD. This has led the few researchers involved in PD pumps studies to prefer experimental tests over numerical methods.

The experimental methods, which are the only techniques utilized so far because of their high level of accuracy, usually provide the analysts with all the difficulties related on how to take from test rigs crucial information such as the pressure field, the production rate of water vapour and the loss of volumetric efficiency.

For instance the role of the non-condensable gasses in cavitation should not be underestimated as pointed out by Baur (Baur et al. 1998) who carried out an experimental test to demonstrate the interaction of the gas dissolved in water on the bubble dynamics. Experimental tests are not suitable to output data on the interaction between vapour and gas (usually air) as they cannot distinguish between them.

Many authors such as K. Opitz (Opitz & Schlücker 2010) agree on the partitioning of the cavitation types into incipient (also referred to as marginal cavitation), partial and full

cavitation. They are characterized by different features as described in (Opitz & Schlücker 2010) and it is of crucial importance, for the designer, to know which cavitating condition the pump being designed will operate in. In the case of incipient or marginal cavitation, for instance, it is understood (Opitz et al. 2011) that the bubbles number and their distribution do not seem harmful for the pump, avoiding any operative condition in that range would result in a uneconomical device. In the case of partial to full cavitation the damage as well as the loss in performance may be extremely high and allowing the pump to operate at that condition would result in failures and loss of money.

Furthermore the cavitation phenomenon in PD pumps appears to be different from the one occurring in centrifugal pumps. In the latter case cavitation is related to the low pressure induced by the high velocity which affects the rotor at certain operating condition (flow induced cavitation) while, in the case of PD pumps, cavitation may depend on the low static pressure due to the plunger decompression at the beginning of the inlet stroke as well as on the high velocity that the flow through the inlet valve may experience. This was discussed by Opitz (Opitz et al. 2011). The outcomes from researches focused on cavitation in centrifugal pumps are therefore not always applicable to PD pump as well.

Tackett (Tackett et al. 2008) also explains that there are still many applications where PD pumps outperform centrifugal pumps; hydraulic fracturing is one of them, and this is the reason why in the next few years a re-evaluation of this “old” device is to be expected.

The main topic discussed in this thesis focuses on how to correctly estimate the Net Positive Suction Head required (NPSH_r) of the device. The reason for the persistence on the NPSH_r is mainly due to the achievement of the requirement specified in the API 610, API 674 and DIN EN ISO 13710 standards where, both in Positive Displacement (PD) pumps and in centrifugal pumps, a certain safety margin to cavitation is fixed. Since pump manufacturers are required to specify the NPSH_r, researchers are called to develop tools and procedures to study cavitation in pumps and to estimate accurately the NPSH_r. In the case of centrifugal pumps, for instance, many authors such as Ding (Ding et al. 2012), developed a CFD based tool to estimate the NPSH-Head curve to find the operating conditions where the drop of 3% in head occurs as specified by the API. Ding also stated that the definition of the NPSH_r is affected by the content of air in water. Budris (Budris & Mayleben 1998) carried out research oriented to understand the effect of the air content in water in the estimation of the performance of centrifugal pumps. Budris found that a little amount of air reduces significantly the suction pressure pulsation whilst increasing the amount of air above a certain threshold produces no further improvement on the pressure fluctuations results while an increment of the NPSH_r occurs.

The case of PD reciprocating pumps appears to be different. The API 674 still defines the NPSHr as the NPSH where a decrement of 3% in volumetric efficiency occurs but many authors do not agree in considering the NPSHr in PD pumps a precise engineering requirement. Miller (Miller 1995) for instance stated that any suction pressure above the NPSHr would only improve the performance in two ways i.e. increasing the volumetric efficiency and minimizing the effect of the air entrained or dissolved. Other authors such as Opitz (Opitz & Schlücker 2010) presented an experimental study on cavitation in PD pumps indicating that the phenomenon up to a certain limit is harmless and the strict requirement of the API 674 is perhaps not really necessary. The same author (Opitz et al. 2011) discussed the phenomenon of expansion generated cavitation relating it to the incipient cavitation occurring at the initial stage of the inlet stroke when the plunger of the pump moves backward and the inlet valve is still closed and pushed against its seat by the preloaded spring. This phenomenon will be investigated in more details in the dedicated section. The author strongly believes that CFD analysis can contribute significantly in shedding light on the debate.

1.4 Dissertation summary

This dissertation explains and discusses how the related PhD project was carried out over three years of duration. The project was composed of three parts (Figure 1-1):

1. Creation and development of a CFD tool to simulate the real behaviour of PD pumps in cavitating conditions.
2. Validation of the CFD model obtained by means of experimental validation.
3. Use of the CFD model to find a valve design capable of mitigating cavitation.

The three parts were strongly related to each other as highlighted by Figure 1-1. The valve optimization process was actually carried out at the same time the test rig was built because of time issues whereas the CFD study was carried out from the beginning and went on also as background activity during the experimental rig design and the tests.

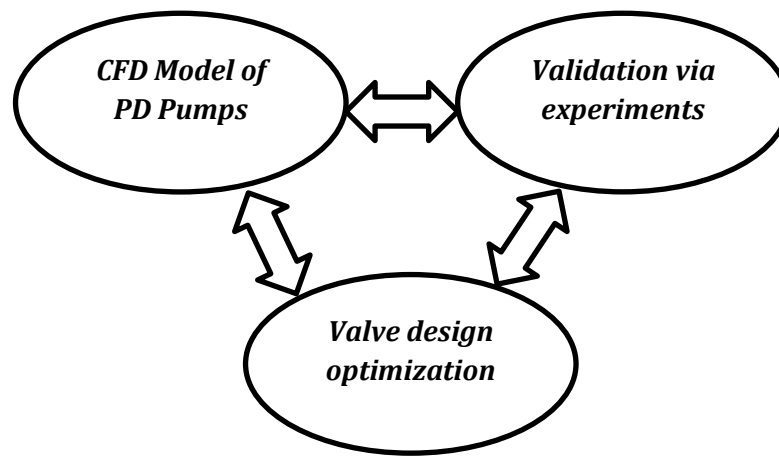


Figure 1-1: Project tasks, the three parts are strongly related to each other.

After the introduction and an overview on PD pumps and their capability discussed in chapter 2, chapter 3 describes in detail the specific device which was utilised for the whole analysis both numerical and experimental. Chapter 3 also describes the theory which was utilised for the design of PD reciprocating pumps. The discussion on the theory and the numerical modelling of cavitation is developed in chapter 4 while chapter 5, 6, 7 and 8 are dedicated to the discussion of the numerical model developed and the results obtained, chapter 7, 8 and 9, describe all the sensitivity analysis and the results which were carried out, they made use of the CFD model developed and tested it to study the sensitivity on:

- a) *Different inlet boundary conditions*
- b) *Different crank rotational velocities*
- c) *Different valve spring preload*
- d) *Different liquid properties*
- e) *Different valve and valve seat designs*

Chapter 10 is dedicated to the discussion of the new valve design which was found capable of mitigating the cavitation. The same chapter also describes how the optimised shape was found. The dissertation then moves to the experimental part. Chapter 11 is dedicated to the description of the test rig setup and layout. Chapter 12 describes the experimental tests which were carried out; the problems encountered are listed and pointed out either in both 11 and in chapter 12. The last chapter draws conclusions and illustrates the improvements that the author suggests for possible future development of the project.

2 PD pump use

2.1 Introduction

The term pump defines a device that raises, transfers or delivers liquids which sometimes can be mixed with slurries. They are operated mainly by two kinds of mechanisms which transfer the energy from a power source (e.g. an engine or a motor) to the device itself: they are the reciprocating mechanism and the rotary mechanism. Many kinds of pumps have been designed and built over the centuries for different applications.

This paragraph will provide a brief overview of the main type of pumps which are currently utilized for modern industrial applications, they are the positive displacement pumps and the velocity pumps. They can be defined and further classified as follows:

1) *Positive displacement pumps*. In this kind of device a constant volume (displacement volume) of fluid is forced to move from the inlet pipe to the outlet pipe. PD pumps in industry can further be divided into:

a. *Rotary PD pumps*. Gear pumps, lobe pumps, screw pumps and all kinds of vane pumps belong to this category. They are all characterized by the presence of mechanical components which create the displacement volume by means of a rotational motion.

b. *Reciprocating PD pumps*. A crankshaft and connecting rod system create an oscillating motion to which a piston, a plunger or a diaphragm are subjected so that the displacement volume can be created.

2) *Velocity pumps*. In these devices kinetic energy is added to the flow by a moving component, this energy is converted into pressure energy by a static component.

These pumps can be divided into the following sub-categories:

a. *Radial flow pumps*. The fluid enters into a centrifugal impeller along the axial direction, kinetic energy is added to the flow by the impeller, the liquid then exits from the impeller radially and is conveyed into the volute where it is decelerated, this converts the kinetic energy into pressure.

b. *Axial flow pumps*. In this device flow is accelerated by means of an axial fan (propeller) which is located in between the inlet and the outlet pipe.

c. *Mixed flow pumps*. Their behavior can be considered halfway between the axial and radial flow pumps. In this device flow enters the impeller axially but the inclination of the blades provides both radial and axial components at the impeller exit, stator blades are usually utilized to convert the radial component of velocity into pressure.

There are two main parameters which are taken into account in order for the end user to choose the kind of pump which is suitable for the application being designed:

- 1) The mass flow to be processed
- 2) The delivery pressure to be achieved

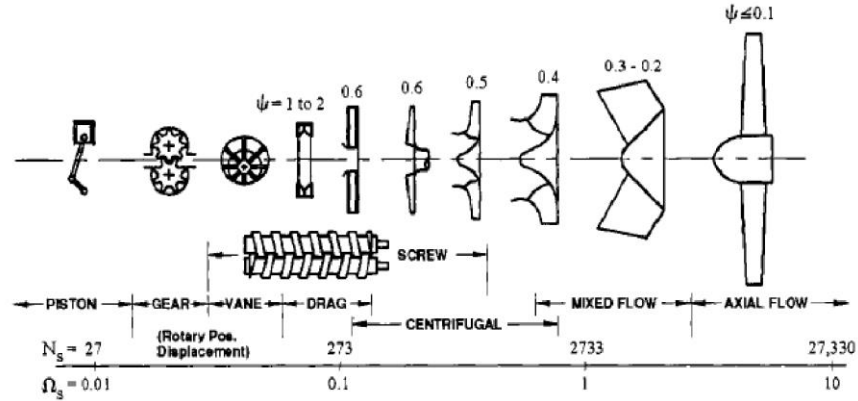


Figure 2-1: Pump classification according to the specific speed N_s (Karassik et al. 2001)

Karassik (Karassik et al. 2001) defined a criterion for choosing the kind of pump according to the pump specific speed required for the application N_s . This parameter is defined as:

$$N_s = \frac{N\sqrt{Q}}{\Delta H^{\frac{3}{4}}} \quad 2.1$$

In equation 2.1 N is the rotational speed defined in [rpm], Q is the mass flow rate defined in [gpm] and ΔH is the head defined in [ft]. The pump specific speed is a parameter that relates the mass flow rate with the pressure head, the higher the mass flow with respect to the pressure head the higher the pump specific speed. Figure 2-1 shows the pump types along the N_s axis. On the opposite ends of the axis one can find the piston (or plunger) pumps and the axial flow pumps. This means that the piston/plunger PD pumps are suitable for applications where the mass flow rate is relatively low with respect to the pressure head. Conversely the axial pumps are suitable to process high mass flows with a low head.

2.2 PD pump Vs Centrifugal pumps

The most important feature which distinguishes PD pumps with respect to the centrifugal counterpart is their mass flow rate which is independent from the delivery pressure. The head-flow characteristic curve for PD pumps does not make sense as the mass flow is defined by the crankshaft velocity, the crankshaft parameters and the piston diameter; this is shown and explained by Figure 2-2.

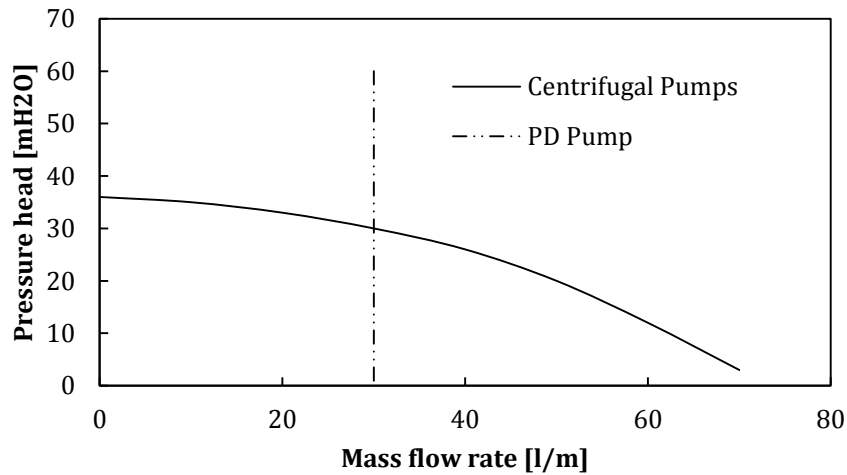


Figure 2-2: PD Vs Centrifugal pumps: Head-flow qualitative curve.

This implies that the design of pipelines where fluid is moved by means of PD pumps should account for relief valves calibrated (with a certain safety factor) on the maximum pressure the pump is designed to operate or the maximum power the motor or engine can provide. In cases when the pressure in the pipelines reaches that value, the relief valve must open to discharge the liquid and avoid damage on the pump, pipelines or both. Centrifugal pumps do not have the same issue as increments of the pressure resistance of the pipeline will result in a mass flow decrement as explained by Figure 2-3. The actual mass flow rate the pump operates at is fixed by the pressure resistance of the pipeline system.

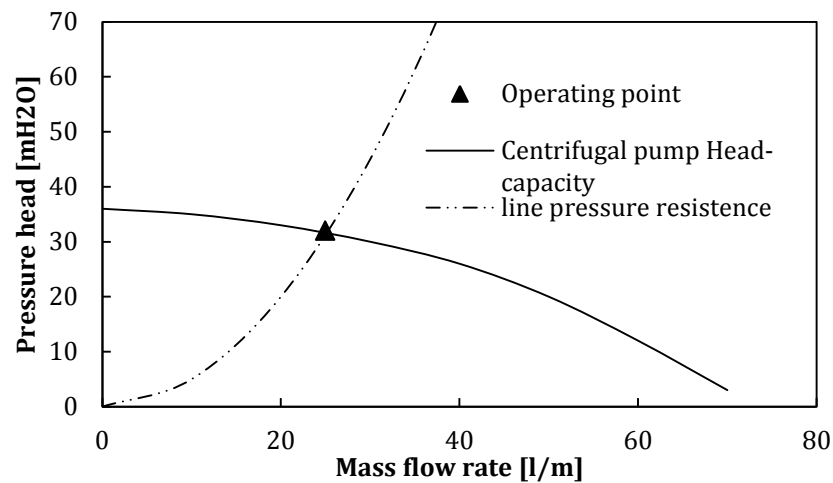


Figure 2-3: Centrifugal pumps. The mass flow rate is defined by the pipeline pressure resistance curve

Although centrifugal pumps can work over a wide range of mass flow rates and pressure heads, they are designed to work efficiently only around a design point, performance usually drops quite significantly away from that range. Figure 2-4 shows, for both centrifugal and

PD pumps, the qualitative trends of the efficiency over the pump delivery pressure. The figure points out that PD pumps efficiency is in fact independent of the delivery pressure. Figure 2-4 does not account for the overall efficiency loss due to the decrement of the volumetric efficiency when the PD pumps cavitate. However this topic will be abundantly discussed later in this dissertation. Unlike PD pumps, Figure 2-4 shows that centrifugal pumps work efficiently only in a narrow range of delivery pressures and the designer should make sure the system accounts for the pump operating point location.

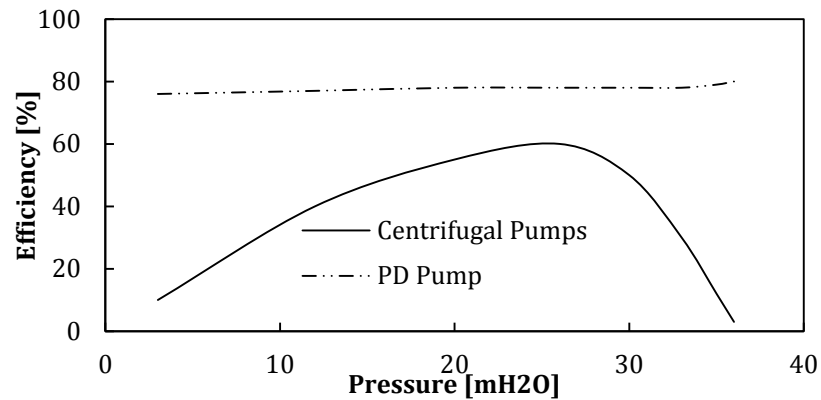


Figure 2-4: Centrifugal Vs PD pumps. Efficiency-head qualitative trend.

Centrifugal and PD pumps also behave differently with different kind of fluids, the viscosity affects performance significantly. Figure 2-5 shows that centrifugal pumps lose capacity when processing highly viscous liquids while PD pumps lose capacity working with low viscosity fluids. PD pumps actually slightly their capacity for high viscosity liquids. Figure 2-6 also demonstrates that centrifugal pumps are not the right choice to process high viscosity liquids as the efficiency of the device deteriorates very quickly with increasing the kinematic viscosity. For PD pumps the rate of deterioration is less steep. This explains the reason why PD pumps are preferred for oils which have, in general, higher viscosity.

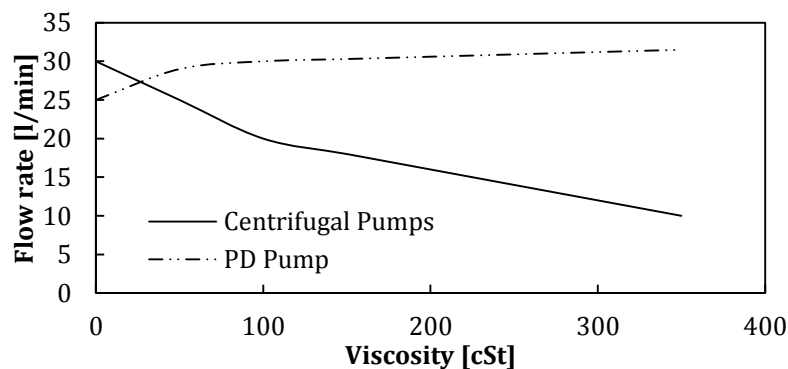


Figure 2-5: Centrifugal Vs PD pumps, the qualitative dependence of the flow rate to the liquid kinematic viscosity is shown.

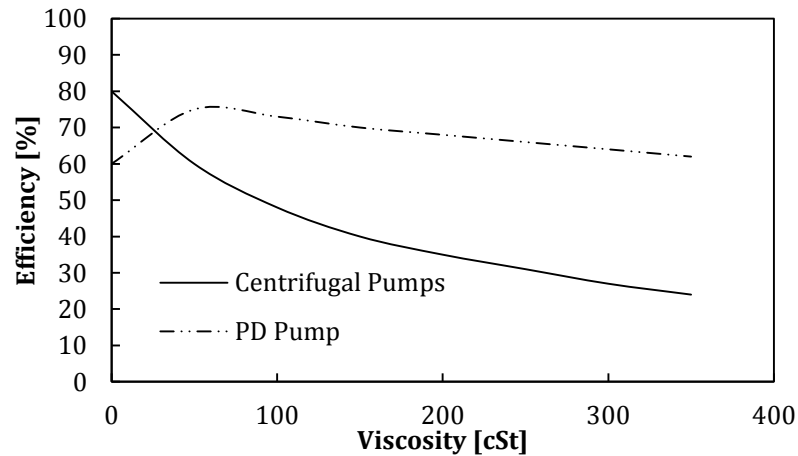


Figure 2-6: Centrifugal Vs PD pumps, the qualitative dependence of the efficiency to the liquid kinematic viscosity is shown.

2.3 PD pump applications in industry

There are many industrial applications where PD pumps are employed. Apart from the considerations discussed in paragraph 2.1 and in Figure 2-1, PD pumps are utilized in all the applications where the mass flow rate must be independent from the pressure head or when a constant and stable average mass flow rate is needed to achieve good efficiency of the system. The author decided to list and briefly discuss a few industrial application where PD pumps are utilized in order to give the reader the industrial background behind the kind of device being discussed in this dissertation.

2.3.1 Hydraulics

PD pumps are widely utilized to move oil in hydraulic actuators. To ensure a constant velocity of the stem of the actuator, in fact, a constant mass flow rate is required despite the pressure resistance of the system. A centrifugal pump which provides a mass flow rate dependent on the pressure resistance of the piping system would not be acceptable. Figure 2-7 shows the schematic of an axial piston pump which achieves the objective of constant mass flow rate required for hydraulic applications. Axial piston pumps are compact multi cylinders PD pumps (usually 8) which, for instance, are widely used in aeronautics to actuate the moving parts of aircrafts control surfaces. The high number of pistons keeps the mass flow rate constant with respect to the crank angular position.

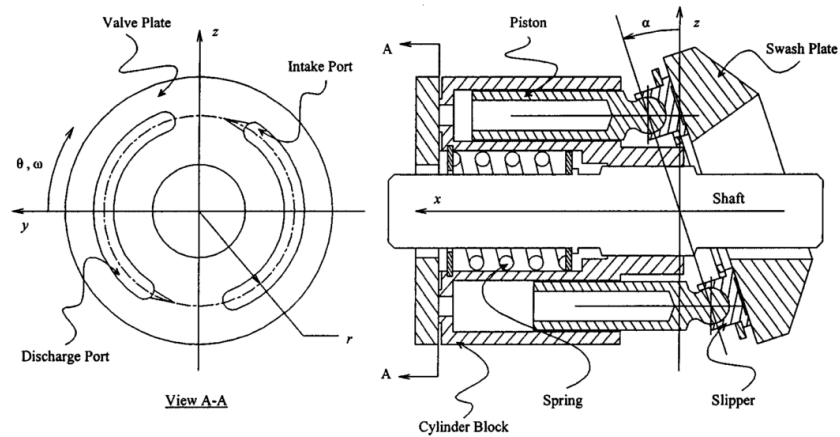


Figure 2-7: Axial piston pump schematic (Manring 2003)

2.3.2 Sea water desalination

The process of sea water desalination is used to produce drinking water or water for irrigation in places like tropical zones which are affected by fresh water shortage. There are different techniques utilized nowadays to desalinate sea water, one, in particular, requires the use of PD pumps. This process is called reverse osmosis. Reverse osmosis makes use of particular membranes which filter sea water not allowing the passage of many types of molecules or ions when the osmotic pressure is applied across them. In order for the process to be efficient the pressure difference a desalination system should apply has to range very closely to the osmotic pressure and should not change when the membrane changes its properties over time. PD pumps are the only device capable of achieving this task.

2.3.3 Water jet cutting technology

Within manufacturing industry, high velocity (up to hypersonic conditions) water jets are used to cut a wide variety of materials. This technology is preferred every time the manufacturing technology must not heat up the items being manufactured or when damage due to high temperature should be avoided. Water jet cutting machines pressurise water and push it through a small diameter nozzle which creates the jet after mixing it with abrasive materials. The jet is then moved by a CNC (Computer Numerical Control) machine on the piece to be cut. To accelerate a low mass flow rate jet to the velocity required, a high pressure pump is utilized. In fact, for this application Figure 2-1 and equation 2.1 suggest to the reader that PD pumps are the most suitable device as the specific speed is expected to range around the left end of the picture (400 MPa of pressure is not uncommon in water jet cutters).

2.4 Hydraulic fracturing

The process of hydraulic fracturing or fracking (Daneshy 2001) consists of making use of Positive Displacement pumps for pumping a mix of water, chemical substances and slurries into a wellbore which has been previously drilled in the ground to reach the shale rocks in which oil is contained thanks to the porous nature of them. The high pressure pumping flow breaks the rocks and the slurries keep the fractures open when the pumping has come to an end and lets the oil to flow out of the rocks and up to the surface along the wellbore to be collected. The pressure needed to create the fractures depends on the site but is usually very high (up to 15000 psi which corresponds to 100 MPa). The target pressure cannot be achieved by any device apart from PD reciprocating pumps. In this case the pump specific velocity remains quite low mostly because of the high head rather than the low capacity, Figure 2-1 suggests to the reader that PD reciprocating pumps are again the best option although the very high pressure, impossible to achieve with different devices makes PD pumps not just the best option but also the only option for hydraulic fracturing.

3 Positive displacement reciprocating pumps

3.1 Introduction

A reciprocating pump is a kind of pump that makes use of a reciprocating motion to push the working fluid from the suction to the delivery line. The reciprocating motion is obtained by means of a rotating crank and a connecting rod. In basic configurations, the rotational velocity, the crank diameter and the connecting rod length are the only parameters needed to define the reciprocating motion. A positive displacement (PD) pump is a common sub-category of the reciprocating pumps which delivers one fixed displaced volume of fluid each pumping cycle. In plunger and in piston pumps, the fixed displaced volume is created by means of the displacement of, a plunger or piston respectively which moves back and forth covering the distance that is commonly known as the stroke. The maximum and the minimum position achieved by the plunger during the stroke are called Top Dead Centre (TDC) and Bottom Dead Centre (BDC) respectively. They correspond to the maximum and minimum distance between the plunger and the rotating shaft. The TDC and BDC positions respectively identify the passage from the delivery stroke to the suction stroke (TDC) and from the suction stroke to the delivery stroke (BDC). During the suction stroke that theoretically lasts for half pumping cycle (180° of crank rotation) a self-actuated inlet valve opens because of the pressure difference between the chamber and the inlet manifold and allows the filling of the displacement volume as the plunger moves backwards. Once the plunger reaches the BDC, the pressure equilibrium between the chamber and the inlet manifold is restored and the preloaded spring closes the inlet valve. During the outlet stroke the displacement volume flows through the outlet valve as the plunger moves forward. The outlet valve which is self-actuated and placed usually in line with respect to the inlet valve, opens when the pressure difference between the chamber and the outlet line exceeds the outlet valve spring preload. Figure 3-1 shows two perpendicular cross section of a PD pump and also explains the nomenclature of the items composing the pump. Figure 3-2 shows the TDC and BDC position of the plunger.

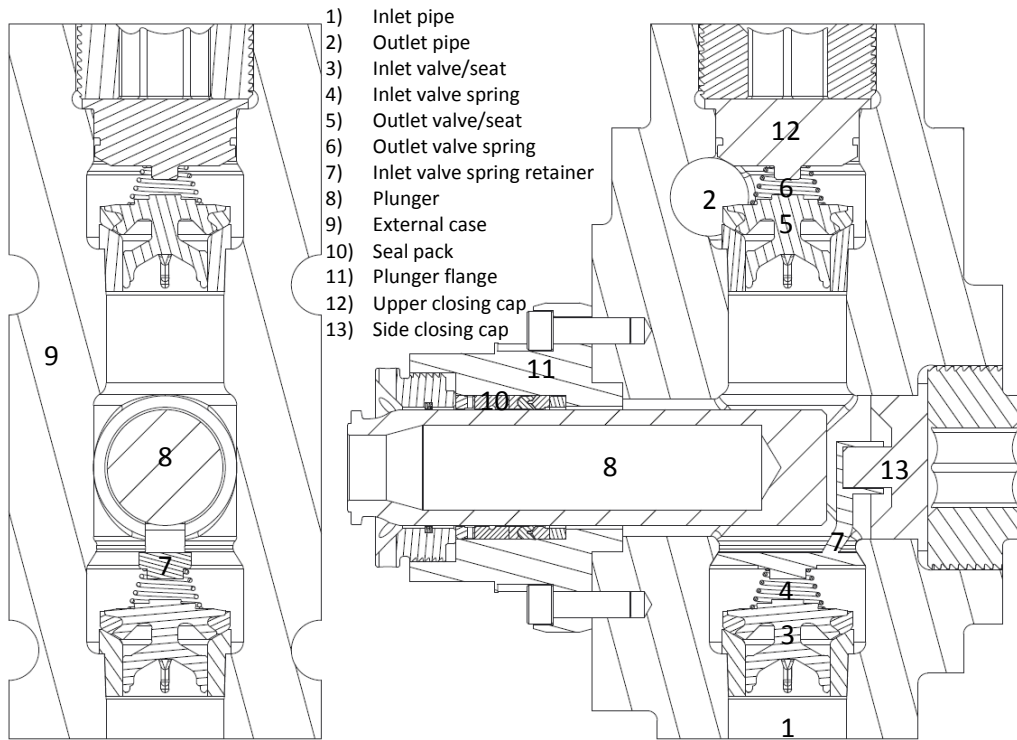


Figure 3-1: Perpendicular sections of a single chamber PD reciprocating pump. Component legend

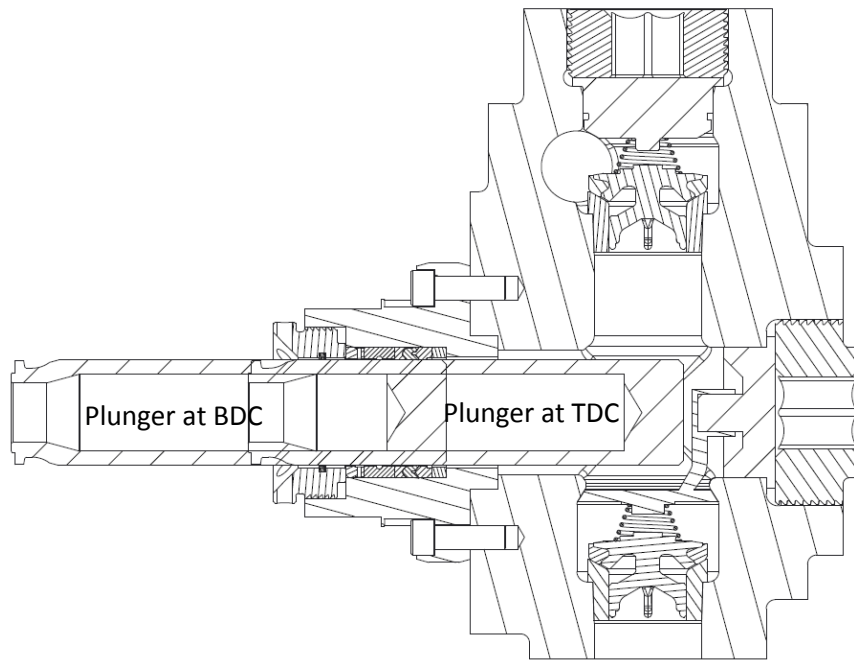


Figure 3-2: Plunger stroke, Top Dead Centre (TDC) and Bottom Dead Centre (BDC), the displacement volume is swept.

To increase the capacity of a PD plunger pump more than one chamber may be designed. Figure 3-3 shows the typical configuration of a PD pump with three chambers (triplex)

equipped with one plunger each. The plungers usually act out of phase to obtain a mass flow over time which is as constant as possible. To increase the capacity for a given angular speed, single chamber or multi chamber PD pumps may also be designed as double acting. In this case two displacement volumes per chamber are delivered for every shaft revolution. However, the discussion on multiple chambers or double acting PD pumps is beyond the scope of the project which is being presented in this document.

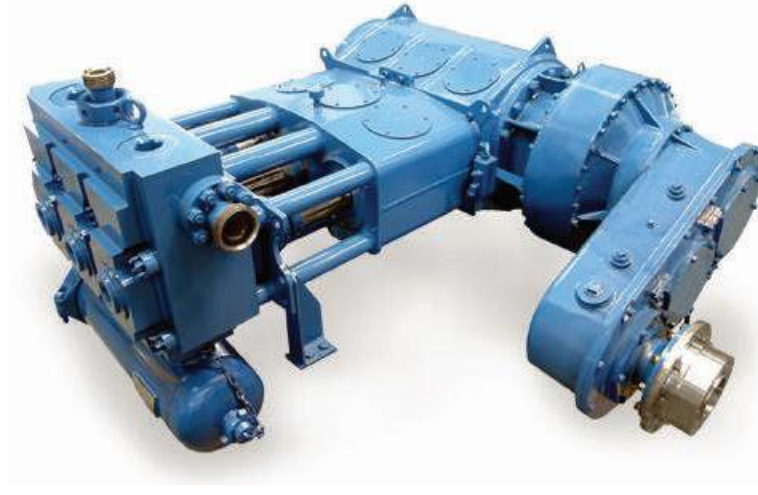


Figure 3-3: Triplex PD reciprocating pump, WEIR SPM Destiny TWS 2500.

3.2 PD pump components

A positive displacement reciprocating pump (Figure 3-3) is composed of two main parts:

- *Power end.* It can be thought to be the group of items which are employed to create the power and transform it into the reciprocating motion provided to the plunger. The power end is composed of the engine, the gear box and the crankshaft.
- *Fluid end.* It can be thought of as the zone where the pumping of the liquid takes place. It is the only part of the pump under investigation in the present document. The fluid end is composed (Figure 3-1) of:
 1. *Inlet manifold.* The pump chambers are fed by a single manifold (which is shown in the bottom left corner of Figure 3-3). The manifold is usually pressurised by an external centrifugal pump to increase the safety factor against cavitation problems (NPSHa) which may occur during the inlet stroke.
 2. *Outlet pipe.* The first part of it is cast inside the external steel block which is connected to the external pipes and manifolds of other pumps in the system.
 3. *Inlet valve and seat.* The valve main body is composed of an inner steel part and a urethane external ring which seals the pumping chamber when it

comes into contact with the seat. The valve assembly is shown in Figure 3-12.

4. *Inlet valve spring* (Figure 3-4). The inlet valve is initially pushed against the seat by means of a preloaded spring, the behaviour of which is not entirely linear as demonstrated by Figure 3-13.

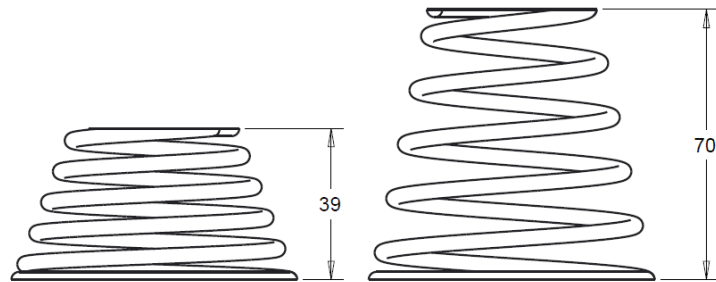


Figure 3-4: Inlet valve spring. On the left the initial (preloaded) configuration, on the right the released configuration. Dimensions are in [mm].

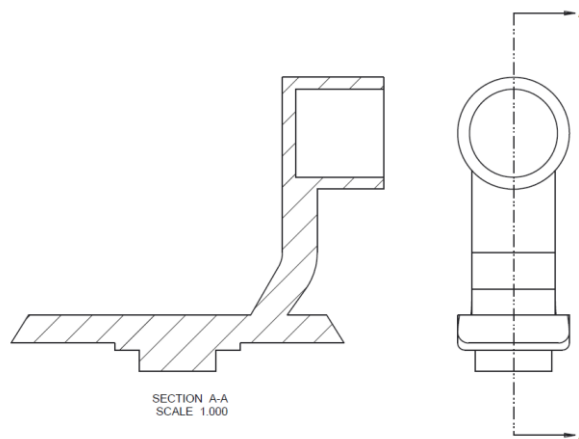


Figure 3-5: Inlet valve spring retainer

5. *Inlet valve spring retainer*. The inlet valve spring preload is kept by means of a retainer (Figure 3-5). The retainer should take the minimum amount of space in order not to obstruct the flow from the valve (located upstream) to the chamber (located downstream).
6. *Pump side closing cap*. The retainer is kept in the correct position by means of the closing cap of Figure 3-6. Figure 3-1 explains how it (item 13) interfaces with the retainer (item 7).
7. *Outlet valve and seat*. The outlet and inlet valve designs are usually the same. The valve main body is composed of a urethane ring and a steel body.
8. *Outlet valve spring* (Figure 3-8). It is usually the same spring as utilised for the inlet valve, the preload could be different as shown by Figure 3-13.

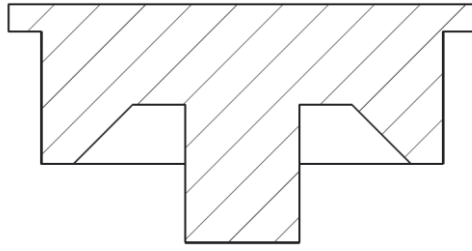


Figure 3-6: Side closing cap, It also hooks the spring retainer to keep it in the correct position.

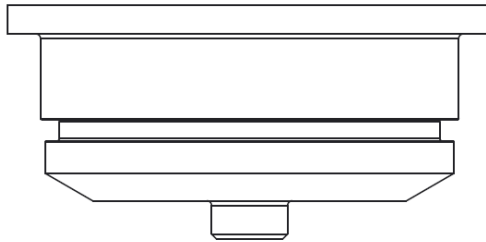


Figure 3-7: The top cap closes on the upper part the pump case and also maintains the outlet valve spring initial compression.

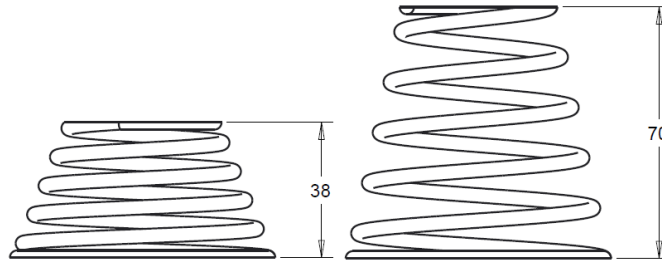


Figure 3-8: Outlet valve spring. On the left the initial (pre-loaded) configuration, on the right the released configuration. Dimensions are in [mm]

9. *One plunger per each chamber* (Figure 3-9). The plunger diameter defines the displacement volume delivered by each pumping cycle together with the stroke. The plunger pump differs from a piston pump by the location of the seals. In plunger pumps the seals are static and the plunger slides inside them. In piston pumps the seals are located on the piston and move with respect to the piston bore in the pump external case.



Figure 3-9: Plunger section

10. *Plunger seals.* The plunger slides inside a bore equipped with a pack of seals which can be tightened by means of an external threaded cap to account for the chamber pressure which can exceed 12000 psi (83 MPa circa). Both are shown in more details in Figure 3-10.

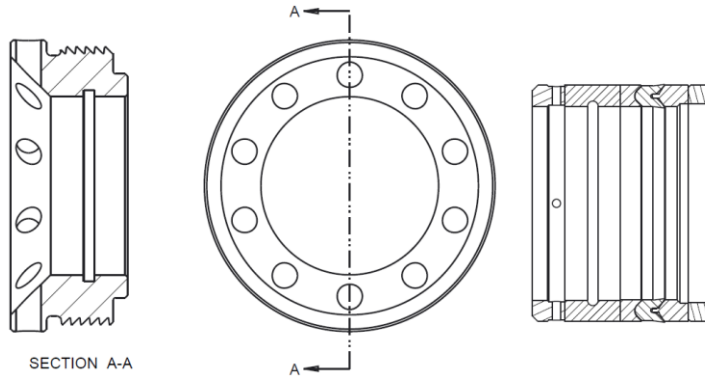


Figure 3-10: (On the left) plunger threaded cap. (On the right) seals pack. The cap tightens the seals.

11. A set of threaded cylinders (Figure 3-11) to resist to the significant pressure force to which the closing caps (respectively) of Figure 3-6 and Figure 3-7 are subjected because of the high pressure in the pump chamber. They are assembled as shown in Figure 3-1 (they are attached to items 12 and 13).
12. A *massive external steel case* (Item 9 in Figure 3-1) which is designed to house the items explained above and to resist the huge stresses that the chamber inner pressure creates.

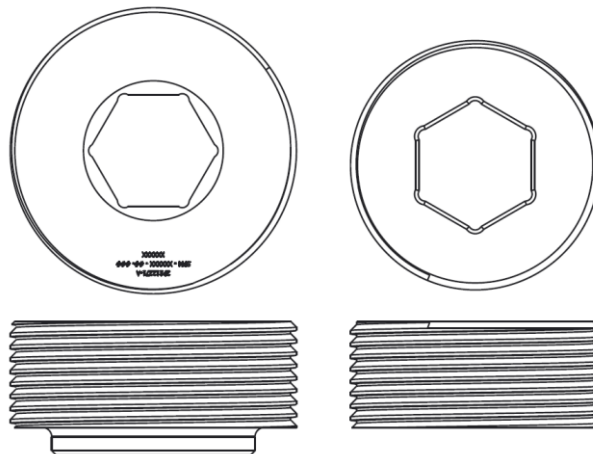


Figure 3-11: (left) Side threaded cylinder. (Right) Top threaded cylinder.

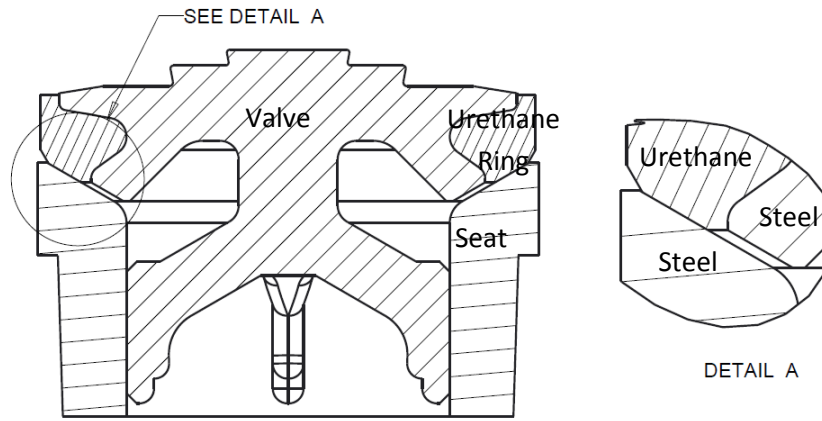


Figure 3-12: inlet (and outlet) valve and seat assembly. The step between the valve main body and the urethane ring prevents the metal-metal contact.

When the urethane ring is not compressed, the valve-seat section presents a *step* due to the urethane shape which prevents the metal-metal contact. However, when the high pressure occurs during the delivery stroke, the urethane ring is subjected to very high forces which cause its compression and a metal-metal contact of the inner parts of the valve with its seat. This is shown in Figure 3-14. The outlet valve is affected by the same phenomenon which, conversely, occurs during the inlet stroke when the chamber pressure decreases with respect to the outlet pipe pressure. The CFD simulation presented in this dissertation did not account for the high delivery pressure and the deformation and the urethane ring deformation was, therefore, neglected.

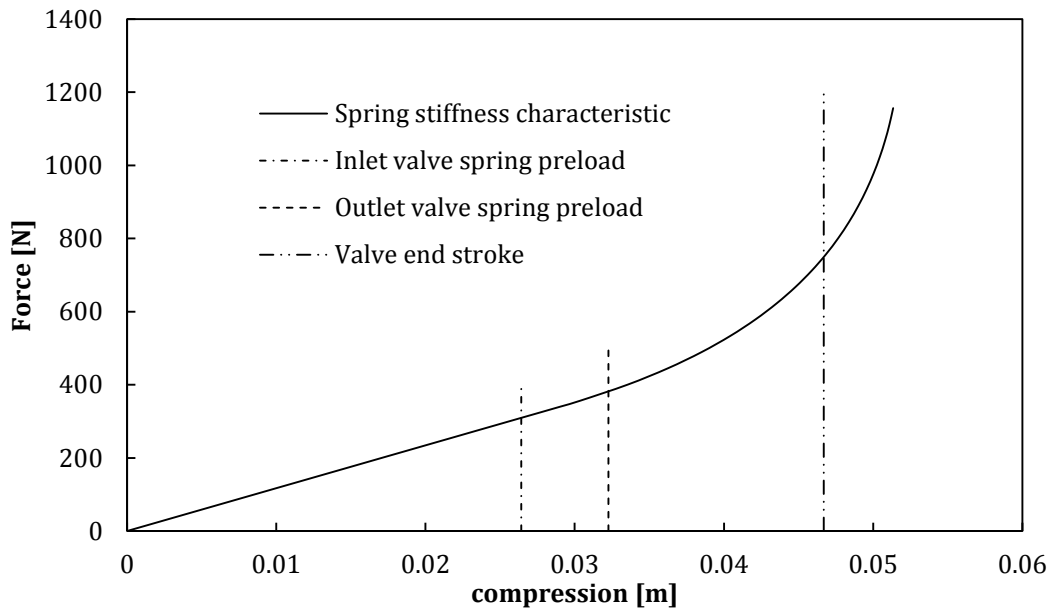


Figure 3-13: Spring stress-strain characteristic curve.

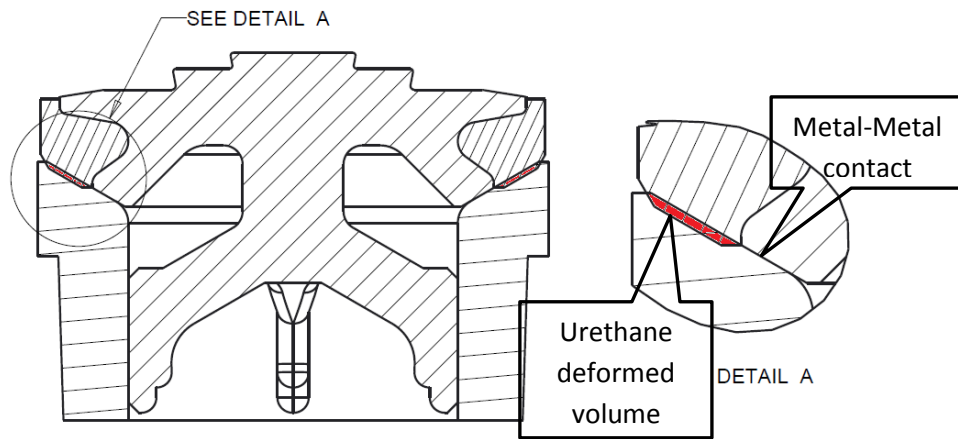


Figure 3-14: urethane deformation when the pressure difference across the valves approaches the operating delivery pressure.

3.3 Kinematics

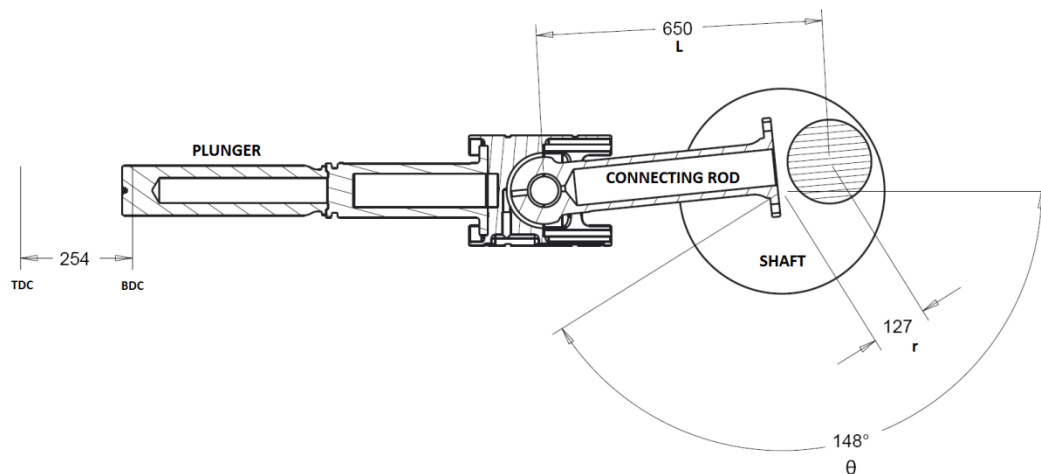


Figure 3-15: Reciprocating motion, parameters for the WEIR SPM Destiny TWS 2500 pump. Dimensions are expressed in [mm].

When the plunger axis passes through the center of the shaft, the reciprocating motion equation is fully described by the angular velocity ω and the parameters discussed in Figure 3-15. It is common to gather the connecting rod length L and the shaft radius r in a term defined by their ratio $\mu=L/r$. Simple considerations of trigonometry lead to the equation of the stroke with respect to the crank rotation angle $s(\theta)$ (equation 3.1). The first and second derivative of 3.1 lead to the equation of the plunger velocity $v(\theta)$ (3.2) and the plunger acceleration $a(\theta)$ (3.3).

$$s(\theta) = r(1 - \cos \theta + \mu - \sqrt{\mu^2 - \sin^2 \theta}) \quad 3.1$$

$$v(\theta) = r\omega \left[\sin \theta + \frac{1}{2} \frac{\sin 2\theta}{\sqrt{\mu^2 - \sin^2 \theta}} \right] \quad 3.2$$

$$a(\theta) = r\omega^2 \left[\cos \theta + \frac{1}{2} \frac{2 \cos 2\theta (\mu^2 - \sin^2 \theta) + \sin^2 2\theta}{\sqrt{(\mu^2 - \sin^2 \theta)^3}} \right] \quad 3.3$$

Figure 3-16 to Figure 3-18 represent the graph of the equations 3.1-3.3 when the geometric parameters of the WEIR SPM Destiny TWS 2500 pump are chosen:

- Connecting rod length $L = 0.65085$ m
- Shaft radius $r = 0.127$ m
- Crank velocity $\omega = 13.61$ rad/s (130 rpm or Strokes Per Minute, SPM)

130 SPM is a typical operational velocity for this kind of pump which runs within the range of 90-300 SPM.

Multiplying the velocity of the plunger by its area one can obtain the volume flow rate needed to fill the positive displacement volume which is created throughout the pumping cycle (Figure 3-19). Multiplying the volume flow rate by the density of water at standard condition (998.2 kg/m^3), the theoretical mass flow at 100% volumetric efficiency can be plotted (Figure 3-20). Figure 3-20 is considered the theoretical mass flow rate which will be used when a comparison with the ideal situation is needed. The hypothesis behind this considers the valve to have no inertia and a perfectly incompressible liquid as working fluid. As a result neither the inlet valve nor the outlet valve is affected by any delay in opening or closing. The theory implies that the valves open instantaneously. Figure 3-20 will be taken as reference when comparison between theory and CFD is made in the next chapters.

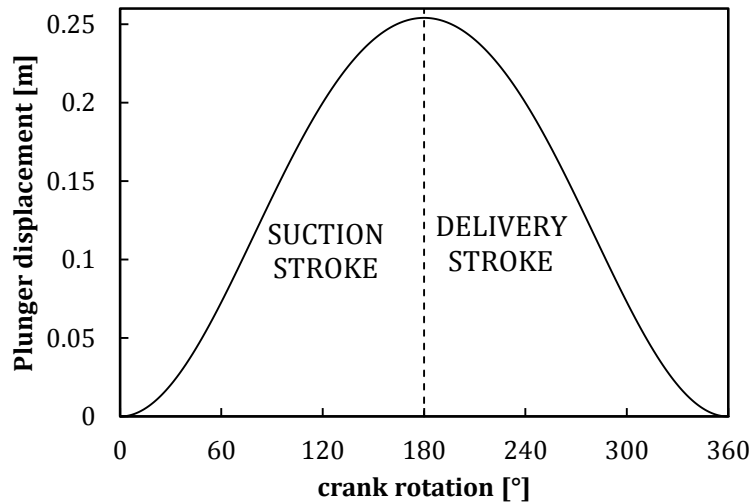


Figure 3-16: Plunger displacement law, $s(\theta)$.

Figure 3-16, as well as any of the following, shows also the norm adopted in this document to refer to the parts of the pumping cycle. At the initial time, the plunger is positioned at the TDC and the shaft is at 0° . In the range 0° - 180° the plunger moves backwards performing the suction stroke which is the first half of the cycle as the total volume of the chamber increases up to the positive displacement volume. At 180° the plunger reaches the BDC then moves forward performing the delivery stroke throughout the range 180° - 360° . Figure 3-17 shows the maximum positive value of the plunger velocity as well as the maximum negative. They occur at 80° and 280° respectively. Figure 3-18 shows the difference between the maximum positive acceleration and the maximum negative one.

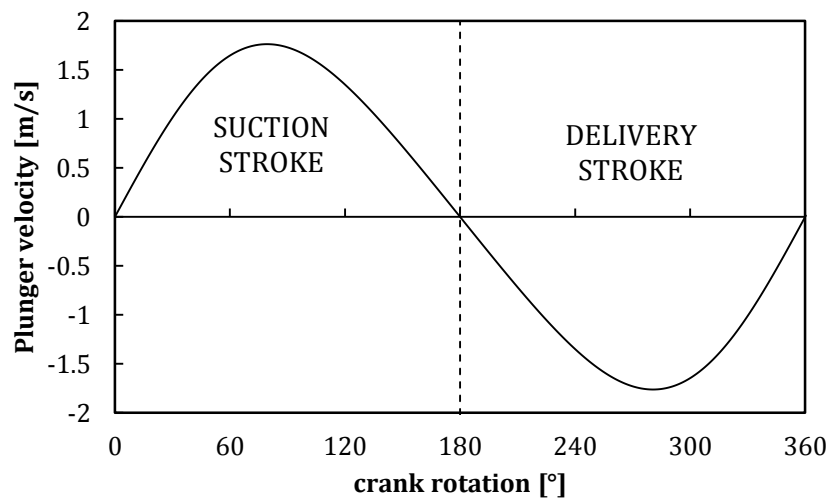


Figure 3-17: Plunger velocity law, $v(\theta)$.

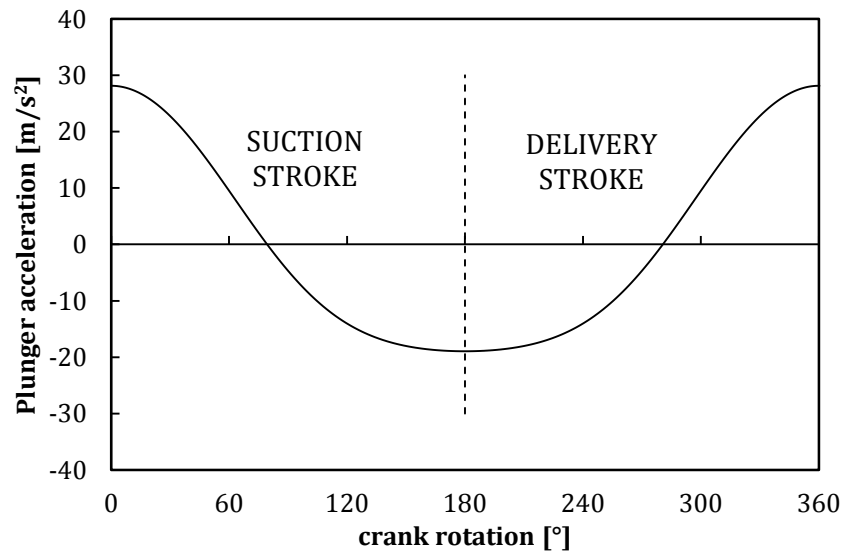


Figure 3-18: Plunger acceleration law, $a(\theta)$.

3.4 Theory

The simplest approach in the analysis of PD reciprocating pumps is the one based on the theory of kinematics explained in the previous paragraph. The theory's main hypothesis is that the mass flow rate is proportional to the plunger velocity, the plunger top surface and the density of water at ambient condition. Figure 3-19 and Figure 3-20 show the simple multiplication needed to turn the velocity of the plunger into the mass flow passing through the volume flow rate. For the main hypothesis to be valid the following phenomena have to be verified:

- Zero compressibility of the liquid
- Zero inertia of the valve which has to lift up as soon as the plunger begins the motion from the TDC and BDC
- Zero cavitation or air content.

It is clear that the standard theory based on the kinematics of the pump is too simplified to estimate the pump performance, such as the volumetric efficiency, which the theory always estimates as 100% because of the applied assumptions.

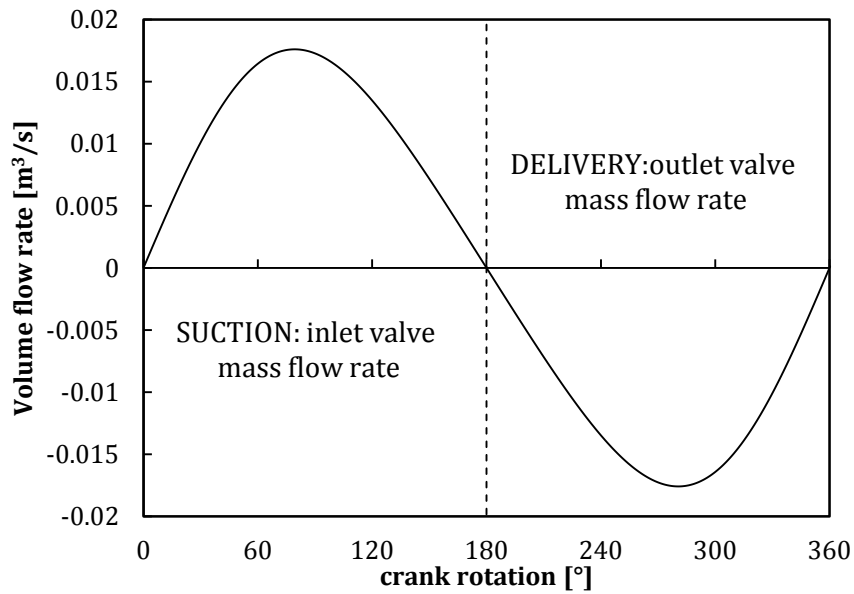


Figure 3-19: Volume flow rate throughout the pumping cycle.

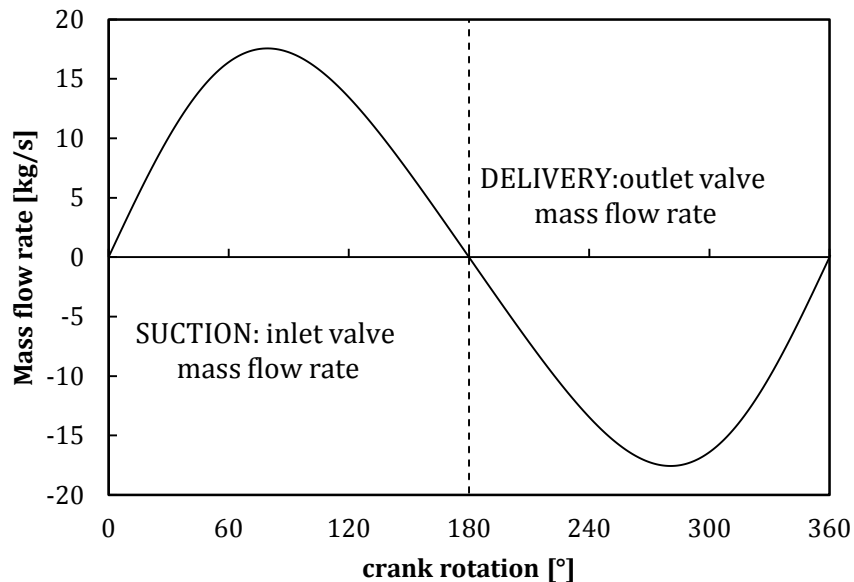


Figure 3-20: Theoretical mass flow rate @ standard condition ($\rho=998.2 \text{ kg/m}^3$).

When the PD pump is composed of more than one chamber, the suction mass flow rate as well as the delivery flow rate is the sum of the different chamber mass flow rates. The higher the number of the chambers the smaller is the mass flow rate fluctuation of the pump throughout the 360° of crank rotation. Figure 3-21 represents the theoretical suction mass flow rate for a triplex pump when the three plungers act out of phase of 120° . From the theory one can see that the suction mass flow rate oscillations lie within the range of -24% , $+7\%$ from the mean value when the reciprocating motion parameters (crank diameter and connecting rod length) are the ones already introduced to plot Figure 3-16 to Figure 3-20.

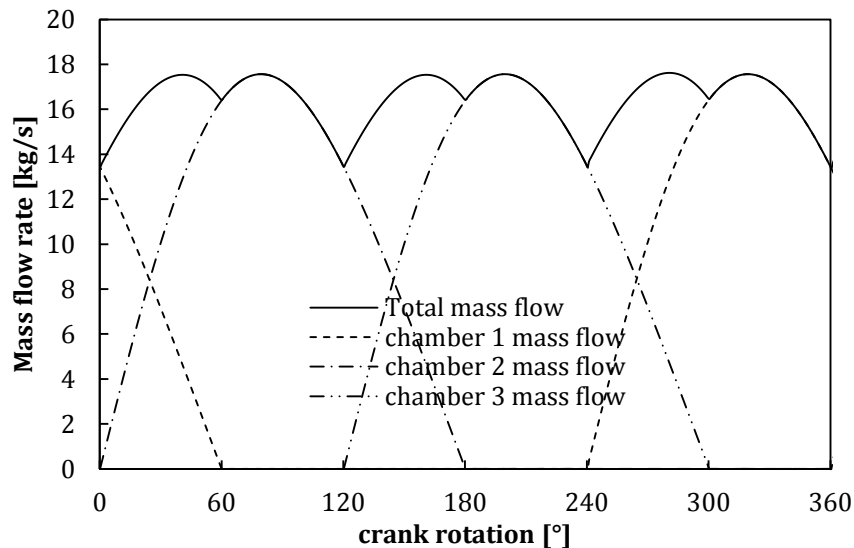


Figure 3-21: Theoretical inlet mass flow rate Vs crank rotation for a triplex PD pump.

3.5 Reciprocating pump efficiency

Figure 3-19 depicts the ideal situation when the pump works at 100% of volumetric efficiency. It means that a volume of fluid of the amount of the displacement volume is delivered every pumping cycle. In real situations the amount of liquid delivered per pumping cycle may be less than that. The difference is usually referred to as the volumetric efficiency loss. It usually depends on the design of the pump and on the operating conditions or, in more details:

- Compressibility of the liquid (not negligible when operating at high delivery pressure).
- Grade of pureness of the liquid. When water is used, the air content dissolved may increase the compressibility of the mixture in cases when the inlet manifold pressure is low.
- The valve inertia. The capability of the inlet valve to quickly close once the inlet stroke has come to an end affects the fluid leakage. The higher the inlet valve closing delay the higher the leakage and the lower the volumetric efficiency.
- Cavitation. When the pressure falls near the vapour pressure, vapour may be generated and this affects the valve closing delay since it creates a significant pressure difference in the pump chamber. This will be discussed in more detail later on in this document.

Tackett (Tackett et al. 2008) defines the volumetric efficiency by the following equation:

$$VE = 1 - [P_{\Delta}\beta\rho + V_L] \quad 3.4$$

Where P_{Δ} is the pressure difference (discharge – sucking), β is the inverse of the liquid bulk modulus, V_L is the valve loss from fluid leakage and ρ is the ratio of chamber total volume, when the plunger is at full forward position (maximum volume), and the displacement volume. It is important to note that the ideal case where the maximum chamber volume (not achievable) equals the displacement volume would result in the minimum value of ρ of 1. In real cases ρ is higher than 1 and the compressibility effects are higher than in the ideal case.

3.6 NPSH

The Net Positive Suction Head (NPSH) defines how safely the pump is operating from cavitation. The NPSH definition is always split into two parameters which really matter: $NPSH_A$ (available) and $NPSH_R$ (required). The $NPSH_A$ is the absolute pressure at the pump inlet and is a design characteristic of the pipeline where the pump is working. $NPSH_R$ is the minimum pressure required at the pump inlet for cavitation to appear and is a pump characteristic which should be provided by the pump designer. Therefore, to operate safely without any cavitation effects, the following condition must be achieved:

$$NPSH_A > NPSH_R \quad 3.5$$

The $NPSH_R$ usually comes as result of a standard test procedure while $NPSH_A$ may be estimated as the sum of several factors:

$$NPSH_A = H_S + H_Z - H_F + H_A - H_{VP} \quad 3.6$$

H_S is the absolute pressure at the surface of the water in the supply vessel which could equal the atmospheric pressure or could be higher (case of pressurized vessels). H_Z is the pressure due to the height of the inlet pump location with respect to the water surface in the vessel. H_F is the friction loss amount which depends on the design of the pipeline and may be estimated either via CFD simulations or analytic tools. H_{VP} is the vapour pressure of the liquid which depend on the temperature at which the pump is operating and may be estimated from the liquid phase diagram. H_A is the acceleration head and is an extra term which accounts for the accelerations and decelerations to which the flow in the inlet pipe is subjected due to the

pumping cycles. Tackett (Tackett et al. 2008) suggests the following formula to roughly estimate that value:

$$H_A = \frac{LVNC}{gk} \quad 3.7$$

Where L is the pipe length, V is the mean suction velocity (estimated by Figure 3-19 and the inlet pipe diameter), N is the crank angular velocity, g is the gravity acceleration, k and C are empirical constants and can be taken from Table 3-1.

Table 3-1: Valuation of k and C coefficients to estimate the acceleration head (Tackett et al. 2008).

C		k	
0.2	Simplex double acting	2.5	For highly compressible hydrocarbons
0.2	Duplex single acting		
0.4	Simplex single acting	2	For most hydrocarbons
0.115	Duplex double acting		
0.066	Triplex single or double acting	1.5	For water, amine, glycol
0.04	Quintuplex single or double acting		
0.028	Septuplex single or double acting	1.4	For deaerated water
0.022	N cylinders single or double acting		

The definition of NPSH is not problematic in cases of pumping circuits equipped with centrifugal pumps but, for positive displacement pumps, many authors agree on the fact that the definition of NPSH loses significance. Tackett and Pawn (Tackett et al. 2008; Pawan J. Singh 1996) recall that, according to the Hydraulic Institute, the NPSH_R for PD pump is the inlet pressure head at which the pump volumetric efficiency falls down the threshold of 97% at a specific pressure and speed. The definition of NPSH in PD pumps is therefore related to the volumetric efficiency loss rather than cavitation. This does not mean necessarily that cavitation and volumetric efficiency loss are not correlated phenomena but it means that the volumetric efficiency is affected by many other parameters along with cavitation. According to Miller (Miller 1995), in fact, the NPSH in a PD pump does not provide a precise engineering requirement. Miller states that although a PD pump may operate at a fair volumetric efficiency with a minimum suction head, any additional suction pressure above that NPSH will improve the performance of the pump in the following ways:

1. Improve the volumetric efficiency

2. Reduce the effect of dissolved or entrained air or gas in the liquid
3. Allow higher pumping temperature
4. Offset the effect of instantaneous pressure drop through the valves
5. Minimize effects introduced in multiple pump installations
6. Reduce the amount of leakage through plunger or rod packing

On the other hand to achieve a very high inlet pressure is technically difficult. It is important to note that a high inlet pressure will result in a double beneficial effect in terms of improvement of the volumetric efficiency it will offset the risk of cavitation and will reduce the volumetric efficiency loss due to the compressibility of the liquid as the suction-delivery pressure difference will reduce according to equation 3.4.

3.7 Introduction to CFD modelling of PD pumps

Although PD pumps are considered simple devices, creating numerical models based on CFD of PD pumps is a very hard task to achieve. To estimate the volumetric efficiency, in fact, provides the analyst with technical problems which cannot be underestimated. According to the author's opinion the difficulty lies in the fact that very few simplifying hypothesis can be applied to PD pump models before losing the significance of the CFD simulation. A PD pump designer's interest is focused on the details that can only be caught by a comprehensive model such as the one discussed later on in this document. This paragraph will provide the crucial features a CFD model of a PD pump must have to provide analyst with the information needed to improve the engineering design of PD pumps. It will be carried out via examples.

The aim of such a model can be summarized in the correct estimation of the volumetric efficiency and this comes directly from the discussion of paragraphs 3.5 and 3.6. What is not yet clear is how to achieve a good estimation of that parameter as it is affected by many factors as already mentioned. According to equation 3.4 one must account for the compressibility of the working fluid and the correct dynamics of the valves as one need to estimate the inlet valve closing delay which causes valve leakage. When the NPSHa falls below the NPSHr the valve dynamics will also be affected by the interaction between vapour generation and the pump chamber pressure field. The model should also account for the content of dissolved air or gas as it affects the compressibility of the liquid (Miller 1995). The cavitation model and the problem of the air content in real liquids will be discussed in detail in the next section. The model should also account for the interaction of the chambers in all cases of multiple pump chambers (triplex for instance).

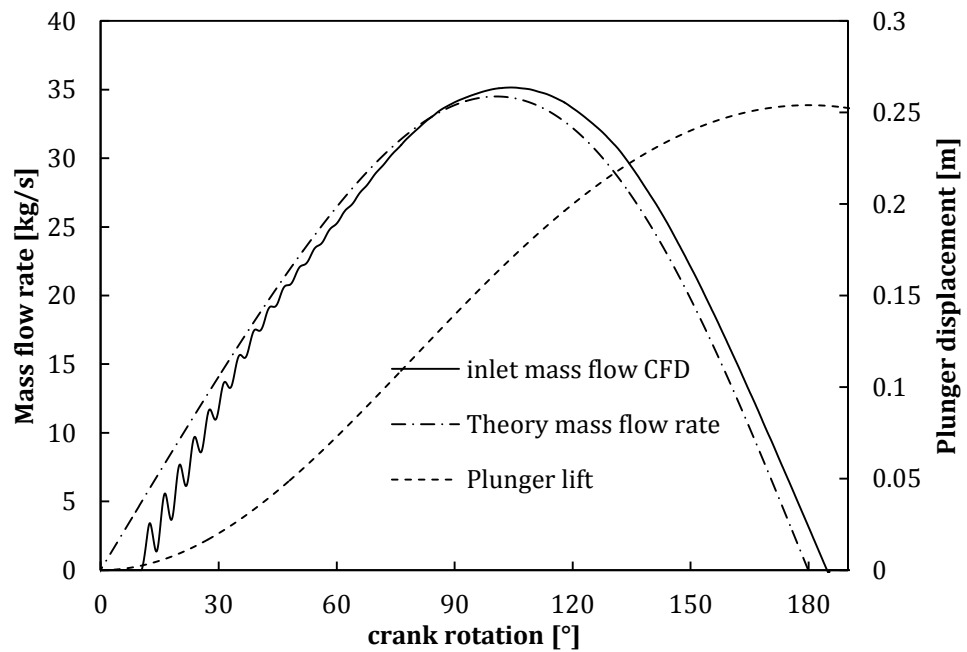


Figure 3-22: Mass flow inlet throughout the inlet stroke, comparison of the theoretical curve with the real behaviour simulated via a one phase CFD model without cavitation effects.

Figure 3-22 and Figure 3-23 provide an example of a comparison between the theoretical mass flow rate and the one calculated via a CFD model. The details of the CFD model are not under investigation in this chapter and therefore will not be discussed. For the time being the reader should only know that in the CFD results shown in Figure 3-22 to Figure 3-24 the compressibility of water and the dynamics of the valves were taken into account. The integral of the curves divided by the density of water at standard condition returns the volumetric efficiency of the CFD model. The theoretical curve returns a value of 100% by definition as it does not account for the compressibility of the liquid nor for the valve dynamics as the curve is simply the one of Figure 3-19 times the water density at standard condition. The CFD curve of this simplified CFD model shows the delay of the valves in opening and closing. This model is already capable of simulating the flow leakage through the inlet valve. The estimation of the volumetric efficiency loss is still affected by the absence in the model of any quantity of dissolved air which carries errors in the correct estimation of compressibility of the mixture (water and air). In the particular case depicted by Figure 3-22 and Figure 3-23, a sufficiently high suction head was simulated and this avoided cavitation problems which could not be simulated as no cavitation model was added to the simulation.

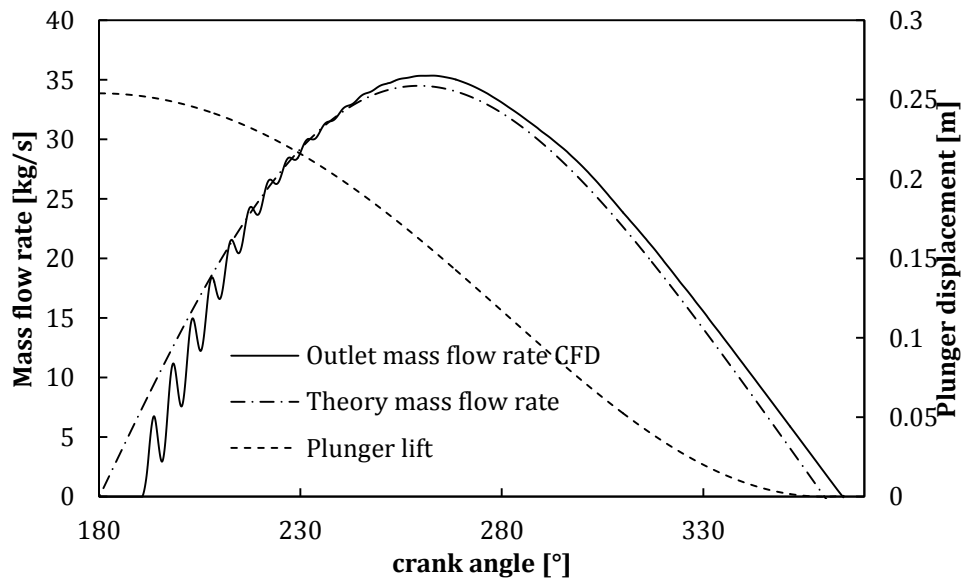


Figure 3-23: Mass flow outlet throughout the outlet stroke, comparison of the theoretical curve with the real behaviour simulated via a one phase CFD model without cavitation effects.

Figure 3-24 and Figure 3-25 show the comparison of the inlet stroke pressure history between the CFD model mentioned and the experimental test carried out at the same operating conditions simulated by the CFD model (A. Iannetti et al. 2014). The pressure values refer to a static chamber location near the TDC position of the plunger in both experimental and CFD cases. CFD pressure trends show high frequency oscillations in this zone when the inlet valve opens a quick damping occurs. Such a phenomenon is totally absent in the experimental curve and this demonstrates that CFD does not estimate correctly the internal damping of the flow due to the turbulence.

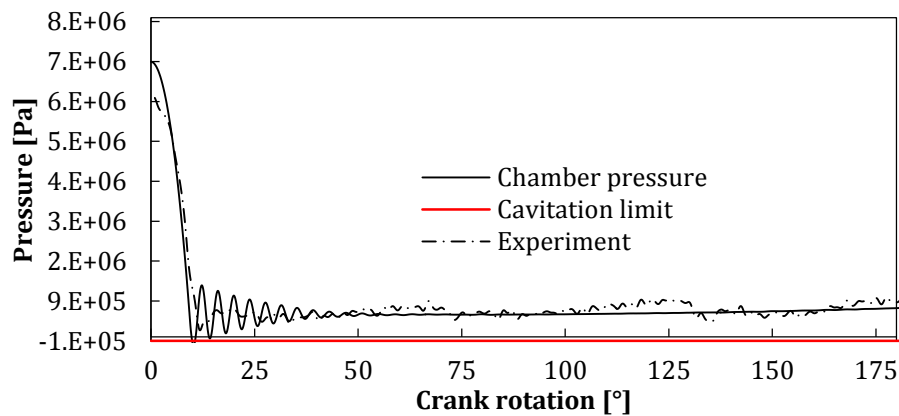


Figure 3-24: Numerical Vs Experimental data, comparison of the inlet stroke chamber pressure. Experiments by Wilson (Wilson et al. 2011).

The experimental pressure trend shows a non-constant behaviour throughout the inlet stroke after the initial decompression part. This was caused by the interaction of the three chambers

(a triplex pump was utilised). The CFD model did not account for the interaction of the chamber and its curve after the oscillations follows the average experimental trend obtained by Wilson (Wilson et al. 2011).

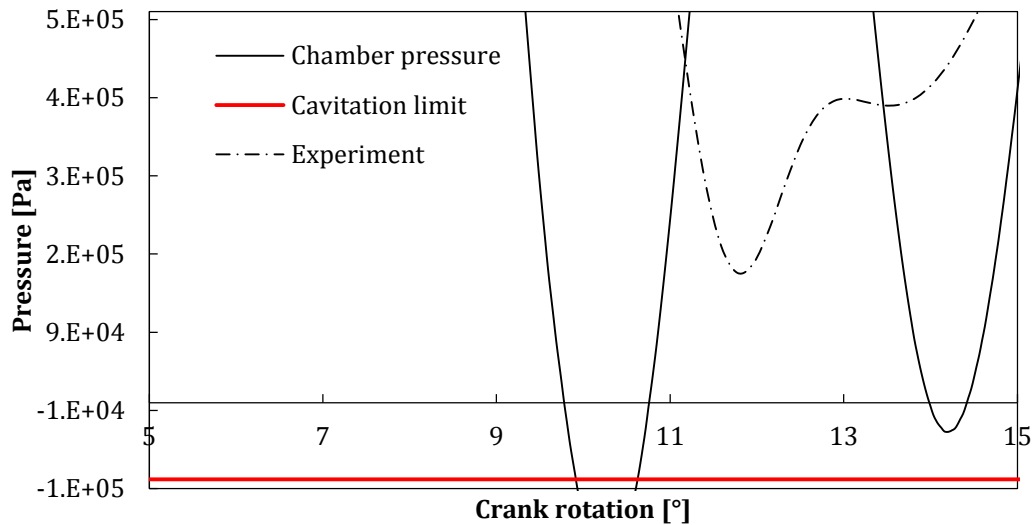


Figure 3-25: Detail of the negative pressure spikes occurred in the CFD simulations. Experiments by Wilson (Wilson et al. 2011).

The analysis discussed in the basic model of Iannetti (A. Iannetti et al. 2014) pointed out that:

- Analytical models based on the simplified theory are inappropriate to predict PD pump performance.
- CFD models have to account for the valve dynamics and the behaviour of the real fluid. The compressibility characteristics of the liquid are crucial to simulate correctly the pressure-time history and, as demonstrated later, the cavitation dynamics.
- One phase CFD model does not estimate the real compressibility of the liquid as a small amount of non-condensable gas mass fraction has to be expected in the water and therefore a change in the physical properties of the fluid with respect to the theory should be also considered.

4 Cavitation Models

4.1 Introduction

The aim of the present chapter is to provide a quick overview of the physics and to focus on the numerical models the analyst may rely on.

Cavitation is the formation and development of vapour structures in an originally liquid flow (Franc & Michel 2004; Franc 2007). Vapour in a liquid can be generated either by increasing the temperature or decreasing the pressure. In both cases it is needed that the microscopic nuclei (Franc & Michel 2004) already present in the liquid volume reach the vapour pressure which is described by Figure 4-1.

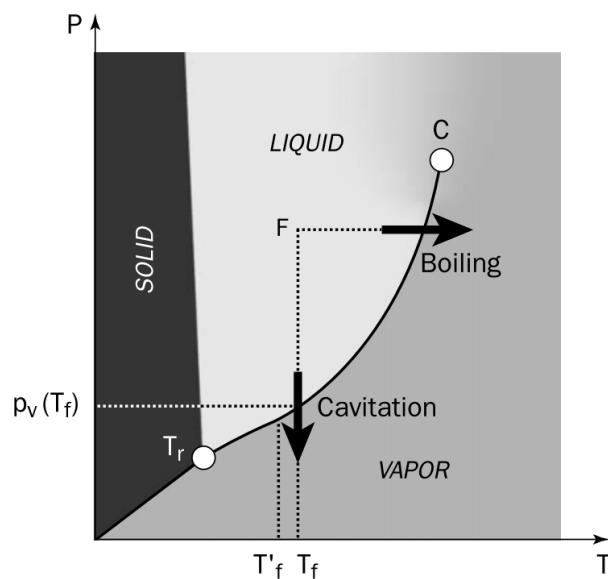


Figure 4-1: Qualitative phase diagram for water (Franc & Michel 2004).

The first, constant pressure case is commonly known as boiling while in the second case the formation of vapour takes place at almost constant temperature and is known as cavitation. There are two main different reasons why a liquid flow may experience a pressure drop and, as shown in the following chapters, they may all occur in PD pumps: high flow velocity which results in a high dynamic pressure and, according to Bernoulli's law, a static pressure drop and a low velocity expansion of the fluid volume which results in a drop in the static pressure. The expansion at low velocity is a typical phenomenon in PD pumps whilst the phenomenon related to the flow speed, commonly known as flow induced cavitation, is very common in different engineering processes and devices such as marine propellers and centrifugal pumps.

Flow induced cavitation has been widely studied in the research environment using both experimental and numerical approaches and many cavitation models have been developed and tested on flow induced cavitation. Numerical studies on PD pumps are currently quite rare in the literature and one may say that the additional effect of cavitation due to expansion on the flow induced cavitation has not been sufficiently discussed to date. To answer the question on whether the low speed expansion is an independent effect or is somehow related to the flow induced cavitation, it is crucial to dispose of a reliable cavitation model.

Cavitation in clean water starts from the presence of microscopic nuclei composed of gas and vapour already present in the flow (Franc & Michel 2004), they may be located on the wall filling the small wall cervices which are not filled with water. In this case the wetting capacity of liquid is crucial (surface tension) but they also can be located inside the liquid bulk. What is important to note is that the presence of nuclei is an intrinsic property of the liquid. In real liquids (Franc & Michel 2004) nuclei of various sizes are present and their density may vary depending on different factors such as the pureness of the water. Figure 4-2 shows the density of nuclei activated by an experimental rig based on a Venturi pipe. In the figure p_c is the critical pressure of the nuclei which will be discussed in the following paragraph.

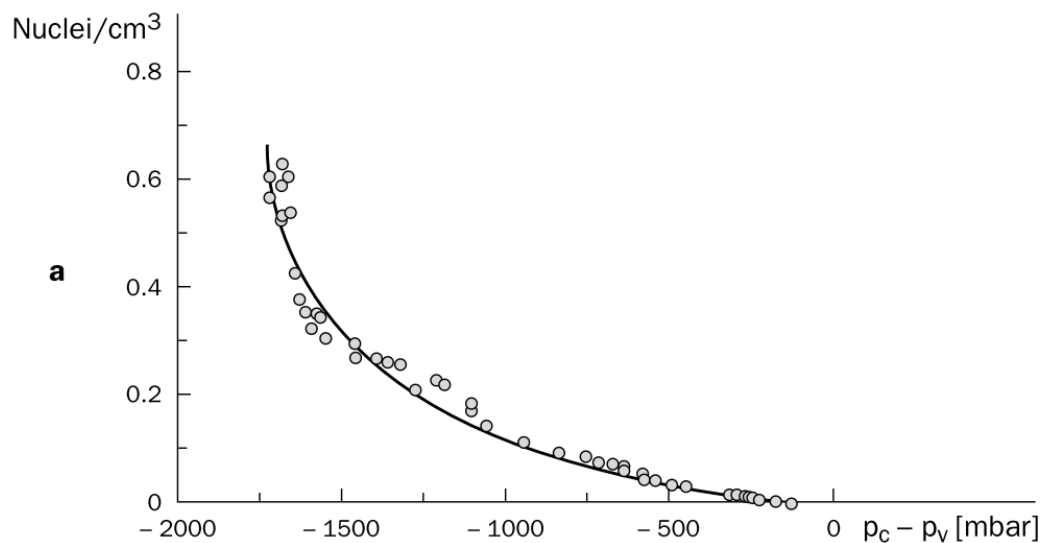


Figure 4-2: Number of nuclei activated in a measurement rig based on a Venturi (Franc & Michel 2004).

It is known that nuclei are in equilibrium status when the velocity is null, pressure and temperature are at standard condition but they may grow in fluid zones where low pressure condition or high temperature is achieved.

The effects of the number of pre-existing nuclei on cavitation is a topic much debated in the technical literature (Arora et al. 2007). However, what is not open to debate is that in most numerical algorithms which model cavitation, the number of nuclei is usually a constant number which has to be specified by the user and this may lead to a source of errors in the model.

As pointed out in the next paragraph, the cavitation phenomenon is also affected by the pureness of the water as it affects the partial pressure inside the nuclei. The amount of non-condensable gas mass fraction dissolved in the water is also a topic discussed in the technical literature (Baur et al. 1998) as it affects the bubble radius dynamics. This document will also show that in PD reciprocating pumps the dissolved gasses may delay vapour cavitation.

4.2 Rayleigh-Plesset equation

The main mathematical tool widely used to study cavitation is the Rayleigh-Plesset equation. It may be considered the dynamics equation of bubbles which describes the relationship between their radius and the external forces once the vapour pressure conditions are achieved. The Rayleigh-Plesset equation does not describe the inception of cavitation nor does it describe the bubble collapse, it applies to a single spherical bubble in an infinite liquid medium at rest at infinity (Franc 2007). If \mathfrak{R}_{B0} is the initial radius of bubbles (Franc 2006; Franc 2007), $\mathfrak{R}_B(t)$ is the radius of bubbles at time t, $P_\infty(t)$ is the pressure at infinite distance from the bubble, and $v(r, t)$ is the radial velocity of the flow at a distance, r, from the bubble center while $v(\mathfrak{R}_B, t)$ and $P(\mathfrak{R}_B, t)$ are respectively the radial velocity and pressure of the interface vapor-liquid. As the bubble contains vapor and gas, the pressure inside the bubble P_B is supposed to equal the partial vapor pressure p_{sat} which is a characteristic of the working fluid (from now on the working fluid will be referred to as water as no other liquids will be discussed in this document) plus the gas partial pressure $p_g(t)$ which changes as the radius of the bubble increases from the starting value p_{g0} . The initial gas partial pressure is related to the instantaneous gas pressure by equation 4.1:

$$p_g(t) = p_{g0} \left[\frac{\mathfrak{R}_{B0}}{\mathfrak{R}_B(t)} \right]^{3\gamma} \quad 4.1$$

Where γ is the ratio of the specific heat capacities of the gas. In an isothermal case the equation changes to the one shown in equation 4.2:

$$p_g(t) = p_{g0} \left[\frac{\mathfrak{R}_{B0}}{\mathfrak{R}_B(t)} \right]^3 \quad 4.2$$

The overall equilibrium equation of the bubble, therefore, may be written as shown in equation 4.3:

$$p_{g0} \left[\frac{\mathfrak{R}_{B0}}{\mathfrak{R}_B(t)} \right]^{3\gamma} + p_{sat} = P(\mathfrak{R}_B, t) + \frac{2\sigma}{\mathfrak{R}_B} - 2\mu \left. \frac{\partial v}{\partial r} \right|_{r=\mathfrak{R}_B} \quad 4.3$$

This equation takes into account the surface tension σ and the viscous stress due to the dynamic effects and refers to the non-equilibrium conditions. In isothermal and steady state cases where the flow velocity is negligible and the external pressure is constant ($P(\mathfrak{R}_B, t) = P_\infty(t) = P$) one can calculate the relationship between the radius and the pressure needed for the equilibrium, equation 4.4:

$$P = p_{g0} \left[\frac{\mathfrak{R}_{B0}}{\mathfrak{R}_B} \right]^3 + p_{sat} - \frac{2\sigma}{\mathfrak{R}_B} \quad 4.4$$

Equation 4.4 is usually used to discuss the stability of bubble under the internal pressures which tends to increase the bubble radius and the external pressure which tries to decrease it. The equation, plotted in Figure 4-3 has a minimum value located at the following coordinates:

$$\begin{cases} \mathfrak{R}_{BC} = \sqrt{\frac{3p_{g0}\mathfrak{R}_{B0}^3}{2\sigma}} \\ P_c = p_{sat} - \frac{4\sigma}{3\mathfrak{R}_{BC}} \end{cases} \quad 4.5$$

The region located on the left of the dotted line of Figure 4-3 defines the situation where stability may be achieved; in this region a pressure reduction leading the pressure to a value lower than the minimum value P_c will bring to a new equilibrium status with a bigger radius while a reduction leading the pressure to a level lower than P_c will result in an unrestrained bubble radius growth. The region on the right side of the dotted line describes an intrinsic unstable situation because any further reduction of the pressure will cause an unlimited growth of the bubble radius (Franc 2007; Franc 2006) and the consequent inception of cavitation. P_c and \mathfrak{R}_{BC} may be considered the critic pressure and bubble radius necessary for cavitation to appear.

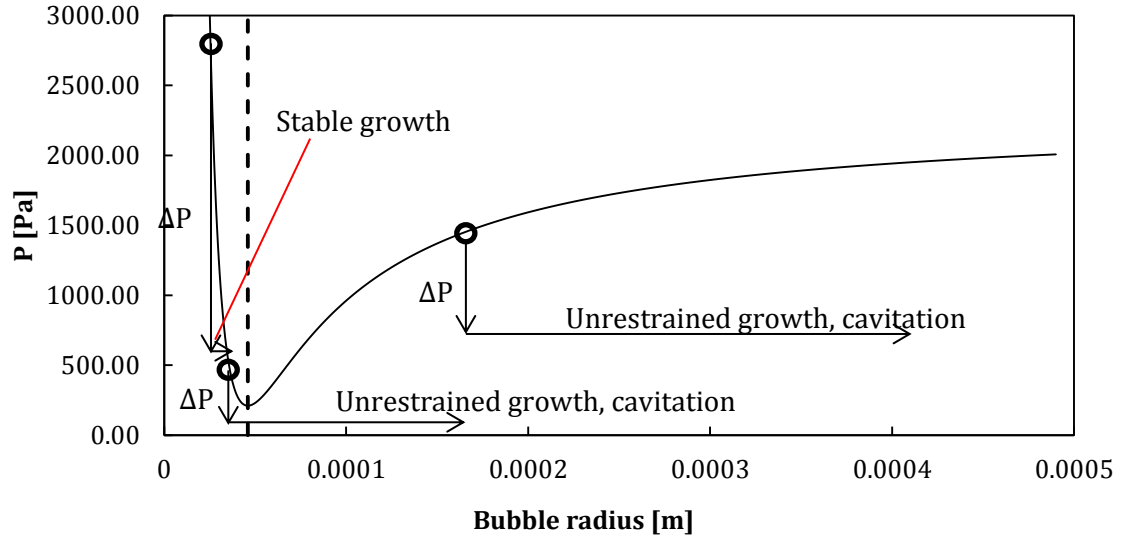


Figure 4-3: Bubble radius stability. Water at room temperature and initial pressure was considered as well as a 0.01 mm initial bubbles radius.

Equation 4.3 may be worked considering:

1. The mass conservation equation for incompressible flows $div \vec{v} = 0$, which may be written in a cylindrical coordinate system from the velocity of the interface, \dot{R} , as:

$$v(r, t) = \dot{\mathfrak{R}}_B \frac{\mathfrak{R}_B^2}{r^2} \quad 4.6$$

2. The radial projection (Franc 2006) of the momentum equation:

$$-\frac{1}{\rho} \frac{\partial P}{\partial r} = \frac{\partial v}{\partial t} + v \frac{\partial v}{\partial r} \quad 4.7$$

Substituting the velocity from equation 4.6 into equation 4.7 and integrating the resulting equation from radius r to infinity one can obtain:

$$\frac{P(r, t) - P_\infty(t)}{\rho} = \ddot{\mathfrak{R}}_B \frac{\mathfrak{R}_B^2}{r} + 2\dot{\mathfrak{R}}_B^2 \left[\frac{\mathfrak{R}_B}{r} - \frac{\mathfrak{R}_B^4}{4r^4} \right] \quad 4.8$$

On the bubble interface $r = \mathfrak{R}_B$, and equation 4.8 becomes:

$$\frac{P(\mathfrak{R}_B, t) - P_\infty(t)}{\rho} = \ddot{\mathfrak{R}}_B \mathfrak{R}_B + \frac{3}{2} \dot{\mathfrak{R}}_B^2 \quad 4.9$$

Substituting equations 4.9 and 4.6 into equation 4.3 the Rayleigh-Plesset equation is obtained:

$$\rho \left[\dot{\mathfrak{R}}_B \mathfrak{R}_B + \frac{3}{2} \dot{\mathfrak{R}}_B^2 \right] = [p_{sat} - P_\infty(t)] + p_{g0} \left[\frac{\mathfrak{R}_{B0}}{\mathfrak{R}_B(t)} \right]^{3\gamma} - \frac{2\sigma}{\mathfrak{R}_B} - 4\mu \frac{\dot{\mathfrak{R}}_B}{\mathfrak{R}_B} \quad 4.10$$

Making use of equation 4.10, many aspects of cavitating flows may be studied, for instance, one can calculate the temporal response of the bubble radius $\mathfrak{R}_B(t)$ under any $P_B(t)$ pressure history although the cavitation models usually make use of the Rayleigh-Plesset equation to estimate the rate of phase change between phases rather the bubble evolution in time. As the reader will see, cavitation models simplify equation 4.10 and solve it to estimate, on a steady state basis, the amount of vapour volume fraction per unit fluid volume. The first assumption the numerical models have do make is to apply equation 4.10 to n bubbles where n is the cavitation nuclei per unit volume and then consider the pressure value at each cell centre $P(t)$ rather than the pressure at infinity $P_\infty(t)$.

The author will refer to equation 4.10 as the Rayleigh-Plesset equation (Franc 2006) even though other authors suggest that the Rayleigh-Plesset equation is equation 4.10 with all second order terms neglected (Rayleigh 1917). It is important to point out that the viscosity and surface tension terms were added by Plesset (Plesset & Prosperetti 1977).

Equation 4.30 represents the starting point for the discussion on the numerical algorithms one may find in CFD solvers to account for cavitation effects in multiphase models. All the numerical cavitation models developed so far which may be found in literature come from the Rayleigh-Plesset equation. All of them add a few more hypotheses to the original equation in order to simplify it further. In the opinion of the author, the analyst should be aware of the simplifications in order to choose the suitable model for his application. The next section will discuss three of them.

4.3 Singhal et al. Cavitation model

Singhal (Singhal & Athavale 2002) explained his model by starting from the Rayleigh-Plesset equation written in the following form:

$$\mathfrak{R}_B \frac{D^2 \mathfrak{R}_B}{Dt^2} + \frac{3}{2} \left(\frac{D \mathfrak{R}_B}{Dt} \right)^2 = \frac{P_B - P}{\rho_l} - \frac{4\nu_l}{\mathfrak{R}_B} \dot{\mathfrak{R}}_B - \frac{2\sigma}{\rho_l \mathfrak{R}_B} \quad 4.11$$

The total derivative is utilised in the left hand side of the equation as Eulerian solvers are usually employed in conjunction with numerical cavitation models. The liquid density, ρ_l , is stated explicitly as the vapour density is also utilised in the algorithm. The partial pressure of the gas contained in the bubble is now included in the term P_B and will be discussed later. The first assumptions that Singhal makes is to neglect the second order terms with respect to the first order terms and the viscous damping term reducing the equation 4.11 to the form:

$$\frac{3}{2} \left(\frac{D\mathfrak{R}_B}{Dt} \right)^2 = \frac{P_B - P}{\rho_l} \quad 4.12$$

Moreover he utilises equation 4.12 to calculate the phase change source term needed in the continuity equations of the mixture (water and vapour) and the second phase (vapour) as follows.

Combining the continuity equation of the liquid phase:

$$\frac{\partial}{\partial t} [(1 - \alpha_v)\rho_l] + \nabla \cdot [(1 - \alpha_v)\rho_l \vec{v}] = -R \quad 4.13$$

Where R is the net phase change rate and α is the second phase volume fraction, the continuity equation of the vapour phase:

$$\frac{\partial}{\partial t} [\alpha_v \rho_v] + \nabla \cdot [\alpha_v \rho_v \vec{v}] = R \quad 4.14$$

Considering the continuity equation of the mixture:

$$\frac{\partial}{\partial t} [\rho] + \nabla \cdot [\rho \vec{v}] = 0 \quad 4.15$$

One can obtain the relation between the mixture density and the vapour fraction:

$$\frac{D\rho}{Dt} = -(\rho_l - \rho_v) \frac{D\alpha_v}{Dt} \quad 4.16$$

The vapour volume fraction α can be related to the bubble number n in the following equation:

$$\alpha_v = n \frac{4}{3} \pi \mathfrak{R}_B^3 \quad 4.17$$

Substituting equation 4.17 into equation 4.16:

$$\frac{D\rho}{Dt} = -(\rho_l - \rho_v) (n4\pi)^{1/3} (3\alpha_v)^{2/3} \frac{D\mathfrak{R}_B}{Dt} \quad 4.18$$

Finally, combining equations 4.13,4.14,4.16 and 4.18 the expression for R is obtained:

$$R = (n4\pi)^{1/3} (3\alpha_v)^{2/3} \frac{\rho_l \rho_v}{\rho} \left[\frac{2}{3} \left(\frac{P_B - P}{\rho_l} \right) \right]^{1/2} \quad 4.19$$

In equation 4.19 all of the terms except n are either known constant or depend on fluid dynamics field variable. Equation 4.19 may also be written in terms of bubble radius instead of bubble number. Neglecting temporarily, the influence of the non-condensable gas, substituting the vapour pressure P_v to the bubble pressure P_B one can obtain :

$$R = \frac{3\alpha_v \rho_l \rho_v}{\Re_B \rho} \left[\frac{2}{3} \left(\frac{P_v - P}{\rho_l} \right) \right]^{1/2} \quad 4.20$$

So that the following estimation of the bubble radius can be applied:

$$\Re_B = \frac{0.061 We \cdot \sigma}{2\rho_l v_{rel}^2} \quad 4.21$$

Where We is the Weber number. Equation 4.21 reintroduces the influence of the surface tension that was temporarily neglected moving from equation 4.11 to 4.12. Equation 4.21 relates the radius of the bubbles to the one which results from the equilibrium of the surfaces tension forces and aerodynamic drag forces generated by the relative velocity v_{rel} . Since the relative velocity is always very low (less than the 10% of the main flow) the dependency between the radius and the relative velocity may be considered linear and approximated with the squared root of the turbulent kinetic energy \sqrt{k} as explained by the author (Singhal & Athavale 2002). Equation 4.20 may thus be rewritten and decomposed in the evaporation and condensation terms which apply depending on the sign of the pressure difference $P_v - P$:

$$R_e = C_e \sqrt{k} \frac{\rho_l \rho_v}{\rho \sigma} \left[\frac{2}{3} \left(\frac{P_v - P}{\rho_l} \right) \right]^{1/2} (1 - \alpha_v) \quad 4.22$$

$$R_c = C_c \sqrt{k} \frac{\rho_l \rho_l}{\rho \sigma} \left[\frac{2}{3} \left(\frac{P_v - P}{\rho_l} \right) \right]^{1/2} \alpha_v \quad 4.23$$

The effect of non-condensable gas mass fraction f_g is reintroduced in equation 4.22 and 4.23 rewriting 4.22 and 4.23 in terms of mass fraction instead of volume fraction, taking into account that:

$$\frac{1}{\rho} = \frac{f_v}{\rho_v} + \frac{f_g}{\rho_g} + \frac{1 - f_v - f_g}{\rho_l} \quad 4.24$$

$$\rho_g = \frac{WP}{RT} \quad 4.25$$

$$\alpha_g = f_g \frac{\rho}{\rho_g}; \quad \alpha_v = f_v \frac{\rho}{\rho_v} \quad 4.26$$

$$\alpha_l = 1 - \alpha_v - \alpha_g \quad 4.27$$

Where 4.25 is the ideal gas law, R (in that equation only) defines the ideal gas constant (8.31 J/mol K), W is the molecular weight of the gas (0.02928 kg/mol) and T is the temperature. Equation 4.22 and 4.23 can be written:

$$R_e = C_e \sqrt{k} \frac{\rho_l \rho_v}{\sigma} \left[\frac{2}{3} \left(\frac{P_v - P}{\rho_l} \right) \right]^{\frac{1}{2}} (1 - f_v - f_g) \quad 4.28$$

$$R_c = C_c \sqrt{k} \frac{\rho_l \rho_l}{\sigma} \left[\frac{2}{3} \left(\frac{P_v - P}{\rho_l} \right) \right]^{\frac{1}{2}} f_v \quad 4.29$$

This cavitation model also accounts for the influence of turbulence on the saturation pressure therefore the bubble pressure equals the real vapour pressure after the turbulence influence. A correction term related to the turbulence kinetic energy is added by equation 4.30 (ANSYS 2011a):

$$P_v = p_{sat} + \frac{1}{2} (0.39 \rho k) \quad 4.30$$

Equations 4.28, 4.29 with 4.30 define the mathematical basis of the “full” cavitation model developed by Singhal et al. The coefficients C_e and C_c are adjusted as explained by Singhal to be 0.02 and 0.01 respectively. It has to be pointed out once again that:

1. The Singhal et al. cavitation model does not model the growth dynamics of the vapour bubbles and thus the bubbles collapse even though it makes use of the Rayleigh-Plesset equation which describes the dynamics of the growth of a single bubble under an external pressure field. A certain vapour phase fraction appears and disappears following the interphase change rate R calculated explicitly by equation 4.28, 4.29.
2. The Singhal et al. cavitation model makes use of the Rayleigh-Plesset equation only to estimate the phase change rate. It is in fact a simplification of the second order terms which are important during the first part of the bubble growth when the accelerations are high. A further demonstration of this is the time steady radius of the bubbles which is considered by equation 4.21.
3. The surface tension forces and the non-condensable gas effects are taken into account under simplifying hypothesis.

Nonetheless the hypothesis discussed by the Singhal et al. cavitation model is considered the most advanced numerical model in literature and it is also referred to as the “Full” cavitation model for the same reason.

4.3.1 Vapour and air in the Singhal et al. cavitation model

The mathematical model of the Singhal et al cavitation model reveals that the model handles three phases: water, vapour and air but the air is managed in an explicit way inside the secondary phase, despite the kind of multiphase model the analyst decides to utilise there is only one transport equation handling the secondary phase volume fraction. It is interesting therefore to split the second phase volume fraction in the two components. Equations 4.25 and 4.26 suggest a simple method based on the known quantities of:

- Air mass fraction, which is a known constant set by the user
- The pressure field, which is known as it is calculated by the CFD solver
- The reference temperature (standard condition) and the ideal gas constant

At this purpose Equations 4.25 and 4.26 can be rearranged together in equation 4.31 where all the quantities are either constant or calculated by the CFD multiphase solver.

$$\alpha_g = f_g \frac{\rho RT}{WP} \quad 4.31$$

Equation 4.31 can be implemented easily as a custom field function and the volume fraction of air can be calculated as an explicit value.

It is important to note that equation 4.31 describes a weak interaction between the air and the pressure field, in fact, the air expansion affect the pressure field indirectly as no transport equation of the air is solved. It is also important to point out that the expansion of the air described by equation 4.31 follows the pressure drop without any delay as no dynamic effects are taken into account, this implies that air instantaneously fills the empty spaces left by the plunger retraction within each time step as the interphase change rate is calculated explicitly.

4.4 Zwart-Gerber-Belamri cavitation model

The Zwart-Gerber-Belamri (ANSYS 2011a) cavitation model is based on the assumption that all bubbles are of the same size, and the interphase mass transfer rate per unit volume is:

$$R = n \left(4\pi \mathfrak{R}_B^2 \rho_v \frac{D\mathfrak{R}_B}{Dt} \right) \quad 4.32$$

Equation 4.32 represents the mass phase change rate of a single bubble multiplied by the bubble density, n . Combining equation 4.17 with 4.30 and using the simplified Rayleigh-Plesset equation 4.12 the phase change rate R is calculated as:

$$R = \frac{3\alpha_v \rho_v}{\mathfrak{R}_B} \left[\frac{2}{3} \left(\frac{P_B - P}{\rho_l} \right) \right]^{1/2} \quad 4.33$$

Comparing 4.33 with 4.20 one can see that the difference lies on the density term. In the Zwart-Geber-Belamri model the phase change rate depends on the vapour density and does not depend on either on the liquid density or the mixture density.

Another important difference and approximation of this cavitation model is that the bubbles radius \mathfrak{R}_B is fixed by the user while in the Singhal et al. cavitation model the bubble radius was calculated via a simplified model which took into account the surface tension forces. Surface tension forces and non-condensable gas effects play no role in the Zwart-Geber-Belamri model.

For the sake of completeness the final equations used in this cavitation model for evaporation and condensation are:

$$R_e = F_{vap} \frac{3\alpha_{nuc}(1 - \alpha_v)\rho_v}{\mathfrak{R}_B} \left[\frac{2}{3} \left(\frac{P_v - P}{\rho_l} \right) \right]^{\frac{1}{2}} \quad 4.34$$

$$R_c = F_{cond} \frac{3\alpha\rho_v}{\mathfrak{R}_B} \left[\frac{2}{3} \left(\frac{P - P_v}{\rho_l} \right) \right]^{\frac{1}{2}} \quad 4.35$$

Where F_{vap} and F_{cond} are empirical constants equal to 50 and 0.01 respectively (ANSYS 2011a) and α_{nuc} is the nucleation site volume fraction fixed at 5×10^{-4} .

4.5 Schnerr and Sauer cavitation model

The Schnerr and Sauer (ANSYS 2011a) cavitation model is based on the assumption that the phase change rate, R , and the vapour volume fraction, α , follow the equations:

$$R = \frac{\rho_v\rho_l}{\rho} \frac{d\alpha_v}{dt} \quad 4.36$$

$$\alpha = \frac{n \frac{4}{3} \pi \mathfrak{R}_B^3}{1 + n \frac{4}{3} \pi \mathfrak{R}_B^3} \quad 4.37$$

Then Schnerr and Sauer derived the equation for R by following a similar approach to Singhal et al. and achieved the following equations:

$$R = \frac{\rho_v\rho_l}{\rho} \alpha(1 - \alpha_v) \frac{3}{\mathfrak{R}_B} \sqrt{\frac{2}{3} \frac{(P_v - P)}{\rho_l}} \quad 4.38$$

$$\mathfrak{R}_B = \left(\frac{\alpha_v}{1 - \alpha_v} \frac{3}{4\pi n} \right)^{1/3} \quad 4.39$$

Equation 4.38 can be specified for the evaporation and condensation cases:

$$R_e = \frac{\rho_v \rho_l}{\rho} \alpha_v (1 - \alpha_v) \frac{3}{\Re_B} \sqrt{\frac{2(P_v - P)}{3\rho_l}} \quad 4.40$$

$$R_c = \frac{\rho_v \rho_l}{\rho} \alpha_v (1 - \alpha_v) \frac{3}{\Re_B} \sqrt{\frac{2(P - P_v)}{3\rho_l}} \quad 4.41$$

In the Shnerr and Sauer cavitation model, the bubble radius is calculated by means of the bubble number density n (Equation 4.39). Comparing equation 4.28-4.29, 4.34-4.35 and 4.38-4.39 one can see that, beside the surface tension forces and the non-condensable gas effect which are considered only in the Singhal et al. cavitation model, the three models differ in the density term in the equation for the phase change rate. For instance, in the Zwart-Geber-Belamri cavitation model, R depends on the density of the vapour while in the Singhal et al. cavitation model R depends on the ratio of the product of the liquid and vapour phase with the mixture density.

5 Comprehensive CFD model

5.1 Introduction

The present chapter is dedicated to a detailed discussion of the CFD model which is the core part of the entire project. The model being described is in fact composed of several different overlapped models, each one of them handles one of the features which characterize the fluid dynamics of pumping. One may refer to it as a modular model which was created in several intermediate steps of increasing complexity. The reader can understand quite easily the intermediate steps the author made use of in order to achieve the advanced model.

Below is a brief summary of the features which will be discussed in the following paragraphs:

1. Customized boundary conditions.
2. Water compressibility model.
3. Moving mesh technique.
4. Valve dynamics User Defined Function (UDF).
5. Multiphase model with mass transfer due to cavitation.

5.2 Boundary and initialization conditions

The CFD model simulated a complete pumping cycle composed of (in order) an inlet stroke and an outlet stroke as already described in chapter 2. The model considers only one out of three chambers of the triplex WEIR SPM TW2500 Destiny pump showed in Figure 5-1, the section of the chamber is shown in Figure 5-2.

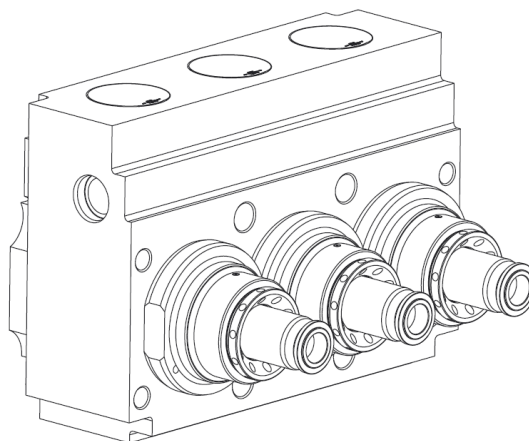


Figure 5-1: Fluid end of the pump utilised.

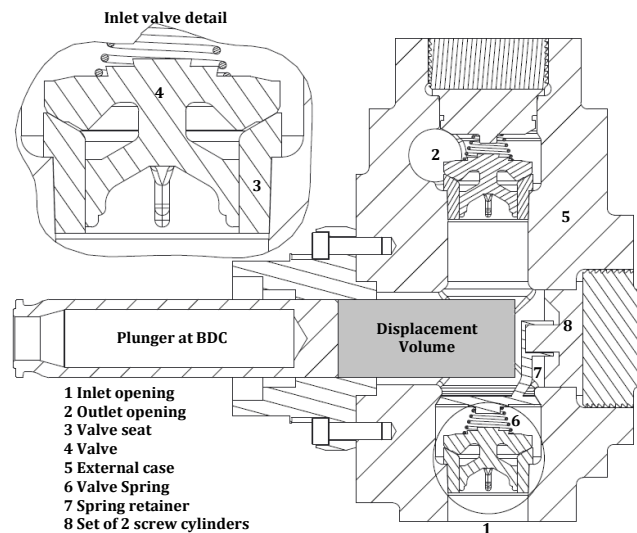


Figure 5-2: Schematic of the chamber section of a triplex pump including the nomenclature.

As described in chapter 2 as well as by Iannetti (A. Iannetti et al. 2014) the simulation begins with the plunger positioned in its Top Dead Centre (TDC) and the valves on their seats closed and sealed by two preloaded springs. At the beginning of the inlet stroke the plunger moves backwards expanding the pumping chamber and creating a pressure difference between the inlet manifold and the chamber itself. When the pressure difference exceeds the spring preload the inlet valve lifts off the seat following the dynamics imposed by its mass, the stretch of the spring and the pressure field in the valve vicinity. The water then fills the displacement volume created by the plunger motion. At the end of the suction stroke when the plunger approaches its Bottom Dead Centre (BDC) the pressure difference between the inlet manifold and the chamber is restored and the valve returns to the seat. At the beginning of the delivery stroke the plunger moves forward increasing the chamber pressure until its value exceeds the delivery line pressure by the amount provided by the outlet valve spring preload. Then the outlet valve opens and follows its dynamics so that the displacement volume previously filled by water is delivered to the outlet.

The dynamics of the pumping cycle needed:

- The initialized geometry of the fluid volumes as the valves and the plunger motion changes the geometry each time step of the simulation.
- The initialization velocity (time 0 of the simulation) and pressure inside the volume and on the boundary surfaces (inlet and outlet pipes).
- The variation of the inlet and outlet pressure as mass flow is sucked or delivered. As the inlet and outlet lines were not modelled entirely, the model was provided

with the pressure drop-mass flow characteristic curves of the inlet and outlet pipes to allow a mass flow dependent inlet and outlet pressure which is more realistic.

- The law of the plunger motion.

Figure 5-3 shows the operation of the extraction of the fluid volumes from the solid ones. The operation was performed making use of the CAD solid volume of the pump with the valve closed and the plunger at the TDC position (pump configuration at initialization time). The reader may rely on Figure 5-2 and Figure 5-3 to recognize the position of the outlet surface which is perpendicular to the schematics section plane.

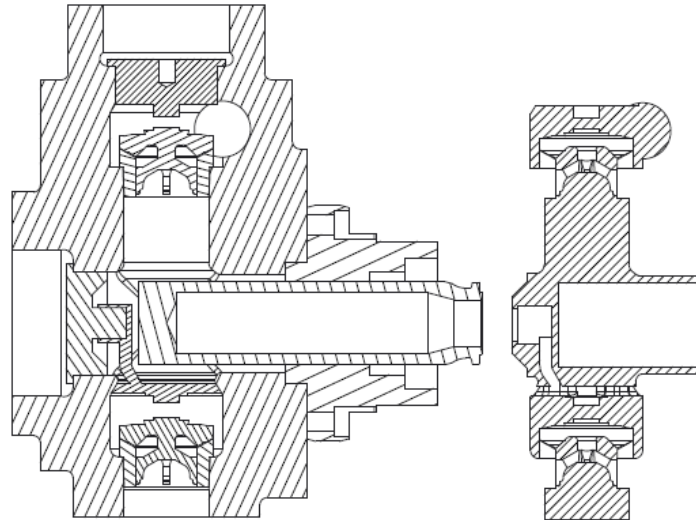


Figure 5-3: Solid to fluid volumes: the plunger is located in the TDC position and the valves are both closed, just the parts of the inlet and outlet pipes close to the pump were modelled.

The inlet stroke was thought to come from a previous outlet stroke which provided the initial chamber volume velocity and pressure. A good approximation of these values is:

- Zero flow velocity in the whole chamber volume as well as in the outlet and inlet surfaces. This is justified considering that the plunger ends the outlet stroke with a zero velocity at the TDC.
- Initial chamber pressure equal to the outlet pressure. The outlet stroke is carried out at a pressure which is greater or equal to the outlet pressure. The assumption of chamber pressure equal to the outlet pressure at the end of the stroke was considered reasonable.

The inlet and outlet pressure boundary conditions deserve a further description. As explained in (A. Iannetti et al. 2014), mass flow dependent pressure inlet and outlet conditions were chosen to introduce the correct behaviour of the inlet and outlet pipe as the major part of the

inlet and outlet pipeline was absent from the model. The mass flow dependent pressure condition, in fact, accounts for the presence of the missing parts of the pipes.

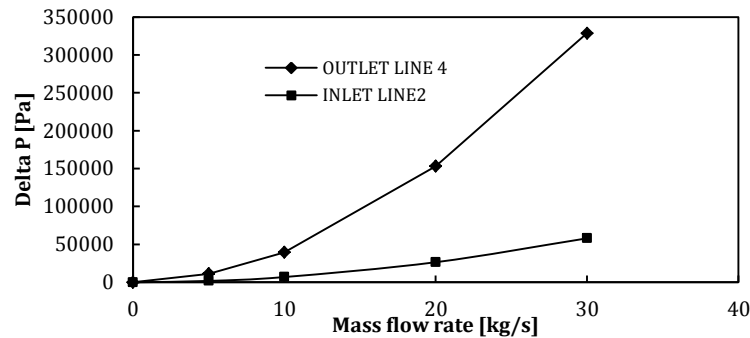


Figure 5-4: Pressure loss-mass flow characteristics of the inlet and outlet pipes. The values were calculated via independent CFD simulations carried out by fixing the geometry of the pipes at 4 different mass flow rates.

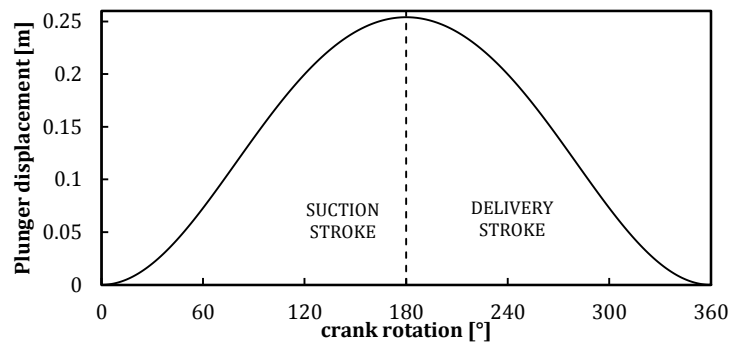


Figure 5-5: Plunger displacement Vs crank rotation angle.

Figure 5-4 represents the piecewise linear law of the pressure drop imposed on the inlet and outlet boundary surfaces. The trends were calculated using independent steady state CFD models of the complete geometries of the pipes using the four mass flow rates highlighted by the markers. The geometry of the pipes was not presented because it is beyond the scope of the present chapter. The figure shows the hypothesis chosen to utilise a pressure loss higher in the outlet pipe than in the inlet one. This kind of boundary condition performs a check on the inlet (and outlet) flow after each iteration and updates the pressure value according to it. The mass flow rate is in turn dependent on the position of the valves and plunger which are driven by independent tools.

5.3 Water compressibility model

In the fluid dynamic model of the flow, the assumptions of continuous and isothermal fluid were made. The Reynolds averaged method to deal with the velocity fluctuation due to turbulence was chosen along with a standard k-epsilon model to solve for the Reynolds

stress tensor. The working fluid (clean water) was considered to be a single-phase Newtonian fluid. The set of the Reynolds Averaged Navier-Stokes equations (RANS) for an incompressible flow they are:

$$\frac{\partial U_i}{\partial x_i} = 0 \quad 5.1$$

$$\rho \frac{\partial U_i}{\partial t} + \rho U_j \frac{\partial U_i}{\partial x_j} = -\frac{\partial P}{\partial x_i} + \frac{\partial}{\partial x_j} \left[\mu \left(\frac{\partial U_i}{\partial x_j} + \frac{\partial U_j}{\partial x_i} \right) + \tau_{ij} \right] \quad 5.2$$

$$\tau_{ij} = 2\mu_T \left(\frac{\partial U_i}{\partial x_j} + \frac{\partial U_j}{\partial x_i} \right) - \frac{2}{3} \rho k \delta_{ij} \quad 5.3$$

$$\mu_T = \frac{\rho C_\mu k^2}{\varepsilon} \quad 5.4$$

$$\rho \frac{\partial k}{\partial t} + \rho U_j \frac{\partial k}{\partial x_j} = \tau_{ij} \frac{\partial U_i}{\partial x_j} - \rho \varepsilon + \frac{\partial}{\partial x_j} \left[\left(\mu + \frac{\mu_T}{\sigma_k} \right) \frac{\partial k}{\partial x_j} \right] \quad 5.5$$

$$\rho \frac{\partial \varepsilon}{\partial t} + \rho U_j \frac{\partial \varepsilon}{\partial x_j} = C_{\varepsilon 1} \frac{\varepsilon}{k} \tau_{ij} \frac{\partial U_i}{\partial x_j} - C_{\varepsilon 2} \frac{\varepsilon^2}{k} + \frac{\partial}{\partial x_j} \left[\left(\mu + \frac{\mu_T}{\sigma_\varepsilon} \right) \frac{\partial \varepsilon}{\partial x_j} \right] \quad 5.6$$

According to (ANSYS 2011b), an essential modification of the standard set of equations 5.1 to 5.6 was needed to account for liquid compressibility. A PD pump chamber is, in fact a closed volume until the valves open. Because of valve inertia there are times within the pumping cycle (e.g. the beginning of the inlet stroke) when the inlet and outlet valves are both closed. In these cases a compressible model of the liquid is crucial to fulfil the continuity equation. A compressible model is also essential in cases of very high delivery pressure.

The hypothesis of *slightly* compressible flow was made. The density, ρ , constant in 5.2 to 5.6, was replaced with a suitable function of pressure $\rho(P)$. The slightly compressible flow hypothesis considered the density to be affected by the pressure whilst the pressure not affected by the density variation. The coupling density-pressure may therefore be considered one way. The compressibility model UDF can be seen in the appendix.

The explicit function of *equation 5.7* was considered for this purpose:

$$\rho = \rho_{REF} \left(1 - \frac{P - P_{REF}}{B} \right) \quad 5.7$$

Equation 5.7 comes from the definition of the modulus of compressibility of water (bulk modulus) B given in *equation 5.8*:

$$B = \rho \frac{\partial P}{\partial \rho} \quad 5.8$$

To transform *equation 5.8* into *equation 5.7* the hypothesis of constant bulk modulus with respect to the change of pressure was made.

$$c = \sqrt{\frac{B}{\rho}} \quad 5.9$$

The speed of sound c in the media is also taken into account by *equation 5.9*.

The unknown quantities $U_x, U_y, U_z, P, k, \varepsilon$ were calculated by means of iterative solution of the set of *equations 5.1 to 5.6* while the density was treated explicitly by *equation 5.7* which utilised the result of the pressure field calculated by the pressure correction equation.

5.4 Moving mesh

To allow the motion of the valves and the plunger surfaces a further decomposition of the fluid volumes of *Figure 5-3* was needed. *Figure 5-6* shows the decomposition pattern discussed in (Aldo Iannetti, M. Stickland, et al. 2014) to handle the moving mesh technique.

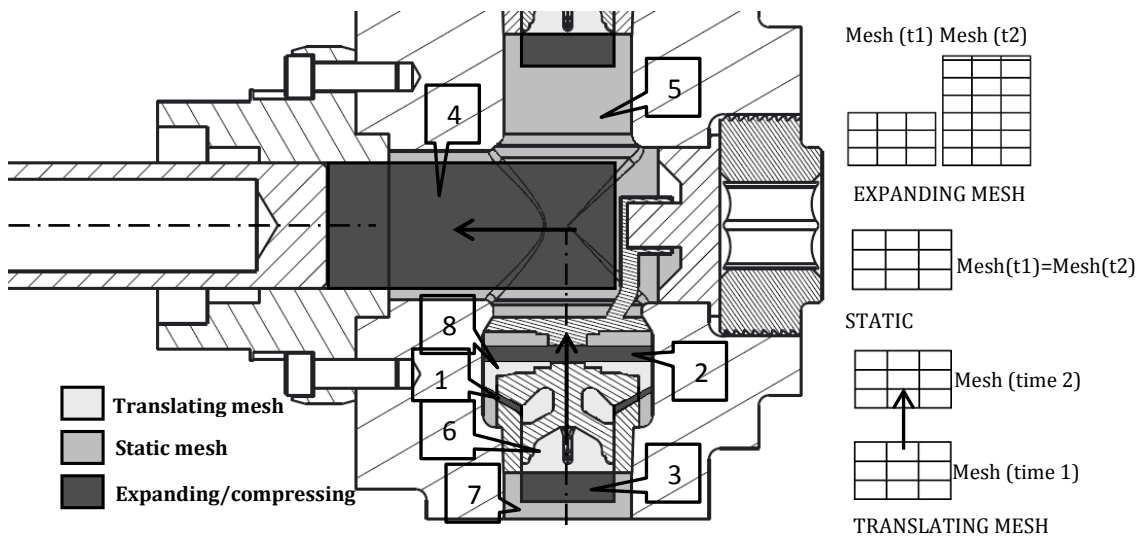


Figure 5-6: decomposition pattern of the fluid volumes in the vicinity of the inlet valve and plunger essential to handle the moving mesh algorithms. The numbered items are listed in *Table 5-2*.

Figure 5-6 shows the detailed subdivision of the fluid volumes around the inlet valve and the plunger. The motion of the plunger was simulated by the expansion of the initial displacement volume. For this purpose a cylindrical volume attached to the plunger top surface was considered in the subdivision of the overall fluid volume and a full hexahedral mesh was chosen to mesh it. The expansion of the chamber volume was simulated by means of parallel layers of hexahedral cells created from the TDC to the BDC. The rate of layer

creation was governed by the “In-Cylinder” technique already mentioned which turned the set of reciprocating motion parameters provided to the solver (shaft angular speed and phase, connecting rod length and crank diameter) into the plunger velocity so that its position at every time step followed the trend shown in Figure 5-5. The “In-Cylinder” technique therefore linked together the reciprocating motion with the moving mesh (ANSYS 2011a).

The motion of the valves was managed in a similar way. Two cylindrical volumes were considered in the decomposition pattern of the fluid volume in the vicinity of the valves. They were placed on the top surface of the valve and on the bottom of it respectively. They were meshed by means of hexahedral cells. When the valve lifted up, the top volume compressed destroying cell layers while the bottom volume expanded adding cell layers instead and vice versa during the valve closing motion. To simulate the growth of the valve-seat gap volume during valve opening, an annular volume was inserted between the valve and the valve seat (all volumes are visible in Figure 5-6) and meshed by means of hexahedral cells. The expansion/reduction of the gap volume process is similar to the one explained above. The volumes in between the expanding/compressing parts meshed using tetrahedral cells and a rigid translational motion strictly following the gap layering generation was applied to them in order to keep the external valve shape unchanged during the valve motion. The valve layering motion and rigid motion were governed by a single User Defined Function (UDF) discussed in the next paragraph.

To ensure volumetric continuity throughout the flow stream, the valve-seat gap volume thickness was initialised as 0.25 mm as described by Iannetti (Aldo Iannetti, M. Stickland, et al. 2014) instead of 0 mm. In order to avoid any mass flow when the valves were closed, a cylindrical check surface within the gap volume was set. The check surface was converted from wall type to interior when the incipient motion condition was achieved and converted back to wall at the end of the valve motion when it returned to the seat again. The initial height of this volume was the result of a balanced choice between two opposite objectives:

- To keep as much as possible the valve-seat configuration close to the real design.
- Not to exceed the minimum dimensions required by the pre-processing CAD software.

A preliminary mesh sensitivity analysis was carried out when the simplified single phase simulations were undertaken. The analysis was aimed at defining the best mesh size and spacing within the opposite needs of achieving good accuracy and keeping low the computational time. For this purpose three mesh sizes were tested: 3, 5 and 6 Million overall

initial cells respectively. The 5 M cells model was chosen as the starting point to define the proper mesh for the multiphase model tests. For all of the models tested and discussed in this dissertation the mesh spacing specification were kept consistent with the ones utilised by the mesh sensitivity analysis. The details of the meshes are listed in Table 5-1 and Table 5-2.

Table 5-1: Mesh sensitivity test, three mesh sizes were tested.

Mesh	Number of Cells [M]	Average Skewness [-]	Approx computational time [h]
1	3	0.24	48
2	5	0.26	60
3	6	0.22	72

Table 5-2: Mesh 2 details summary.

Location (see Figure 5-6)	Volume description	Mesh type	Size details min- max [mm]	Mesh motion
1	Valve-seat lift	Hexahedral	0.2-1	Expanding
2	Inlet valve	Wedge	1-3	Compressing
3	Inlet valve	Hexahedral	2-3	Expanding
4	Displacement	Hexahedral	2.5	Expanding
5	Pump chamber	Tetrahedral	2.5-5	Static
6	Valve internal	Tetrahedral	1-2.5	Translating
7	Inlet manifold	Tetrahedral	2-4	Static
8	Valve top volume	tetrahedral	1-2	Translating

5.5 Valve Dynamics UDF

An important contribution the project being discussed provides to the scientific literature is the capability of the model to manage the relationship between the valve lift and the pressure field within a CFD solver. The valve lift is driven by the pressure generated in the chamber which, in turn, depends on the plunger displacement and the valve position. To deal with a two-way coupling problem, an automatic tool capable of updating the valve lift every time step according to the pressure field generated by the geometry configuration at the previous time step was needed. Such a tool is missing in the CFD model discussed by Ragoth (Ragoth & Nataraj 2012). The hypothesis of a one-dimensional dynamics equation of the valve movement was made as it was thought to move along its axis of symmetry while the translation along the perpendicular axis and the three rotations were neglected. The dynamics equation 5.10 results:

$$F_{TOT} = F_p + F_s + mg \quad 5.10$$

F_p was calculated by means of integration of the pressure forces on the valve surfaces and was updated every time step. F_s , the spring force, was a known non-linear function of the valve stretch (shown in Figure 3-13) was updated every time step. The UDF, called once per time step, also integrated the equation 5.11 of motion of the valve:

$$m\ddot{x}_{[i]} = F_{P[i-1]} + k(x)x_{[i-1]} + mg$$

5.11

The result of the integration was the current valve position $x_{[i]}$ needed to update the mesh layering algorithm and fixed the spring force for the next time step. In the force balance of equation 5.10 the structural damping of the spring, as well as the damping due to friction between the valve body and the seat, were neglected.

Figure 5-7 summarises the steps executed by the UDF attached to the valve surfaces to drive the layering algorithm. The figure shows also how the UDF relates to the RANS solver.

A sensitivity analysis on the time step was also carried out. Three time step sizes were tested (0.03125°, 0.0625° and 0.125° of crankshaft rotation). The three of them were chosen to be sufficiently small to be compatible with a first order explicit Euler algorithm defined by equation 5.11. As direct consequence, the outcomes of the time step sensitivity analysis highlighted no differences among the three cases' results.

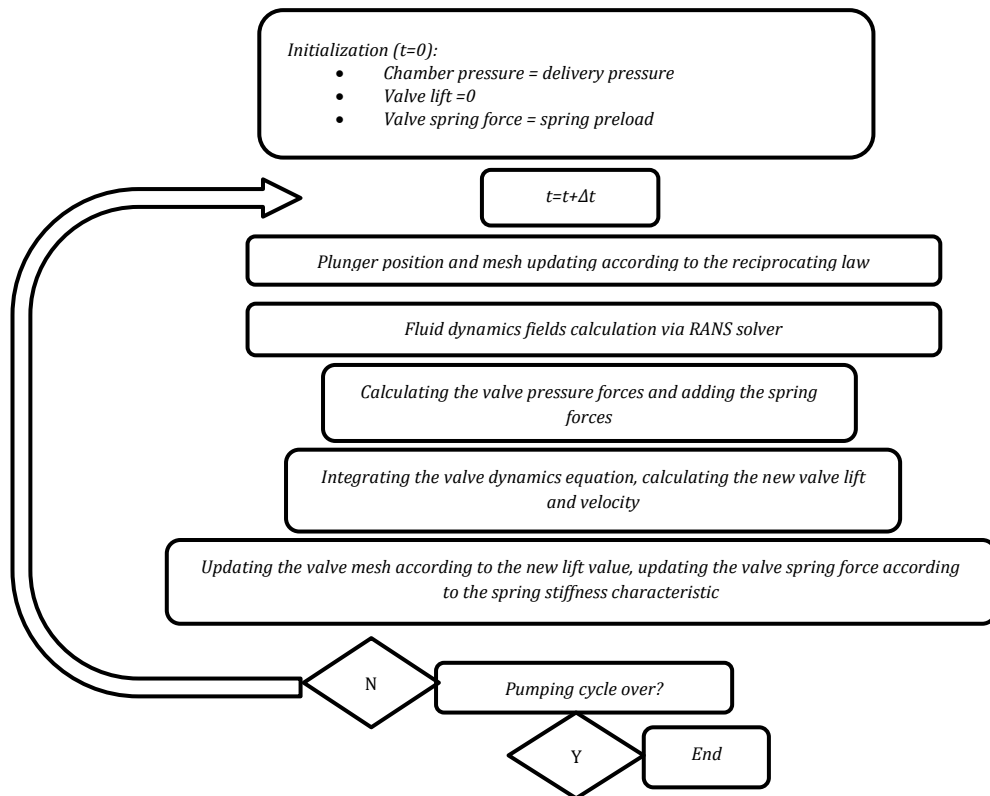


Figure 5-7: Valve motion UDF: the diagram shows how the UDF interacts with the RANS solver to achieve the self-actuating valve model (Aldo Iannetti, M. Stickland, et al. 2014), the C++ code can be viewed in the appendix.

5.6 CFD model settings

Table 5-3 summarises the settings chosen for the solver. Because of the wide range of flow velocity, y^+ varied significantly in space and time. Therefore the enhanced wall treatment (ANSYS 2011a) was considered for the near wall function. The enhanced wall treatment adjusts the standard wall function in cases where its requirements is not achieved (slow flow velocity, $y^+ < 100$).

The k- ϵ turbulence model was preferred over the k- ω because it provided better convergence behaviour. The need for improving the convergence also drove the decision on the SIMPLE Pressure-Velocity coupling algorithm chosen (ANSYS 2011a). The second order spatial discretization scheme of the upwind type provided robustness together with good accuracy against numerical diffusion. The transient formulation of first order implicit was the only option available with the multiphase model and was chosen for this reason.

The mixture model (ANSYS 2011a) was chosen for the multiphase approach because it does not require significant computational costs. It is important to specify the set of transport equations the mixture model solves for:

- 1) Continuity equation of the mixture (water and secondary phase together).
- 2) Momentum equation for the mixture (water and secondary phase together).
- 3) Volume fraction equation for the secondary phase (vapour and air together).

It is clear that the mixture equation is a simplified and cheap numerical model which does not couple the phases strongly with respect to the Eulerian model (ANSYS 2011a) which solves:

- 1) Continuity equation for the mixture (water and secondary phase together).
- 1) One Momentum equation for each phase.
- 2) Volume fraction equation for the secondary phase (vapour and air together).

Table 5-3: Solver Settings summary

Solver	RANS, pressure based, transient			
	Mixture model (ANSYS 2011a)			
Models	Multiphase	Phases	Water liquid	Primary phase
			Water vapour	Secondary phase
	Turbulence	k- ϵ Standard	Enhanced wall treatment	
	Cavitation	Singhal et al.	15 ppm air (ideal gas)	
Pressure-Velocity coupling	SIMPLE			

Spatial discretization	Momentum	Second order upwind
	Vapour	First order upwind
	Turbulent kinetic energy	Second order upwind
	Turbulent dissipation rate	Second order upwind
Transient formulation	First order implicit	
Under relaxation factors	Pressure	0.3
	Momentum	0.7
	Vapour	0.5
	Turbulent kinetic energy	0.8
	Turbulent dissipation rate	0.8
Residuals	10^{-3}	
Time step	0.125° crank rotation $\equiv 1.6 \times 10^{-4}$ s @130 rpm	
Max Iteration per time step	35	
UDFs	Compressibility of water (see paragraph 5.3)	
	Valve dynamics (see paragraph 5.5)	

A 12 GB RAM computer with an Intel Xeon W3670 @ 3.2GHz processor was employed for the simulation and the time needed for a single run (1 pumping cycle only) took between 48 hours (the smallest mesh with a single phase model) to around 3-4 weeks (the biggest mesh with a multiphase model).

5.7 Mesh sensitivity test

When the multiphase and cavitation models were added, the mesh sensitivity analysis was performed again. In this new analysis, two different sizes of mesh were tested in order to make sure that the solution did not depend on the grid and also to find the optimum mesh size capable of bringing down the computational costs in all the simulations where the multiphase model was employed. Because of the higher computational time needed, for the complete multiphase simulations, the analyst made use of the symmetry feature of the pump chamber. Therefore, half the pump was modelled and meshed. This significantly reduced the number of cells required. Figure 5-8 shows the detailed view of the two sizes of mesh tested in the vicinity of the valve where special care was taken. Figure 5-8 represents the coarse mesh of 2.5 million of cells (corresponding to the 5M cells test of the preliminary mesh sensitivity analysis) and the fine mesh of 3.7 million of cells respectively on the left and the right. It is important to point out that the amount of cells specified refers to the initial configuration at initialization time of the simulation. The number of cells increased during the calculation as the displacement volume as well as the valve-seat gap volume increased.

To refine the mesh and move from 2.5 to 3.7 million of cells a proportional smaller size of mesh was chosen, the cell size was decreased further in the vicinity of the valve gap (the region highlighted in Figure 5-8) as the maximum flow velocity was expected in that zone.

Obviously the setting controls, operating and boundary condition chosen to run the different mesh size models was kept consistently the same in order to compare the results. The only different choice the author made before launching the two models concerned the pressure inlet boundary condition. It was decided to carry out the set of mesh sensitivity analysis using a constant inlet pressure of 0 PaG instead of the mass flow adjustable pressure inlet which was shown in Figure 5-4.

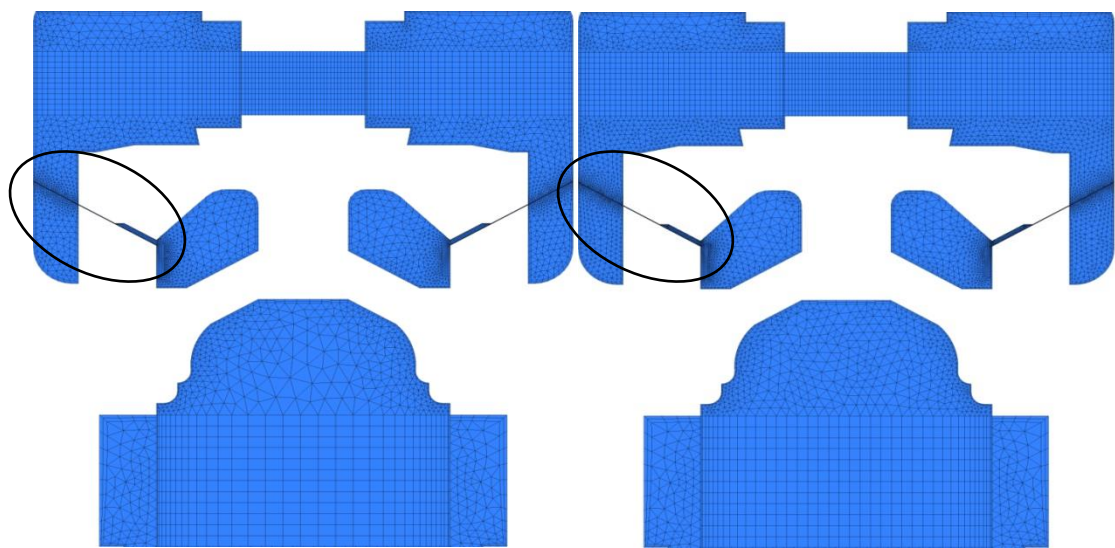


Figure 5-8: (left) 2.5 M cells mesh, (right) 3.7 M cells mesh.

For the comparison of the physical quantities the following monitors were chosen:

1. *Chamber pressure.* The pressure-time history recorded by a virtual probe located at a static point close to the TDC position of the plunger.
2. *Plunger 2nd phase mean fraction.* The 2nd phase (vapour + air) volume fraction in the vicinity of the top surface of the plunger. The surface monitor moves together with the plunger top surface.
3. *Gap volume 2nd phase mean fraction.* The average 2nd phase fraction present in the valve gap volume.
4. *Inlet mass flow.* The mass flow calculated on the inlet surface. Its integral is compared to the theoretical mass of the displacement volume filled with water at ambient conditions in order to estimate the volumetric efficiency loss.

5. *Inlet valve lift history.*
6. *Valve-seat gap volume integral of 2nd phase.* Shows the time history of the volume occupied by the 2nd phase within the valve-seat gap.
7. *Chamber integral of 2nd phase.* Shows the time history of the volume occupied by the 2nd phase within the pump chamber.

The list of monitor will be utilised also to discuss the results in the analysis of the following chapters, a few exceptions will be made and discussed as soon as necessary.

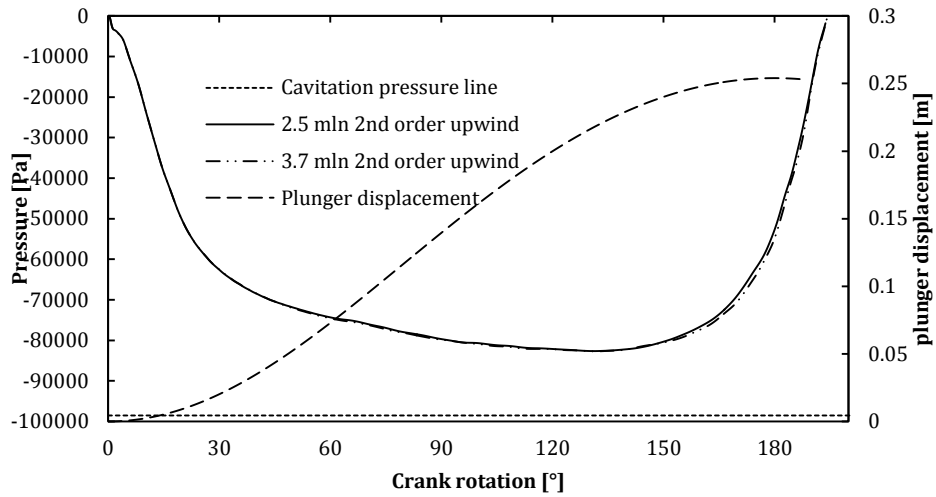


Figure 5-9: Chamber pressure time history.

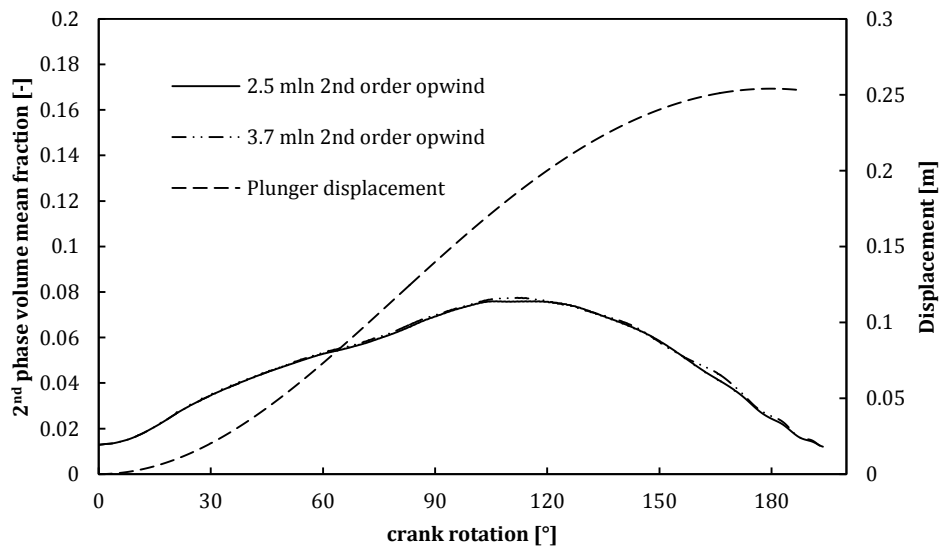


Figure 5-10: Plunger vicinity 2nd phase volume fraction

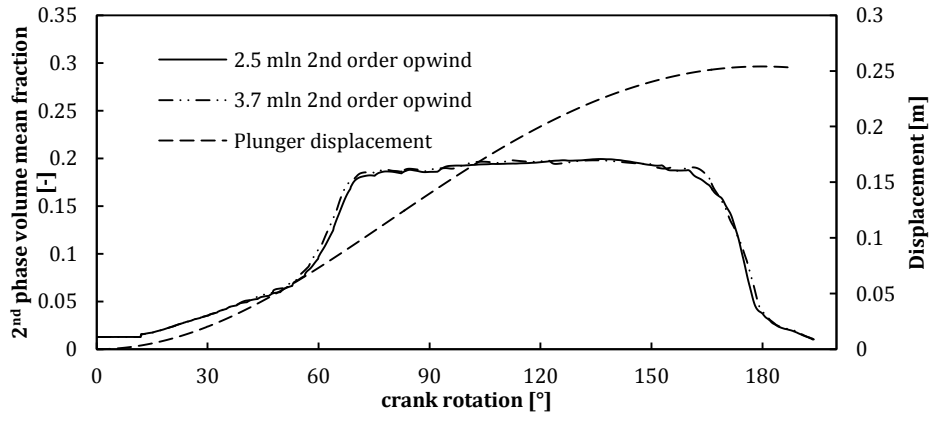


Figure 5-11: 2nd phase valve-seat gap volume mean fraction

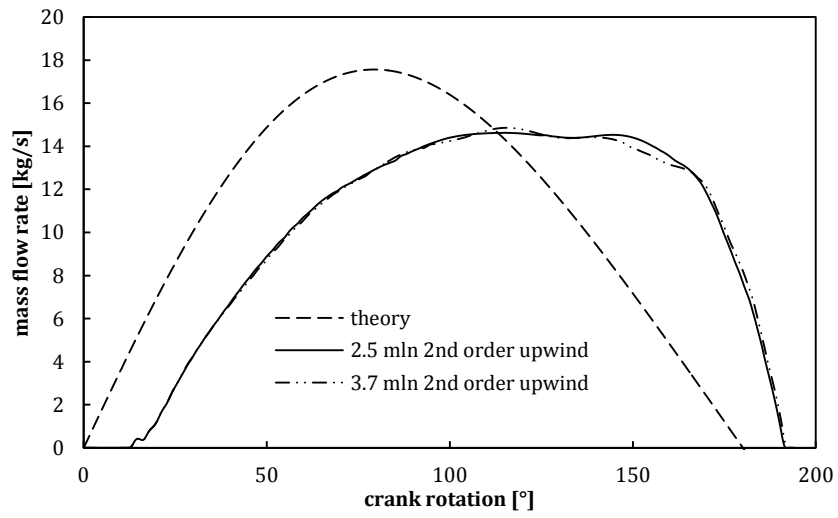


Figure 5-12: Inlet mass flow.

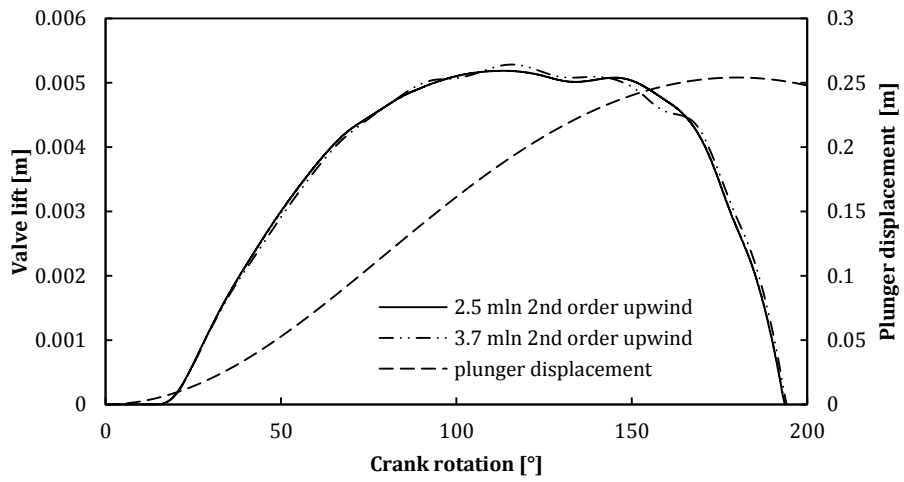


Figure 5-13: Inlet valve lift.

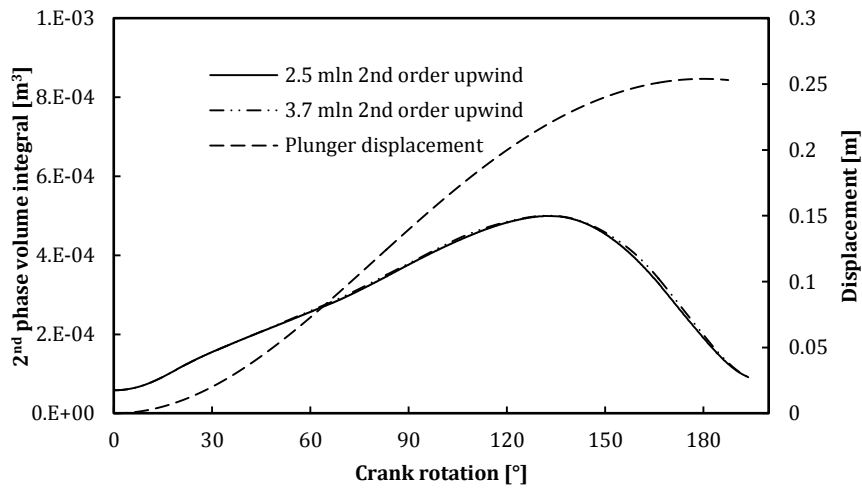


Figure 5-14: 2nd phase chamber volume integral.

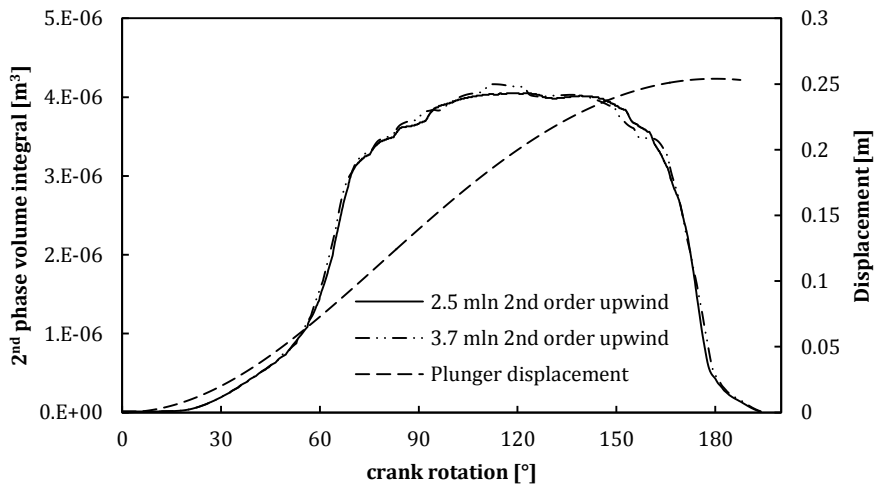


Figure 5-15: Valve-seat gap volume integral of the 2nd phase

Figure 5-9 to Figure 5-15 show the plots of the monitor data discussed above. They compare the same quantities for the mesh sensitivity analysis. The scientific meaning of the trends shown in the figures will be discussed in chapter 7, 8 and 9. What the author would like to point out to the reader in this paragraph is that the situation described by all the figures demonstrates with no doubt that qualitatively the two meshes provided very similar results as the curves are nearly overlapped. This is clear evidence that the 3.7 million cells grid did not provide further improvement to the CFD model when compared to the 2.5 million cell grid.

Table 5-4: Quantitative comparison of the performance of the grids tested

Grid	Inlet valve opening time [Crankshaft°]	Inlet valve closing time [Crankshaft°]	Volumetric efficiency [%]	Max chamber 2 nd phase integral [m^3] × 10 ⁻³	Max valve gap 2 nd phase integral [m^3] × 10 ⁻⁶
2.5 M cells	12	193.75	97.16	0.4996	4.05

3.7 M cells	12	194.25	97.12	0.50044	Difference [%] 0.168	4.1643	Difference [%] 2.82
----------------	----	--------	-------	---------	----------------------------	--------	---------------------------

Table 5-4 confirms quantitatively what was stated earlier; the difference in performance of the two grids tested never exceeded 3%. The reader may assume that the grids provided almost identical results. The analyst chose to carry on the project making use of the coarsest mesh and when new geometries needed to be meshed the overall cell size was chosen according to the specifications utilised for the 2.5 million cells grid discussed in this paragraph.

5.8 Conclusion

In this chapter the author explained how it was created the comprehensive CFD model to simulate the pumping cycle of a PD pump in cavitating conditions. The main features of the model can be summarised as follows:

- Fully transient model which made use of the moving mesh technique to handle the displacement of the plunger as well as the valves lift.
- Compressibility of the liquid taken into account by means of a UDF
- Two-way coupling between the valves lift and the chamber pressure field so that the valves are self-actuated
- The Mixture model (ANSYS 2011a) took care of the 2-phase flow model composed of water and vapour
- The “full” cavitation model by Singhal et al. (Singhal & Athavale 2002) was added to drive the phase change. Within the Singhal cavitation model, the non-condensable air effect which was considered as an ideal gas and treated as an explicit term. The presence of non-condensable gas results in a three-phase flow rather than two-phase.
- The inlet and outlet pipe were cut five diameters upstream and downstream the valves to account for the presence of the inlet manifold and the outlet pipe. A mass flow adjustable pressure inlet and outlet boundary conditions were set. This advanced type of boundary condition produced a mass flow/pressure drop characteristic of the pipes which is shown on the left of Figure 5-4. The curves were estimated by means of separate, steady state, CFD simulations focused on the inlet manifold and outlet pipe only.

A mesh sensitivity test was also carried out and discussed to prove the validity of the 2.5 million cells mesh which will be utilised in the following parts of the project.

6 Cavitation in PD pumps

6.1 Introduction

In order to facilitate the reading of the results discussion of the chapters 7, 8 and 9, this chapter aims at providing, in advance, an overview of what has been already published in the free technical literature concerning the analysis of cavitating flows in PD pumps. It is a concern of the author to explain also a few physics concepts which will be useful to complete the description of the phenomenon. As already stated the lack of literature on the topic is not beneficial in shedding light on the physics of cavitating flow in PD pumps and this increases the importance of the project presented to fill this gap.

According to many authors cavitation in any device can be classified on the basis of the regime the phenomenon is subjected: incipient, partial and full cavitation. It can be classified also according to the causes which generate the phenomenon in PD pumps which are the expansion of the plunger, the high velocity flow and the viscous forces in the valve-seat lift volume. Literature usually refers to them as expansion cavitation, flow induced cavitation and pseudo adhesion respectively. Furthermore, there are aspects of the physics of the phenomenon which should not be underestimated in the previous classification of cavitation causes and regimes:

1. *Location.* Cavitation may appear in a localised zone within the pump chamber or may be randomly present in a wide region of it.
2. *The presence of dissolved air in water.* In the real world water contains a little quantity of air which is dissolved. The amount (volumetric fraction) depends on the pressure and temperature. When the conditions change, air may come out of the liquid in the form of air bubble. Once generated, air bubbles behave as an ideal gas. They expand or compress following the external pressure field and, under high pressure, they disappear returning back into the liquid phase in the form of dissolved gas. This process is called gas cavitation and is different from vapour cavitation as it deals with gas instead of vapour and does not cause damage.

6.2 Cavitation Regimes

Opitz (Opitz & Schlücker 2010; Opitz et al. 2011) categorized cavitation in PD pumps as the following regimes:

- *Incipient cavitation.* It occurs in the very first part of the induction stroke when the plunger starts to move backwards and the valve is still on the seat because of the

spring preload. According to Opitz, in this case the chamber experiences the vapour pressure for a very short time during which bubbles are randomly distributed in the entire chamber without getting in contact with walls. He states that this cavitation is not harmful for the pump but he does not specify if incipient cavitation deals with the expansion of the dissolved air (air cavitation), vapour cavitation or both. It is important to point out to the reader that Opitz carried out an experimental study only where it was very difficult to distinguish between air and vapour.

- *Partial cavitation.* In this regime the chamber pressure remains constant at the level of the vapour pressure from the beginning of the suction stroke to the end of it when bubbles collapse. No significant delay in the suction stroke end is observed. The bubble implosion which takes place because of certain pressure conditions which can be associated to the water hammer, does not affect the outlet stroke. Depending on when the water hammer appears the partial cavitation can be divided into:
 1. *Incipient partial cavitation.*
 2. *Advanced partial cavitation.* As the incipient partial cavitation, it is characterized by the impact within the first half of the suction stroke. Bubbles are distributed in the pump chamber and even if Opitz observed their implosions in the vicinity of the chamber walls, he “could not find any hint of damage”. This kind of regime is, thus, harmless.
 3. *Distinctive partial cavitation.* It is characterized by the backformation of volume expansion generated cavitation during the second half of the suction stroke. Opitz is not certain on the grade of harmfulness of this regime of cavitation.
- *Full cavitation.* According to Opitz it occurs when the bubble implosion takes place in the first part of the outlet stroke. A very high pressure surge is expected along with a significant decrement of the performance. There is no doubt on the fact that full cavitation is very dangerous for the pump.

6.3 Cavitation Causes

Many authors have also classified cavitation in PD pumps according to the triggering causes which may differ depending on the regimes of cavitation and the location where it appears. Opitz (Opitz et al. 2011) identified the following main causes: plunger expansion, pseudo-adhesion and flow induction.

6.3.1 Cavitation due to expansion

The opening of the inlet valve is always affected by a certain delay because of the inertia. Therefore at the beginning of the suction stroke the flow through the valve is lower than the equivalent flow rate generated by the plunger which is moving backwards. This generates an expansion of the working liquid thus a low pressure. Sometimes the vapour pressure can be exceeded and cavitation may arise in the pump chamber and/or near the plunger. Opitz does not explain whether the cavitation due to expansion is real vapour cavitation or just gas cavitation.

6.3.2 Cavitation due to pseudo-adhesion

Just after the liquid expansion, when the inlet valve spring preload is exceeded, the valve starts to lift off the seat, in the very first part of the valve lift, the gap is so small that it cannot be filled quickly enough by the flowing liquid because of the high viscous forces. A low pressure region within the gap is generated and cavitation may take place. Once the gap height exceeds a certain threshold, cavitation disappears. Other authors such as Price (Price et al. 1995) referred to the same phenomenon as viscous adhesion or sticktion and identified an equation to estimate the sticktion force:

$$F_S = \frac{\mu b^3}{(y + e_0)} \cdot \frac{de}{dt} \cdot L \quad 6.1$$

According to Price, in fact the viscous adhesion force F_S depends on:

- μ = Liquid absolute viscosity
- b = width of seat
- e = film thickness
- e_0 = film initial thickness
- y = valve lift
- L = circumferential length of the seat

6.3.3 Flow induced cavitation

Opitz and many other authors also identified the most common cause of cavitation which is due to a high flow velocity and a consequent low static pressure. In PD pumps this kind of cavitation is localised in the valve-seat gap volume after the pseudo-adhesion takes place. The gap height is not affected by significant viscous forces and the plunger position approaches the location of maximum velocity which induces the maximum flow rate through

the valve. According to the Bernoulli's effect the pressure may reach the vapour pressure. It is known that cavitation due to expansion always precedes the flow induced cavitation which overlaps the former after a certain delay.

6.4 Cavitation in PD pumps

A literature review on cavitation in PD pumps has not shed light on the relationship between the gas cavitation and the vapour cavitation which depends on the effect of the air dissolved in the liquid phase. According to the physics of the phenomenon, the air content in water depends on the external conditions. Lowering the pressure or increasing the temperature would let the dissolved gas out of the liquid phase. In a closed and expanding volume such as a pump chamber during the inlet stroke, air behaves like an ideal gas. It expands before the surrounding liquid as the bulk modulus of air is lower than the bulk modulus of water. It is, therefore plausible that gas cavitation precedes vapour cavitation which takes places when air expansion cannot mitigate the pressure drop any more due to the small amount (at ambient pressure 15 parts per million in mass fraction). A plausible theory which is under investigation and will be discussed in the next sections is the one relating expansion cavitation to gas cavitation as both of them must precede the flow induced cavitation.

Table 6-1 summarises the multiple phenomena occurring in PD pumps in regimes of full and developed cavitation. The first column defines the approximate (qualitative) temporal range within the inlet stroke (0° to 180° of crankshaft rotation) when the phenomena take place. Following is a further explanation of the time frames:

1. 0° - 15° *circa*. The plunger starts to move backward from the TDC position and a 0 velocity. The valve is still closed because of the spring preload and the possible high initial chamber pressure which approximately equals the delivery pressure as the inlet stroke comes from a former delivery stroke. The chamber is being decompressed by the plunger and the air comes out of the liquid phase as, at ambient temperature, the lower the pressure the lower the amount of air that can be dissolved in the water. In the technical literature it is not specified if, during this temporal range, vapour is generated but considering the very low plunger velocity the author doubts it. This justifies the “?” in the third column of Table 6-1. This statement was supported by the results published in (Aldo Iannetti, M. T. Stickland, et al. 2014).
2. 15° - 20° *circa*. The valve starts to lift off the valve seat, the valve-seat gap volume height is sufficiently small to cause the pseudo-adhesion cavitation. The author assumes that pseudo-adhesion effect is harsh enough to induce both vapour and air cavitation as viscous forces may be significant. Expansion cavitation overlaps.

3. 20° - 50° *circa*. The valve-seat gap volume height exceeds a certain threshold and viscous effects decrease. Pseudo-adhesion cavitation disappears but expansion cavitation still goes on as the plunger accelerates. As the valve is open and the flow through it is not zero it is unlikely that vapour is generated by the plunger. However the phenomenon needs further investigation.
4. 50° - 120° *circa*. The plunger reaches the maximum velocity and the valve achieves the maximum lift. The high velocity flow through the valve generates flow induced cavitation and a significant amount of vapour is generated in the same location, it spreads into the chamber afterwards. Flow induced cavitation is the most common cause of cavitation as it also affects other devices such as centrifugal pumps. Flow induced cavitation is also affected by gas cavitation as discussed by Ding (Ding et al. 2012).Expansion cavitation may continue also during this temporal frame as shown by Opitz (Opitz et al. 2011).
5. 120° - 180° *circa*. Expansion cavitation disappears as the plunger decelerates but, due to the inertia delay, the flow induced cavitation through the valve still goes on until the plunger compresses the vapour generated once the outlet stroke has started after 180° of crankshaft rotation.

Table 6-1: Full/developed cavitation cases, causes types and locations.

Crank rotation [°] (circa)	Expansion Cavitation			Flow induced cavitation			Viscous adhesion cavitation		
	Gas	Vapour	Location	Gas	Vapour	location	Gas	Vapour	Location
0-15	✓	?	Chamber and plunger vicinity						
15-20	✓	?	Chamber and plunger vicinity				✓	✓	Pseudo-adhesion in valve-seat gap volume
20-50	✓	?	Chamber and plunger vicinity						
50-120	✓	?	Chamber and plunger vicinity	✓	✓	Valve-seat gap volume			
120-180→				✓	✓	Valve-seat gap volume			

To assist the reader, Table 6-1 content can be further summarised as follows:

- Plunger expansion at low velocity causes a low chamber pressure field which generates gas cavitation which is usually not followed by vapour cavitation. This situation lasts for the first half of the inlet stroke.
- As soon as the inlet valve lifts off the valve seat cavitation takes place because of the pseudo-adhesion but this situation lasts only as long as the valve lift is small enough to create a high viscosity force in the small valve gap. Vapour is generated.
- When the plunger accelerates the high flow velocity through the valve triggers flow induced cavitation which is supported, but not caused by, the plunger expansion as it comes in a low static pressure situation created by the plunger displacement.

Table 6-1 was drawn utilising the notion previously present in the technical literature but also anticipating a few results obtained by the author which were also published such as (Aldo Iannetti, M. T. Stickland, et al. 2014) and (A. Iannetti et al. 2015). The challenging task of the CFD model creation is to simulate the three causing phenomena and highlight the relationship between them. The situation depicted by Table 6-1 points out that cavitation in PD pumps is different from other devices such as marine propellers or centrifugal pumps where the phenomenon is driven mainly by flow induced cavitation. The coexistence of the three phenomena described above is the peculiarity of cavitation in PD devices.

7 CFD Simulation of cavitation in PD pumps

7.1 Introduction

This chapter discusses the regimes of cavitating flow in PD pumps by means of four test cases by utilising CFD. The discussion is purely numerical as the data was generated by making use of the CFD model explained in chapter 5. At this part of the project the experiment data was not available yet and the accuracy of the results shown could not be verified. On the other hand the test cases were chosen in order to achieve the different cavitation regimes discussed in the previous chapter so that the consistency of the model could be investigated by qualitative comparison with literature data and consideration of the physics of the phenomenon. Furthermore, the criterion of changing the inlet pressure boundary conditions also led the analyst to:

- Shed light on the dynamics of the phenomenon. Again the author highlights the unlimited potential of CFD methods for post-processing the output. By storing the fluid dynamics field data of as many time steps as possible throughout the simulation that lasts for the entire pumping cycle, the analyst was able to record information which is nearly impossible to obtain by means of experimental tests. The dynamics of the phenomenon include:
 1. The causes
 2. The development of the phenomenon (e.g. where and when within the chamber the vapour is generated)
 3. The effects (e.g. performance drop)
- Understand the typical features of cavitation in PD pumps. The analysis carried out showed qualitative and quantitative features of the cavitating flow which could be related to literature data.

7.2 Test Cases

Four test cases were selected (Aldo Iannetti, M. Stickland, et al. 2014), all of them represented the same pump at four different operating conditions. The CFD model utilised was the same as presented in chapter 5, with slightly different pressure inlet boundary conditions and the same shaft angular velocity (130 rpm). Table 7-1 specifies that the inlet pipe pressure discussed in paragraph 5.2, was applied along with an additional drop supposed constant for each case and increasing from 0 (case 1) to 100 kPa (case 4). In the results discussion section the reason for additional pressure drop will be made clear. The analyst aimed at obtaining the worst case of a full cavitation regime in case 1 and to slowly

move to the non-cavitating scenario in the last case by the means of increment of the inlet manifold pressure.

Table 7-1: Test cases boundary conditions summary, ΔP trends were shown by figure 5.3.

Case	Pressure: function of the mass flow rate	
	Inlet pressure [kPaG]	Outlet pressure [kPaG]
Case 1	$0 - \Delta P_{inlet}$	$0 + \Delta P_{outlet}$
Case 2	$25 - \Delta P_{inlet}$	$25 + \Delta P_{outlet}$
Case 3	$50 - \Delta P_{inlet}$	$50 + \Delta P_{outlet}$
Case 4	$100 - \Delta P_{inlet}$	$100 + \Delta P_{outlet}$

7.3 Results discussion

7.3.1 Case 1

(Figure 7-1) The chamber pressure fell close to the vapour level and remained fairly constant throughout the temporal range of 100° - 170° of the inlet stroke. A significant amount of vapour was produced in the valve-seat gap as shown in Figure 7-2. During the 17° - 70° range the second phase volume fraction-time trend in the valve-seat gap was steep demonstrating a high level of phase change, whereas it remained constantly at around 20% in the interval 70° - 190° . When the inlet stroke ceased (180°) the gap mean secondary phase volume fraction was still 17.5%, it quickly turned back to liquid water during the initial part of the outlet stroke (180° - 200°). Figure 7-3 shows that the phase change occurred also in the vicinity of the plunger and started very soon after the beginning of the induction stroke. Its trend may be considered linear ascending in the range 17° - 105° , then a peak of 10% occurred and eventually showed a descending trend which terminated at 200° of crank rotation. Figure 7-2 and Figure 7-3 demonstrate the presence of two types of cavitation which were occurring simultaneously in the pump chamber. The first, cavitation due to expansion, affected the low pressure and low velocity regions such as the zones in the vicinity of the plunger where the maximum flow velocity can be considered equal to the plunger velocity (0 to 1.74 m/s) and was insufficient to produce any flow induced cavitation effects. The second type, the flow induced cavitation, affected mainly the zones with a high velocity flow such as the inlet valve-seat volume once the valve lifted. Figure 7-2 which quantifies the amount of second phase volume fraction present in the inlet valve-seat gap volume, shows a non-linear trend and a higher rate with respect to Figure 7-3. The rate of second phase fraction increased as the gap volume mean velocity increased (Figure 7-4) and caused by the pressure drop (Bernoulli's effect). The delay in vapour condensation affected the inlet mass flow and the inlet valve lift histories as shown in Figure 7-5 and Figure 7-7. This effect is also shown in Table 7-2 which quantifies it as 205.3° , 25.3° after the start of

the outlet stroke. Figure 7-8 shows the consequent delay in outlet valve opening which proves the assessed 7% loss of volumetric efficiency as shown in Table 7-2. According to the described phenomena, one can assume that the pump was operating at full cavitating condition in accordance with Opitz (Opitz & Schlücker 2010; Opitz et al. 2011).

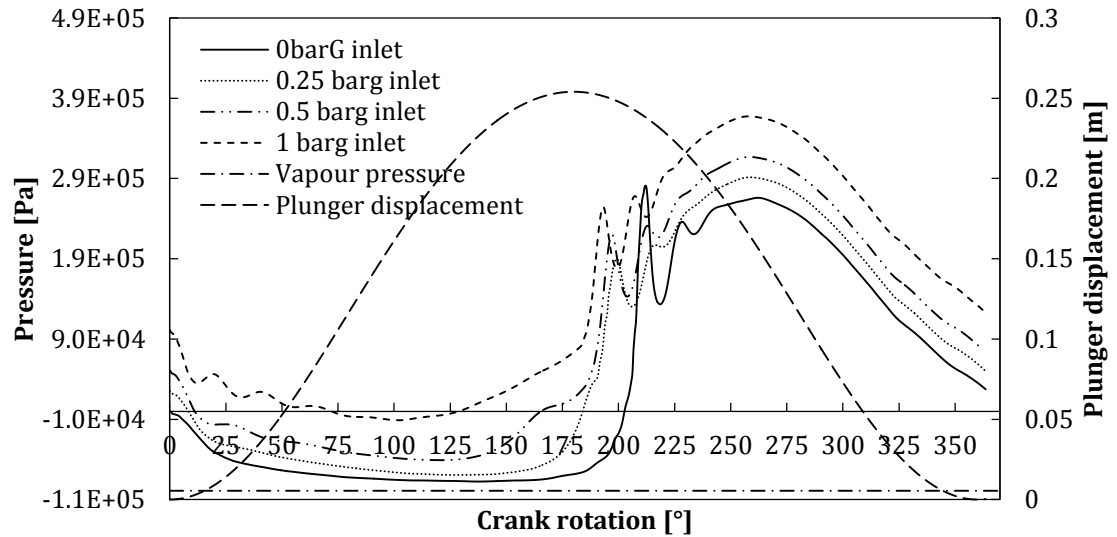


Figure 7-1: Chamber Pressure –time history, case 1 to 4. The pressure is monitored at a fixed point near the TDC position of the plunger

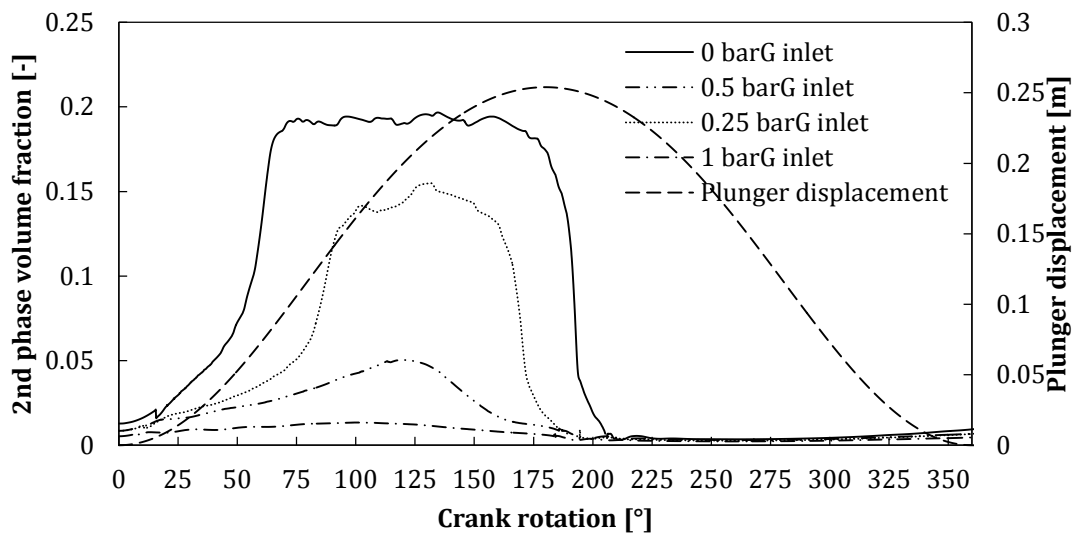


Figure 7-2: Inlet valve-seat gap volume mean 2nd phase fraction time history, case 1 to 4.

Table 7-2: Summary of the quantitative results, the volumetric efficiency related to the inlet valve closing time

	Inlet Max pressure [kPa]	Volumetric efficiency Vs standard conditions [%]	Inlet valve opening time [crank rotation °]	Inlet valve closing time [crank rotation °]
Case 1	0	93.36	15.6	205.3

Case 2	25	97.93	11.5	194.6
Case 3	50	98.26	9.6	185.8
Case 4	100	98.87	6.7	183.7

7.3.2 Case 2

(Figure 7-1) The chamber monitor pressure during the induction stroke closely approached the saturation vapour pressure. Figure 7-2 shows a fairly similar to case 1 behaviour of the 2nd phase fraction in its trend but the maximum values estimated by the CFD solver were lower (15%) and remained almost constant over a narrower range (90°-165°). It can be observed from Figure 7-3 that, in the vicinity of the plunger, the 2nd phase fraction followed a similar trend to case 1 with a smaller peak (6%) and a linear increment in the vapour volume fraction but with a lower rate. All the observations on the flow induced cavitation and cavitation due to expansion made for case 1 are also qualitatively valid for case 2. The smaller overall amount of vapour generated produced a smaller delay in valve closing which can be observed in Figure 7-7. Table 7-2 quantifies the delay as 14.6° and a volumetric efficiency loss within the limit of 3% discussed by Miller (Miller 1995). One can assume that case 2 describes a pump operating in partial cavitating condition in accordance with Opitz (Opitz & Schlücker 2010; Opitz et al. 2011).

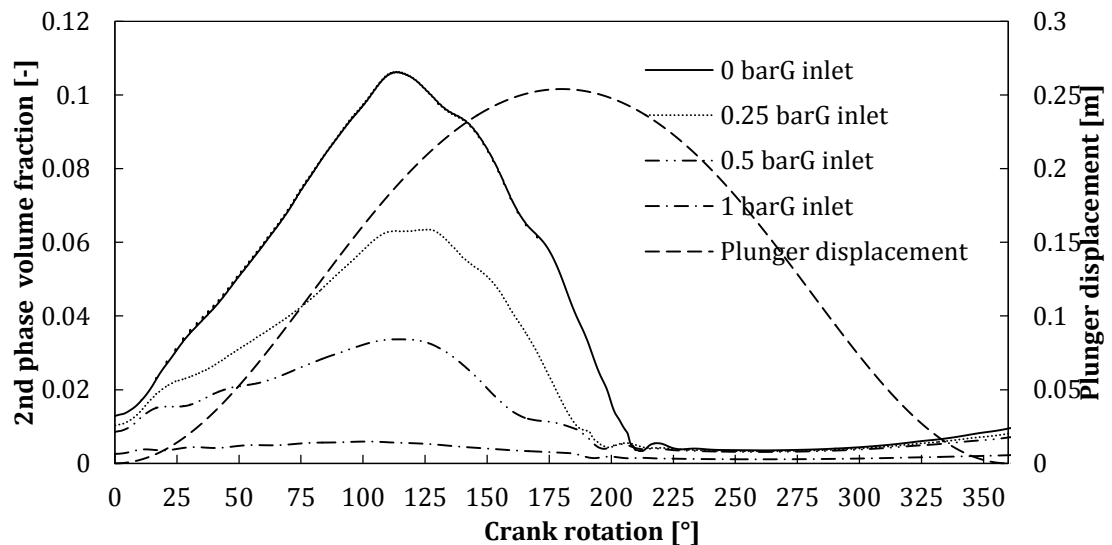


Figure 7-3: Plunger surface mean 2nd phase fraction, case 1 to 4.

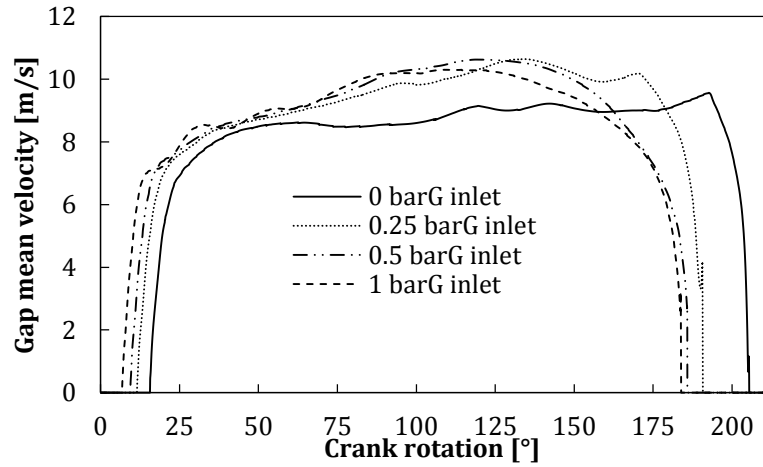


Figure 7-4: Inlet valve-seat gap volume mean flow velocity, case 1 to 4.

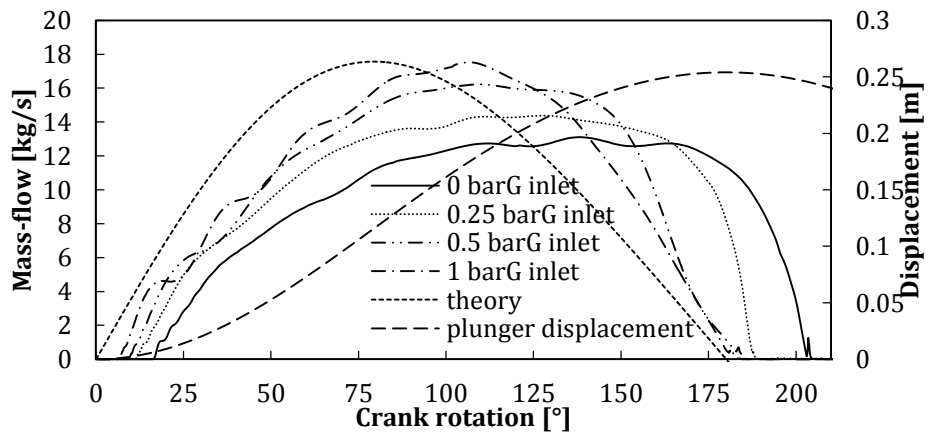


Figure 7-5: Inlet mass flow-time history, case 1 to 4. The theoretical curve is calculated as the positive displacement volume times the density of water at standard conditions.

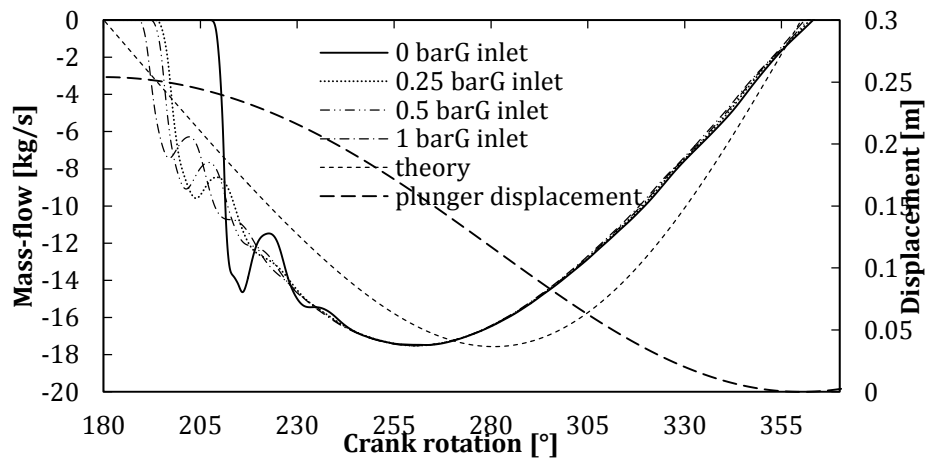


Figure 7-6: outlet mass flow-time history, case 1 to 4. The theoretical curve is calculated as the positive displacement volume times the density of water at standard conditions.

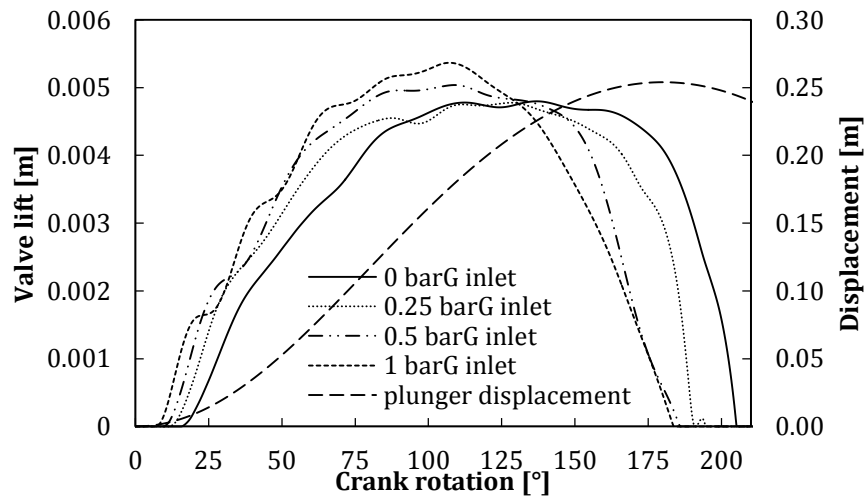


Figure 7-7: Inlet valve lift-time histories. Case 1 to 4.

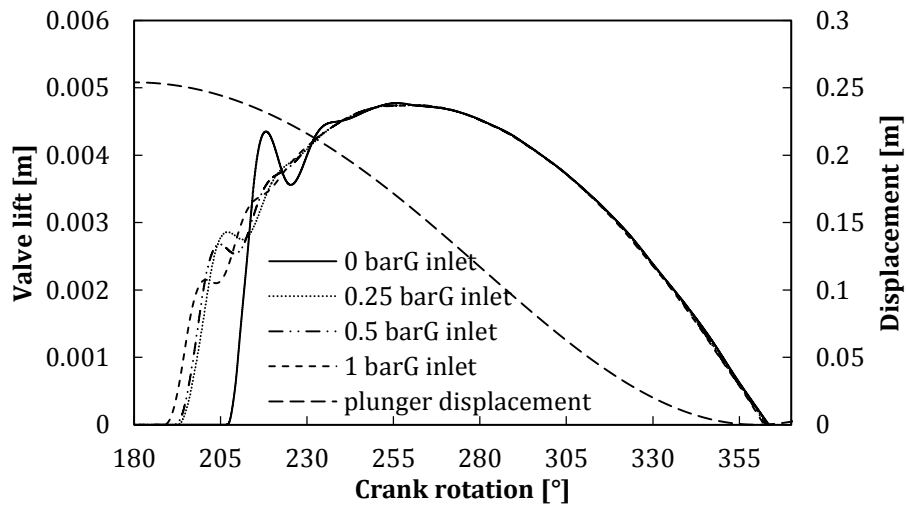


Figure 7-8: Outlet valve lift-time histories. Case 1 to 4.

7.3.3 Case 3

Although the monitor pressure in the chamber during the inlet stroke remained generally above the saturation vapour pressure (see Figure 7-1), a 5% peak of 2nd phase fraction was present in the gap volume as shown in Figure 7-2 and occurred at 120° of crank rotation. One may say that on the whole the pressure remained above the vapour limit but locally there were regions affected by low pressure. In this case Figure 7-2 shows a linear trend which was different with respect to case 1 and 2 where the secondary phase volume fractions revealed a strongly non-linear behaviour before reaching the maximum.

In fact Figure 7-4 indicates that the high velocity in the inlet valve-seat gap volume, as well as the induced localized pressure drop, is evidence of flow induced cavitation. The low level of 2nd phase volume fraction resulted in a shorter delay in valve closing and an inlet mass

flow rate/time history curve closer to the theoretical one (Figure 7-7 and Figure 7-5). The low level of volumetric efficiency loss (<3%) implied that the pump was operating at incipient cavitating condition since cavities do not disturb and modify the main flow (Franc & Michel 2004).

7.3.4 Case 4

Chamber minimum pressure remained either generally or locally safely above the vapour limit, the minimum monitor pressure/time curve ranged around the ambient pressure as shown in Figure 7-1. Figure 7-2 shows a flat trend of the vapour volume fraction throughout the pumping cycle. The graph indicates a 1% quantity of the second phase but, rather than water vapour this may be interpreted as the initial non-condensable mass fraction which slightly expanded during the inlet stroke. The model correctly calculated the expansion of that gas providing a minimum variation of its volume fraction, such a phenomenon is commonly known as “gas cavitation” (Baur et al. 1998). Among all cases this one is the closest to the theory in terms of inlet mass flow as pointed out by Figure 7-5 and it is affected by the least amount of volumetric efficiency loss (Table 7-2).

7.4 Conclusion

The model estimated the interphase change in the three conditions of incipient to full cavitation, good interaction of the phase change with the pressure field and valve lift was also achieved. In case 1, where the higher second phase generation was observed, the vapour trapped in the vicinity of the inlet valve, at the end of the inlet stroke, kept the pressure close to the vapour pressure. The integral of the forces on the valve surfaces prevented the valve from closing until the plunger compressed the vapour and turned it into water again.

The model was accurate enough to quantify the amount of second phase produced and destroyed in the chamber and therefore the efficiency loss throughout the four operating conditions. Table 7-2 demonstrated the capability of the model to simulate the behaviour of the non-condensable gas dissolved in water in terms of the inlet valve opening delay. The model also demonstrated the capability of CFD methodologies in providing the analyst with the information needed to understand the mechanisms leading to cavitation as well as all the information concerning the cavitation dynamics. For instance, this chapter showed and discussed the two different type of cavitation affecting PD reciprocating pumps which the numerical model identified; the flow induced cavitation and cavitation due to expansion.

On the other hand the analysis carried out did not shed light on the influence of the non-condensable gas dissolved in the working fluid as no distinction was made between the two

components of the secondary phase: air and vapour. It is of great interest to understand how much of the second phase volume fraction depicted in Figure 7-2 and Figure 7-3 is composed of water vapour and how much is air.

8 CFD Sensitivity test on the non-condensable gas mass fraction

8.1 Introduction

This chapter aims at answering the question that the analysis of the previous chapter left unsolved; how the generation of vapour during the cavitation phenomenon relates to the non-condensable gas dissolved in the water. The new analysis proposed is again purely numerical and the accuracy cannot be verified yet but the results were correlated to the physics of the phenomenon to provide the analyst with an estimation of the consistency of the model.

It is known (Kuiper 2010) that clean water at ambient conditions contains approximately 15 ppm (parts per million) of air which is dissolved. As the static pressure decreases during the suction stroke, air separates from the liquid and gathers in bubbles which interact with the pressure field as air is much more compressible than water (Wood et al. 1998). It is also known (Eisenberg 1963) that water contains a large amount of nuclei which are microscopic bubbles containing water vapour and air which are located in the crevices of the solid boundaries or on dust particles. This amount of air which is not dissolved may increase the overall amount of the gas. The interaction of the air with the pressure field implies an expansion of the former: this phenomenon is usually called gas cavitation as outlined previously. Gas cavitation results in a pressure drop slowdown which may result in a delay in the achievement of the vapour cavitation condition and a mitigation of the water vapour generation. The accuracy of the estimation of the pump performance depends also on the correct estimation of the interaction between air and vapour. The CFD model utilized can be considered a slight variation of the one discussed in chapter 5. An improvement of the monitoring capabilities was made. The model interrogates the cavitation model utilized to decompose the second phase into its two components i.e. the air which expands following the pressure field and the water vapour which is generated in the region of low static pressure. This is of great interest to investigate cases with different air content and to study its influence.

8.2 Test cases

Two CFD test cases were created and launched, and their results were compared. The cases dealt with a single chamber PD pump subjected to the same operating and boundary conditions of the test case number 1 discussed in the previous chapter. They differed only in the property of the fluid processed, the first case utilised water with 15 ppm of dissolved air at standard conditions (case 1 previous chapter) while the second case utilised a lower air content of 1.5 ppm (now referred to as case 2). It has to be pointed out that for this analysis the analyst chose a slightly different kind of valve (stem valve) which in the case 1 might

provide slightly different results with respect to case 1 described in chapter 7. Table 8-1 shows the solver controls chosen for this analysis while Table 8-2 shows the inlet and boundary conditions.

Table 8-1: Solver settings summary

Solver	RANS, pressure based, transient			
	Mixture model (ANSYS 2011a)			
Models	Multiphase	Phases	Water liquid	Primary phase
			Water vapour	Secondary phase
	Turbulence	k-ε Standard	Enhanced wall treatment	
	Cavitation	Singhal et al.	15 ppm air (Case 1), 1.5 ppm (Case 2)	
Pressure-Velocity coupling	SIMPLE			
Spatial discretization		Momentum	Second order upwind	
		Vapour	First order upwind	
		Turbulent kinetic energy	Second order upwind	
		Turbulent dissipation rate	Second order upwind	
Transient formulation	First order implicit			
Under relaxation factors		Pressure	0.3	
		Momentum	0.7	
		Vapour	0.5	
		Turbulent kinetic energy	0.8	
		Turbulent dissipation rate	0.8	
Residuals	10 ⁻³			
Time step	0.125° crank rotation \equiv 1.6 x 10 ⁻⁴ s @130 rpm			
Max Iteration per time step	35			
UDFs	Compressibility of water (A. Iannetti et al. 2014)			
	Valve dynamics			

Table 8-2: Inlet pressure boundary and initial conditions for both cases under investigation.

Case	Pressure: function of the mass flow rate	Chamber initialization pressure [kPa]
	Inlet pressure [kPaG]	
Case 1 and 2	0 - ΔP (see Figure 5.4)	0

As decided for the analysis described in chapter 5 the analyst chose the following set of monitors which in the author's opinion define completely the outcomes of the simulations. They will remain consistent also for the analysis shown in chapter 9 as well:

- Gauge pressure history at a point located in the TDC position of the plunger. This provides an estimation of the minimum chamber pressure.

- The valve-seat gap volume average of the water vapour fraction. This gives information on how much vapour is generated in the valve-seat gap volume.
- The plunger top surface area average of the vapour volume fraction. This provides information on how much vapour is generated in the plunger vicinity.
- The inlet mass flow
- The inlet valve lift
- Valve-seat gap volume vapour integral. This completes the information on how much vapour is generated in the gap volume.
- Chamber vapour volume integral. This completes the information on how much vapour is generated in the plunger vicinity.

All the transient quantities will be plotted against the crank angular rotation during the inlet stroke (0° - 180°) instead of the time domain because this provides the reader with a better understanding of the phenomena.

8.3 Numerical results and discussion

Figure 8-1 shows the time history of the chamber static pressure throughout the inlet stroke for both cases of air mass fractions of 15 and 1.5 ppm. The pressure monitor point was a point close to the TDC plunger position. The simulations showed that the lower the air content the closer the minimum chamber pressure to the vapour pressure. Figure 8-1 also shows that, in case of low air content, the pressure drops quicker and this results in low pressure regimes which last longer and increases the generation of vapour as shown in Figure 8-2 and Figure 8-5.

Figure 8-2 shows the situation in terms of second phase volume fraction in the valve-seat volume throughout the inlet stroke. An important remark that has to be pointed out is how the second phase volume fraction is actually divided into vapour and air. Figure 8-2 demonstrates that case 1 is affected by a higher second phase fraction (solid line, 15 ppm air mass fraction) but Figure 8-3 demonstrates that the vapour generation was actually higher in the dotted line of case 2 (25% against 16%, Figure 8-3), case 1 is affected by a higher air expansion rather than vapour generation as shown by Figure 8-4. Furthermore, while in the first case air and vapour split evenly (16% against 16% circa), in the second case the difference between vapour and air is significant (25% against 2.5% circa).

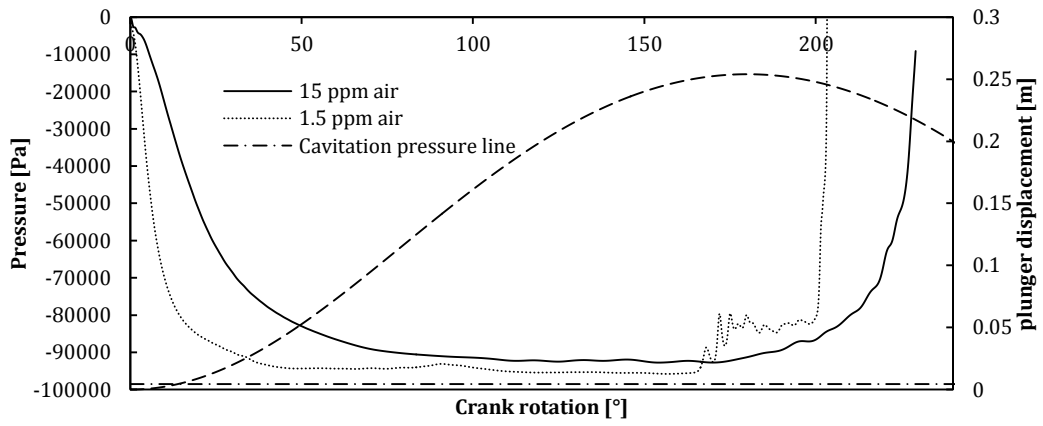


Figure 8-1: Pump chamber pressure history. A liquid with lower air mass fraction is affected by a higher pressure drop.

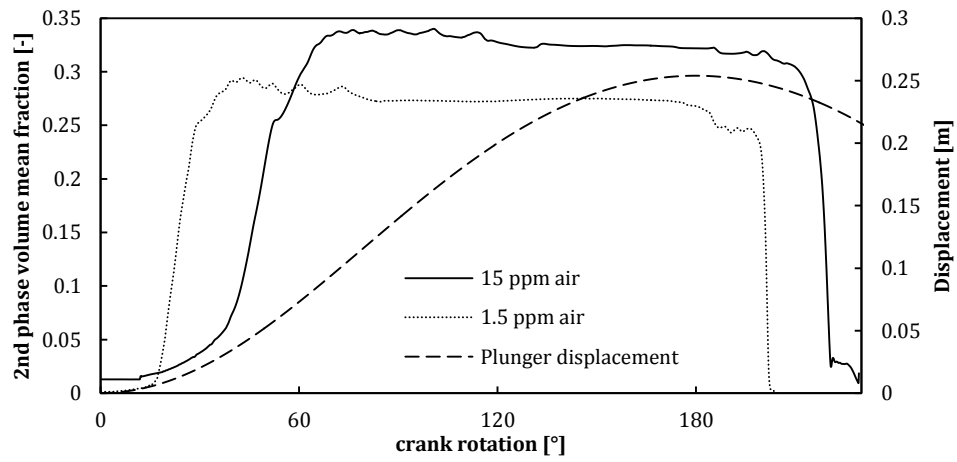


Figure 8-2: 2nd phase (water + air) volume fraction in the valve-seat lift volume when the air mass fraction is 15 and 1.5 ppm.

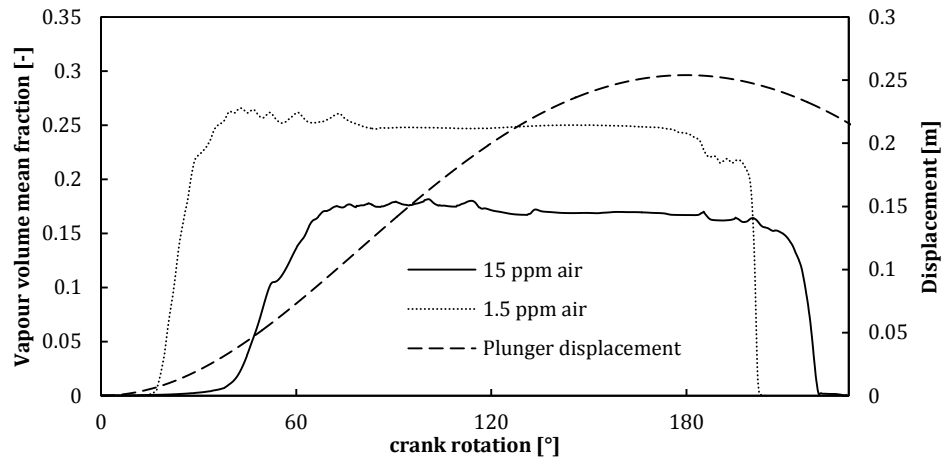


Figure 8-3: Vapour volume fraction in the valve-seat lift volume when the air mass fraction is 15 and 1.5 ppm.

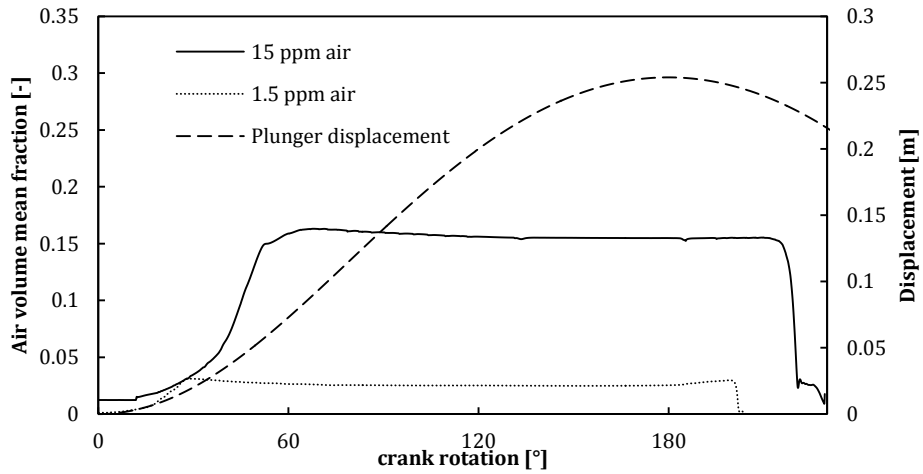


Figure 8-4: Air volume fraction in the valve-seat lift volume when the air mass fraction is 15 and 1.5 ppm.

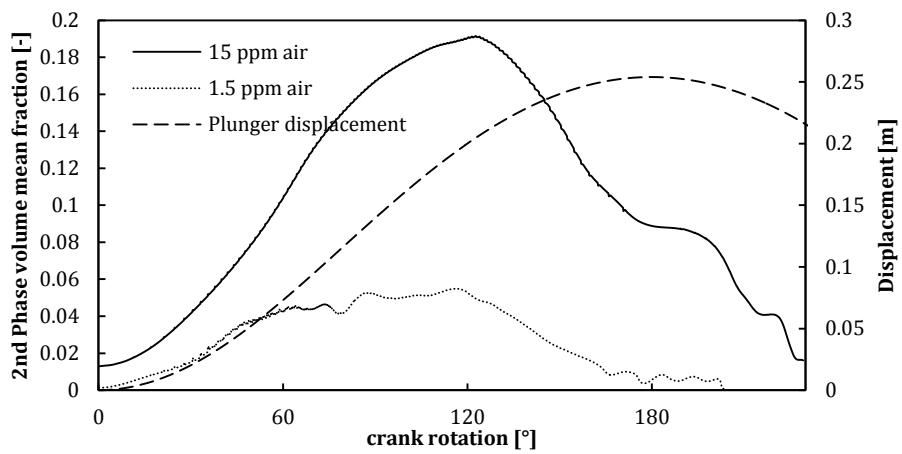


Figure 8-5: 2nd phase (water + air) volume fraction in the vicinity of the plunger when the air mass fraction is 15 and 1.5 ppm.

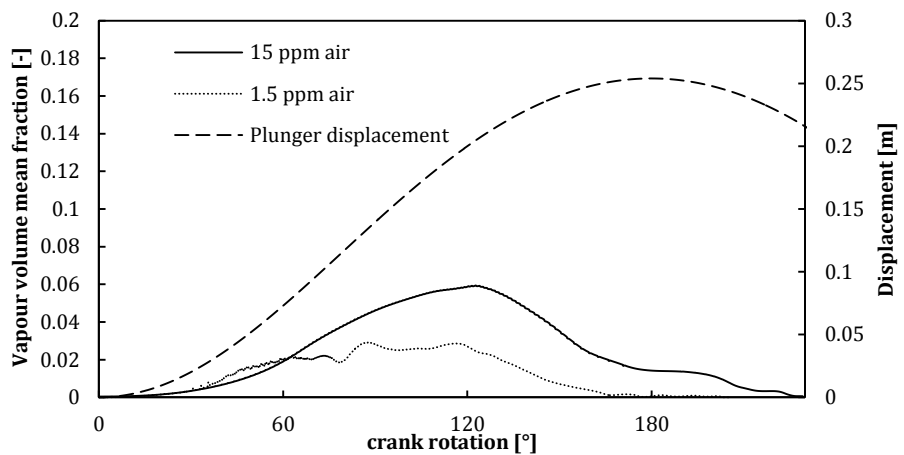


Figure 8-6: Vapour volume fraction in the vicinity of the plunger when the air mass fraction is 15 and 1.5 ppm.

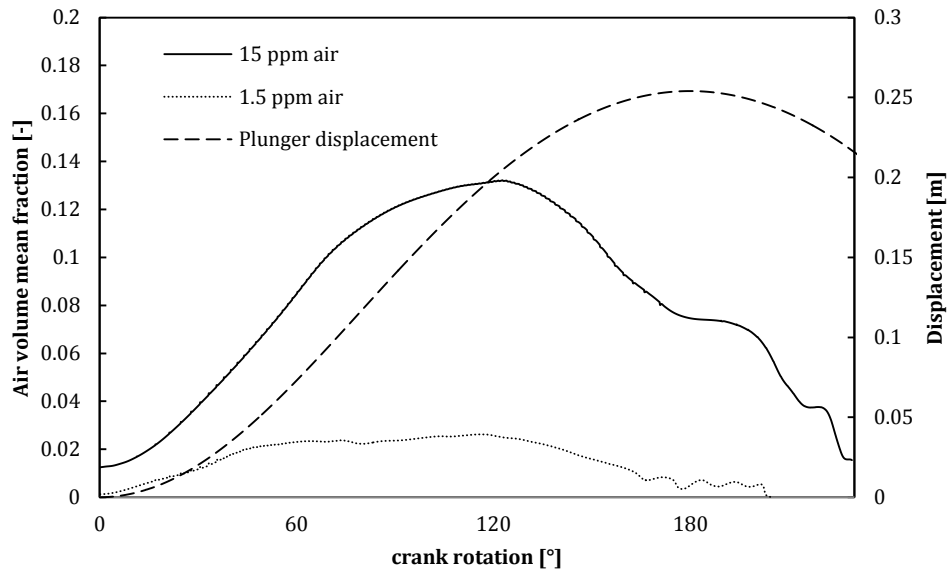


Figure 8-7: Air volume fraction in the vicinity of the plunger when the air mass fraction is 15 and 1.5 ppm.

Figure 8-5 shows the second phase volume fraction in the vicinity of the plunger top surface throughout the inlet stroke. The plunger region was affected by a lower vapour volume fraction than the valve region. For instance, considering case 1, the maximum second phase volume fraction was 32% circa (valve-seat gap volume, Figure 8-2), close to the plunger the amount was 19% (Figure 8-5 left). Furthermore, near the plunger the liquid richer of air showed an uneven subdivision of air and vapour volume fraction, respectively 6% and 13% (solid line Figure 8-6 and Figure 8-7). Case 2 showed an even subdivision of 2% circa air and vapour instead.

The trends of Figure 8-2 to Figure 8-7 are confirmed by the chamber volume integral of second phase depicted in Figure 8-8 to Figure 8-12. When operating with a 15 ppm air mass fraction, the pump shows twice the integral of second phase volume (1.28 l against 0.64 l) but in large part the second phase is composed of air rather than vapour (respectively 0.86 l against 0.42 l, Figure 8-9 and Figure 8-10). The case of 1.5 ppm of air mass fraction shows a slightly higher vapour volume integral (0.49 l against 0.42 l) and a much lower air volume integral (0.15 l against 0.49 l of vapour).

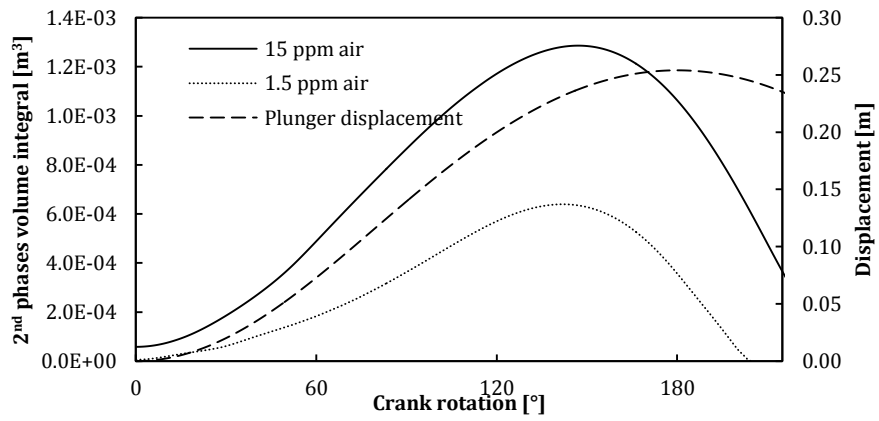


Figure 8-8: Chamber volume integral of the 2nd phase (vapour + air), when air mass fraction is 15 ppm (case 1) and 1.5 ppm (case 2).

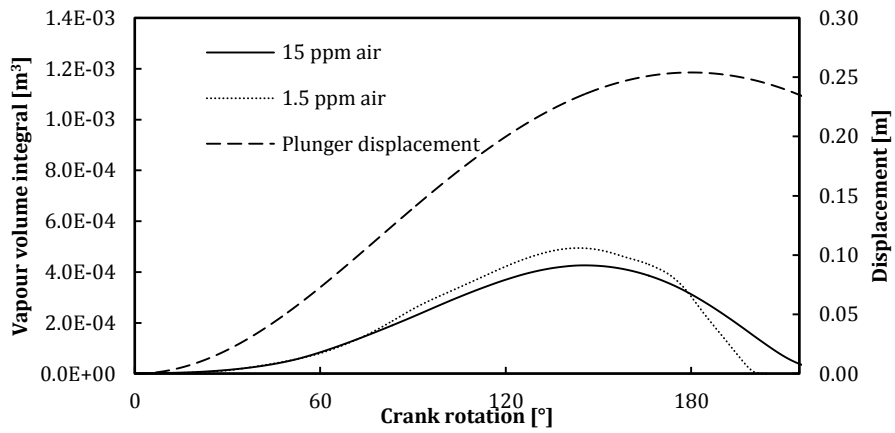


Figure 8-9: Chamber volume integral of the vapour when air mass fraction is 15 ppm (case 1) and 1.5 ppm (case 2).

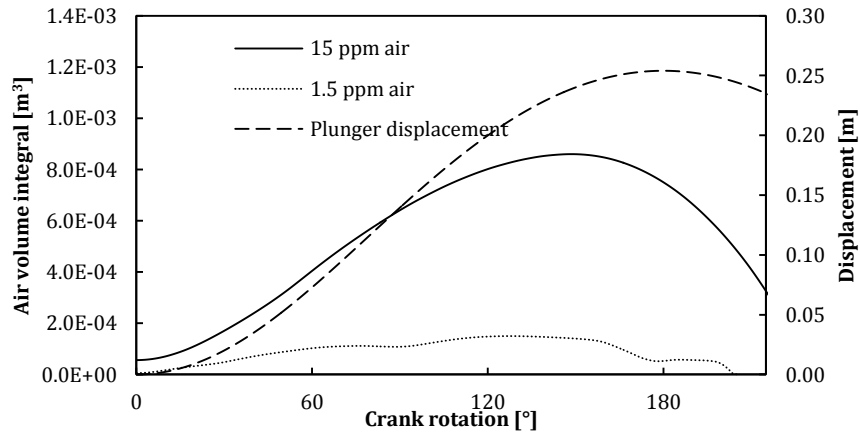


Figure 8-10: Chamber volume integral of the air when air mass fraction is 15 ppm (case 1) and 1.5 ppm (case 2).

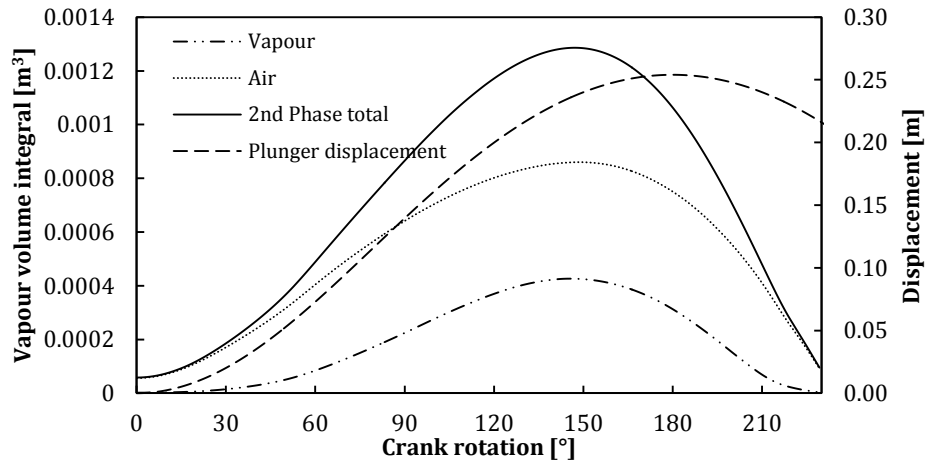


Figure 8-11: Chamber volume integral of the second phase components Case number 1, air mass fraction 15 ppm.

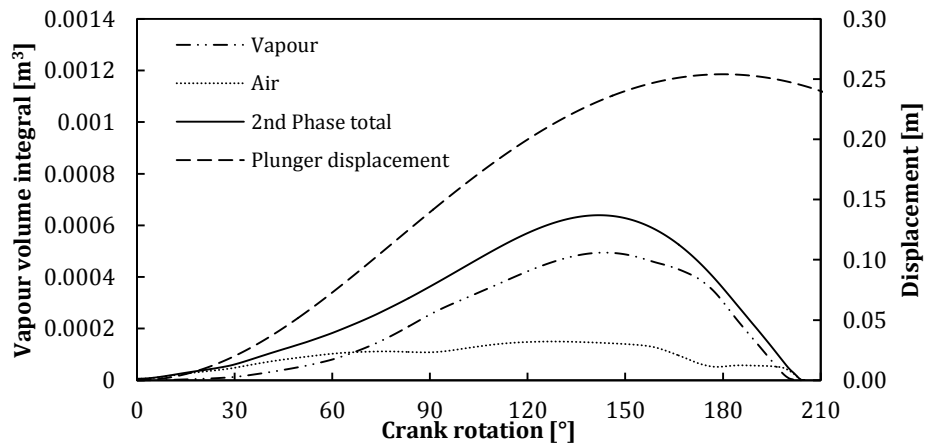


Figure 8-12: Chamber volume integral of the second phase components Case number 2, air mass fraction 1.5 ppm.

Table 8-3 summarises and quantifies the performance of the pump. In both cases studied, the volumetric efficiency loss was higher than 3% but case 1 showed a much lower volumetric efficiency (78.5% against 95%) because of the much higher air content which demonstrated a great influence on the performance deterioration. Table 8-3 also shows that the higher the volumetric efficiency loss the bigger the inlet valve closing delay (the theory indicates the end of the inlet stroke at 180° of shaft rotation), this can be explained by the time needed for the plunger to compress the second phase and turn it back to the liquid phase. Furthermore the higher air content resulted in bigger inlet valve opening delay (12° against 4°) because of the air expanding and slowing down the chamber pressure drop.

Table 8-3: Pump performance estimation summary, comparison of the two fluid properties 15 ppm vs 1.5 ppm air mass fraction

	Air mass fraction [ppm]	Volumetric efficiency Vs standard conditions [%]	Inlet valve opening time [°]	Inlet valve closing time [°]
Case 1	15	78.5	12	229
Case 2	1.5	95	4	205

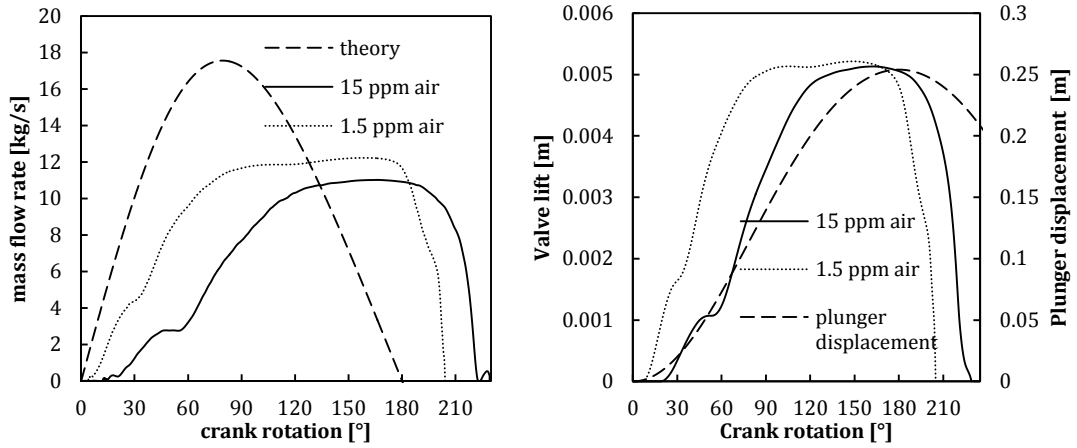


Figure 8-13: (left) mass flow rate throughout the inlet stroke when the air mass fraction is 15 and 1.5 ppm. (right) valve lift history.

Figure 8-13 shows the mass flow rate (left) and inlet valve lift (right) trends of the two cases under investigation. The mass flows are compared to the theory curve which is calculated considering a one phase incompressible fluid with zero inertia inlet valve (displacement volume times the density of water at standard condition). Case 2 shows an average mass flow rate higher than case 1 which explains the higher volumetric efficiency, the valve lift plot shows clearly the difference in closing delay highlighted also in Figure 7-6.

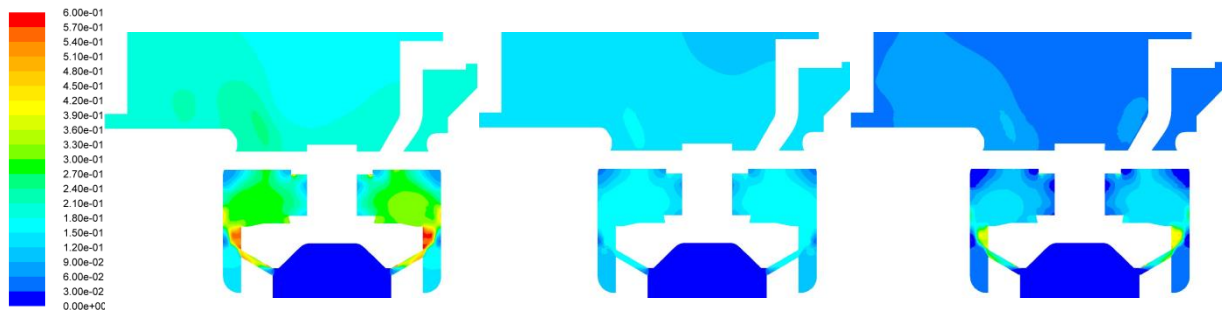


Figure 8-14. Case 1 (15 ppm air mass fraction) at 120° of crank rotation . (left) total second phase volume fraction. (Middle) air volume fraction. (Right) vapour volume fraction.

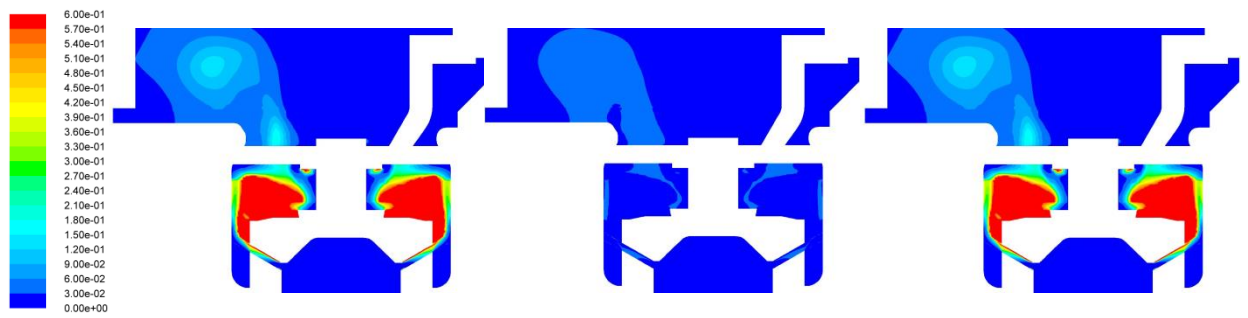


Figure 8-15. Case 2 (1.5 ppm air mass fraction) at 120° of crank rotation . (left) total second phase volume fraction. (Middle) air volume fraction. (Right) vapour volume fraction.

Figure 8-14 and Figure 8-15 show the contour of the second phase volume fraction respectively for case 1 and 2. Both figures represent a picture taken when the plunger rotation was 120° which is close to the maximum vapour generation for both cases. The contours confirm what was already stated in the discussion of Figure 8-1 to Figure 8-13. Vapour is generated mainly in the valve-seat gap volume and propagates downstream. According to the CFD simulation and supported by Figure 8-14, the expansion provided by the plunger generates a wide region where the air comes out of the fluid phase as dissolved gas and expands randomly around the plunger. This phenomenon is known as gas cavitation and was observed by Opitz (Opitz & Schlücker 2010). As the amount of air mass fraction was very low, case 2 showed the typical features of vapour cavitation (Figure 8-15) where the second phase was concentrated in the vicinity of the valve where it was mainly generated.

8.4 Conclusion

A transient and comprehensive CFD model of a one chamber PD pump was created to estimate the performance of the device under different working fluid properties. Two cases were investigated; in case 1 water with 15 ppm of air mass fraction content was considered. Case 2 dealt with a 1.5 ppm air mass fraction. The operating conditions (i.e. shaft angular speed and inlet pressure) were designed to achieve the full cavitating conditions so that the effect of the non-condensable gas mass fraction content on cavitation could be investigated. The CFD model made use of the Singhal et Al cavitation model (Singhal & Athavale 2002), the multiphase mixture model (ANSYS 2011a; ANSYS 2011c) and two UDFs modelled the compressibility of the fluid and the two-way coupling between the valve lift and the pressure field. The valve spring effect and the valve inertia was also taken into account. A complete inlet stroke was simulated, from the initialization point (plunger located at the TDC) until the end of the valve lift history. The two cases, in fact demonstrated different dynamics and in case 2 the valve ended the lift sooner than case 1.

General remarks on cavitation

According to the CFD model and under the investigated operating conditions, the plunger expansion created the pressure drop needed for vapour cavitation to appear but the air expansion (gas cavitation) mitigated the vapour formation in the vicinity of the plunger which was mainly affected by the vapour generated upstream by the valve rather than generated by the plunger itself. Once the average static pressure in the chamber approached the vapour pressure and the flowing velocity in the valve-seat gap volume exceeded a certain threshold, vapour cavitation appeared and affected primarily the lift volume moving downstream towards the plunger afterwards. The triggering cause of cavitation was the high flow velocity (flow induced cavitation, Opitz (Opitz & Schlücker 2010)) rather than the expansion cavitation which created the cavitating pressure conditions without actually triggering the phenomenon.

Influence of the non-condensable mass fraction on cavitation

Non-condensable gas mass fraction influences the chamber pressure history (Figure 8-1), the dissolved air slows down the pressure drop while it comes out of the liquid and expands. Air expansion tends to fill the void left by the plunger at the beginning of the inlet stroke when the valve is closed and delays vapour cavitation appearance. Case 1, which deals with saturated air liquid, shows a lower vapour volume integral than case 2 which deals with a lower air content instead (Figure 8-8 to Figure 8-12). On the other hand the air content is itself a source of volumetric efficiency loss as shown by Table 8-3. Figure 8-11 and Figure 8-12 together with Table 8-3 demonstrates that the overall second phase content (vapour and air) defines the volumetric efficiency rather than the vapour content itself. In fact case 1, which shows the highest second phase volume integral also shows the lowest volumetric efficiency. Figure 8-1 demonstrates also that the higher the air content the higher the minimum pressure. This provides a further safety factor on cavitation and increases the NPSH of the pump and this confirms what stated by Miller (Miller 1995).

The analysis demonstrated the importance of the working liquid properties for an accurate estimation of the performance of the pump as well as the prediction of the cavitation damage. Although the overall content of air (dissolved air plus the nuclei content) is not harmful for the pump, taking into account the non-condensable air mass fraction in cavitation results in a better estimation of the vapour volume fraction prediction. Despite air cavitation, vapour bubbles can harm the pump significantly. An accurate prediction of the

amount and the location may result in a better understanding of the design and operating parameters affecting cavitation and this implies a reliable support for pump designers and manufacturers.

9 CFD Sensitivity tests on the parameters acting on cavitation in PD pumps

9.1 Introduction

The analysis discussed in the previous chapter revealed that cavitation in PD pumps is a complex phenomenon to study. All the fluid dynamics phenomena such as the vapour generation and the pressure fields are strongly coupled both to each other and to the valve dynamics. A simplified model which does not account for a two-way coupling would not be able to provide analysts with the information needed to improve the design of the device. Simulating the two way coupling between the valve dynamics and the pressure field represents one of the originalities of this research as the free literature review revealed that no such comprehensive tool was developed at the time the present document was written.

The next step of the project which is the objective of the present chapter is to utilise the model to investigate the influence of geometric and operating conditions of the pump on cavitation. For the analysis the following sensitivity tests were chosen:

1. *Valve/seat design sensitivity test:* In full cavitating conditions created by a low inlet pressure. The pump equipped with a set of 5 different valve/seat geometries was tested to assess the influence of the valve design parameters on cavitation.
Within the valve/seat sensitivity test, a detailed analysis focused on the influence of the valve-seat angle was carried out. The influence of this design parameter is under debate in industrial environment and patents regarding the choice of that angle have been also released.
2. *Shaft angular speed sensitivity test:* In full cavitating conditions created by low inlet pressure, the pump equipped with two valve designs discussed in 1 was tested with a crankshaft velocity twice as high as the previous case (260 rpm instead of 130rpm).
3. *Spring preload sensitivity test:* In full cavitating conditions generated by low inlet pressure, the pump equipped with the original valve geometry was tested twice, with 26 mm and 13 mm initial valve stretch which corresponded to a spring preload of 300 N and 150 N.
4. *Valve mass sensitivity test:* In full cavitating conditions generated by low inlet pressure, the pump equipped with the original valve geometry was tested twice, with a 2.5 kg and 1.25 kg valve mass. Results were compared afterwards.

9.2 Valve/seat design sensitivity test

9.2.1 Valve/seat designs description

A set of five valve/seat modified configurations were considered for the analysis. Figure 9-1 represents the original geometry of which Figure 9-2 to Figure 9-6 are the modifications under investigation.

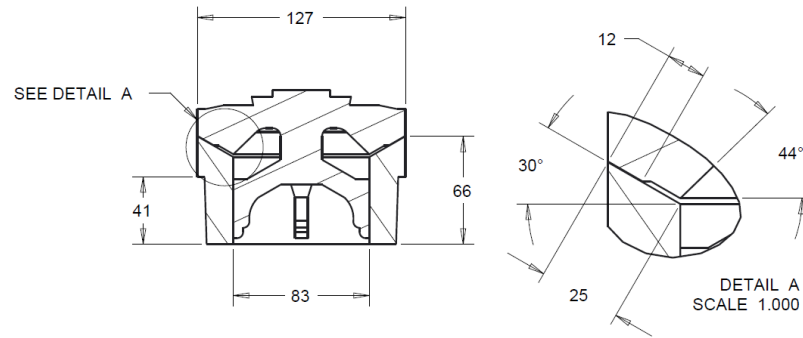


Figure 9-1: Original valve shape: the four legs slide inside the inner bore of the seat to allow a 1-DOF motion.

Figure 9-1 shows that the original valve is composed of a body which slides inside the 83 mm diameter bore by means of four legs which allow one DOF motion (translation along the axis). The detail A of the same figure shows the valve-seat angle of 30° and the overall seat contact length of 25 mm. Detail A also shows a step in the vicinity of the contact area. This is due to the urethane ring profile (not shown in the picture because it is merged to the valve main body) and it disappears because of its elasticity when the valve is pushed against the seat in the operating conditions where the delivery pressure exceeds a certain threshold. This was explained in chapter 3.

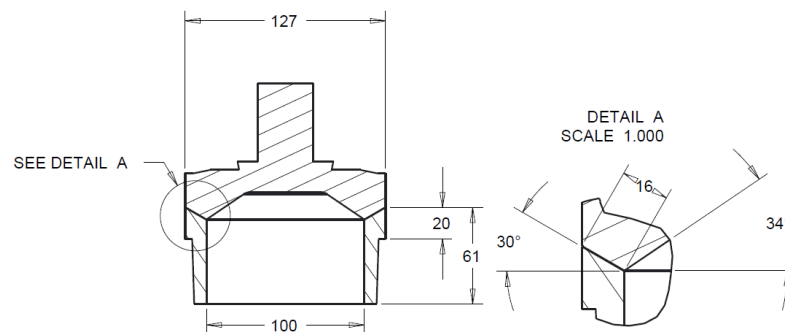


Figure 9-2: Modified geometry number 1: a stem slides in a bore drilled in the spring retainer replaced the legs, the inner diameter of the seat is smaller.

The first modification of the valve/seat configuration is shown in Figure 9-2. The four legs were replaced by a stem located on the top of the valve body. The stem slides in a bore drilled in the retainer in order to allow the one DOF motion of the valve. The seat has a wider diameter of 100 mm and the valve seat angle is still 30°. The step in the urethane ring is not present anymore.

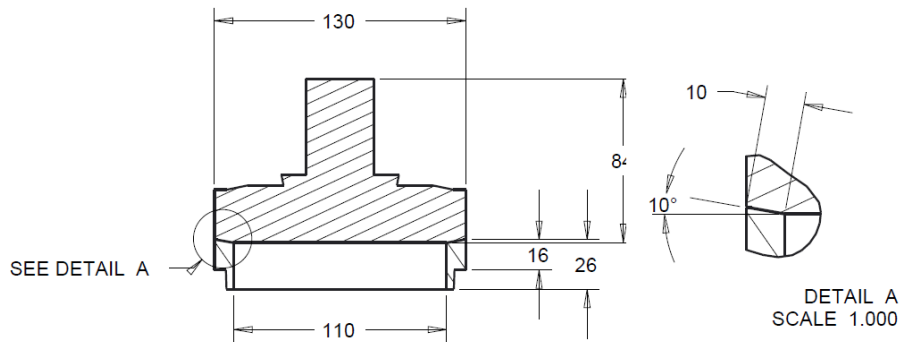


Figure 9-3: Modified geometry number 2: as the geometry number 1 a stem drives the valve motion, the inner diameter of the seat was reduced further, the valve/seat angle was reduced to 10°.

The modification number 2 of the valve/seat geometry is shown in Figure 9-3. It differs from geometry modification number 1 because of the seat angle, which was decreased to 10°. The seat inner diameter, which was increased by 10 mm, and the flat inner surface of the valve main body were also changed.

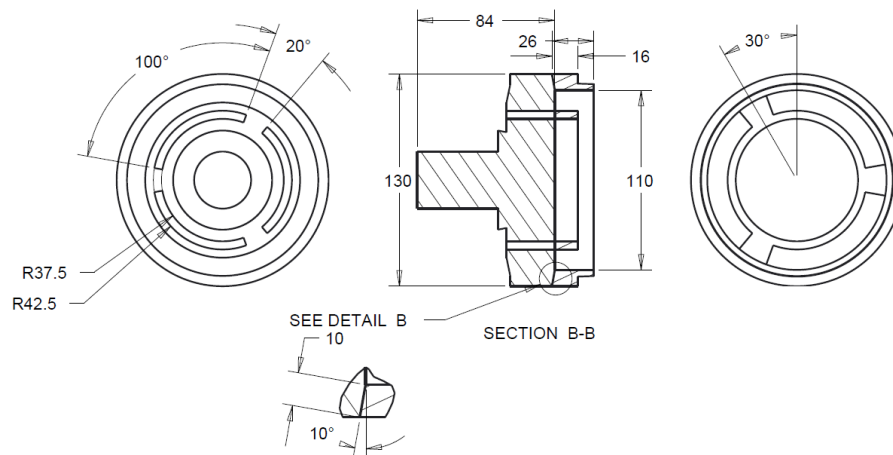


Figure 9-4: Modified geometry number 3, three additional opening areas were cut in the valve body, an additional body inside the seat was added to seal them.

The modified valve/seat geometry number 3 is shown in Figure 9-4. It differs from the geometry of Figure 9-3 by the three additional openings drilled in the valve main body. The picture shows also an additional body designed in the seat to provide the additional openings with the contact surfaces in order to seal them at zero valve lift situations.

The geometry modification number 4 is shown in Figure 9-5, In this case a single additional opening was present and it was cut in the stem. An additional body providing the sealing of the stem central opening was needed and thus designed in the seat.

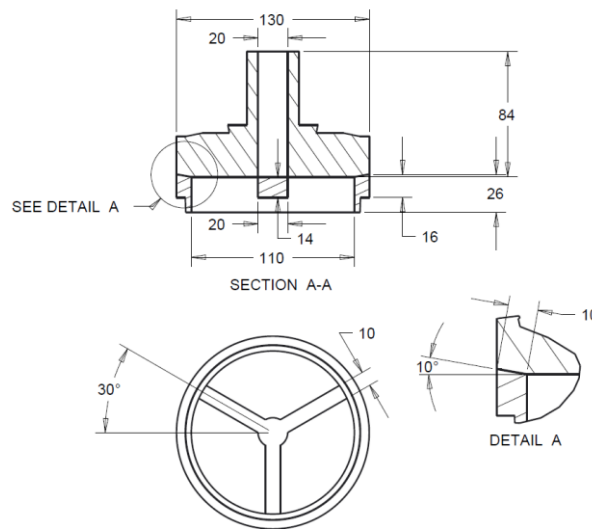


Figure 9-5: Modified geometry number 4: an additional opening area was cut in the stem, an additional body inside the seat was needed to seal it.

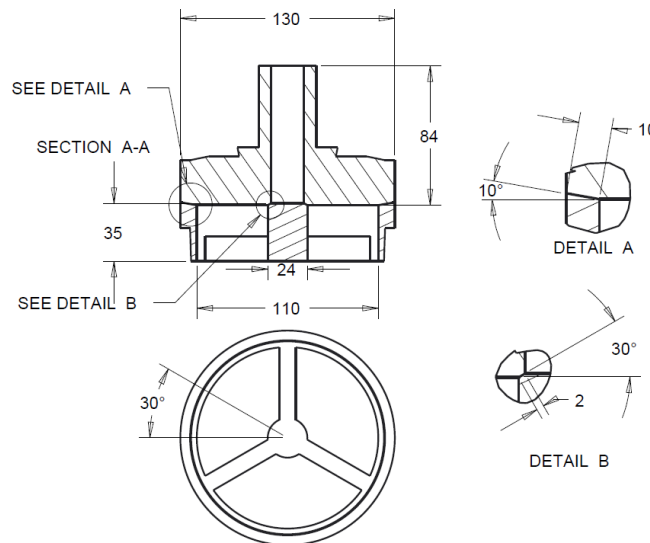


Figure 9-6: Modified geometry number 5: a little modification on the detail B and the additional seat contact body makes it different from the geometry number 4.

The last modified geometry (number 5) is represented in Figure 9-6. It is a design similar to the previous one with a slightly different additional contact area profile (Detail B) and an additional contact body. The seat additional contact body was enlarged and its angle with the valve was set to 30°. The interest in testing this further design was justified by the need to

understand the sensitivity of the results when very similar designs are tested but also to understand the behaviour of a more feasible design as Mod4 and Mod3 are not feasible geometries. Mod3 and Mod4, in fact were characterised by the same additional contact/opening surfaces which did not provide sufficient sealing properties that would be required in real operating conditions. Mod3 and Mod 4 were tested to verify the physical principle rather than providing a geometry which could be usable in the field.

Table 9-1: Summary of the advantages and disadvantages of the design configuration from Original to Mod5.

	Advantages	Disadvantages
Original	<ul style="list-style-type: none"> • Simple design • Wide contact area, good sealing 	<ul style="list-style-type: none"> • Small seat inner diameter • Small Opening
Mod1	<ul style="list-style-type: none"> • No obstacle in the stream due to the legs • Wider flow area 	<ul style="list-style-type: none"> • Spring retainer must be properly redesigned to allow the sliding stem • Smaller contact area and sealing area
Mod2	<ul style="list-style-type: none"> • No obstacle in the stream due to the legs • Flow area even wider than Mod1 	<ul style="list-style-type: none"> • Spring retainer must be redesigned to house the sliding stem • Contact and sealing area even smaller than Mod1
Mod3	<ul style="list-style-type: none"> • No obstacle in the stream due to the legs • Flow area as wide as Mod1 • Valve/seat smaller angle, 10° • 3 additional opening areas 	<ul style="list-style-type: none"> • Spring retainer must be redesigned to house the sliding stem • Contact and sealing area as small as Mod1 • Additional contact body obstructs the flow and may result in an additional non-beneficial pressure drop • The additional opening areas subtract useful pushing areas, this may cause a decrement in the maximum valve lift and flow area. • The additional contact area should be wider than the one represented in Figure 9-4
Mod4	<ul style="list-style-type: none"> • No obstacle in the stream due to the legs • Flow area as wide as Mod1 • Valve/seat smaller angle, 10° • 1 additional opening areas in the stem which brings flow in the plunger vicinity 	<ul style="list-style-type: none"> • Spring retainer must be redesigned to house the sliding stem • Contact and sealing area as small as Mod1 • Additional contact body obstructs the flow and may result in an additional non-beneficial pressure drop • The additional opening areas subtract useful pushing areas, this may cause a decrement in the maximum valve lift and flow area. • The additional contact area should be wider than the one represented in Figure 9-5.
Mod5	<ul style="list-style-type: none"> • No obstacle in the stream due to the legs • Flow area as wide as Mod1 • Valve/seat smaller angle, 10° • 1 additional opening areas in the stem which brings flow in the plunger vicinity 	<ul style="list-style-type: none"> • Spring retainer must be redesigned to house the sliding stem • Contact and sealing area as small as Mod1 • Additional contact body obstructs the flow and may result in an additional non-beneficial pressure drop • The additional opening areas subtract useful pushing areas, this may cause a decrement in the maximum valve lift and flow area. • Is the additional contact area wide enough for the proper sealing?

Table 9-1 summarizes the potential advantages and disadvantages which drove the analyst in the definition of the five geometries (Mod1 to Mod5). To allow easier reading the following nomenclature is used:

- **Flow area.** (Figure 9-7) Is the area of the inner (minimum) cylindrical surface between the valve and the seat, the author will also refer to this as the main flow area since there are geometries equipped with more than one flow area. This area is a function of the inner seat diameter and the valve lift. In the following description it can also be referred to as opening area.
- **Pushing area.** (Figure 9-8) Is the area of the inner valve surface where the integral pressure drop across the valve acts and determines the pressure forces which move the valve. This area affects the maximum valve lift and indirectly the main flow area because of geometrical considerations.
- **Additional flow area.** In the following description it can also be referred to as the additional opening area and is the area of the cut(s) created in the valve main body of the modified valve geometries number 3, 4 and 5 to increase the overall flow area. This area can be calculated as:
 1. Perimeter of the additional opening area(s) multiplied by the valve lift if it returns a value less than the area of the cut.
 2. The area of the cut considered constant with respect to the valve lift if the previous calculation returns a value higher than the area of the cut.

The reason for the evaluation above depends on geometrical considerations. According to Bernoulli's law, the geometric parameter defining the minimum pressure is in fact the minimum flow area which may change depending on the valve lift when additional openings are cut in the valve main body.

- **Contact area.** Is the main contact area between the valve and the seat.
- **Additional contact area.** Is the secondary contact area needed by the modified geometries number 3, 4 and 5 to seal the additional flow area.
- **Additional contact body.** Is the secondary body included in the seat design which provides the additional contact surface.

For a perfect sealing the additional contact area should be wider than the additional opening area even though Mod 3 and 4 (Figure 9-4 and Figure 9-5) show two equal areas. Mod5 (Figure 9-6) shows an additional contact area wider than the additional opening area instead.

At this stage it is important to point out that for all the configurations introduced there is a geometric relationship between the seat inner diameter, the main flow area and the pushing area. Increasing the seat inner diameter results the beneficial effects of increasing the flow area per unit of lift but also increasing the pushing area and thus the overall driving force which increases the maximum valve lift and therefore the flow area. On the other hand, a high inner seat diameter results in a low contact area and a worse sealing as pointed out in Table 9-1.

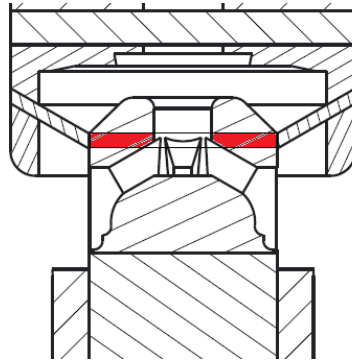


Figure 9-7: Fluid volumes in the vicinity of the valve, the cylindrical flow area is shown

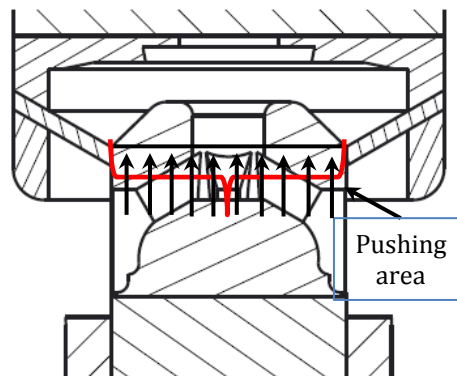


Figure 9-8: The pushing area is the area where the integral of pressure forces acts and determines the maximum valve lift

The valve-seat angle is a geometric parameter which deserves further discussion. According to the trigonometry and also fluid dynamics, the valve-seat angle affects significantly the flow area in two opposite ways:

1. To maximise the height of the valve-seat lift volume per valve lift unit the valve-seat angle should be as close as possible to 0° . This would increase the real flow area height as it is proportional to the lift multiplied by the cosine of the valve-seat angle.

2. To avoid the bends in the streamlines of the flow, the valve-seat angle should be as close as possible to 90° .

One-phase steady state simulations, suggested that the optimum angle value was located between 10° and 20° . Figure 9-9 and Figure 9-10 are the result of the a set of simulations carried out using a flat inner surface valve body similar to Mod 2 of Figure 9-3 at different valve-seat angles (0° - 45°) considering a fixed valve lift of 5 mm and a constant flow rate of 17 kg/s.

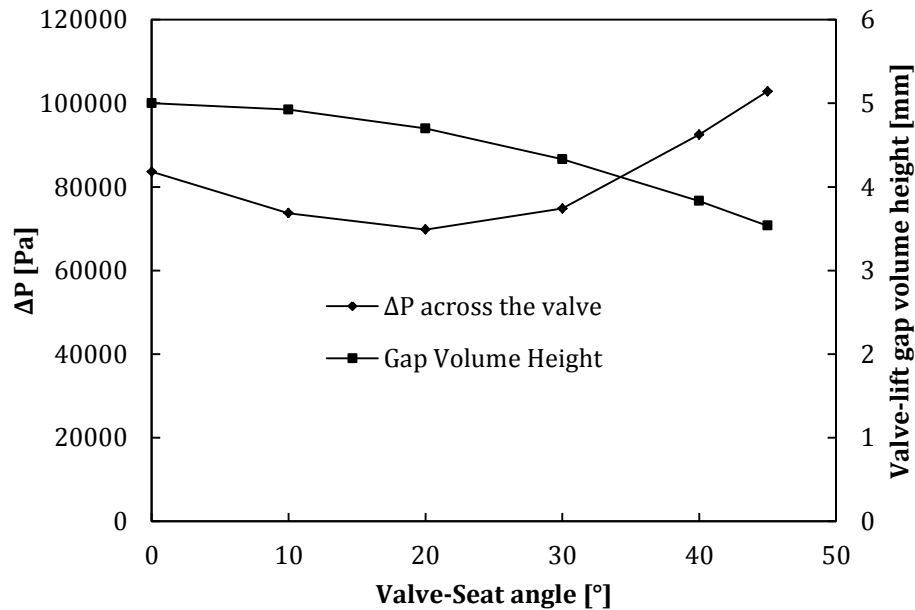


Figure 9-9: Pressure drop across a flat pushing area valve at different valve-seat angles, one-phase steady-state simulations.

Figure 9-9 shows the pressure drop across the valve which is an indicator of the fluid dynamic resistance of the valve. Figure 9-10 shows the maximum velocity occurring in the vicinity of the valve (not necessarily in the valve-seat gap volume) which affects the minimum pressure and thus cavitation. In the first case the optimum situation occurs at 10° while in the second case it occurs at 20° valve-seat angle.

On the other hand, the reader should be aware that steady state simulations in a highly coupled problem such as the one affected by the interaction between the pumping cycle in cavitating conditions and the valve dynamics, give only a rough estimation of the optimum solution to adopt. A further and more detailed investigation was carried out and presented in the paragraph 9.2.3.

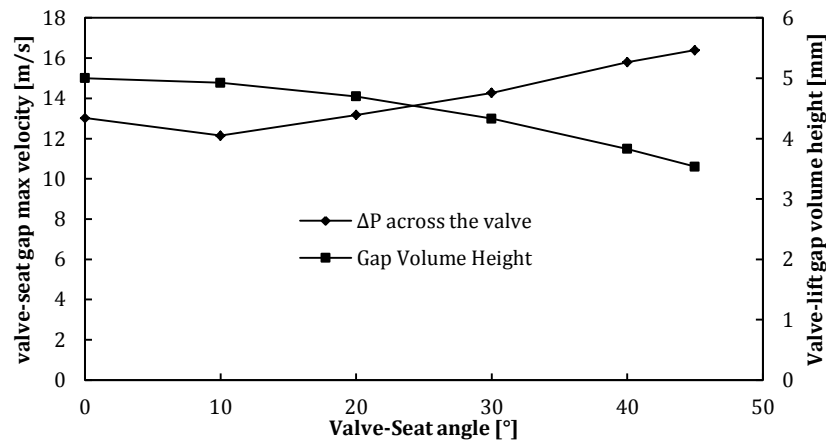


Figure 9-10: Valve-seat gap volume maximum velocity for a flat valve at different valve-seat angles, one-phase steady-state simulations. The maximum velocity affects the minimum pressure and thus cavitation.

9.2.2 Valve/seat design sensitivity test results

Figure 9-11 shows the chamber pressure comparison between the six configurations throughout the induction stroke. The figure demonstrates clearly that moving from the original valve/seat shape to Mod2 a significant increment of the minimum pressure in the chamber was achieved. While the original shape pressure approached the vapour pressure, Mod1 which was characterised by a slightly bigger seat inner diameter showed an increased pressure with respect to the original valve. Mod2 showed the highest pressure instead, even though Mod3 to Mod5 configurations showed similar trends as the minimum pressure achieved was similar for the three of them. Figure 9-15 shows the valve lift trends. The highest maximum lift was achieved by the Mod2 configuration which also showed (Figure 9-16) the widest flow area. This explains the reason why Mod2 showed the maximum absolute pressure. Mod3 showed the least valve lift but the second widest maximum flow area which can be explained by taking into account the additional opening area which increases the flow area per valve lift unit. On average it is clear that in Mod3, 4 and 5 the cut performed in the main valve body to create the additional opening area decreased the valve surface over which the pressure force acts and caused a decrement in the valve lift force and maximum valve lift. This also caused a reduction in the main flow area which was just partially balanced by the additional opening area in the valve body. Even though Mod3 showed the highest gain in overall flow area it was not sufficient to overcome and improve on the Mod2 trend. Analysis of the Mod1 results revealed an unexpected behaviour. It showed the second highest maximum lift (Figure 9-15) and overall flow area (Figure 9-16) but the pressure trend (Figure 9-11) revealed the second lowest pressure which resulted in the second worst cavitation behaviour. This seems not to agree with the average trend. The reasons for this phenomenon are to be found in the geometric differences between Mod1

and2 that one can see in Figure 9-2 and Figure 9-3 and will be investigated further. Small variations in the geometry did not result in significant differences in behaviour as demonstrated by Mod5 which showed all trends of Figure 9-11 to Figure 9-18 consistent with its Mod4 counterpart.

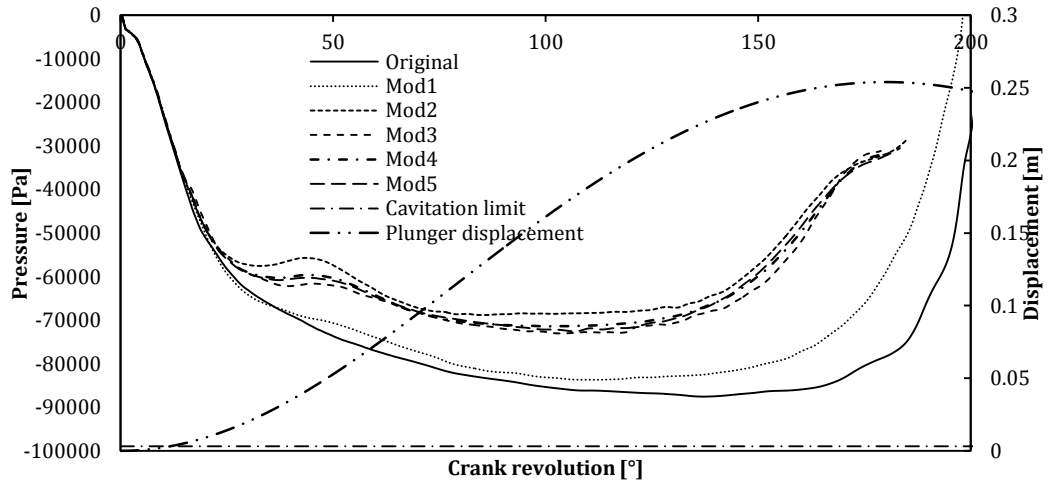


Figure 9-11: Chamber pressure throughout the inlet stroke

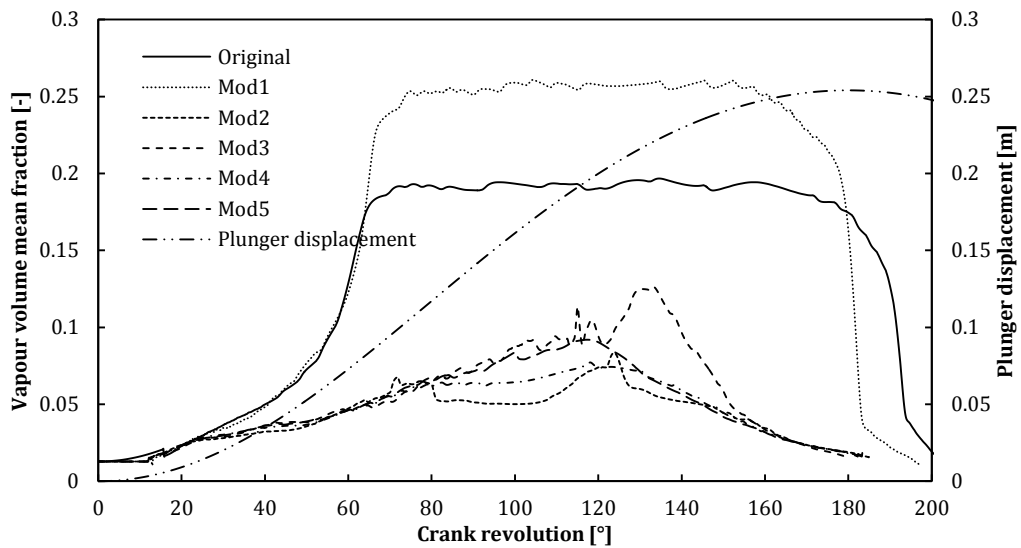


Figure 9-12: Valve-seat gap 2nd phase (vapour+air) mean vapour fraction.

Figure 9-18 shows the chamber second phase volume integral (vapour and air) for all of the configurations whereas Table 9-2 summarizes the most relevant outcomes of the CFD simulations. The pump equipped with the original valve/seat configuration was affected by the highest amount of 2nd phase fraction, this caused the lowest volumetric efficiency as one can see in Table 9-2. As expected, Mod2 was the least affected by the 2nd phase generation

even though Mod3 to 5 did not show a significantly different trend with respect to Mod2. Table 9-2 relates the volumetric efficiency with the 2nd phase integral peak of Figure 9-18 and the inlet valve opening and closing times. The original valve showed the highest delay in opening which was related to the smallest valve area where the pressure drop operated due to the smallest inner valve-seat diameter. Mod1 and 2 which have a larger inlet diameter (100 and 110 mm respectively) were subjected to a higher lifting force which exceeded the spring preload sooner than the original valve case. From Mod3 to 5 the cut in the valve body generated a reduction in the pushing area and thus the valve lifted off the seat later than Mod2 case. Another important remark which Table 9-2 reveals is the strict link between the volumetric efficiency, the 2nd phase generation and the valve closing time delay. The higher the pump chamber vapour production the higher the delay and the lower the volumetric efficiency.

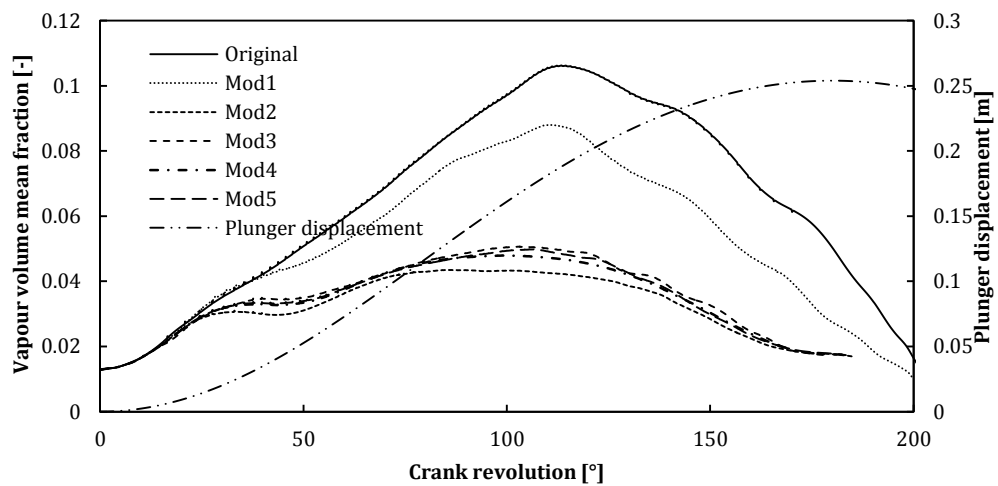


Figure 9-13: Plunger top surface mean vapour fraction.

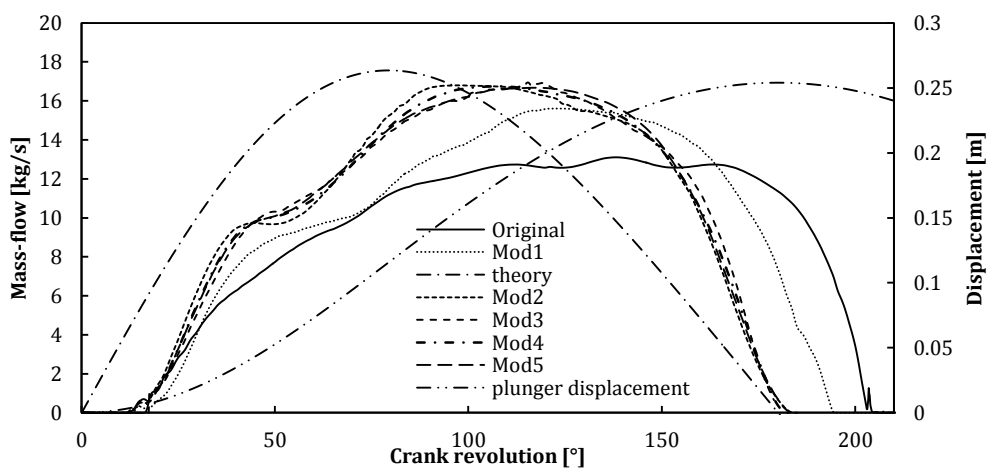


Figure 9-14: Inlet Mass flow rate.

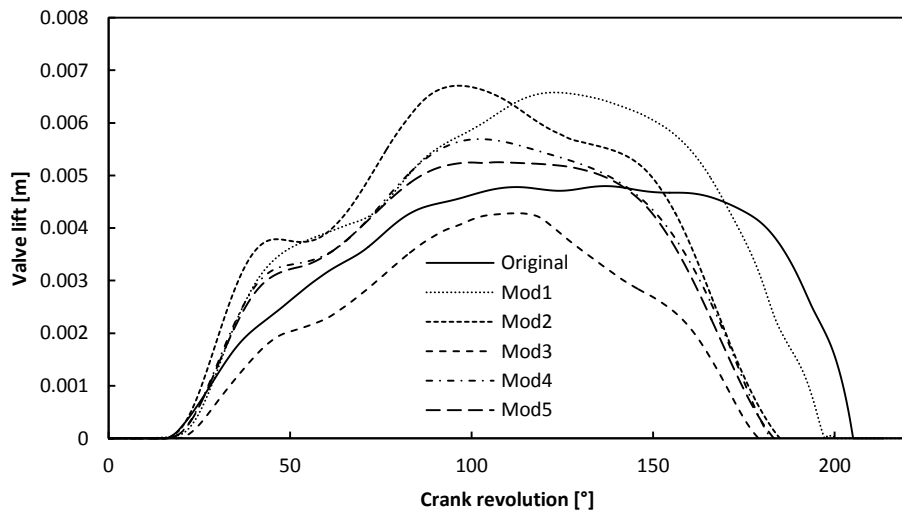


Figure 9-15: Inlet Valve lift.

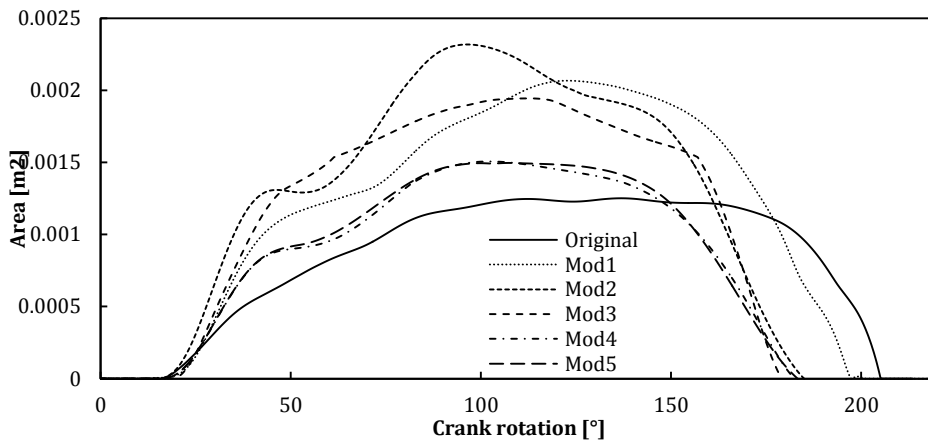


Figure 9-16: Total flow area, sum of the main flow area and the additional one where present.

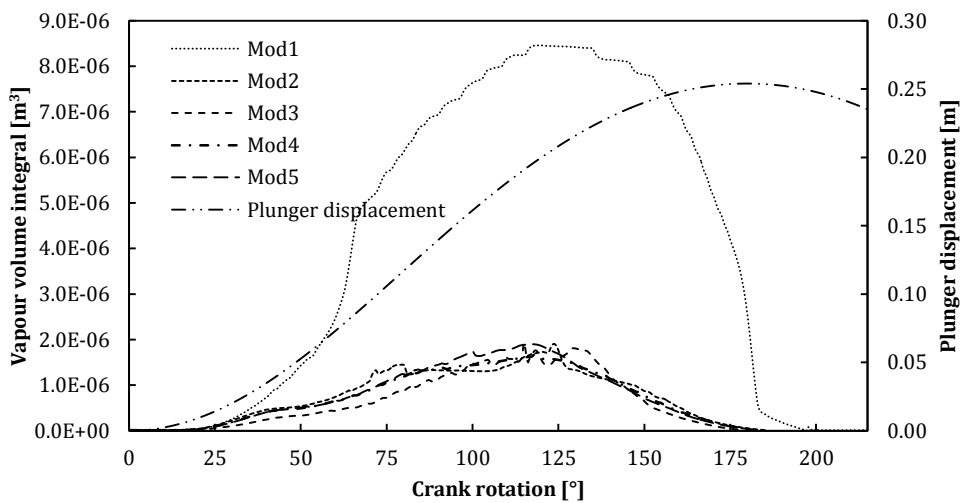


Figure 9-17: Valve-seat gap volume vapour integral.

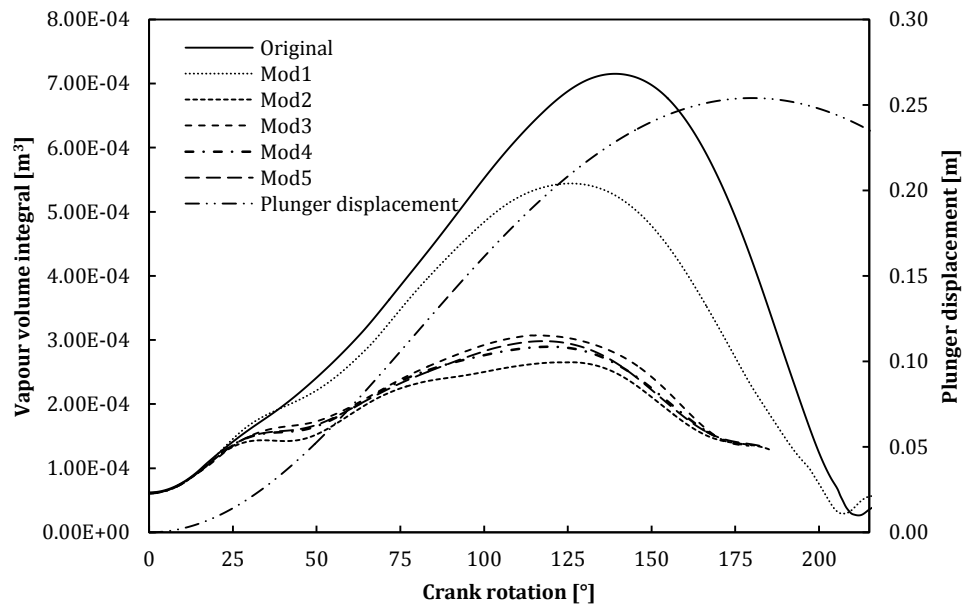


Figure 9-18: Chamber volume vapour integral.

Table 9-2: Summary and comparison of the six configurations

	Volumetric efficiency [%]	Inlet valve opening time [°]	Inlet valve closing time [°]	Maximum chamber 2 nd phase volume × 10 ⁻³ [m ³]	Maximum Valve-seat gap 2 nd phase volume × 10 ⁻⁶ [m ³]
Original CAD23	93.36	15.6	205.3	0.7151	-
Mod 1 CAD24	95.1	12.25	200.75	0.5441	8.46
Mod 2 CAD25	97.07	11.74	185.06	0.2652	1.90
Mod 3 CAD26	96.78	12.5	179.12	0.3075	1.93
Mod 4 CAD27	97.04	12.0	182.62	0.2895	1.66
Mod 5 CAD28	97.01	12.0	183.37	0.2982	1.89

9.2.3 Valve-seat angle sensitivity test

Due to the high non linearity of the problem a further sensitivity test focused on the valve-seat angle only was carried out. Three geometries were chosen to carry out the transient CFD simulations accounting for the vapour generation. The three valve designs differed by the valve-seat angle. Angles of 10°, 20° and 30° were chosen (Figure 9-19 to Figure 9-21).

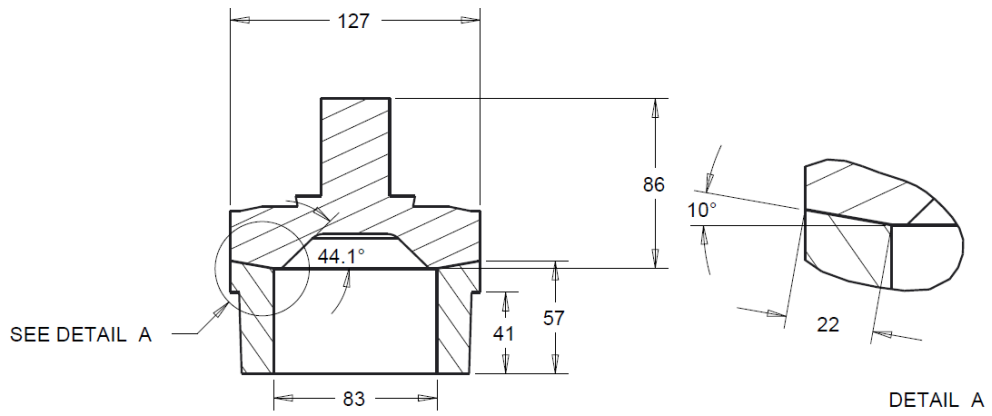


Figure 9-19: Stem valve, urethane ring step neglected, 10° valve-seat angle.

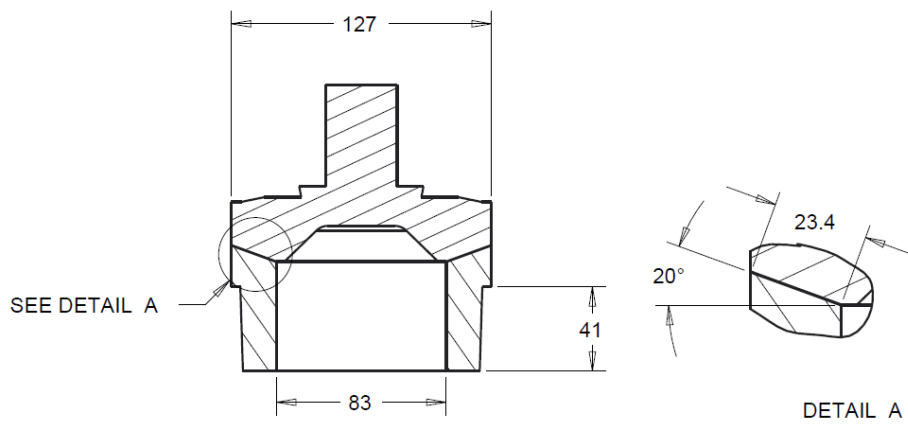


Figure 9-20: Stem valve, urethane ring step neglected, 20° valve-seat angle.

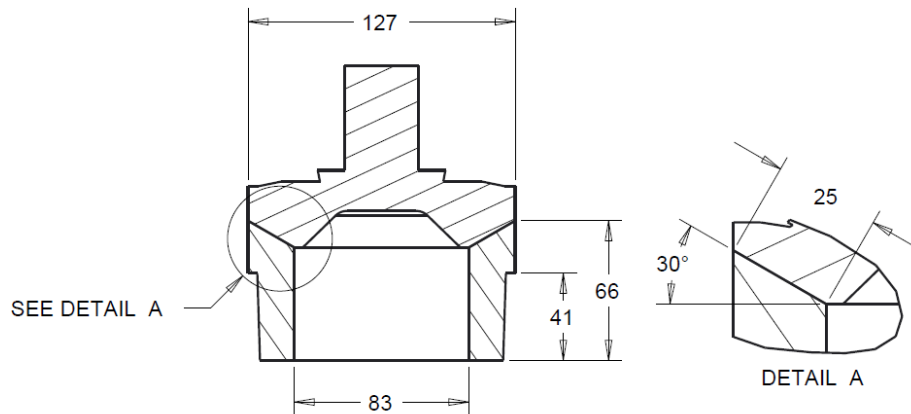


Figure 9-21: Stem valve, urethane ring step neglected, 30° valve-seat angle.

A Stem guided type of valve was chosen and the real shape of the urethane ring was neglected to simplify the geometric model as the analyst's intention was to create a consistent set of models to discuss the differences.

9.2.4 Valve-seat angle sensitivity test results

Figure 9-22 demonstrates that the three configurations chosen do not show significant differences in the chamber pressure trend. The situation is different if one observes the second phase fraction in the valve-seat gap volume where one can say that the higher the angle the lower the vapour-air fraction which is 40% in the 10° configuration and decreases to approximately 34% in the 30° configuration. A maximum of 24% of 2nd phase integral difference can be observed in Figure 9-27 and this confirms the data on the volume fraction. As the valve-seat gap volume was negligible compared to the overall chamber volume, either the chamber 2nd phase fraction or its integral does not show any difference among the three configurations, this is demonstrated by Figure 9-24 to Figure 9-26.

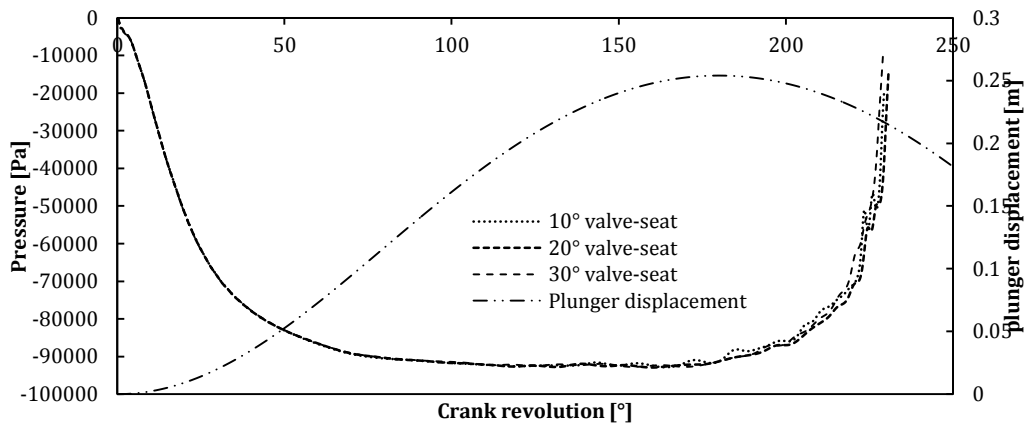


Figure 9-22: Valve-seat angle sensitivity test, chamber pressure for the 10°, 20° and 30°.

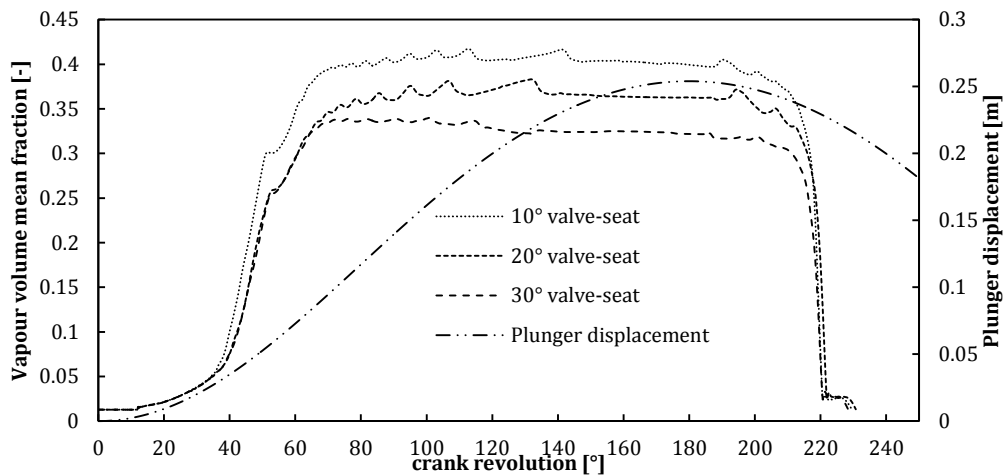


Figure 9-23: Valve-seat angle sensitivity test, Valve-seat gap volume 2nd phase fraction for the 10°, 20° and 30°.

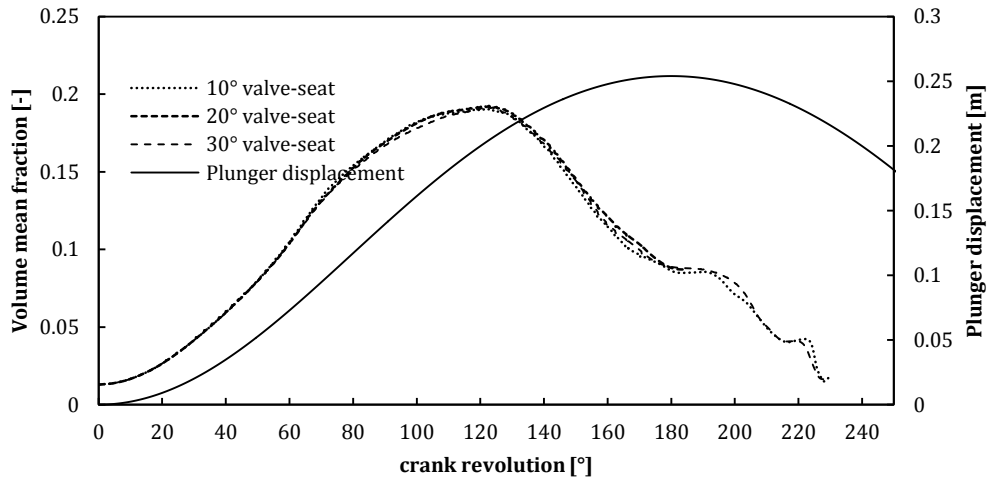


Figure 9-24: Valve-seat angle sensitivity test, 2nd phase volume fraction in the vicinity of the plunger for the 10°, 20° and 30°.

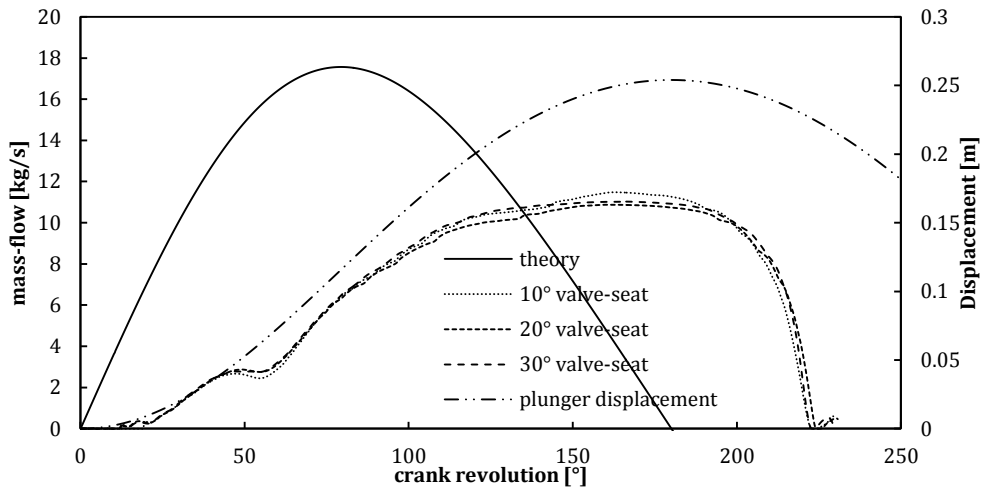


Figure 9-25: Inlet mass flow for the 10°, 20° and 30° configurations.

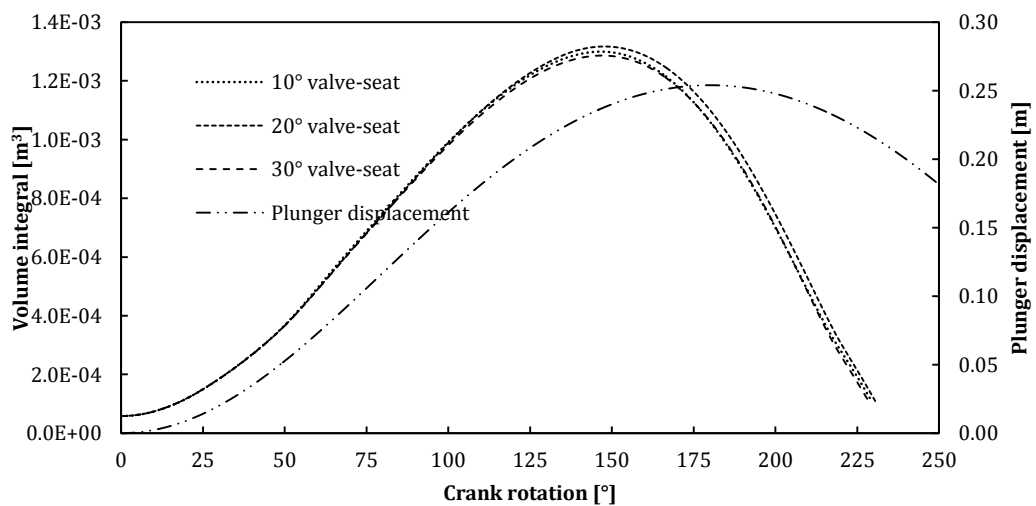


Figure 9-26: Chamber 2nd phase integral for the 10°, 20° and 30° configurations.

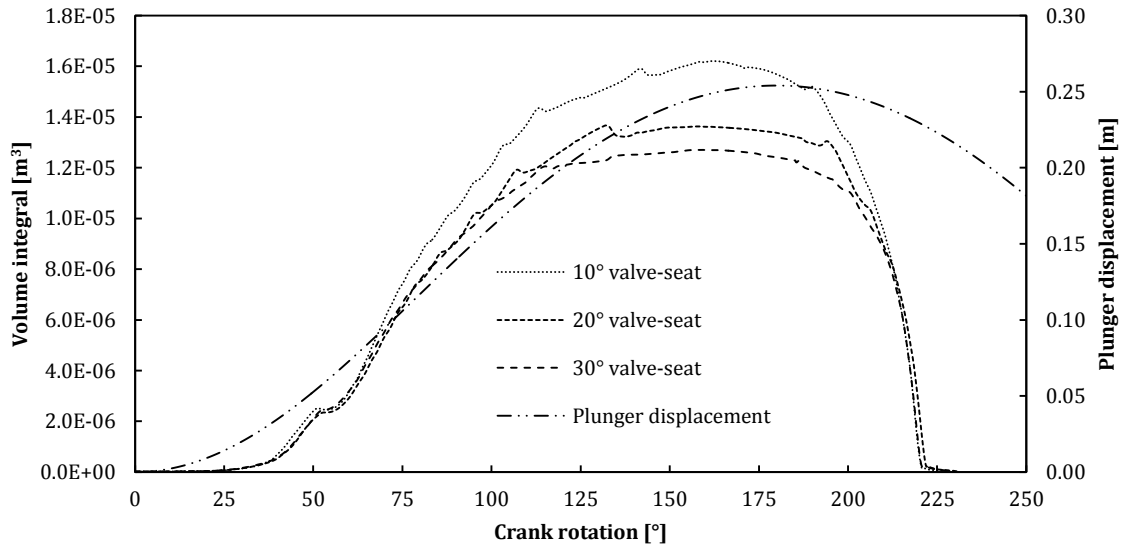


Figure 9-27: Valve-seat gap volume 2nd phase integral for the 10°, 20° and 30° configurations.

Table 9-3 summarises the data of Figure 9-26 and Figure 9-27. The volumetric efficiency increases slightly moving from the 10° to the 30°, furthermore, no significant difference was observed in the inlet valve opening and closing time.

This detailed analysis rejects in part the results of single phase steady state analysis carried out and discussed in the paragraph 9.2.1. This points out once again the highly non-linear behaviour of the pump due to the transient effects and also to the cavitation.

Table 9-3: Summary and comparison of the three valve-seat angle configurations

	Volumetric efficiency [%]	Inlet valve opening time [°]	Inlet valve closing time [°]	Maximum chamber 2 nd phase volume × 10 ⁻⁶	Maximum Valve-seat gap 2 nd phase volume × 10 ⁻⁶ [m ³]
10° Valve-seat	77.66	11.62	229.25	1.3	16.2
20° Valve-seat	79.9	12	230.87	1.31	13.6
30° Valve-seat	78.46	12	229.12	1.28	12.7

9.3 Shaft angular speed sensitivity test

Mod2 and 5 were tested by means of the same CFD model also at higher shaft speed. Figure 9-28 to Figure 9-34 show the results in terms of pressure, vapour generation, mass flow and valve lift obtained by CFD simulations where 260 rpm shaft angular speed was set instead of 130 rpm. The situation depicted reveals a general worsening of the performance as the generation of vapour is higher in both cases if compared to the 130 rpm cases. This is quantitatively highlighted by Table 9-4. The table quantifies the second phase generated

relating it to the volumetric efficiency and valve opening and closing delays for each of the geometries and crankshaft angular velocities. The reader may also see that the volumetric efficiency decreases by approximately 4% in both the geometries when accelerating the shaft from 130 to 260 rpm.

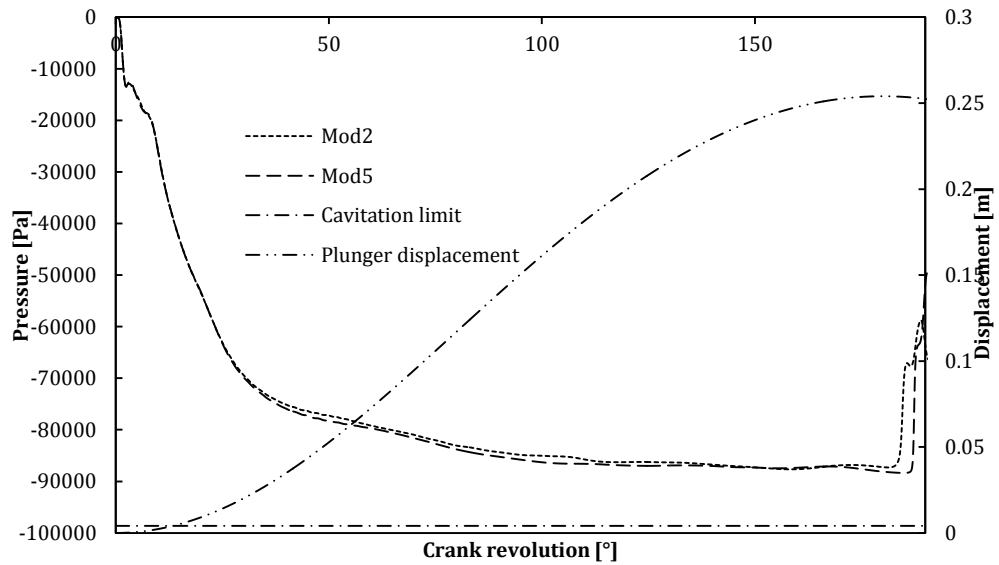


Figure 9-28: Mod2 and 5 at 260 rpm of shaft angular speed, chamber pressure during the inlet stroke

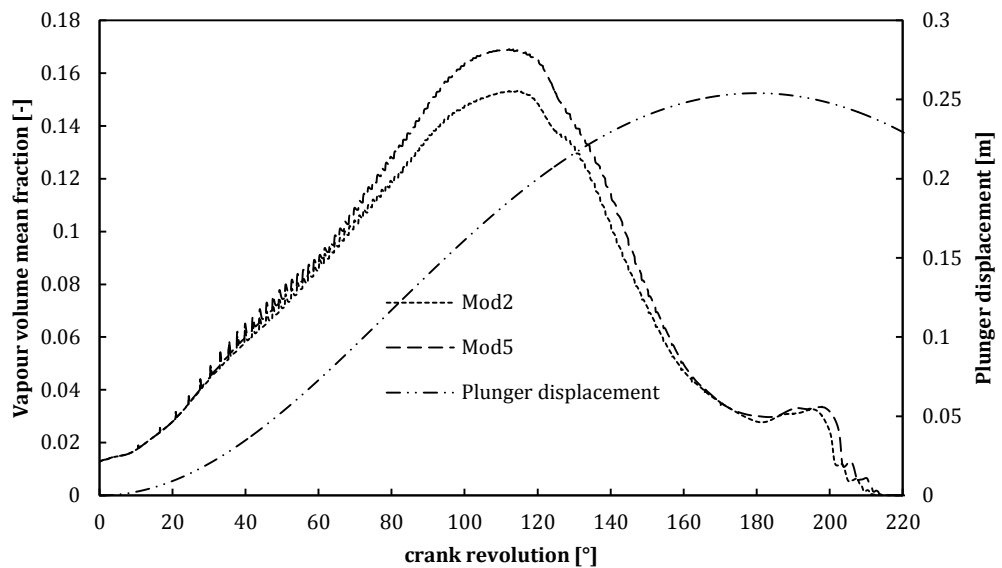


Figure 9-29: Mod2 and 5 geometry at 260 rpm, plunger top surface vapour fraction

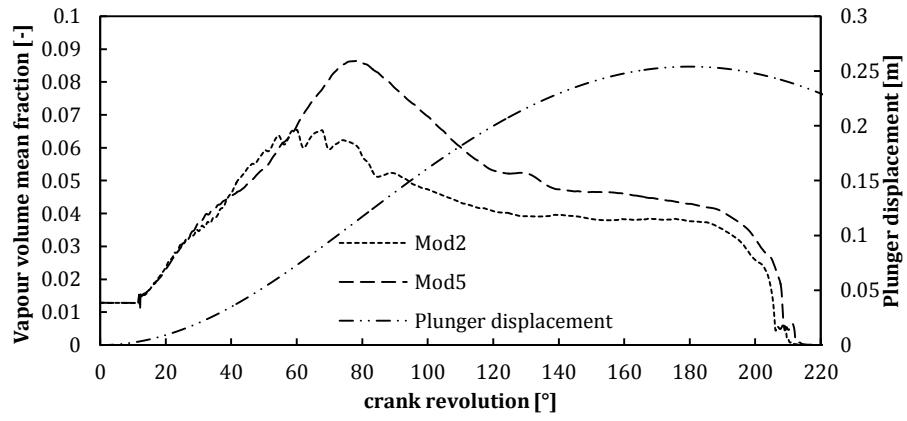


Figure 9-30: Mod2 and 5 geometry at 260 rpm, valve-seat gap volume vapour fraction

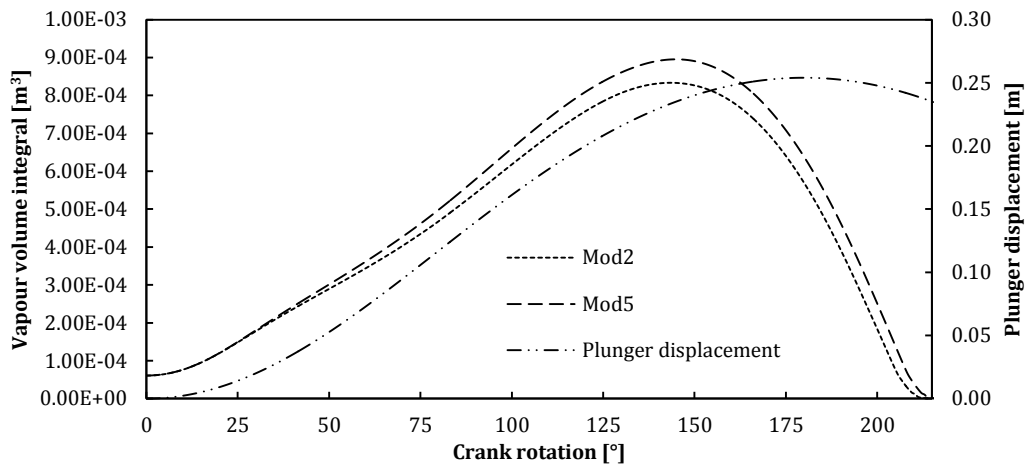


Figure 9-31: Mod2 and 5 geometry at 260 rpm, chamber vapour volume integral

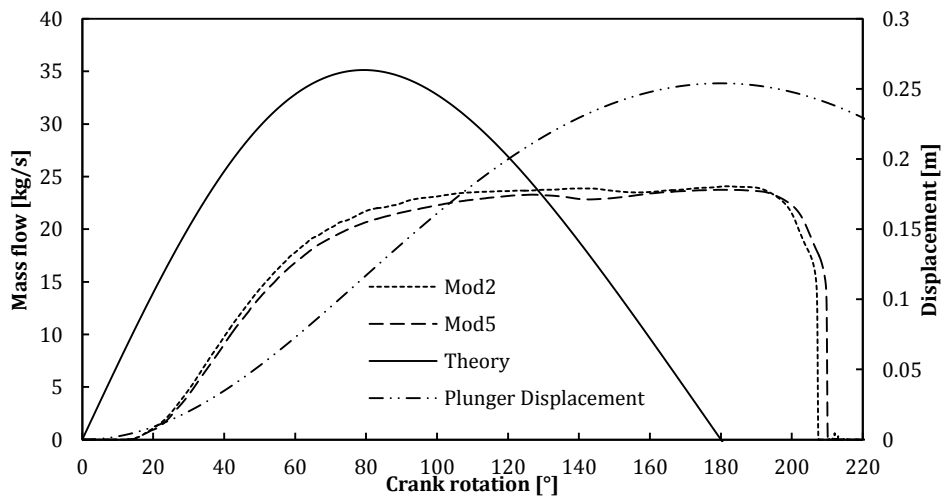


Figure 9-32: Mod2 and 5 geometry at 260 rpm, mass flow rate compared with theory

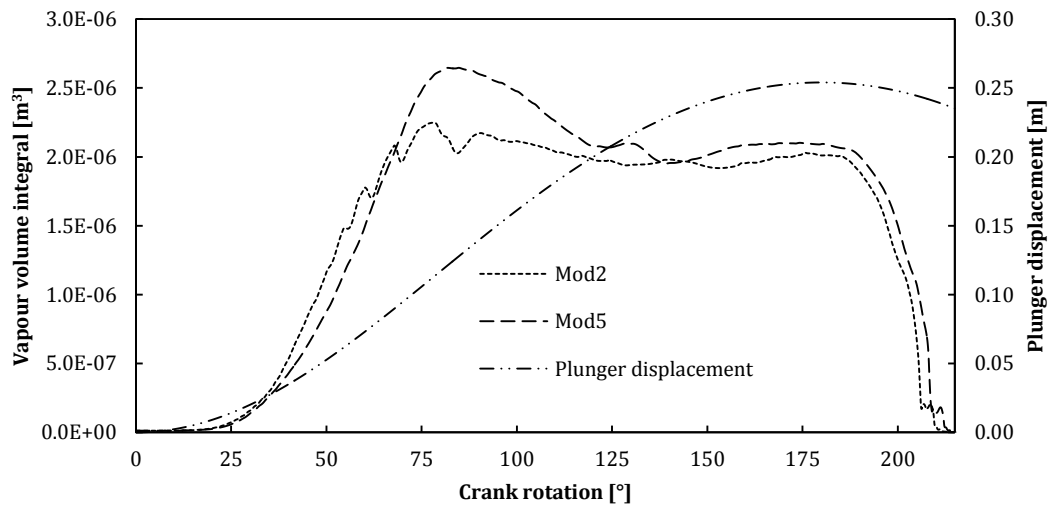


Figure 9-33: Mod2 and 5 geometry at 260 rpm, valve-seat gap volume vapour integral

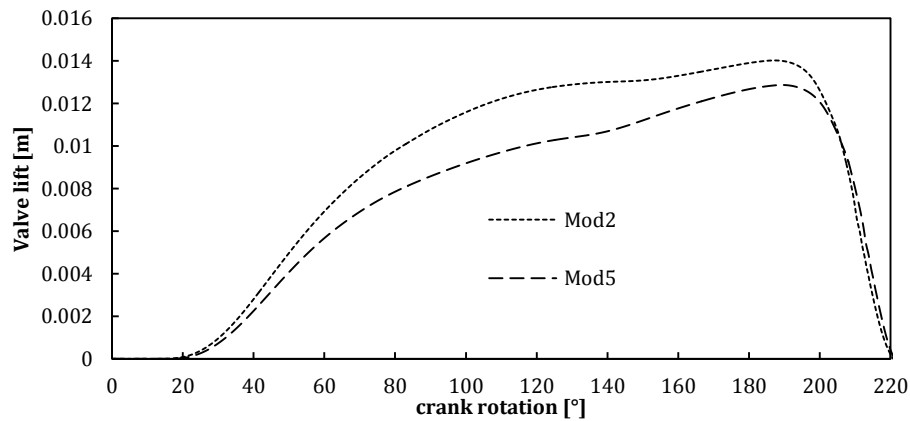


Figure 9-34: Mod2 and 5 geometry at 260 rpm, valve lift history

Table 9-4: Mod2 and 5 at 260 rpm, volumetric efficiencies and their relation with vapour generation and valve delays

	Volumetric efficiency Vs standard conditions [%]	Inlet valve opening time [°]	Inlet valve closing time [°]	Maximum chamber 2 nd phase volume ×10 ⁻³ [m ³]	Maximum Valve-seat gap 2 nd phase volume ×10 ⁻⁶ [m ³]
Mod 2 CAD25@ 260 rpm	94.5	11.6	220.9	0.83	2.25
Mod 2 CAD25@ 130 rpm	97.07	11.74	185.06	0.2652	1.90
Mod 5 CAD28@ 260 rpm	93.2	12.2	221.2	0.89	2.64

Mod 5 CAD28@	97.01	12.0	183.37	0.2982	1.89
130 rpm					

9.4 Spring preload sensitivity test

Figure 9-35 shows in more details the stiffness characteristic of the spring which was fed into the UDF (Aldo Iannetti, M. Stickland, et al. 2014). The pump model with the original valve-seat geometry configuration was simulated in two cases. In the first case which was the original, the spring preload was defined by fixing the spring compression at the closed position at 26 mm and that gave an initial preload of approximately 300 N, in the second case the spring was compressed of 13 mm at zero lift and this gave a preload of approximately 150 N. The objective in this further analysis was to obtain higher valve lift under similar external pressure forces and to estimate how much this affects the vapour generation. This was accomplished by comparing the second case with the first one.

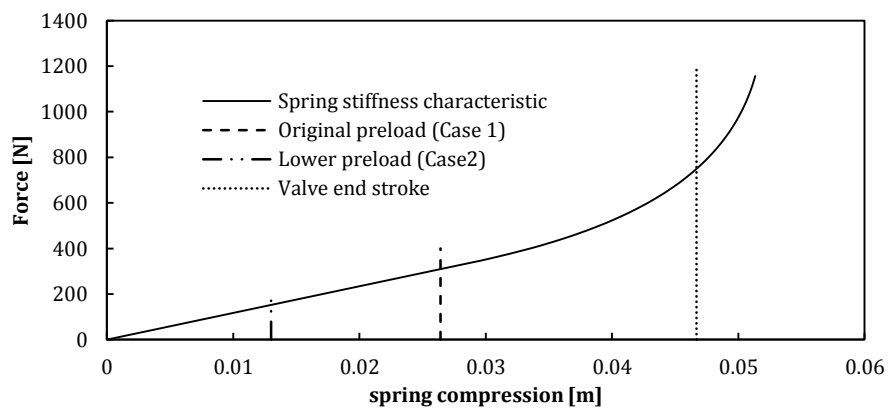


Figure 9-35: Valve stiffness characteristic and chosen preload for the two cases discussed

9.4.1 Valve spring preload test results

As shown in Figure 9-36 the spring preload significantly affects the chamber pressure, case 2 minimum pressure was approximately 10kPa higher than case1. This depended on the higher valve lift achieved by the lower preload case as one can see in Figure 9-37. The higher lift resulted in an increased flow area and a consequently lower velocity which caused a lower pressure drop across the valve. Figure 9-38 and Table 9-5 complete the overview of this analysis showing the amount of second phase generated in the pump chamber and correlate the delay in opening and closing time with the vapour generation. Decreasing the spring preload creates a smaller delay in the valve opening. Furthermore, the higher lift caused a lower amount of vapour creation which lowered the closing delay. As explained by Iannetti (Aldo Iannetti, M. Stickland, et al. 2014) the pump utilised the initial part of the outlet stroke to compress the vapour and change it into water at constant pressure (vapour pressure),

therefore a lower amount of vapour usually means a smaller delay because the compressing process lasts for a shorter period of time.

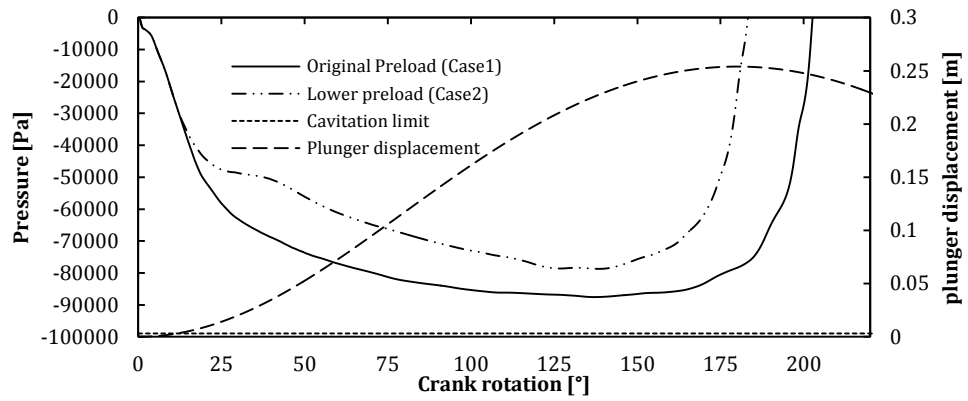


Figure 9-36: Chamber pressure history, original and lower spring preloads cases in the original valve-seat geometry

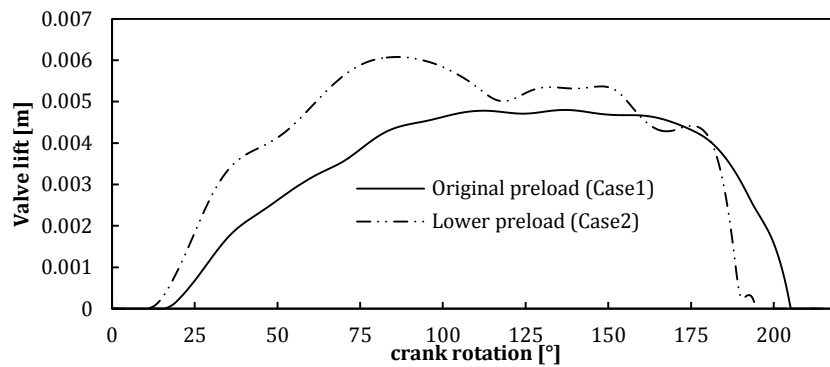


Figure 9-37: Valve lift-time histories. Case 2 shows a higher maximum lift and as a consequence, a wider flow area.

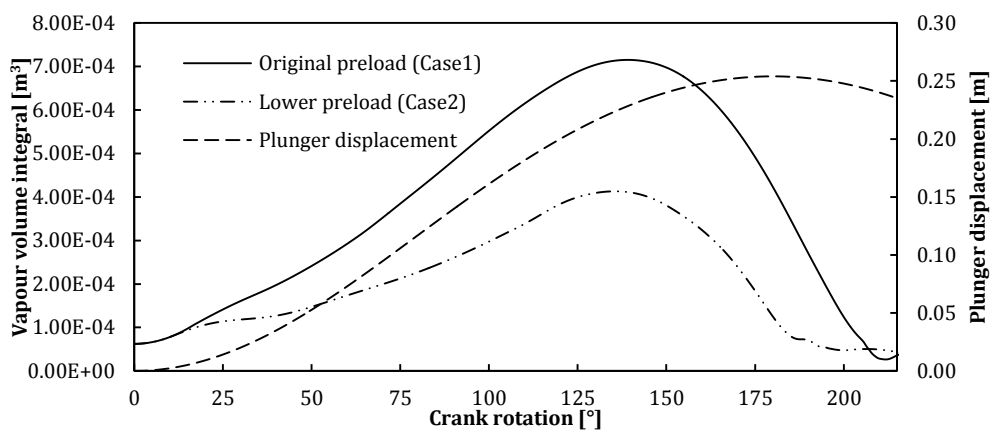


Figure 9-38: Pump chamber vapour integral throughout the inlet stroke, Case 2 showed a significant reduction in vapour generation.

Table 9-5: Summary of the spring preload sensitivity test. Case 2 shows a lower valve opening and closing delay and higher efficiency

	Volumetric efficiency [%]	Inlet valve opening time [°]	Inlet valve closing time [°]	Maximum chamber 2 nd phase volume × 10 ⁻³ [m ³]
Valve original preload (Case1)	93.36	15.6	205.12	0.7151
Lower spring preload (case2)	98.54	10.25	194.75	0.4129

9.5 Valve mass sensitivity test

A sensitivity test on the valve mass was performed to understand the influence of the mass on the cavitation phenomenon. The model of the pump equipped with the original valve and valve seat geometry was re-launched with the UDF modified. By adjusting the UDF a smaller valve mass model was simply obtained. The results were then compared to those obtained with the original mass valve model. The choice of halving (from 2.4 to 1.2 kg) the original valve mass was made and the Figure 9-39 to Figure 9-42 show the comparison.

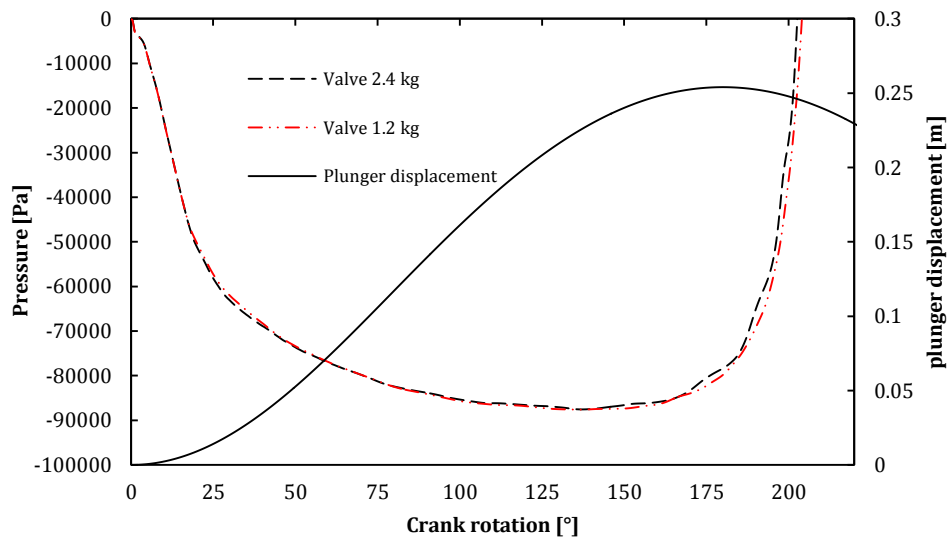


Figure 9-39: Chamber pressure of the original valve and valve seat geometry when halving the valve mass

Figure 9-39 to Figure 9-42 demonstrate that the valve mass has a very low influence on the outcomes. For instance, the valve lift trends of the two cases are basically overlapped, as shown in Figure 9-42. The pressure field, which is directly related to the valve lift behaves in a similar way, as shown in Figure 9-39. The difference in vapour generated in the valve-seat

gap volume is therefore negligible as the difference of volumetric efficiencies which one may calculate integrating the mass flow rate of Figure 9-41.

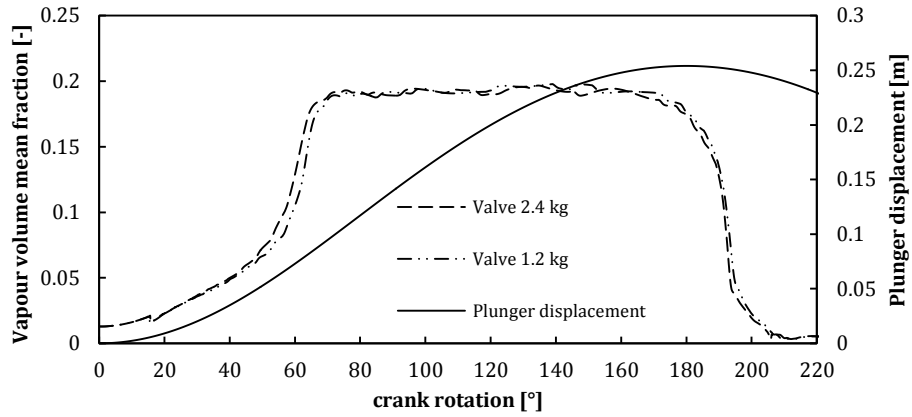


Figure 9-40: Vapour generated in the valve-seat gap volume, case of original valve mass compared to the lighter valve case

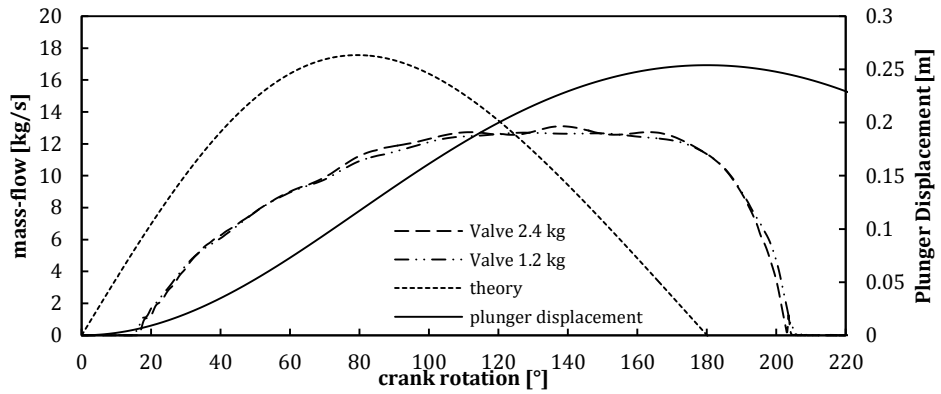


Figure 9-41: mass flow rate during the inlet stroke, original valve mass and shape compared to the lighter valve mass case and the theory valve

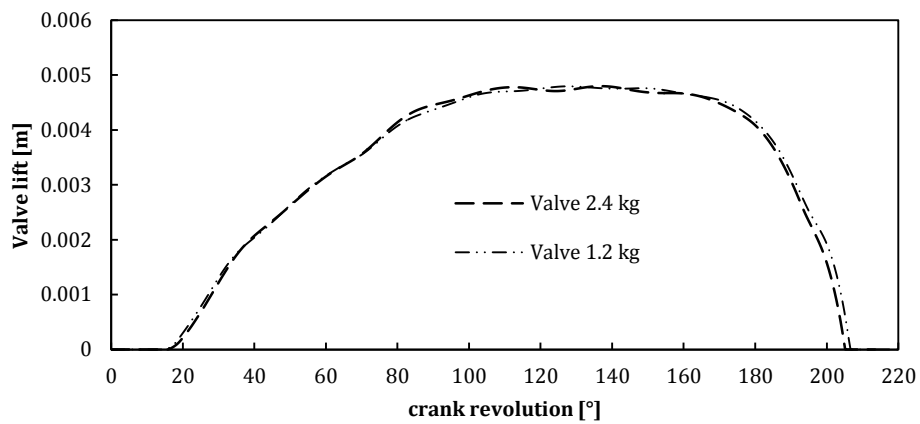


Figure 9-42: Valve lift history, original valve mass case and lighter valve case

9.6 Conclusion

The detailed analysis of the geometric and operating parameters acting on cavitation together with the analysis of the non-condensable gas dissolved in the working fluid carried out in Chapter 7, 8 and 9, pointed out the importance of some of them with respect to the others. The author chose to investigate the following parameters:

1. Valve and valve seat design, particularly the following aspects:
 - a) Valve seat inner diameter.
 - b) Valve-valve seat angle.
 - c) Effect of alternative designs with additional opening areas on the main valve body: influence of the valve inner pushing area.
2. Valve mass.
3. Valve spring initial preload.
4. Non condensable dissolved gas.
5. Inlet pressure.

The analysis revealed that one of the most influential parameters affecting the performance of PD pump in cavitating condition is the inlet valve seat inner diameter. This statement is supported by Figure 9-18 and Table 9-2 which show that moving from the original configuration to Mod 2 (from 83 mm to 110 mm of seat inner diameter) a decrement of the second phase of 63% is achieved. The second most influential parameter on PD pump performance on cavitation is the valve spring preload. This is demonstrated by Figure 9-38 and Table 9-5. Decreasing the initial valve spring preload by 50% a decrement of the maximum 2nd phase generation in the pump chamber of 42% was achieved.

The shaft angular velocity is also a crucial parameter in cavitation. In fact comparing Table 9-2 and Table 9-4 one can see (Mod 2 configuration) that increasing the shaft rotation velocity from 130 rpm to 260 rpm an increment of the second phase maximum of 69% was achieved (from 0.26 l to 0.83 l circa).

The inlet pressure affects significantly the performance of the pump as it is the source of the low pressure triggering cavitation together with the crank angular velocity. Adjusting the inlet pressure may result in the appearance of any regimes of cavitation as demonstrated by table 7-2, figure 7-2 and figure 7-3.

The analysis demonstrated that all other parameters listed above have a very low or negligible influence on cavitation. For instance the valve-seat angle of 30° appears to cause a slightly lower vapour generation in the valve-seat gap volume but an overall negligible

influence on the vapour generation in the pump chamber. This aspect will be taken into account for the study of the final optimized valve but it cannot be considered a parameter worthy to focus on in the next chapter. Altering the initial design and moving to non-ordinary valve shapes (e.g. Mod 3 to 5) which had additional opening areas cut in the valve main body, does not provide any better results as the increment of the flow area, which is beneficial, is entirely covered by the loss in the valve pushing area and therefore in the valve maximum lift. The quality of the working fluid (usually water) has a non-negligible influence on cavitation but as it is very complicated to adjust the quantity of the dissolved gas, this parameter will no longer be considered.

Non-conformal valve designs are also very difficult to manufacture and would suffer from important sealing problems which have not been considered as the physical principle only was under investigation. Obviously, because of their poor performance the author will not consider the feasibility of them and from this point on.

The discussion now moves to a more sophisticated step, it is not clear at the moment how to use the technical information pointed out above. Furthermore it is not even clear on which of the most influential parameters to act in order to define a final and optimized valve shape geometry. This topic will be discussed in the next chapter in more details.

10 Optimised valve geometry

10.1 Introduction

The previous chapter provided the reader with much detailed information on the influence of cavitation in PD pumps due to either operating or geometric design parameters. It was concluded that the following set of parameters significantly affect the amount of vapour generated by cavitation (in order of importance):

- Shaft angular speed
- Valve seat inner diameter
- Spring preload
- Inlet pressure

Obviously not all of them are suitable to be adjusted in order to improve the performance of the pump in cavitating conditions. Indeed, there are operating, structural and geometric constraints which the analyst has to bear in mind. Furthermore, given that this kind of pump is subjected to many problems apart from cavitation as already mentioned in the introductory chapter, solutions which might look logical are, in fact, not feasible. This chapter will provide justification to support the design of the final and optimised valve design presented at the end of the chapter.

The angular shaft velocity, which in PD pumps is directly related to the mass flow rate, is an operating parameter which is usually defined by the need of the application the pump is used for but also it is adjusted depending on the layout of the pumping system where the pump is located. Moreover, the shaft angular velocity is one of the parameters together with the maximum pressure and power which manufacturers strive to increase in order to gain market share. Any solutions which restrict angular velocity would result in a non-competitive device on the market. The goal of the project is to redesign the valve shape obtaining better behaviour against cavitation for a given shaft angular velocity. For this reason crank velocity will no longer be considered in the list of the variable parameters.

The inlet pressure is the main source of the cavitation problems. It does not affect directly the competitiveness of the device as it does not involve the application directly. It is a matter of fact that the inlet pressure affects the NPSHa which can be interpreted as a safety factor against cavitation. The higher the inlet pressure the higher the NPSHa and the farther the pump is operating from cavitation. As already explained in this dissertation, the NPSHa depends also on the design of the inlet pipe which is usually a specification of the end user rather than the manufacturer who should provide minima requirements for the installation of

the pump in the system. Oil & gas users usually pressurize the inlet manifold of each PD pump in the system. In some application, for instance, the manufacturer suggest to make use of centrifugal pumps upstream the PD pump inlet manifold in order to improve the NPSHa and gain a higher safety margin against cavitation which can keep the pump safe even when high shaft rotational speeds increase the transient effects and the occurrence of negative pressure spikes. It is clear that the pressurization of the system upstream of the pumps has technical limitations that may vary for each customer. For this reason an optimization process based on the inlet pressure parameter is meaningless. The optimization should be carried out by making use of inlet pressure boundary conditions which should be the same for all the geometries under investigation. In this study, the inlet boundary conditions were consistently kept as discussed in chapter 5 where a mass flow dependent pressure was applied to the inlet duct in order to simulate the pressure drop due to the upstream inlet pipeline.

The spring preload is usually a design parameter which is chosen in conjunction with the crankshaft rotational velocity and therefore the plunger maximum velocity. The higher the velocity the higher should be the spring preload as it increases the force pushing the valve back to the valve seat once the inlet stroke comes to the end. According to Tackett (Tackett et al. 2008) the higher the spring preload the quicker the valve closes, this is important in order to avoid valve leakage and thus the volumetric efficiency loss. On the other hand the higher the spring preload the worse the regime of cavitation as a higher amount of vapour is generated as highlighted by the analysis carried out in the previous chapter. For this reason this parameter was discarded from the list above.

The valve seat inner diameter is the only parameter left to discuss. To introduce the topic the following comparison figure is brought to the reader's attention:

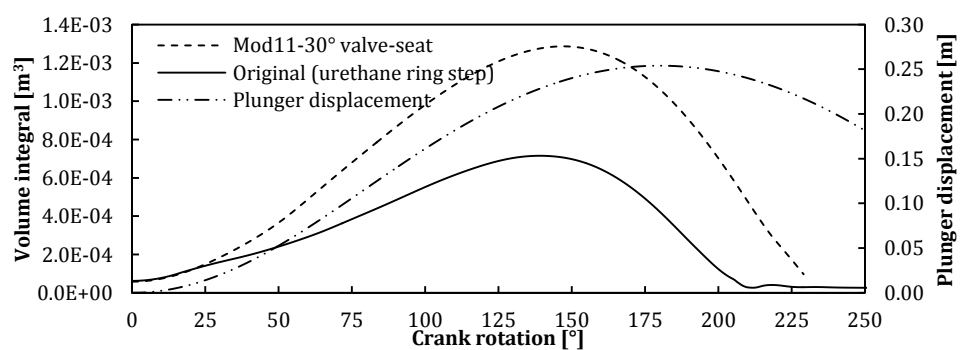


Figure 10-1: Effect of the urethane ring section on the 2nd phase integral (vapour + air) in the pump chamber throughout the inlet stroke, the configuration without the step in the urethane ring (Mod1) shows lower content.

Figure 10-1 shows the amount of the second phase (water + vapour) present in the pump chamber throughout the inlet stroke. The figure comes from two simulations which made use of the two valves shown in Figure 10-2. The figure demonstrates that the configuration with the step in the urethane ring section has better behaviour over the flat counterpart. Under the operating and boundary conditions discussed in chapter 5 a lower amount of vapour is generated. The reason will be explained in the next section.

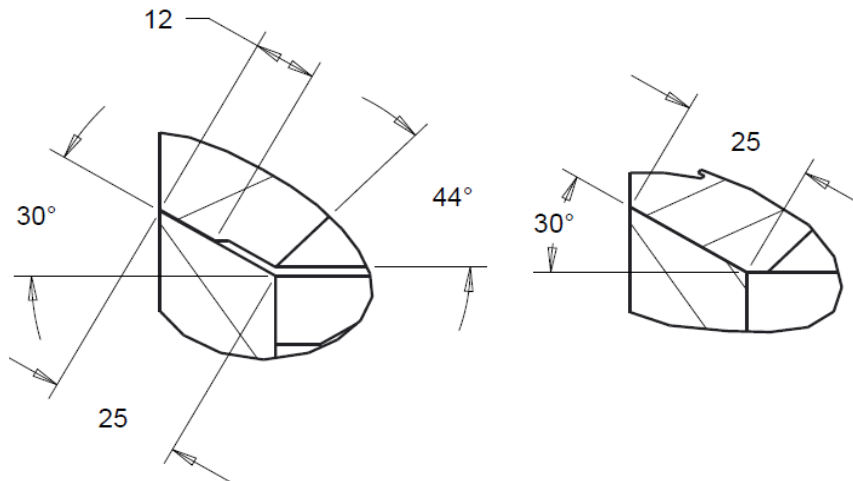


Figure 10-2: (Left) original valve equipped with the urethane ring step, (right) mod 11 without step in the ring and a perfect valve-seat contact. Dimensions are expressed in [mm].

10.2 Effect of the urethane ring shape

The urethane ring section shape of the valve seems to have a significant influence on the performance of the pump. To investigate this, the author needs to draw the reader's attention to some of the principles discussed in chapter 6:

- Flow induced cavitation is one of the causes of cavitation in PD pumps and occurs mainly in the valve-seat gap volume where the flow velocity is high.
- Velocity, area and pressure in the valve-seat gap volume are dependent on each other via Bernoulli's law. Fixing the flow area, the higher the velocity the lower the static pressure. Increasing the flow area one can achieve lower velocity and higher minimum pressure.
- A wider flow area results in a lower NPSHr and therefore a higher safety factor against cavitation.

The flow area is the minimum cylindrical passage area between the valve and the seat which is shown in Figure 10-3. According to simple geometric considerations the flow area depends on:

1. The seat inner diameter.
2. The valve lift.
3. The shape of the urethane ring section: Step thickness, urethane inner radius (where the step starts with respect to the radial coordinate).
4. (weak dependency) The valve seat angle.

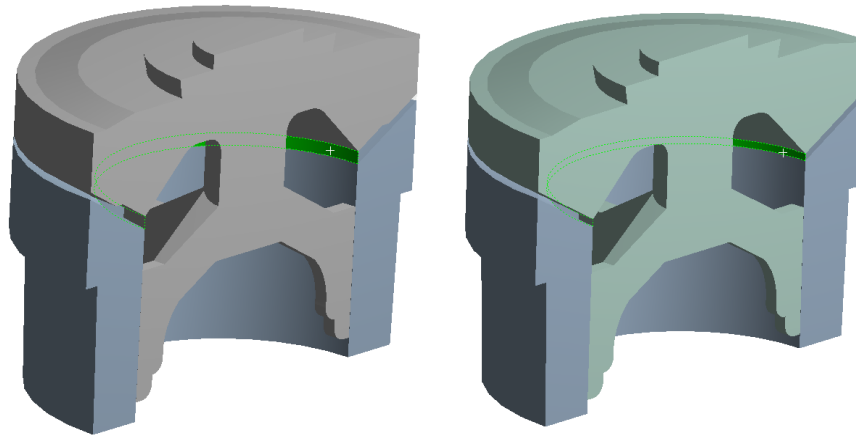


Figure 10-3: Fixed valve lift of 2 mm, (left) urethane step configuration can have a wider minimum passage area than the configuration without step (right). In this second case the minimum area is always the inner annulus highlighted in green colour in the figure on the right.

According to simple considerations based on the geometry, one can say that in the flat configuration (without the step in the urethane ring) the minimum passage area depends on the valve lift only and it is located always in the inner position along the radial coordinate as shown in Figure 10-4 (Table 10-1 summarises the hypothesis under which the curves in Figure 10-4 were drawn). In this case, the inner flow area is fixed by the seat inner diameter only. In the original valve case, the step in the urethane ring section plays an important role in defining the minimum flow area which depends also on the shape of the urethane ring and its step. In this case the minimum flow area is generally larger than in the previous case but also it can be located on the inward edge of the step according to the dimension of the step itself (Figure 3-12). In fact, geometric parameters such as the step starting location along the radial coordinate and its thickness determine the flow passage area. Figure 10-5 defines the nomenclature of geometric parameters already mentioned and provides a comparison between the two geometries under investigation. Figure 10-6 shows graphically the location of the minimum passage area for both the configurations (original Vs no-step). Figure 10-7, Figure 10-8 and Figure 10-9 show respectively:

- How the distribution vary with the valve lift (constant step thickness and urethane ring inner radius)
- How the distribution vary with the step thickness (constant lift and urethane inner radius)
- How the distribution vary with the urethane ring inner radius (constant lift and step thickness)

The figures demonstrate that the minimum flow area is always bigger in the step configuration than in the no-step configuration of Figure 10-4, they also demonstrate that the minimum flow area is always located in the inner step edge and, more importantly they demonstrate that increasing the urethane inner radius the analyst would increase the minimum flow area at every valve lift. Also increasing the step thickness up to a certain value which depends also on the valve lift itself (apparently 0.5 mm circa is the limit for 2 mm lift) a beneficial effect would be achieved, above that limit no further improvement would result. Figure 10-3 shows a qualitatively comparison between the inner flow areas of the original and no-step configuration counterpart.

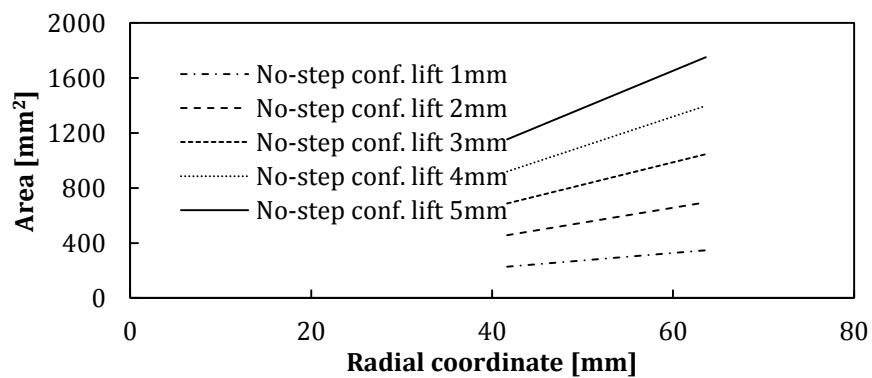


Figure 10-4: No-step urethane ring configuration, how the radial distribution of flow area changes with the valve lift.

Table 10-1: Summary of the parameters defining the flow area distribution of Figure 10-6.

	Valve-seat angle [°]	Seat inner radius [mm]	Valve outer radius [mm]	Step thickness [mm]	Urethane inner radius [°]	Valve lift [mm]
Original shape	30	42	64	1.5	51	2
No-step config.	30	42	64	-	51	2

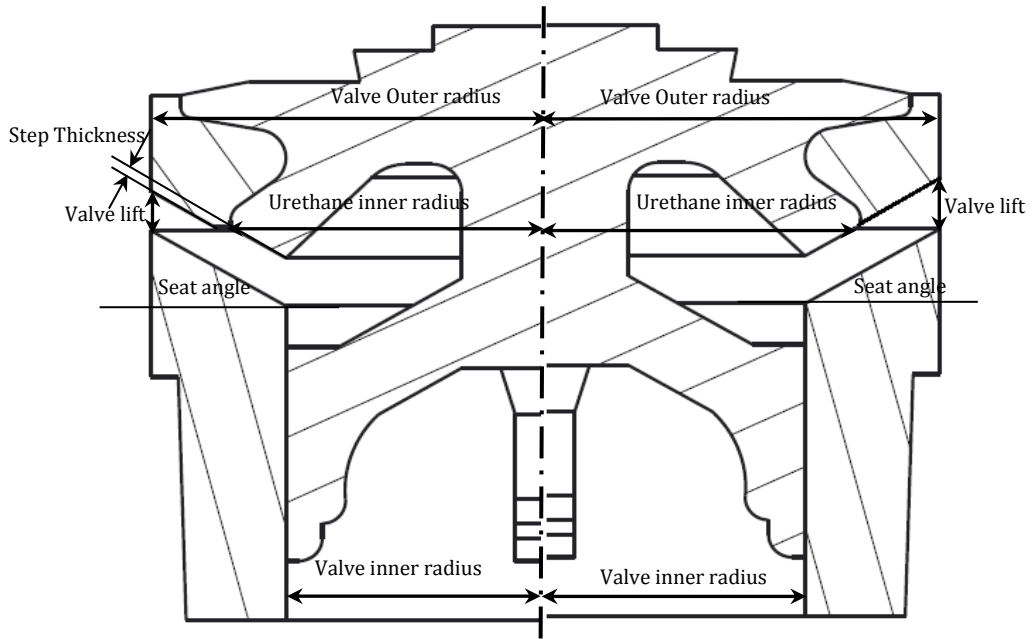


Figure 10-5: Original (left of the axis) Vs No-step configuration valve geometry (right).

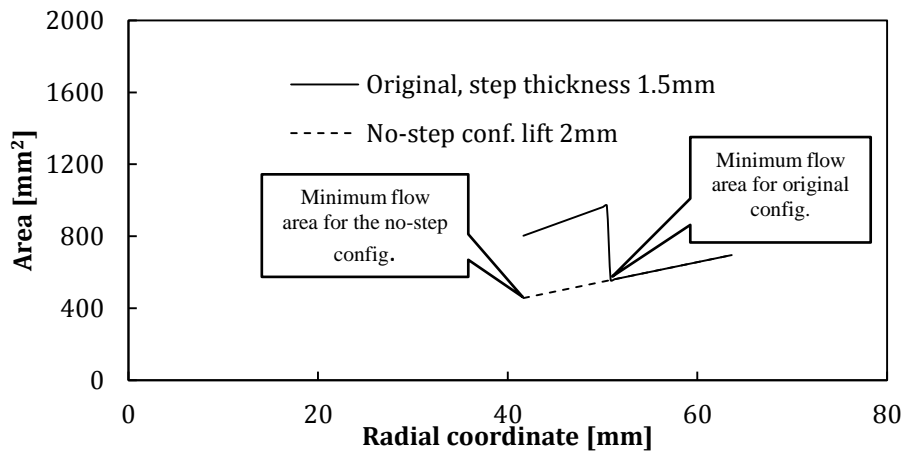


Figure 10-6: Radial distribution of flow area when the lift is 2 mm. Original Vs no-step configuration comparison.

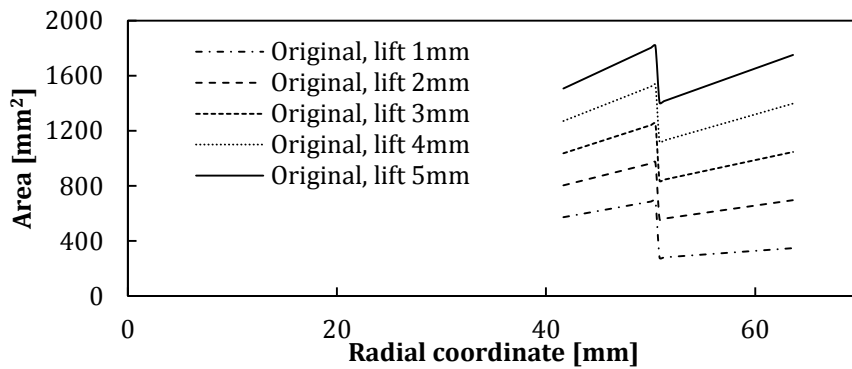


Figure 10-7: Original valve shape, how the radial distribution of flow area changes with the valve lift.

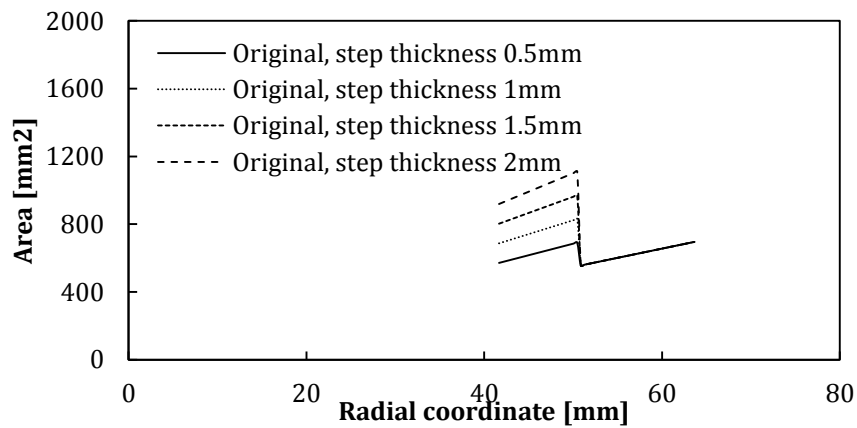


Figure 10-8: Original valve shape, how the radial distribution of flow area changes with the step thickness at fixed (2mm) lift.

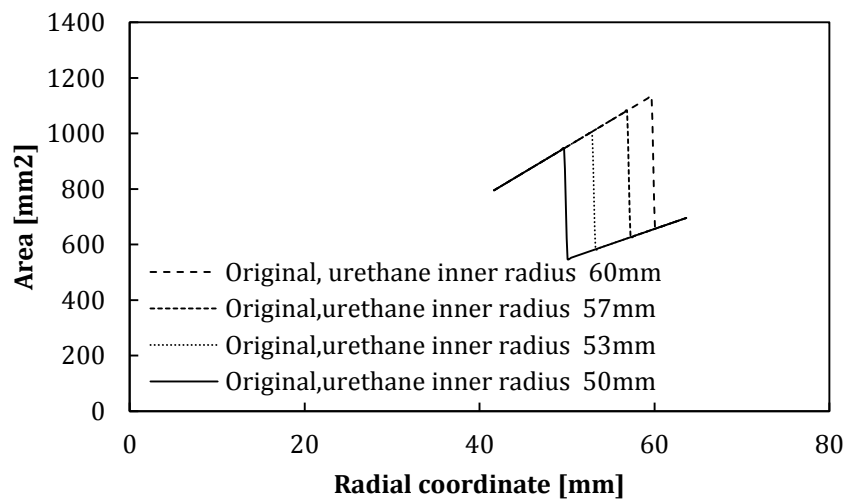


Figure 10-9: Original valve shape, how the radial distribution of flow area changes with the urethane ring inner radius at fixed (2mm) lift.

Indeed when the designer changes the shape of the valve, a modification of the valve lift history has to be expected as well. This is supported by Figure 10-10. The phenomena occurring in the pump chamber are, in fact, non-linear which is the reason why the analyst developed the two way coupling UDF to relate the valve lift to the fluid dynamic field. However, very small geometry adjustments such as the modification of the urethane ring section already discussed, should not result in a significant difference in the valve maximum lift which is the only parameter capable of affecting the benefits of the urethane ring step on performance. Regardless of the different shape of the valve lift-time history shown in Figure 10-10, the maximum lift is around 5 mm in both the configurations investigated.

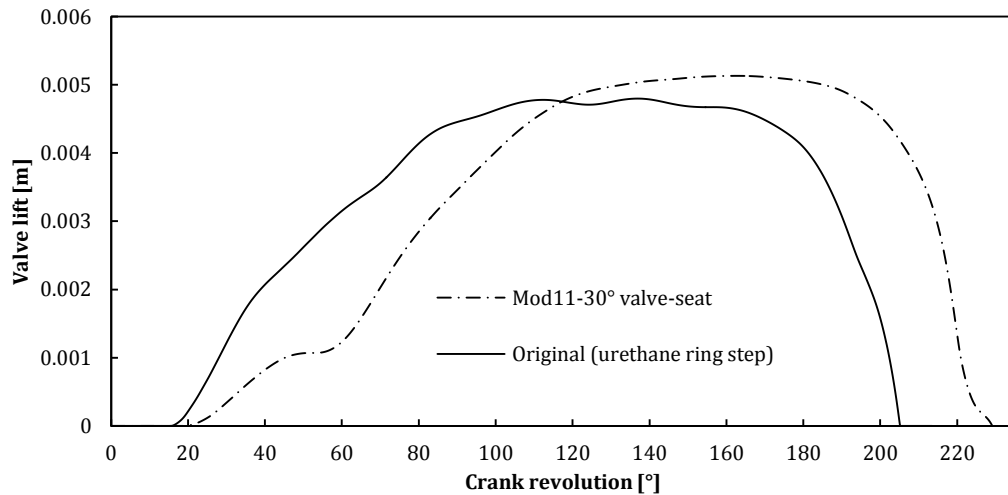


Figure 10-10: How the valve lift history changes with/without the step in the urethane ring.

Making use of the no-step configuration which is not feasible, the author showed the physical mechanisms which lead to the results depicted in Figure 10-1. The considerations discussed suggested that the author make use of the physical principles in a clever way. According to the figures shown in this section and bearing in mind the physics of flow induced cavitation, it is clear that the presence of the step in the urethane ring is beneficial because it increases the actual flow area leaving unchanged the seat inner diameter.

From a structural point of view this result is very important because the seat minimum thickness is limited by the need for structural stiffness. The designer cannot get rid of the seat inner part because when operating at very high pressure, the urethane ring must deform in order for the inner part of the valve main body to provide a metal-metal contact wide sufficiently to release the energy of the high pressure on the seat. Without the inner part of the seat the high forces would be released onto the urethane ring which would wear very quickly and this is not acceptable.

10.3 Optimised valve configuration

Figure 10-7, Figure 10-8 and Figure 10-9 suggest utilising the benefits of the urethane ring step and to improve them fulfilling the principles discussed in the previous paragraph. For this purpose, the following actions might be taken:

1. Increase the step thickness.
2. Increase the urethane inner radius.

3. Introduce a variable thickness distribution of the urethane along the radial coordinate.

Each action listed above has drawbacks that depend mainly on structural and sealing specifications. Increasing the step thickness, for instance, may result in a stiffer urethane ring which means a higher level of internal stresses. This might not be acceptable. On the other hand increasing the urethane inner radius would affect the sealing capabilities of the valve.

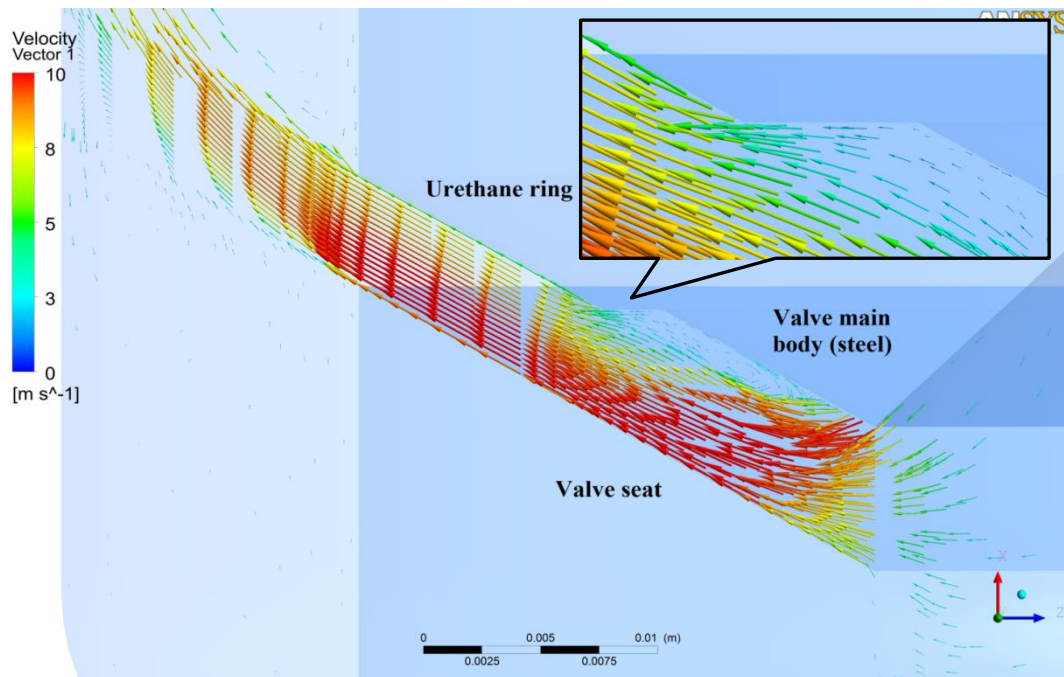


Figure 10-11: Flow velocity in the vicinity of the urethane-steel interface between the ring and the valve main body. A high erosion rate is expected.

Moreover the presence of the step itself introduces in the flow a geometric discontinuity which is not beneficial in mitigating against erosion problems. Figure 10-11 shows a detailed view of the fluid flow in the vicinity of the steel-urethane interface of the valve main body where the step edge is located. The small zoomed picture, located on the top right of the figure, shows a region of flow bending and a consequent acceleration. In that location is reasonable to expect a higher erosion rate because solid particles would not be able to follow the water streamlines because of their inertia. A high impact angle impingement zone is to be expected in this location. The third option in the above list can solve the structural problems as it would give the designer the possibility to obtain:

- An overall good stiffness and therefore lower urethane internal stresses
- Similar sealing capability

- Avoid high angle particle impact because of the absence of hard edges and thus small radius bends in the streamlines

On the right of Figure 10-12 one can observe the new configuration proposed and its differences with the original valve. Table 10-2 summarises the main differences and similarities between the two designs under investigation.

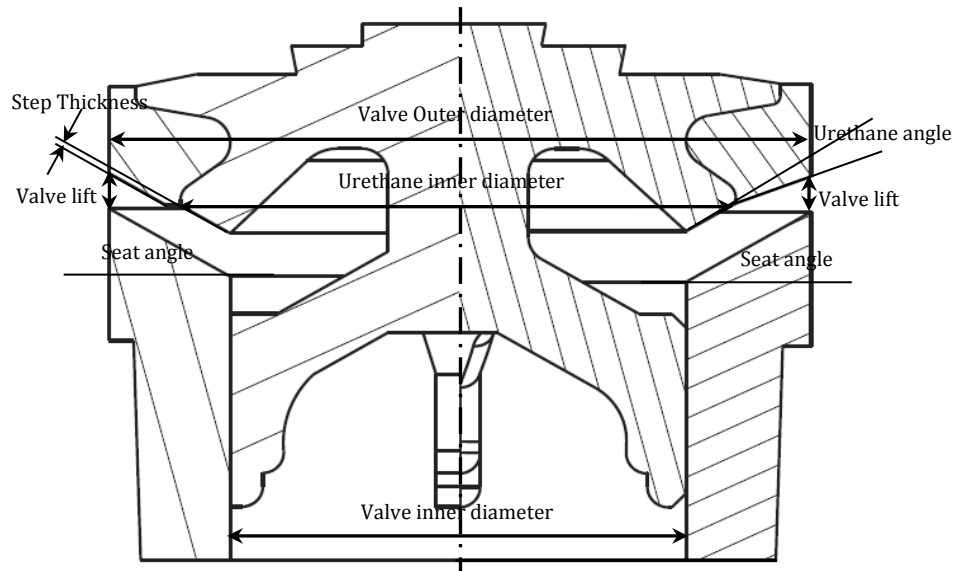


Figure 10-12: Original (left) Vs proposed Optimized valve geometry (right).

Table 10-2: Original-New generation valve geometry detail comparison

	Valve-seat angle [°]	Seat inner radius [mm]	Valve outer radius [mm]	Step thickness [mm]	Urethane inner radius [°]	Urethane ring angle [°]	Valve lift [mm]
Original shape	30	42	64	1.5	51	0	2
No-step config.	30	42	64	-	51	0	2
Proposed Optimised	30	42	64	-	51	10	2

Figure 10-6 can be completed to show how the proposed modification of the urethane ring section relates to the former and discussed geometries, Figure 10-13 results. Table 10-2 summarises the assumptions under which the curve of Figure 10-13 was drawn. The new and proposed geometry shows a great improvement over the others. Under the hypothesis of Table 10-2 the new design shows a minimum flow passage area increased with respect to the

original case, this minimum flow area moved to the valve-seat exit point along the radial coordinate. Therefore the new configuration should generally show lower velocity and higher pressure and they must be observed along the radial coordinate downstream the steel part of the valve main body. Figure 10-14, Figure 10-15 and Figure 10-16 show the influence on the minimum flow area on the urethane ring-seat angle, the urethane ring inner diameter and valve lift respectively. They demonstrate that:

- Increasing the *urethane ring-valve seat angle* the minimum flow area increases and skips to higher radial coordinate positions.
- Decreasing the *urethane inner radius* the minimum flow area increases and skips to higher radial coordinate positions.
- The higher the *valve lift* and the higher the minimum flow area.

The three parameters highlighted in *italic* are strictly connected together, for instance higher urethane-seat angles would result in higher urethane inner radius acceptable and vice versa.

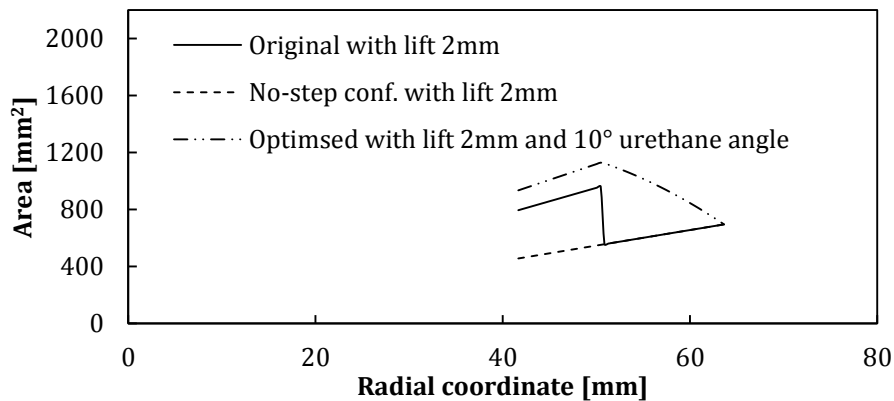


Figure 10-13: Original, no-step and new proposed valve comparison. Fixes valve lift of 2 mm and fixed urethane inner radius of 51 mm

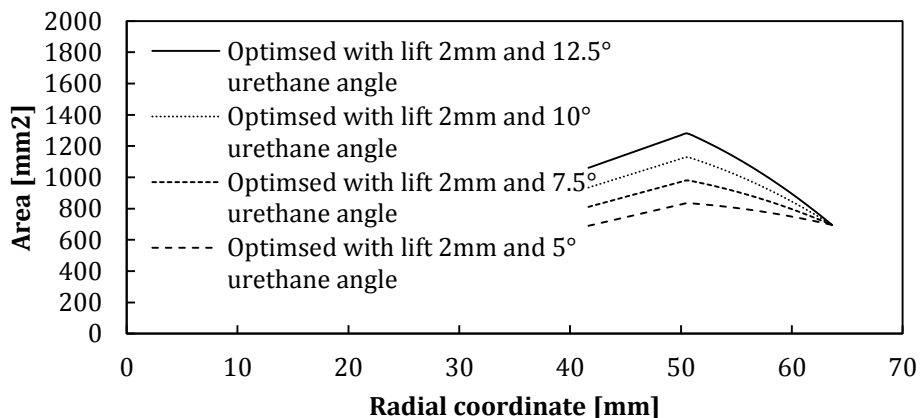


Figure 10-14: Proposed valve geometry, how the radial distribution of flow area varies with the urethane – seat angle at fixed (2mm) lift and fixed urethane inner radius (51 mm).

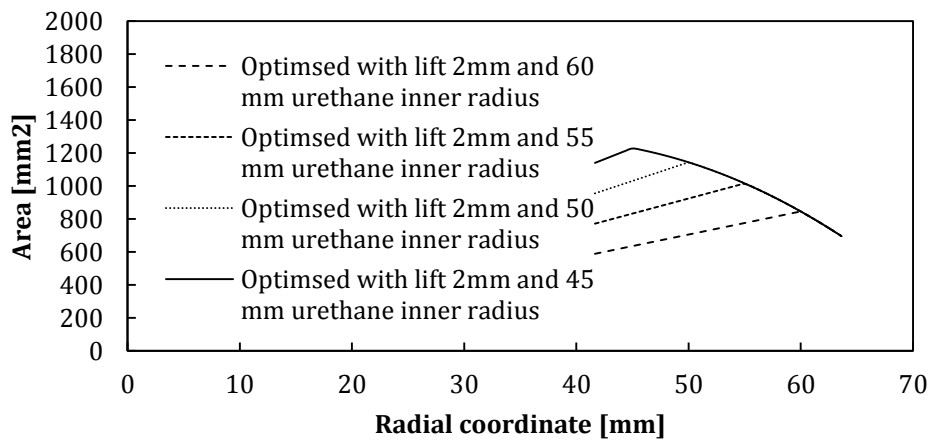


Figure 10-15: Proposed valve geometry, how the radial distribution of flow area varies with the urethane inner radius at fixed (2mm) lift and fixed urethane-seat angle (10°).

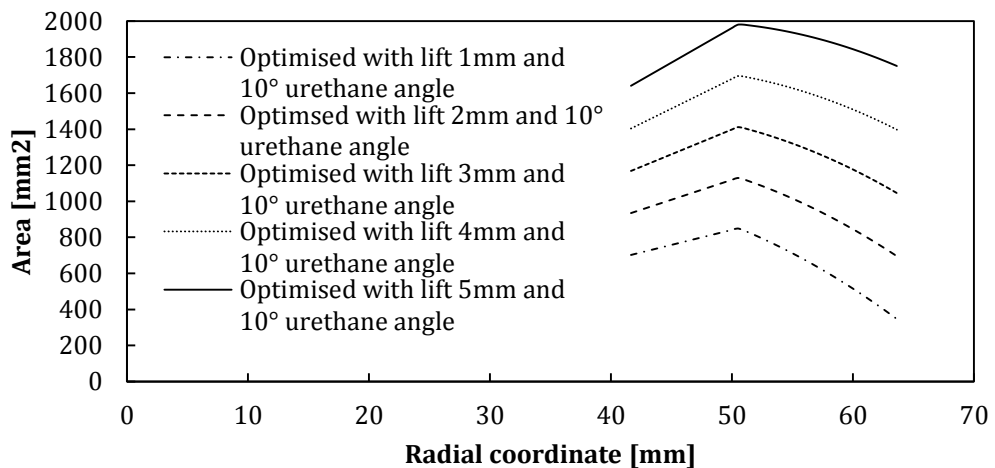


Figure 10-16: Proposed valve geometry, how the radial distribution of flow area varies with the valve lift at fixed urethane-seat angle (10°) and fixed urethane inner radius (51 mm).

To gather and summarise the information contained in Figure 10-14, Figure 10-15 and Figure 10-16, Table 10-3 and Table 10-4 were drawn. The tables show the summary of the minimum flow area to expect in the new geometry, for the range of valve lift 1-5 mm and for the range of 5°-12.5° of urethane-seat angle in the two scenarios of 51 mm and 45 mm of inner urethane radius respectively. The tables may also be utilised to accurately choose the design parameters according to the specifications. The yellow cells define the parameter sets optimised in order to obtain the widest flow area located on the exit edge of the urethane ring with respect to the radial coordinate. The blue cell zones define regions in which the combination of the parameters (lift and urethane/seat angle) is not optimised in order to place the minimum flow area on the exit of the valve-seat annular channel. As one can see Table 10-3 shows wider blue zones with respect to Table 10-4 to confirm that a smaller inner

urethane ring radius would give the designer much more flexibility in choosing the urethane ring-seat angles.

Table 10-3: Summary and integration of Figure 10-14, Figure 10-15 and Figure 10-16. How the minimum flow area changes with respect to the valve lift and urethane-seat angle with fixed urethane inner radius of 51 mm. The table shows the extension of the area and the location: inner= close to the urethane/steel interface, outer= urethane exit edge.

Lift [mm]	Min area [mm ²] For 5° urethane angle config.	Min area [mm ²] For 7.5° urethane angle config.	Min area [mm ²] For 10° urethane angle config.	Min area [mm ²] For 12.5° urethane angle config.
1	347 outer	347 outer	347 outer	347 outer
2	689 outer	695 outer	695 outer	695 outer
3	922 inner	1043 inner	1045 outer	1045 outer
4	1155 inner	1278 inner	1397 outer	1397 outer
5	1391 inner	1514 inner	1640 inner	1750 outer

Table 10-4: Summary and integration of Figure 10-14, Figure 10-15 and Figure 10-16. How the minimum flow area changes with respect to the valve lift and urethane-seat angle with fixed urethane inner radius of 45 mm. The table shows the extension of the area and the location: inner= close to the urethane/steel interface, outer= urethane exit edge.

Lift [mm]	Min area [mm ²] For 5° urethane angle config.	Min area [mm ²] For 7.5° urethane angle config.	Min area [mm ²] For 10° urethane angle config.	Min area [mm ²] For 12.5° urethane angle config.
1	347 outer	347 outer	347 outer	347 outer
2	695 outer	695 outer	695 outer	695 outer
3	1022 inner	1045 outer	1045 outer	1045 outer
4	1256 inner	1397 outer	1397 outer	1397 outer
5	1492 inner	1669 inner	1750 outer	1750 outer

10.4 Optimised valve design results

The proposed geometry valve was tested by means of the CFD model already discussed in the previous sections of this dissertation, under the same operating and boundary conditions. Figure 10-17 shows the chamber pressure throughout the suction stroke. The proposed modifications on the design of the urethane ring demonstrate a higher average pressure which results in a lower NPSHr.

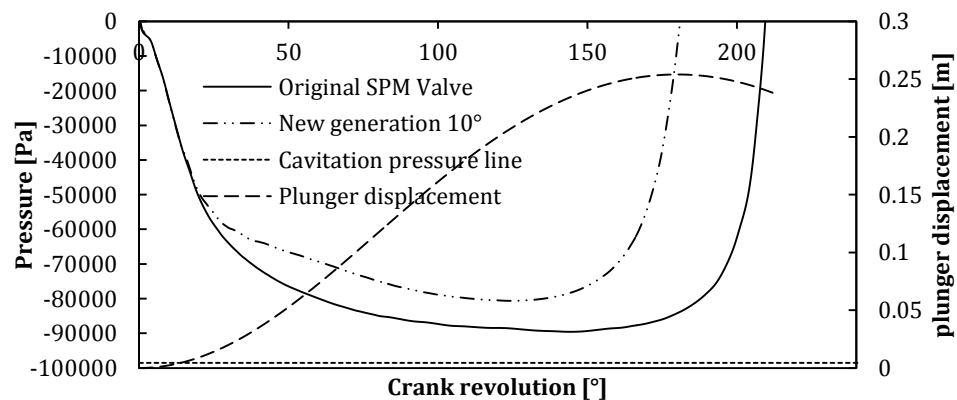


Figure 10-17: Chamber pressure, Original valve Vs new proposed modification with 10° urethane-seat angle.

Figure 10-18 compares the vapour fraction in the valve-seat gap volume demonstrating that the modifications proposed have a huge impact on the generation of vapour. The original valve shows the typical trend of full cavitation regime as discussed in chapter 7 whereas the new valve works in the incipient cavitation regime as the vapour volume fraction is very low. Figure 10-21 highlights that in the vicinity of the plunger, a low level of vapour fraction is present as well, Figure 10-19 and Figure 10-22 show the amount of the air as it expands while the pressure decreases during the suction stroke in the valve-seat gap volume as well as in the vicinity of the plunger respectively. Figure 10-20 and Figure 10-23 show the overall amount of second phase volume fraction which is the sum of vapour and air, they confirm the better performance of the new geometry over the original one as the overall 2nd phase fraction is significantly lower than in the first case.

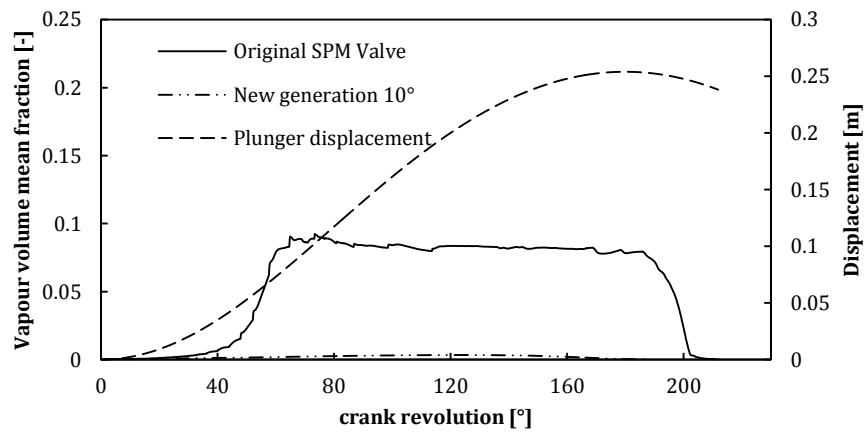


Figure 10-18: Valve-seat gap volume, original Vs modified valve comparison of vapour volume fraction.

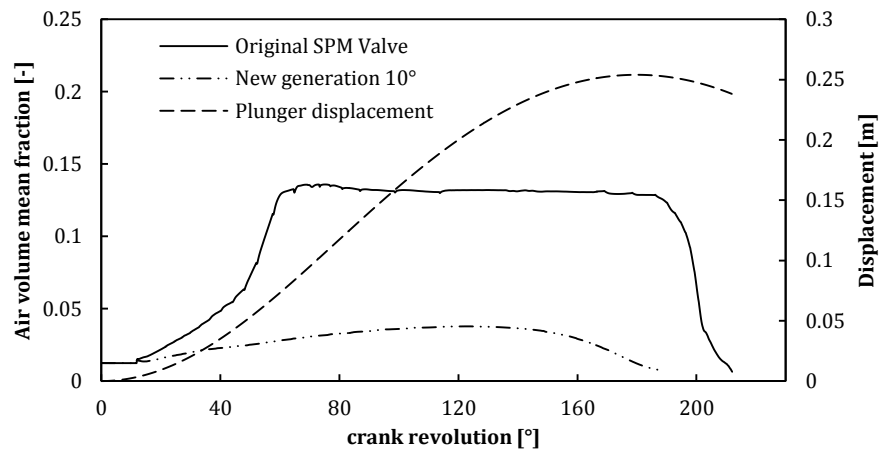


Figure 10-19: Valve-seat gap volume, original Vs modified valve comparison of air volume fraction.

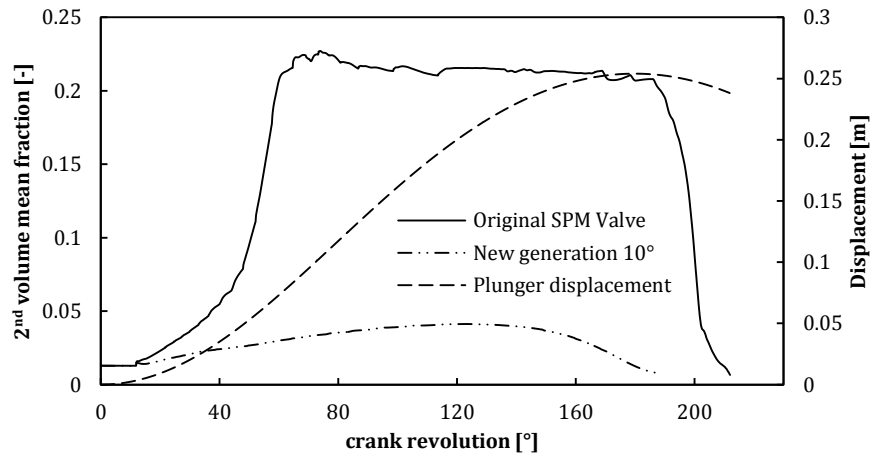


Figure 10-20: Valve-seat gap volume, original Vs modified valve comparison of 2nd phase volume fraction (water + vapour)

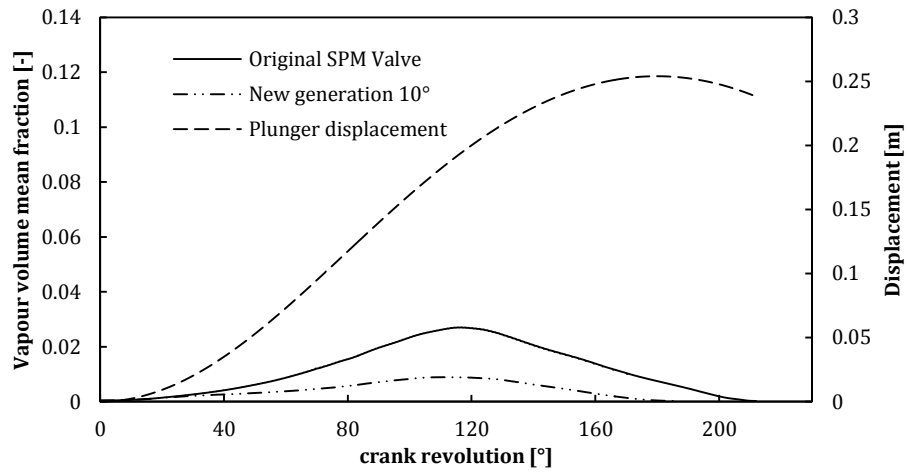


Figure 10-21: Plunger vicinity, original Vs modified valve comparison of vapour volume fraction.

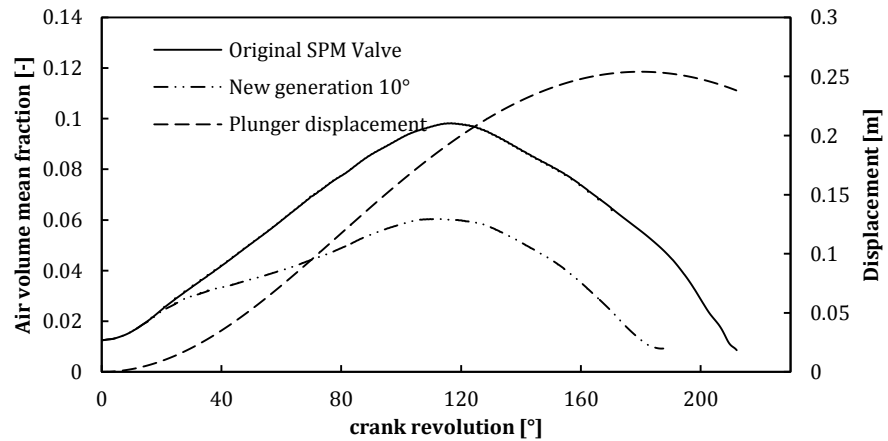


Figure 10-22: Plunger vicinity, original Vs modified valve comparison dissolved air volume fraction.

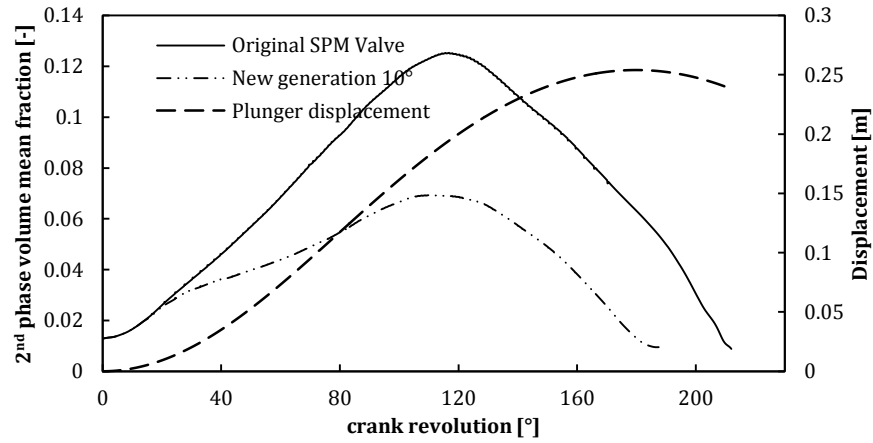


Figure 10-23: Plunger vicinity, original Vs modified valve comparison of 2nd phase volume fraction (water + vapour).

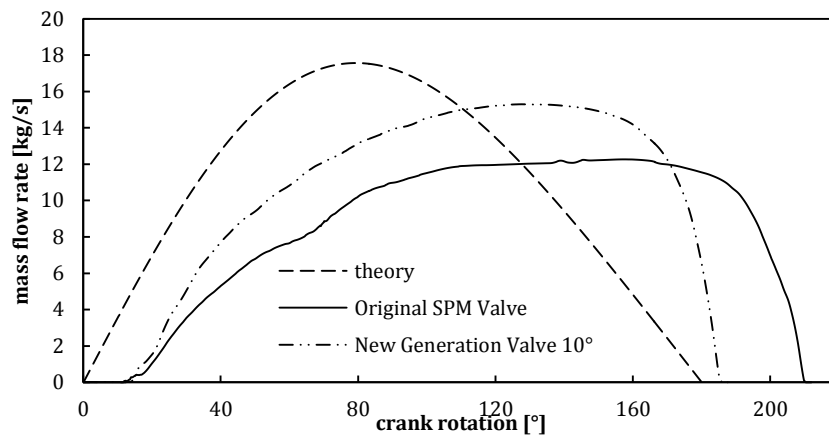


Figure 10-24: Original valve Vs new geometry. (a) Inlet mass flow, the theory curve is also included.

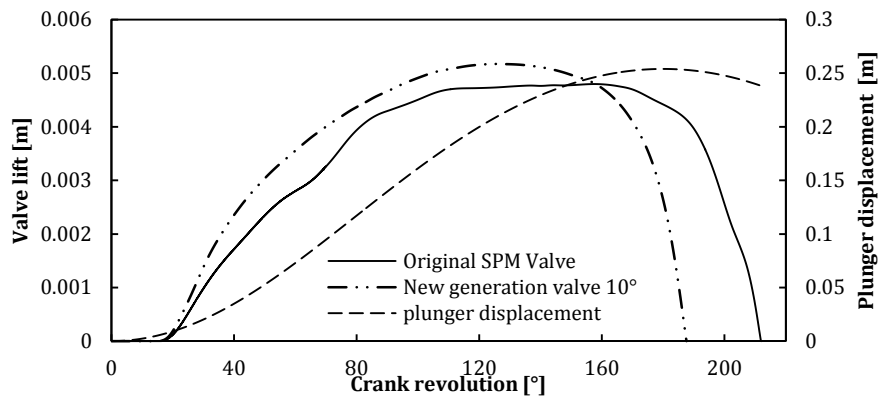


Figure 10-25: Original valve Vs new geometry. Inlet valve lift history.

Figure 10-24 shows the inlet mass flow time history of both the original and the proposed valves and their comparison with the theoretical curve. The proposed valve showed a mass flow rate closer to the theoretical than the original valve. It also reveals a higher maximum value. Figure 10-25 represents the valve lift-shaft rotation trend; it appears consistent with

the mass flow trend figure as the original valve maximum lift is lower than the proposed one. The original valve also shows a larger delay in closing. Figure 10-24 and Figure 10-25 depict the typical situation of different cavitation regimes which was already discussed in chapter 7. In this case the lower cavitation regime is due to a variation in the design of the valve rather than an increment of the inlet pressure as discussed in the same chapter.

Table 10-5: Original valve Vs new geometry. Summary of the performance data.

Configuration	Inlet valve opening time [Crankshaft°]	Inlet valve closing time [Crankshaft°]	Volumetric efficiency [%]	Max chamber vapour integral [m^3] $\times 10^{-3}$	Max valve gap vapour integral [m^3] $\times 10^{-6}$	
Original Valve	12	212	91.4	0.1928	1.59	
New proposed geometry	12	188	99.4	0.056	Difference	
					[%]	0.1
					71	94

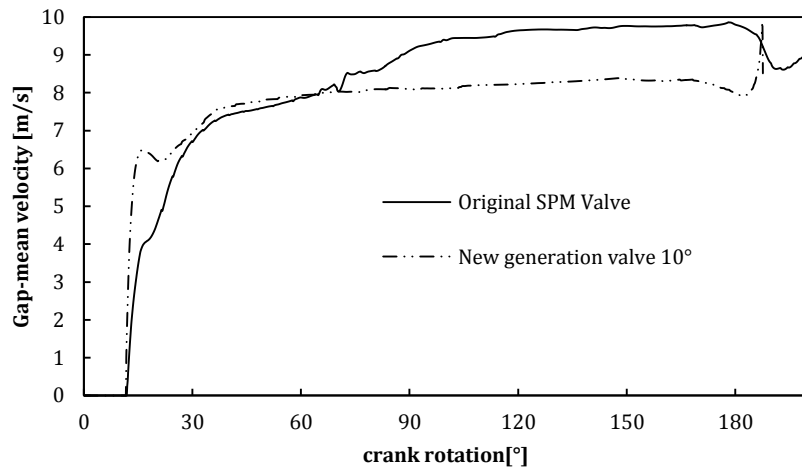


Figure 10-26: Original valve Vs new geometry. Flow velocity through the valve-seat gap volume.

Figure 10-26 points out an important feature of the proposed geometry design. It reveals an average velocity lower than the original valve case. The flow velocity was calculated in the valve gap exit area. The lower velocity justifies the lower generation of vapour which is once again illustrated in Figure 10-27 to Figure 10-29. Figure 10-27 and Figure 10-29 show the volume integral of the vapour present in the chamber and in the valve gap volume respectively whereas Figure 10-28 and Figure 10-30 show the volume integral of the air expanded in the chamber and in the valve gap respectively. The figures confirm what was already stated in the previous paragraph. The geometry modification proposed have generated an improvement in the performance which is quantified in Table 10-5 in terms of the delay in inlet valve closing and the volumetric efficiencies difference.

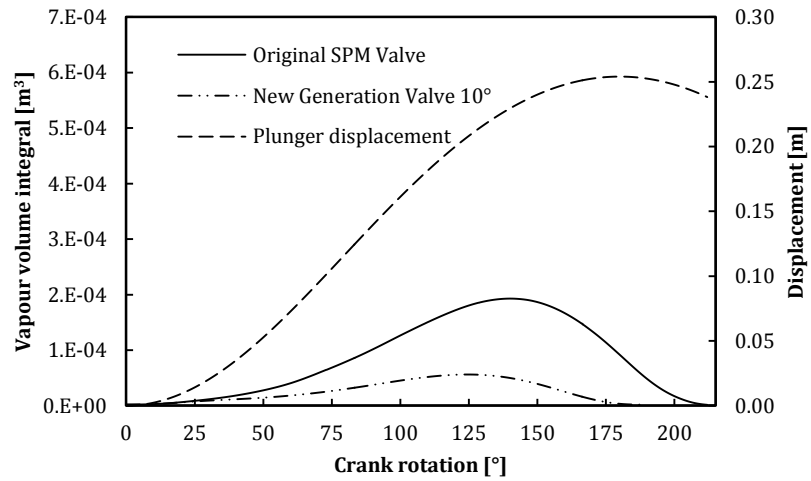


Figure 10-27: Original valve Vs new geometry. Chamber vapour integral.

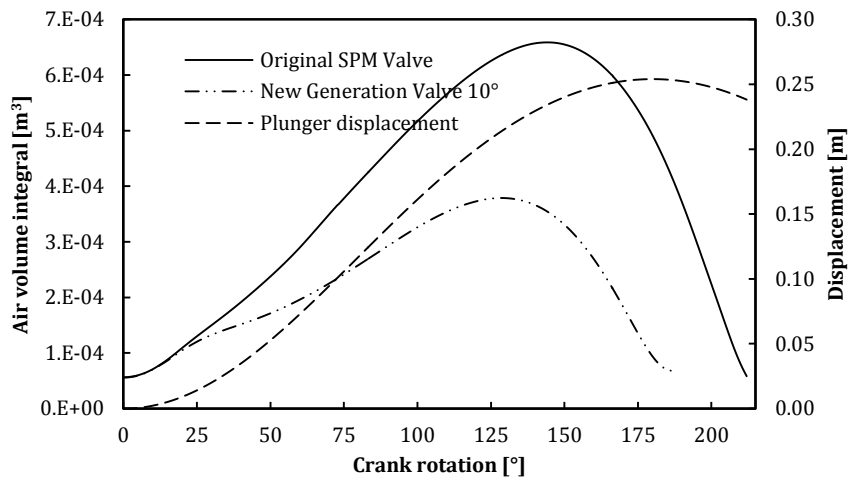


Figure 10-28: Original valve Vs new geometry. Chamber air volume integral.

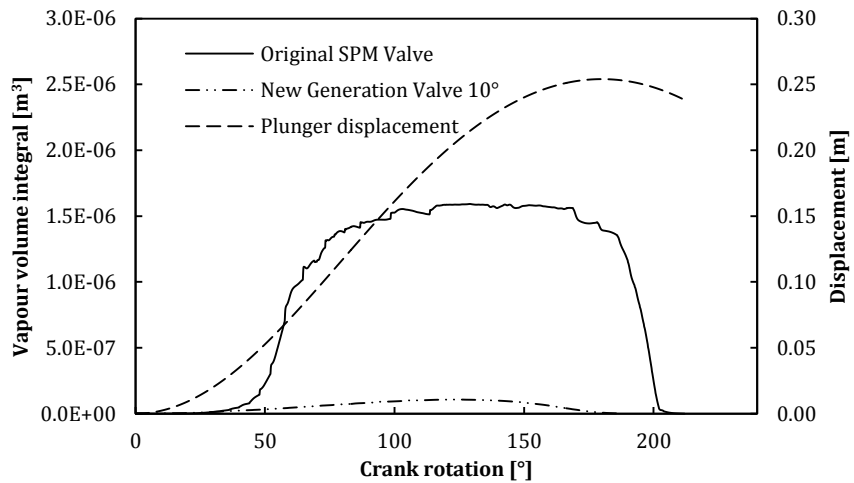


Figure 10-29: Original valve Vs new geometry. Valve-seat gap vapour integral.

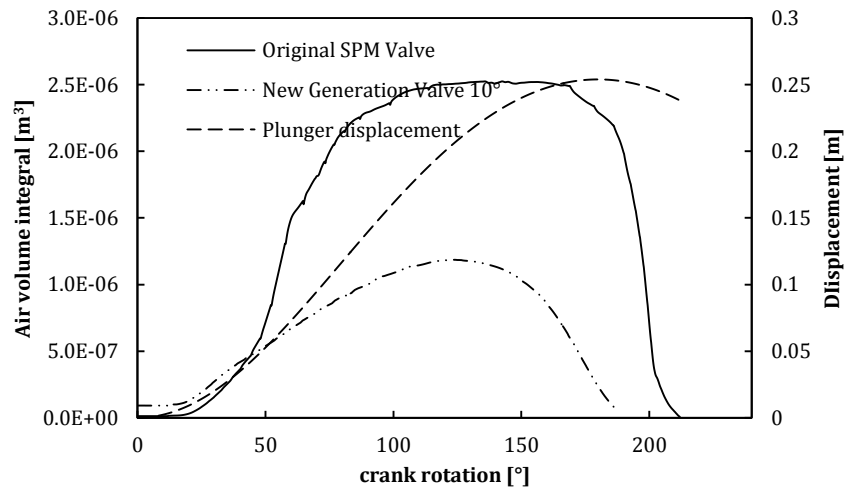


Figure 10-30: Original valve Vs new geometry. Valve-seat gap air volume integral.

10.5 Conclusion

The influence of the operating condition as well as the geometric parameters of the valve on cavitation were discussed in more details, they came out as results of the previous chapter discussion. The author then made a choice of which one was to take as the main object of the topological optimization process, based on operating constraints which accounted also for the erosion problem. The author decided to carry on with the analysis of the valve-valve seat contact shape. For this purpose a modification of the urethane ring section was proposed, analysed, discussed and justified by means of CFD comparative simulations with the original valve geometry. The new valve design under the same operating conditions already discussed, demonstrated 71% and 94% (Table 10-5) lower volume vapour integral in the chamber and in the valve-seat gap respectively, showing in fact the capability to move to a lower regime of cavitation with a volumetric efficiency loss smaller than the 3% limit which is the maximum allowed by the API 674 requirement. The new valve section provided a volumetric efficiency of 99.4% whereas the original valve gave 91.4%.

11 Experimental test rig set-up

11.1 Introduction

Chapter 7 discussed the capability of the numerical tool developed by the author in simulating the typical features of incipient, partial and full cavitation in PD pumps. The model provided realistic results as increments of inlet pressure resulted in the gradual movement from full to incipient cavitating conditions. The author could not quantify the accuracy of the model as it was difficult to estimate it by means of numerical models. A test rig was design for this purpose. It aimed at replicating as precisely as possible the CFD tests discussed in chapter 7 in order to validate the numerical models by means of data comparison and to estimate their accuracy. The main interest of the author is the accuracy estimation of case 1 which was subjected to the full cavitation regime and the generation of vapour was not negligible. In this case the high interphase change rate might bring down the accuracy of the numerical multiphase model. The modality of the data comparison to achieve the goal is not trivial as the entire process is affected by the difficulty in gathering crucial information on physical quantities from a test rig. The data acquisition usually depends on the rig layout and will be discussed later on in this chapter but it should be clear at this point that acquiring data such as the volume integral of the vapour which is very easy in a CFD model is almost impossible in a test rig and was not carried out. The data comparison involved quantities related indirectly to the cavitation phenomenon instead.

11.2 Test rig specifications

The test rig analysis objective was to provide the analyst with sufficient data to validate the numerical analysis within the overall need to keep the costs reasonably low both in terms of time and money spent whilst designing a device simple to use. For this purpose the test rig and the CFD models should describe the same situation in terms of both boundary and operating conditions as well as the same geometry. Without this basic feature the operation might result in inconsistent numerical-experimental data comparison. The experimental campaign should provide both qualitative as well as quantitative data. Fluid dynamics fields such as the vapour fraction are very complicated to measure. Also, other kinds of data such as the valve lift are technically very difficult and expensive to measure and therefore the author utilised a non-invasive method as explained later in this chapter. Because of their relevance in a CFD validation by means of comparison with experimental results, the following acquisition parameters were initially identified by the author to be included into the rig design list of specifications as measured quantities:

1. Mass flow inlet
2. Inlet pressure
3. Pump chamber pressure
4. Valve –seat gap volume pressure
5. Outlet pressure
6. Valve lift

The mass flow inlet can be utilised to estimate the volumetric efficiency which is related to the vapour generation as demonstrated in chapter 7. The test rig was also equipped with transparent windows in the vicinity of the inlet valve as well as in the vicinity of the plunger in order to visualise and record qualitative images of the generation of vapour in these locations. Qualitative pictures together with the mass flow trend and the volumetric efficiency can be considered complementary for completing the investigation. The set of pressure data acquired was not problematic as they could be directly compared to the CFD data.

The test rig was also initially conceived to replicate the operating conditions described in chapter 5 and 7 so that the numerical model could be validated in all the regimes discussed (from incipient to full cavitation). It was decided that a real PD pump should be utilised for the experimental tests as a detailed CAD file of this pump was employed to create the CFD model.

11.3 Test rig layout

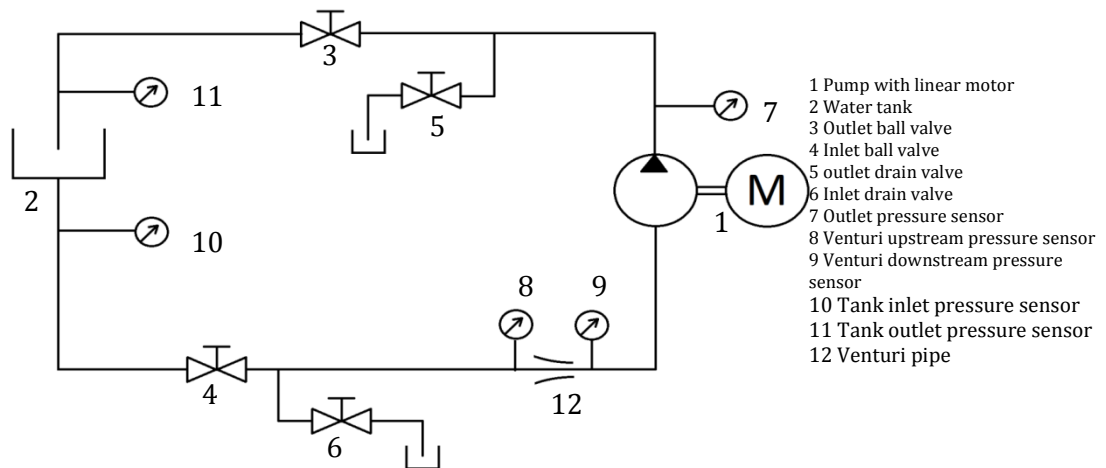


Figure 11-1: Test rig schematic with legend. The pumping system is shown, the pressure sensors on the pump are not shown

Figure 11-1 shows a simplified schematic of the test rig which can be seen in drawing 000 located in the Appendix. A closed loop pipeline system was chosen. The reason for this

choice lies in the need to restrict the overall imprint of the rig in order to fit it in the designated laboratory room. Water was pumped to and from a water vessel by means of the inlet and outlet lines. Although the vessel was designed to accommodate a flexible bladder whose inflation would increase the pressure inlet boundary conditions, as discussed later on, the tests were carried out with the vessel top hatches open and the inlet pressure always equal to ambient. The pump sits on a frame designed to host a linear motor which drove the plunger. The frame was designed to resist the application of the force provided by the motor and with negligible deformation. This will be demonstrated later on in this chapter. The parts composing the rig are listed as follows:

1. Single chamber pump
2. Linear motor
3. Frame
4. Inlet pipe
5. Venturi pipe
6. Outlet pipe
7. Water vessel
8. High speed camera
9. Data acquisition system

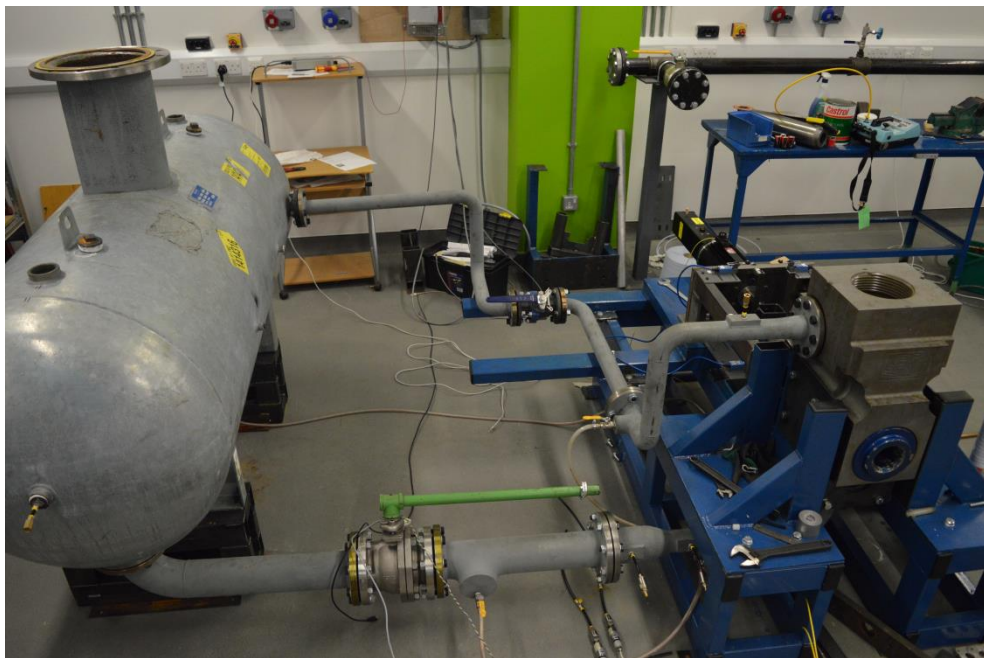


Figure 11-2: Test rig in the laboratory room where the tests were carried out.

11.3.1 Single chamber pump

The single chamber pump shown in drawing 001 which is included in the Appendix, was obtained by cutting the central chamber of a triplex WEIR SPM Destiny TW2500 pump and modified according to the test rig specifications. The actions taken to modify the original pump and satisfy the experimental rig specifications are listed as following:

- Three 51 mm diameter holes were drilled and 10 mm thick transparent polycarbonate disks were placed in front of them, the closing cap shown in the drawing 001-08, 001-09, 001-12 were utilised to create the inspection windows. Rubber rings were placed between the polycarbonate disks and the steel caps in order to improve the sealing and avoid direct contact between the two different materials. The detailed section of the portholes assembly can be seen in the details H, I and J of drawing 001-01 and 001-02. The thickness of the polycarbonate disks was chosen in order to provide a sufficient safety factor against the yield stress of the composing material. It is known from literature that polycarbonate yield stress is around 90 MPa. Finite Element Analysis simulations were carried out making use of the 10 mm thick polycarbonate window under 20 bar of chamber internal pressure. Figure 11-3 demonstrates that the pressure load chosen (20 bar) leads the material to the yield point. For a reasonable safety factor ≥ 2 , the internal load of 10 bar should not be exceeded.

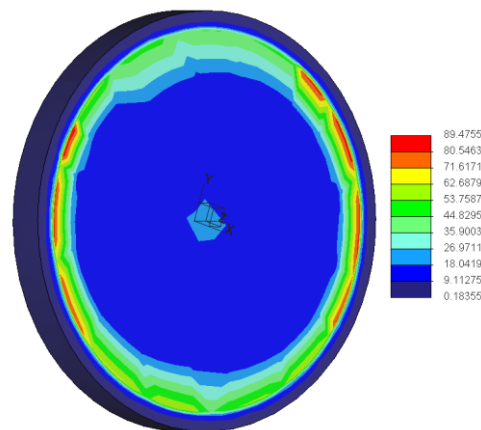


Figure 11-3: Von Mises stresses [MPa] of a 10 mm thick polycarbonate window under 20 bar of pressure.

Figure 11-4 which was already presented in chapter 7, estimates by means of a CFD tool a maximum chamber pressure of 4 bar. This points out that the thickness chosen for the windows defines a safety factor against the yield point of approximately 5.

- A threaded hole to place a pressure transmitter in the vicinity of the TDC position of the plunger. The position of this gauge is shown in section A-A of drawing 001-01

and also in 001-07 which shows the lateral closing cap where the hole was drilled and threaded. According to Figure 11-4 the pressure transmitter should be able to measure absolute pressures in the range of 0-5 bar. Table 11-1 summarises the technical specifications of the device chosen. The technical sheet is also attached in the appendix.

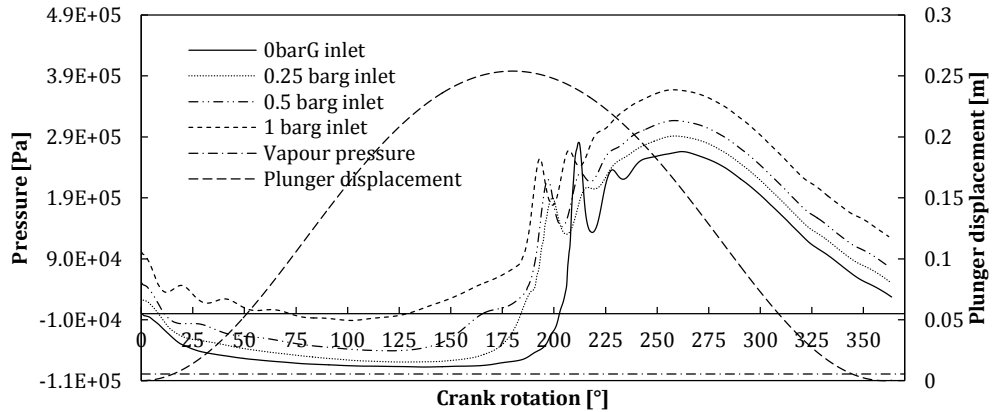


Figure 11-4: Chamber pressure, the maximum value can be estimated as 4 bar (1 barG inlet case).

Table 11-1: Technical specifications of the pump chamber pressure transmitter GEM 220SAB1001F3EA.

Position	Output signal	Pressure connection	Electrical connection	Measurement range	Type (abs/relative)	Non linearity [%]	Response time
Chamber pressure (TDC position)	0-10 Vdc	G1/4 gas male	Shielded cable	0-10 bar	Abs	±0.025 bar	0.5 msec
Valve-seat gap	0-10 Vdc	G1/4 gas male	Shielded cable	0-10 bar	Abs	±0.025 bar	0.5 msec

- A second pressure transmitter was also chosen to acquire the signal of the static pressure in the vicinity of the valve-seat gap volume. For this purpose section A-A, detail E of the 001-01 drawing together with 001-03 drawing show how this was arranged; four holes with a recess cut in the inlet valve seat and a hole drilled in the pump case shown in detail E created a path leading the pressure signal from the valve-lift gap to the pressure sensor. The importance of the mean pressure value in the valve-seat gap volume can be easily demonstrated considering that this pressure is affected by the vicinity of either the inlet manifold or the pump chamber but also it provides information on the dynamic pressure due to the high velocity flow through the valve and therefore cavitation. In fact, during the suction stroke, the manifold pressure was higher than the chamber pressure which was affected by the decompression caused by the action of the plunger moving backwards and this

pressure difference moved the water through the valve. The valve-seat pressure signal can be considered a representative parameter defining the phenomena ongoing in the valve-seat lift volume.

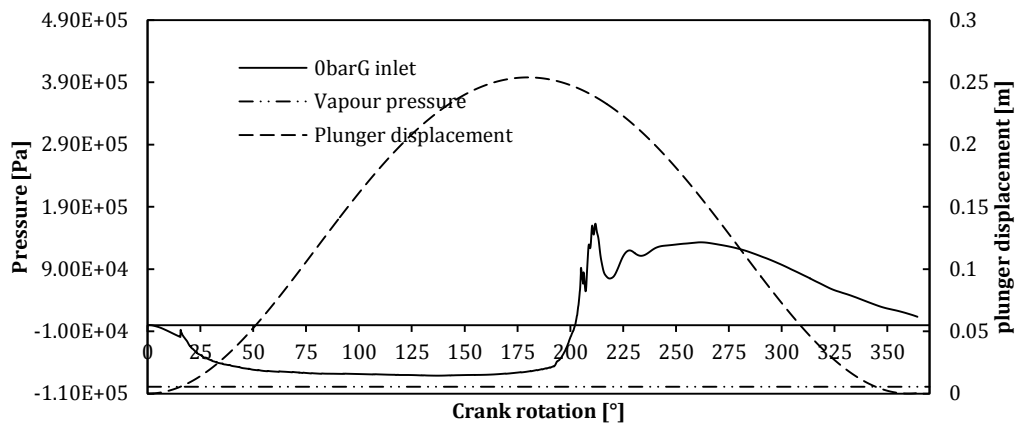


Figure 11-5: Mean pressure in the valve-seat gap volume (0 barG inlet case).

Figure 11-5 which results from CFD simulations, estimates the mean gap static pressure to be in the range 0-3 bar for the full cavitating case (0PaG inlet pressure case). For its acquisition, the pressure sensor defined in Table 11-1 was found suitable.

- The original sealing pack which prevented leaks from the plunger bore was replaced mainly because of the following reasons:
 1. The experimental tests were designed to drive the pump at very low delivery pressure with respect to the real operating conditions the pump was designed for (up to 12 kpsi, 82.7 MPa). This makes the sealing pack over-designed for the experiments the author prepared.
 2. The original material of the seals and their coupling tolerance with the plunger resulted in a very high friction force beyond the capability of the linear motor chosen to drive the plunger during the tests. The problem of the power needed will be fully discussed in the next paragraph but it should be clear that the lower the friction force the more the required force achieved the linear motor power specifications.

Figure 11-6 shows how the sealing system was modified (on the left) starting from the original one (on the right). Two different types of original seals were first tested in order to decrease the friction on the plunger but none of them provided an acceptable value. The analyst removed the entire pack replacing it with one additional metal ring and two soft rings made of packing material (graphite). The

metal ring had the duty of supporting the plunger and driving it along its axis, whereas the graphite rings were placed in the space between the outer ring and the middle ring to seal the chamber and providing a low friction force at the same time. To adjust the sealing properties the threaded closing cap was tightened squeezing the sealing pack as in the original configuration. Grease was also utilised to reduce friction further. A spring balance estimated the friction force for incipient motion of around 300 N which was considered acceptable.

- Minor modifications were made to the pump case in order to connect the inlet and outlet pipe flanges, to close one side of the outlet pipe and to connect a chamber draining pipe. All these modifications are visible in the drawing 001-01 and 001-02 whereas the geometry of the draining pipe is shown in drawings 001-13.

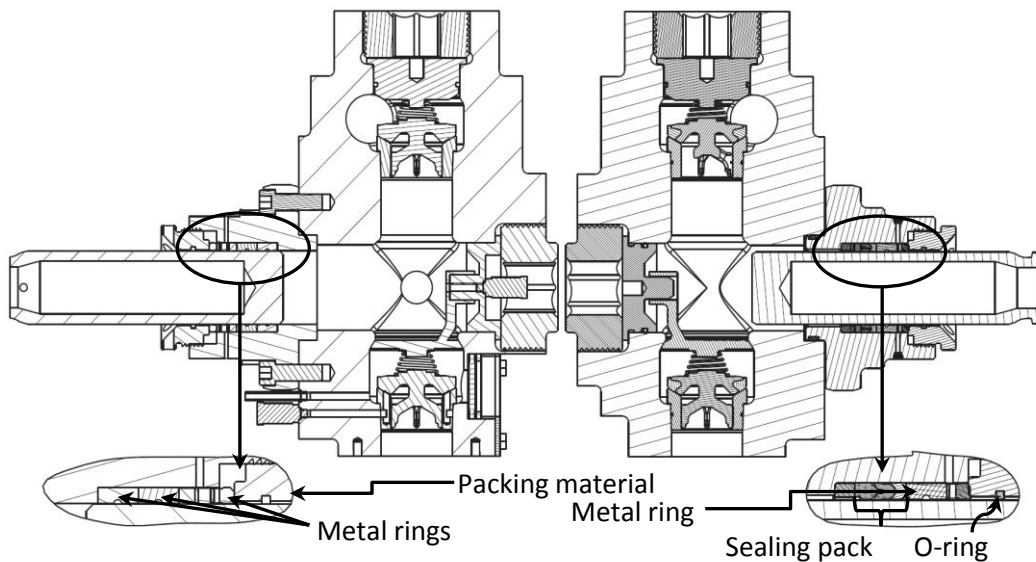


Figure 11-6: (left) Details of the modification carried out on the sealing system compared to the original design (right).

- The original plunger was replaced with a new one which was $2/3$ lighter than the original (10 kg instead of 30 kg), the reason for this will be explained in more details later in this chapter and is related to the inertia force the linear motor had to exceed to achieve the plunger velocity requirements for the tests. The new plunger design is shown in drawing 018: it is composed of three main parts welded together. The main cylindrical part was made of stainless steel to avoid corrosion problems

and was cut from a 200 mm diameter solid stainless steel cylinder using a lathe and a boring machine.

11.3.2 Linear motor

The estimation of the force and power required was a very important part of the preliminary work carried out because it decided the kind of technology to employ in order to drive the plunger during the experimental tests. The location (a closed room with no windows) assigned for the project did not make possible the use of the diesel engine of the original pump which is usually supplied by the WEIR group together with the fluid ends. The lack of space and time for the design and the development of the rig excluded the possibility to choose other kind of devices such as electric motor or hydraulic actuators because they would have required expensive design and manufacturing of the gear box and reciprocating system, for the former case, and the hydraulic system for the latter. A linear motor appeared to be the quickest and most versatile choice from the test rig preliminary design. A linear motor which is fully programmable is also more flexible in applying the motion of the plunger capable of providing it with any kind of velocity and displacement trends within a certain range. This feature gives the linear motor a great advantage over the rotational counterpart but also a few drawbacks. In fact, linear motors are usually not very powerful devices and limited in the maximum axial force they can provide. To find a suitable one on the market was not an easy task.

The research on the market carried out in the preliminary study, identified a high power and high performance linear motor which is the most powerful on the market to date. Therefore the problem was then to demonstrate whether or not the device found was capable of achieving the test rig specifications and then worthwhile buying it.

The motor identified is shown in Figure 11-7. It is manufactured by the Moog group and, according to the technical sheet, is capable of delivering the axial force needed for the tests at the velocity required. According to the research on the market carried out, despite the screw motors, the tubular linear servomotor technology is capable of achieving a velocity nearly 10 times higher than the fastest screw motor per unit axial force.



Figure 11-7: Moog high performance linear servomotor.

The technical sheet for the motor, which is attached in the Appendix, claims that it is possible to choose between two main groups of different stator diameter each one of them with three different coil number and two winding types. It was also possible to choose the stroke length and the type of linear encoder. The choice of the motor size was based on the axial force/velocity specification curve (Figure 11-8), due to the high force needed to move the plunger the most powerful type was chosen, the stroke length was fixed by the real maximum stroke (10 in, 254 mm) therefore the 12 in motor stroke was chosen as 1 inch extra on both ends of the stroke was needed as a minimum tolerance.

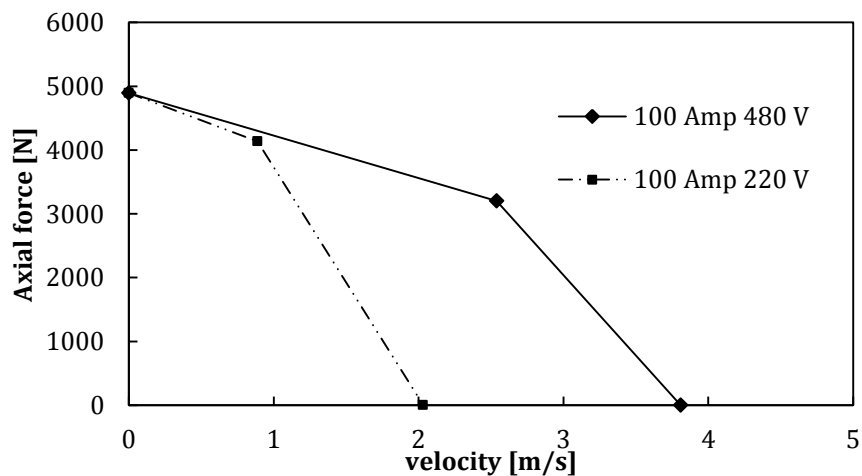


Figure 11-8: linear motor performance of maximum axial force Vs piston velocity

Figure 11-8 shows the linear motor application range for the two cases of 220V and 480V supply. The supply current and voltage is a parameter fixed by the power supply, by the driver and the user in the driver administrator software discussed later. The choice of the driver and the power supply were driven by the need to achieve the performance defined by the continuous line of Figure 11-8 which represents the maximum performance line the

linear motor can provide and should not be exceeded. Figure 11-9 compares the axial force available of Figure 11-8 to the real force needed for the inlet stroke only. The four test cases of chapter 7 are considered. Figure 11-10 compares the same quantities throughout the outlet stroke.

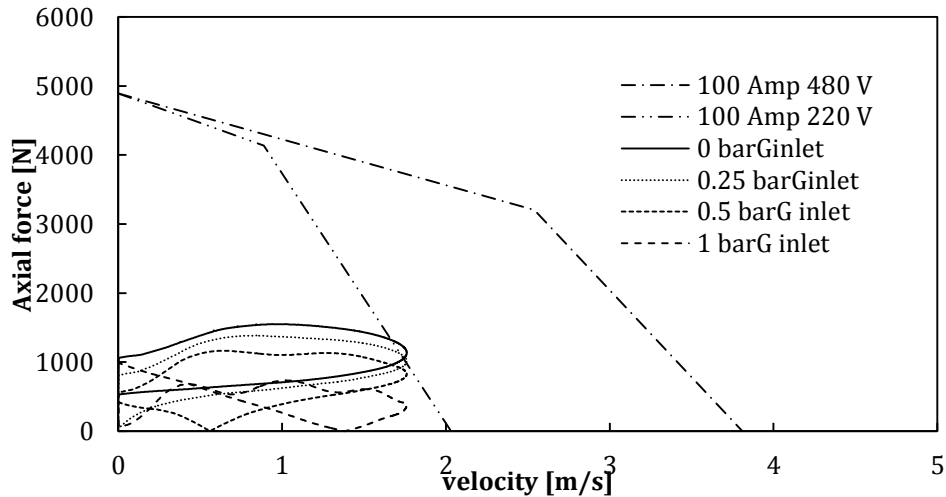


Figure 11-9: Inlet stroke, total axial force needed Vs axial force available. Test cases 0, 0.25, 0.5, 1 barG inlet pressure.

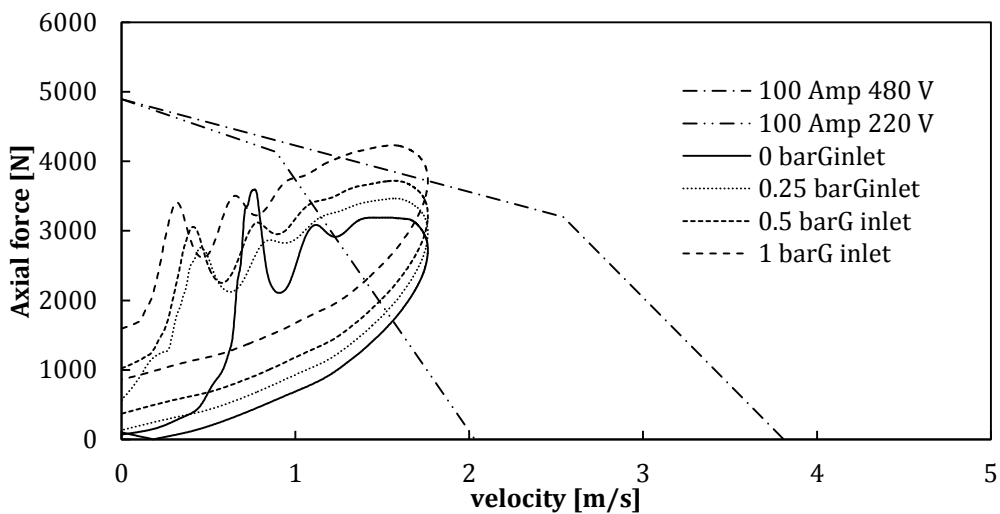


Figure 11-10: Outlet stroke, total axial force needed Vs axial force available. Test cases 0, 0.25, 0.5, 1 barG inlet pressure.

The estimation of the overall force needed (Figure 11-9 and Figure 11-10) was based on the pressure force on the plunger calculated by means of CFD to which the inertia of the plunger as well as the estimation of the friction force was added. The total force required is shown in Figure 11-11. For the estimation of the inertia the original 30 kg plunger was used. A fixed friction force of 300 N was considered for conservative reasons.

Figure 11-9 and Figure 11-10 show that for all the tests (0 to 100kPa inlet pressure), the inlet stroke does not provide any problem as the area swept by the four curves of the force required lay inside the area swept by the 100 Amp- 480 V mode. For the outlet stroke the highest pressure test is not entirely below the available force curve, therefore this test should be avoided. The author decided that this was not a real issue which could have invalidated the experimental campaign as the scope of the experimental analysis is the cavitation which arises during the inlet stroke only. As the outlet stroke was only needed to bring the plunger back to the initial position to perform the inlet stroke again, the analyst did not pay much attention to the issue. In fact, despite the real crankshaft, a fully programmable linear servomotor which simulated its behaviour, allowed the operator to decouple the inlet and outlet stroke so that they could be performed at a different velocity and therefore could require a lower power with respect to the curves shown in Figure 11-9 and Figure 11-10.

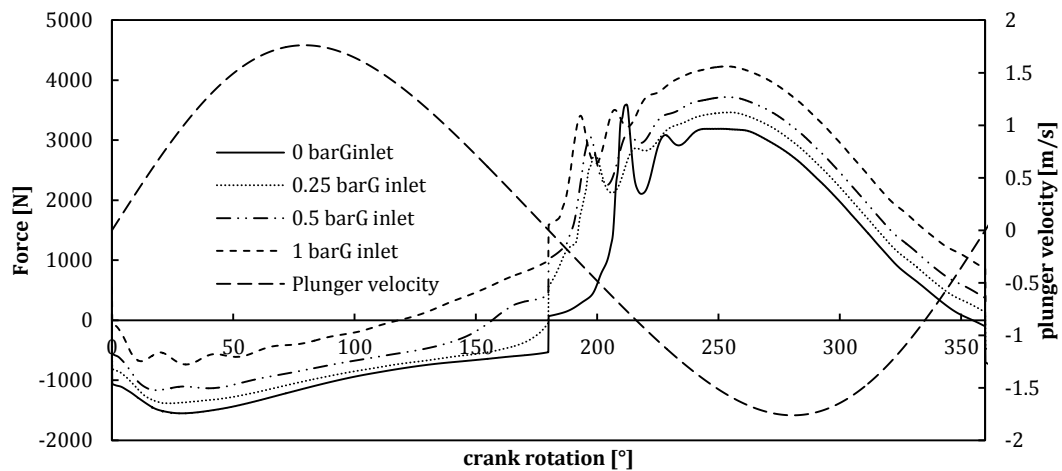


Figure 11-11: Total axial force needed throughout the pumping cycle.

However, as there was no possibility to opt for a more powerful linear motor it was clear that not all the test cases could be replicated experimentally exactly as they were planned. This important topic will be discussed in more detail later in this chapter as the experimental test modifications depended also on critical parts which should be discussed first.

An important part of the linear motor was the linear encoder, the motor and the encoder, in fact worked in conjunction with their driver. The encoder provided the driver with the feedback position of the motor shaft which was managed by the closed loop control system. All the linear encoder types listed in the motor technical sheet were found suitable for the designed tests. The choice of the encoder was driven by non-technical considerations such as the availability of the type with the chosen motor and the lead time.

Together with the linear motor the driver shown in Figure 11-12 was also needed to perform the following operations:

- To interface with the administration software installed on the laptop computer (discussed later in this chapter) in order to drive the linear motor and make it perform the operations set by the analyst via the administration software. It is important to note that the linear motor was not plugged directly into the power source but it received the power from the driver which managed the voltage and current needed to achieve the target operations.
- To manage the feedback signal of the encoder in order to control the position and velocity of the motor shaft and make sure that the displacement read matched the one set by the user.

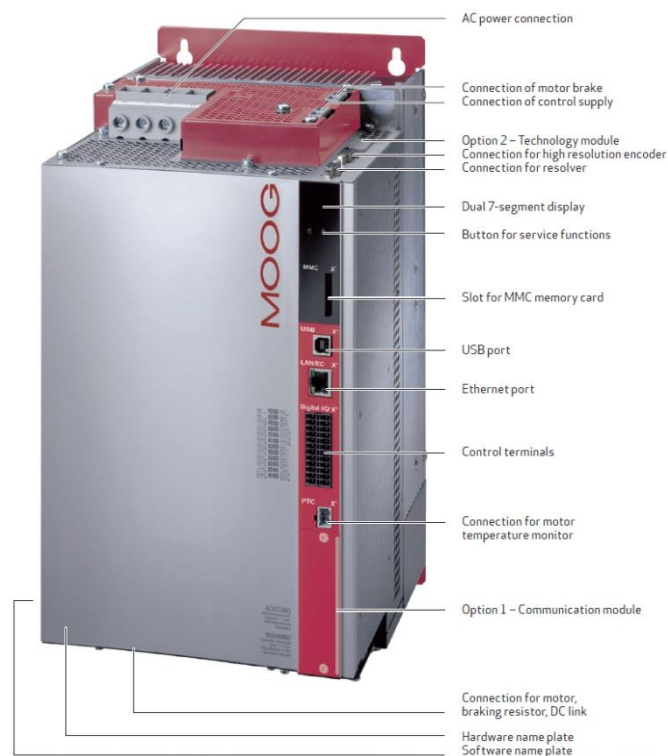
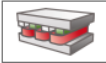


Figure 11-12: MOOG linear motor Servo Drive MSD G392-045-020-001

The driver administration software was utilised in order to:

- Set the control loop parameters
- Set the parameters defining the type and characteristics of the motor and encoder
- Defining the limits in terms of current and voltage not to be exceeded
- Set the parameters defining the shaft displacement

Figure 11-13 and Figure 11-14 show the Graphical User Interface of the Moog Administrator software dedicated to the linear motor and linear encoder parameters respectively. The specified parameters were set according to the type of the motor and encoder chosen. The maximum velocity the linear motor could handle was entered in the window shown in Figure 10-12 but during the preliminary tests that parameter could be multiplied by a further safety coefficient entered in the windows shown in Figure 11-15. The resulting value was utilised by the feedback control system which could stop the shaft safely in case the velocity limit was exceeded. The information provided by means of the window shown in Figure 11-14 were utilised to set up the feedback control system. The parameter set up was an operation performed once for the first commissioning and was never repeated again.

Calculation of control settings for linear PS motor 

Motor name

Rating plate data

Rated voltage	<input type="text" value="222.513"/> V	Rated current	<input type="text" value="32"/> A
Maximum speed	<input type="text" value="1.74"/> m/s	Magnet pitch (NN)	<input type="text" value="23.4"/> mm
Rated force	<input type="text" value="2745"/> N		

Weight

Motor weight (coil)	<input type="text" value="5.5"/> kg	Total weight	<input type="text" value="8"/> kg	<input type="button" value="Info ..."/>
---------------------	-------------------------------------	--------------	-----------------------------------	---

Motor impedances

Stator resistance	<input type="text" value="0.6"/> Ohm	Stator inductance	<input type="text" value="7.25"/> mH	<input type="button" value="Info ..."/>
-------------------	--------------------------------------	-------------------	--------------------------------------	---

Encoder

Encoder period μ m

Figure 11-13: Moog Drive Administrator: Linear motor parameters

Encoder configuration channel 1 (X7)

Encodename

Cyclic position via

Absolute interface

Gear ratio (if encoder is not fitted at the motor)

Motor	<input type="text" value="1"/>
Output drive	<input type="text" value="1"/>

Signal correction (GPOC)

Figure 11-14: Moog drive Administrator: Encoder parameters

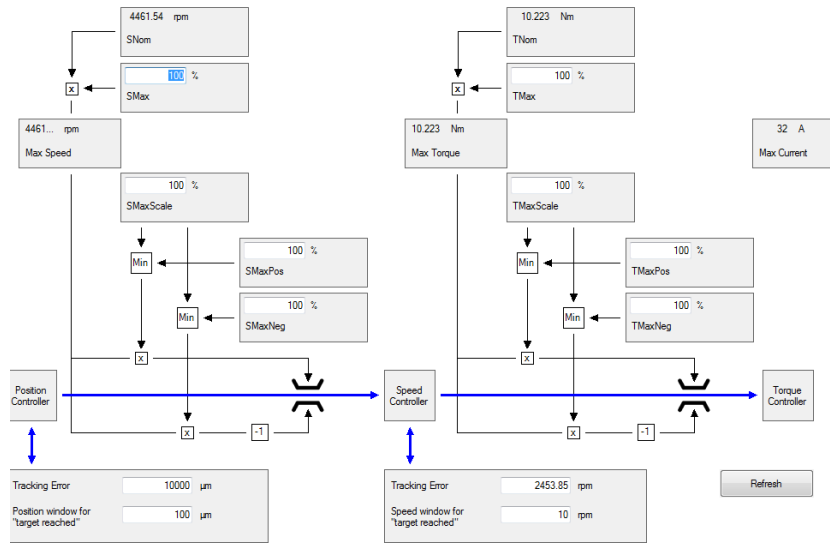


Figure 11-15: Moog Drive Administrator: Limits

According to the drive Administrator guide, there were several ways to feed the shaft time-displacement law:

1. Automatic
2. Manual
 - a. Velocity control
 - b. Position control

To utilise the automatic mode, the operator is asked to compile the set table shown in Figure 11-16. In this mode the displacement reference curve is fed into the driver by means of a piecewise linear function where the internal points are defined by the set table. The operator can define up to 16 points and for each of them he should not only provide the time and velocity but also the acceleration and deceleration which will be used by the system to calculate the continuous displacement function by means of interpolation among the points.

Control mode	TERM(1) - via terminals	
Set number	0	1
Reference	100 μm/s	100 μm/s
Acceleration	100 mm/s/s	100 mm/s/s
Deceleration	100 mm/s/s	100 mm/s/s
Time delay in Auto mode	0 ms	0 ms
Max table index in Auto mode		
Actual table index		
	Teach position	

Figure 11-16: Automatic control: Setpoint table

Regardless of its great capability, the automatic mode was more complicated to use as it was less user friendly as no detailed technical material covering the topic was provided by the supplier.

In the manual mode “velocity control” the operator is asked to provide the reference velocity he needs to achieve without setting the displacement limits. This mode was specifically created for standard rotational motors but was found not suitable for linear motors where the shaft maximum displacement is fixed by the stroke. The manual mode “position control” was the only one which was very simple to use even without any training or technical material. It was found suitable for the application. In this mode the operator is asked to provide (see Figure 11-17) the following parameters:

1. Shaft maximum stroke
2. Constant acceleration value
3. Constant velocity value
4. Constant deceleration value

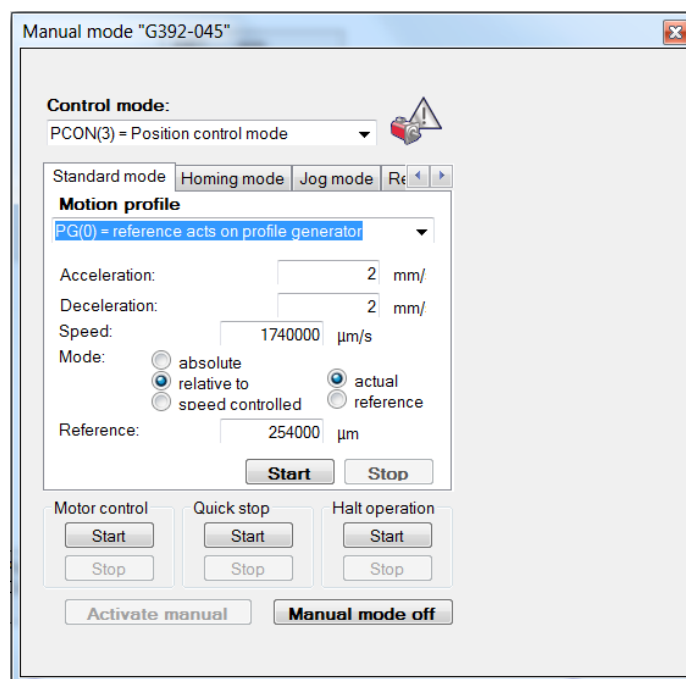


Figure 11-17: Moog drive Administrator: Manual mode

The software utilises the parameters set to create the displacement-time motion displayed by the dashed line in Figure 11-18. In the figure it is shown that the displacement line is continuous as the accelerating and decelerating parts are connected to the constant velocity part (middle) in a continuous way. The shaft displacement-time function shown was obtained utilising 23.5 m/s^2 as acceleration/deceleration whereas 1.7 m/s was chosen as the constant

velocity. The reader may also see that there is no significant difference between the dashed line and the continuous line which was obtained using the crankshaft parameters of the WEIR Destiny pump and the equation discussed in chapter 3 (130 rpm). This demonstrates that the manual mode with position control could be utilised to simulate the behaviour of the crankshaft with negligible errors.

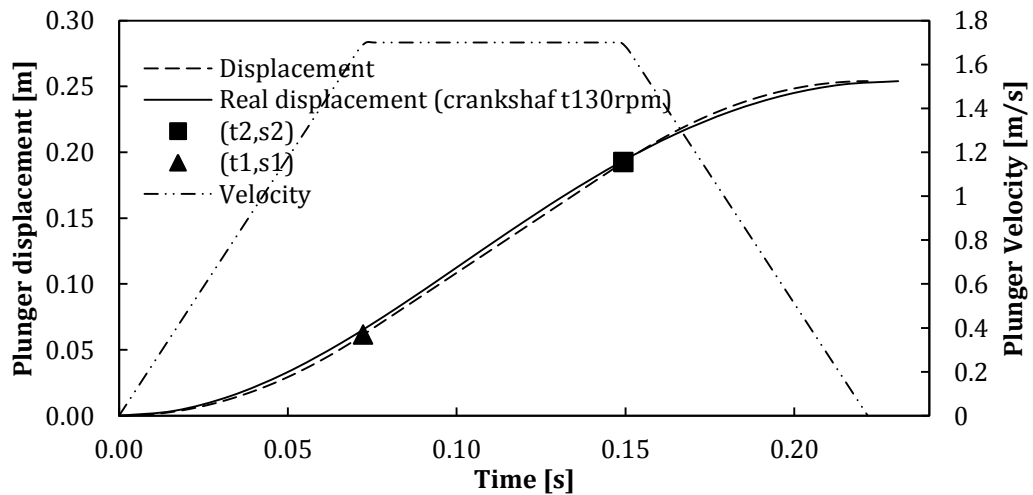


Figure 11-18: Example of shaft displacement compared to the crankshaft motion @ 130rpm. There is a combination of parameters which makes the two functions matching closely.

11.3.3 Rig frame

A carbon steel modular frame was designed to support the pump and the linear motor. It was composed of 6 separate parts which were then assembled together by means of bolts. They are listed as following:

- Two pump supports (drawing 004 and 005). Their task was to support the pump on the right and left sides and interface it with the two main frames. The pump could not be supported directly from the bottom as that space was needed in order to house the inlet pipe connecting flange.
- Motor support assembly (drawing 007). Its task was to provide a planar and rigid surface used to arrange and adjust the linear motor holding frame.
- Linear motor holding frame (drawing 013). Its task was to support the linear motor and match the motor-shaft/pump-plunger alignment requirements.
- Two main supporting frames (drawing 009 and 010). Their task was to support all the items listed above and to constrain the rig on the ground.

All the components of the welded frameworks were composed of the following standard items:

1. 5 mm thick carbon steel plates
2. 8 mm thick carbon steel plates
3. 25 mm thick carbon steel plates
4. Hollow box section beam 100 mm X 50 mm, 3 mm thickness
5. M16 bolts of various length and nuts.

The size of the standard items was decided upon to fulfil the requirement of the framework rigidity and internal stresses. The framework had to be stiff enough in order to make the maximum displacements negligible so that the relative distance between the items (e.g. linear motor, plunger, etc.) remained constant during the plunger motion. The framework internal stresses had also to be safely far from the material yield stresses and furthermore safe from the phenomena of mechanical resonance.

To check for maximum displacements and stresses and also to estimate the framework natural frequencies a FEM (Finite Elements Method) analysis was performed. For the modal analysis the frame was constraint on the ground fixing the 6 DOF of the nodes of the four steel plates in contact with the ground. Frequencies are shown in Table 11-2. The first structural frequency found was significantly lower than the external forcing frequency which was thought to be the one corresponding to the 130 rpm test (2.16 Hz) discussed in chapter 7. The frame was considered therefore safe from any structural resonance problems.

Table 11-2: Modal analysis results, the first structural frequency is significantly lower than the external force frequency.

	Frequency [Hz]
Pump cycle	2.16
Mode 1	67.4
Mode 2	74.1
Mode 3	80.5
Mode 4	84

To check for internal stress, the frame was tested under two external force cases which represented the positive (inlet stroke) and negative (outlet stroke) motor maximum axial force. The load in both cases was chosen as 5kN which is approximately the maximum motor axial load at zero velocity (Figure 11-8).

Figure 11-19 shows the contour plot of the Von Mises stress in both of the load cases. The outlet stroke gave a maximum stress of 66 MPa on the flange to which the linear motor was bolted. The inlet case gave 98 Mpa on the same location. Given that the frame material (mild

steel) yield stress is 220 MPa, the safety factor calculated was higher than 2 in both cases as summarised in Table 11-3.

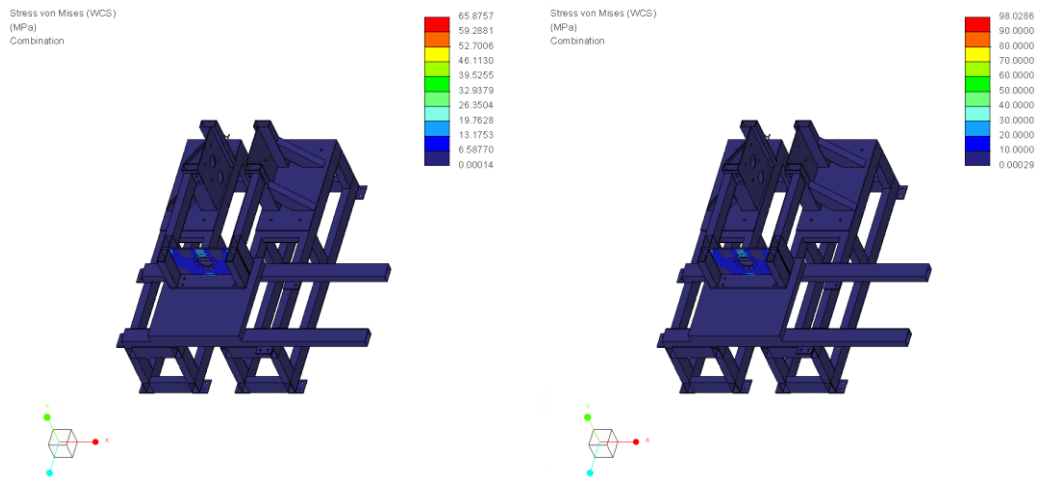


Figure 11-19: Contour plot of the Von Mises Stress on the frame, Outlet stroke (left), Inlet stroke (right).

Table 11-3: Safety factor against yield.

	Von Mises Max stress [MPa]	Safety Factor [Mpa]
Outlet stroke	65.9	3.3
Inlet Stroke	98	2.2

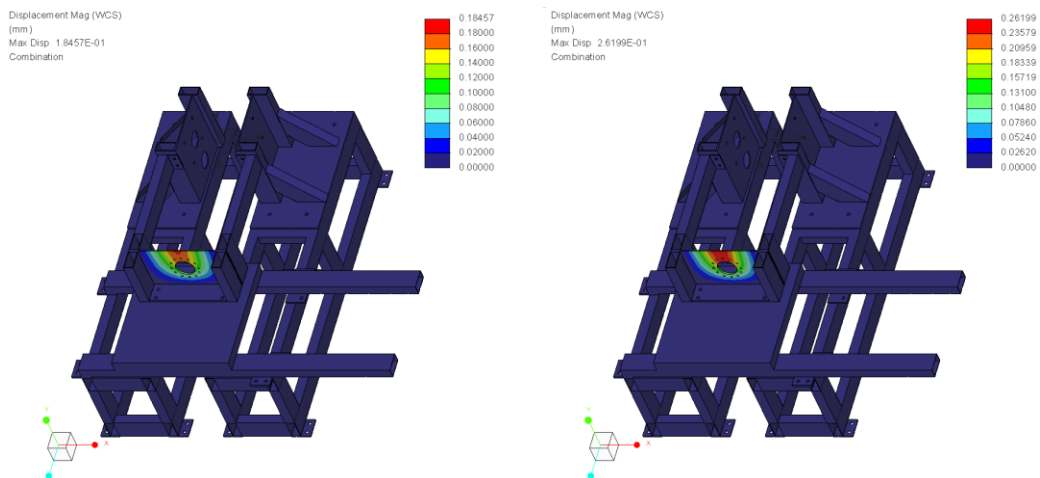


Figure 11-20: Contour plot of the maximum displacements, Outlet stroke (left), Inlet stroke (right).

Figure 11-20 Demonstrates that the frame was not subjected to significant displacements. Under the two load configurations the calculated displacements were 0.26 mm and 0.18 mm for the inlet and outlet stroke case respectively. In any case the displacement found was not important and the frame was rigid enough for the scope of the experiments.

The frame was equipped with four additional plates (drawing 013-05 and 013-06) properly positioned along the plunger stroke. They were designed to house three limit switches which were activated by the plunger during the stroke in order to send to the acquisition system the signal of the position of the plunger. In fact, the steel box utilised for coupling the motor shaft and the plunger, which will be discussed in the next paragraph, was equipped with two side wings which activated the limit switches when in contact with their levers. The limit switches were manually placed in three locations which were chosen in order to activate the relative switch:

1. When the plunger started the suction stroke at the TDC position (start switch)
2. When the plunger reached the mid-stroke location (middle limit switch)
3. When the plunger accomplished the stroke getting to the BDC position (end limit switch)

The paragraph dedicated to the data acquisition system will explain how the signals generated were manipulated.

11.3.4 Inlet pipe

The inlet pipe was composed of three parts (drawings 002, 003 and 008) which connected the water vessel with the pump inlet opening. The diameters of the pipes were chosen from among the standard imperial sizes in order to be big enough to provide the least pressure loss possible and achieve the mass flow rate measurement specification (part shown in the 002 drawing) of the Venturi pipe which is discussed in the next paragraph. The designer also tried to avoid bends as much as possible as they increase the fluid dynamics resistance of the pipe increasing the pressure drop across it for a given mass flow. One of the interests of the analysis was also to investigate the importance of the pressure loss in the inlet pipe. A ball valve was also placed in order to:

1. Isolate the water vessel from the pump in order to drain the pump without draining the vessel. A small drain valve was positioned upstream the ball valve for this purpose.
2. To be partially closed in order to increase the pressure loss in case a further inlet pressure loss was needed to enhance the cavitation.

The inlet line pressure loss at ball valve fully open is represented in Figure 11-21 and it accounts also for the Venturi pipe which was placed between the items shown in drawings 003 and 008, this will be discussed in the next paragraph. The trend was obtained simulating the inlet pipe by means of steady state CFD.

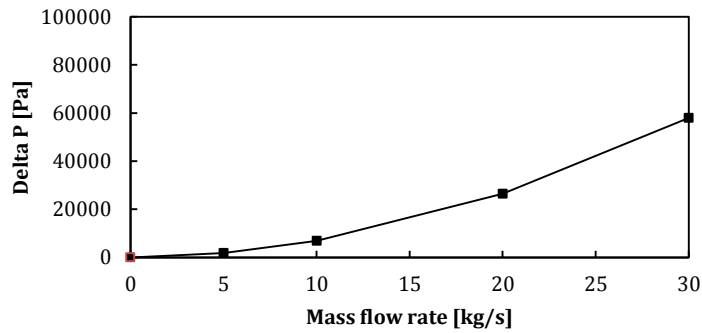


Figure 11-21: Inlet line pressure loss calculated by means of four steady state CFD simulations.

11.3.5 Venturi pipe

The Venturi pipe was placed in between the two parts creating the inlet line (drawing 003 and 008). It is shown in drawing 002. Its duty was to estimate the mass flow rate by means of measurement of static pressure drop across it. The inlet and outlet diameter ratio of the convergent duct was chosen in order to provide the least pressure loss with a measurable pressure difference at the expected mass flow rate and accounted for the sensitivity of the pressure sensor chosen for the purpose.

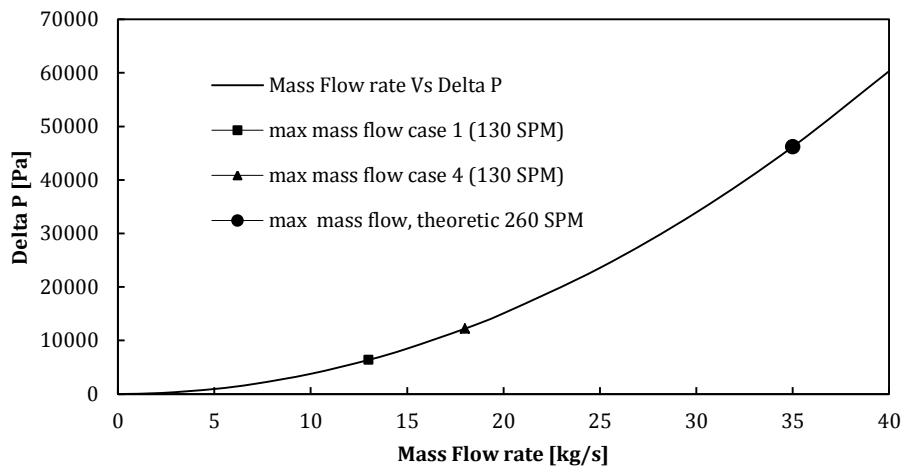


Figure 11-22: Venturi pipe ΔP Vs mass flow rate calculated by means of the Bernoulli's equation.

Figure 11-22 shows the trend of the theoretical mass flow rate with respect to the pressure drop of the Venturi pipe with the diameter ratio chosen. The figure highlights the mass flow rate estimated by the CFD analysis discussed in chapter 7 (case 1 and case 4) where the hypothesis of 130 rpm (130 SPM) was made. Also the maximum theoretical flow rate when the speed of 260 rpm (260 SPM) was used. The characteristic of the pressure sensors used to acquire the pressure drop across the Venturi pipe should account for the phenomenon described in Figure 11-22. In other words, the maximum pressure measurable by the gauge within its linearity limit should range around the value specified by the maximum flow rate

that the analyst is expecting to measure. For instance, if the analyst would like to carry out experimental tests simulating the behaviour of the crankshaft at 260 rpm, the maximum pressure value to measure is 46 kPa (0.46 bar circa), for 130 rpm that value decreases approximately to 10 kPa (depending on the cavitation regime).

Table 11-4: Venturi tube pressure sensors, characteristics summary. GEMS 2200SAA2501F3EA (upstream and downstream) and a Model z Wet/Wet RDP differential pressure transducer (Venturi differential)

Position	Output signal	Pressure connection	Electrical connection	Measurement range	Type (abs/relative)	Accuracy	Response time
Venturi upstream	0-10 Vdc	G1/4 gas male	Shielded cable	0-2.5 bar	Abs	±0.00625 bar	0.5 msec
Venturi Downstream	0-10 Vdc	G1/4 gas male	Shielded cable	0-2.5 bar	Abs	±0.00625 bar	0.5 msec
Venturi Differential	2mV/V	G1/4 gas male	Shielded cable	0-1 bar	Differential	±0.0025 bar	N/A

Table 11-4 summarises the characteristics of the pressure probe chosen for the Venturi tube. The measurement range 0-2.5 bar was chosen considering the availability of the devices on the market. The table (bottom row) highlights that a third sensor was utilised. This extra probe was a differential gauge sensor which measured directly the pressure difference between the upstream and the downstream ports. The reason for the use of this extra sensor lies on the strict requirement of the mass flow rate measurement. As discussed in the next chapter the tests eventually revealed that the accuracy achieved in measuring the mass flow rate was not sufficient and the differential pressure sensor was tested to achieve better results. It was thought that one single pressure reading provided by the differential transmitter was expected to carry half the maximum error as the two absolute pressure sensors. The accuracy of these three gauges is the same as their absolute counterparts (0.25% of the overall range). This will be discussed in more details in the next chapter.

11.3.6 Outlet pipe

The outlet pipe was composed of three parts (drawing 006, 011 and 014) and connected the outlet opening of the pump to the water vessel in order to close the loop. A ball valve was utilised to isolate the pump from the water vessel in order to drain the pump without draining the whole system. A draining valve was also positioned upstream the ball valve for this purpose.

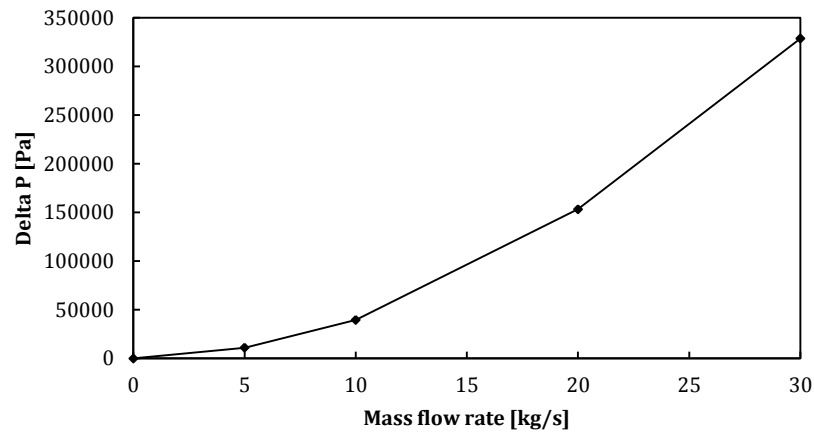


Figure 11-23: Outlet line pressure loss calculated by means of four steady state CFD simulations.

As the diameter of the outlet opening of the pump was smaller than the inlet one, it was possible to choose a smaller size of the pipe and this resulted in a bigger pressure loss of the overall pipe as suggested by Figure 11-23. The points in the figure were obtained by a set of 4 steady state CFD simulations of the outlet line (from the pump to the tank). It is important to note that Figure 11-21 and Figure 11-23 were utilised to set the boundary condition in the CFD analysis discussed in chapter 7 and 8 and 9. In those simulations, in fact, the author tried to utilise boundary condition as close as possible to the real experimental situation.

11.3.7 Water vessel

The 1 m³ capacity water vessel shown in drawing 017 was utilised to store the water needed for the experiment. For this purpose a water tank for domestic applications was bought and then modified. The modifications are shown in more detail in the technical drawing and can be summarised as following:

1. Two openings (100 and 50 mm of diameter) were cut to create the flanged connection with the inlet and outlet pipe.
2. Two big openings on the top and bottom were cut to place the 200 mm pipe which was designed to house the bladder utilised for pressurising the vessel in order to avoid the contact between the compressed air and the stored water.
3. Two pressure sensors were placed in the vicinity of the inlet and outlet pipe connecting flange in order to measure the pressure fluctuations in the tank during the experiments and make sure their magnitude was negligible. This was necessary to check the compatibility of the numerical and experimental conditions. A summary of the sensor characteristics is shown in Table 11-5.

Table 11-5: Tank pressure sensor (Gefran TSAN1FBV25GTV) characteristics summary.

Position	Output signal	Pressure connection	Electrical connection	Measurement range	Type (abs/relative)	Accuracy	Response time
Tank/inlet pipe	0-10 Vdc	G1/4 gas male	Shielded cable	0-0.25 bar	Rel	±0.000625 bar	< 1 msec
Tank/outlet pipe	0-10 Vdc	G1/4 gas male	Shielded cable	0-0.25 bar	Rel	±0.000625 bar	< 1 msec

The capacity of the tank was calculated making sure that temperature increment after a complete replacement of the water contained in it was negligible. As the vapour pressure depends on the temperature, a constant temperature during the tests was needed. The calculation was performed under the following assumptions:

- Vessel, pipelines and pump were adiabatic.
- 100% of the power needed by the motor was dissipated by heat.
- The average pumping cycle power is considered

The following equation was utilised for the estimation of the temperature increment:

$$\int_0^{t_1} P_M dt = m c_p \Delta T \quad 11.1$$

Where P_M is the pumping cycle average power needed to drive the plunger at 130 strokes per minute, t_1 is the time needed by the pump to replace completely the water contained in the tank at 130 strokes per minute, m is the amount of water contained in the vessel (1000 kg), c_p is the specific heat of water.

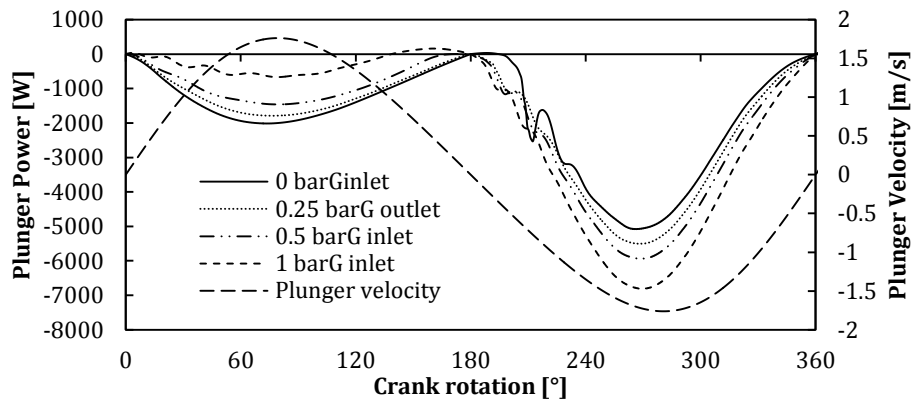


Figure 11-24: Plunger power throughout the pumping cycle estimated by the CFD analysis discussed in chapter 7.

Averaging the plunger power estimated by the test at ambient pressure (continuous line of Figure 11-24) the value of P_M needed results 1.78kW whereas considering a crankshaft

velocity of 130 rpm and the mass of a single displacement volume amount of water (2.5 kg circa), t_1 is calculated as 92 s. ΔT is then simply estimated as 0.04 K which was considered negligible, 1m³ tank was therefore big enough for the purpose.

11.3.8 High speed camera

A high speed camera (Figure 11-25) was utilised to take pictures of the valve during the tests. The camera was placed approximately 1 m far from the pump side inspection window (detail I of 001 drawing in the appendix). The camera recorded the frames in its hard drive which was connected to a computer from which the images could be downloaded via dedicated software. The frames were then mounted to create video clips.

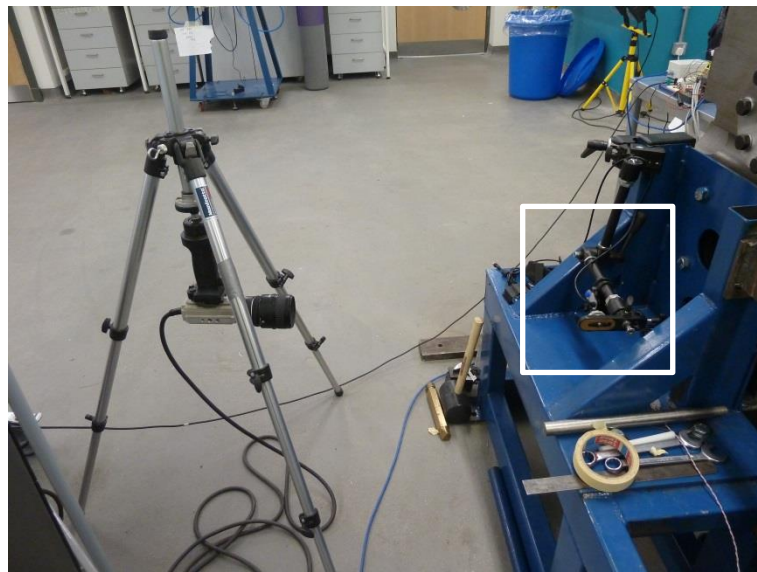


Figure 11-25: High speed camera placed 1 m from the side inspection window

To be employed the camera needed a source of light, Figure 11-25 shows the flashlight utilised and the arm where it was attached.



Figure 11-26: view of the inspection window

Figure 11-26 shows the frontal view of the inspection window which was the zone that the camera was aimed at during the tests. Figure 11-27 clarifies that the high speed camera

aimed at the middle of the inspection window in order to focus on the inlet valve-seat region, this allowed the operator to see the valve lift and also the vapour bubble formation. A further LED light was attached to the window in order to be visible in the images taken by the camera. This LED was activated by the stroke starting limit switch discussed in paragraph 11.3.3. The author opted for this system in order to synchronise the image sequence taken by the camera with the data acquired by the acquisition system discussed in the next paragraph. The camera was triggered manually a little bit before the plunger started the stroke. This means that once the movie frames were collected there was no possibility to relate precisely the frame sequence and the data flow. The problem was solved by LED light which was activated by the stroke starting switch and became clearly visible in the images identifying the starting photograph so that the sequence could be synchronised with the data flow of the pressure sensors.

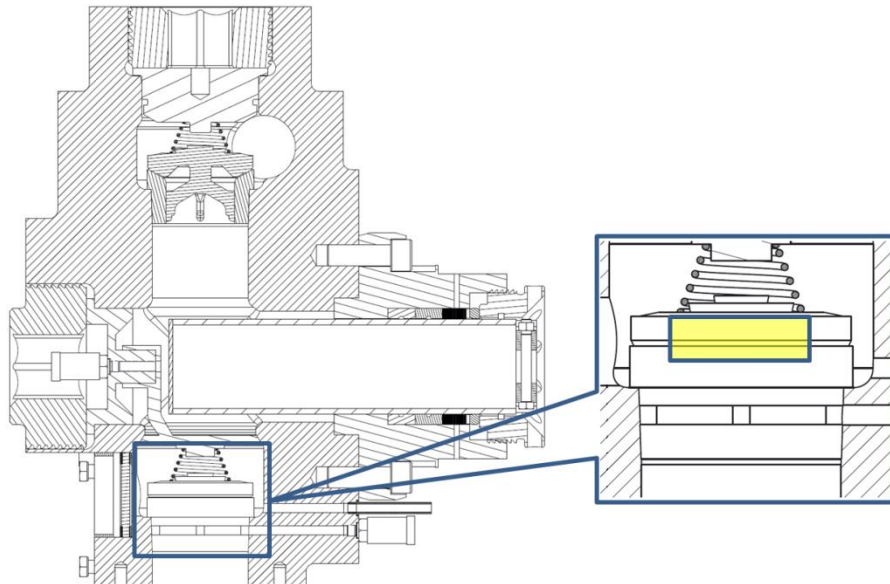


Figure 11-27: The yellow area highlights the position of the inspection window where the camera aimed at during the experiments.

A graphical post processing programme was written to manipulate the images and extract the information of the valve lift. The programme measured the valve lift by comparing the displacement of a reference mark from the initial frame (zero lift) to the mark's location on subsequent frames. All the tests were run twice in order to acquire images at the frequency of 1kHz and 0.5 kHz in order to have different resolution sequences and valve lift-time histories.

11.3.9 Data acquisition and driving system

According to the technical information discussed in paragraph 11.3.1 to 11.3.8, the acquisition quantities listed in paragraph 11.2 can be now updated as follows:

1. Mass flow rate
2. Inlet pressure
3. Pump chamber pressure
4. Valve–seat gap volume pressure
5. Outlet pressure
6. Valve lift
7. Plunger position
8. Tank/inlet-pipe connection static pressure
9. Tank/outlet-pipe connection static pressure

To successfully carry out the tests all the signals listed above had to be acquired at the same time in order to relate them to each other. The only exception was the valve lift which was related to plunger displacement by utilising the method described in paragraph 11.3.8. A real time acquisition system was therefore needed to achieve the scope. The whole acquisition system was composed of sensors, data acquisition hardware and data acquisition software. The components chosen can be described in more detail by the following list:

- *Sensors*. Pressure probes to acquire signals of mass flow rate and static pressure as previously discussed, and limit switches for the plunger position acquisition, introduced in paragraph 11.3.3.
- *National Instrument 16 bit Analog input module NI 9205* (Figure 11-28) to collect the analog signals of the pressure probes.
- *National Instruments 9401 8-Channel TTL Digital Input/Output module* (Figure 11-29) to collect the digital signal from the limit switches
- *National Instrument cRIO-9076 Integrated Controller and Chassis System* (Figure 11-30) to integrate the 9205 and 9401 modules and to interface them with the laptop utilised.
- *Laptop computer* where the NI LabView with its Real-Time module software was installed.



Figure 11-28: NI9205 Analog input module

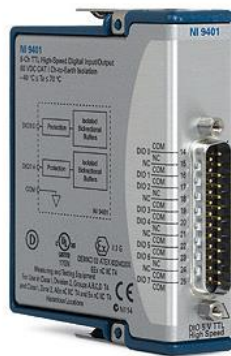


Figure 11-29: NI9401 Digital input module



Figure 11-30: NI-CRIO-9076 integrated controller and Chassis System

The pressure probes were wired into the NI9205 module whereas the limit switches were wired into the NI9401. Both the NI9401 and NI9205 were plugged into the chassis NI-CRIO9076 which was powered and connected to the laptop by means of a LAN cable. Two programmes were written in Labview in order to:

- a) Calibrate the pressure sensors
- b) Manage the whole set of signals and store it in a data file for post-processing

The calibration of the pressure sensors was needed to transform the voltage read by the data acquisition system into pressure data but also to check for the linearity of the sensors. For this purpose an external calibrator was utilised. The device allowed the operator to apply known pressures to the transmitters and read the output voltage by means of the LabView programme written for the specific purpose in order to build the calibration lines. Figure 11-31, Figure 11-32 and Figure 11-33 show the calibration line obtained for all pressure sensors. All the figures show a perfect linear behaviour, the coefficient of linearity and the offset term is also shown in the figures.

Figure 11-31, Figure 11-32 and Figure 11-33 also point out that the coefficient of determination R^2 was very close to 1. R^2 is defined as:

$$R^2 = 1 - \frac{\sum_i (y_i - f_i)^2}{\sum_i (y_i - \bar{y})^2} \quad 11.2$$

In equation 11.2 y values refer to the measured value of pressure while f refers to the calculated linear value of pressure. R^2 very close to 1 means that utilising the interpolated linear trend the error expected is negligible over the sensor linearity range.

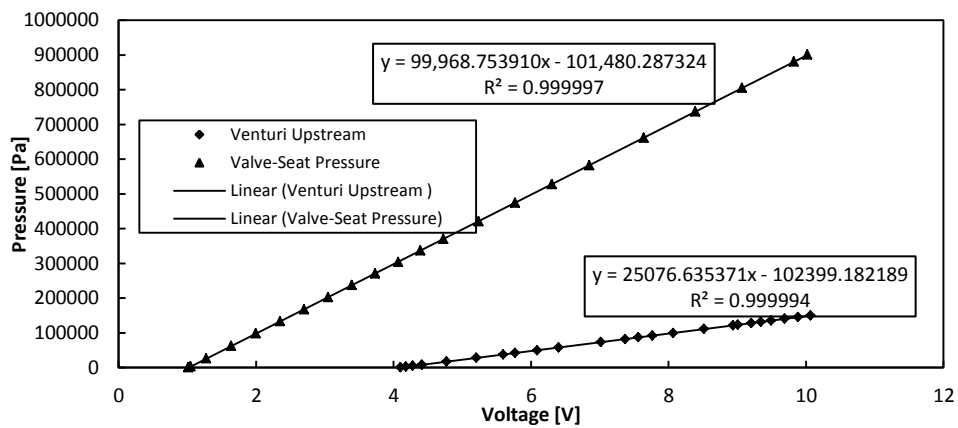


Figure 11-31: Calibration line of the Venturi Upstream and Valve-seat sensors. The coefficients of linearity are provided.

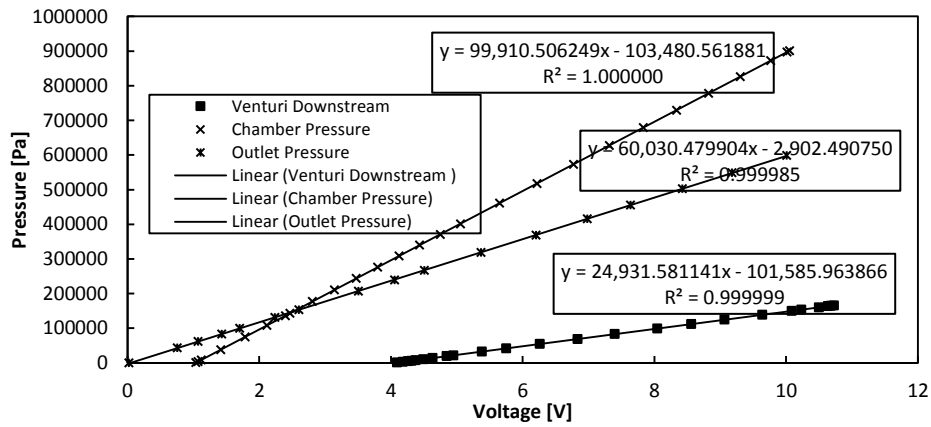


Figure 11-32: Calibration line of the Venturi Downstream, pump chamber and outlet sensors. The coefficients of linearity are provided.

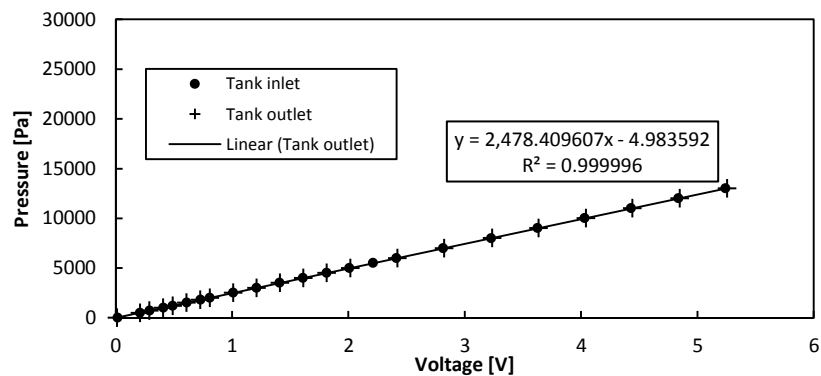


Figure 11-33: Calibration line of the tank pressure sensors. The coefficients of linearity are provided.

The coefficients of linearity obtained by the calibration process were fed into the main Labview acquisition programme to turn the voltage signals into pressure. Figure 11-34 shows the part of the block diagram of the main acquisition programme where this operation occurred. The signals were acquired inside a real time loop where the acquisition frequency of 1 kHz was set. Outside the time loop each voltage signal was converted to pressure by means of:

- Multiplication by the linearity coefficient calculated via the calibration operation.
- Addition of the offset term which was calculated by the calibration operation as well.

As shown in Figure 11-34 the time information was stored in the data file as well as the digital signal of the limit switch, without any further manipulation. As all the acquisitions took place at the same time, this technique allowed the analyst to have a direct relation between the pressure phenomena and the time when they occurred. The limit switch digital signal together with the time gave the analyst the information on the time when the plunger

reached the known positions where the limit switches were placed (TDC, middle, BDC), this information was also utilised to synchronize the image sequences as explained.

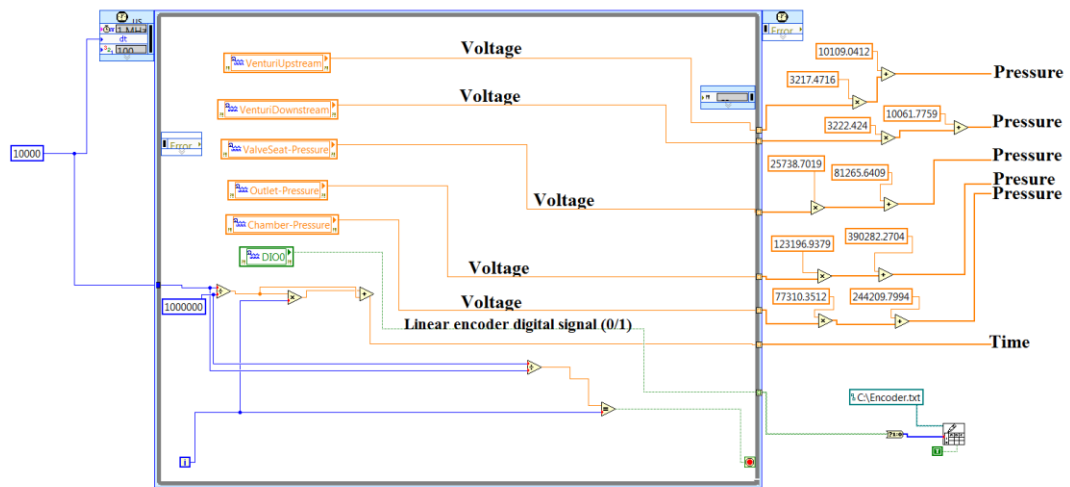


Figure 11-34: LabView acquisition main programme: how the calibration coefficients were utilised to transform the voltage signal to pressure.

Figure 11-35 shows the second part of the block diagram of the LabView programme which completes Figure 11-34. The pressure signals of the Venturi tube (upstream and downstream) were manipulated further in order to calculate the mass flow rate by utilising Bernoulli's equation as well as the continuity equation and the geometric properties of the Venturi tube. Figure 11-35 shows also that the downstream Venturi pressure probe signal was utilised to provide the pump inlet pressure. All the manipulated signals were visualised and stored as shown by the diagram.

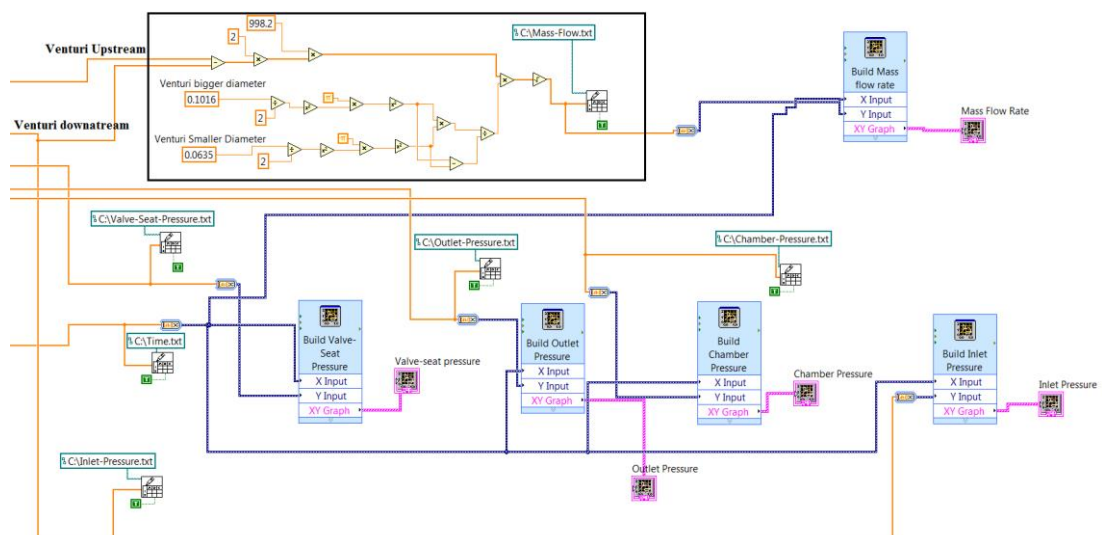


Figure 11-35: Labview acquisition main programme. How the signals are manipulated, visualised and stored.

11.4 Motor use issues

As shown in drawing 000-01, the linear motor was bolted on the rig frame part which is shown in more detail in drawing 013-01. The plate on which the motor was bolted was manually adjusted to allow for an acceptable alignment between the motor shaft and the plunger. The coupling between the motor and the pump was a critical issue to focus on. In fact, according to the motor user manual, the maximum misalignment acceptable at full load to avoid any damage on the motor coils was only $\pm 1^\circ$ which can be considered quite strict for a manual alignment operation. Furthermore, to allow for the misalignment within the specified range a non-rigid connection between the shaft and the plunger had to be designed.

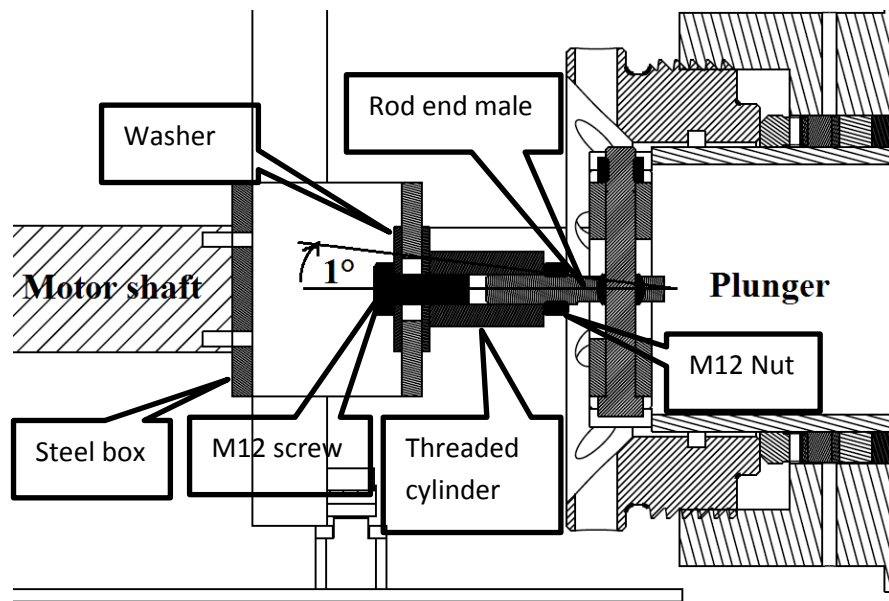


Figure 11-36: Motor shaft-Plunger coupling, detail of the items utilised

The solution found is represented in Figure 11-36. The idea was to avoid a direct coupling between the shaft and the plunger and to use the items highlighted in the figure instead. A rod end male allowed rotation around the ball joint located on its head to satisfy the requirement of flexibility of the coupling. As the direct connection between the rod end male and the motor shaft was impossible because of lack of space, a steel box (021 drawing), a M12 screw, two 3 mm thick washers, a threaded cylinder and an M12 nut were utilised instead.

The solution described provided the flexibility of the coupling but also a few drawbacks:

1. Avoiding the direct coupling between the shaft and the plunger some more space was needed, the steel box and the threaded cylinder (56 mm overall length) caused a decrement of the available plunger stroke of approximately 2 in (50 mm). It was

in fact impossible to move the frame part (013 drawing of the Appendix) which was already manufactured. For this reason the analyst was obligated to change from a 10 inch stroke test to an 8 inch instead, different from originally planned.

2. Achievement of the $\pm 1^\circ$ range depended on the skill of the technicians.

It is important to point out that the linear encoder attached to the motor was not absolute. This meant that turning on the motor the driver did not know the position along the stroke the shaft was located and utilises the starting position, which may change, as the reference position. This operation of setting the reference position is called “commutation” and is performed automatically by the driver the first time the linear motor is activated after every reboot of the driver. The commutation has to be carried out without load attached to the shaft and shaft-plunger decoupling was required. This was a time consuming process.

No solution was found that allowed a quick decoupling of the plunger from the shaft and therefore, if possible, the operation was not suitable to be performed often. However this issue was not considered as high priority.

Bearing in mind the time needed to redesign the coupling which might involve the complete modification of the frame, the solution described was accepted provided the following action to protect the linear motor from damage:

- **In any load configuration (inlet and outlet stroke) the maximum axial force was fixed in order not to exceed the maximum allowable force of the linear motor with a safety factor of 2.**

The safety factor accounted for the uncertainties of the estimation of the friction force which may vary during the experiment due to the variation of lubrication as well as and the real alignment, provided that the limit of $\pm 1^\circ$ was valid at full load only. Manufacturing of a lighter plunger having a lower inertia aimed also at reducing in any condition the force needed by the motor to accelerate the plunger and achieve the required displacement motion law.

The reason for the caution in the use of the linear motor was justified by the fact that the motor was the most expensive part of the rig as it cost £12k worth alone.

The motor user manual also recommended to make sure that the shaft never hit the internal stroke ends during the operations performed at high velocity because it might damage the encoder and the coils. As the encoder was not absolute this implied that it was up to the operator to make sure that the starting position was compatible with the application of the entire displacement law in a safe way within the stroke ends. An external system to safely

stop the shaft in case it approaches the shaft stroke ends was strongly recommended in order not to leave the responsibility to the operator who may make a mistake. This will be discussed in the future improvements section of this dissertation.

12 Experimental tests and CFD model validation

12.1 Introduction

Chapter 11 revealed some technical issues due to the use of the linear motor which led the author to slightly change the experimental conditions previously planned. The modification of the experimental conditions was followed by a slight modification of the CFD model which was previously designed (chapter 7) for CFD validation via experiments. This chapter will discuss in more details the tests as they were eventually carried out and also the small changes performed on the numerical model. The comparison of the experimental and numerical data will also be provided and discussed.

12.2 Experimental tests

Differently from the boundary condition discussed in chapter 7, it was decided to move from the full cavitating condition to null/incipient cavitating condition by decreasing the plunger velocity instead of increasing the water tank inlet pressure. Also, in order to satisfy the requirement of low shaft maximum force, the maximum plunger velocity was limited to 1.1 m/s. This increased the axial force available of further 10% and achieved a safety factor in the use of the motor of 2 as the author suggested in the previous chapter. The results will demonstrate that this decision does not affect the requirement of achieving the full cavitating condition.

Three tests at three different plunger speeds were carried out. Figure 12-1 shows the displacement-time history and the velocity chosen for each of them:

- A constant acceleration part of 4, 5.5, 7 m/s² respectively for test number 1, 2 and 3.
- A constant velocity part of 0.8, 0.95, 1.1 m/s respectively for test number 1, 2 and 3.
- A constant deceleration part of 4, 5.5, 7 m/s² respectively for test number 1, 2 and 3.

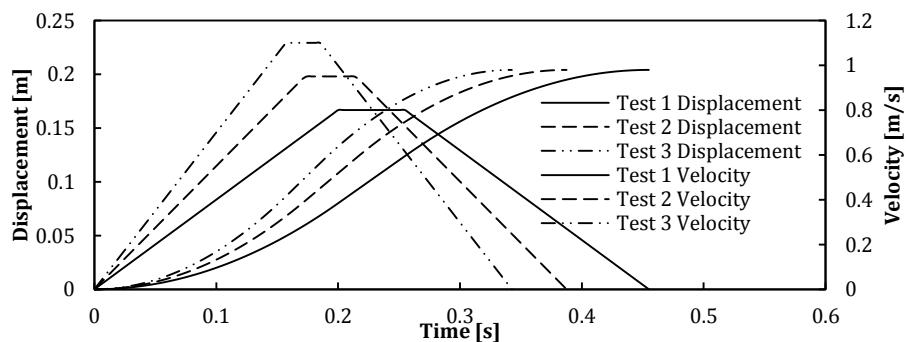


Figure 12-1: Plunger displacements and velocities created by means of the motor drive administrator (Aldo Iannetti et al. 2015).

In all tests the stroke was 204 mm instead of 254 mm chosen for the numerical set described in chapter 7. Figure 12-1 represents the suction stroke only as the delivery stroke was carried out very slowly only to reposition the plunger to the TDC position again for the following suction stroke test. The acceleration and velocity were designed to achieve the null/incipient, partial and full cavitation regimes as described by Opitz (Opitz et al. 2011; Opitz & Schlücker 2010) and Iannetti (Aldo Iannetti et al. 2015).

12.3 CFD model modification

For the numerical side of the analysis the CFD model described in chapter 7 was modified to account for the modifications of the experimental test specifications. The reciprocating motion which was achieved by feeding ANSYS Fluent with the connecting rod length, crank diameter and velocity within the In-Cylinder technique (ANSYS 2011c), was replaced by three new UDFs where the velocities of the plunger of Figure 12-1 were set as piecewise linear laws. These UDFs were attached to the plunger top wall and drove the displacement volume moving mesh in a similar way to the In-Cylinder technique in the previous analysis.

As the aim of the experimental tests was to investigate the inlet stroke only, the analyst excluded the outlet valve from the numerical model which resulted in a smaller mesh and lower computational resources need. Furthermore, in this new CFD model, the inlet boundary conditions were slightly changed. In the model discussed in chapter 7 the inlet pipe was cut a few diameters upstream and a mass-flow variable pressure condition was set on the inlet surface. In this case the smaller mesh allowed the analyst to model the entire length of the inlet pipe and also the volume of the water vessel. The inlet boundary condition was moved onto the top opening of the water vessel and set as a constant ambient pressure. In this way the inlet pipe pressure resistance could be estimated. The validity of this boundary condition depended on the water level oscillation inside the tank which resulted in a non-constant inlet pressure which signal was provided by the pressure transducer attached to the vessel.

Table 12-1: Solver settings summary

Solver	RANS, pressure based, transient		
	Mixture model (ANSYS 2011a)		
Models	Multiphase	Phases	Water liquid
			Primary phase
			Water vapour
			Secondary phase
	Turbulence	k-ε Standard	Enhanced wall treatment
	Cavitation	Singhal et al.	3 ppm air (test 1,2 and 3), 1.5 and 4.5 ppm (test3)
Pressure-Velocity coupling	SIMPLE		
Spatial discretization	Momentum	Second order upwind	

	Vapour	First order upwind
	Turbulent kinetic energy	Second order upwind
	Turbulent dissipation rate	Second order upwind
Transient formulation	First order implicit	
	Pressure	0.3
	Momentum	0.7
Under relaxation factors	Vapour	0.5
	Turbulent kinetic energy	0.8
	Turbulent dissipation rate	0.8
Residuals	10^{-3}	
Time step	2×10^{-4} s	
Max Iteration per time step	45	
UDFs	Valve dynamics (see chapter 7)	
	Plunger displacement-time (Figure 12-1)	

Table 12-1 summarises the solver settings used for the modified CFD model. They were very close to those described in chapter 7.

During the CFD simulation the models were set to monitor every time step and store the data of the following quantities:

- *Chamber pressure.* A monitor point close to the TDC position of the plunger was created
- *Valve seat pressure.* This monitor returned every time step the volume weighted average of the static pressure in the valve-lift volume.
- *Inlet pressure.* The static pressure downstream the Venturi tube.
- *Mass flow rate.*
- *Inlet valve lift.*

The monitor locations in the CFD were set to the same location as the pressure sensors in the experimental counterpart to allow a consistent comparison with the experimental data.

It was also decided that the following monitors, which had no counterpart in the experimental tests, were of interest for the analysis:

- *Valve-seat vapour volume fraction.* This is the valve-seat lift volume weighted average of the vapour fraction
- *Valve-seat air volume fraction.* This is the valve-seat lift volume weighted average of the air fraction which comes out of the solution because of the low static pressure.

12.4 CFD-Experiments results comparison

12.4.1 Test 1: Incipient cavitation

Test 1 was designed to achieve the lowest cavitation regime (incipient) by means of low plunger velocity and acceleration, the CFD model was set with 3 ppm of air mass fraction. Figure 12-2 and Figure 12-3 show the trend of chamber and valve-seat static pressure respectively. Figure 12-2 shows that the minimum pressure in the chamber remains sufficiently above the vapour pressure and also shows a trend which is not perfectly flat in its behaviour (between 0.07 and 0.2 s). Figure 12-3 shows that the valve-seat minimum pressure is always higher than the chamber pressure too; this is evidence of incipient cavitation. A small amount of vapour generation cannot be excluded as the static pressure could approach the vapour pressure locally in zones of high velocity and turbulence, this is demonstrated by the frame sequence of Figure 12-6 where in some of them the valve is partially not visible because of the vapour bubbles propagating from the external edge of the valve body. The slope of the pressure decrement calculated by CFD, in both Figure 12-2 and Figure 12-3 is slightly lower than their experimental counterpart although the trends are in good agreement in the first half of the suction stroke.

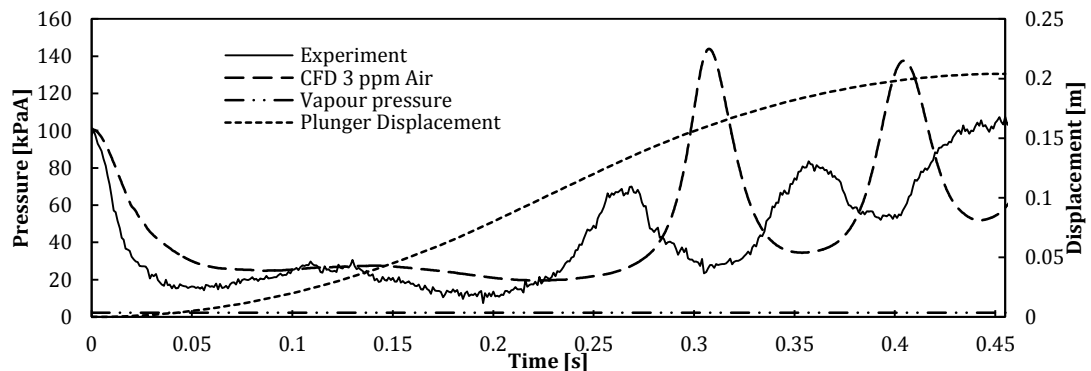


Figure 12-2: Pump chamber static pressure. Experiments Vs CFD (test 1).

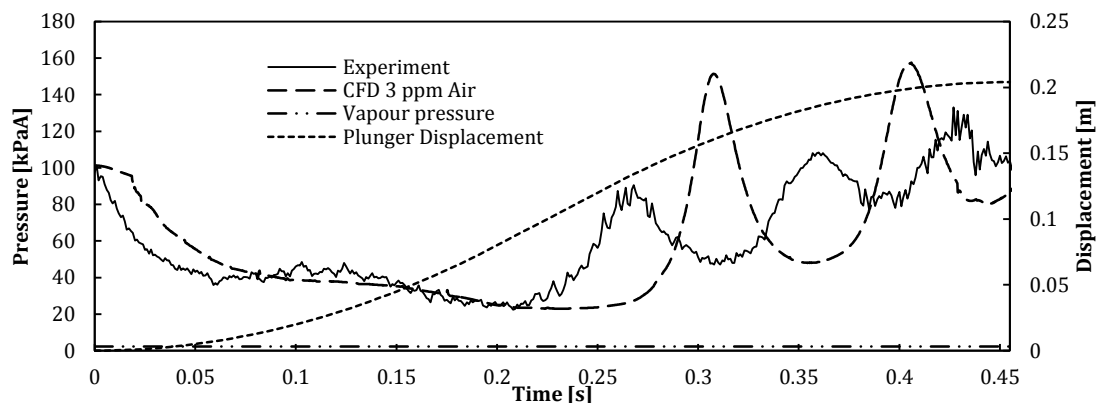


Figure 12-3: Valve-seat static pressure. Experiments Vs CFD (test 1).

Pressure spikes affect the second half of the suction stroke. They are present in both the experiment and the CFD plots although the latter show a delay in the occurrence. It would appear that the CFD pressure trends are stretched along the time axis with respect to the experimental counterparts.

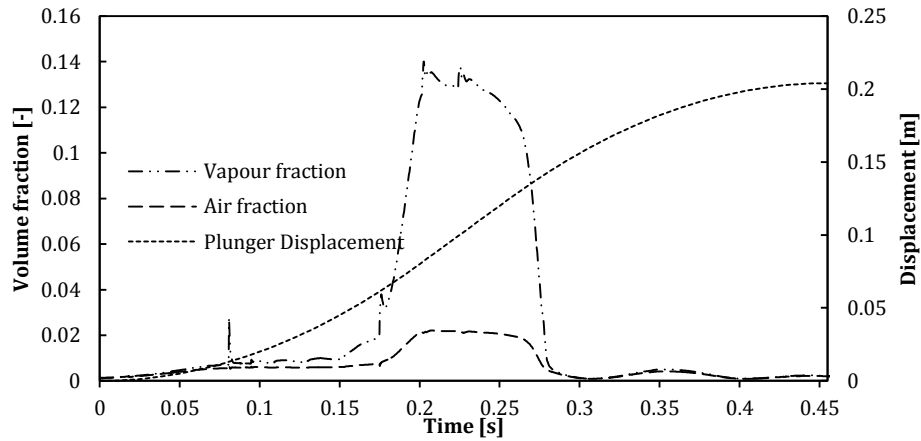


Figure 12-4: Second phase fraction composition according to CFD (test1).

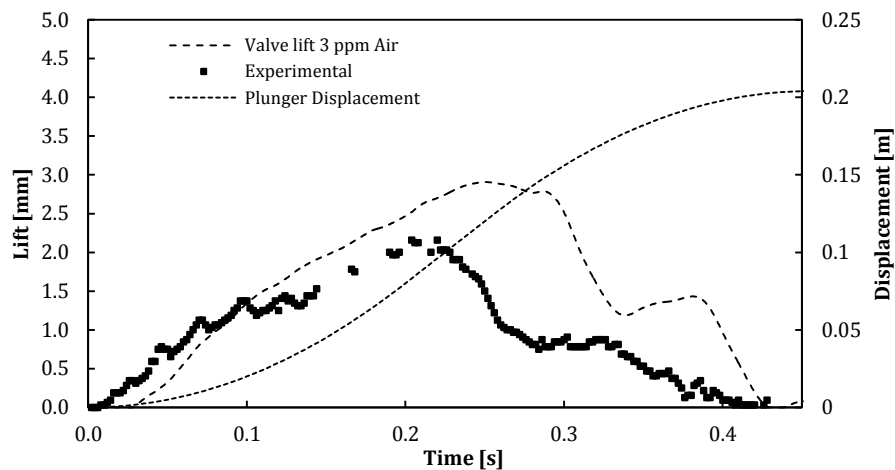


Figure 12-5: Valve lift, Experiment Vs CFD (test1).

As the CFD is affected by low pressure longer than the experiment, the maximum valve lift achieved by CFD is as highlighted by Figure 12-5, which also shows the delay of the maximum valve lift occurrence compatible with the delay in the occurrence of the pressure spikes shown in Figure 12-2 and Figure 12-3. Figure 12-5 demonstrates that the pressure spikes are the results of the water hammer effect related to the valve closing as the spikes temporal location corresponds to the negative valve velocity part on the right side of the valve-lift trend in both CFD and experiment. Errors in estimating the valve dynamic, affect the estimation of the pressure peak temporal location and magnitude. However, beside the delay, in this case the trends are in good agreement with each other.

Figure 12-4 shows how CFD estimates the composition of the second phase volume fraction in the valve-lift volume. The maximum vapour fraction calculated was 14% and occurred roughly in the middle of the suction stroke. However the average results very low as the vapour quickly returned to negligible values.

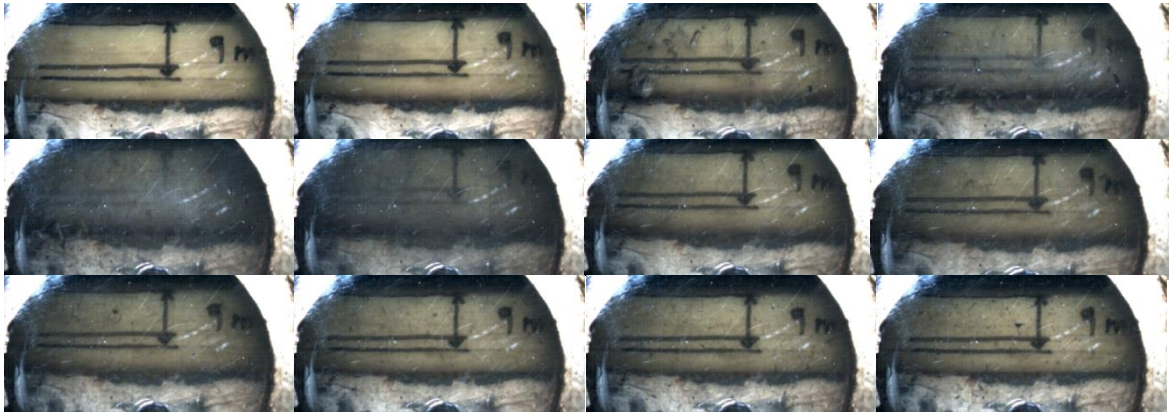


Figure 12-6: Null/incipient cavitation, only three frames show second phase presence which never obscures the view of the valve.

12.4.2 Test 2: Partial cavitation

Test 2 was designed to achieve the partial cavitating conditions. The CFD model was set with 3 ppm of air mass fraction as was previously done in test 1. Figure 12-7 and Figure 12-8 show that the static pressure in both the chamber and the valve-seat locations were closer to the vapour pressure for a longer time, in the first half of the suction stroke, than test 1. The CFD lines were again shifted with respect to the experiments but the trends were in good agreement with each other from a qualitative view. In this test, the CFD predicted the water hammer effect but it overestimated the magnitude of the resulting pressure spikes more than test 1.

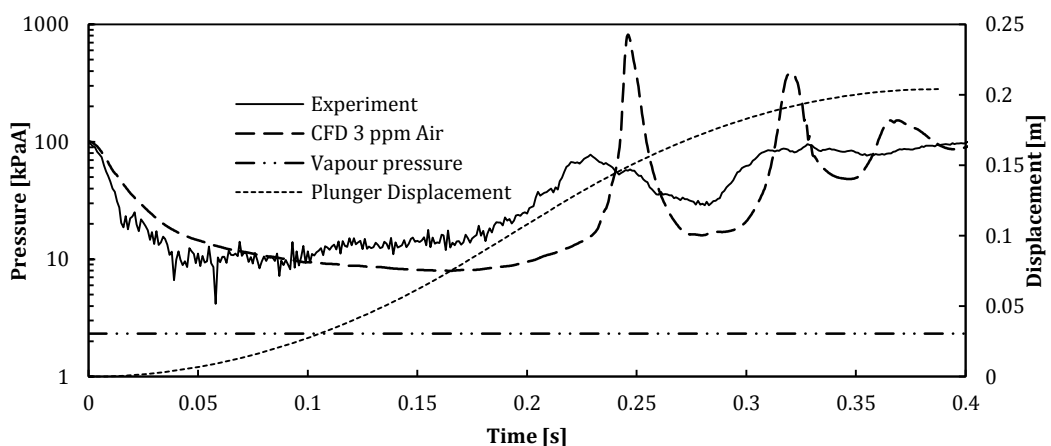


Figure 12-7: Pump chamber static pressure (Log scale). Experiments Vs CFD (test 2).

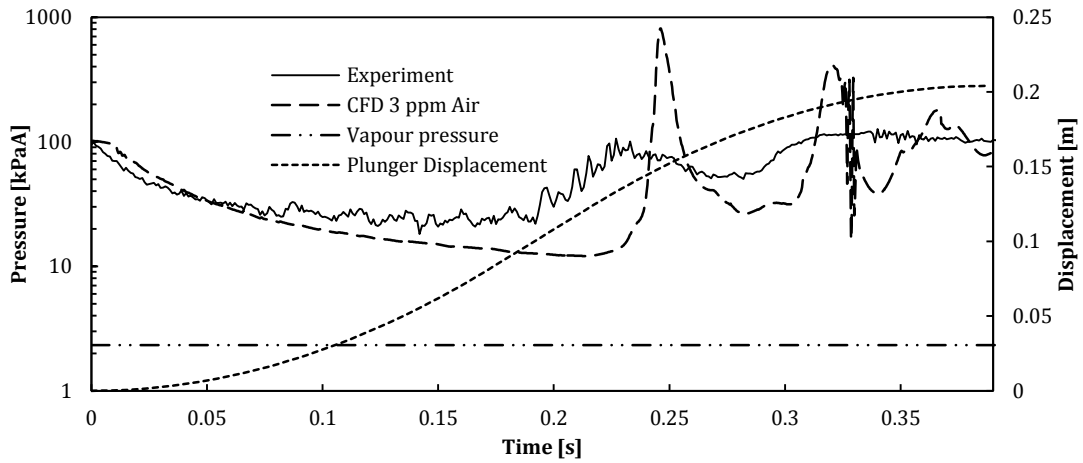


Figure 12-8: Valve-seat static pressure (Log scale). Experiments Vs CFD (test 2).

Also in this case, because the CFD's lower pressure lasted longer than the experimental counterpart, it may be assumed that the pressure forces across the valve induced the lift acceleration for a longer period of time, this resulted in a bigger and delayed valve lift achieved by CFD as shown in Figure 12-11. Figure 12-11 also revealed that the CFD pressure spikes magnitude was overestimated because of behaviour of the valve lift trend. In fact, while returning to the seat, according to CFD, the valve reversed its motion twice (approximately at 0.27 and 0.3 s). The experimental trend results much smoother instead and provided much less disturbance to the flow. It is important to show that the pressure peaks occur a little after the valve reverses the motion and, according to the author's opinion, the valve reverse motion is the actual cause of the pressure spikes. The relation between the valve velocity and the pressure spikes is shown in Figure 12-9.

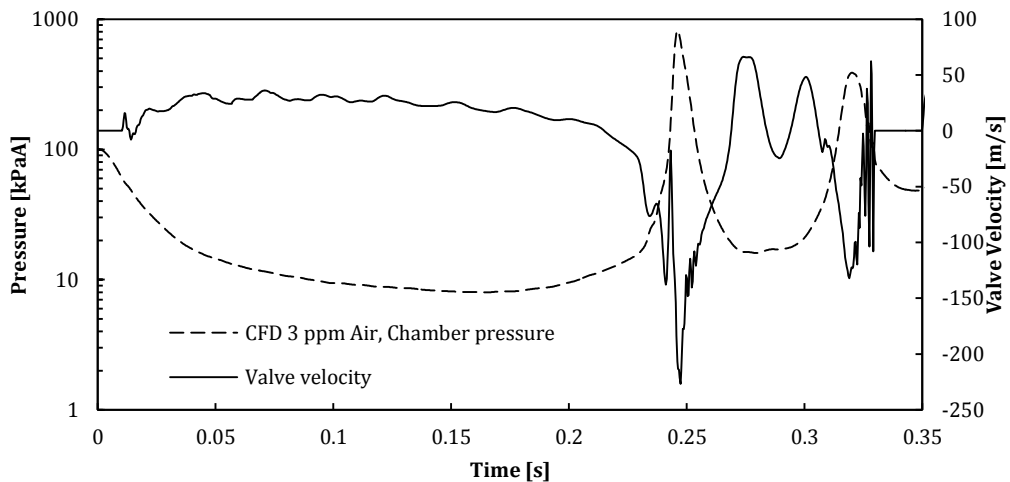


Figure 12-9: Test 2, Chamber pressure Vs valve velocity, the pressure peaks occur in the same time of the valve minimum velocity.

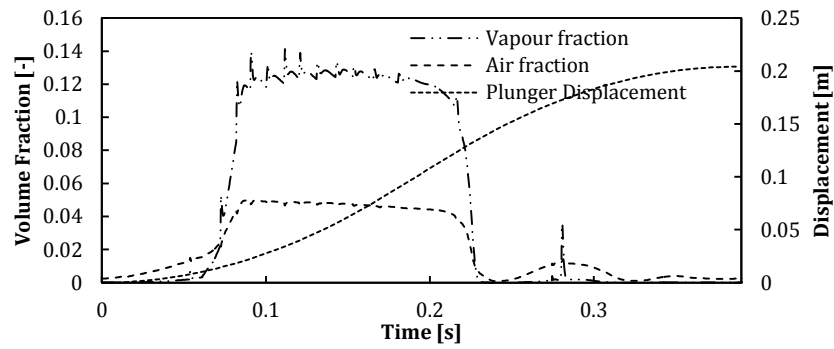


Figure 12-10: Second phase fraction composition according to CFD (test 2).

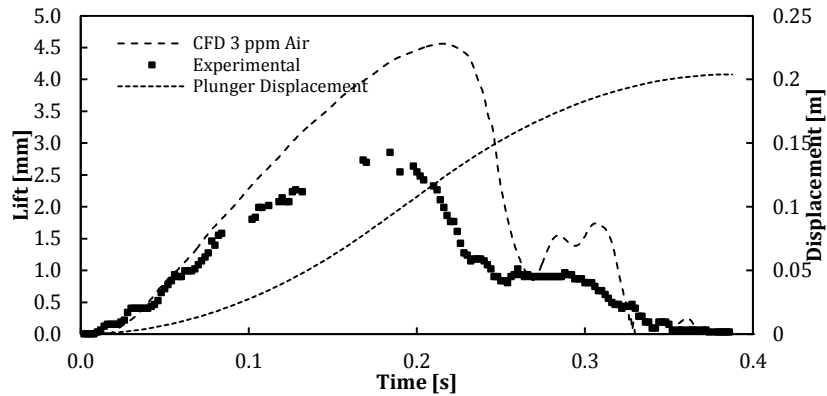


Figure 12-11: Valve lift, experiment Vs CFD (test2)

The maximum vapour fraction in the valve-seat lift volume, estimated by CFD and revealed by Figure 12-10 for test 2, was 14% and thus similar to test 1 but this time the maximum level was kept for more than a third of the overall suction stroke duration resulting in a more significant vapour overall integral. Figure 12-12 shows twelve frames evenly separated taken by the high speed camera. The vapour generation was demonstrated to be non-negligible as in two of the images the valve is completely obscured by the vapour cloud.

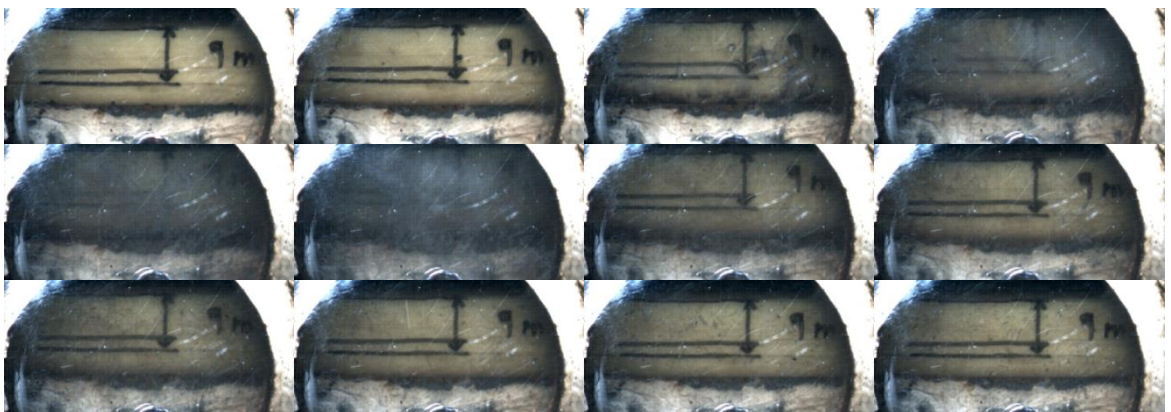


Figure 12-12: Partial cavitation. Four frames show a vapour cloud around the valve-lift gap, in two of them the view of the valve was obscured almost completely.

12.4.3 Test 3: Full Cavitation

Test 3 was the highest plunger speed test designed to achieve the full cavitating condition as explained by Opitz (Opitz & Schlücker 2010). In this case the CFD simulations ran four times with 1.5, 3, 4.5 and 15 ppm of air mass fraction to shed light on the sensitivity of the CFD solution to the air content in the water.

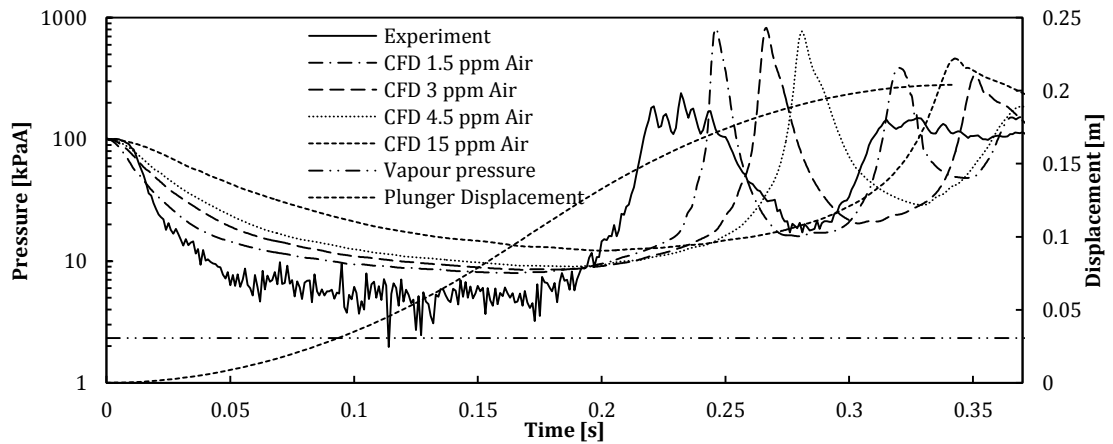


Figure 12-13: Pump chamber static pressure (Log scale). Experiments Vs CFD (test 3), the sensitivity to the air mass fraction is shown.

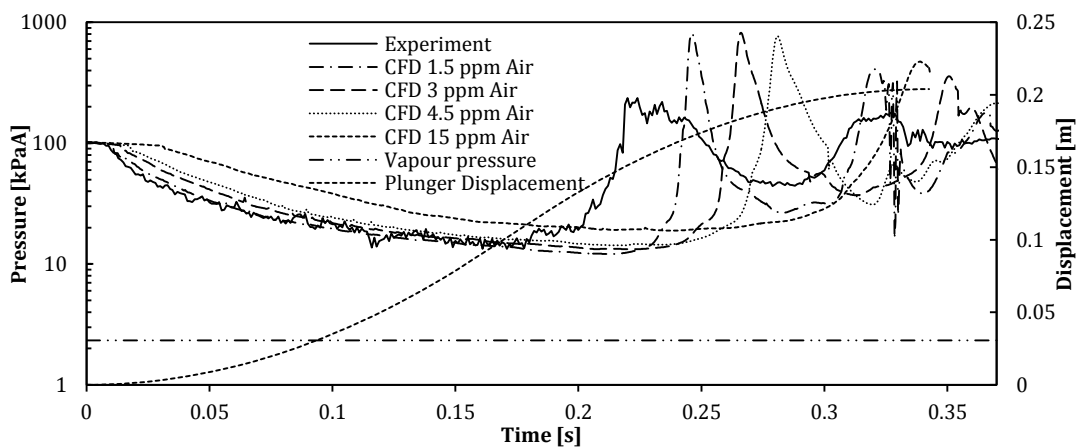


Figure 12-14: Valve-seat static pressure (Log scale). Experiments Vs CFD (test 3). The sensitivity to the air mass fraction is shown.

Figure 12-13 and Figure 12-14 show the trend of chamber pressure and valve-seat lift volume static pressure respectively. In both cases, the experimental curve highlights a flat and low pressure trend which affects the first half of the suction stroke after the initial decompression. During the first part of the suction stroke the experimental line and the 1.5 ppm CFD line are overlapped in Figure 12-14, the same lines are very close to each other in Figure 12-13. High magnitude pressure spikes affected the second half of the suction stroke. The water hammer effects, in the experimental case produces lower magnitude pressure spikes with respect to the CFD lines. In this case the magnitude of the pressure peaks

(experimental line of Figure 12-13 and Figure 12-14) is overestimated by the CFD because of the valve bounces which are visible in Figure 12-17. The peak's magnitude occurrence was affected by a delay as stated for test 1 and 2. Both Figure 12-13 and Figure 12-14 explain that the delay was affected by the air mass fraction, the more the air mass fraction the bigger the delay in the CFD pressure spikes occurrence. The 1.5 ppm curve produced the closest fit to the experimental line while the 15 ppm CFD curve shows the biggest delay.

Figure 12-15 and Figure 12-16 were obtained by the CFD analysis and show respectively the vapour volume fraction and the air volume fraction in the valve-seat lift volume. The figures show that the higher the air content the lower the vapour generation and this agrees with what was postulated by Iannetti (Aldo Iannetti, M. T. Stickland, et al. 2014).

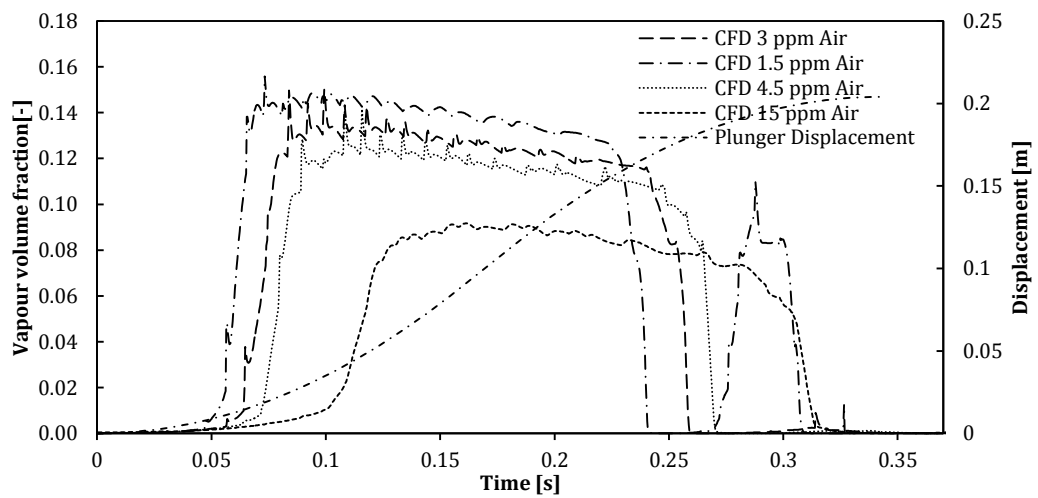


Figure 12-15: Vapour volume fraction in the valve-seat lift volume according to CFD (test 3).

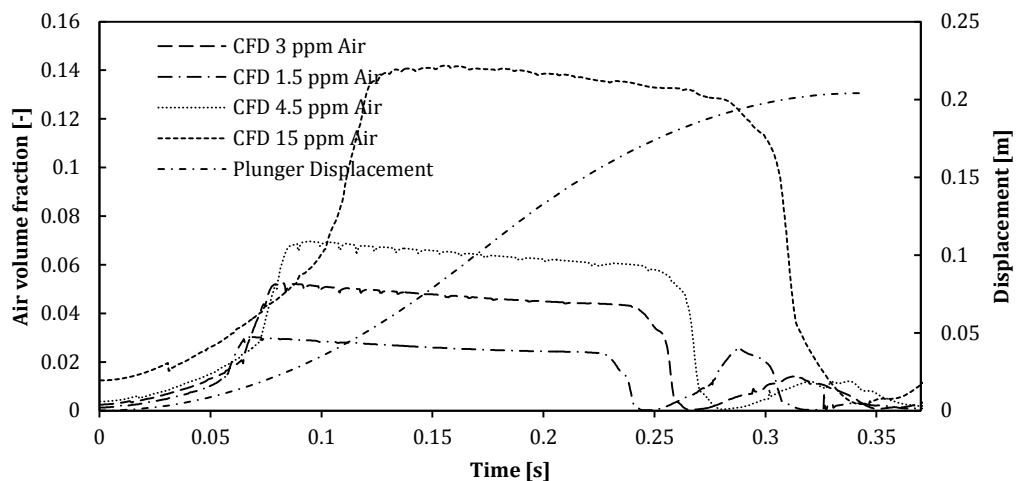


Figure 12-16: Air volume fraction in the valve-seat lift volume according to CFD (test 3)

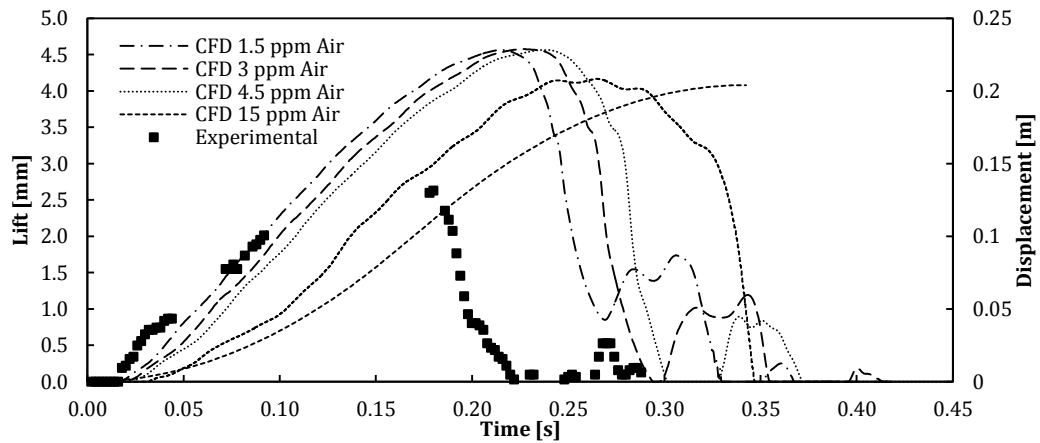


Figure 12-17: Test 3 valve lift, experiment Vs CFD, the sensitivity of the CFD solution to the air mass fraction is also shown

A similar correlation between the air content and the NPSHr which affects vapour cavitation was also observed by Ding studying centrifugal pumps (Ding et al. 2012).

As the air expansion, shown by Figure 12-16 reveals a second peak after it reaches the zero value around 0.25 s, it may be assumed that the valve bounces on and off the seat once before completely closing. This is confirmed by the valve lift trend of Figure 12-17, the 3 and 4.5 ppm CFD simulations clearly show that the valve touches the seat after 0.3 s and then lifts off it to close completely at the end (or a little after) of the suction stroke. The 1.5 ppm simulation does not follow exactly the same pattern as in this case, the valve reversed the motion at 0.27 s before touching the seat. The 15 ppm curve does not show the same behaviour as, for this case the valve closes approximately when the plunger motion comes to the end. The 1.5, 3 and 4.5 ppm CFD trend of the valve lift show a similar maximum value which was higher than the 15 ppm case, this can be explained by the bigger amount of vapour generated which keeps the force across the valve on a low value for a longer time, it can be assumed that vapour and air have a similar effect on the valve force.

The valve lift experimental trend deserves a further discussion. The frame sequence shown in Figure 12-18 demonstrates the big amount of vapour generated as in four frames out of 12 the valve is not visible because of the significant content of vapour bubble which is clear evidence of full cavitation. In these frames, in fact, the graphical post processing programme, which estimated the valve lift, failed and caused the gap in the experimental valve lift trend which may be seen in Figure 12-17. However, the maximum valve lift can be estimated by interpolation and can be assessed to range between 3 and 3.5 mm which demonstrated that CFD in any case, once again overestimated the maximum valve lift. As discussed for test 1 and 2 the reason for the overestimation of the valve lift is the longer application of the lifting

pressure force on the valve. Furthermore, until 0.1 s, the 1.5 ppm CFD simulation follows the experimental valve lift trend closely while the 15 ppm case is the least accurate even though 15 ppm is expected to be the real air content in the water utilised (tap water). The 3 and 4.5 ppm case lay consistently in between the 1.5 and the 15 ppm case.

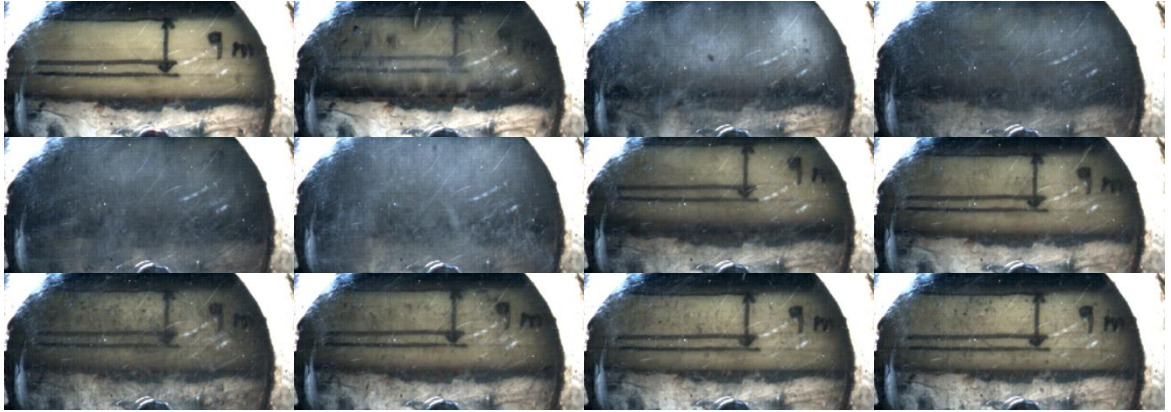


Figure 12-18: Full cavitation, five frames show a vapour cloud around the valve-lift gap, in four of them the view of the valve is completely obscured.

12.5 Conclusion

According to the observations on the experimental and numerical data together with the discussion of the results in the previous paragraph, the following brief summary can be drawn:

- All the phenomena related to the fluid dynamics of cavitation were predicted by the CFD (the decompression, the interaction with the non-condensable gas, the vapour generation and the water hammer pressure peak which marks the end of cavitation). Increasing the plunger velocity the cavitation regime worsen as expected, increasing the air content in the water, the vapour generated decreases, this proves the consistency of the model.
- CFD overestimates the valve maximum lift due to the overestimation of the low pressure duration. The reason for this is the failure of the cavitation model which accounts for the influence of the air mass fraction in cavitation. CFD overestimates influence of the expansion of air on cavitation.
- CFD pressure lines are generally slightly above the experimental line in the low pressure region. CFD overestimates also the magnitude of the pressure spikes in figure 7, 10 and 13 as a consequence of the wrong valve velocity trend prediction.

- Although the analyst expected to see a good matching between the experiments and the 15 ppm CFD case, the 1.5 ppm CFD simulations were, in fact the closest to the experimental trends.

The author identified the influence of the air expansion on the fluid dynamics of the pump in cavitating condition. It should be investigated further as in the opinion of the author it is the main cause of the mismatch between the CFD and the experimental data.

It is clear that the explicit algorithm managing the volume fraction estimation and thus the influence of the air (discussed in paragraph 4.3.1) did not work accurately. The numerical model overestimated the expansion of the non-condensable gas during the low pressure part (first half of the suction stroke), this affected the time the recompression (carried out at approximately constant pressure) needed to "eliminate" the air, this resulted in the longer application of the lifting force on the valve. Therefore all the phenomena observed such as the overestimation of the valve maximum lift and the pressure peaks magnitude and frequency, should be considered a direct consequence rather than a further source of problems.

The reason why the air expansion in the mixture is not predicted correctly lies in the assumptions and the simplifications made by the cavitation model explained in chapter 4. Concerning the air mass fraction, the only effect accounted by the model was the volume fraction which appeared and disappeared according to the pressure value in all the cells of the discrete model. The air volume fraction affected back the pressure field only indirectly through the second phase volume fraction transport equation. No momentum equation of the air was solved neither by the cavitation model nor the multiphase mixture model. The energy involved in the air expansion is not present in the fluid dynamic field as the energy equation was not solved and the mixture momentum equation did not account for the exchange of momentum between the second phase and the primary phase. As a result the dynamics of the vapour bubbles was not taken into account, the bubbles expanded without any constraints and this justifies the 15 ppm CFD spectrum. As stated in chapter 4 the cavitation model does not account for the dynamics of the bubbles as the second order terms of the Rayleigh-Plesset equation were neglected. It is obvious that the model did not account correctly for the wave propagation because of an inaccurate estimation of the compressibility of the mixture which is not proportional to the composition as highlighted by Chung (Chung et al. 2004).

Moreover there is another aspect the author would like to point out. During the experiments no measurement of the dissolved air content was carried out, however the numerical model assumed the condensation of the entire mass of the dissolved gas. It would be interesting at this point to know whether or not fluid dynamic phenomena (for instance turbulence) can prevent part of the dissolved gas to get out of the solution and take part in the expansion of the second phase either in localised zones or in the whole pump chamber.

12.6 Experimental tests repeatability

The repeatability test was actually carried out prior to the tests. The reason for running such a test lies on the need of making sure that under the same operating condition the test results did not change. Each of the tests discussed in the previous paragraph were performed several times in different days and the results were compared. In between them, maintenance and cleaning activities were carried out on the rig. Figure 12-19 to Figure 12-24 compare the results obtained by the same tests which ran in different times, TestX-1, TestX-2, Test X-3 and Test X-4 where carried out after a complete drainage of the system which needed nearly one day to be accomplished, Test 1-X, Test 2-X and Test 3-X were carried out one after another instead without any action on the pump or pumping system.

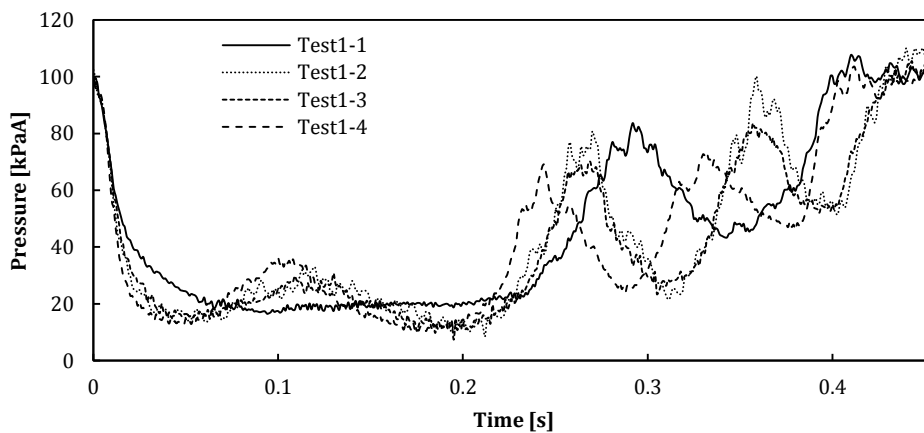


Figure 12-19: Repeatability analysis on Test 1: lower plunger velocity. The Chamber pressure comparison is shown.

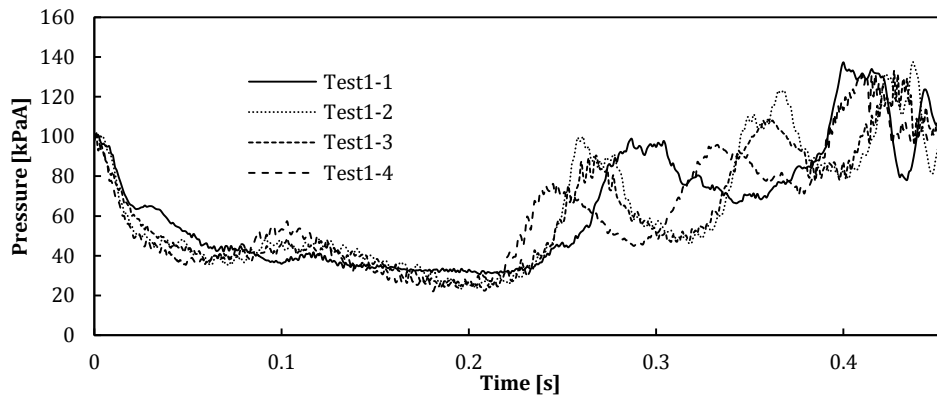


Figure 12-20: Repeatability analysis on Test 1: lower plunger velocity. The valve-seat pressure comparison is shown.

Figure 12-19 and Figure 12-20 show that the behaviour of both the chamber pressure and valve-seat pressure was similar for tests 1-2, 1-3 and 1-4 as the pressure trends result basically overlapped each other on the left part of the figure, the pressure spikes which characterize the right part of the figure appeared slightly shifted to each other although the compatibility and repeatability can be considered acceptable. Test 1-1 showed a quite different behaviour instead. In the first half of the suction stroke the pressure drop gradient was lower than all the other counterparts, this is visible especially in Figure 12-19 around time 0.05 s, the pressure spikes on the second half of the figures were affected by a further delay in the occurrence.

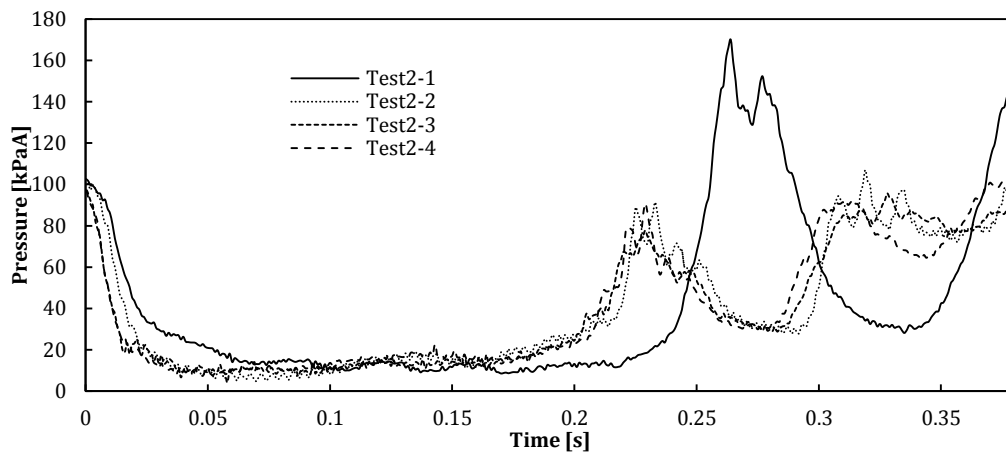


Figure 12-21: Repeatability analysis on Test 2: middle plunger velocity. The Chamber pressure comparison is shown

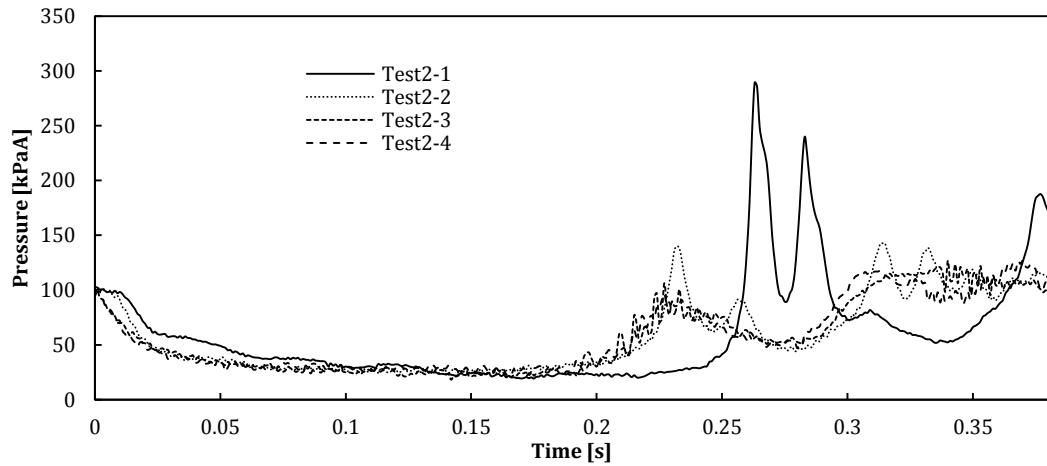


Figure 12-22: Repeatability analysis on Test 2: middle plunger velocity. The valve-seat pressure comparison is shown

Figure 12-21 and Figure 12-22 show the chamber pressure and the valve-seat pressure relative to tests 2-1 to 4. What was previously said about the compatibility and repeatability of test 1 is still valid for test 2. For both the pressure signals, in fact, tests 2-2 to 2-4 are overlapped to each other and this is evidence of good repeatability. Despite test 1 counterparts test 2-2 to 2-4 are highly compatible in both the initial and final part of the suction stroke, no significant delay in the spikes occurrence was recorded. Test 2-1 as test 1-1 provided with different results in terms of:

1. Pressure gradient drop, at the beginning of the suction stroke
2. Delay of the occurrence of the pressure spikes in the second half of the suction stroke
3. Pressure spikes magnitude, which was higher than test 2-2 to 2-4

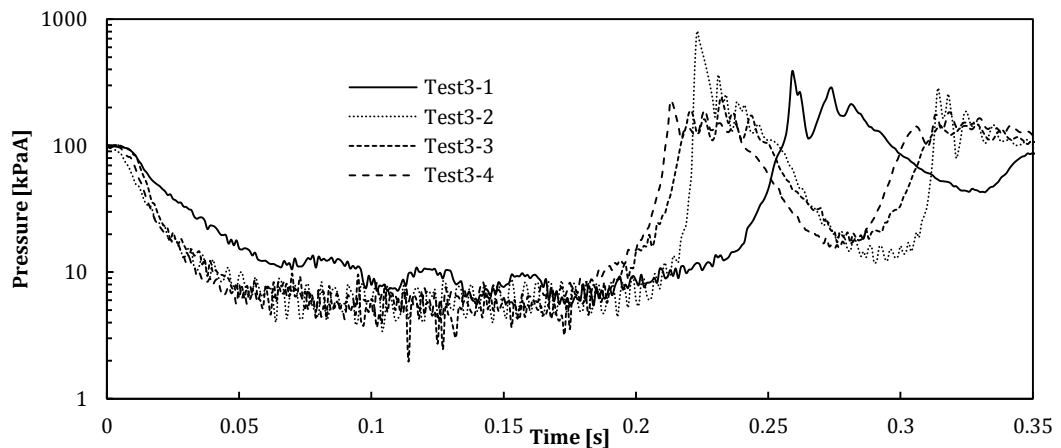


Figure 12-23: Repeatability analysis on Test 3: high plunger velocity. The Chamber pressure (Log scale) comparison is shown.

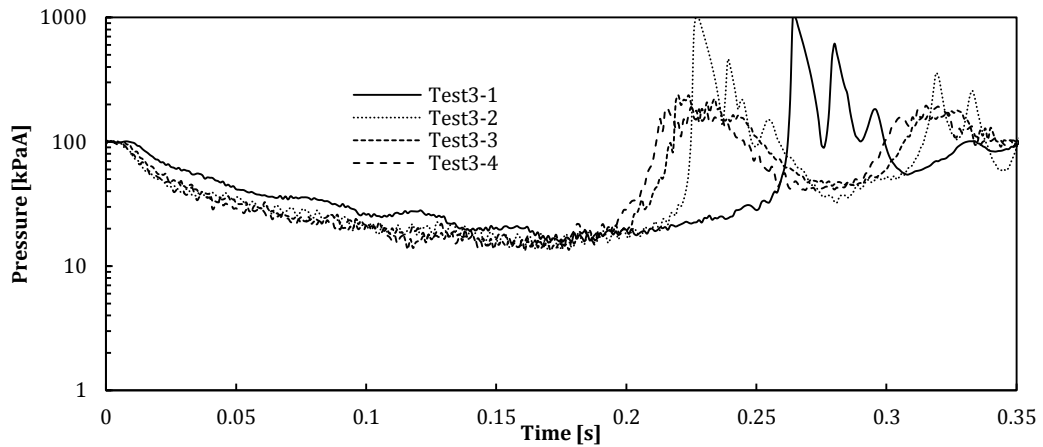


Figure 12-24: Repeatability analysis on Test 3: high plunger velocity. The valve-seat pressure comparison is shown.

Figure 12-23 and Figure 12-24 show the repeatability analysis results relative to test 3. Once again the curves corresponding to tests 3-2, 3-3 and 3-4 are overlapped in the first half of the figures, in the second half the occurrence of the pressure peaks is slightly delayed among the three trends but the most visible difference was demonstrated by the test 3-2 curve which shows a much higher magnitude pressure peak. Test 3-1 presented as test 2-1 a high magnitude pressure peak significantly shifted towards the end of the suction stroke and this behaviour was completely different from tests 3-2, 3-3 and 3-4.

Tests X-1 were the first tests carried out at the beginning of the experimental campaign when the analyst was still getting familiar with the equipment. Thanks to the experience collected over the months spent on the rig, it was understood that although the experiments were subjected to the same conditions, there were a few phenomenon interfering with the outcomes. Unfortunately, the analyst had not complete control on them. These phenomena can be listed as follows:

1. *Water level in the vessel.* The influence of this parameter is thought to be low but trying to keep the water to a constant level during the experimental campaign is good practice.
2. *Water quality degradation over time.* This parameter was found to be very important on the outcomes of the experiments. All the system of the pipelines and the pump was made of steel which is affected by corrosion, because of the closed loop system the electrolytes due to corrosion remained in the system which made the water dirty very quickly. Also the graphite seals released solid flakes in the water every plunger stroke, the influence of the solid particulate on the performance is unknown therefore replacing the water as often as possible is good practice.

3. *Trapped air in the system.* The operation of tank filling leaves room for air pockets in the system. As air is a compressible media the influence of the air trapped in the system has a huge impact on the results, the significant delay of pressure spikes occurrence in tests X-1 was most likely caused or enhanced by the air. It is recommended in such cases to move the plunger back and forth and purge the system unscrewing the pressure sensor to let the air out from the sensors tapping. After the purge operations a little amount of water may remain trapped in the system and cause the little discrepancies which were observed among tests X-2, X-3 and X-4.

The author decided to discard the results obtained in Tests X-1, Tests X-2 were taken as reference and discussed in the data post processing.

12.7 Remarks on CFD-Experiments comparison

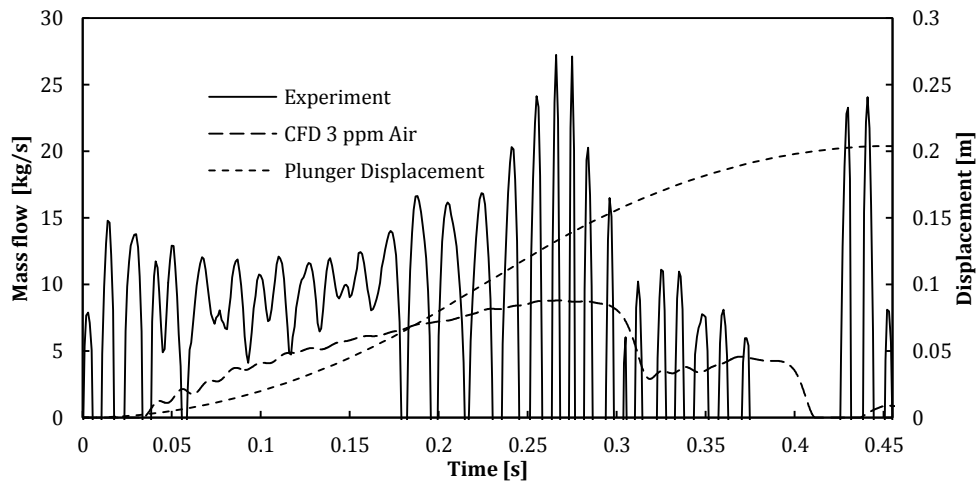


Figure 12-25: Test 1 mass flow rate, experiment Vs CFD, the Venturi pipe absolute pressure sensors output a not reliable signal.

Figure 12-25 shows the output signal of mass flow rate for test 1. It can be assumed that the two absolute pressure sensors across the Venturi pipe failed to provide a reliable signal during this experiment. The noise in the signal results in fact significant over the signal magnitude to be measured (static pressure drop across the pipe). Figure 12-26 confirms the same behaviour for test 2, the oscillations and the spikes in the signal are not acceptable. Figure 12-27, which refers to test 3 (full cavitation, highest plunger velocity) shows a mass flow spikes on the right part of the figure whereas the trend looks corrugated in the first half of the suction stroke, however, in this part the signal is above any of the CFD lines and on the whole it cannot be considered accurate.

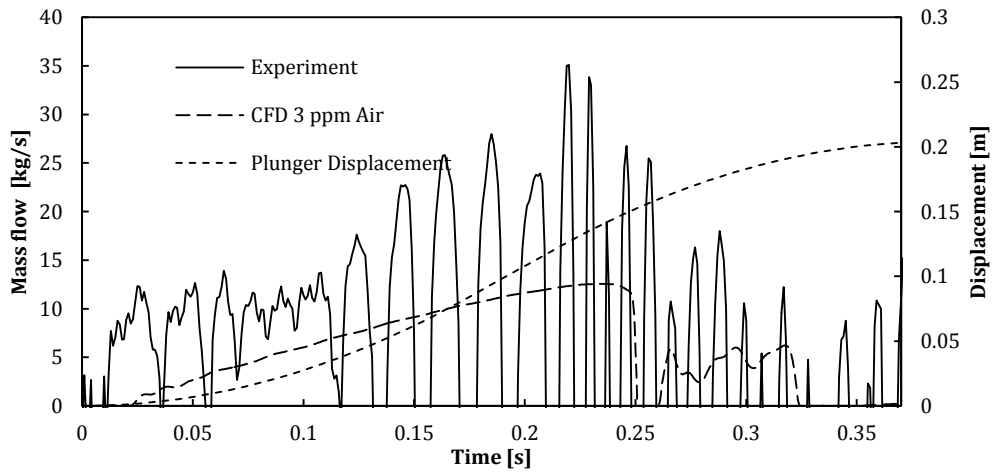


Figure 12-26: Test 2 mass flow rate, experiment Vs CFD, the Venturi pipe absolute pressure sensors output a not reliable signals.

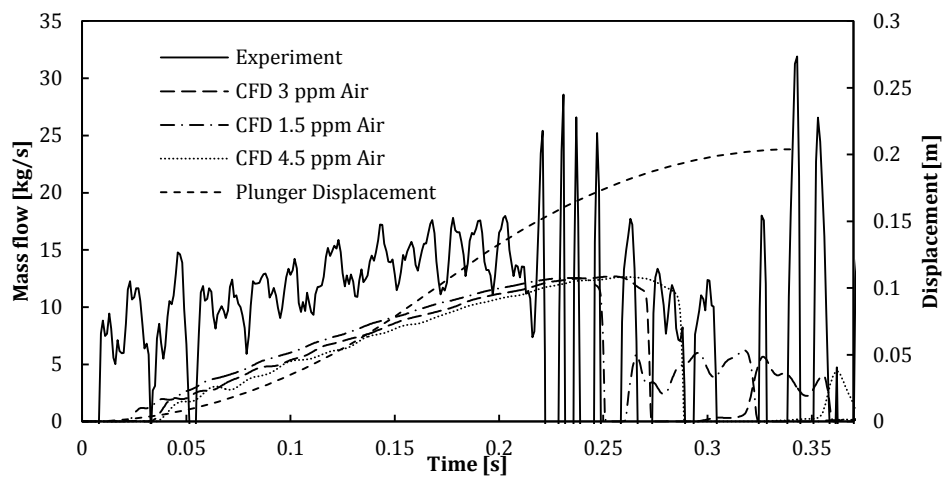


Figure 12-27: Test 3 mass flow rate, experiment Vs CFDs, the Venturi pipe absolute pressure sensors output a not reliable signals.

As explained in chapter 7, the integral of the mass flow rate over time gives the mass of the liquid being pumped, its ratio with the displacement volume standard mass considering the same liquid at ambient condition returns the volumetric efficiency. In all the three tests the experimental volumetric efficiency calculated was not either consistent or accurate as demonstrated by Table 12-2. In fact, as was discussed in chapters 7, 8 and 9 the lower the inlet pressure or the higher the plunger velocity, the lower the volumetric efficiency has to be, this applies within cases of same air mass content. In this case the experimental tests highlighted an unphysical trend as the test 3 volumetric efficiency estimated exceeded the 100% and the test 2 showed a higher efficiency than test 1 which was carried out at lower

velocity. However the figures provided by the third column of Table 12-2 should be considered meaningless.

Table 12-2: Volumetric efficiency estimation: CFD Vs Experiments

	CFD Volumetric efficiency [%]			Experimental volumetric efficiency [%]
	1.5 ppm Air	3 ppm Air	4.5 ppm Air	
Test 1	97.3			68.5
Test 2	98.5			95.2
Test 3	98.7	97.5	97.05	102.3

On the other hand, all the CFD simulations estimated very similar volumetric efficiencies within narrow range which can be considered within the numerical accuracy, without showing the trend expected.

The reason for this behaviour can be found in the low plunger velocities tested (Figure 12-1). All of them were lower than the displacement-time trend used by the simulation discussed in chapter 7. Therefore it can be assumed that all the CFD results in terms of volumetric efficiency lay within a narrow range because the three low velocities tested did not enhance the differences unlike what happened in the analysis discussed in chapter 8 and 9. Figure 12-28 show the difference between the crankshaft displacement-time history utilised in the simulation presented in chapter 7 and 8 (130 rpm) and the one utilised to simulate test 3, the reader may see that although cavitation took place the experimental tests were carried out at a lower velocity than it was previously planned.

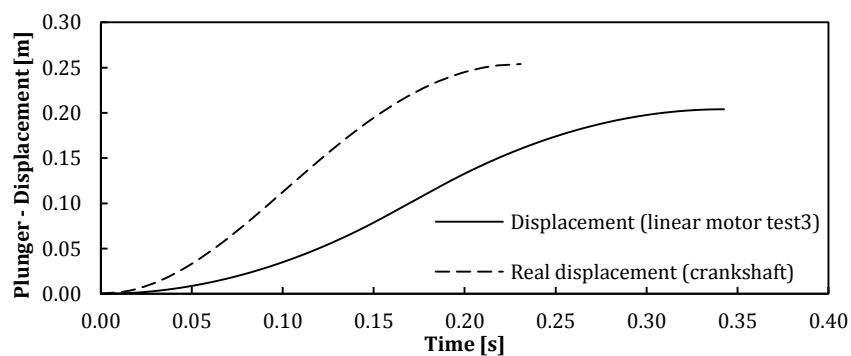


Figure 12-28: Crankshaft @130rpm Vs Linear motor (test 3), comparison of the displacement-time histories.

To improve the mass flow rate measurements a differential pressure sensor was also utilised and placed across the ends of the Venturi pipe. The differential pressure sensors have the

capability to output directly the pressure drop across the locations where the sensors were placed and this characteristic might decrease the measuring errors.

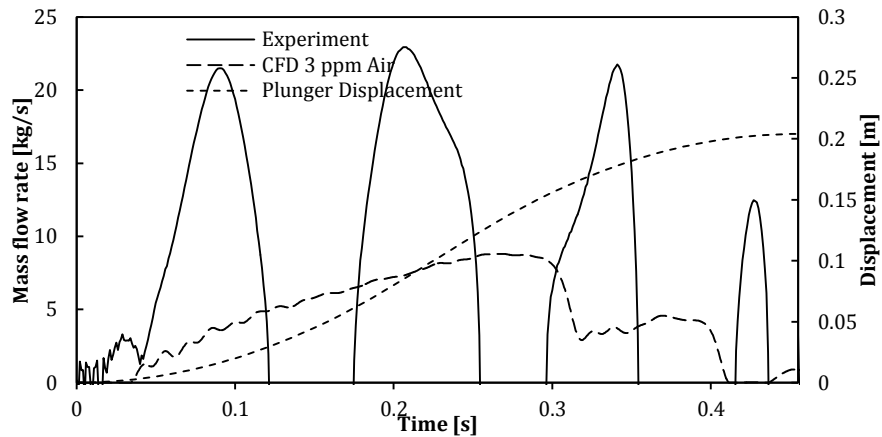


Figure 12-29: Test 1 mass flow rate, experiment Vs CFD, the Venturi pipe differential pressure sensor outputs not reliable signals.

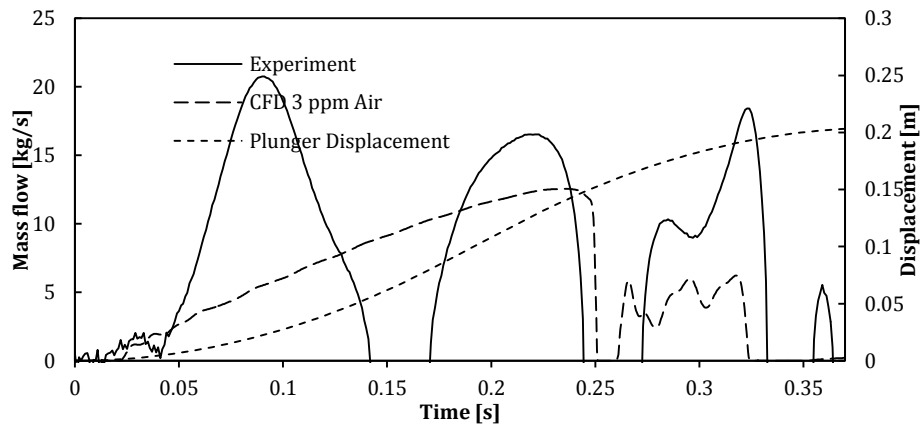


Figure 12-30: Test 2 mass flow rate, experiment Vs CFD, the Venturi pipe differential pressure sensor outputs not reliable signals

Unfortunately the differential pressure sensor did not solve the problem. Figure 12-29, Figure 12-30 and Figure 12-31 show the mass flow rate signal as acquired by the differential pressure sensor and manipulated by the data acquisition system respectively for test 1, 2 and 3. In all the cases the oscillations of the signals are not physical. A further proof of the scarce accuracy of the mass flow signal is provided by Table 12-3 which shows that every time any test was carried out the integral of the mass flow returned a different value so that the volumetric efficiency resulted different every times.

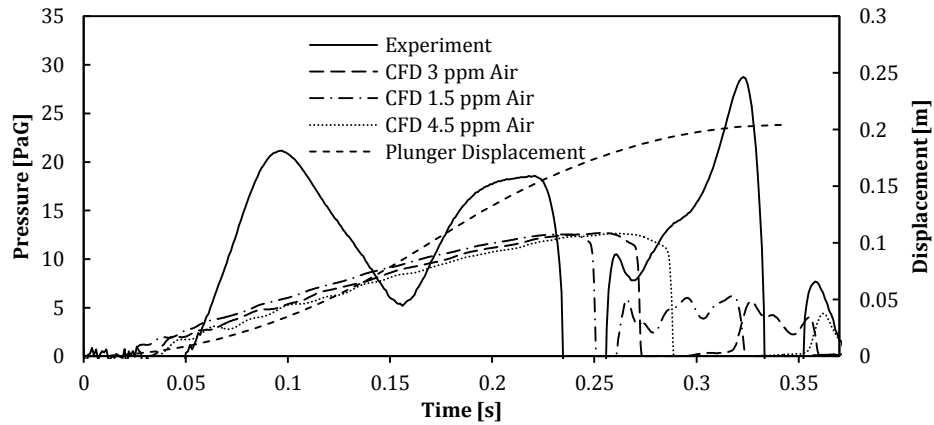


Figure 12-31: mass flow rate, experiment Vs CFD, the Venturi pipe differential pressure sensor outputs not reliable signals

Table 12-3: The volumetric efficiency calculated by means of the differential pressure sensor gives different results every time the test is performed.

	Attempt 1	Attempt 2	Attempt 3
Test 1	60%	94%	70%
Test 2	51%	88%	83%
Test 3	43%	131%	130%

In the end it was understood that using a Venturi pipe to measure the mass flow rate was not the best choice because of the number of problems which affected the tests. They can be listed as following:

1. *Small pressure drop magnitude due to the mass flow.* Provided the dimension of the Venturi pipe and according to the Bernoulli's law, the maximum pressure drop expected across the pipe when 15 kg/s of water is flowing, results 9kPa circa. This value is quite low and any kind of error has a non-negligible effect on the accuracy of the measurements.
2. *Electromagnetic interferences.* During the operations, the linear motor produced electromagnetic signals which interfered with the pressure sensors measurements. The nature of those interference signals was random, their influence on the signals of the chamber and valve-seat pressure was negligible as those pressures variability range was above 1 bar but on the mass flow the percentage error could not be considered negligible.
3. *Water hammer effects combined with the water sloshing in the tank.* The sudden closing of the inlet valve triggered transient effects related to the water hammer which resulted in the generation of pressure waves inside the inlet line. These pressure oscillations induced movements of the water vessel free surface. The

water level oscillations changed the inlet pipe pressure over time and this interfered with the Venturi pressure sensor measurement. The non-steady pressure inlet boundary conditions, in fact, were not related to any mass flow and interfered with the pressure reading because the Venturi pressure sensors interpreted the pressure waves as mass flow variations. Figure 12-32 shows the reading of the pressure sensor tapped on the water vessel in a location close to the inlet pipe connection flange. Figure 12-32 points out that the period of inlet pressure oscillations in test 3 was lower than the inlet stroke duration. This affected the measurement of the mass flow. Also the maximum magnitude of 400 Pa resulted sufficiently high to interfere with the mass flow measurement as entering 400 Pa into figure 11.21 a mass flow of 3 kg/s results. If the reader considers 15 kg/s of maximum mass flow rate the error expected will be up to 20% which justifies the low accuracy of the volumetric efficiency estimation.

4. *Transient effects due to the hydraulic inertance.* The Venturi pipe is a device designed to measure the mass flow rate in steady state conditions. When the mass flow rate changes quickly the hydraulic inertance affects the measurement of the pressure across the pipe and the disturbance is proportional to the variation of the mass flow rate according to the definition of the hydraulic inertance.

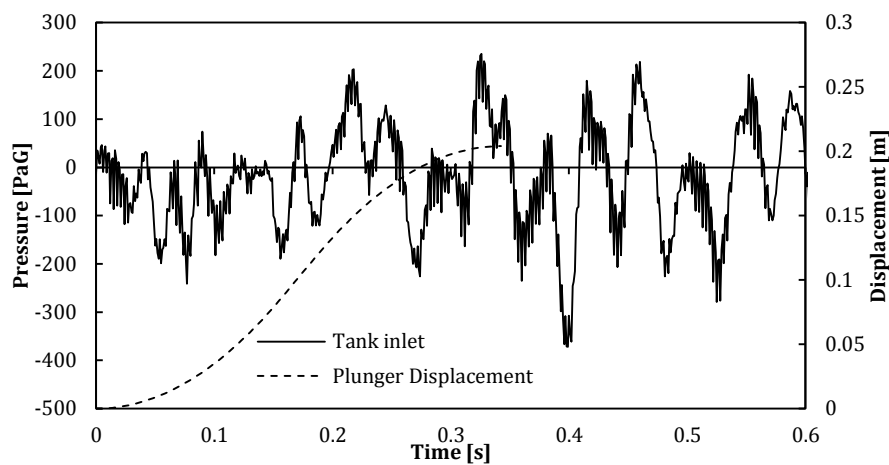


Figure 12-32: Test 3, full cavitation. The water vessel pressure sensor reading close to the inlet pipe is shown.

The issue of the mass flow rate measurement was not solved, the next chapter will discuss the methods the author suggests to improve the accuracy in the future improvements of the project.

13 Conclusion and future improvements

13.1 Brief summary of the project

A comprehensive and transient CFD model of a positive displacement reciprocating pump based on the commercial code ANSYS Fluent was created and improved. The model simulated the middle chamber of a WEIR SPM Destiny TWS 2500 pump triplex pump running at 130 rpm with an inlet pressure of 1 bar (ambient condition). The operating condition was chosen in order to achieve full cavitation. The model, in fact, accounted for the generation of vapour by means of the mixture multiphase model (ANSYS 2011a) and the Singhal et al (Singhal & Athavale 2002) cavitation model which also accounted for the influence of the non-condensable air mass fraction content in the water. Although the device is usually utilised to pump slurries as well as water, the model did not account for the solid particulates as this was beyond the scope of this project. The CFD model was equipped with two UDFs accounting for:

1. *The compressibility of water.* At the beginning of the inlet and outlet stroke, both the valves are closed and the compressibility of the liquid must be accounted in order to satisfy the continuity equation.
2. *The valve dynamics.* The valves are actuated by the spring force and preload and the pressure force which is an output of the simulation and unknown a priori. The UDF was called at the end of the each time step in order to calculate the composition of the pressure force and the spring force acting and estimate the valve lift by integration of the acceleration and then the velocity. The lift value was used to update the moving mesh in the vicinity of the valve and prepare the new mesh for the following time step operations.

Although cavitation takes place during the inlet stroke only, in chapter 7 a model simulating the outlet stroke as well as the inlet stroke was discussed. In that model the inlet and outlet pipes were not entirely simulated and a pressure varying with the mass flow was set as boundary condition. This choice was also made in the analysis discussed in chapter 8 and 9.

Chapter 7, 8 and 9 discussed a set of analyses in order to test the consistency of the CFD model on the estimation of its sensitivity on:

1. *Inlet pressure.* The sensitivity to 0, 25, 50, 100 kPaG inlet pressure boundary condition was investigated.

2. *Crank velocity.* The sensitivity to 130 and 260 rpm crankshaft angular velocity was investigated.
3. *Non-condensable gas mass fraction.* The sensitivity to 15 and 1.5 ppm air mass fraction in the water was investigated.
4. *Valve shape and design.* Five different valve designs were simulated in order to estimate the influence of the design parameters on the performance.
5. *Valve mass.* A reduced mass valve was simulated together with the original mass valve to investigate the sensitivity on the performance of the pump to this parameter.
6. *Valve spring stiffness.* A reduced spring stiffness valve was simulated together with the original one to investigate the sensitivity on the performance of the pump to this parameter.

Due to structural issues which could not allow the analyst to reduce cavitation by decreasing the valve seat thickness, the analysis focused attention on the shape of the valve-seat contact and was carried out to demonstrate the influence of the valve urethane ring section on the performance and this suggested a new modification of the urethane part of the valve. Chapter 10 presents and discusses the new valve design which is capable of lowering the vapour generation in full cavitating conditions and demonstrates it via CFD.

To validate the results obtained and discussed in chapter 10 a test rig was built. The first idea was to replicate via experimentation the geometry and operating conditions utilised by the CFD model discussed in chapter 7 and to proceed with the validation via CFD-Experiments data comparison. Technical problems related to the use of the linear servomotor chosen to drive the plunger led the analyst to modify slightly the operating condition specifications in terms of plunger maximum velocity and stroke which resulted in a slight modification of the CFD model which the experimental data had to be compared to. A closed loop test rig was designed and built, the middle chamber of a full scale WEIR destiny pump was utilised for the tests and a programme provided by the linear motor supplier was employed to create the displacement motion to feed into the linear motor driver. Pressure sensors acquired the signals of chamber pressure and valve-seat pressure while the mass flow rate was monitored by means of a Venturi pipe and two pressure sensors across it. A high speed camera took photographs of the inlet valve up to a frame rate of 1000 images per seconds. The pictures were post processed afterwards to measure the valve lift. Three tests were carried out at different plunger velocities in order to achieve the condition of incipient, partial and full cavitation. The same plunger velocities were utilised to run comparable numerical models. Despite the lower plunger velocity, experimental test 3 clearly showed the feature of full cavitation which was the aim of the experimental campaign. The analyst did not choose to

increase the plunger velocity in order not to put the linear motor at risk. The experiments highlighted a few issues. Neither the mass flow rate measurement nor its integral was reliable. The analyst tried to lower the errors in the reading by using a differential pressure sensor on the venture pipe replacing the absolute sensors. This action failed.

13.2 Conclusion

Considering the significant complexity of the numerical model utilised and according to what was shown in chapter 12, the accuracy of the CFD model developed can be considered reasonable as all the CFD trends were in good qualitative agreement with the experiments but also because good consistency was proved. The CFD demonstrated a smaller gradient of pressure drop at the beginning of the suction stroke and also a certain delay in the pressure spikes occurrence during the second part of the suction stroke. The pressure drop gradient and the delay in pressure spike occurrence depended on the air mass fraction; the lower the air content the lower the delay and the steeper the pressure gradient. CFD always overestimated the valve lift; the CFD maximum lift was higher and shifted with respect to the experimental counterpart. The reason for the difference in predicted lift was the longer application of the lifting pressure force on the valve predicted by CFD. All the evidence collected drove the author to identify the main source of error in the overestimation of the air volume fraction as described in paragraph 12.5. It is known, in fact, that the presence of air decreases the gradient of the pressure drop as the air expansion slows down the pressure drop but the tests revealed that the 15 ppm CFD analysis, which was thought to be the more realistic as 15 ppm is the air content in tap water at ambient condition, presented significant delay in the pressure spikes occurrence and pressure drop gradient. This proved that the algorithm managing the air expansion overestimated the effect.

The set of simulations compared with their experimental counterparts demonstrated consistency in the performance variation with respect to the operating conditions modification and this validated the analysis carried out in chapter 10 where the optimised valve was presented and the performance estimated by means of CFD. The consistency is the result of the capability that the CFD analysis demonstrated. It also proved the capability of accounting for all the fluid dynamics phenomena occurring in the pump chamber during the suction stroke. They can be listed as following:

1. Chamber and valve-seat pressure drop at the beginning of the suction stroke due to the plunger decompression
2. Constant and low pressure in the middle of the induction stroke due to the achievement of the vapour pressure.

3. Pressure spikes in the end of the suction stroke due to the water hammer effect which were also observed by Opitz (Opitz et al. 2011)

13.3 Future improvements

Studies on the CFD model should be carried out in order to understand how to fix the weakness of the cavitation model. This investigation would be easier if the analyst had the possibility to measure the second phase fraction and integral during experiments. Unfortunately this is a very difficult task to achieve. On the other hand (Aldo Iannetti, M. T. Stickland, et al. 2014) the vapour fraction and integral are strictly related to the volumetric efficiency loss which means that estimating the volumetric efficiency may help the analyst in this investigation. Therefore efforts should be put in improving the way the mass flow rate is measured during the experimental tests. Instead of a Venturi pipe with pressure sensors across it, different devices could be utilised. For instance, a mass flow meters could be able to provide accurate reading less sensitive to the electromagnetic interference caused by the linear servomotor but also insensitive to the pressure fluctuations in the inlet pipe. Increasing the plunger velocity would result in a higher and more measurable volumetric efficiency loss in full cavitating conditions. More accurate experimental data would support and lead the study on how to improve the accuracy of the numerical models utilised. The following investigations should be carried out:

- *The influence of the regimes of turbulence.* RANS based CFD codes assume that the flow is always fully turbulent, this assumption is not valid when modelling PD pumps. During the pumping cycle, in fact, these devices experience all the regimes of turbulence and Reynolds number from laminar to fully turbulent. Other turbulence models than the k-epsilon should be tested. As a long term plan, other approaches than the RANS could also be employed (e.g. Large Eddy Simulation techniques).
- *More accurate multiphase models.* The Mixture model utilised (ANSYS 2011a) does not require important computational resources but it is not indicated when the second phase fraction amount is significant. The Eulerian model (ANSYS 2011a) should be employed instead. This model provides a better coupling of the two phases as it solves one momentum transport equation for each phase rather than solving one momentum equation for the mixture (water and vapour). Treating the air mass fraction in an implicit way as a real third phase within a more realistic multiphase model could also help to improve the accuracy of the overall model.

- *Modification and customization of the cavitation model.* Although the “full” cavitation model accounts for all the first order terms of the Rayleigh-Plesset equation adjustments on the model based on the experimental results may be considered.

Accelerating the motor shaft, as discussed in chapter 11, may be detrimental for the motor itself which was the most expensive part of the rig. Investigation by means of strain gauge on the real axial force provided by the motor would be beneficial to estimate the real safety factor on the maximum force allowable and this would give to the analyst room to increase safely the motor velocity. Therefore, before doing this, it is recommended that safety limit switches which activate when the shaft approaches the TDC and BDC positions be installed. The signals of the limit switches could be utilised for sending to the motor driver the shutdown signal and safely stop the motor. Higher plunger velocity experimental tests would enhance the difference between the three cavitation regimes and lead measurable data in terms of mass flow rate and efficiency.

Laser Doppler Anemometry could also be used to measure the flow velocity vectors in the vicinity of the valve. This could shed light on the dynamic pressure in the same location and complete the experimental data collection.

For future development of the project the analyst suggests that the real air mass fraction content in the water being pumped be measured as this will shed light on the real properties of the working fluid and will help the investigation on the numerical model improvement.

After improving the experimental test rig it would be of interest to manufacture the valve models proposed in chapter 9 and 10 with the modified urethane ring section and quantify the improvement of the performance in terms of volumetric efficiency gain from the experimental side.

13.4 Legacy

At the end of three years there are a few marks that this project leaves in the scientific community. These legacies are related not only to the specific problem the project was created to solve, but also to a wider overview of the analysis approach in engineering.

To date, this project has resulted in the only one based entirely on a comprehensive numerical approach in studying the behaviour of PD pumps in cavitating condition as no such a study has been published to date. So far, research and development studies of PD pumps have always been based on either experimental tests or analytical methods, CFD has

been applied only in a simplified way as it has been difficult to handle until recently because of computational issues. The numerical approach presented, which was supported by the experimental campaign encourages researchers and engineers who are involved in the study of PD pumps, to follow the same path drawn by this project. The CFD model, whose consistency was demonstrated, provides the engineers, researchers and designers with a cheap tool to analyse the device being designed before manufacturing it. This results in money and time saving which would reflect in the competitiveness of the pump on the market. Furthermore, CFD also provides much detailed information which may be helpful in the decision making regarding the design.

In the opinion of the author the numerical approach discussed cannot only be applied to the kind of pump which was investigated in the project but also to any kind of PD device, safety valves, and generally speaking to analyse hydraulic systems.

Concerning the specific project, the validation of the Singhal et al. cavitation model defines further evidence of the originality of the project as to date that cavitation model has been abundantly discussed in hydro dynamics applications such like marine propellers or centrifugal pumps but, according to the literature review carried out, never tested in PD pumps where the mechanisms leading to cavitation are slightly different from the cited previous cases.

Bibliography

- ANSYS, 2011a. ANSYS Fluent Theory Guide. , 15317(November).
- ANSYS, 2011b. ANSYS FLUENT UDF Manual. , 15317(November).
- ANSYS, 2011c. ANSYS FLUENT User' s Guide. , 15317(November).
- Arora, M., Ohl, C.D. & Lohse, D., 2007. Effect of nuclei concentration on cavitation cluster dynamics. *The Journal of the Acoustical Society of America*, 121(6), pp.3432–6. Available at: <http://www.ncbi.nlm.nih.gov/pubmed/17552694> [Accessed November 14, 2013].
- Baur, T., Köngeter, J. & Leucker, R., 1998. Effects of dissolved gas on cavitation inception in free surface flows. In *Third International Symposium on Cavitation*.
- Budris, A.R. & Mayleben, P.A., 1998. Effects of entrained air, NPSH margin, and suction piping on cavitation in centrifugal pumps. In *Proceeding of the 15th international pump users symposium*. Houston, Texas, USA, pp. 99–108.
- Chung, M.S., Park, S.B. & Lee, H.K., 2004. Sound speed criterion for two-phase critical flow. *Journal of Sound and Vibration*, 276(1-2), pp.13–26.
- Daneshy, A., 2001. Hydraulic Fracturing To Improve Production. *SPE Tech 101*, 6(3), pp.14–17.
- Ding, H., Visser, F.C. & Jiang, Y., 2012. A practical approach to speed up NPSHR prediction of centrifugal pumps using CFD cavitation model. In *Proceedings of the ASME 2012 Fluids Engineering Summer Meeting*. Rio Grande, Puerto Rico, USA, p. Paper No. FEDSM2012–72282.
- Edge, K. a et al., 1997. Pressure pulsations in reciprocating pump piping systems Part 2: experimental investigations and model validation. *Proceedings of the Institution of Mechanical Engineers, Part I: Journal of Systems and Control Engineering*, 211(3), pp.239–250.
- Eisenberg, P., 1963. *Cavitation Damage*, Office of Naval Research.
- Franc, J., 2007. *Fluid Dynamics Of Cavitation and Cavitating Turbopumps* L. D'agostino & M. V. Salvetti, eds., Springer Vienna.
- Franc, J., 2006. *Physics and Control of Cavitation University of Grenoble*,
- Franc, J.P. & Michel, J.M., 2004. *Fundamental of Cavitation*, Kluwer academic publishers.
- Iannetti, A., Stickland, M.T. & Dempster, W.M., 2015. A CFD study on the mechanisms which cause cavitation in positive displacement reciprocating pumps. *Journal of Hydraulic Engineering*, 1(1), pp.47–59.

- Iannetti, A., Stickland, M.T. & Dempster, W.M., 2014. A computational fluid dynamics model to evaluate the inlet stroke performance of a positive displacement reciprocating plunger pump. *Proceedings of the Institution of Mechanical Engineers, Part A: Journal of Power and Energy*, 228(5), pp.574–584.
- Iannetti, A., Stickland, M.T. & Dempster, W.M., 2014. An advanced CFD model to study the effect of non-condensable gas on cavitation in positive displacement pumps. In *11th international symposium on compressor & turbine flow systems theory & application areas SYMKOM 2014 IMP2*. Lodz, Poland.
- Iannetti, A., Stickland, M.T. & Dempster, W.M., 2015. Experimental validation of the Singhal et al . cavitation model on Positive Displacement pumps. *Engineering applications of Computational Fluid Mechanics*, In Press.
- Johnston, D.N., 1991. Numerical modelling of reciprocating pumps with self-acting valves. *Journal of Systems and Control Engineering, Part I*, pp.87–96.
- Karassik, I.J. et al., 2001. *Pump Handbook*,
- Kuiper, G., 2010. *Cavitation in ship propulsion*, Delft: Delft University of Technology.
- Manring, N.D., 2003. Valve-Plate Design for an Axial Piston Pump Operating at Low Displacements. *Journal of Mechanical Design*, 125(1), p.200.
- Miller, J.E., 1995. *The reciprocating pump, theory design and use* Second Edi., Krieger publishing company.
- Opitz, K. & Schlücker, E., 2010. Detection of Cavitation Phenomena in Reciprocating Pumps using a High-Speed Camera. *Chemical Engineering & Technology*, 33(10), pp.1610–1614.
- Opitz, K., Schlücker, E. & Schade, O., 2011. Cavitation in reciprocating positive displacement pumps. In *Twenty-seventh international pump users symposium*. Houston, Texas, pp. 27–33.
- Pawan J. Singh, S.D.A., 1996. Determination of NPSHR for reciprocating positive displacement pumps: a new approach. In *Proceedings of the thirteenth international pump user symposium*. pp. 131–139.
- Plesset, M.S. & Prosperetti, A., 1977. BUBBLE DYNAMICS AND CAVITATION. *Annual Reviews*, 9, pp.145–185.
- Price, S.M., Smith, D.R. & Tison, J.D., 1995. The effects of valve dynamics on reciprocating pump. In *Proceedings of the twelfth international pump users symposium*. Texas A&M University, pp. 221–230.
- Ragoth, R. singh & Nataraj, M., 2012. Study on Performance of Plunger Pump at Various Crank Angle Using CFD. *IRACST Engineering Science and Technology: An International Journal (ESTIJ)*, ISSN:2250-3498, 2(4), pp.549–553.

- Rayleigh, Lord, 1917. VIII. On the pressure developed in a liquid during the collapse of a spherical cavity. *Philosophical Magazine Series 6*, 34(200), pp.94–98. Available at: <http://www.tandfonline.com/doi/abs/10.1080/14786440808635681> [Accessed January 23, 2014].
- Shu, J., Burrows, C.R. & Edge, K.A., 1997. Pressure pulsations in reciprocating pump piping systems Part 1 : modelling. *Proc Inst Mech Engrs*, 211 Part I(April), pp.229–237.
- Singhal, A. & Athavale, M., 2002. Mathematical basis and validation of the full cavitation model. *Journal of Fluids Engineering*, 124(3), p.617.
- Tackett, H.H., Cripe, J.A. & Dyson, G., 2008. Positive displacement reciprocating pump fundamentals- power and direct acting types. In *Proceedings of the twenty-fourth international pump user symposium*. Texas A&M University, pp. 45–58.
- Wilson, F. et al., 2011. *Reciprocating Pump System Dynamic Analysis Weir SPM*, WRES Inc. report E1142.
- Wood, D.W., Hart, R.J. & Ernesto, M., 1998. Application guidelines for pumping liquids that have large dissolved gas content. In *Proceedings of the 15th international pump user symposium*. Huston, TX, USA, pp. 91–98.

Appendix

Valve dynamics model UDF

```
# include "udf.h"
# include "dynamesh_tools.h"
# include "math.h"

# define DEBUG 1
# define NO_OF_VALVES 1
# define NO_OF_ZONES 11

/***** User Input Starts *****/

# define INITIAL_LIFT 0

static int valveid[NO_OF_VALVES][NO_OF_ZONES]={{ 502,503,461, -1}};

static real lift_min[NO_OF_VALVES]={0};
static real lift_max[NO_OF_VALVES]={0.0199};
static real mass[NO_OF_VALVES]={2.38};

/*static real stiffness[NO_OF_VALVES]={10500};
static real stretch_at_closed[NO_OF_VALVES]={0.026416};

static real rest_conts[NO_OF_VALVES]={0};
static real current_vel_mag[NO_OF_VALVES]={0};

/***** User Input Ends *****/

static real axis[NO_OF_VALVES][ND_ND]={{-1, 0}}; /* normalized */
static real gravity_direction[ND_ND]={1, 0}; /* normalized */
static real r_rp_closed[NO_OF_VALVES][ND_ND]={{0,0}};
static real cur_r_rp[NO_OF_VALVES][ND_ND]={{INITIAL_LIFT, 0}};
static real previous_time[NO_OF_VALVES]={0};

static void f_valve(int valveNo, void *dt, real *cg_vel, real *cg_omega, real time, real dtime)
{
# if !RP_HOST
    real tmp[ND_ND], dv, current_vel[ND_ND], CG[ND_ND], force[3], moment[3], stretch;
    real aero_force[ND_ND], aero_force_axis, spring_force, gravity_force, net_force,
        r_rp_new[NO_OF_VALVES][ND_ND];
    int i;
    Thread * tf;
    Domain * domain;

/*****

static real cg_vel_saved[NO_OF_VALVES][ND_ND];

/*****

/* Do the calculation if the new time step */

if(fabs(previous_time[valveNo]-time)>0.2*dtime)
{
```

```

/* reset velocities */

NV_S (cg_vel, =, 0.0);
NV_S (cg_omega, =, 0.0);

/* Check to see if there is data */

if (!Data_Valid_P ())
{
    Message0("\n\nNo data->No mesh motion!!!\n\n");
    return;
}

/*Calculate force*/

domain = THREAD_DOMAIN (DT_THREAD ((Dynamic_Thread *)dt));

i=0;
NV_S(aero_force,=,0);
while(valveid[valveNo][i]>=0)
{
    tf=Lookup_Thread(domain, valveid[valveNo][i]);

    NV_S (CG, =, 0.0);

    Compute_Force_And_Moment (domain, tf, CG, force, moment, FALSE);
    NV_V(aero_force,+=,force);

    i++;
}

aero_force_axis=NV_DOT(aero_force, axis[valveNo]);

NV_VV(tmp,=,r_rp_closed[valveNo],-,cur_r_rp[valveNo]);
stretch = (stretch_at_closed[valveNo]+NV_DOT(tmp,axis[valveNo]));
spring_force= 1370323771520.00*pow(stretch,6) - 185636068328.00*pow(stretch,5) +
9625259842.50*pow(stretch,4) - 231629611.63*pow(stretch,3) + 2512028.98*pow(stretch,2) +
1977.13*(stretch) + 4.3383 ;
gravity_force = 9.81*mass[valveNo]*NV_DOT(gravity_direction, axis[valveNo]);

net_force=spring_force+aero_force_axis+gravity_force;

dv=net_force/mass[valveNo]*dtime;

/* Calculate the C.G location and velocity if it does not hit the boundary */

NV_VS(current_vel,=,axis[valveNo],*,current_vel_mag[valveNo]);

NV_VS(tmp,=,current_vel,*,dtime);
NV_VV(r_rp_new[valveNo],=,cur_r_rp[valveNo],+,tmp);

    /* Update velocity */

current_vel_mag[valveNo]+=dv;

/* debug info */

#if DEBUG

```

```

Message0("\n\n***** VALVE INLET-1 INFO
*****\n");

Message0("\nCurrent valve lift =% 10.3e\n", -NV_DOT(cur_r_rp[valveNo], axis[valveNo]));
Message0("\nCurrent valve velocity (negative if pointing to positive x) =% 10.3e\n",
current_vel_mag[valveNo]-dv);

Message0("\naero force =% 10.3e\n", aero_force[0]);

Message0("\n(stretching at closed, stretching, force)=(% 10.3e, % 10.3e, % 10.3e)\n",
stretch_at_closed[valveNo], stretch, -spring_force);

Message0("\n(net_force, spring force, aero force)=(% 10.3e, % 10.3e, % 10.3e)\n",
-net_force, -spring_force, -aero_force_axis);

#endif

/* if it hits the lift_min boundary then it stays at lift_min*/

NV_VV(tmp,=,r_rp_closed[valveNo],-,r_rp_new[valveNo]);
if(NV_DOT(tmp,axis[valveNo])<1.000001*(lift_min[valveNo]))
{
NV_V_VS(r_rp_new[valveNo],=,r_rp_closed[valveNo],-,axis[valveNo],*,lift_min[valveNo]);

current_vel_mag[valveNo]=-rest_conts[valveNo]*fabs(current_vel_mag[valveNo]);

#ifdef DEBUG

Message0("\n Valve hits the min valve lift\n");

#endif
}

/* if it hits the lift_max boundary then it stays at lift_max*/

NV_VV(tmp,=,r_rp_closed[valveNo],-,r_rp_new[valveNo]);
if(NV_DOT(tmp,axis[valveNo])>0.9999999*(lift_max[valveNo]))
{
NV_V_VS(r_rp_new[valveNo],=,r_rp_closed[valveNo],-,axis[valveNo],*,lift_max[valveNo]);

current_vel_mag[valveNo]=rest_conts[valveNo]*fabs(current_vel_mag[valveNo]);

#ifdef DEBUG

Message0("\n Valve hits the max valve lift\n");

#endif
}

/* set valve velocity */

NV_VV(tmp,=,r_rp_new[valveNo],-,cur_r_rp[valveNo]);
NV_VS(cg_vel,=,tmp,/,dtime);

/* Update location and velocity */

```

```

NV_V(cur_r_rp[valveNo],r_rp_new[valveNo]);
NV_V(cg_vel_saved[valveNo],cg_vel);

previous_time[valveNo]=time;

/* debug info */

#if DEBUG

Message0("\nNext valve velocity (negative if pointing to positive x)=%11.3e\n",
current_vel_mag[valveNo]);

Message0("\nNext valve lift =%10.3e\n", -NV_DOT(r_rp_new[valveNo], axis[valveNo]));

if(NULL == (pf = fopen("C:/Users/Aldo/Desktop/Destiny/CFD/C000-071-000/C000-071-000-inlet1-
valve-lift-real.dat","a")))
Error("Could not open file for append!\n");
fprintf(pf," %e",time);
fprintf(pf," %e\n",-NV_DOT(r_rp_new[valveNo], axis[valveNo]));
fclose(pf);

Message0("\n***** VALVE INLET-1 INFO END
*****\n\n");

#endif

}
else
{
NV_V(cg_vel,cg_vel_saved[valveNo]);
}
#endif

node_to_host_real(current_vel_mag, NO_OF_VALVES);
node_to_host_real(cur_r_rp[0], NO_OF_VALVES*ND_ND);
node_to_host_real(previous_time, NO_OF_VALVES);
}

DEFINE_CG_MOTION(INLETvalve_1, dt, cg_vel, cg_omega, time, dtime)
{
f_valve(0, dt, cg_vel, cg_omega, time, dtime);

node_to_host_real(cg_vel,ND_ND);
node_to_host_real(cg_omega,ND_ND);
}

```

Water compressibility model UDF

```
# include "udf.h"
# include "dynamesh_tools.h"
# include "math.h"

#define BMODULUS 2.15e9
#define rho_ref 998.2
#define p_ref 101325

DEFINE_PROPERTY(superfluid_density, c, t)
{
    real rho;
    real p, dp;
    real p_operating;
    p_operating = RP_Get_Real ("operating-pressure");
    p = C_P(c,t) + p_operating;
    dp = p-p_ref;
    rho = rho_ref/(1.0-dp/BMODULUS);
    return rho;
}

DEFINE_PROPERTY(sound_speed, c,t)
{
    real a;
    real p, dp,p_operating;
    p_operating = RP_Get_Real ("operating-pressure");
    p = C_P(c,t) + p_operating;
    dp = p-p_ref;
    a = (sqrt(1.-dp/BMODULUS))*(sqrt(BMODULUS/rho_ref));
    return a;
}
```

Technical sheets and Drawings



Main Features

- Ranges: from 0...0.05 bar to 0...60 bar (0...1 to 0...1000 psi)
- Complete range of voltage/current outputs
- Protection rating: IP65/IP67
- Wetted parts: AISI304 , AISI316, NBR, Viton
- Operating temperature range -20...+85°C
- Accuracy: $\pm 0.15\%$ FSO typical
- Fill Fluid: silicone oil
- Available absolute ranges
- Available "Barometric" range (0.8-1.2 bar abs)
- Available low ranges (50mbar and 100mbar)

Series TSA transmitters are based on silicon piezoresistive sensing element in wheatstone bridge configuration.

Thanks to highly stable electronic components, these transmitters can be used in applications requiring long-distance signal transmission or in smart control systems.

TSA pressure transmitters were developed mainly for pressure measurement in industrial refrigeration and air conditioning, compressor and pumps. They are also used for monitoring and control on automatic machines and general purpose industrial applications.

TECHNICAL DATA

	VOLTAGE	CURRENT
Output signal	$\pm 0.15\%$ FSO typical; $\pm 0.2\%$ FSO max (gauge ranges)	
Accuracy (1)	$\pm 0.15\%$ FSO typical; $\pm 0.25\%$ FSO max (absolute ranges)	
Resolution	Infinite	
Overpressure (without degrading performance) (2)	see table	
Pressure containment (Burst test) (3)	see table	
Pressure media	Fluid compatible with AISI 316 Stainless steel, AISI 304, NBR, Viton	
Body materials	AISI 304 Stainless steel and Nylon 66GF35V0	
Power supply	15...30Vdc	10...30Vdc
Supply sensitivity	< 0.0015% FSO/V	
Insulation resistance	> 1000 M Ω @ 50Vdc	
Zero output signal	B, C, M, N, P, Q, R	4mA (E)
Full scale output signal	B, C, M, N, P, Q, R	20mA (E)
Max current absorption	< 13mA	<32mA
Max allowed load	1mA	See diagram
Long term stability	< 0.1% FSO/per year (ranges \geq 250mbar)	
Operating temperature range (process)	-20...+85°C (-4...+185°F)	
Compensated temperature range	-10...+85°C (+14...+185°F)	
Storage temperature range	-30...+90°C (-22...+194°F)	
Temperature effects over compensated range (zero-span)	$\pm 0.01\%$ FSO/°C typical ($\pm 0.02\%$ FSO/°C max.) ranges >1 bar $\pm 0.04\%$ FSO/°C typical ranges \leq 1 bar	
Response time (10...90%FSO)	< 1 msec.	
Start-up time	< 500 msec.	
Mounting position effects	Negligible (ranges \geq 1bar)	
Humidity	Up to 100%RH non condensing	
Weight	110 gr. nominal	
Mechanical shock	100 g / 1 msec. according to IEC 68-2-6	
Vibrations	20 g max @ 15-2000Hz according to IEC68-2-6	
Ingress protection	IP65/IP66/IP67	
Output short circuit and reverse polarity protection	YES	

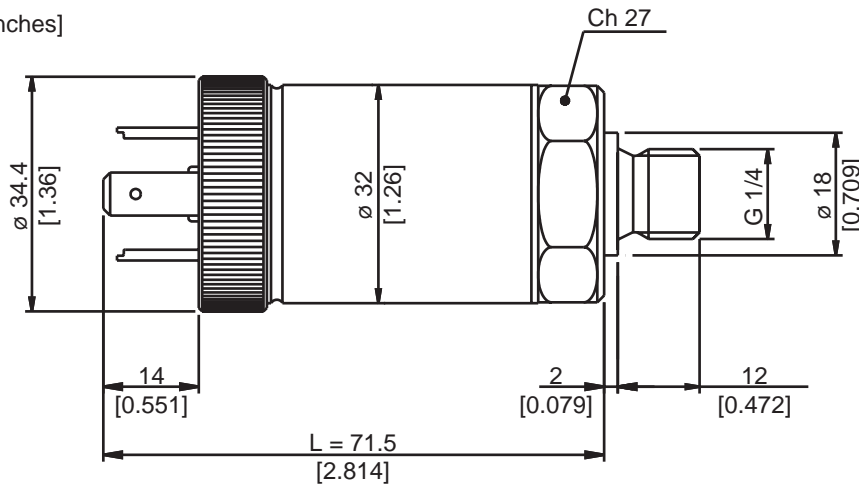
FSO = Full Scale Output 1 BFSL method (Best Fit Straight Line): includes combined effects of Non-Linearity, Hysteresis and Repeatability
 2 tested for more than 1000 strokes with single duration < 2msec. 3 tested for more than 100 strokes with single duration < 2msec.

MEASUREMENT RANGE (Bar)	0.05	0.1	0.25	0.5	1	0.8-1.2	2	2.5	4	5	6	7	10	16	20	25	30	40	50	60
Overpressure	3	3	2	4	5	3	10	12,5	20	20	35	35	40	80	80	90	90	90	90	90
Burst test	10	10	2,5	5	10	10	20	25	40	50	50	70	100	120	120	120	120	120	120	120

Absolute ranges \geq 2 bar: overpressure 3xFS; burst test > 200bar

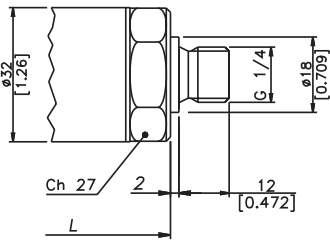
INSTALLATION DRAWINGS

Dimensions: mm [inches]

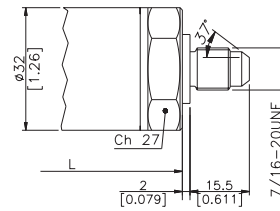


PRESSURE CONNECTION

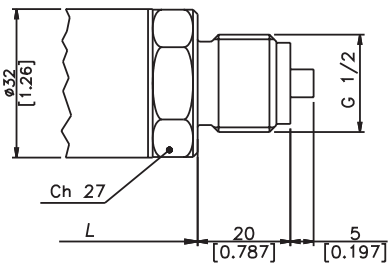
(1) G 1/4 MALE (DIN 3852-A)



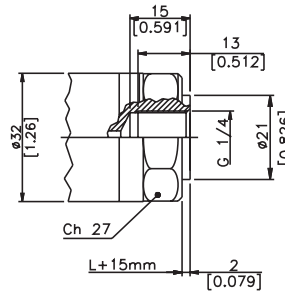
(2) SAE 04 AS4395 - E



(3) G 1/2 A (DIN 16288)

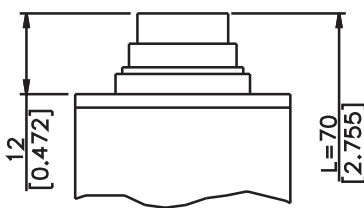


(4) G 1/4 FEMALE

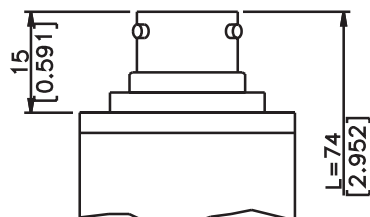


ELECTRICAL CONNECTION

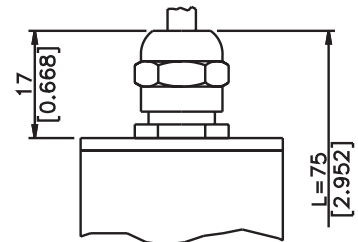
P - 7 pole connector



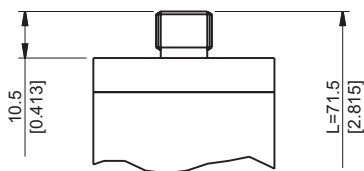
V - 6 pole connector



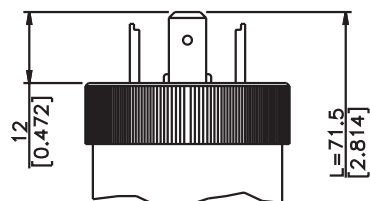
F - 4 pole connector



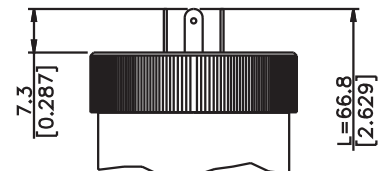
Z - 4 pole connector
M12x1



E - 4 pole connector
solenoid

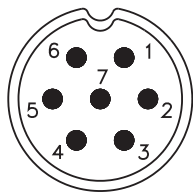


M - 4 pole connector
microsolenoid



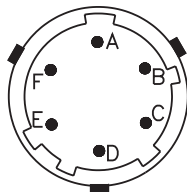
ELECTRICAL CONNECTION - Connectors

P - 7 pole connector



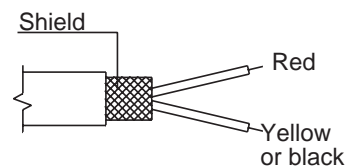
Male connector 09-127-09-07
Protection IP67

V - 6 pole connector



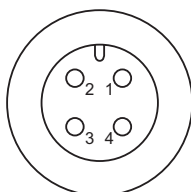
Male connector VPT02A10-6PT2
Protection IP66

F - 2-4 pole cable



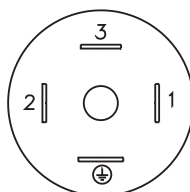
Shielded cable 2x0.25 - 2m. (output E)
Protection IP65

Z - 4-pole male connector M12 x 1

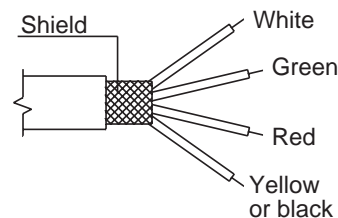


4 pole male connector 713 series
Protection IP67

E - 4 pole solenoid connector M - 4 pole microsolenoid connector



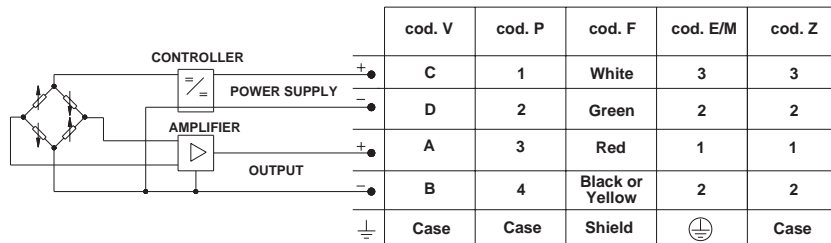
E - Solenoid DIN 43650A - ISO4400
Protection IP65
M - Microsolenoid DIN 43650C - ISO4400
Protection IP65



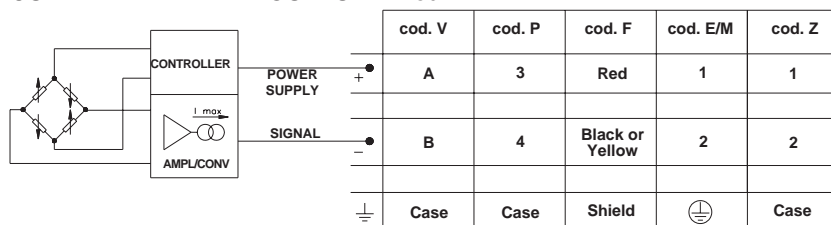
Shielded cable 4x0.25 - 1m
Protection IP65

ELECTRICAL CONNECTION - connection diagrams

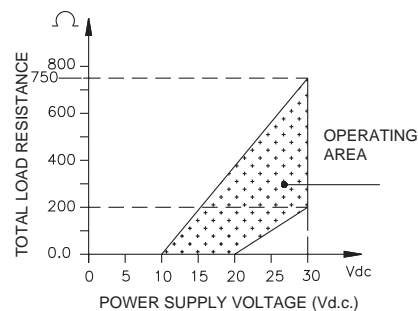
VOLTAGE AMPLIFIED OUTPUT - mod. B/C/M/N/P/Q/R



CURRENT AMPLIFIED OUTPUT - mod. E



LOAD DIAGRAM (Output current)



ACCESSORIES ON REQUEST

Connectors Plugs

Connection E

3 poles connector + ground DIN43650A ISO4400 **CON 006**
Prot. IP65

Connection Z

4 poles connector
Prot. IP67

CON 293

Connection M

3 poles connector + ground DIN43650C ISO4400 **CON 008**
Prot. IP65

Connection P

7 poles female cable connector Prot. IP67 **CON 321**

Connection V

6 poles female cable connector Prot. IP66 **CON 300**

EXTENSION CABLES

6-pin connector with 8m (25ft) cable

C08WLS

6-pin connector with 15m (50ft) cable

C15WLS

6-pin connector with 30m (100ft) cable

C30WLS

Other lengths

consult factory

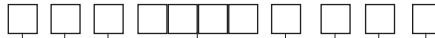
Cable color code

Conn.	Wire
A	Red
B	Yellow/Black
C	White
D	Green
E	Blue
F	Orange

ORDERING INFORMATION

Pressure transmitter

TSA



OUTPUT SIGNAL		
Standard		
4 .. 20 mA	E	
0 .. 10 Vdc	N	
On request		
0.1 .. 5.1 Vdc	B	
0.1 .. 10.1 Vdc	C	
0 .. 5 Vdc	M	
1 .. 5 Vdc	P	
1 .. 10 Vdc	Q	
1 .. 6 Vdc	R	

PRESSURE CONNECTION		
Standard		
G 1/4 gas male	1	
On request		
7/16-20 UNF-2A male (SAE 4 for AS4395-E)	2	
G 1/2A (DIN 16288)	3	
G 1/4 gas female	4	
1/8-27 NPT female	5	
1/4-18 NPT female	6	
1/4-18 NPT male	7	
M14 x 1.5 male	8	
1/8-27 NPT male	9	
G 1/4 male (DIN 3852-E)	E	
M12 x 1.5 male	R	
7/16-20 UNF-2A male (SAE 4 for J1926-2)	K	
7/16-20 UNF-2A female (SAE 4)	F	

ELECTRICAL CONNECTION		
4-pole connector solenoid	E	
Shielded cable	F	
Connector M12x1 4 pole	Z	
4-pole connector microsolenoid	M	
7 pole connector	P	
6 pole connector	V	

Mechanical and/or electrical characteristics differing from standard may be arranged on request.

RESPONSE TIME

V Fast (< 1 msec)

ACCURACY

T ± 0.15%FSO typical

G Gauge

A Absolute

MEASUREMENT RANGE

bar		psi	
BV05	0..0.05	P01U	0..1
BV10	0..0.1	P2V5	0..2.5
BV25	0..0.25	P05U	0..5
BV50	0..0.5	P15U	0..15
B01U	0..1	P18U	11..18
B1V2	0.8..1.2	P03D	0..30
B02U	0..2	P05D	0..50
B2V5	0..2.5	P75U	0..75
B04U	0..4	P01C	0..100
B05U	0..5	P15D	0..150
B06U	0..6	P25D	0..250
B07U	0..7	P03C	0..300
B01D	0..10	P05C	0..500
B16U	0..16	P75D	0..750
B02D	0..20	P01M	0..1000
B25U	0..25		
B03D	0..30		
B04D	0..40		
B05D	0..50		
B06D	0..60		

■ = Range available also "Absolute"

B1V2 = Range available only "Absolute" (Barometric)

P18U = Range available only "Absolute" (Barometric)

Note: The measurement range B1V2 is for absolute pressure from 0.8 to 1.2 bar and is defined as "Barometric". The signal output is scaled from 800mbar (i.e. 4mA) to 1200mbar (i.e. 20mA).

Ex.: **TSA - N - 1 - P - B03D - G - T - V**

Pressure transmitter TSA with 0...10Vdc output signal, G 1/4 male pressure connection, 7 pole connector, pressure range 0...30 bar gauge, ± 0.15% FSO accuracy, 1msec response time.

Sensors are manufactured in compliance with:

- EMC 2004/108/CE compatibility directive
- RoHS 2002/95/CE directive

Electrical installation requirements and Conformity certificate are available on our web site: www.gefran.com

CALIBRATION STANDARDS

Instruments manufactured by Gefran are calibrated against precision pressure calibration equipment which is traceable to International Standards.

GEFRAN spa reserves the right to make any kind of design or functional modification at any moment without prior notice

GEFRAN

GEFRAN spa
via Sebina, 74
25050 PROVAGLIO D'ISEO (BS) - ITALIA
tel. 0309888.1 - fax. 0309839063
Internet: <http://www.gefran.com>

DTS_TSA_0709_ENG

2200 Series / 2600 Series – General Purpose Industrial Pressure Transducers

- ▶ Gauge, Absolute, Vacuum and Compound Pressure Models Available
- ▶ Submersible, General Purpose and Wash Down Enclosures
- ▶ High Stability Achieved by CVD Sensing Element
- ▶ Millivolt, Voltage and Current Output Models

The 2200 series features stability and accuracy in a variety of enclosure options. The 2600 series extends the packaging options via an all welded stainless steel back end for demanding submersible and industrial applications. The 2200 and the 2600 feature proven CVD sensing technology, an ASIC (amplified units), and modular packaging to provide a sensor line that can easily accommodate specials while not sacrificing high performance.

Specifications

Input	
Pressure Range	Vacuum to 6000 psi (400 bar)
Proof Pressure	2 x Full Scale (FS) (1.5 x Fs for 400 bar, ≥ 5000 psi)
Burst Pressure	>35 x FS <= 100 psi (6 bar); >20 x FS >= 1000 psi (60 bar); >5 x FS <= 6000 psi (400 bar)
Fatigue Life	Designed for more than 100 million FS cycles
Performance	
Long Term Drift	0.2% FS/year (non-cumulative)
Accuracy	0.25 % FS typical (optional 0.15% FS)
Thermal Error	1.5% FS typical (optional 1% FS)
Compensated Temperatures	-5°F to +180°F (-20°C to +80°C)
Operating Temperatures	-40°F to +260°F (-40°C to +125°C) for elec. codes A, B, C, 1 -5°F to +180°F (-20°C to +80°C) for elec. codes 2, D, G, 3 -5°F to +125°F (-20°C to +50°C) for elec. codes F, M, P Amplified units >100°C maximum 24 VDC supply
Zero Tolerance	1% of span
Span Tolerance	1% of span
Response Time	0.5 ms
Mechanical Configuration	
Pressure Port	See ordering chart
Wetted Parts	17-4 PH Stainless Steel
Electrical Connection	See ordering chart
Enclosure	316 ss, 17-4 PH ss IP65 NEMA 4 for elec. codes A, B, C, D, G, 1, 2, 3 IP67 for elec. code "F" IP68 for elec. codes M, (max depth 200 meters H ₂ O) IP30 for elec. code "3" with flying leads
Vibration	70g, peak to peak sinusoidal, 5 to 2000 Hz (Random Vibration: 20 to 2000 Hz @ ≈20g Peak per MIL-STD.-810E Method 514.4)
Acceleration	100g steady acceleration in any direction 0.032% FS/g for 15 psi (1 bar) range decreasing logarithmically to 0.0007% FS/g for 6000 psi (400 bar) range.
Shock	20g, 11 ms, per MIL-STD.-810E Method 516.4 Procedure I
Approvals	CE, UR (22ET, 26ET Intrinsically Safe)
Weight	Approx. 100 grams (additional cable; 75 g/m)

Series 2200



Series 2600



Individual Specifications

Millivolt Output units	
Output	100 mV (10 mv/v)
Supply Voltage (Vs)	10 VDC (15 VDC max.) Regulated
Bridge resistance	2600-6000 ohms
Voltage Output units	
Output	see ordering chart
Supply Voltage (Vs)	1.5 VDC above span to 35 VDC @ 6 mA
Supply Voltage Sensitivity	0.01% FS/Volt
Min. Load Resistance	(FS output / 2) Kohms
Current Consumption	approx 6 mA at 7.5V output
Current Output units	
Output	4-20 mA (2 wire)
Supply Voltage (Vs)	24 VDC, (7-35 VDC)
Supply Voltage Sensitivity	0.01% FS/Volt
Max. Loop Resistance	(Vs-7) x 50 ohms

Electromagnetic Capability

Meets the requirement for CE marking of EN50081-2 for emissions and EN50082-2 for susceptibility.

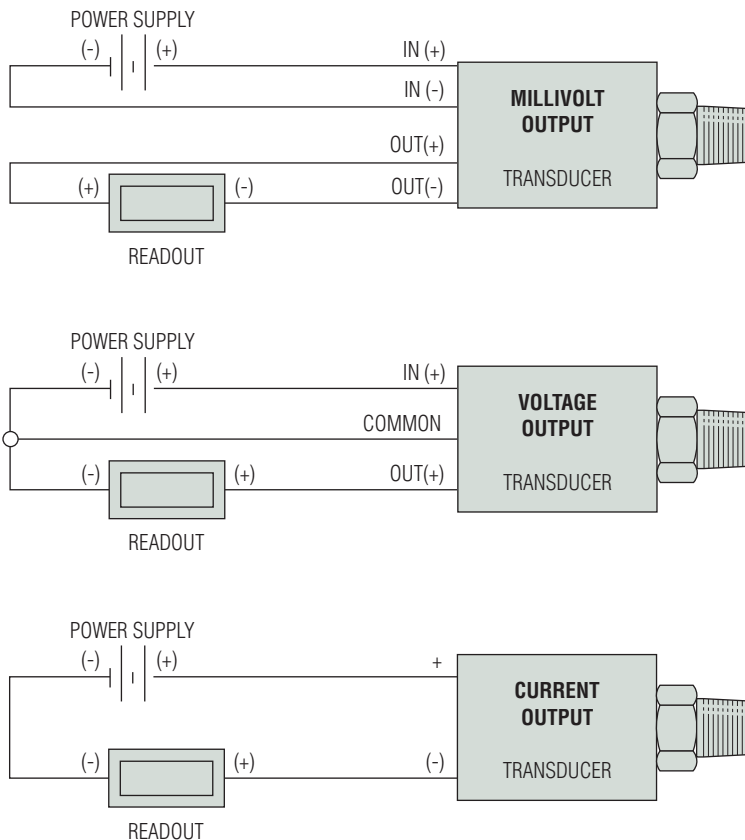
Test Data:

- EN61000-4-2 Electrostatic Discharge. 8kV air discharge, 4kV contact discharge. Unit survived.
- ENV50140 Radiated RF Susceptibility. 10V/m, 80MHz-1GHz, 1kHz mod. Maximum recorded output error was $<\pm 1\%$
- ENV50204 Radiated RF Susceptibility to Mobile Telephones. 10V/m, 900MHz. Maximum recorded output error was $<\pm 1\%$.
- EN61000-4-4 Fast Burst Transient. 2kV, 5/50ns, 5kHz for 1 minute. Unit survived.
- ENV50141 Conducted RF Susceptibility. 10Vms, 1kHz mod, 150kHz - 80MHz. Maximum recorded output error was $<\pm 1\%$

Connection Code		mV units				Voltage units				Current units (4-20mA)		
		IN+	OUT+	OUT-	IN-	IN+	COM	OUT+	EARTH	(+)	(-)	EARTH
A, B, G	"DIN" PIN	1	2	3	E	1	2	3	4	1	2	4
C	"10-6 Bayonet" PIN	A	B	C	D	A	C	B	E	A	B	E
D	"cable"	R	Y	BL	G	R	BK	W	DRAIN	R	BK	DRAIN
F	"IP 67 cable"	R	W	G	BK	R	BK	W	DRAIN	R	BK	DRAIN
M	"Immersible"	R	Y	BL	W	R	W	Y	DRAIN	R	BL	DRAIN
1	"8-4 Bayonet" PIN	A	B	C	D	A	C	B	D	A	B	D
2	"cable"	R	W	G	BK	R	BK	W	DRAIN	R	BK	DRAIN
3	"conduit & cable"	R	W	G	BK	R	BK	W	DRAIN	R	BK	DRAIN

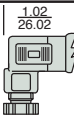
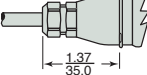
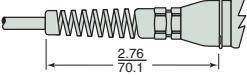
Cable Legend:

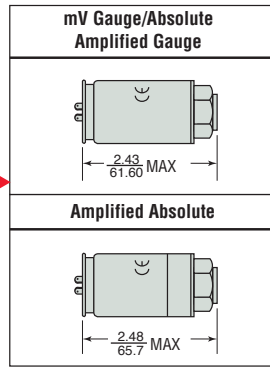
R = Red
 BL = Blue
 BK = Black
 W = White
 Y = Yellow



Dimensions

2200 Series

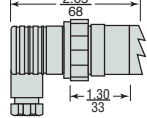
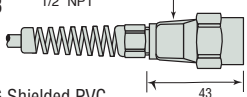
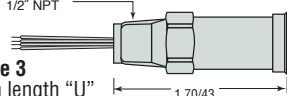
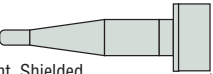
Mini 4 Pin - No Connector
Code B 
Mini 4 Pin - With Connector
Code A  1.02 26.02
IP67 Cable (Waterproof)
Code F  1.37 35.0
24 AWG Shielded PVC
IP65 or NEMA4 Cable
Code D or 2  2.76 70.1
24 AWG Shielded PVC

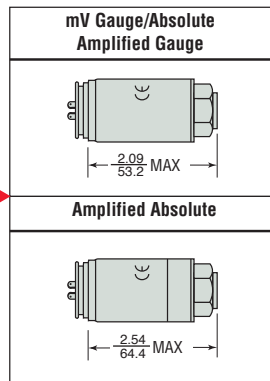


Maximum diameter 1.07" (27.3 mm)

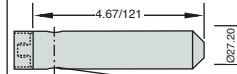
1/8-27 NPT
Code 08  0.59 15
1/4 - 18 NPT
Code 02 with snubber  0.79 20
Code OJ with snubber
1/4-18 NPT Internal
Code 0E  0.95 24
1/2-14 NPT
Code 0H  1.02 26.0
7/16-20 UNF-2A
Code 04  0.75 19
9/16-18 UNF-2A
Code 1P  0.67 17
G 1/8 Internal
Code 09 
G 1/4 External
Code 01  0.67 17
R 1/4
Code 0A  0.79 20

2600 Series

10-6 or 8-4 Mil-C Connector
10-6 Code C  0.87 22
8-4 Code 1
Large DIN 43650 Plug
Code G  2.65 68 1.30 33
Conduit Connector with Cable
Code 3 1/2" NPT  43 1.70
24 AWG Shielded PVC
Conduit Connector with Flying Leads
Code 3 1/2" NPT with length "U"  1.70/43
Moulded, Immersible Cable
Code M 24 AWG, Vent, Shielded, Polyurethane  0.90 23



Maximum diameter 1.07" (27.3 mm)

Nose Cone - Black Acetal
Code 19  0.75 19
Nose Cone Sink Weight
Code 29  4.67/121 0.87/20 Through hole Ø 10.0

inch
mm

PRESSURE TRANSDUCERS

How to Order

Use the **bold** characters from the chart below to construct a product code

2200 B G A60 01 A 3 U A

Series **2200 2600 22 ET⁴ 26 ET⁴**

Output
A - 100 mV **C** - 1-6V **J** - 0.5-5.5V **G** - 0.2-10.2V
B - 4-20mA **D** - 1-11V **R** - 0-5V **F** - 0.1-5.1V
H - 1-5V **S** - 0-10V

Pressure Datum
A* - Absolute **G** - Gauge
 *Max absolute range is 25 bar. (≤ 300 psi)

Pressure Range³ - psi

F07 - 0-7.5	G60 - 0-600	Vac = -15 psi
F15 - 0-15	H10 - 0-1,000	1F5 - Vac-0
F30 - 0-30	H15 - 0-1,500	3F0 - Vac-15
F60 - 0-60	H20 - 0-2,000	6F0 - Vac-45
G10 - 0-100	H30 - 0-3,000	1G0 - Vac-85
G15 - 0-150	H40 - 0-4,000	1G5 - Vac-135
G20 - 0-200	H50 - 0-5,000	2G0 - Vac-185
G30 - 0-300	H60 - 0-6,000	3G0 - Vac-285
G50 - 0-500		

Pressure Range - bar

A10 - 0-1	B25 - 0-25	Vac = -1 bar
A16 - 0-1.6	B40 - 0-40	1A0 - Vac-0
A25 - 0-2.5	B60 - 0-60	1A6 - Vac-0.6
A40 - 0-4	C10 - 0-100	2A5 - Vac-1.5
A60 - 0-6	C16 - 0-160	4A0 - Vac-3
B10 - 0-10	C25 - 0-250	6A0 - Vac-5
B16 - 0-16	C40 - 0-400	1B0 - Vac-9
		1B6 - Vac-15
		2B5 - Vac-24
		4B0 - Vac-39

Pressure Port

08 - 1/8-27 NPT External	European Threads
02 - 1/4-18 NPT External	09 - G1/8 Internal
0J - 1/4 NPT External w/snubber	01 - G1/4 External
0E - 1/4 NPT Internal	0A - R1/4 External
0H - 1/2-14 NPT External	Submersible (2600 only)
04 - 7/16-20 External (SAE #4, J514)	19 - Plastic Nose Cone
1P - 9/16-18 External (SAE #6, J1926-2)	29 - Sink Weight Nose Cone
1J - 7/16-20 External (SAE #4, J1926-2)	

Performance Code
 Accuracy/Thermal
A - .25%/1.5%
B - .15%/1.0%

Cable Length¹
U - No Cable Fitted^{1 2}
D - 1 Metre (3 feet)
E - 3 Metres (9 feet)
F - 5 Metres (16 feet)
G - 10 Metres (32 feet)

Apparatus Protection
2 - mV Only Transient Protection CE Mark, UR
3 - Amplified Only RFI Protected CE Mark, UR
E - Amplified only IS mark (Div. 1 only)⁴
T - Amplified only IS mark (Div. 1 and 2)^{4 5}

Electrical Connection (See Notes)
 2200 Series
A - 4 PIN DIN (Micro) Mating Connector Supplied
B - 4 PIN DIN (Micro) Mating Connector Not Supplied
2 - Cable Nema 4 USA
D - Cable European Color Code
F - Cable Gland Metal IP67

2600 Series
C - Fixed Plug Size 10-6 Mating Plug Not Supplied
G - Fixed Plug To DIN 43650 Mating Plug Supplied
M - Moulded Cable Immersible
1 - Fixed Plug Size 8-4 Mating Plug Not Supplied
3 - Conduit Connector 1/2NPT Ext. 1M Cable²

Notes:

- When electrical connection is cable please select a cable length from Table 1 below. When electrical connection is DIN or plug style "U" must be specified.
- Where electrical connection -3 and cable length -U occur in part number, the unit will be supplied with flying leads (4-1/2" IP30). Additional Pressure Ranges are available. Please consult factory.
- Intrinsically safe transducers are available with amplified outputs only. (ETL, entity approved for Class I, Division 1, Groups C & D, hazardous areas; Class I, Divisions 1 and 2, Groups C & D for Electrical Connection Codes -A, -B, -G or -3 only.
- Apparatus Protection Code -T is available for Electrical Connection Codes -A, -B, -G or -3 only.

Table 1 - Cable Length

(2600 Series) (2200 Series select "U" through "G")

Code	Length (M)	Code	Length (M)
U	No Cable Fitted	M	40
D	1	N	50
E	3	P	75
F	5	Q	100
G	10	R	125
H	15	S	150
J	20	4	170
K	25	5	200
L	30	6	225



High Performance Linear Servomotor

4020, 5020



Precision, powerful linear motion

The brushless DC tubular linear motor's shaft contains rings of powerful rare earth magnets that interact with the stator coils to produce rapid, precise and powerful motion. The stator's length and diameter determine the force level, while the shaft length determines the stroke.

Linear motion is initiated by a motion controller, which relays detailed move profiles to the motor. A precision encoder reports motor position to the controller for closed loop control. The motor's position and force are fully programmable and there is no backlash or compressibility to compromise position accuracy.

Contact us to discuss your application requirements.

TYPICAL APPLICATIONS

- Robotics and factory automation
- Processing equipment
- Packaging equipment
- Pumping / dispensing
- Material / product testing
- Machine tools
- Textile (tufting equipment)
- Paper converting
- Transfer equipment
- Automation welding

FEATURES

- Single moving part – integral bearings
- Compact size
- Brushless direct drive technology
- Fully programmable
- Clean, quiet operation
- 1180 lb peak force
- > 180 in / sec
- 40 G acceleration
- Strokes up to 20 inches
- Clean, quiet operation
- Long life / low maintenance

ADVANTAGES

- Increased throughput, a function of its high acceleration
- Exceptional accuracy
- Consistent repeatability
- Environmentally friendly – no hydraulic fluids
- Exceptionally high force per volume
- High force / weight ratio
- Quiet
- Lifecycle cost savings of up to 50 percent over existing motion control systems because of:
 - Reduced wear and friction – meaning lower repair and maintenance costs because it has just one moving part and integral bearings
 - High operating efficiency
 - Low cost of operations / power consumption

MOOG
COMPONENTS GROUP

Linear Motors

WHAT IS A TUBULAR LINEAR SERVOMOTOR?

The Moog linear motor is essentially a conventional brushless motor with an unconventional twist.

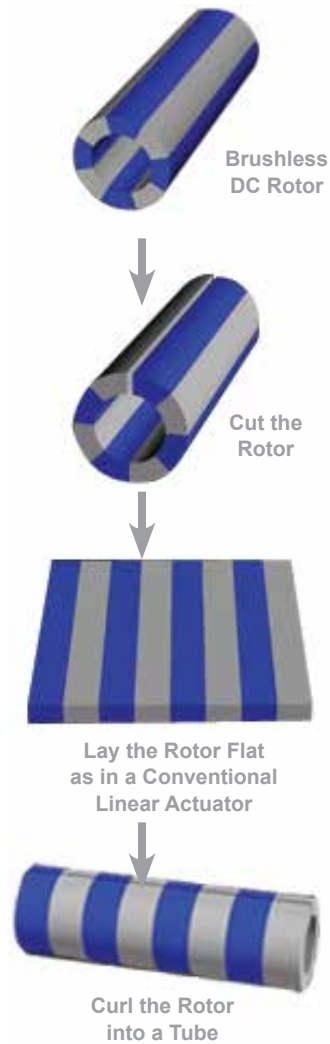
The design of Moog's core patent began with the magnetic design of a rotary brushless motor. Engineers cut the rotor lengthwise, laid it out flat, and then curled the assembly into a tube from the other direction. The permanent magnets now formed a stack of rings in alternating magnetic polarity. Engineers suspended the magnetic shaft in a column of current-carrying coils held in slots along a metallic core – the stator.



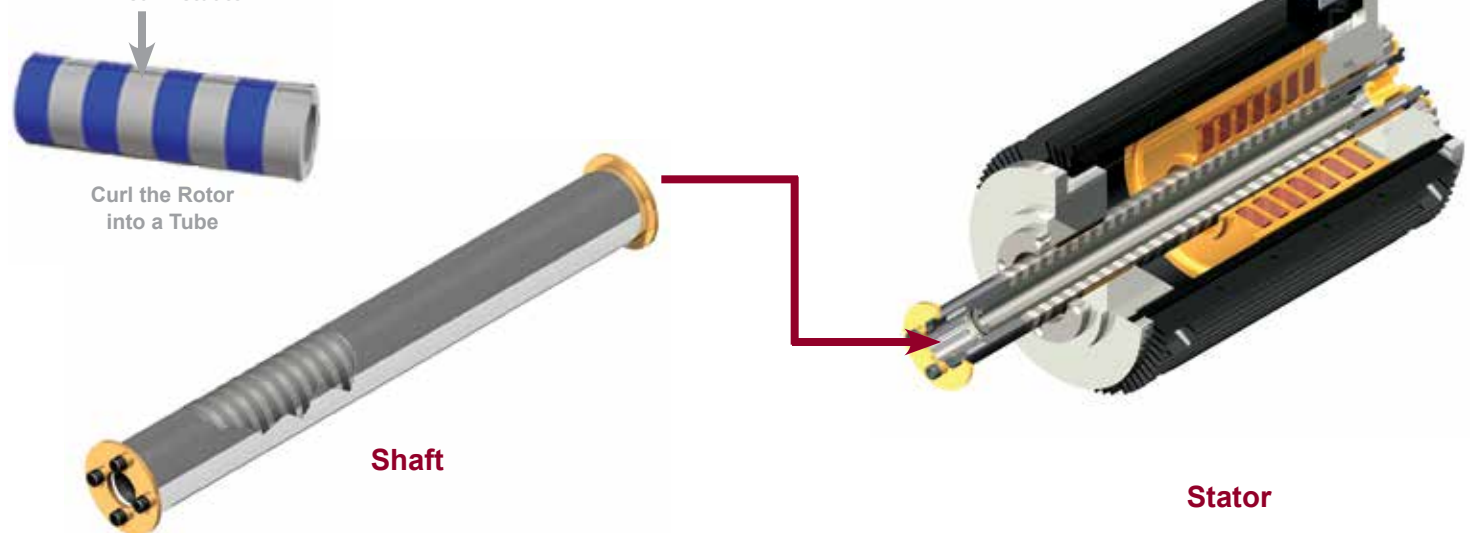
The company's engineers then rebuilt the shaft using more powerful magnets to increase the force produced, and lengthened the motor to create a longer stroke.

The result of these design improvements is the Moog linear motor: a compact motor with all the advantages of existing technology and none of the disadvantages.

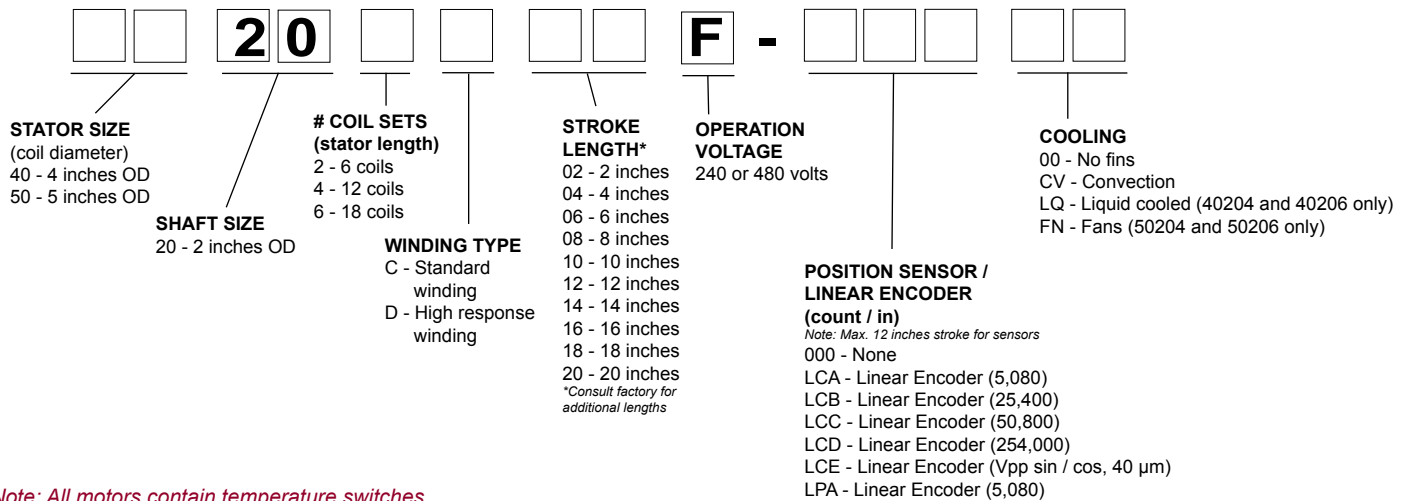
In short: a motor poised to replace a portion of today's pneumatic and ball screw, as well as some hydraulic motion control technology.



The Result:



PART NUMBERING SYSTEM



*Note: All motors contain temperature switches.
Consult factory for controller and feedback devices available.*

SPECIFICATIONS

		4020						5020					
Parameter	Units	2C	2D	4C	4D	6C	6D	2C	2D	4C	4D	6C	6D
Peak Force (1 sec)	lbf	410	410	850	850	1180	1180	360	360	780	780	1100	1100
	N	1824	1824	3781	3781	5249	5249	1601	1601	3469	3469	4893	4893
Peak Force (3 sec)	lbf	310	310	660	660	1020	1020	300	300	680	680	970	970
	N	1379	1379	2936	2936	4537	4537	1334	1334	3025	3025	4315	4315
Peak Current (1 sec)	A	45	90	45	90	45	90	50	100	50	100	50	100
Peak Current (3 sec)	A	25	50	25	50	25	50	30	60	30	60	30	60
Continuous Static Force (nat. convection)*	lbf	80	80	170	170	260	260	160	160	320	320	450	450
	N	356	356	756	756	1156	1156	712	712	1423	1423	2002	2002
Continuous Static Force (forced air)*	lbf	n/a	490	490	710	710							
	N	n/a	2180	2180	3158	3158							
Force Sensitivity (at 50% of 3 sec peak current)	lbf / A	13.7	6.8	27.7	13.8	44.1	22.0	11.7	5.8	26.9	13.4	38.7	19.3
	N / A	60.9	30.2	123.2	61.4	196.2	97.9	52.0	25.8	119.7	59.6	172.1	85.8
Back EMF Constant (ph-ph)	V _{pk} / (in / sec)	2.09	1.05	4.08	2.04	6.44	3.22	1.94	0.97	4.04	2.02	6.04	3.02
	V _{pk} / (m / sec)	82.3	41.3	160.6	80.3	253.5	126.8	76.4	38.2	159.1	79.5	237.8	118.9
DC Winding Resistance (ph-ph at 25° C)	ohms	2.9	0.7	5.9	1.5	8.8	2.2	1.6	0.4	3.2	0.8	4.8	1.2
Winding Inductance (ph-ph)	mH	20.5	5.1	40.3	10.1	60.5	15.1	19.6	4.9	39.2	9.8	58.1	14.5
Motor Constant	lbf / sqrt (watt)	9.2	9.2	13.2	13.2	17.1	17.1	10.6	10.6	17.3	17.3	20.4	20.4
	N / sqrt (watt)	40.9	40.9	58.7	58.7	76.1	76.1	47.1	47.1	77.0	77.0	90.7	90.7
Detent Force (peak)	lbf	10	10	10	10	10	10	10	10	10	10	10	10
	N	44	44	44	44	44	44	44	44	44	44	44	44
Thermal Resistance (nat. convection)	°C / W	0.28	0.28	0.19	0.19	0.13	0.13	0.23	0.23	0.13	0.13	0.09	0.09
Thermal Resistance (forced air)	°C / W	n/a	0.06	0.06	0.04	0.04							
Standard Stroke**	inch	20	20	16	16	12	12	20	20	16	16	12	12
	m	0.508	0.508	0.406	0.406	0.304	0.304	0.508	0.508	0.406	0.406	0.304	0.304
Weight (add 0.62 lbf for each inch of stroke) (add 0.11 kg for each centimeter stroke)	lbf	31	31	44	44	58	58	41	41	58	58	81	81
	kg	14.1	14.1	20.0	20.0	26.3	26.3	18.6	18.6	26.3	26.3	36.7	36.7

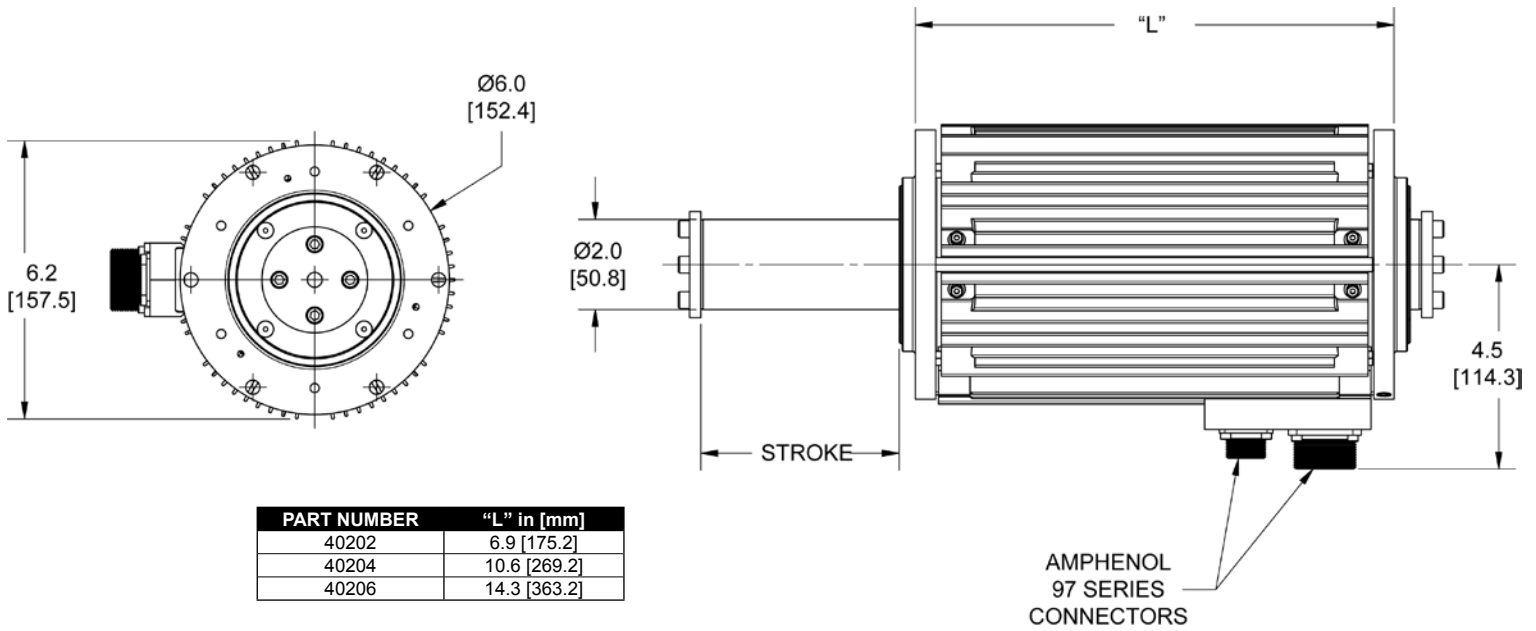
**Consult factory for continuous force capability of standard configuration motors as well as fan and liquid cooled options.*

***Consult factory for stroke lengths in excess of standard values.*

Linear Motors

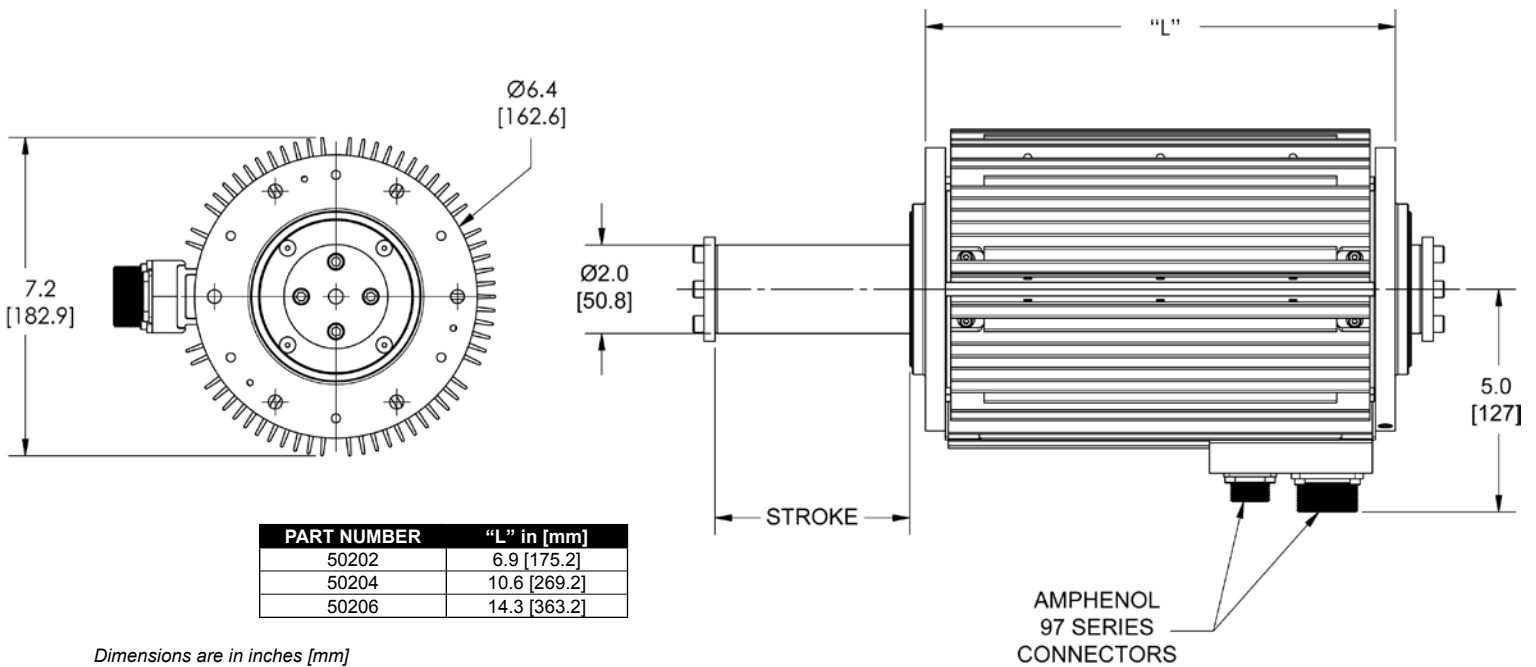
DIMENSIONS

Model 4020



Dimensions are in inches [mm]

Model 5020

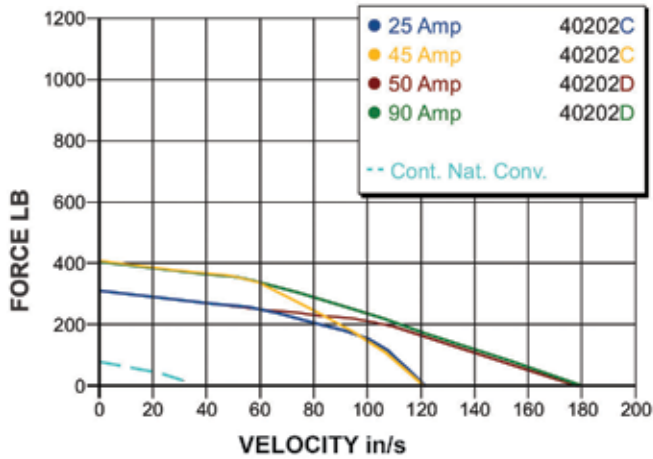


Dimensions are in inches [mm]

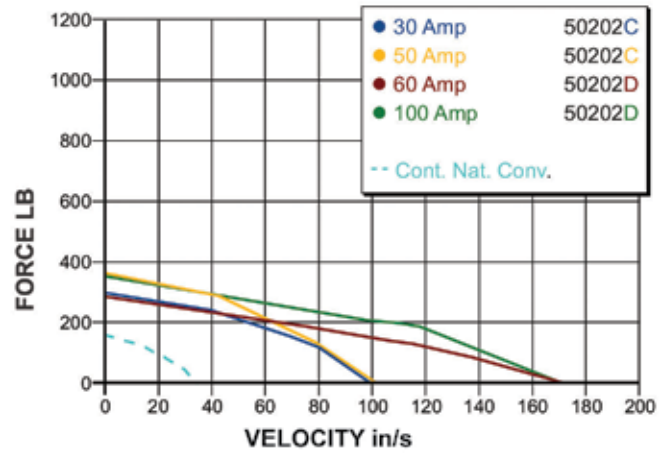
Note: For electrical performance see page 3.

FORCE-VELOCITY CURVES - 220 VOLT MOTORS

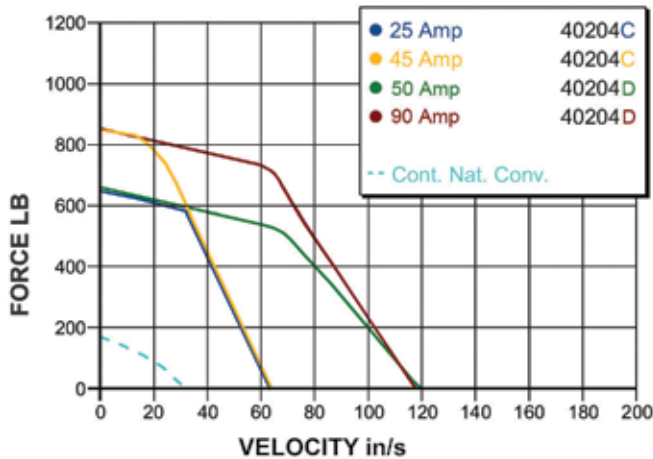
40202



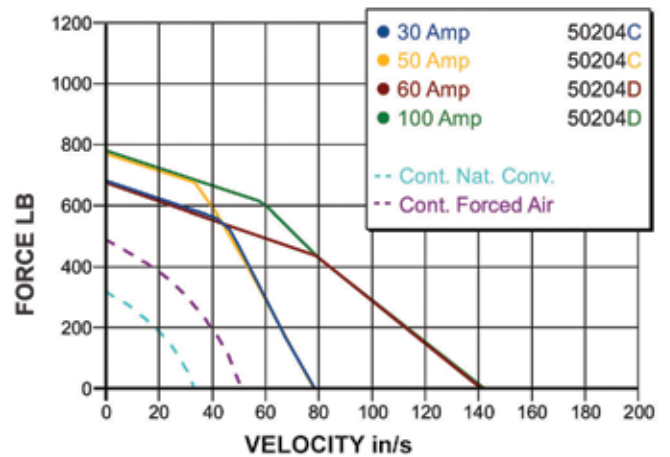
50202



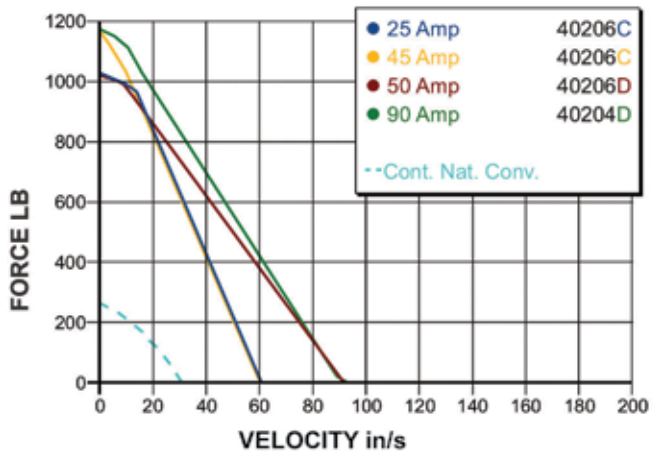
40204



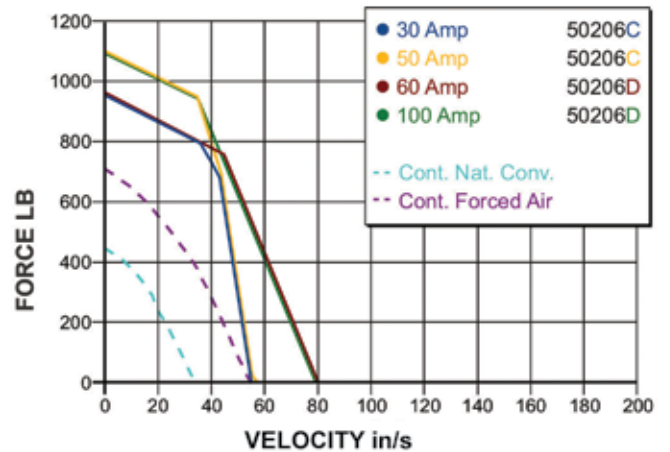
50204



40206



50206

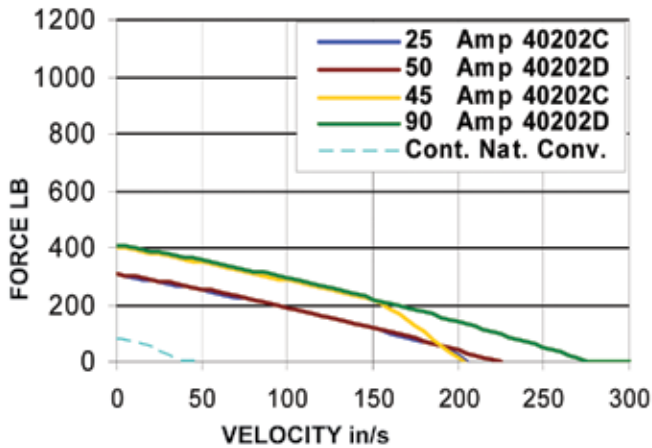


Performance obtained with Delta Tau PMAC2 controller and MTS Powerblock amplifier powered by 220 V 3-phase mains. Motors mounted to an aluminum plate. Allowed coil temperature rise is 75°C.

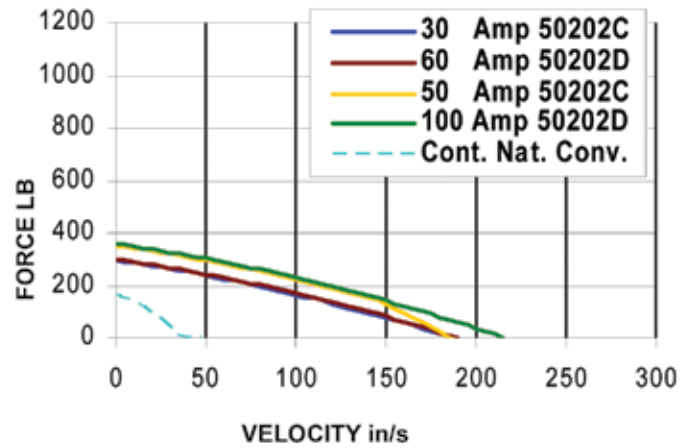
Linear Motors

FORCE-VELOCITY CURVES - 480 VOLT MOTORS

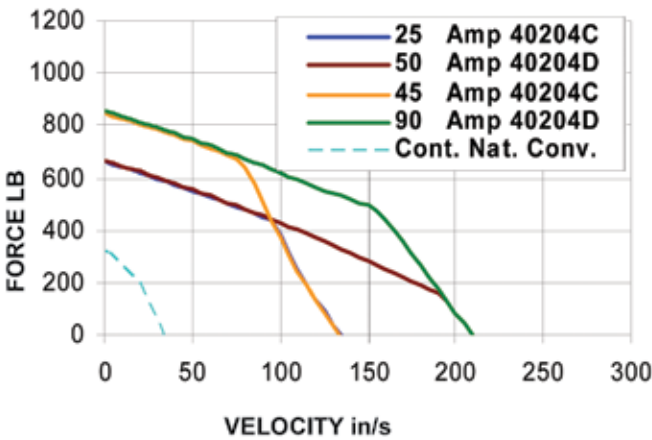
40202



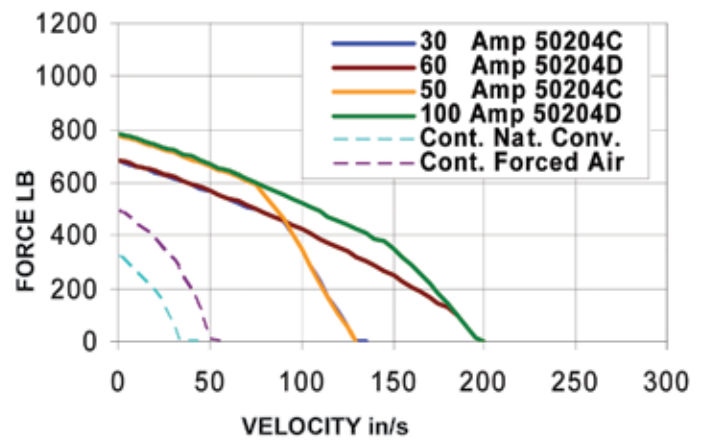
50202



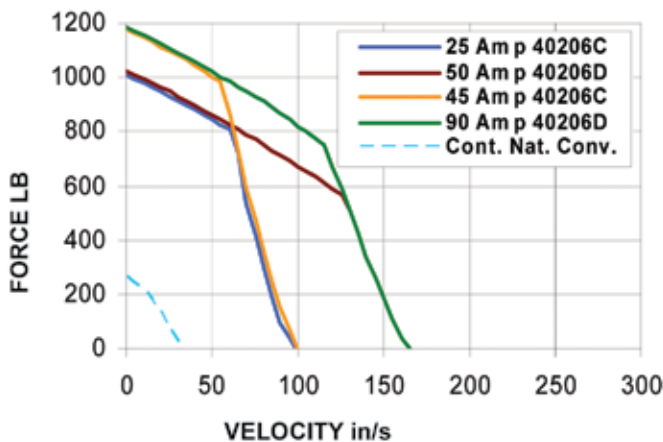
40204



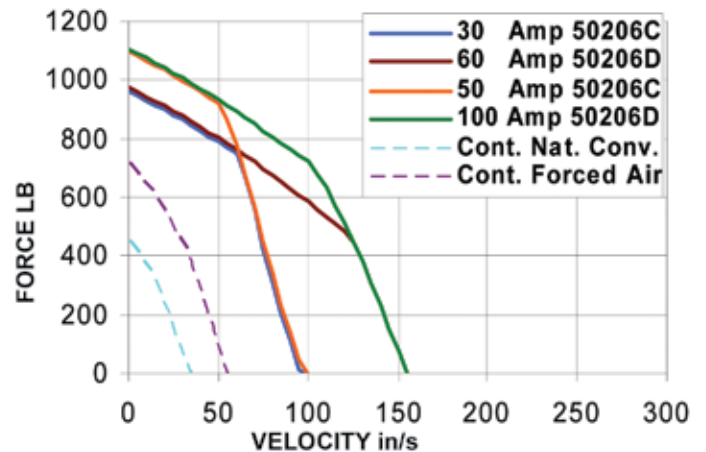
50204



40206



50206

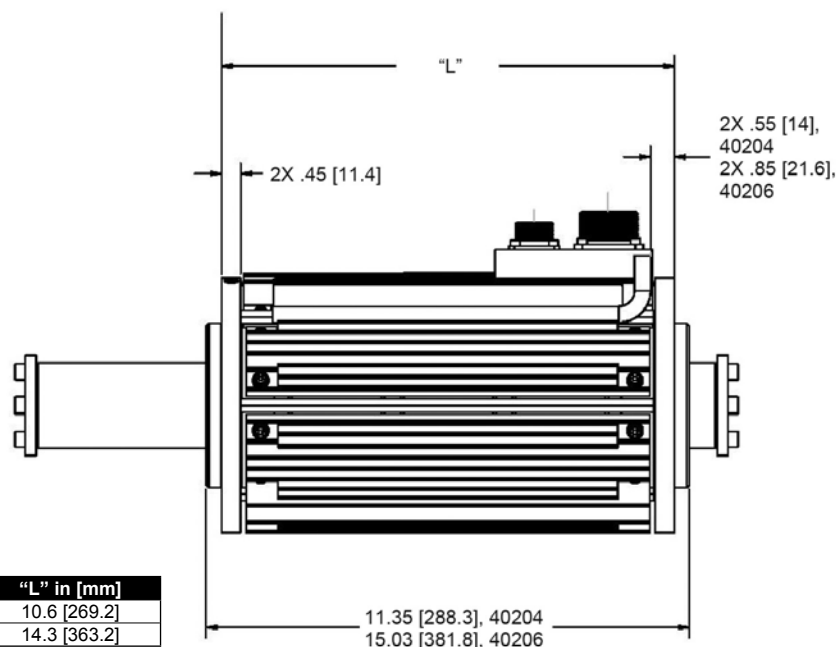
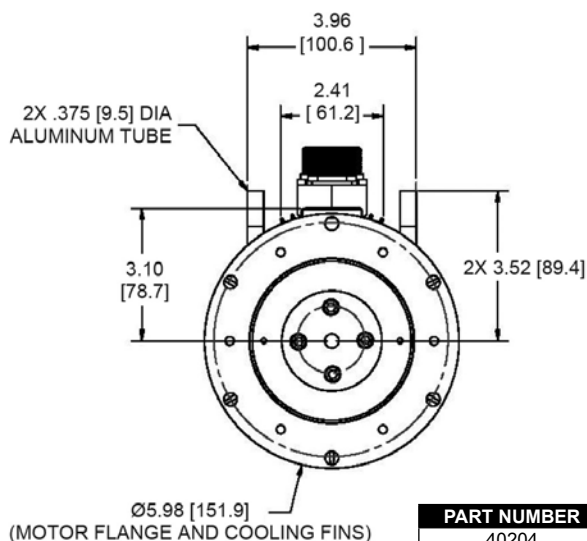


SPECIFICATIONS - LIQUID COOLING

		4020			
Parameter	Units	4C	4D	6C	6D
Peak Force (1 sec)	lbf	850	850	1180	1180
	N	3781	3781	5249	5249
Peak Force (3 sec)	lbf	660	660	1020	1020
	N	2936	2936	4537	4537
Peak Current (1 sec)	A	45	90	45	90
Peak Current (3 sec)	A	25	50	25	50
Continuous Static Force (liquid cooled)*	lbf	360	360	540	540
	N	1601	1601	2402	2402
Force Sensitivity (at 50% of 3 sec Peak Current)	lbf / A	27.7	13.8	44.1	22.0
	N / A	123.2	61.4	196.2	97.9
Back EMF Constant (ph-ph)	$V_{pk} / (\text{in} / \text{sec})$	4.08	2.04	6.44	3.22
	$V_{pk} / (\text{m} / \text{sec})$	160.6	80.3	253.5	126.8
DC Winding Resistance (ph-ph at 25° C)	ohms	5.9	1.5	8.8	2.2
Winding Inductance (ph-ph)	mH	40.3	10.1	60.5	15.1
Motor Constant	lbf / sqrt (watt)	13.2	13.2	17.1	17.1
	N / sqrt (watt)	58.7	58.7	76.1	76.1
Detent Force (peak)	lbf	10	10	10	10
	N	44	44	44	44
Thermal Resistance (liquid cooled)	°C / W	0.09	0.09	0.06	0.06
Maximum Stroke	inch	16	16	12	12
	m	0.406	0.406	0.304	0.304
Weight (add 0.62 lbm for each inch of stroke) (add 0.11 kg for each centimeter stroke)	lbm	45	45	59	59
	kg	20.41	20.41	26.76	26.76

*Consult factory for continuous force capability of standard configuration motors as well as fan and liquid cooled options. Performance parameters and velocity curves are based on a 5°C coolant inlet temperature and a 2 GPM flow rate.

DIMENSIONS - LIQUID COOLING



PART NUMBER	"L" in [mm]
40204	10.6 [269.2]
40206	14.3 [363.2]

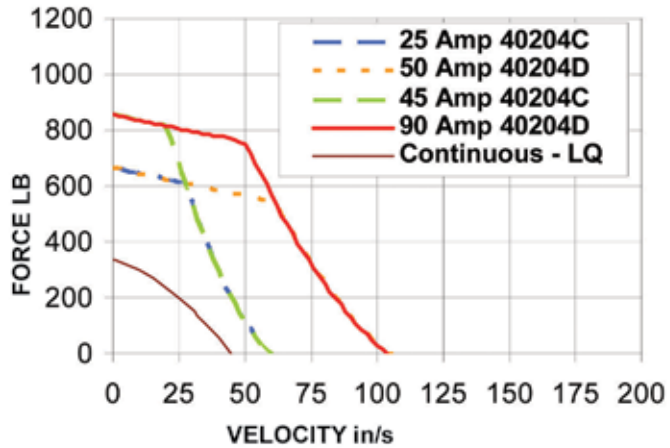
Dimensions are in inches [mm]

Note: For electrical performance see above specifications.

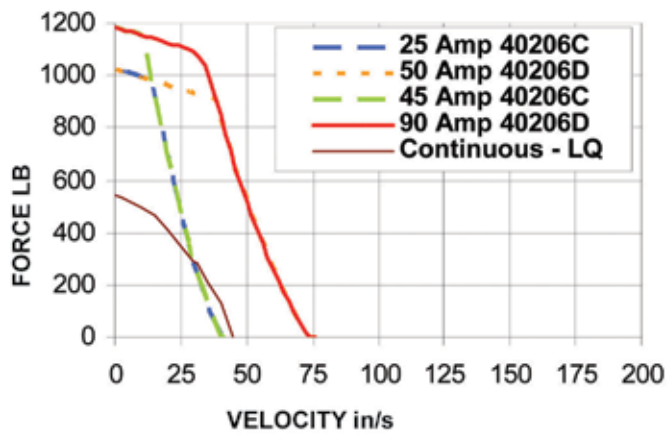
Linear Motors

FORCE-VELOCITY CURVES - LIQUID COOLING

40204



40206



TECHNOLOGY COMPARISON

Tubular linear servomotors offer an advantage in weight, size, maintenance costs, environmental considerations, precision, speed, control, programmability, reliability and noise. The patented technology offers the motion control industry an alternative to hydraulic, pneumatic and mechanical power sources for linear motion control. The linear motors are easy to install and integrate. Position and force are fully programmable and there is no backlash or fluid compressibility to compromise position accuracy.

The superior performance of Moog's linear servomotor results in improved profitability for a broad range of industrial motion control applications. The linear motor's high velocity enables manufacturers to increase throughput. At the same time, its high accuracy and consistent repeatability contribute greatly to improved product quality.



Its unique design incorporates the important features of a single moving part, integral bearings, compact size, and exceptionally high force per volume. These features deliver significant advantages, including cost savings, over not only traditional approaches including hydraulics, pneumatics, ball screws and other electromechanical systems, but also when compared to other linear motors.

With its single moving part and integral bearing system, the Moog linear motor is remarkably easy to install. Its simple design provides robust, reliable operation, and lowers life cycle costs. Its cylindrical configuration yields a highly efficient generation of force, enabling the motor to accelerate quickly to high velocities, even when handling heavy loads.

The linear motor compared to the alternatives:

- Hydraulic systems are environmentally unfriendly, require an external power supply, and cannot match the programmability or reliability of the Moog motor.
- Mechanical devices such as ball screws, cams and pulleys have high maintenance requirements, limited programmability, and lack the velocity that can be achieved with the Moog motor.
- Pneumatic systems cannot achieve the accuracy, velocity, programmability or reliability of the Moog motor, and present environmental concerns similar to those of hydraulic systems.
- Competing linear motors are more costly, more difficult to integrate, and lack the Moog motor's integral bearing system. The external bearing system required for competing flat linear motors can cost as much as the motor alone.

Typical Linear Drive Comparison				
	Tubular Motors	Mechanical Drives	Hydraulics	Pneumatic
Stiffness	High	Medium	Medium	Low
Friction	Medium	Medium	High	High
Temperature Range	125° C max.	125° C max.	50° C max.	50° C max.
Efficiency	50%	40%	25%	25%
Noise	40 dB	80 dB	120 dB	120 dB
Speed	180 in / sec	10 in / sec	10 in / sec	20 in / sec
Accuracy	0.0005 in	0.001 in	0.01 in	0.1 in

For technical assistance please call: 610-328-4000.

Linear Motors

TYPICAL APPLICATIONS

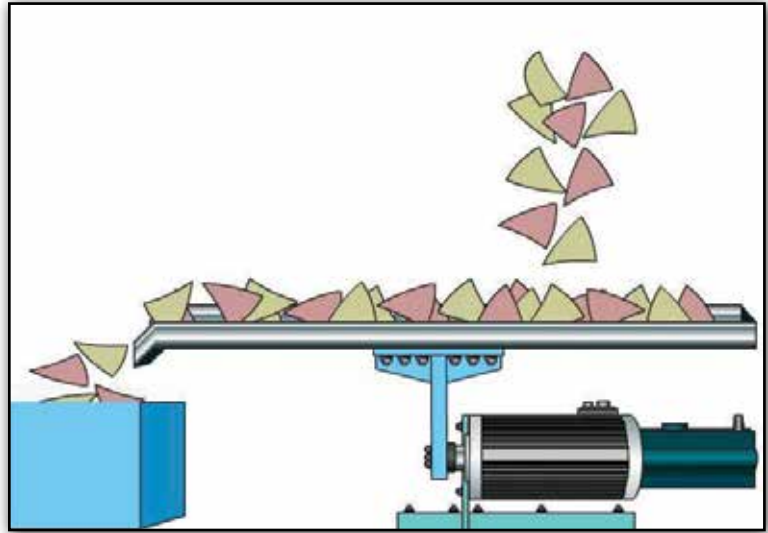
Conveyor

The Function

A fast-back conveyor moves dry goods along a production line, moving the product slowly in one direction and then reversing the conveyor back at high speed. The conveyor motion can be gentle in moving the product without shaking it too much.

This type of conveyor is used to move:

- Potato chips and seasoned foods – flavored potato chips or cereal, seasoned nuts
- Pharmaceuticals
- Rice and grains
- Small finished metal parts



The Problem

Producing just the right type of movement without damaging the product is a complex engineering problem that usually requires intricate mechanical solutions.

The Solution

As part of a linear servo system, the Moog motor's programmability produces optimum motion for any product without the expense and high maintenance of complex mechanical systems. The Moog motor also is used with vibratory conveyors.

The Result

- Faster conveyance speed, even up slopes
- Easy modification of motion profile for products requiring different motion

Moog motors can even be electronically geared together to drive large conveyors – impractical to impossible for mechanical systems to accomplish.

TYPICAL APPLICATIONS

Flying Die

Plastic and metal forming industries rely on motors to manipulate, hold and move product parts.

The Function

A flying die stamps or cuts a product while the product is in motion. The die is accelerated to match product speed, stamps or cuts the product and then returns to its original position. Flying dies are typically found in plastic and metal extruders, metal stamping and embossing.

The Problem

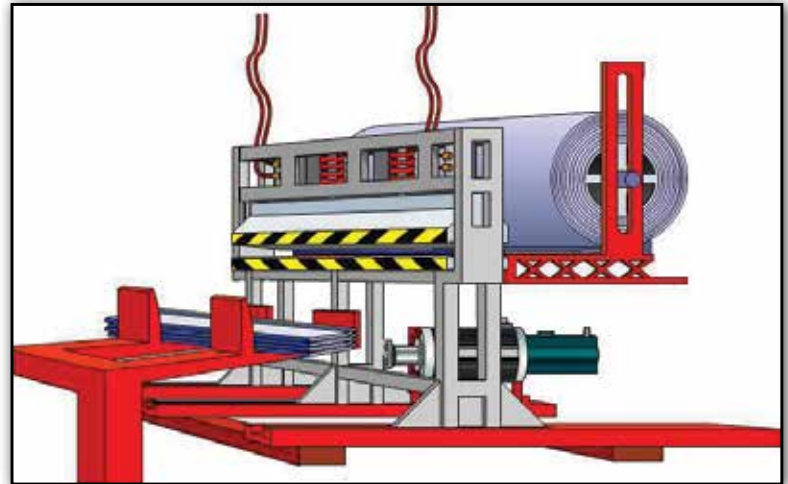
Synchronizing production line speed and die speeds at a precise location is an engineering challenge.

The Solution

The Moog linear motor automatically tracks and matches line speed.

The Result

- Faster throughput
- Reduced error and scrap rate
- Improved consistency



Destacker

The Function

Many raw materials are supplied in large quantity bulk stacks. A destacker unstacks products consistently and precisely for production. Destackers are common in lamination production and in manufacturing CDs, packaging materials, food products, etc.

The Problem

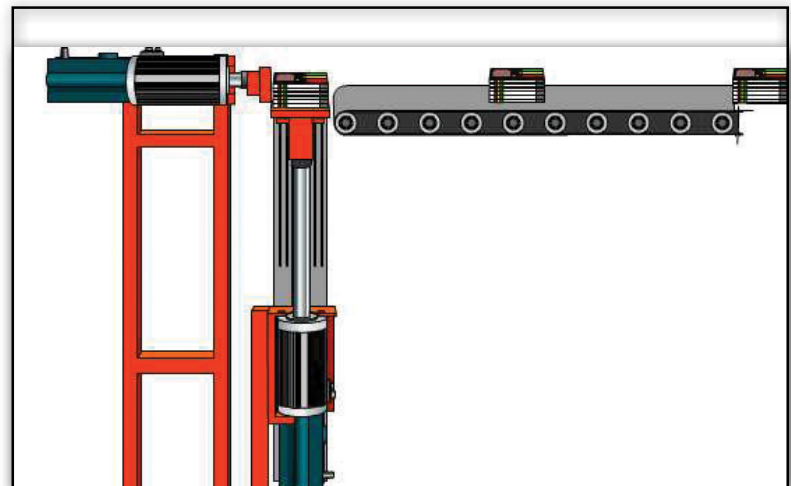
To avoid damaging the product, a destacker must make short, precise movements and stay perfectly in step with a pusher axis.

The Solution

A servo system with Moog motors is fully programmable for a precisely matching product thickness and finely tuned coordination between the axes.

The Result

- Faster line speeds
- Reduction of product damage



Americas

Moog Components Group
1213 North Main Street
Blacksburg, VA 24060
United States

Tel: +1-540-552-3011
Fax: +1-540-557-6400

Europe

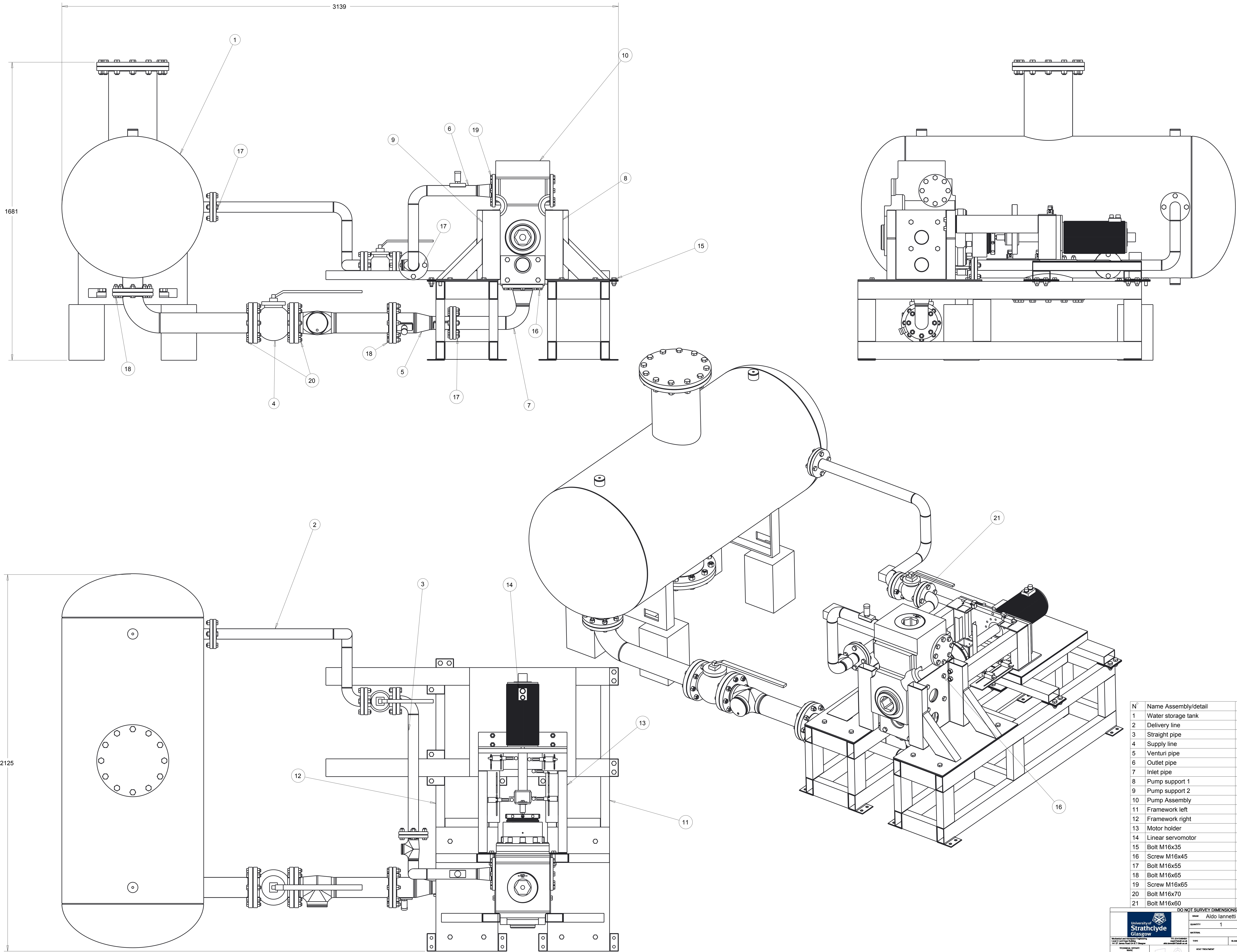
Moog Components Group
30 Suttons Business Park
Reading, Berkshire RG6 1AW
England

Tel: +44 (0) 118-966-6044
Fax: +44 (0) 118-966-6524

MOOG
COMPONENTS GROUP

www.moog.com/components

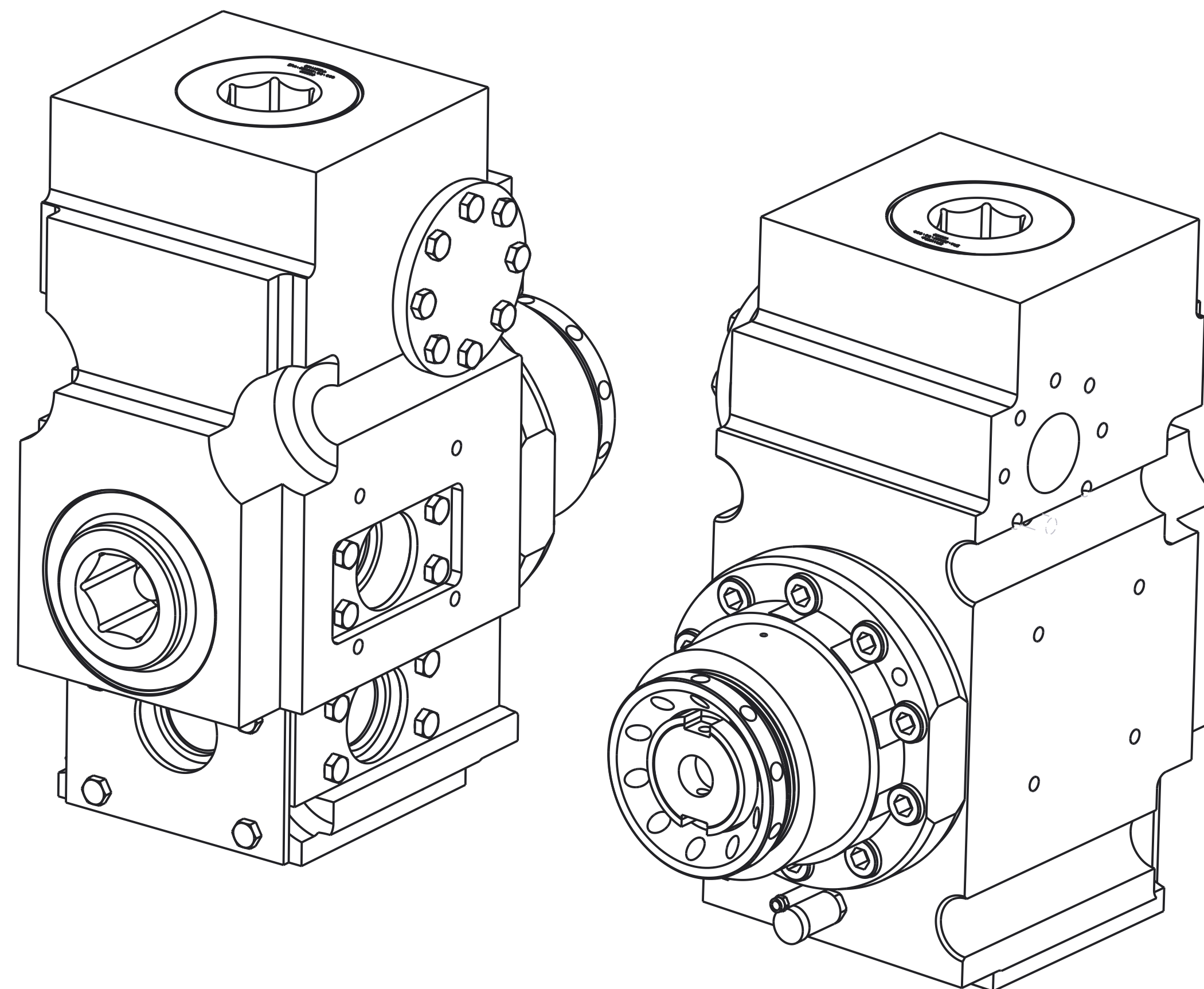
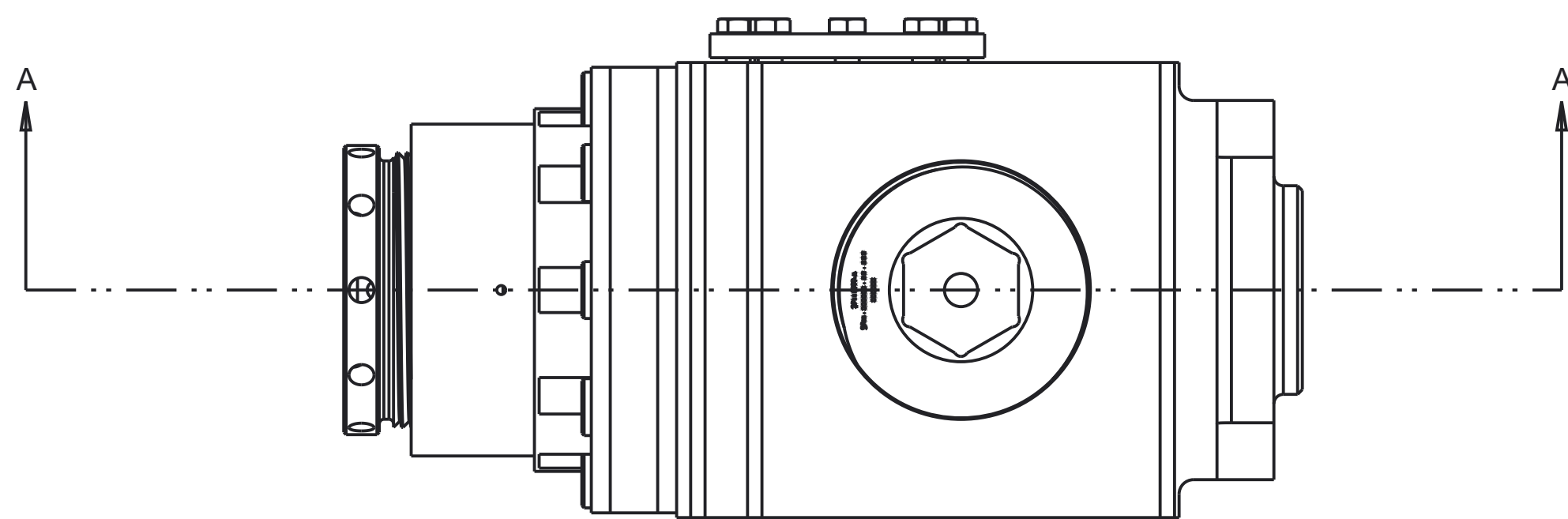
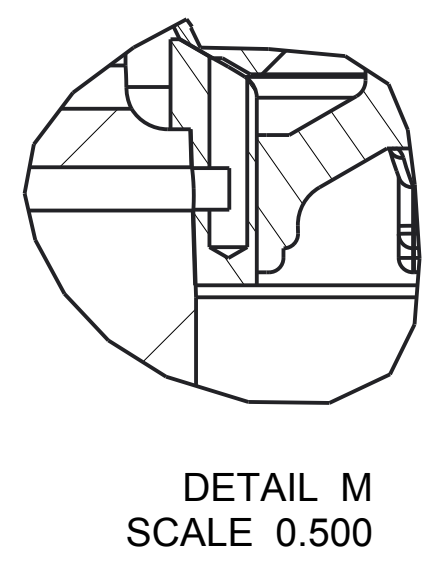
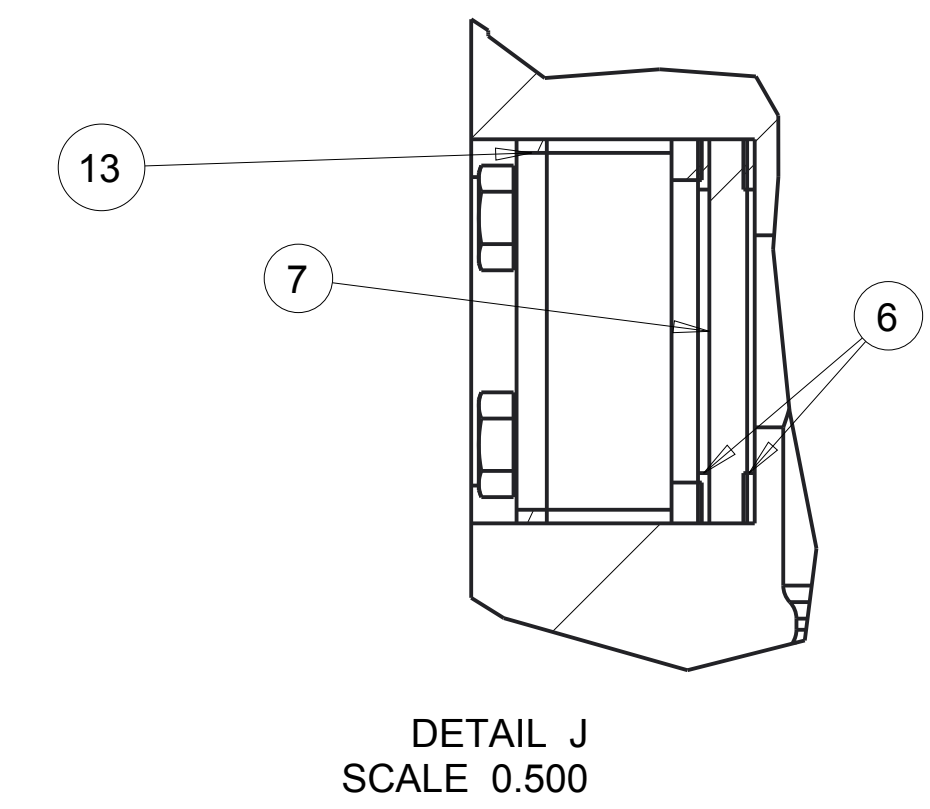
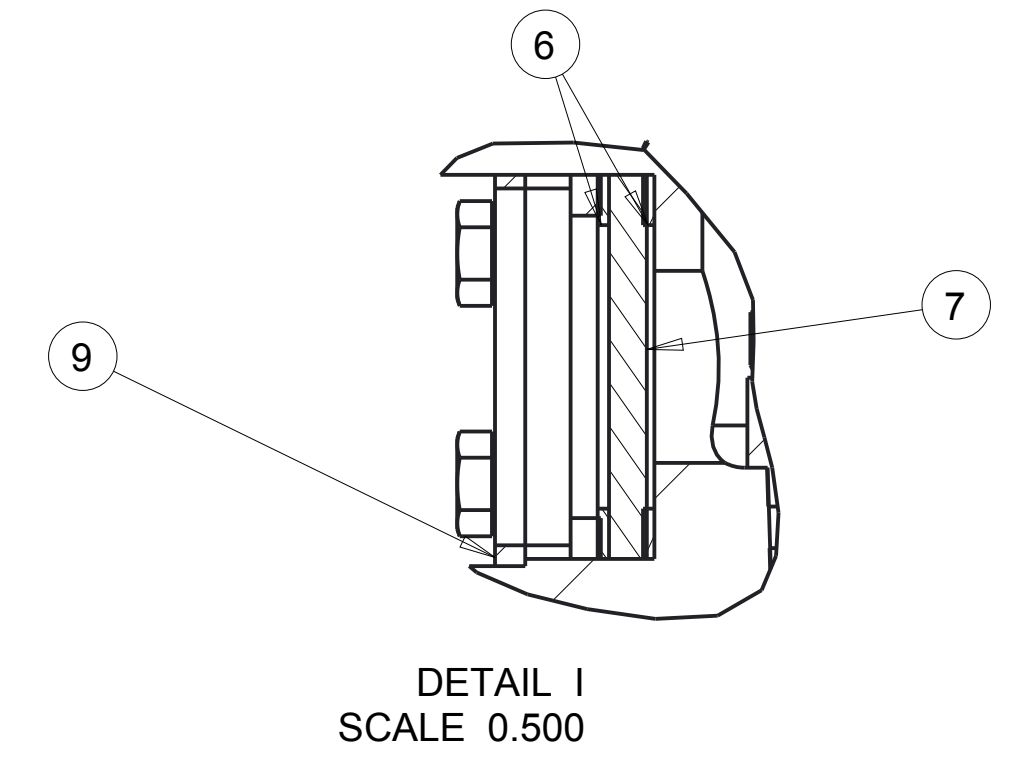
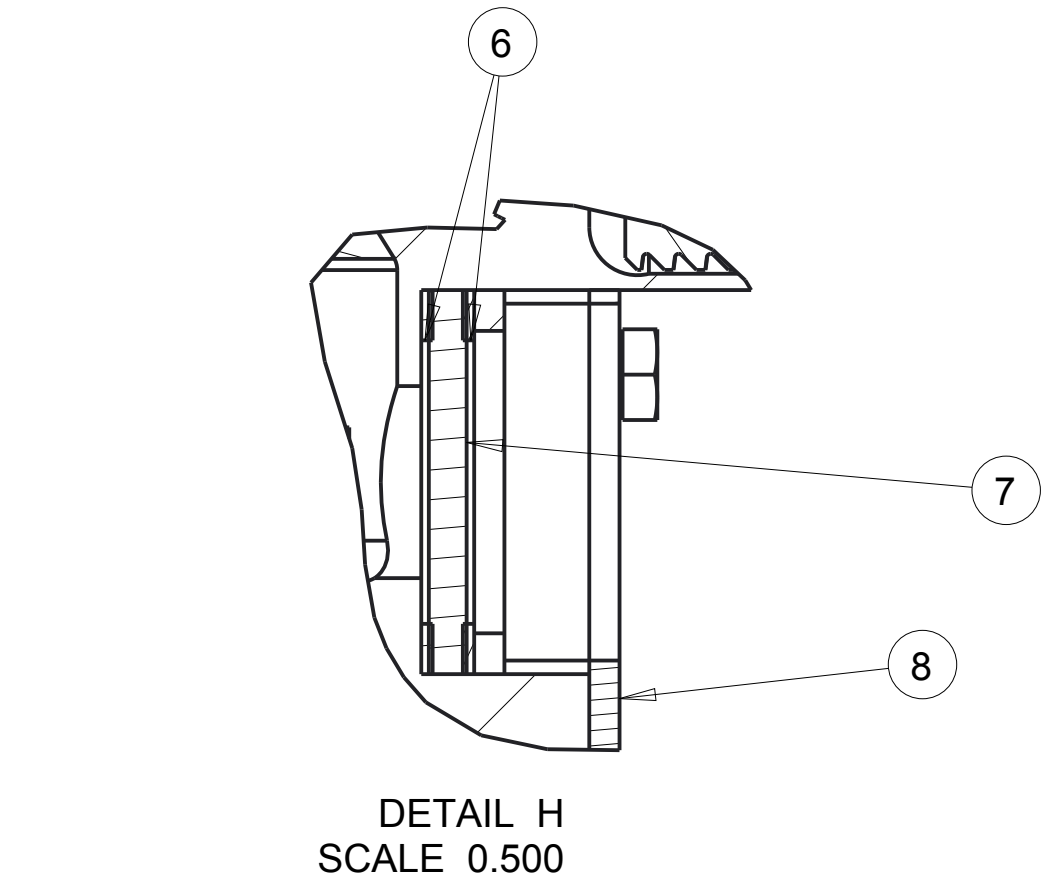
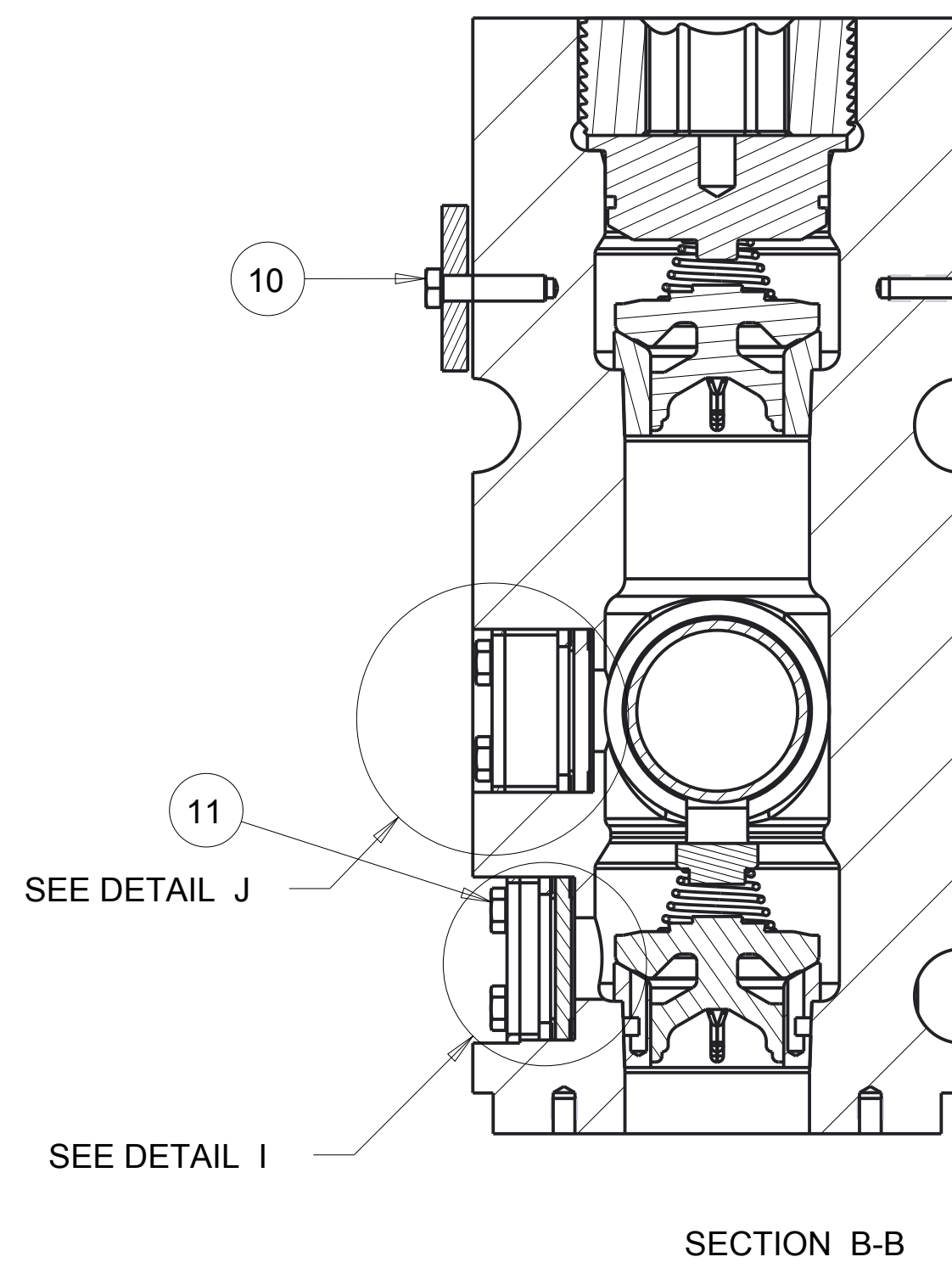
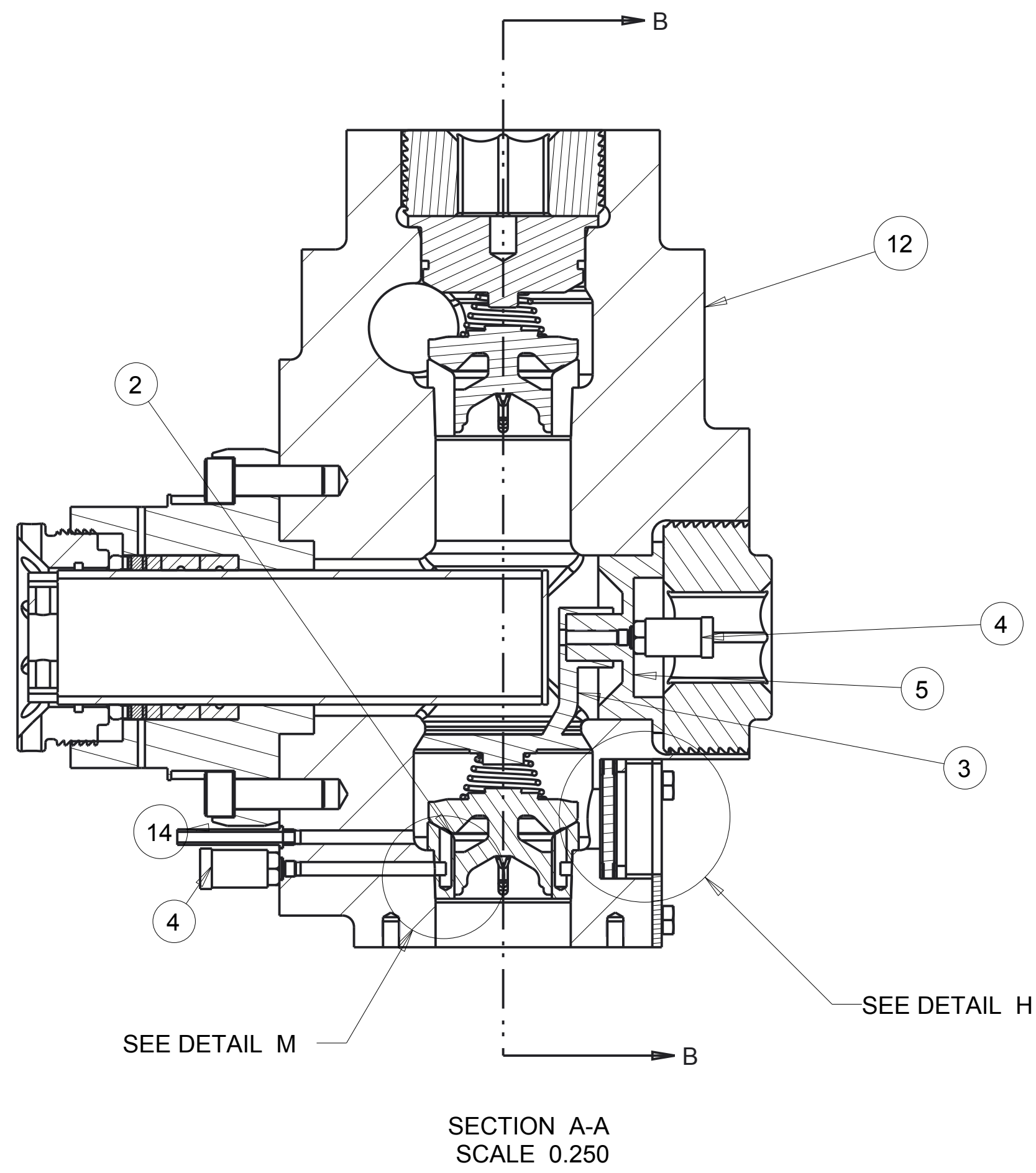
Email: mcg@moog.com



N°	Name Assembly/detail	Drawing	Q.
1	Water storage tank		1
2	Delivery line	011	1
3	Straight pipe	014	1
4	Supply line	003	1
5	Venturi pipe	002	1
6	Outlet pipe	006	1
7	Inlet pipe	008	1
8	Pump support 1	005	1
9	Pump support 2	004	1
10	Pump Assembly	001	1
11	Framework left	010	1
12	Framework right	009	1
13	Motor holder	013	1
14	Linear servomotor		1
15	Bolt M16x35		27
16	Screw M16x45		16
17	Bolt M16x55		12
18	Bolt M16x65		16
19	Screw M16x65		8
20	Bolt M16x70		16
21	Bolt M16x60		4

DO NOT SURVEY DIMENSIONS FROM THE DRAWING

		NAME: Aldo Iannetti QUANTITY: 1 REF: 000-01	DESIGNER: M. Slickland WEEK: 1760 DATE: 25/06/2013	PROJECT: A. Iannetti SCALE: 0.150 STANDARD: Standard
TECHNICAL OFFICE: NAME: A0 SHEET: 1 DRAWING: 000-01	HEAT TREATMENT: None SURFACE FINISH: Paint TEST RIG ASSEMBLY	DATE: 25/06/2013 TEST RIG ASSEMBLY		

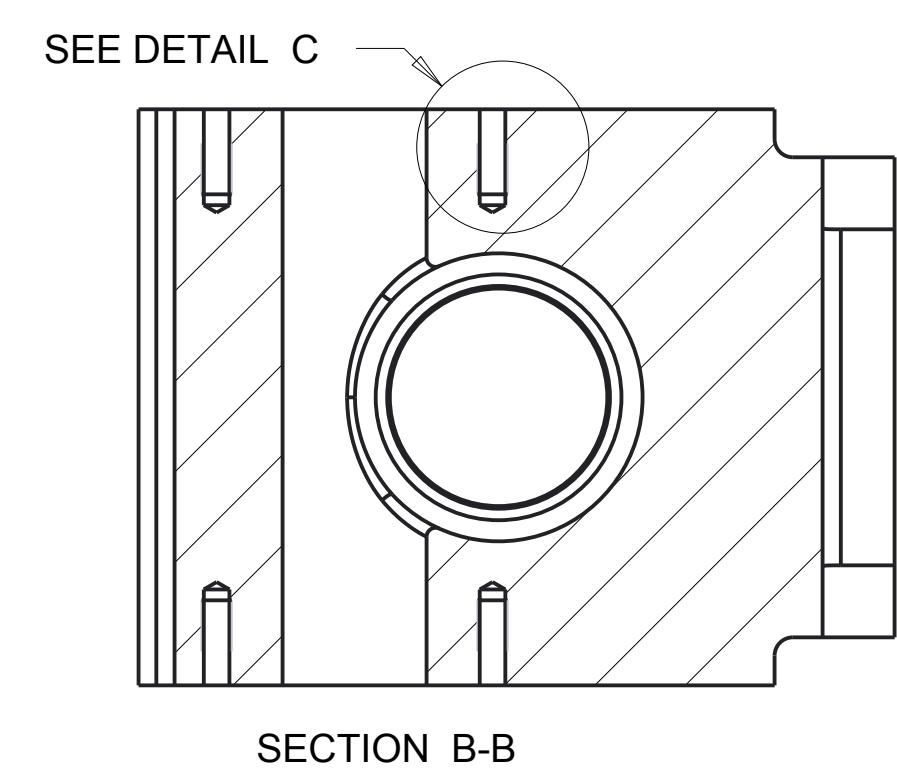
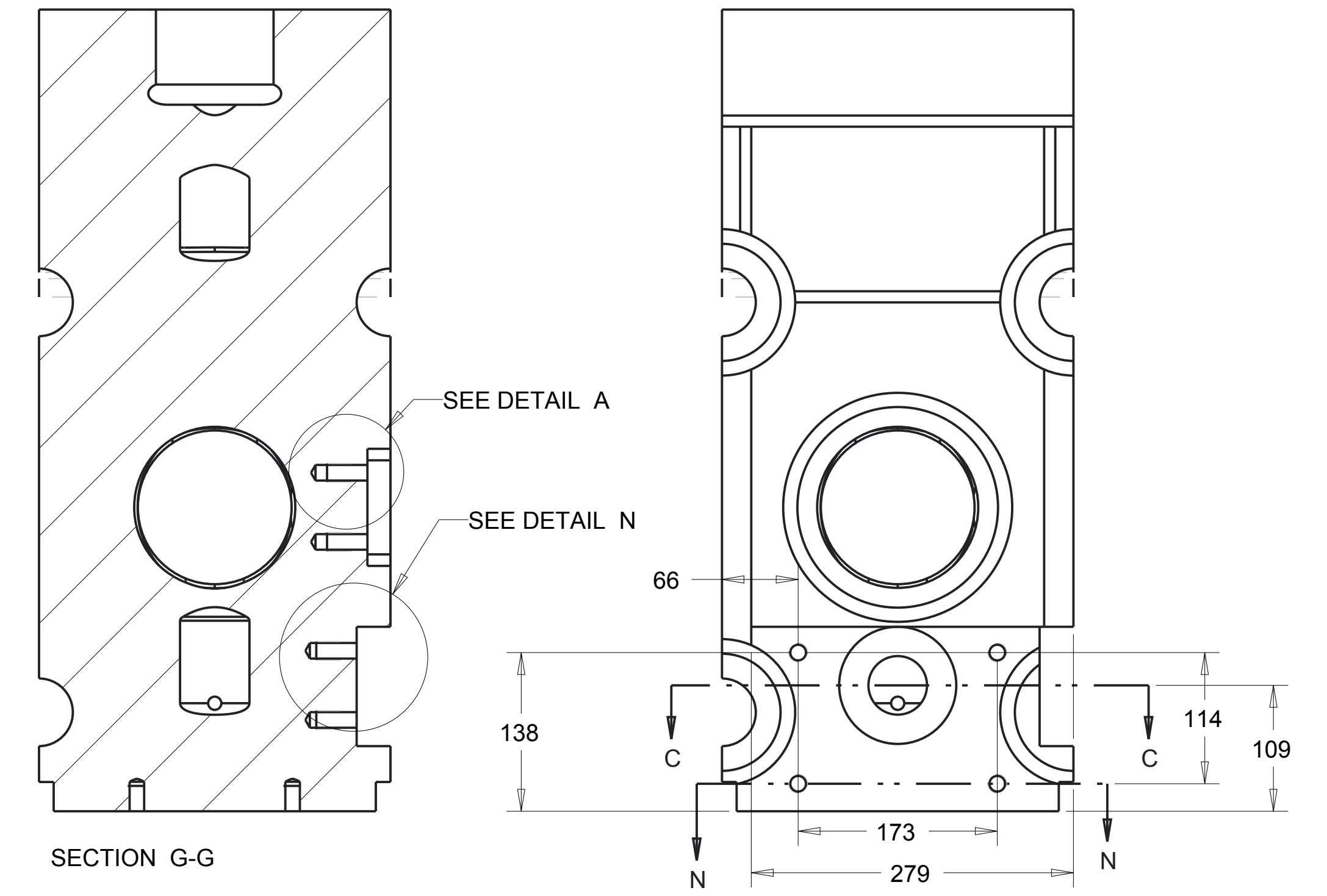
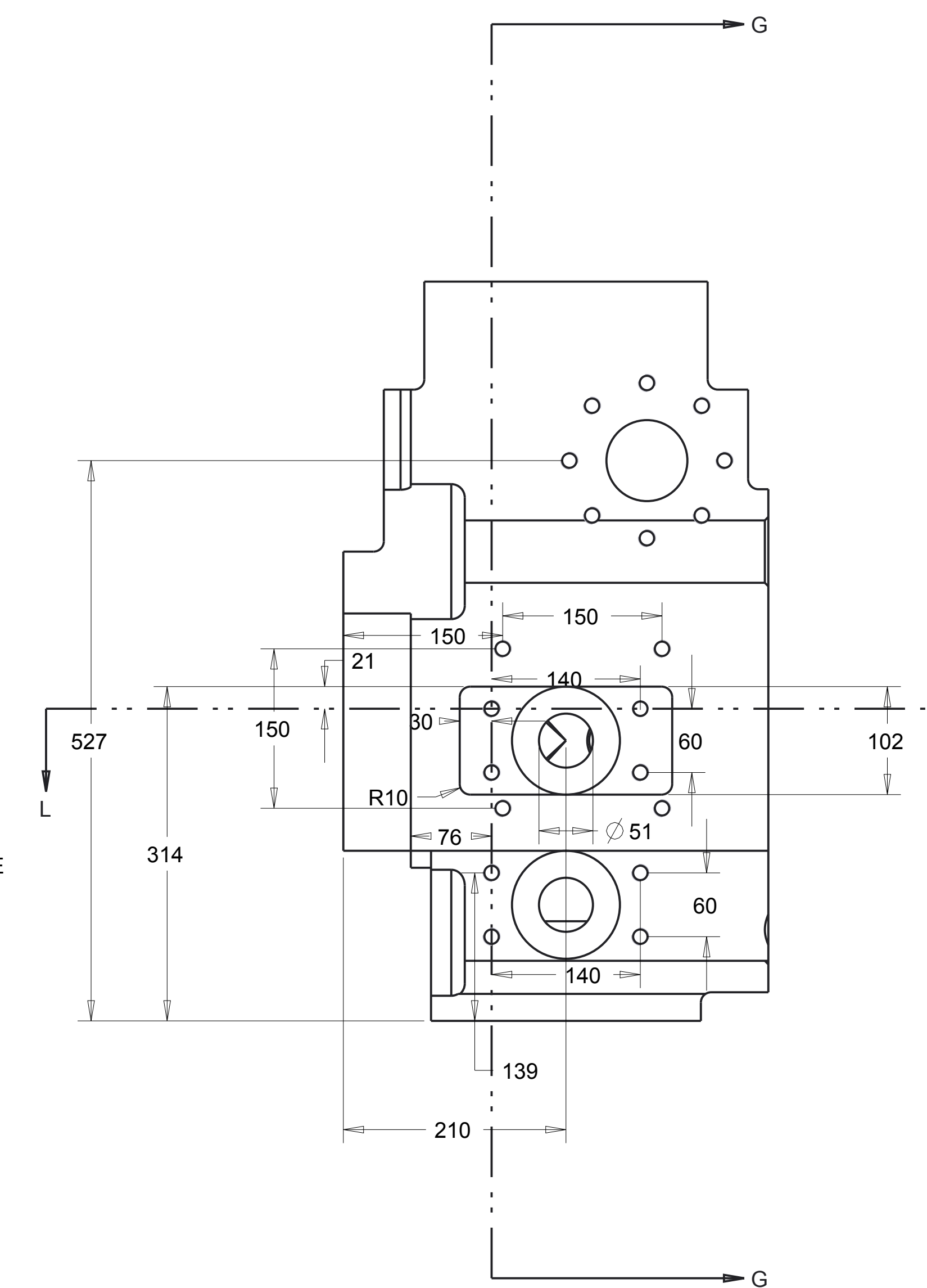
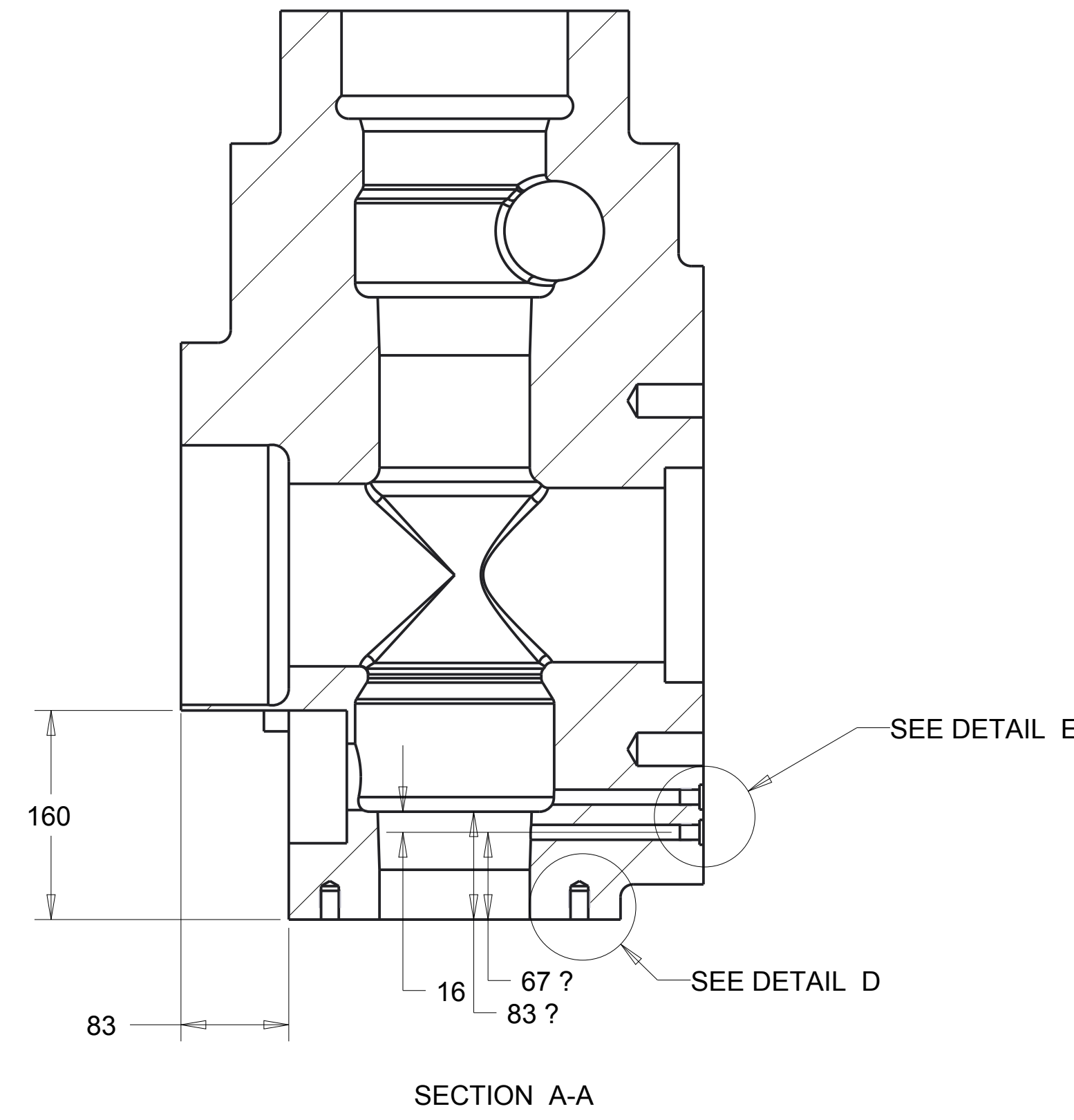
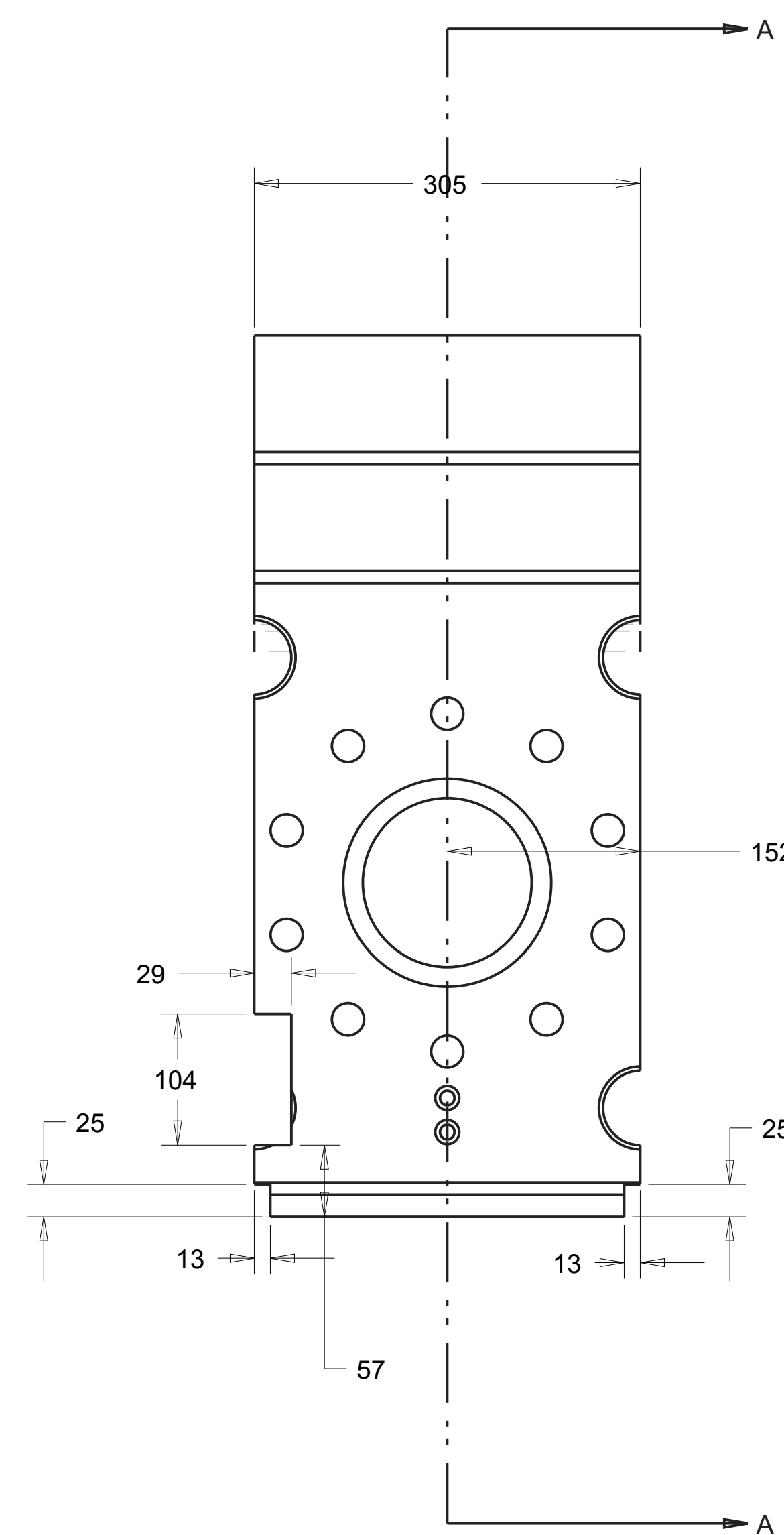
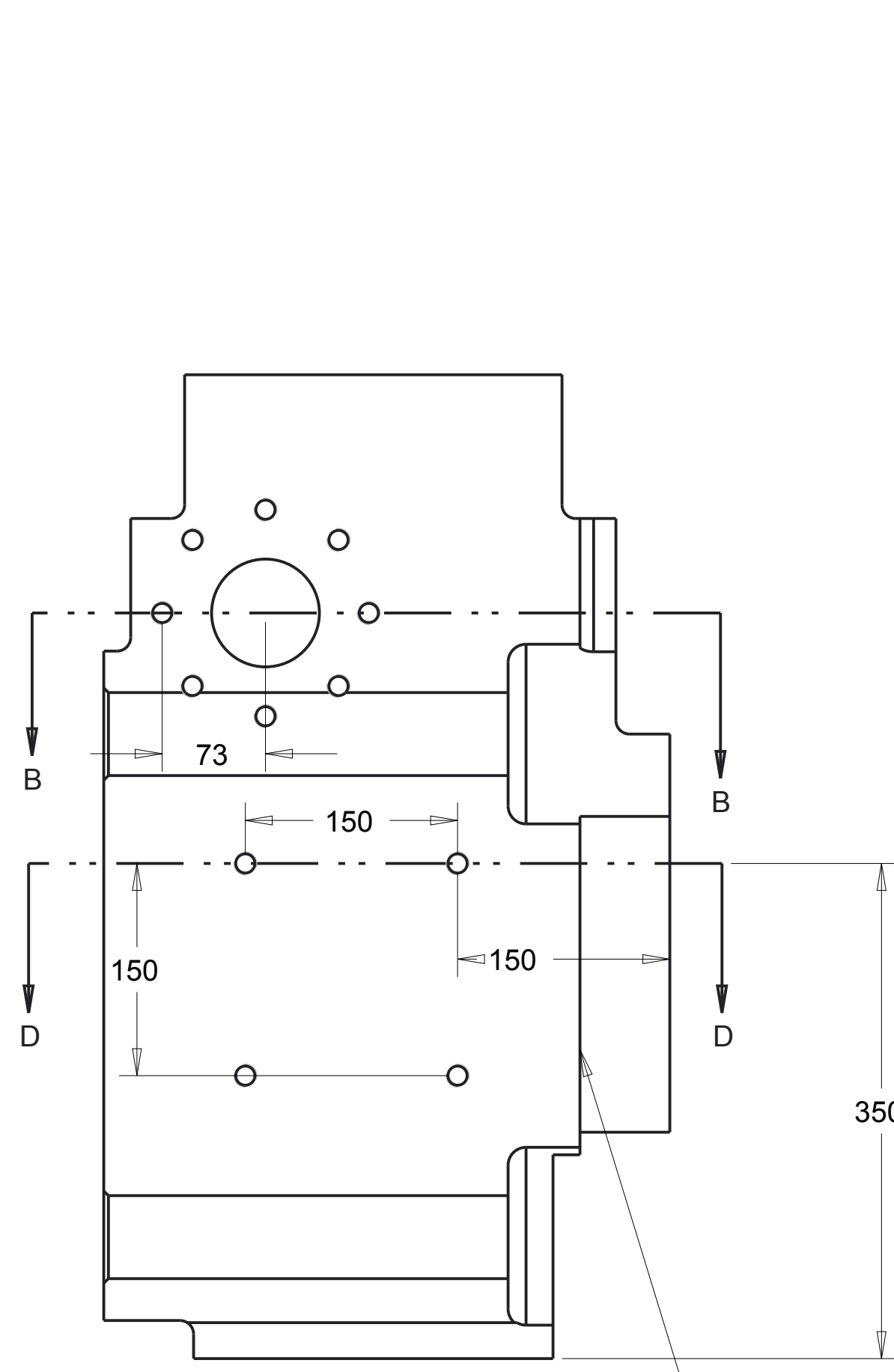
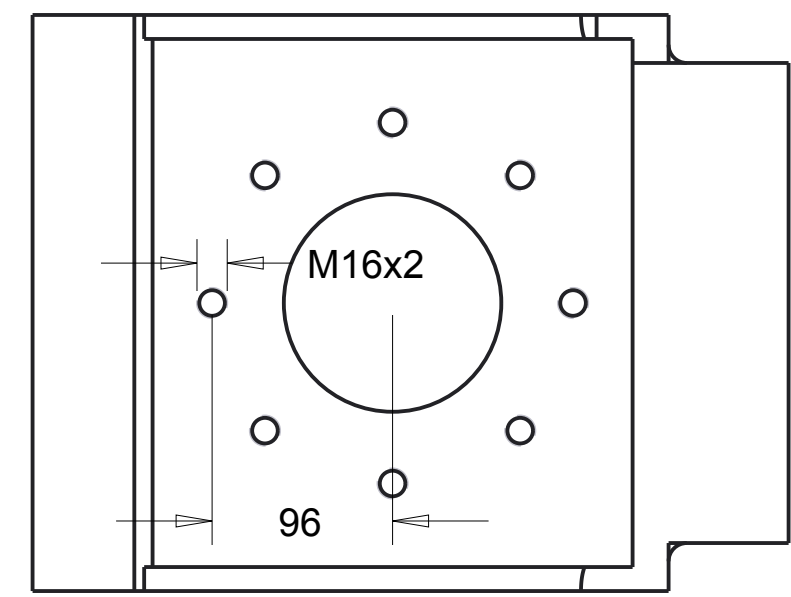


The 001 drawings show the modification needed on the pump assembly:

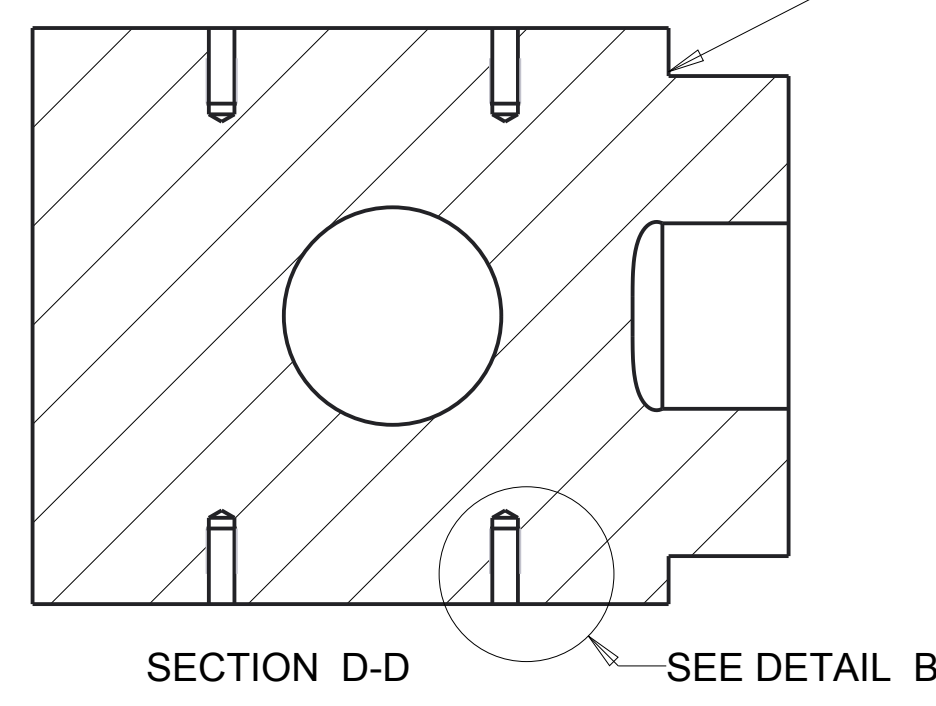
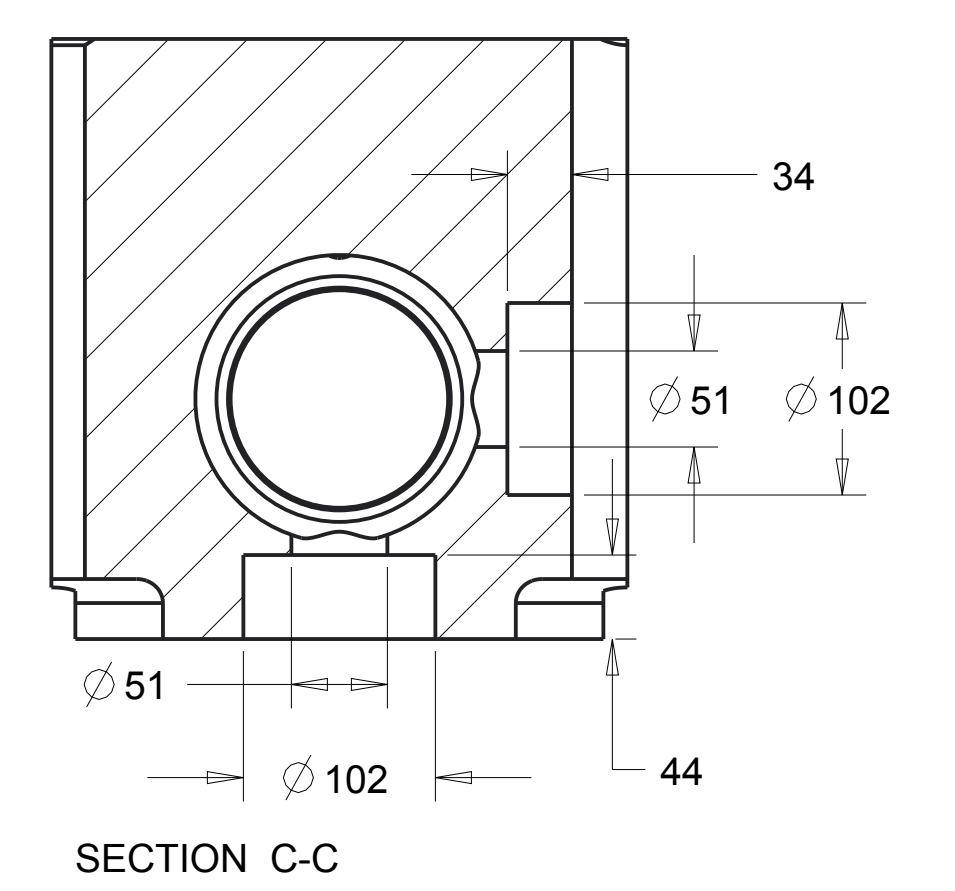
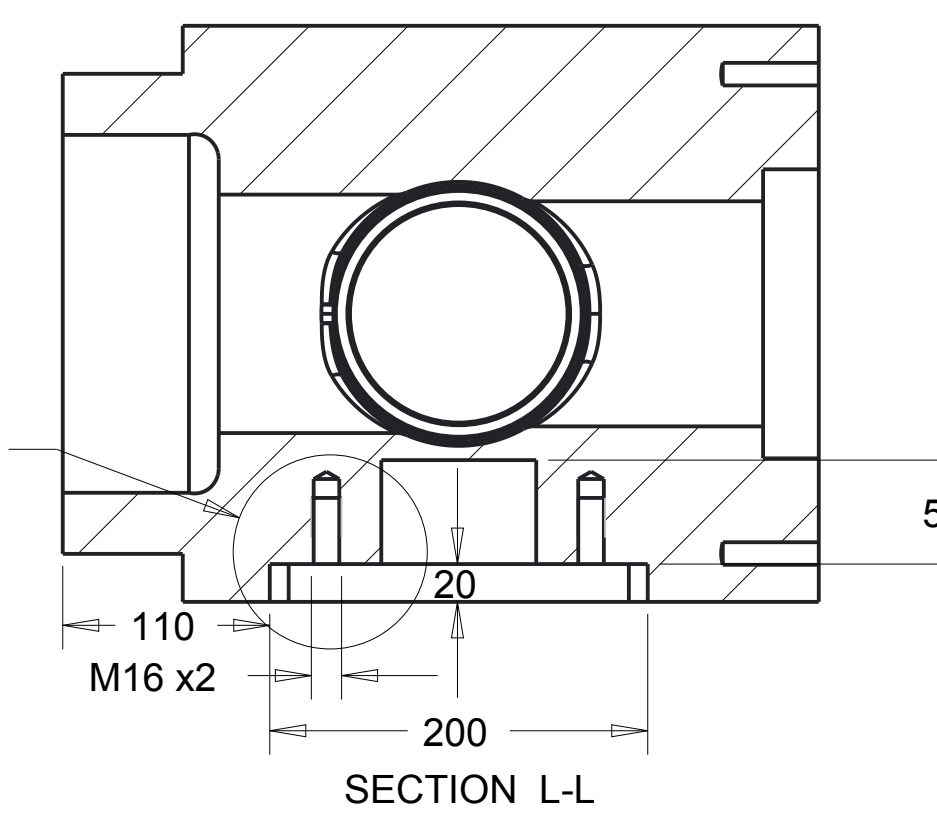
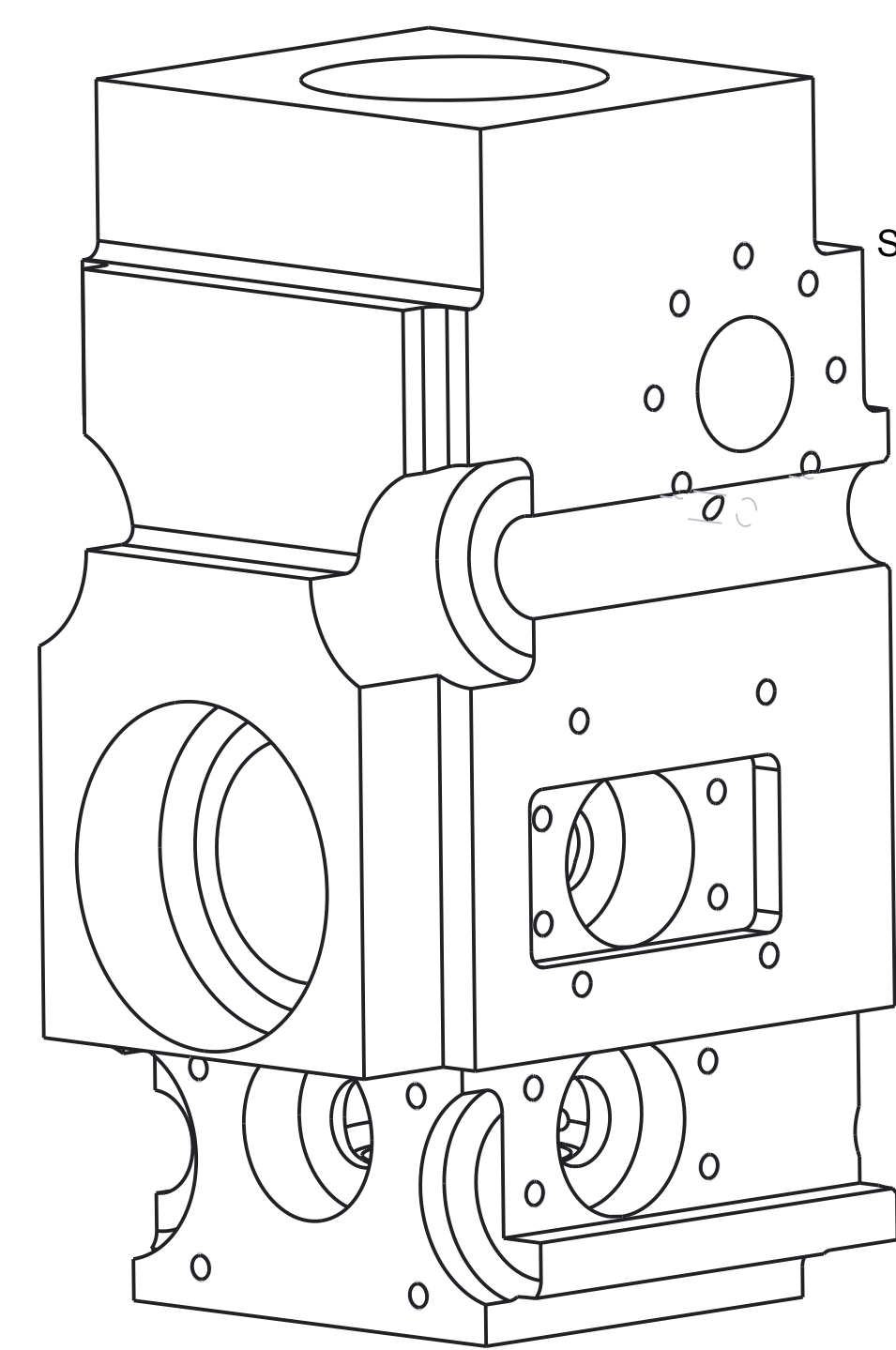
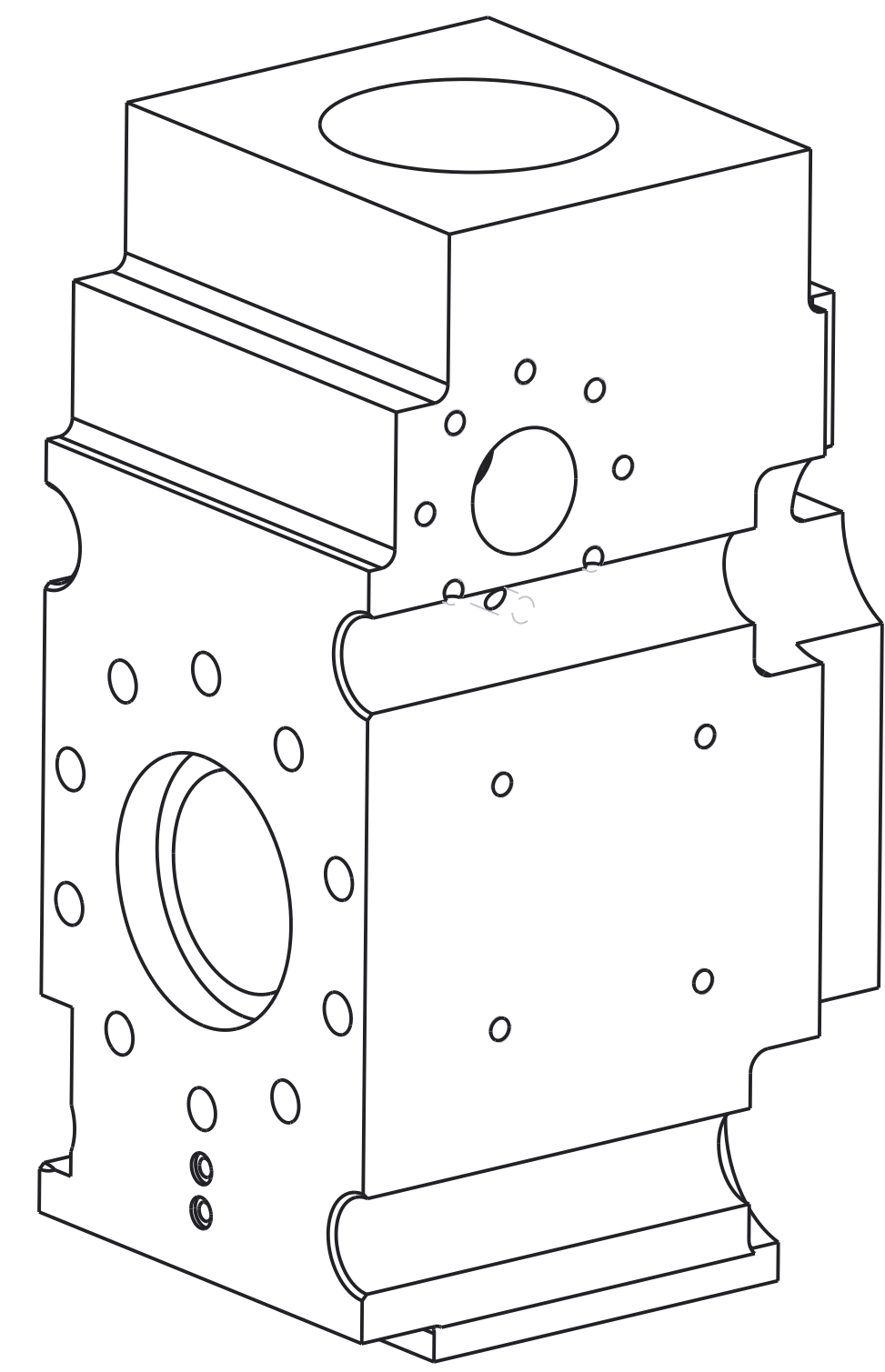
- create 2 transparent windows positioned 90° each other
- position the proximity sensor in the inlet valve seat
- position the pressure transmitter near the Top dead centre position of the plunger
- Close one end of the outlet pipe

N°	Assembly/detail	Drawing	Q.
2	Inlet valve seat	001-03	1
3	Inlet valve retainer	001-06	1
4	Pressure transmitter		2
5	Retainer cap	001-07	1
6	Rubber seal	004-11	6
7	Window	001-10	3
8	Window cover1	001-08	1
9	Window cover2	001-09	1
10	Screw M16x65		16
11	Screw M16x45		12
12	pump external case	001-02	1
13	Window cover 3	001-12	1
14	Chamber drain pipe	001-13	1

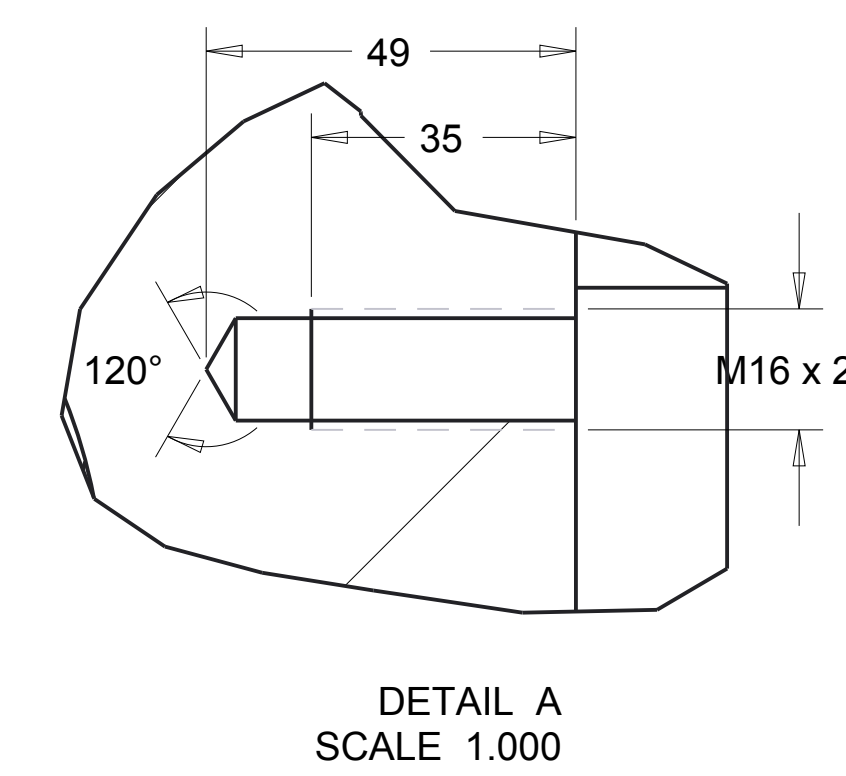
		DRAW: Aldo Iannetti CHECKED: _____ PROJECTE: M. Stickland
QUANTITY: 1 MATERIAL: Standard	MASS: 400 SCALE: 0.250	GENERAL TOLERANCES IN MM UNLESS STATED SIZE TOLERANCE HEAT TREATMENT: None SUPERFICIAL COATING: Paint WEIR SPM Destiny pump
TECHNICAL DEPART: MECH FORMAT: A1 SHEET: 1 N° DRAWING: 001-01	DATA DATE: 25/06/2013	GENERAL TOLERANCES IN MM UNLESS STATED SIZE TOLERANCE HEAT TREATMENT: None SUPERFICIAL COATING: Paint WEIR SPM Destiny pump



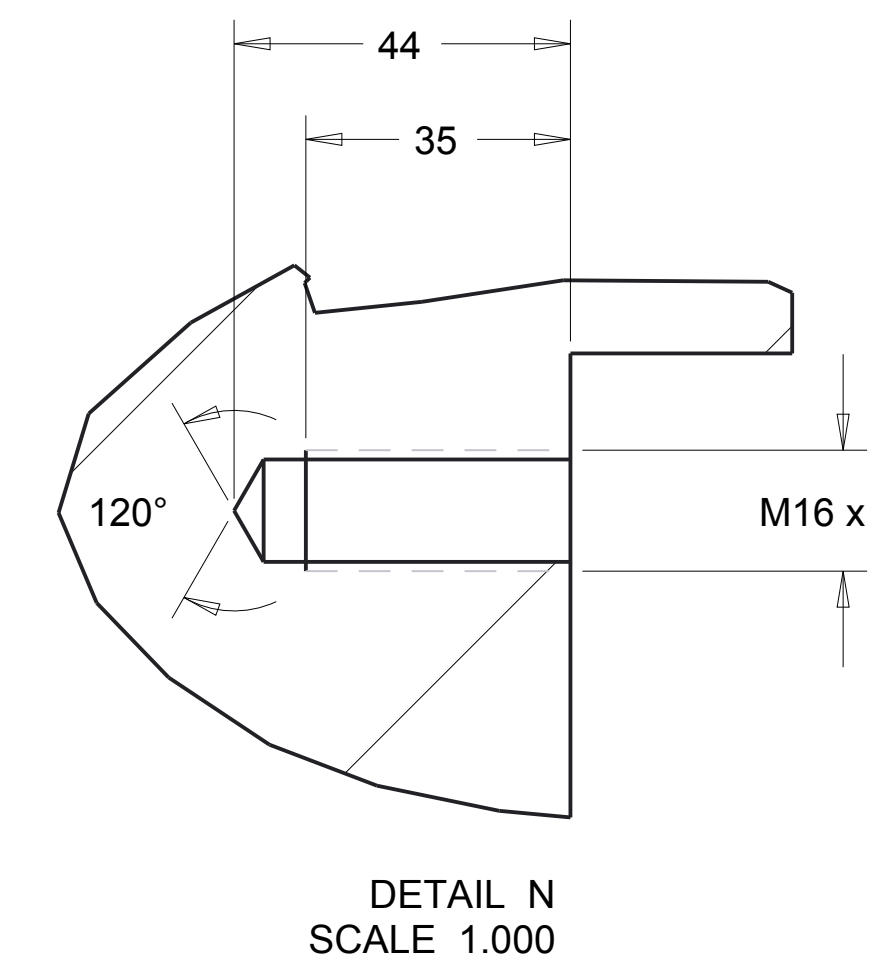
Note: Machine off this round



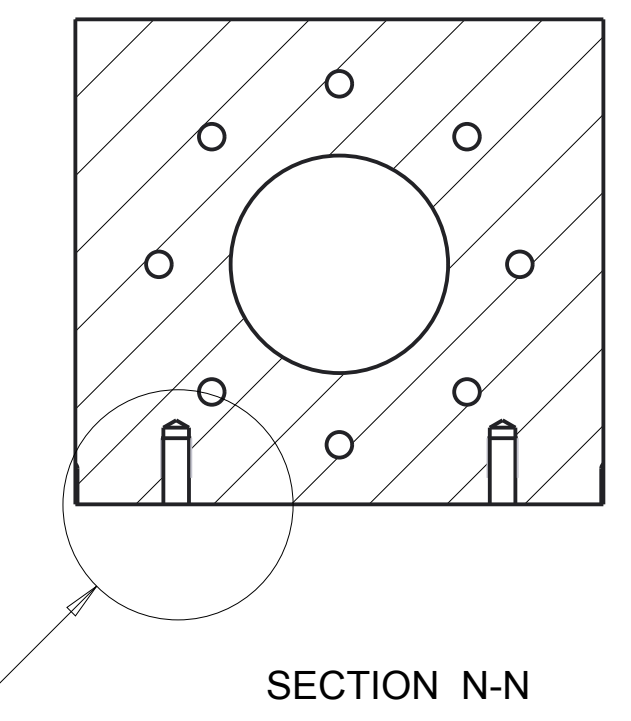
SEE DETAIL B



DETAIL A
SCALE 1.000

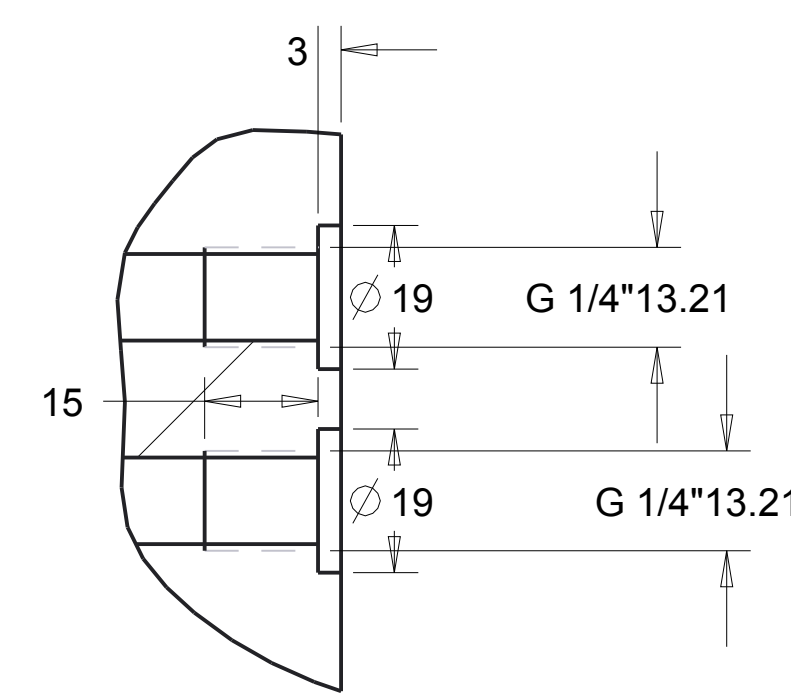


DETAIL N
SCALE 1.000

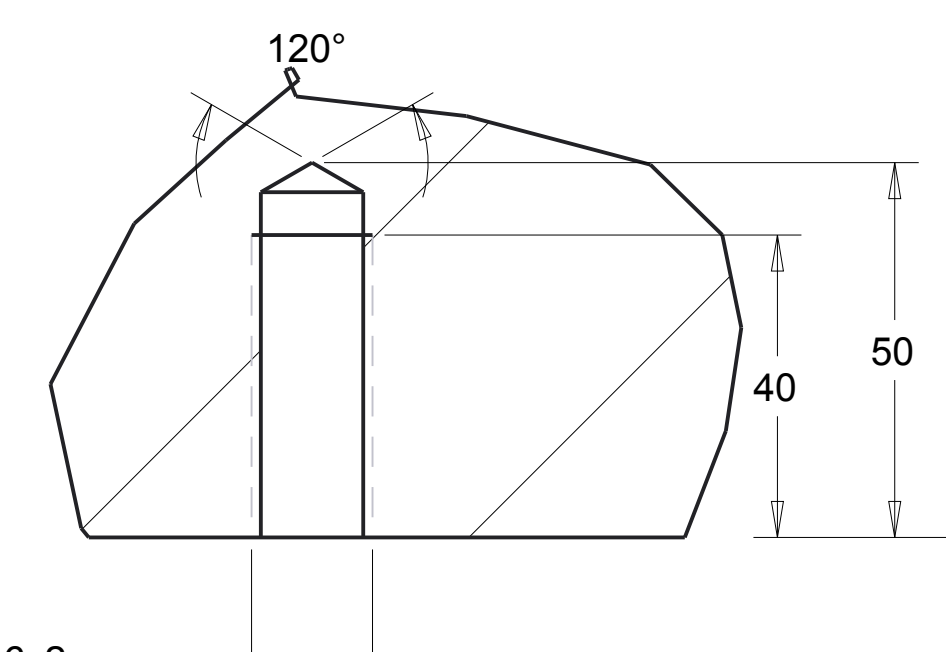


SEE DETAIL F

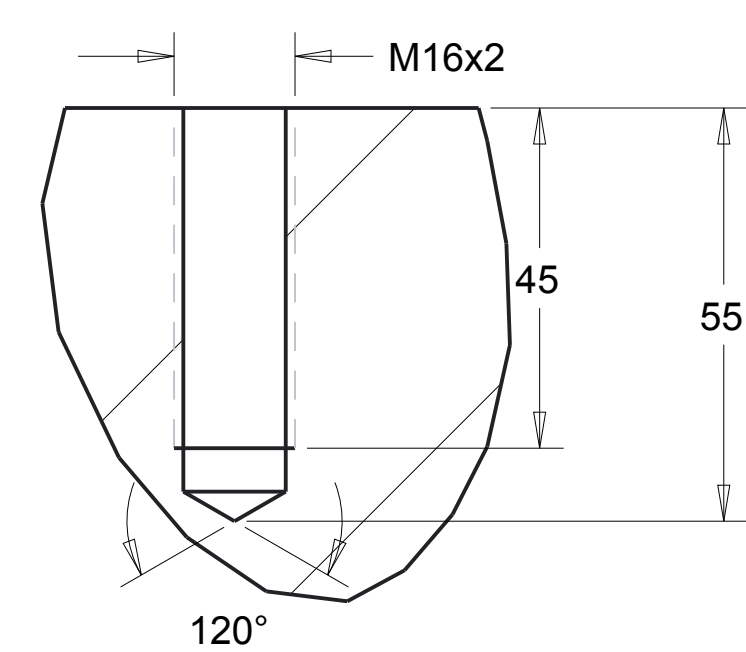
SECTION N-N



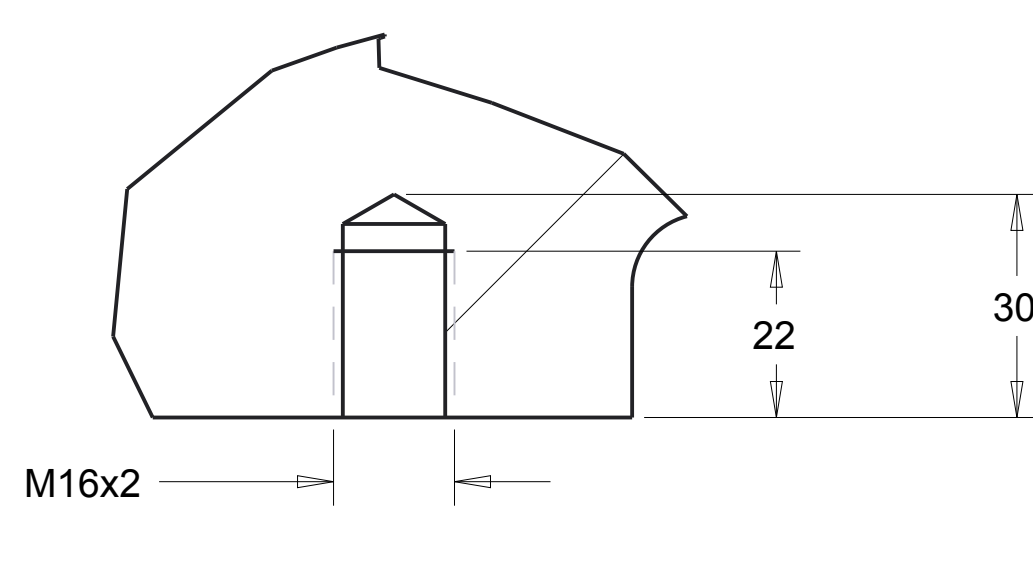
DETAIL E
SCALE 1.000



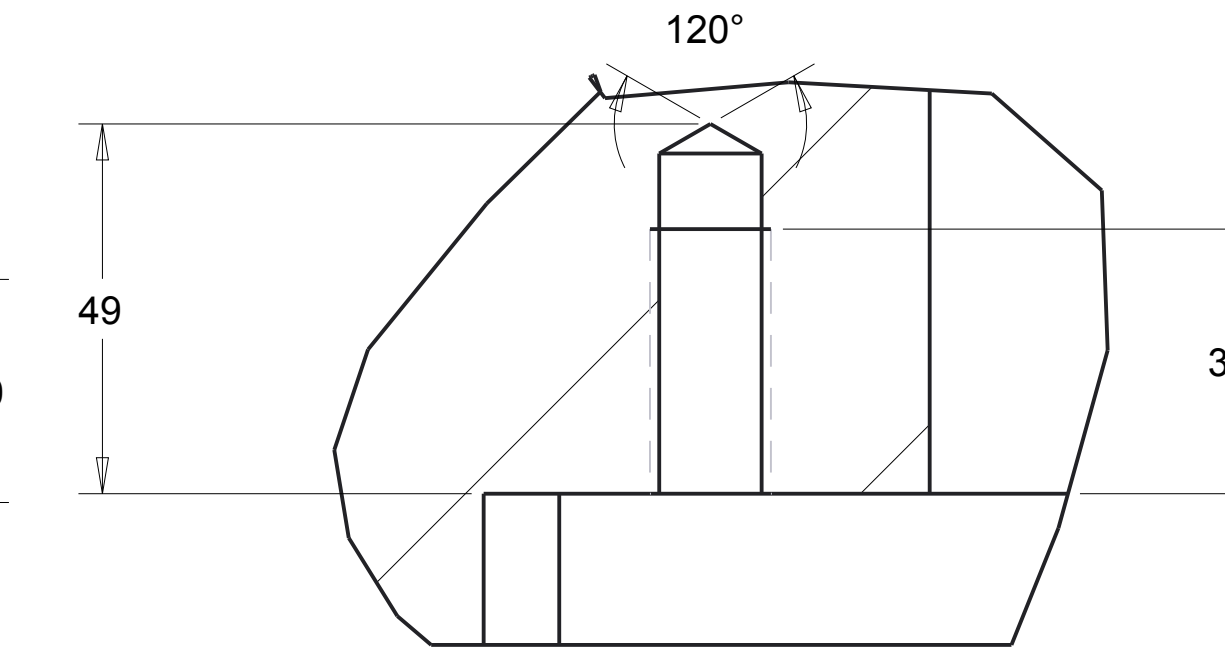
DETAIL B
SCALE 1.000



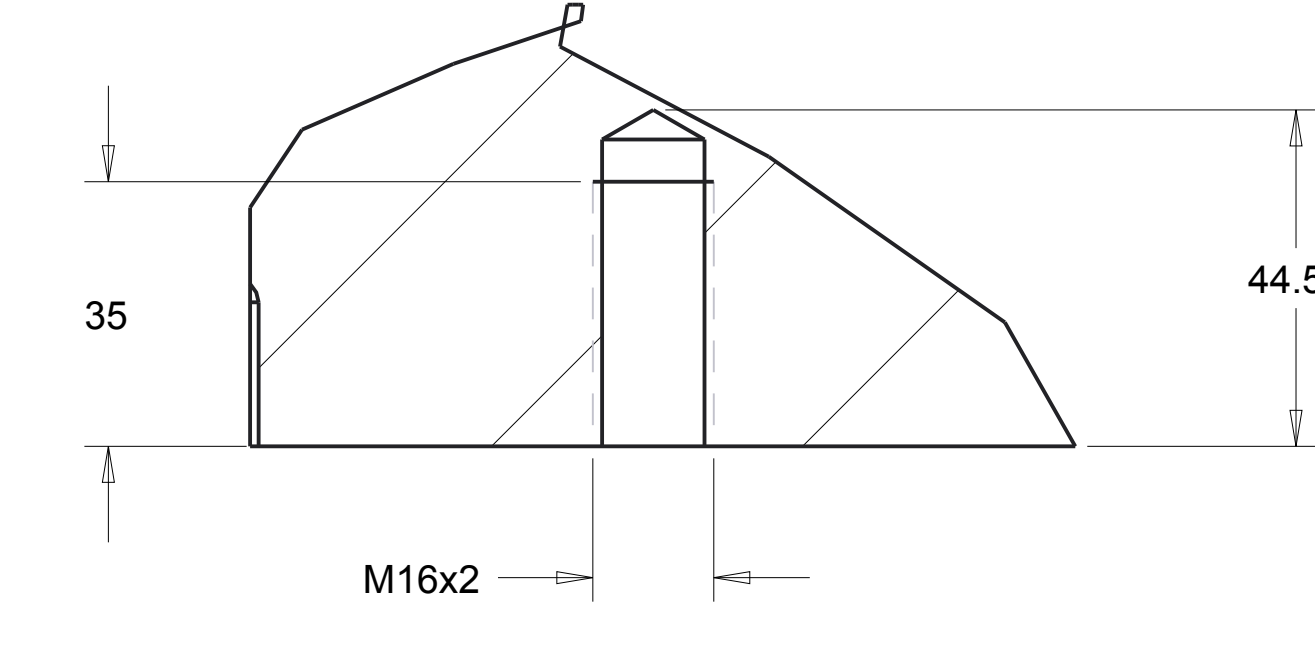
DETAIL C
SCALE 1.000



DETAIL D
SCALE 1.000



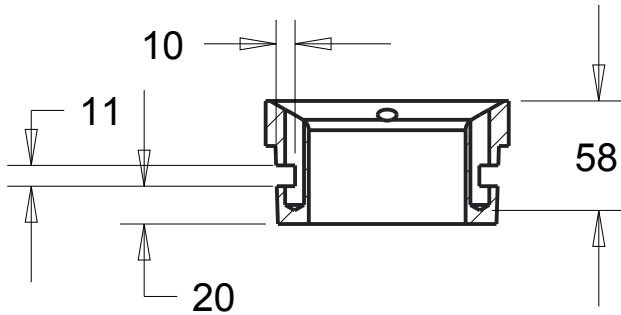
DETAIL K
SCALE 1.000



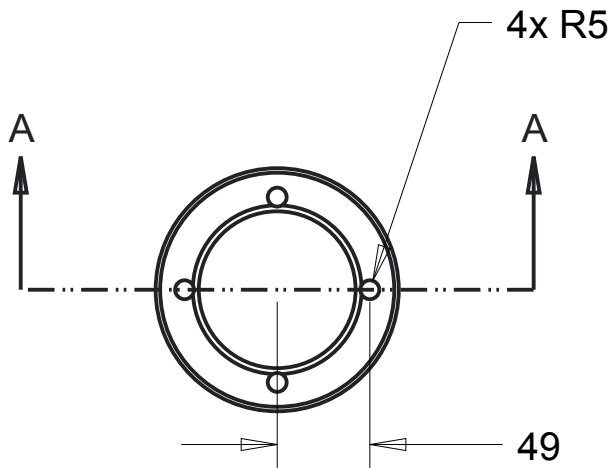
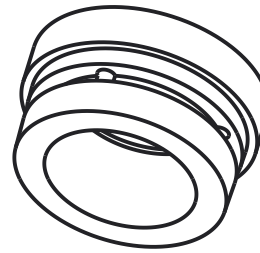
DETAIL F
SCALE 1.000

This drawing shows the modification details only

DO NOT SURVEY DIMENSIONS FROM THE DRAWING			
DESIGNER	Aldo Iannetti	PROJECT	M. Slickland
QUANTITY	1	NO. OF SHEETS	393
SCALE	Standard	DATE	0.250
REVISION		DATE	
APPROVED		DATE	
DATE	25/06/2013	DESCRIPTION	Pump External case
SHEET	2	OF SHEETS	
PROJECT NO.	001-02		



SECTION A-A

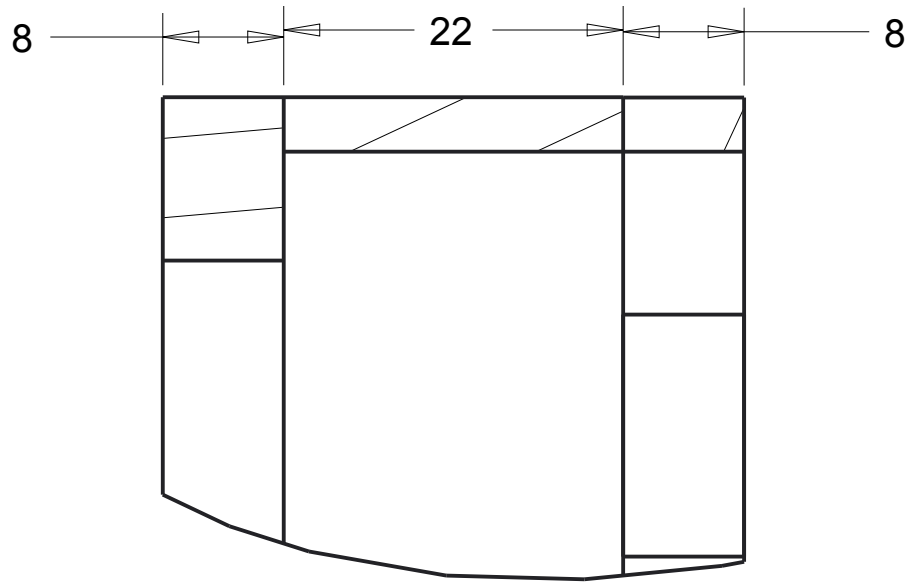
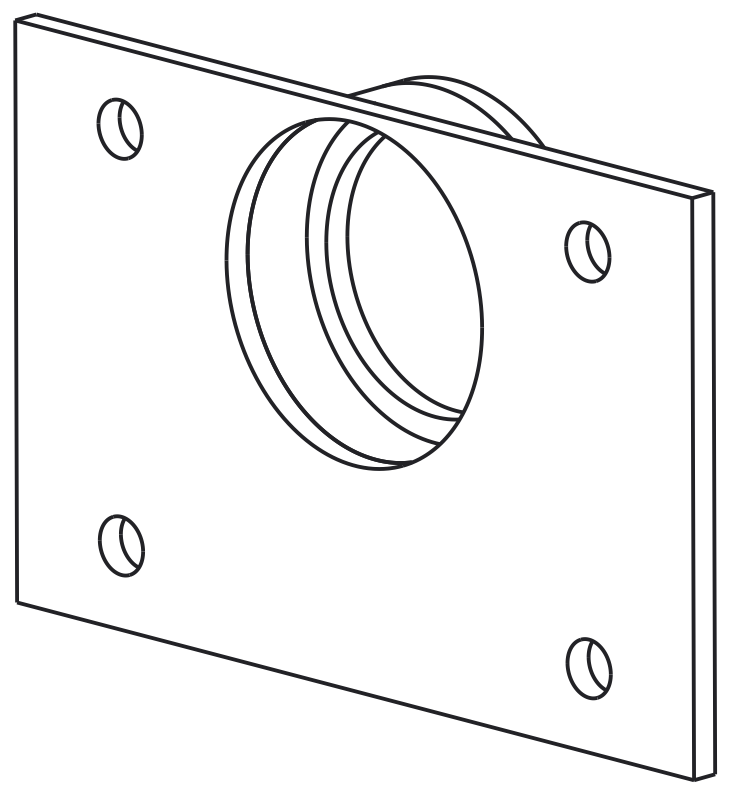
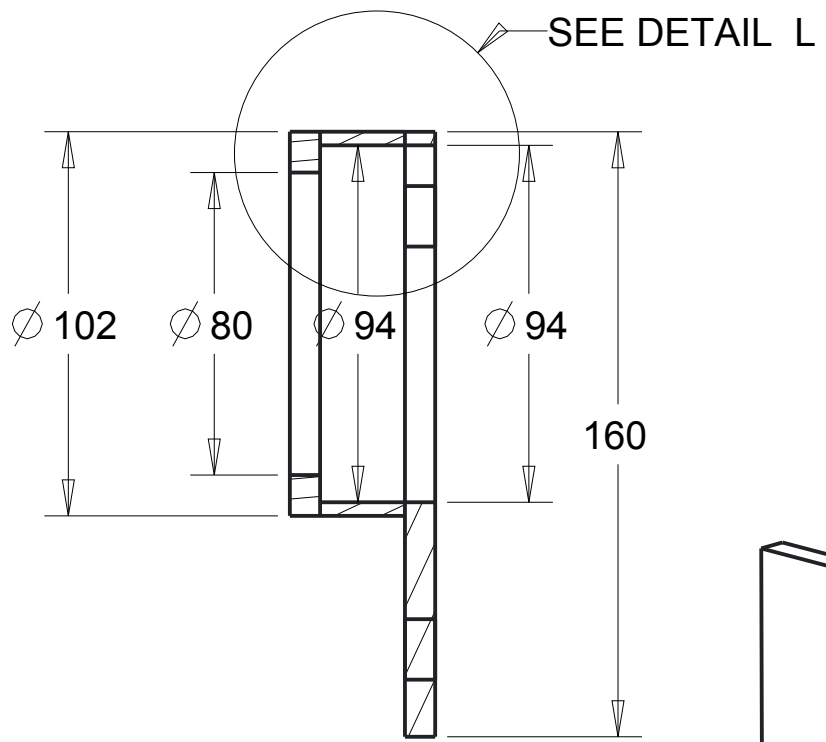
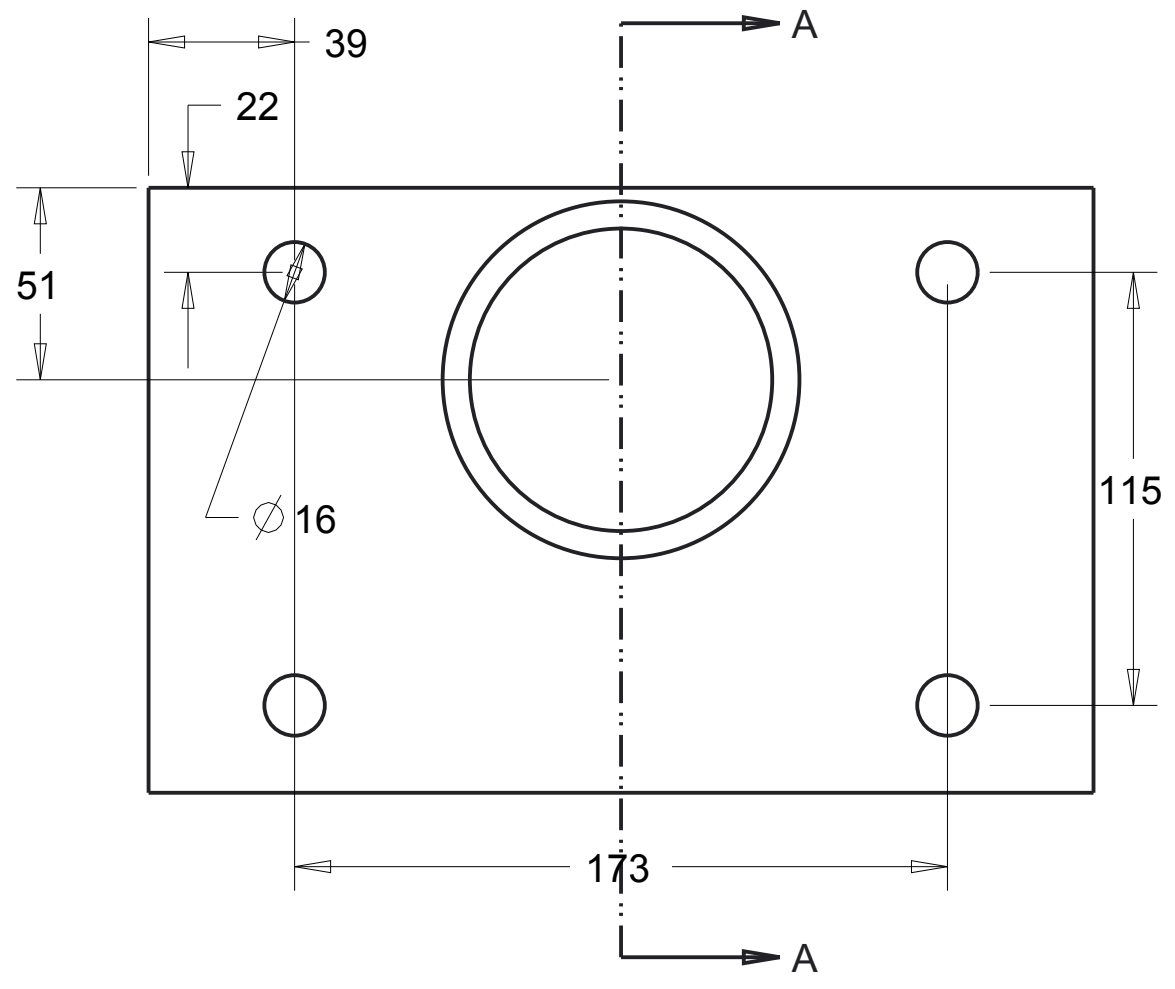


Modification details

REV.	DATE	DESCRIPTION	DESIGN TO DRAW	CONTROL TO CHECKED	VISIT TO PROJECT

DO NOT SURVEY DIMENSIONS FROM THE DRAWING

	DRAW Aldo Iannetti CHECKED	PROJECT E. M.Stickland
	QUANTITY 1 MATERIAL Standard	MASS 2.8 SCALE 0.500
	TYPE BLANK	GENERAL TOLERANCES EN ISO 13920-AE
TECHNICAL DEPART. WARC FORMAT A4 SHEET 3 N° DRAWING 001-03		HEAT TREATMENT None SUPERFICIAL COVERING None DENOMINAT. Inlet valve seat
DATE 25/06/2013	SIZE 2 30 120 400 1000 2000 4000 8000 TOLERANCES ±1 ±20' ±1 ±20' ±1 ±20' ±2 ±15' ±3 ±10' ±4 ±10' ±5 ±10'	



DETAIL L
SCALE 2.000

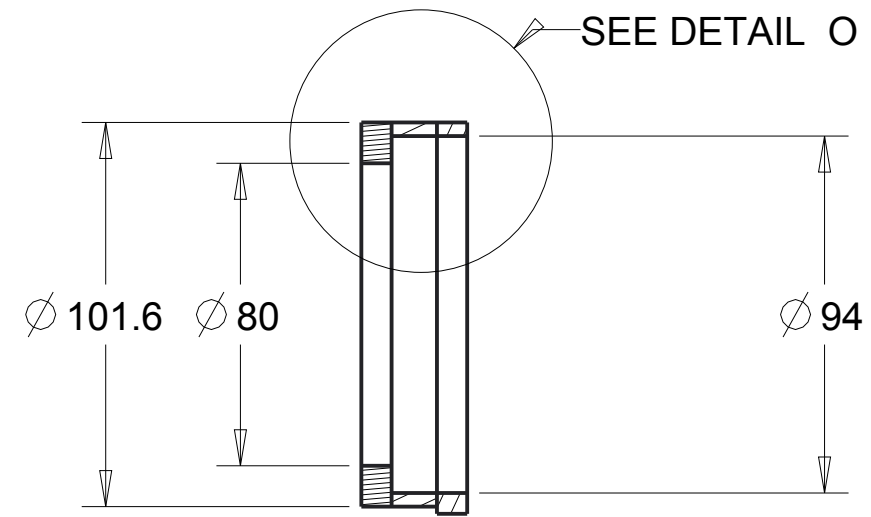
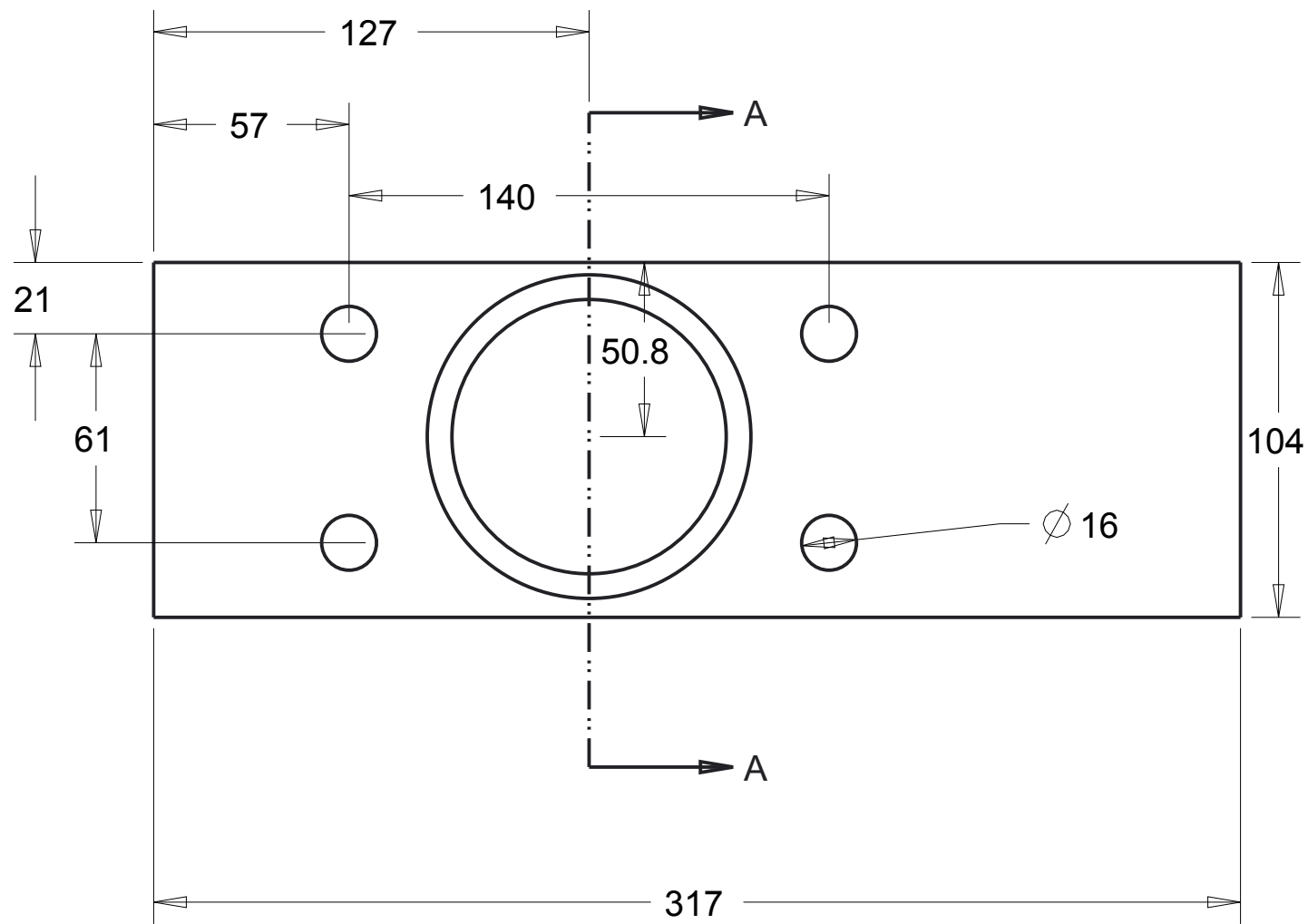
SECTION A-A

SCALE 0.500

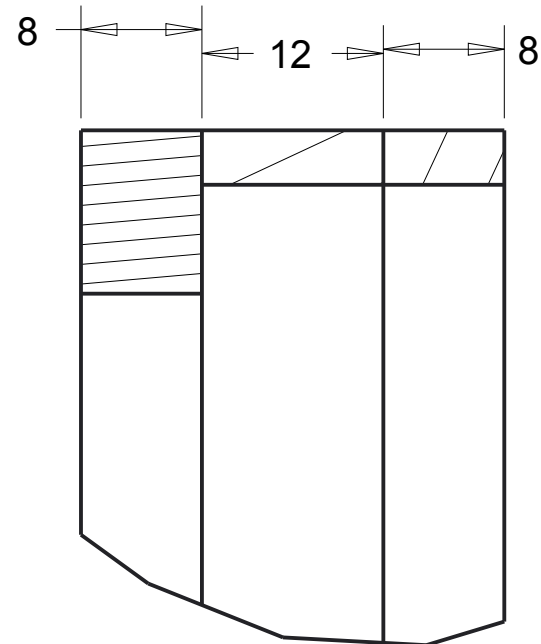
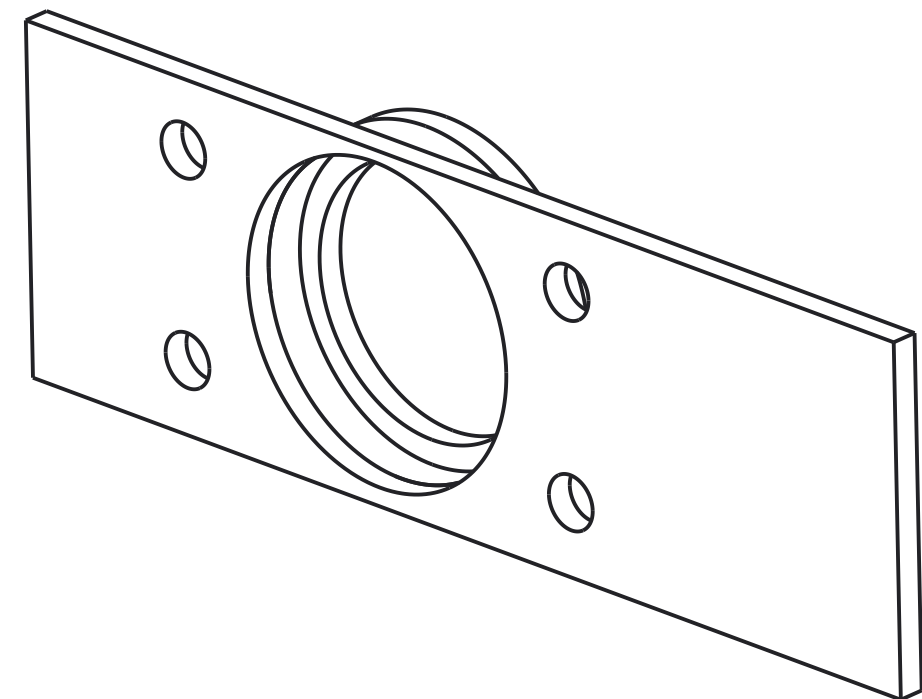
DO NOT SURVEY DIMENSIONS FROM THE DRAWING

<p>Mechanical and Aerospace Engineering Level 4 Lord Hope Building 141 ST James Road G4 0LT Glasgow UK</p> <p>TEL. 01415484851 mae@strath.ac.uk aldo.iannetti@strath.ac.uk</p>	<p>TECHNICAL DEPART. WARC</p>		<p>HEAT TREATMENT</p> <p>None</p>	<p>SIZE</p> <p>2 30 ±1 ±20'</p>
	<p>FORMAT</p> <p>A3</p>	<p>SHEET</p> <p>8</p>	<p>DATE</p> <p>25/06/2013</p>	<p>TOLERANCES</p> <p>30 120 ±1 ±20'</p> <p>120 400 ±1 ±20'</p> <p>400 1000 ±2 ±15'</p> <p>1000 2000 ±3 ±10'</p> <p>2000 4000 ±4 ±10'</p> <p>4000 8000 ±5 ±10'</p>
	<p>N° DRAWING</p> <p>001-08</p>	<p>DRAW</p> <p>Aldo Iannetti</p>	<p>CHECKED</p> <p>MASS</p> <p>3.46</p>	<p>PROJECT E.</p> <p>M. Stickland</p>
	<p>GENERAL TOLERANCES EN ISO 13920-AE</p>	<p>QUANTITY</p> <p>1</p>	<p>SCALE</p> <p>0.5</p>	<p>TOLERANCES</p> <p>None</p>
<p>MATERIAL</p> <p>Carbon steel</p>			<p>TYPE</p> <p>BLANK</p>	<p>DENOMINAT.</p> <p>Window cover1</p>

					PROJECT E.
					CHECKED
					DRAW
					DATE
					REV.



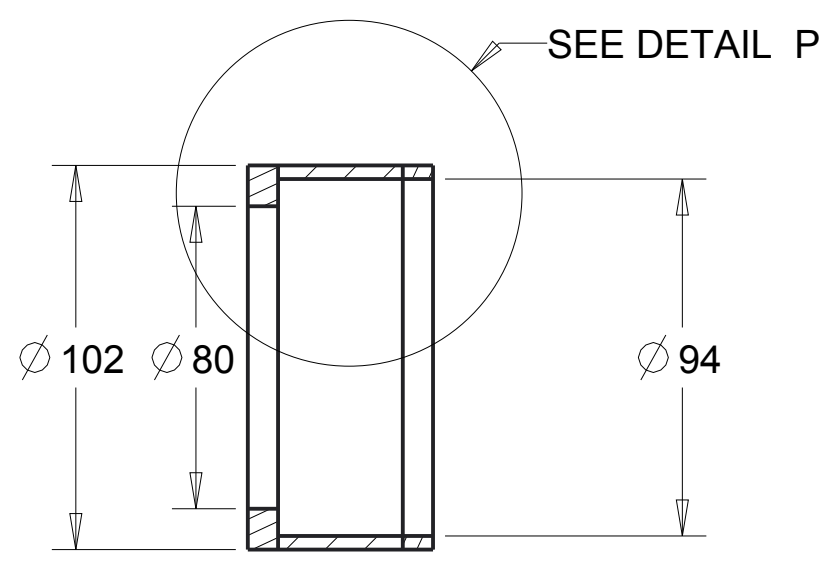
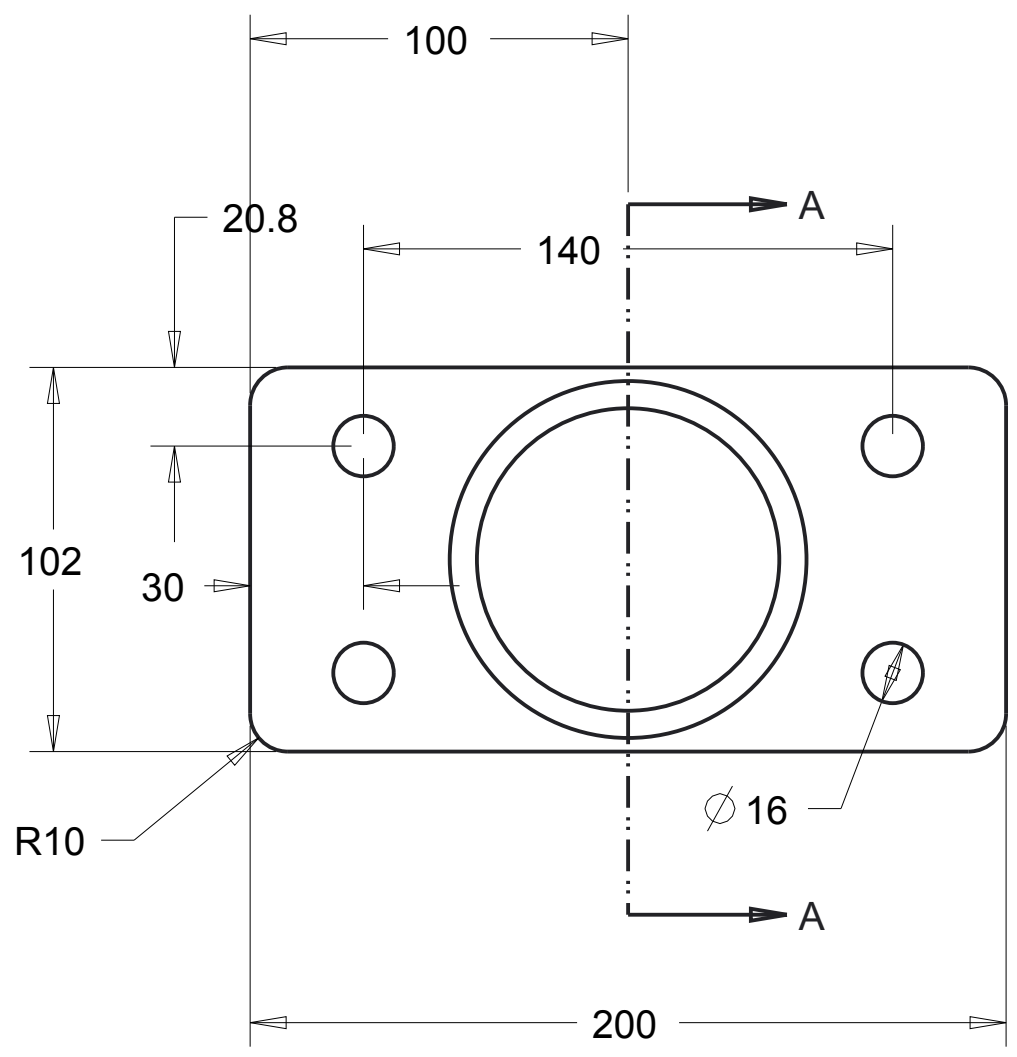
SECTION A-A



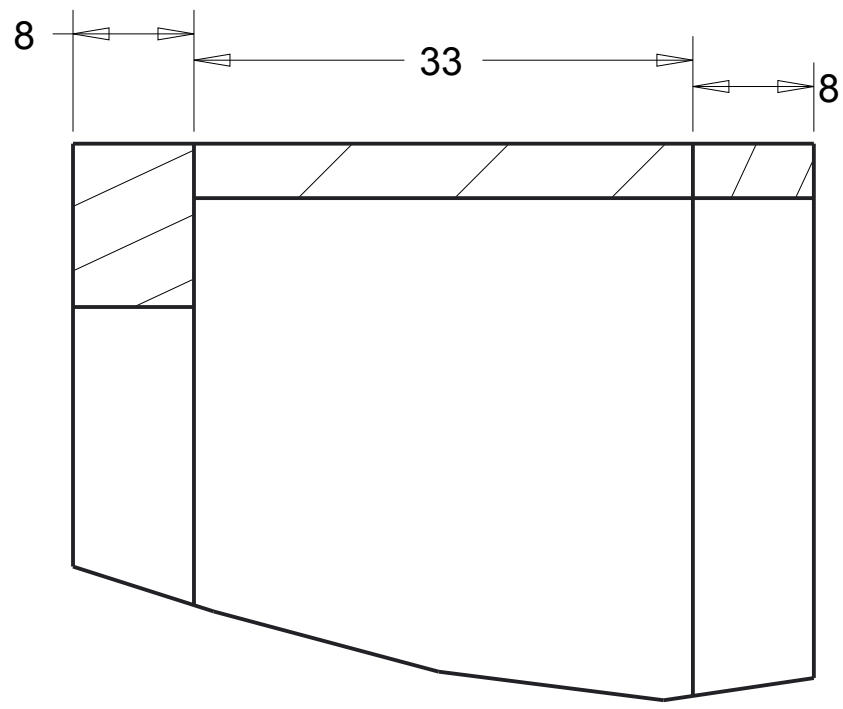
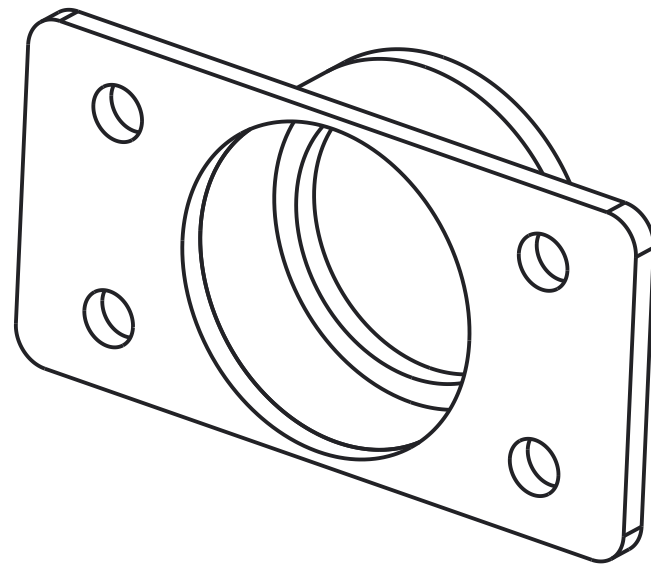
DETAIL O
SCALE 2.000

REV.	DATE	DATE AND MODIFY DESCRIPTION	DRAW	CHECKED	PROJECT E.

DO NOT SURVEY DIMENSIONS FROM THE DRAWING					
<p>Mechanical and Aerospace Engineering Level 4 Lord Hope Building 141 ST James Road G4 0LT Glasgow UK</p> <p>TEL: 01415484851 mae@strath.ac.uk aldo.iannetti@strath.ac.uk</p>	DRAW Aldo Iannetti	CHECKED	PROJECT E. M. Stickland	GENERAL TOLERANCES EN ISO 13920-AE	
	QUANTITY 1	MASS 1.85	SCALE 0.5	SIZE	TOLERANCES
	MATERIAL Carbon steel			TYPE BLANK	<input type="checkbox"/> > <input type="checkbox"/> <= <input type="checkbox"/> <
	TECHNICAL DEPART. WARC	HEAT TREATMENT None	SUPERFICIAL COVERING None	2 30 ±1 ±20'	30 120 ±1 ±20'
FORMAT A3	SHEET 09	DATE 25/06/2013	DENOMINAT. Window Cover 2		120 400 ±1 ±20'
N° DRAWING 001-09	TECHNICAL DEPART. WARC			400 1000 ±2 ±15'	1000 2000 ±3 ±10'
N° DRAWING 001-09			TECHNICAL DEPART. WARC		2000 4000 ±4 ±10'
N° DRAWING 001-09			TECHNICAL DEPART. WARC		4000 8000 ±5 ±10'



SECTION A-A



DETAIL P
SCALE 2.000

				PROJECT E.
				CHECKED
				DRAW
DATE AND MODIFY DESCRIPTION				
				DATE
				REV.

DO NOT SURVEY DIMENSIONS FROM THE DRAWING																						
 Mechanical and Aerospace Engineering Level 4 Lord Hope Building 141 ST James Road G4 0LT Glasgow UK TEL. 01415484851 mae@strath.ac.uk aldo.iannetti@strath.ac.uk	DRAW	A. Iannetti	CHECKED	M. Stickland																		
	QUANTITY	1	MASS	1.54																		
	MATERIAL	Carbon steel																				
	TYPE	BLANK																				
TECHNICAL DEPART. WARC	HEAT TREATMENT			None																		
FORMAT	A3	SUPERFICIAL COVERING			None																	
SHEET	12	DATE	25/06/2013	GENERAL TOLERANCES EN ISO 13920-AE <table border="1"> <tr> <th>SIZE</th> <th>TOLERANCES</th> </tr> <tr> <td>2</td> <td>± 20'</td> </tr> <tr> <td>30</td> <td>± 1</td> </tr> <tr> <td>120</td> <td>± 20'</td> </tr> <tr> <td>400</td> <td>± 15'</td> </tr> <tr> <td>1000</td> <td>± 3</td> </tr> <tr> <td>2000</td> <td>± 10'</td> </tr> <tr> <td>4000</td> <td>± 4</td> </tr> <tr> <td>8000</td> <td>± 10'</td> </tr> </table>	SIZE	TOLERANCES	2	± 20'	30	± 1	120	± 20'	400	± 15'	1000	± 3	2000	± 10'	4000	± 4	8000	± 10'
SIZE	TOLERANCES																					
2	± 20'																					
30	± 1																					
120	± 20'																					
400	± 15'																					
1000	± 3																					
2000	± 10'																					
4000	± 4																					
8000	± 10'																					
N° DRAWING	001-12																					
DENOMINAT. Window Cover 3																						

D

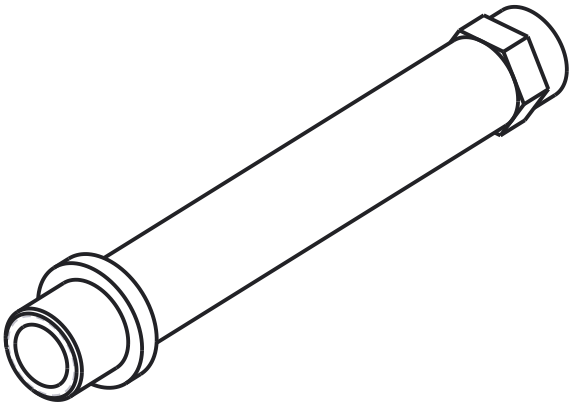
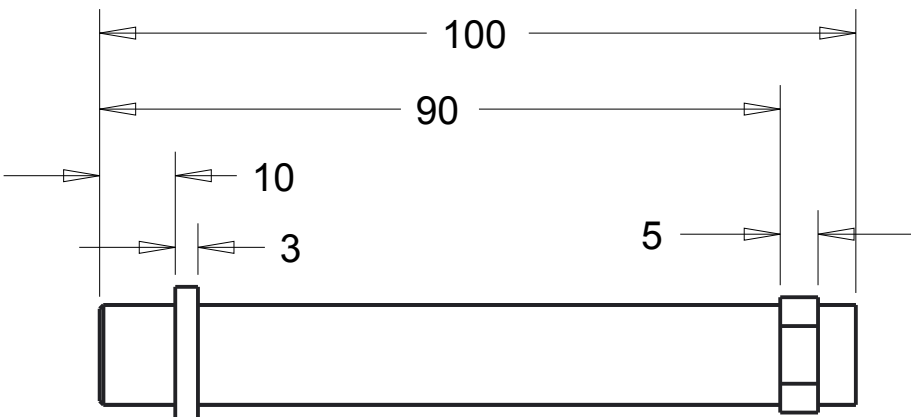
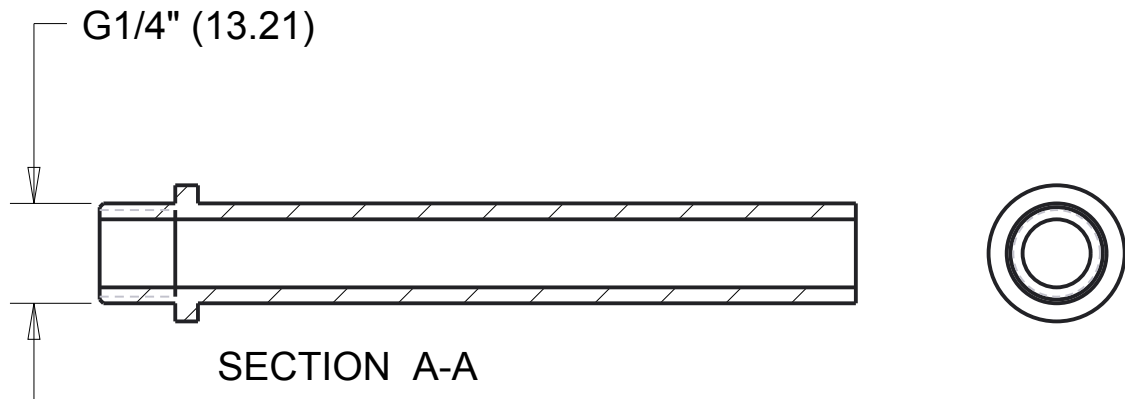
D

C

C

B

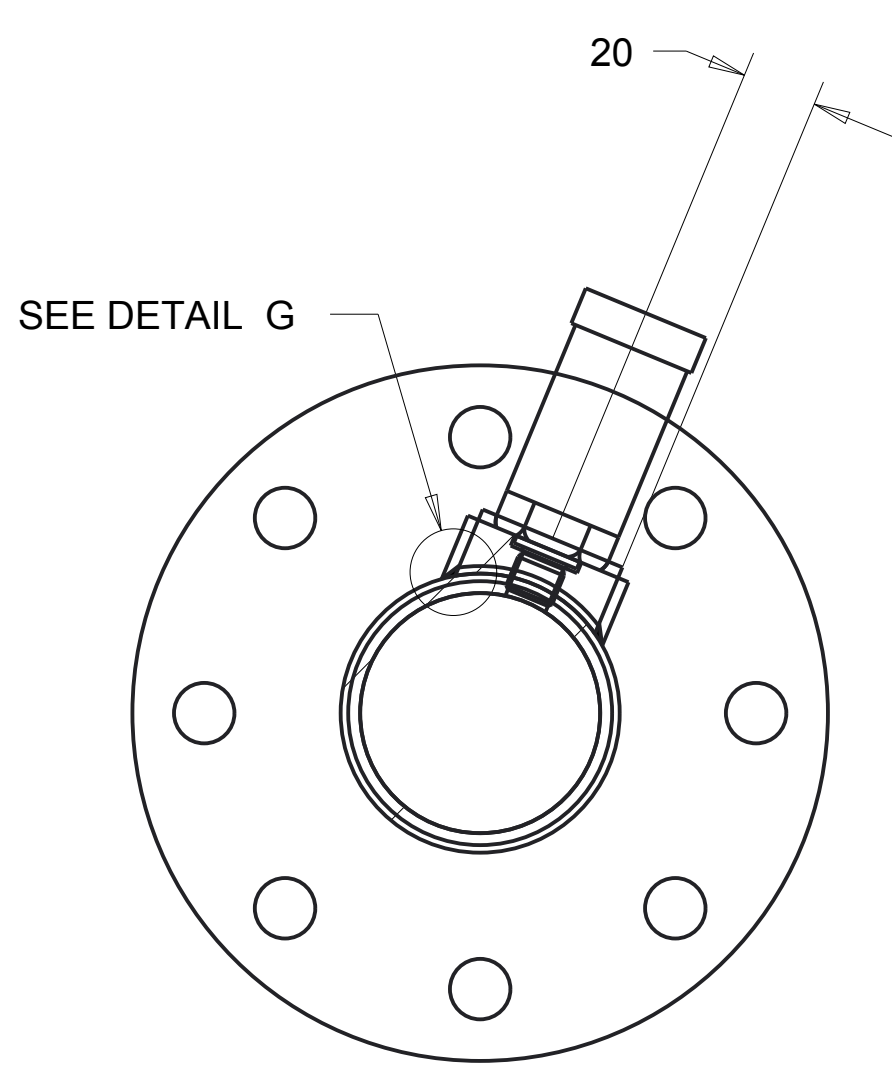
B



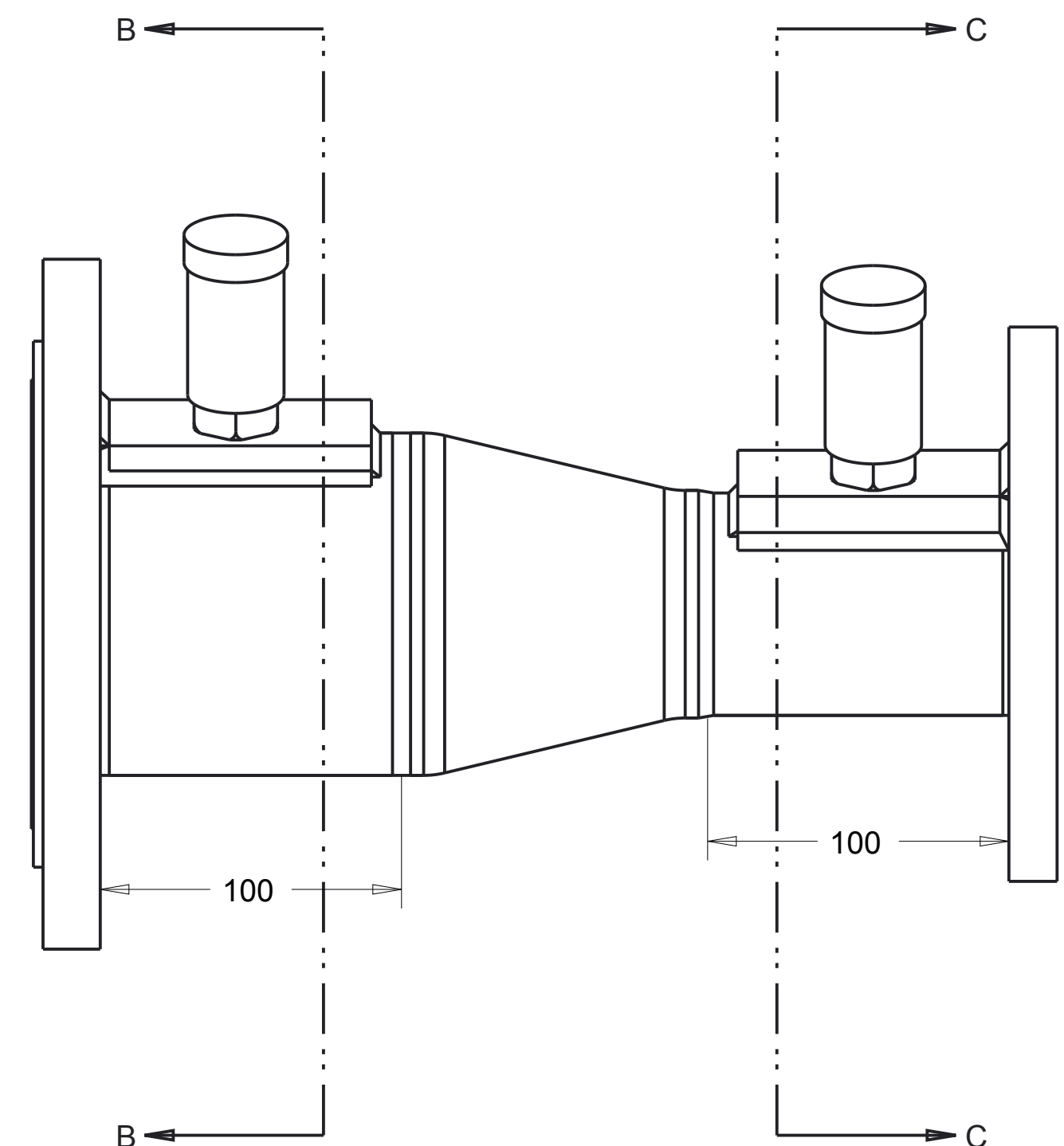
					PROJECTE.
					CHECKED
					DRAW
DATE AND MODIFY DESCRIPTION					
					DATE
					REV.

DO NOT SURVEY DIMENSIONS FROM THE DRAWING

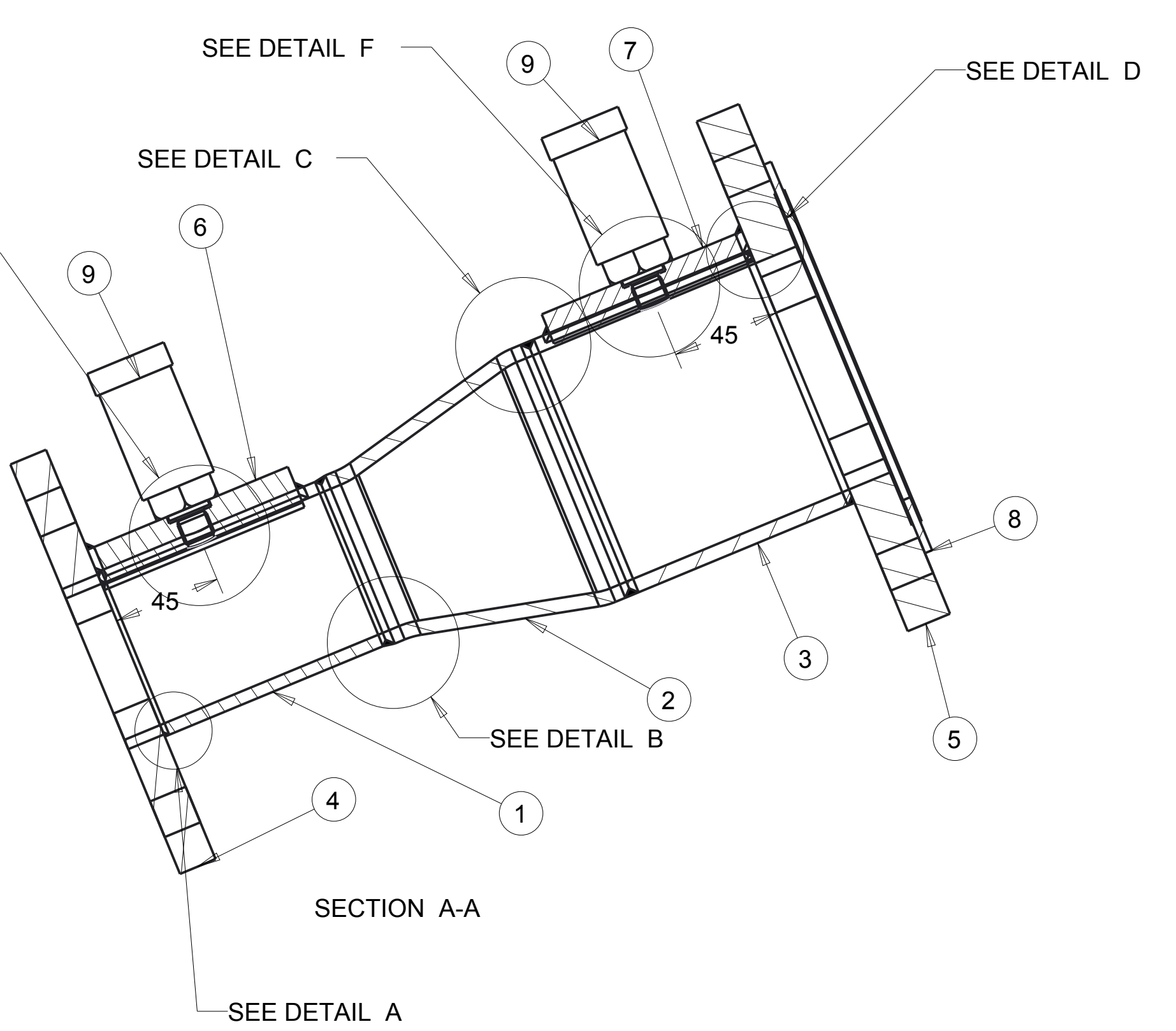
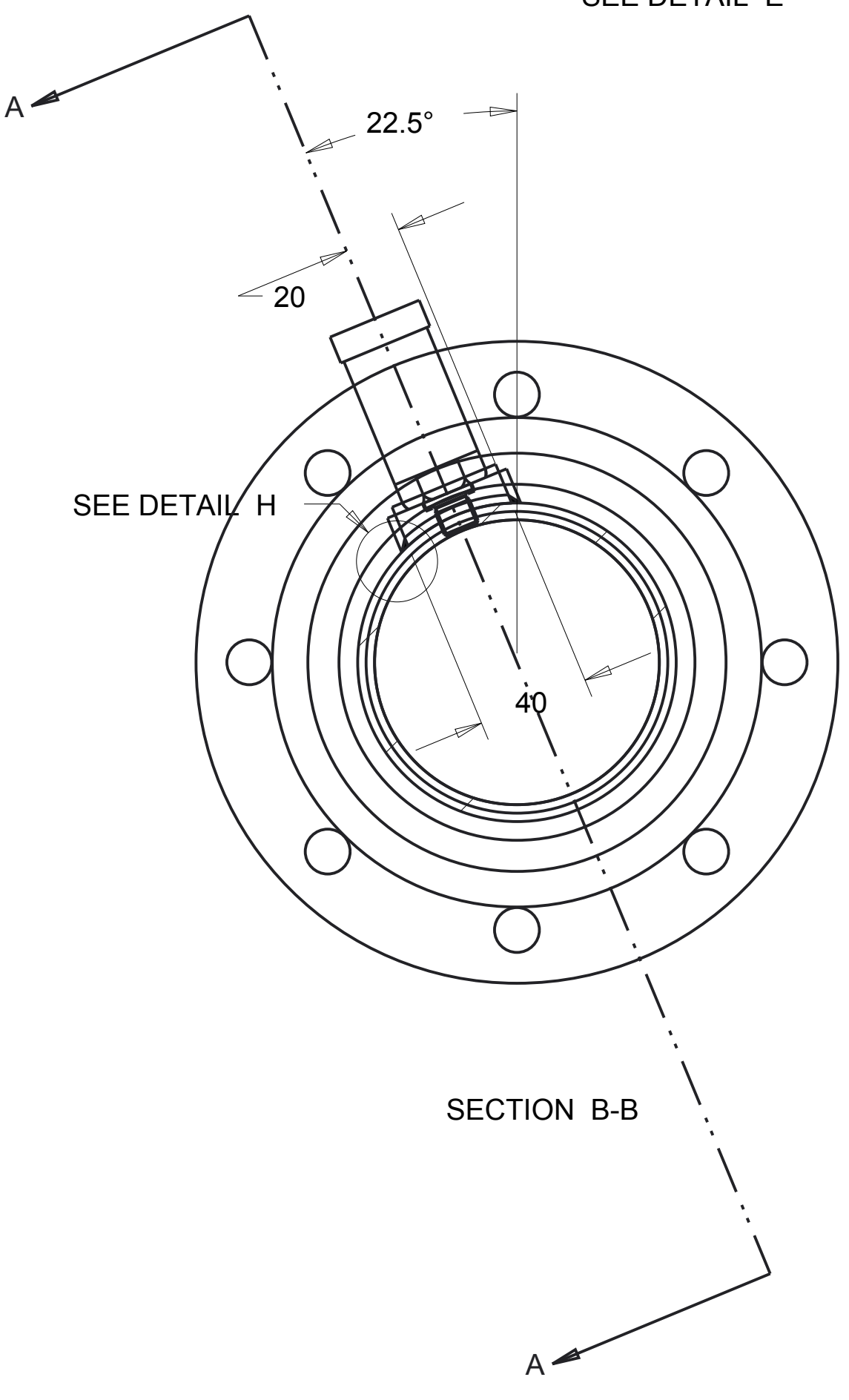
		DRAW A. IAnnetti	CHECKED	PROJECT E. M.Stickland
		QUANTITY 1	MASS 0.06	SCALE 1
MATERIAL Carbon steel		GENERAL TOLERANCES EN ISO 13920-AE		
Mechanical and Aerospace Engineering Level 4 Lord Hope Building 141 ST James Road G4 0LT Glasgow UK	TEL.01415484851 maeATstrath.ac.uk aldo.iannettiATstrath.ac.uk	TYPE BLANK	SIZE TOLERANCES	
TECHNICAL DEPART. WARC		HEAT TREATMENT None	<input type="checkbox"/> >	<input type="checkbox"/> <=
FORMAT A4		SUPERFICIAL COVERING None	2 30 ±1 ±20'	30 120 ±1 ±20'
SHEET 13	DATE 25/06/2013	DENOMINAT. Chamber drain pipe	120 400 ±1 ±20'	400 1000 ±2 ±15'
N° DRAWING 001-13			400 2000 ±3 ±10'	2000 4000 ±4 ±10'
			4000 8000 ±5 ±10'	



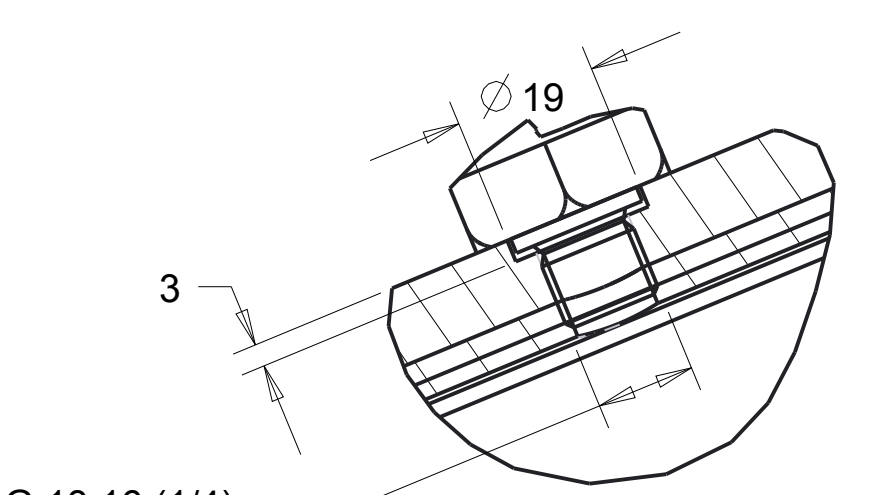
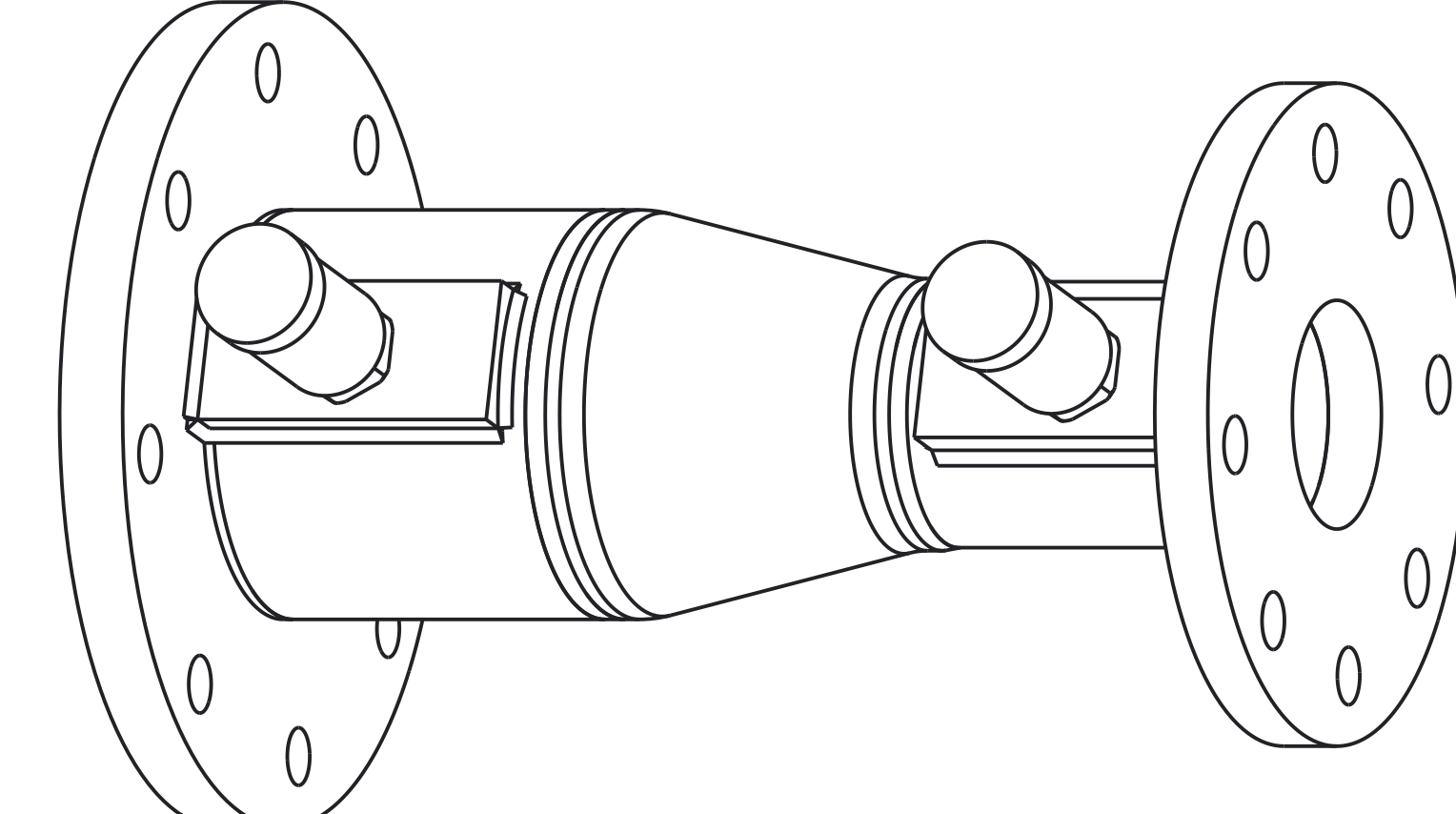
SECTION C-C



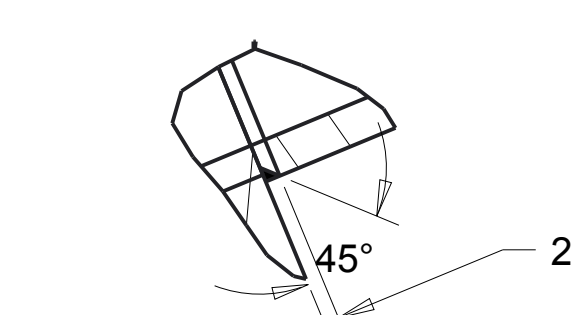
SECTION B-B



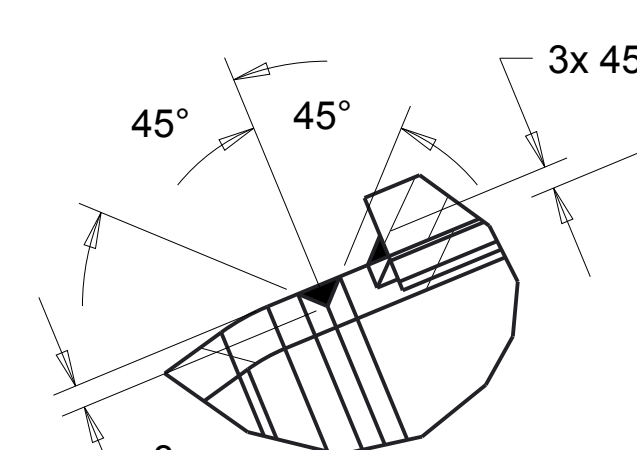
SECTION A-A



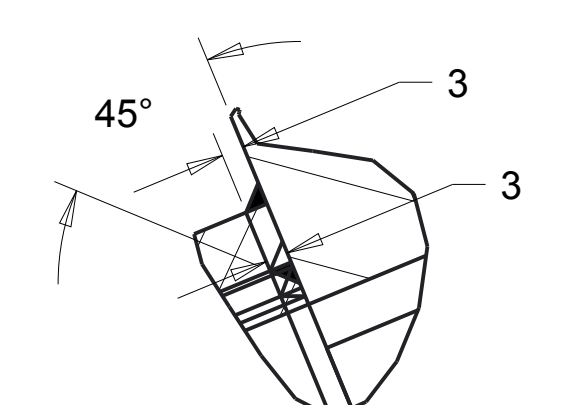
DETAIL E
SCALE 1.000



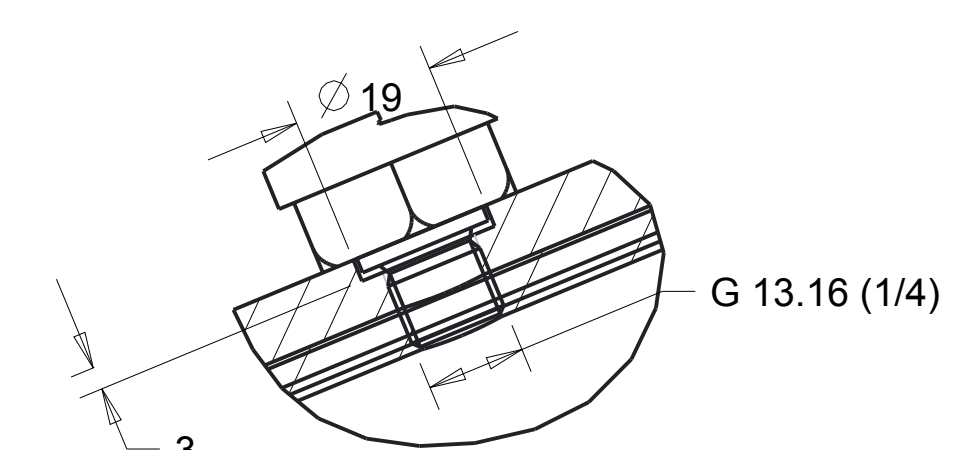
DETAIL A
SCALE 1.000



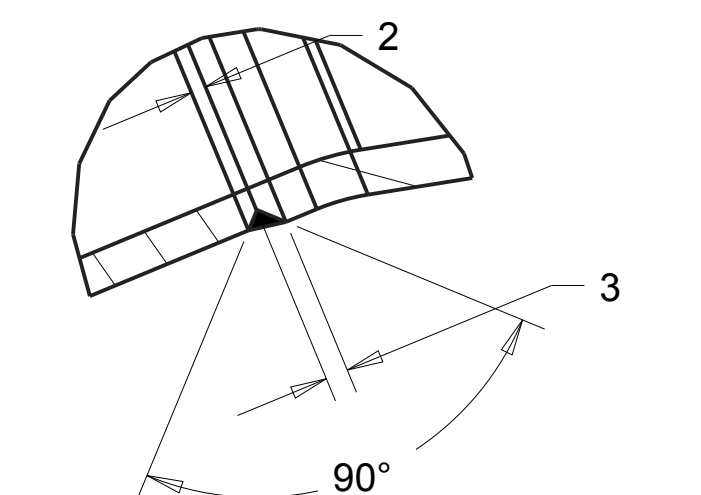
DETAIL C
SCALE 1.000



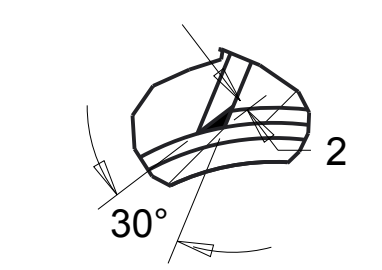
DETAIL D
SCALE 1.000



DETAIL F
SCALE 1.000



DETAIL B
SCALE 1.000



DETAIL G
SCALE 1.000



DETAIL H
SCALE 1.000

N°	Assembly/detail	Drawing	Q.
1	pipe 2" 1/2 Std BS 1387		1
2	concentric reducer 2" 1/2 x 4" BS1640 Std		1
3	pipe 4" Std BS 1387		1
4	flat flange 2" 1/2 BS 10 Tab F		1
5	flat flange 4" BS 10 Tab F		1
6	plate base 2" 1/2 pipe	002-02	1
7	plate base 4" pipe	002-03	1
8	Spiral wound Gasket type CG 4"		1
9	Piezoresistive pressure transmitter 0-0.25 bar		2

DO NOT SURVEY DIMENSIONS FROM THE DRAWING

		DRAW: Aldo Iannetti CHECKED: _____ PROJECT E: M. Stickland
QUANTITY: 1	MASS: 12.11	SCALE: 0.500
MATERIAL: standard		GENERAL TOLERANCES EN ISO 12801-A1
TECHNICAL DEPART: WAVEC	HEAT TREATMENT: None	SIZE TOLERANCE
FORMAT: A1	SUPERFICIAL COVERING: paint	2 30 ±0.1
SHEET: 1	DATE: 25/06/2013	30 120 ±0.1
N° DRAWING: 002-01		400 1000 ±0.2
		1000 2000 ±0.3
		2000 4000 ±0.4
		4000 8000 ±0.5

3

2

1

D

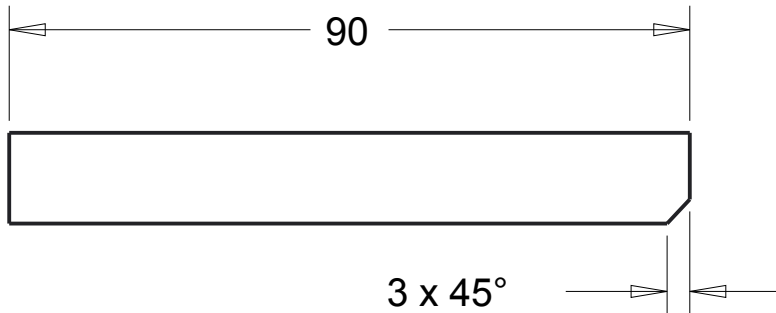
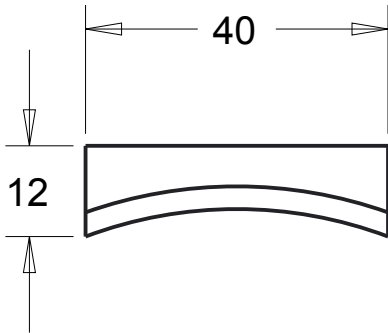
D

C

C

B

B



REV.	DATE	DATE AND MODIFY DESCRIPTION	DRAW	CHECKED	PROJECTE.

DO NOT SURVEY DIMENSIONS FROM THE DRAWING

	DRAW Aldo Iannetti	CHECKED	PROJECT E. M.Stickland
	QUANTITY 1	MASS 0.267	SCALE 1.000
MATERIAL carbon steel			GENERAL TOLERANCES EN ISO 13920-AE
Mechanical and Aerospace Engineering Level 4 Lord Hope Building 141 ST James Road G4 0LT Glasgow UK TEL 01415484851 maeATstrath.ac.uk aldo.iannettiATstrath.ac.uk	TYPE BLANK	SIZE TOLERANCES	
TECHNICAL DEPART. WARC		HEAT TREATMENT None	<input type="checkbox"/> > <input type="checkbox"/> <= <input type="checkbox"/> - <input type="checkbox"/> <
FORMAT A4	SHEET 2	DATE 25/06/2013	2 30 ±1 ±20' 30 120 ±1 ±20' 120 400 ±1 ±20' 400 1000 ±2 ±15' 1000 2000 ±3 ±10' 2000 4000 ±4 ±10' 4000 8000 ±5 ±10'
N° DRAWING 002-02		DENOMINAT. plate base for 2" 1/2 pipe	

3

2

1

3

2

1

D

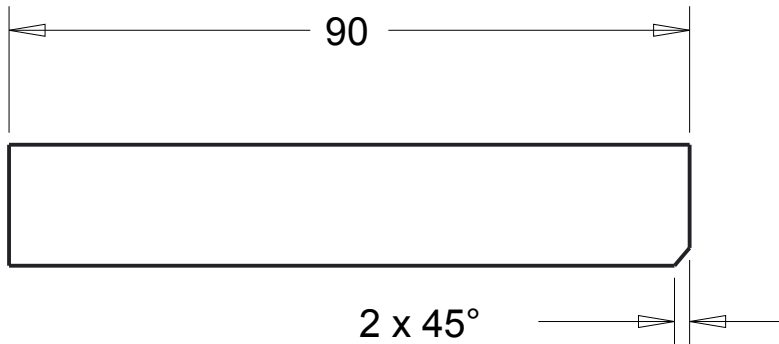
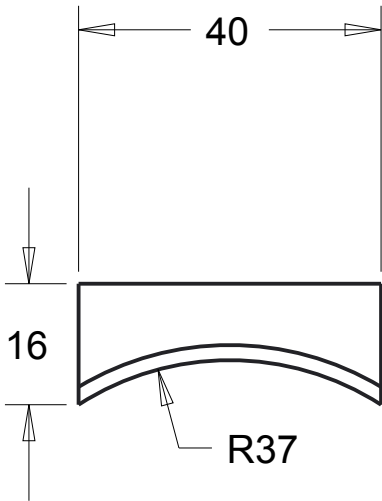
D

C

C

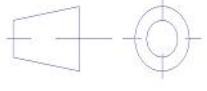
B

B



REV.	DATE	DATE AND MODIFY DESCRIPTION	DRAW	CHECKED	PROJECT E.

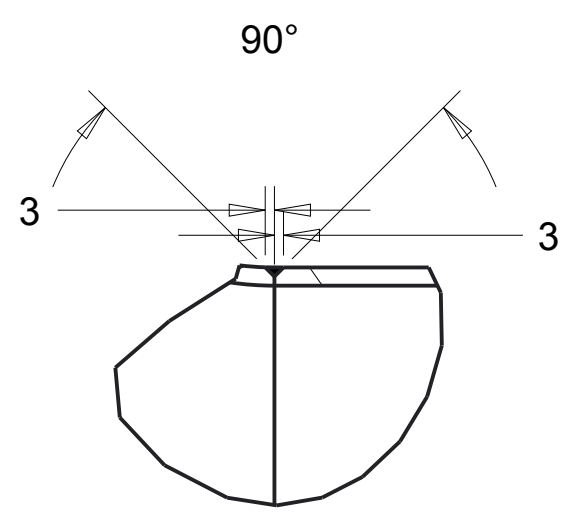
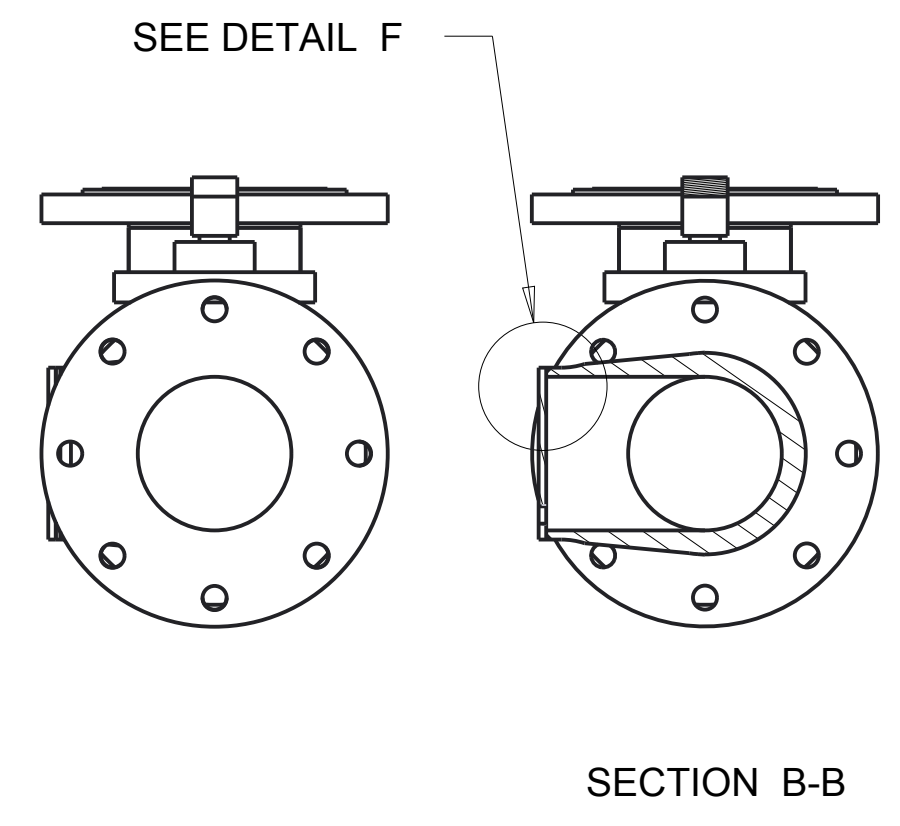
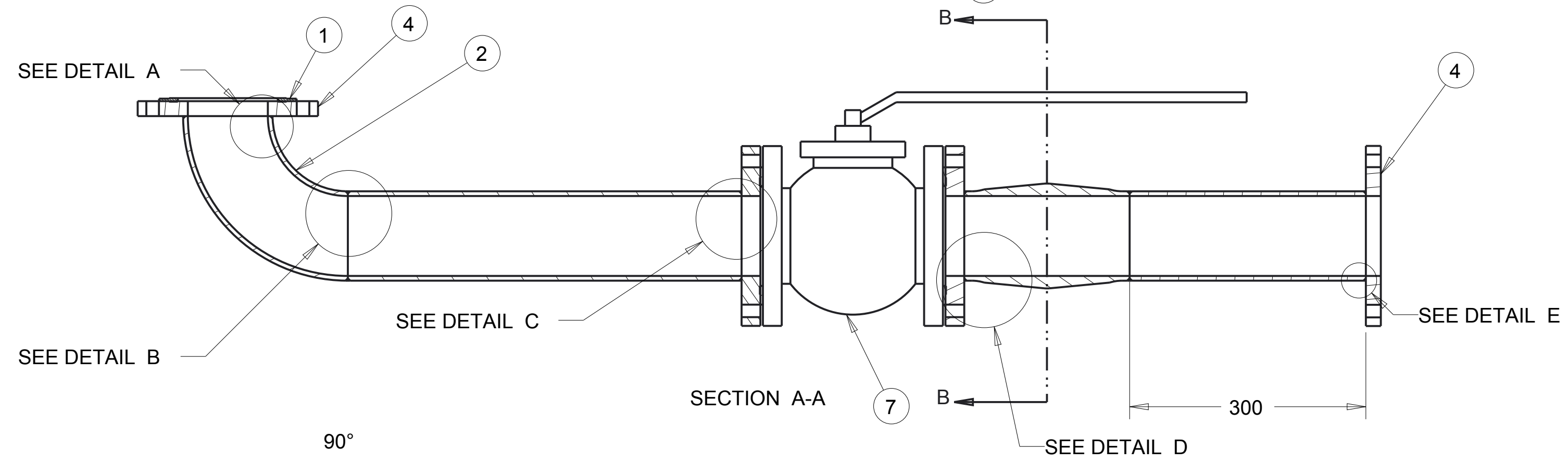
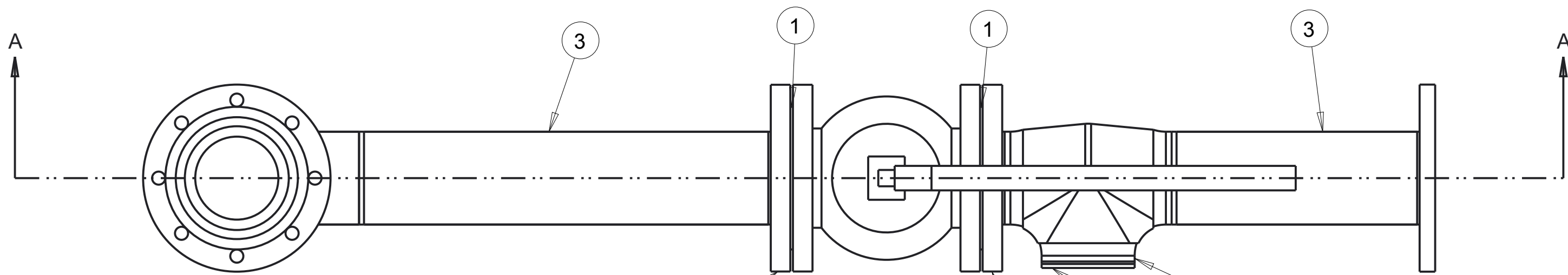
DO NOT SURVEY DIMENSIONS FROM THE DRAWING

	DRAW Aldo Iannetti	CHECKED	PROJECT E. M.Stickland
	QUANTITY 1	MASS 0.336	SCALE 1.000
	MATERIAL carbon steel		GENERAL TOLERANCES EN ISO 13920-AE
Mechanical and Aerospace Engineering Level 4 Lord Hope Building 141 ST James Road G4 0LT Glasgow UK TEL 01415484851 maeATstrath.ac.uk aldo.iannettiATstrath.ac.uk	TYPE BLANK	SIZE	TOLERANCES
TECHNICAL DEPART. WARC		HEAT TREATMENT None	<input type="checkbox"/> > <input type="checkbox"/> <= <input type="checkbox"/> - <input type="checkbox"/> <
FORMAT A4	SHEET 3	DATE 25/06/2013	2 30 ±1 ±20' 30 120 ±1 ±20' 120 400 ±1 ±20' 400 1000 ±2 ±15' 1000 2000 ±3 ±10' 2000 4000 ±4 ±10' 4000 8000 ±5 ±10'
N° DRAWING 002-03	DENOMINAT. base plate for 4" pipe		

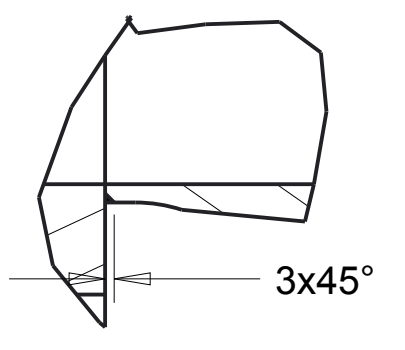
3

2

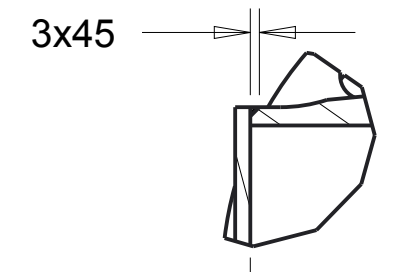
1



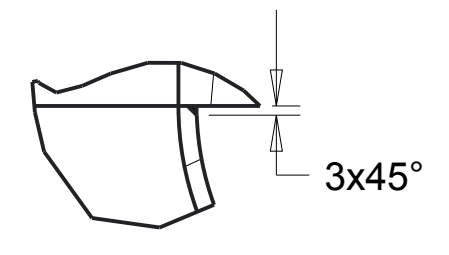
DETAIL B
SCALE 0.400



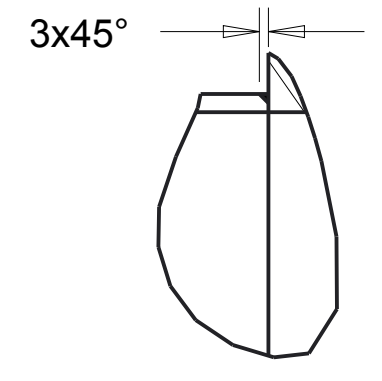
DETAIL D
SCALE 0.400



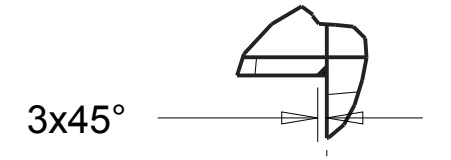
DETAIL F
SCALE 0.400



DETAIL A
SCALE 0.400



DETAIL C
SCALE 0.400



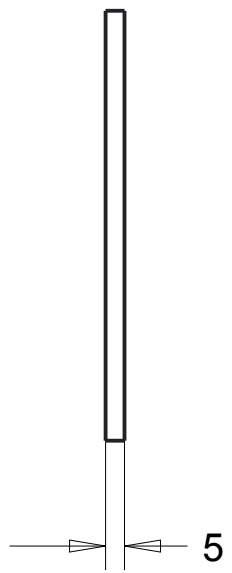
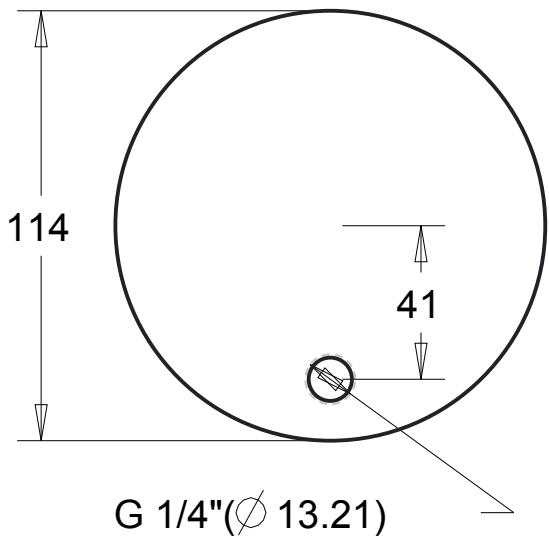
DETAIL E
SCALE 0.400

N°	Assembly/detail	Drawing	Q.
1	Spiral wound gasket CG 4"		3
2	90 deg elbow long radius BS 1640 std		1
3	Pipe 4" BS 1640 Std		2
4	Flat flange BS10 tab F 4"		2
5	Flat flange ANSI B16.5 ASA 150LB 4"		2
6	Equal Tee 4" BS10 1640 Std		1
7	KVC Ball valve, full bore class 150 4"		1
8	Circular cap 5 mm thick	003-02	1

DO NOT SURVEY DIMENSIONS FROM THE DRAWING

		DRAW Aldo Iannetti	CHECKED	PROJECT E. M.Stickland
QUANTITY 1	MASS 80.36	SCALE 0.200		
MATERIAL standard			GENERAL TOLERANCES EN ISO 13920-AE	
TYPE BLANK		SIZE TOLERANCES		
TECHNICAL DEPART. WARC		HEAT TREATMENT None		
FORMAT A2		SUPERFICIAL COVERING paint		
SHEET 1		DATE 25/06/2013		
N° DRAWING 003-01		DEPARTMENT Supply line		

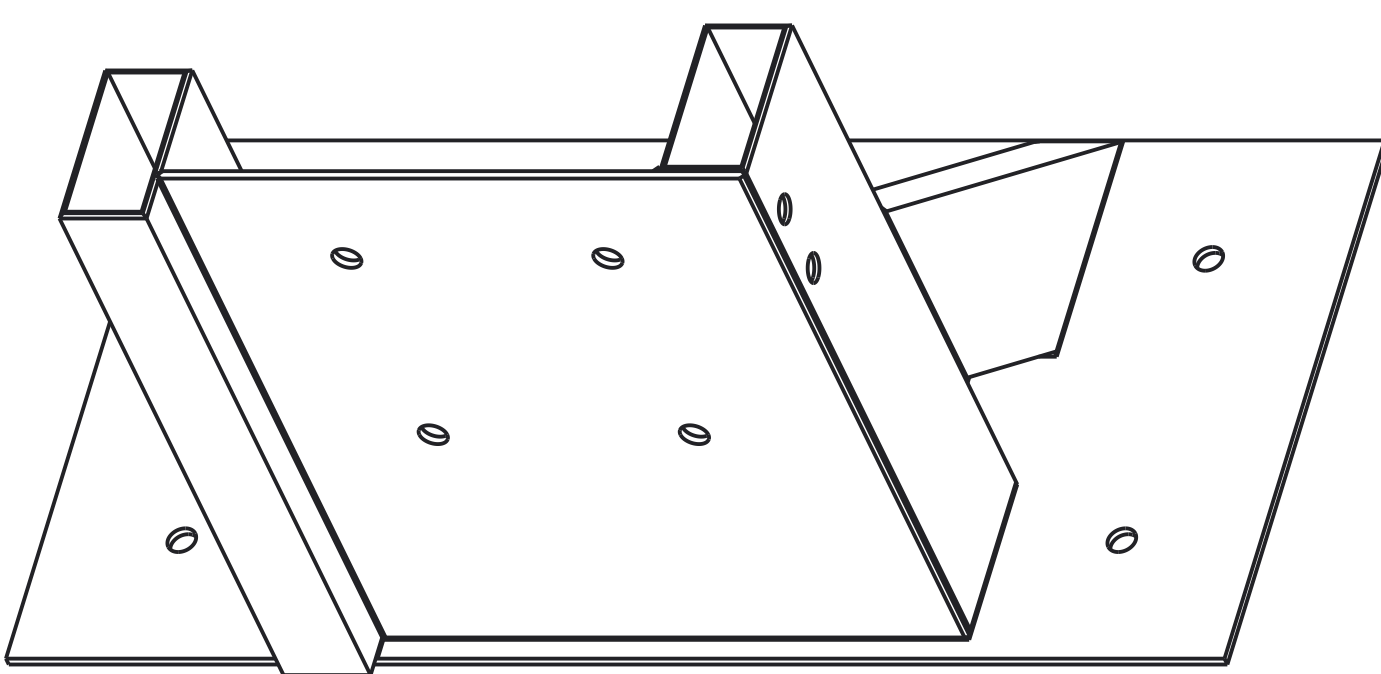
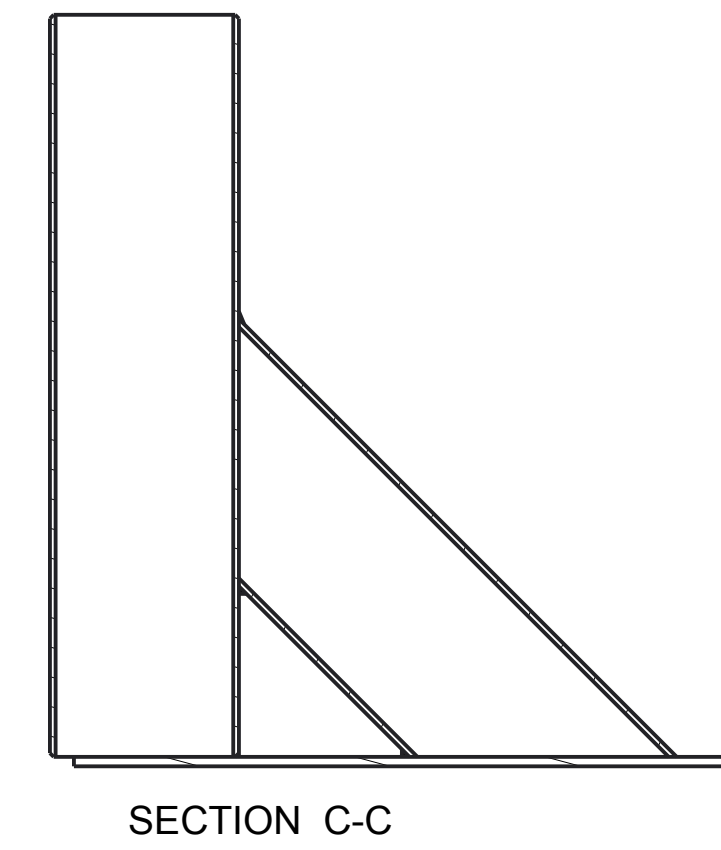
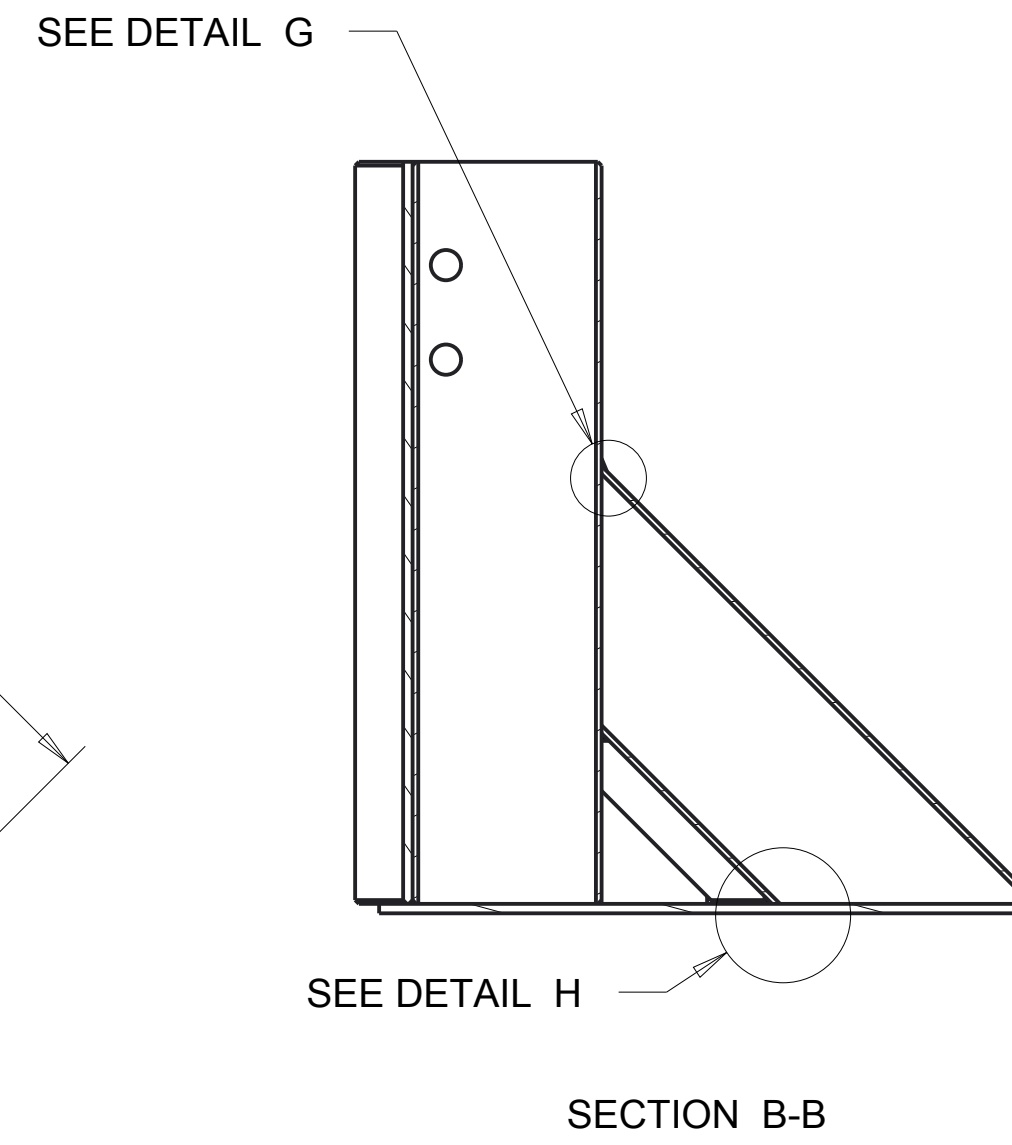
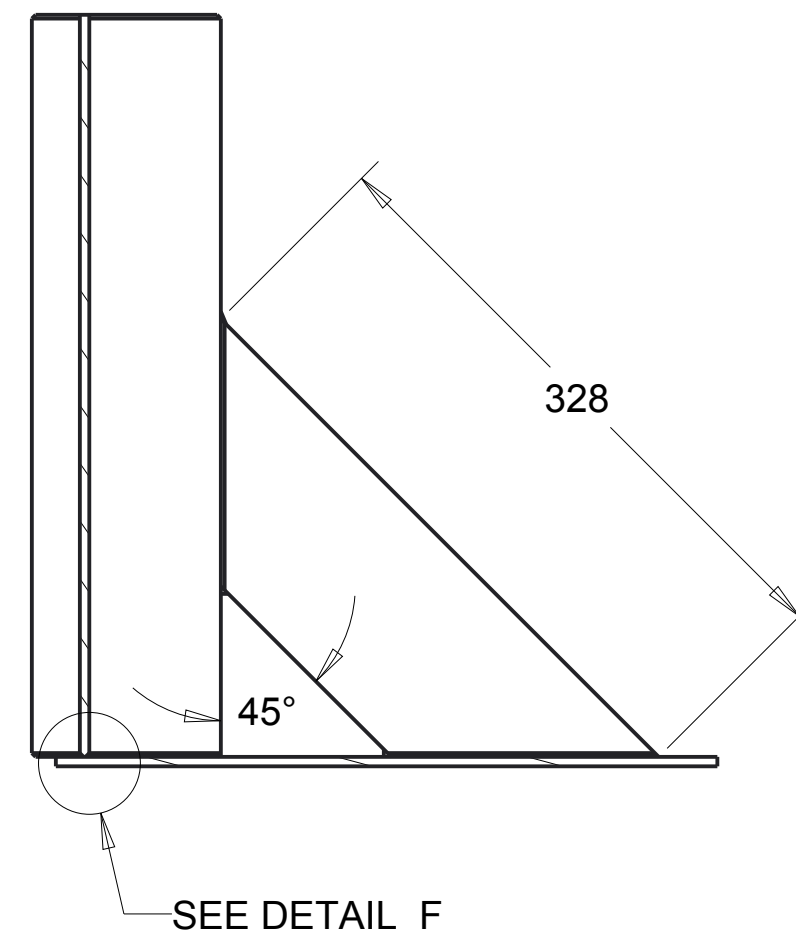
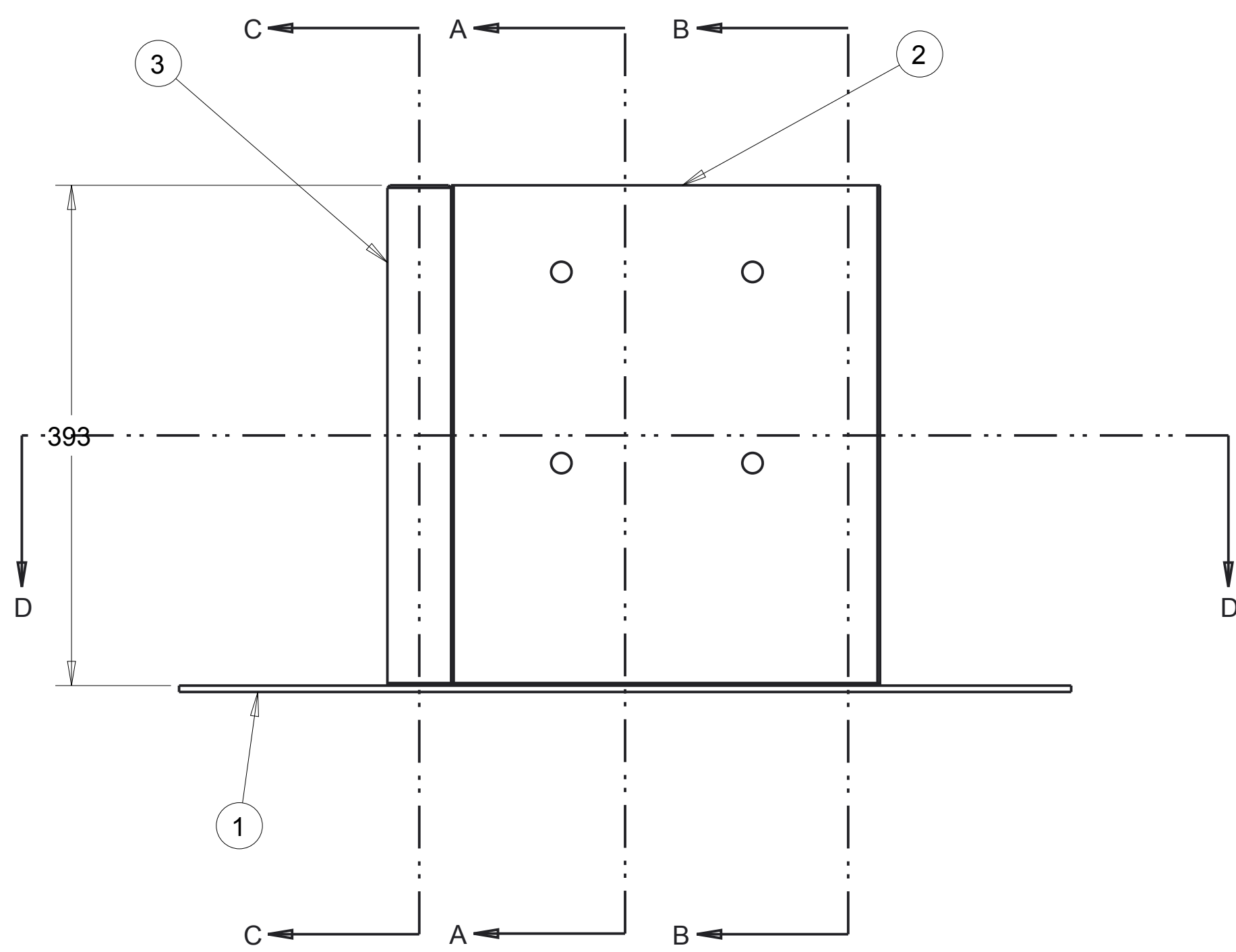
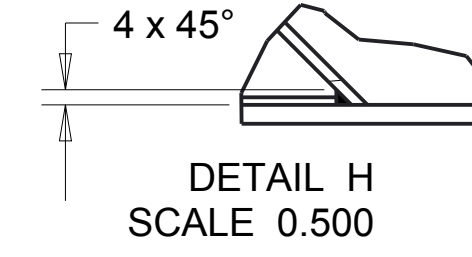
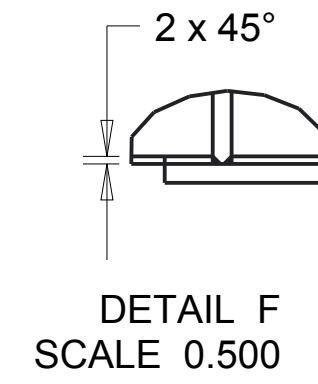
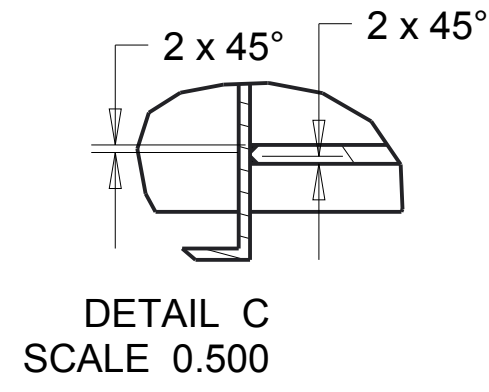
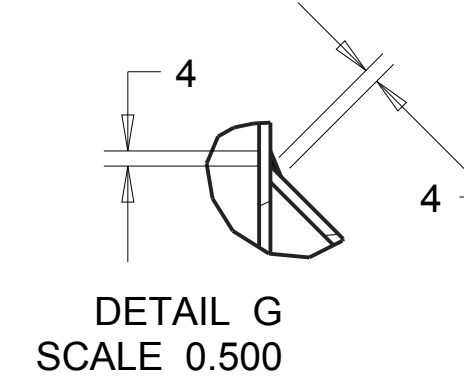
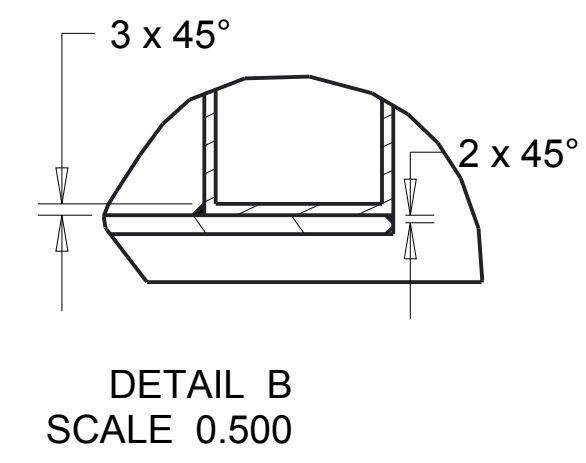
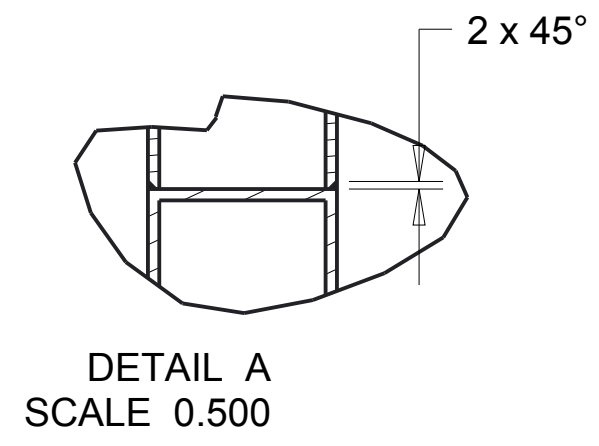
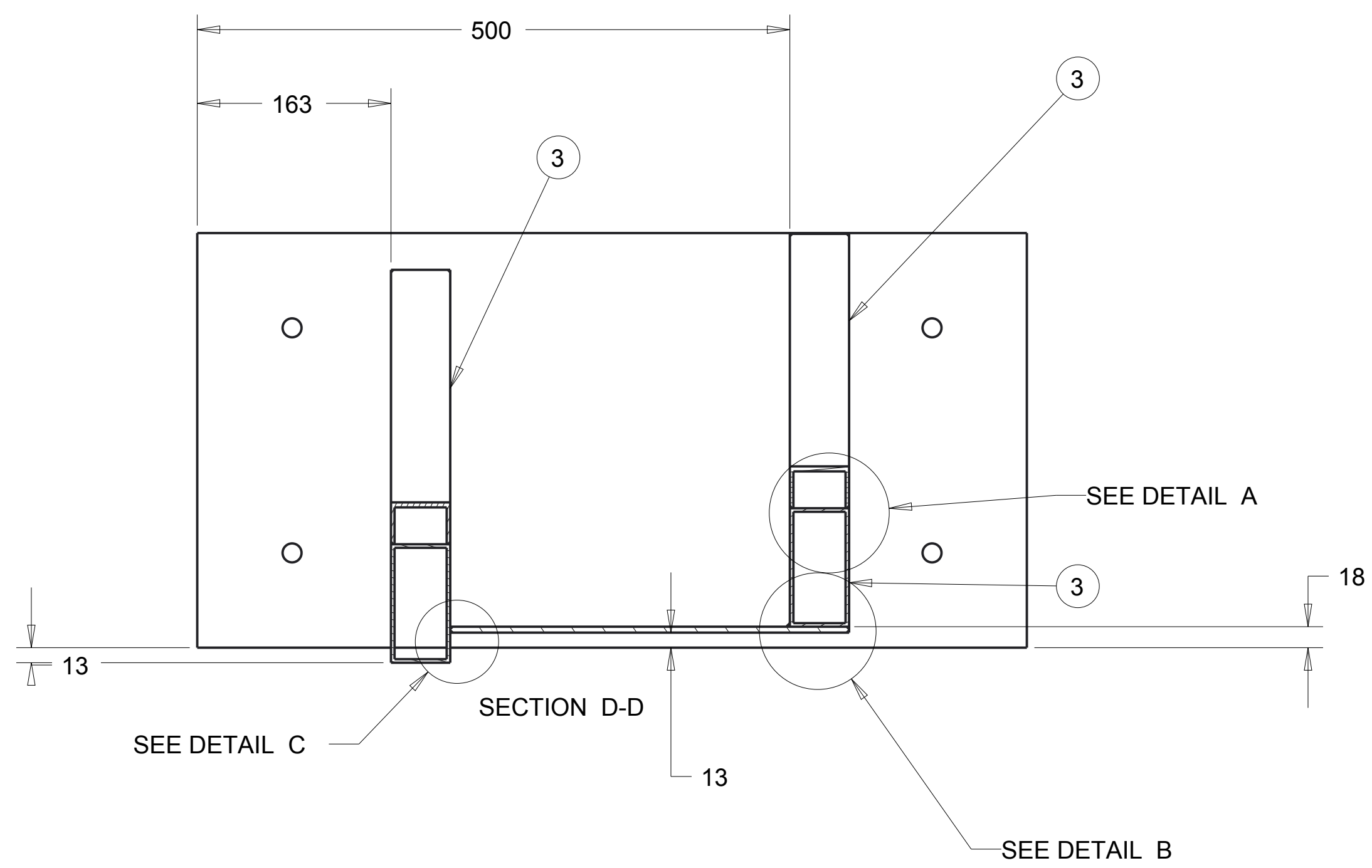
DATE	REV.	DESCRIPTION	DRAWN	CHECKED	PROJECT E.



REV.	DATA DATE	DATA DESCRIZIONE MODIFICA DATE AND MODIFY DESCRIPTION	DISEGNATO DRAW	CONTROLLATO CHECKED	VISTO PROJECT E.

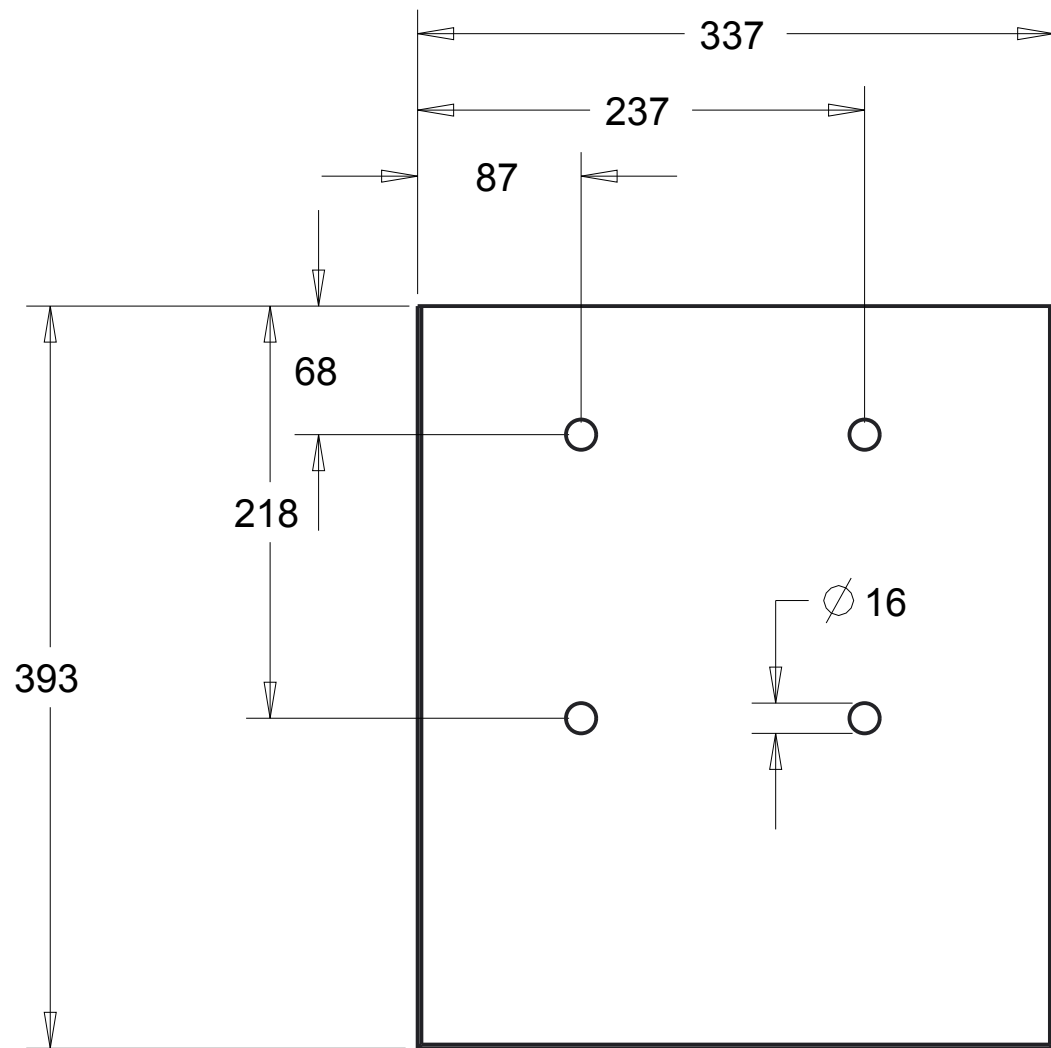
DO NOT SURVEY DIMENSIONS FROM THE DRAWING

	DRAW Aldo Iannetti	CHECKED	PROJECT E. M.Stickland
	QUANTITY 1	MASS 0.395	SCALE 0.500
	MATERIAL Carbon Steel		
Mechanical and Aerospace Engineering Level 4 Lord Hope Building 141 ST James Road G4 0LT Glasgow UK TEL 01415484851 maeATstrath.ac.uk aldo.iannettiATstrath.ac.uk	TYPE BLANK	SIZE	TOLERANCES
TECHNICAL DEPART. WARC	HEAT TREATMENT None	<input type="checkbox"/> > <input type="checkbox"/> <= <input type="checkbox"/> - <input type="checkbox"/> <	2 30 ±1 ±20' 30 120 ±1 ±20' 120 400 ±1 ±20' 400 1000 ±2 ±15' 1000 2000 ±3 ±10' 2000 4000 ±4 ±10' 4000 8000 ±5 ±10'
FORMAT A4	SUPERFICIAL COVERING None	DENOMINAT. Tee Cap 1	
SHEET 2	DATE 25/06/2013	N° DRAWING 003-02	



N°	Assembly/detail	Drawing	Q.
1	Pump support base plate	005-03	1
2	Pump support vertical plate	004-02	1
3	Rectangular section hollow beam 100x50		4

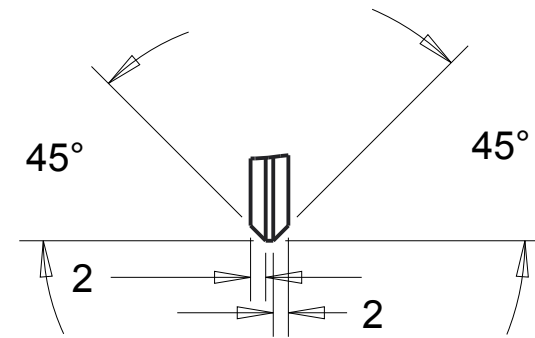
DO NOT SURVEY DIMENSIONS FROM THE DRAWING			
DRAWN: Aldo Iannetti		CHECKED:	PROJECT E: M. Stickland
QUANTITY: 1	MASS: 23.01	SCALE: 0.250	
MATERIALE: standard			
TECHNICAL DEPART: MASC		HEAT TREATMENT: None	SIZE TOLERANCE: 2 30 ±0.20
FORMAT: A1	DATA: 25/06/2013	SUPERFICIAL COVERING: Paint	30 120 ±0.1 ±0.20
SHEET: 1	DATE: 25/06/2013	RESISTANCE: Pump Support 2	100 400 ±0.1 ±0.20
N° DRAWING: 004-01			400 1000 ±0.2 ±0.15
			1000 2000 ±0.3 ±0.15
			2000 4000 ±0.4 ±0.15
			4000 8000 ±0.5 ±0.15



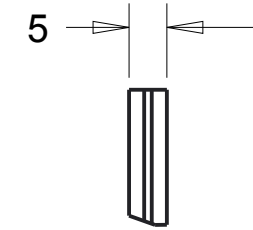
SEE DETAIL E



SEE DETAIL D



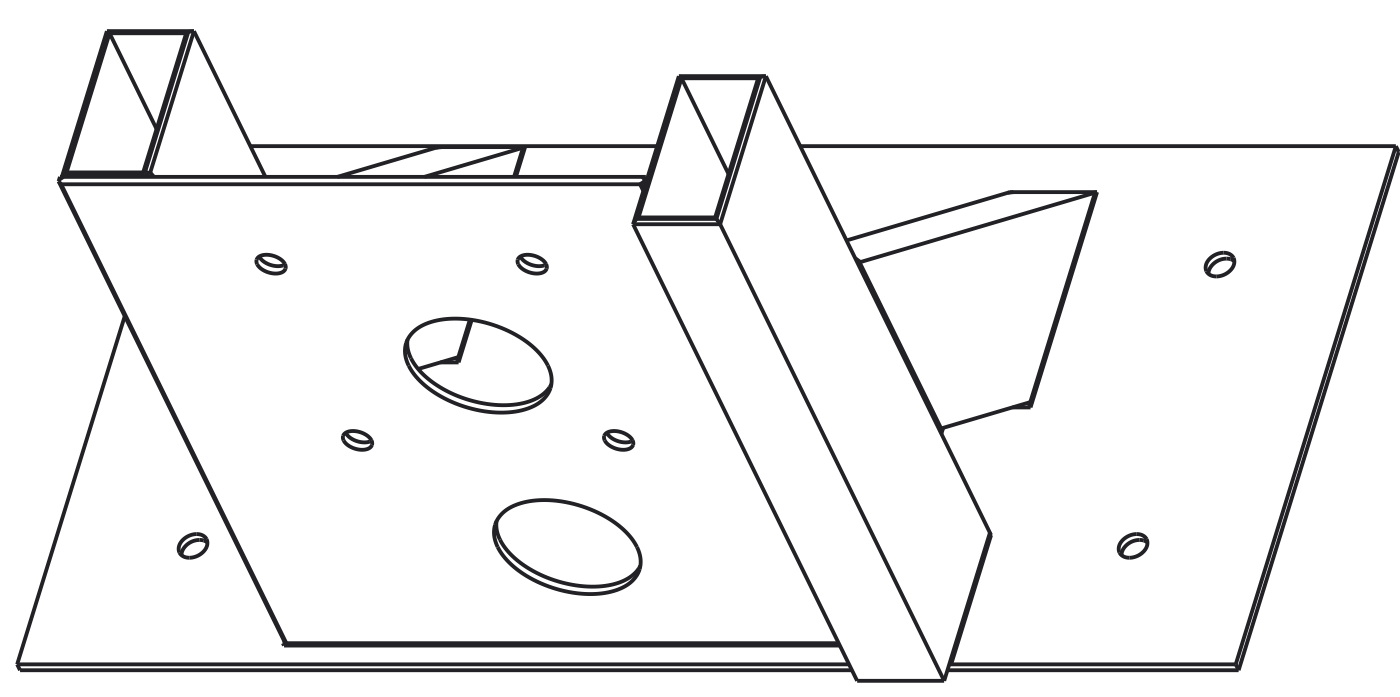
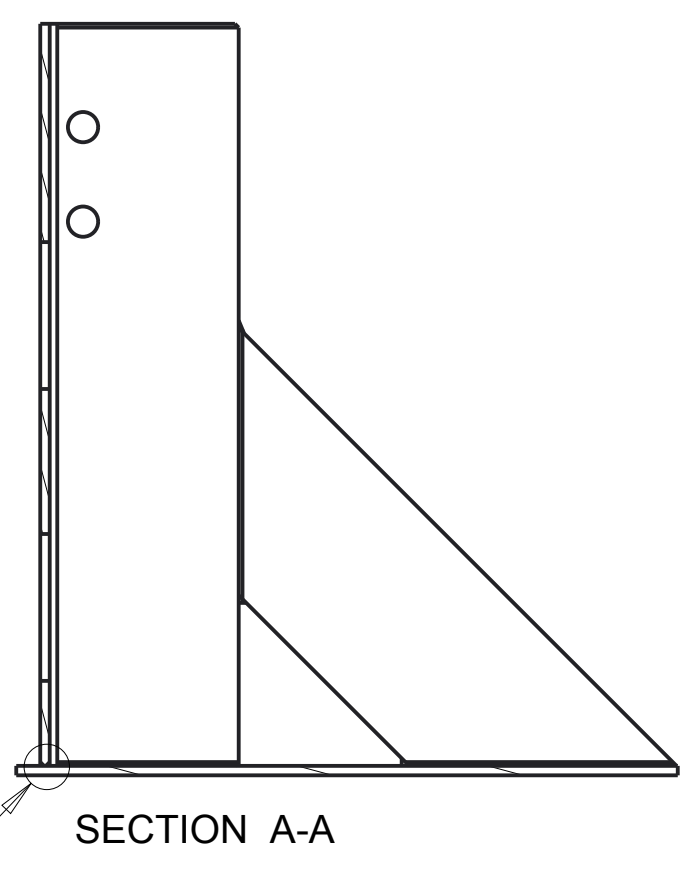
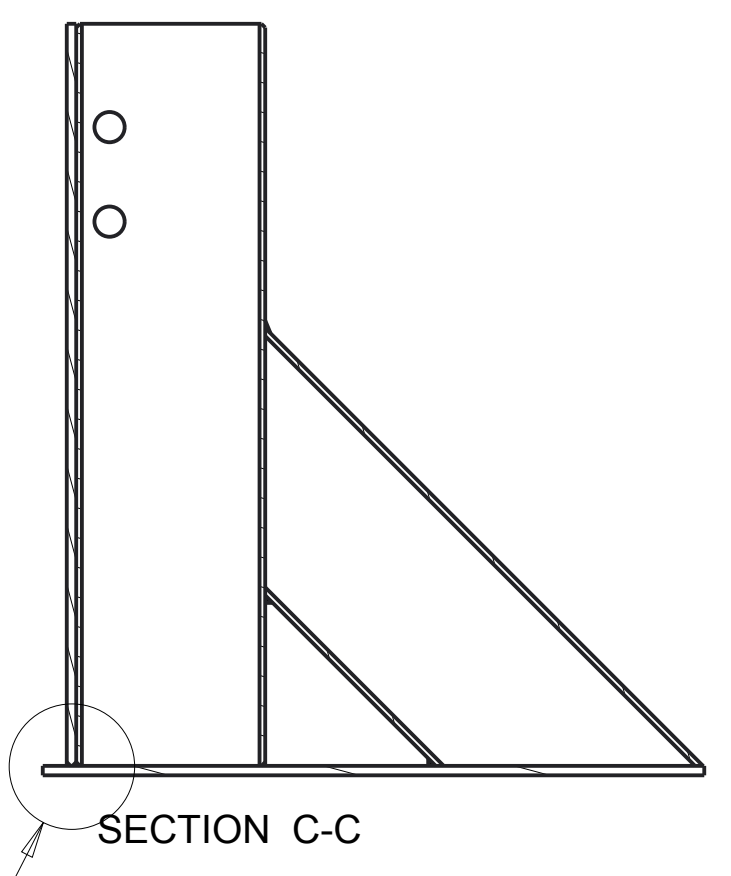
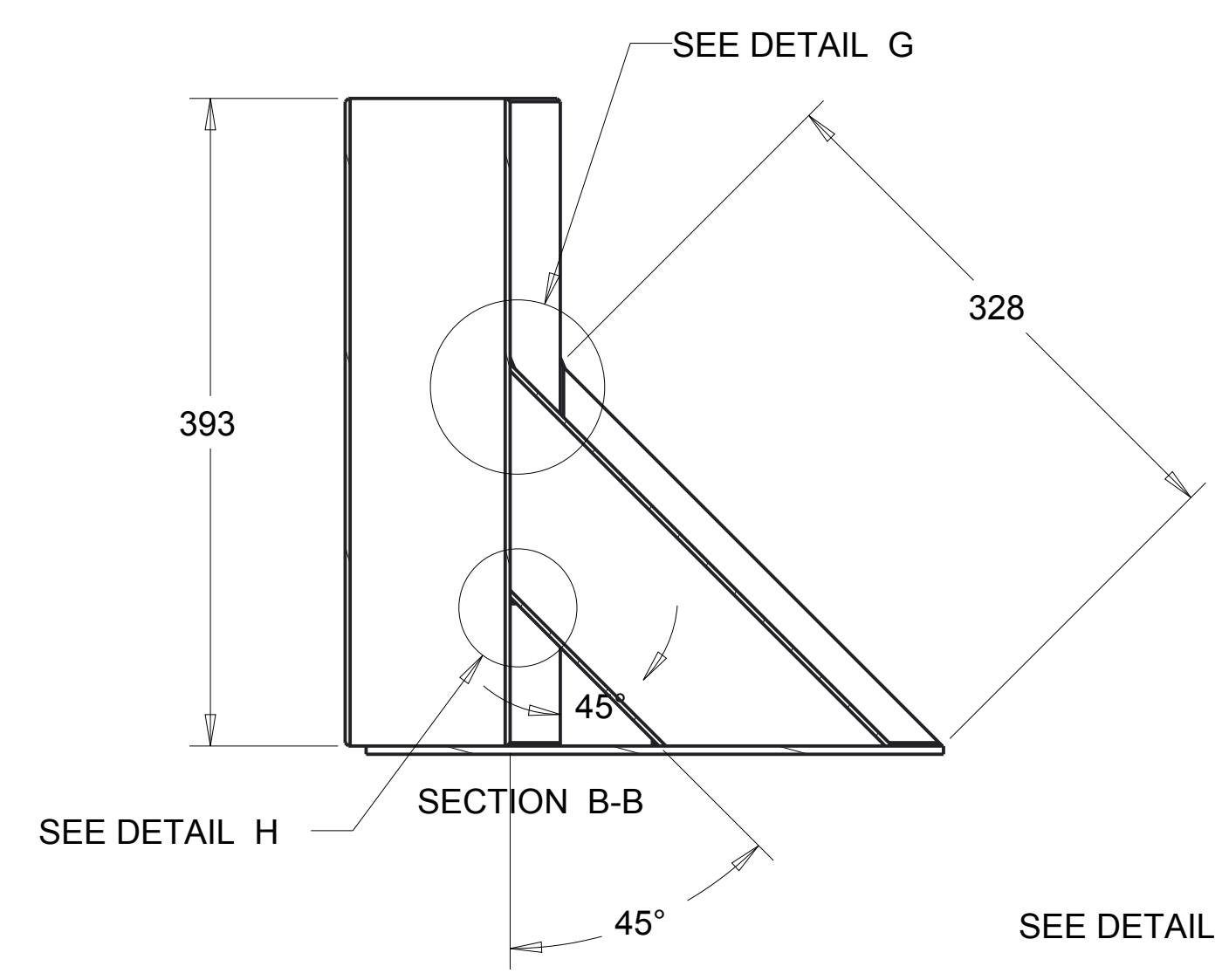
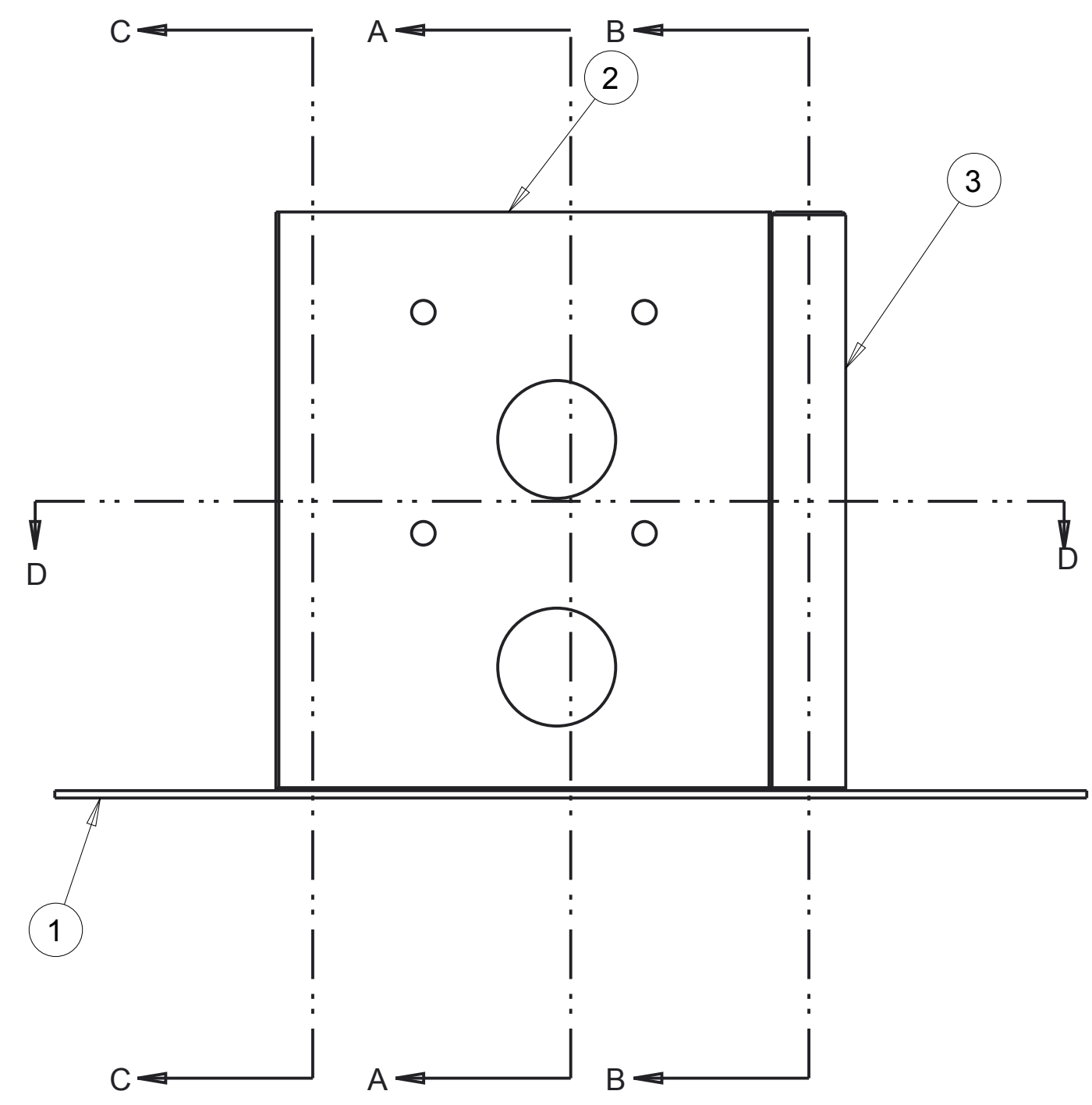
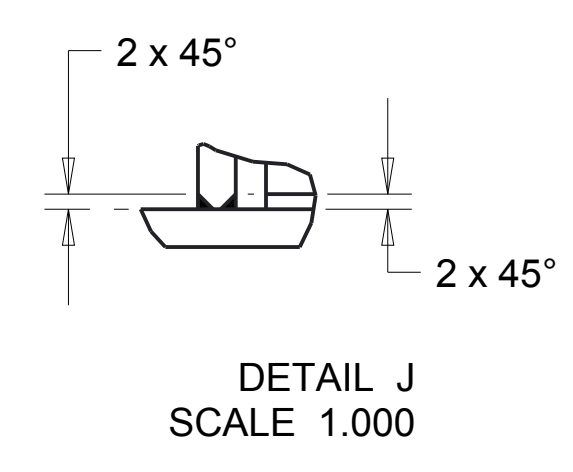
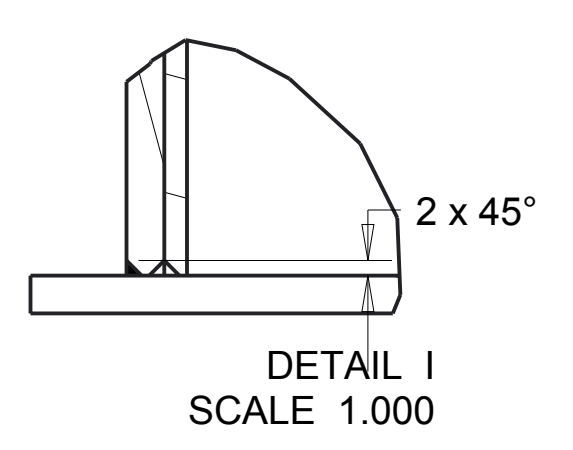
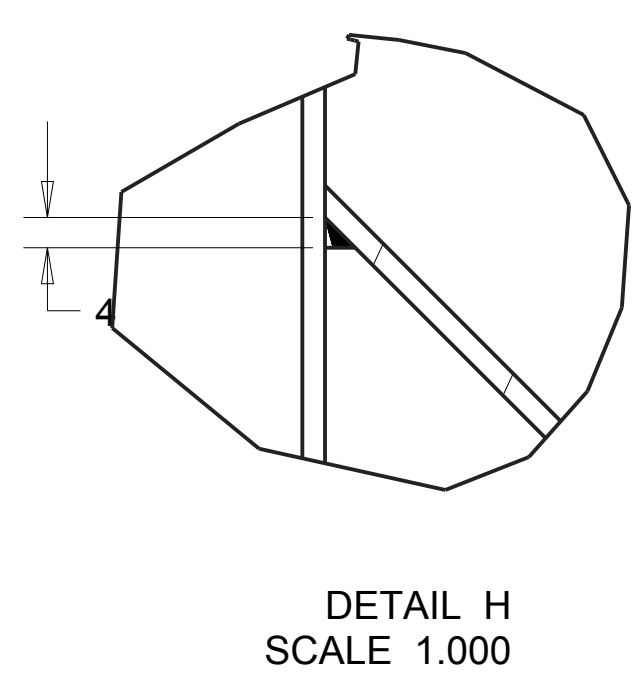
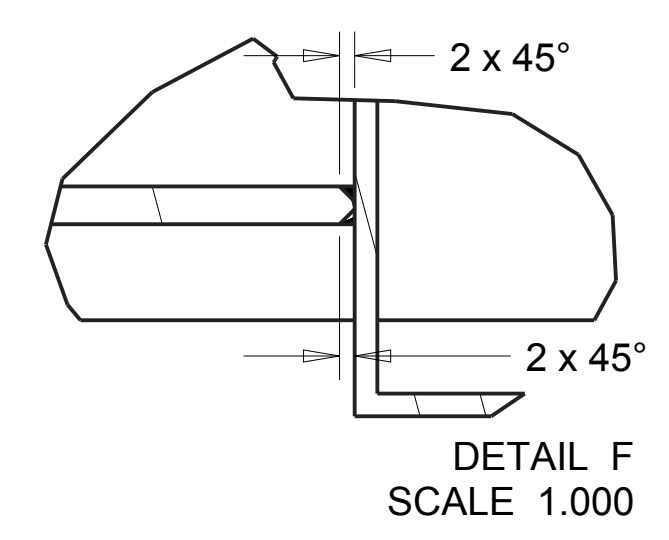
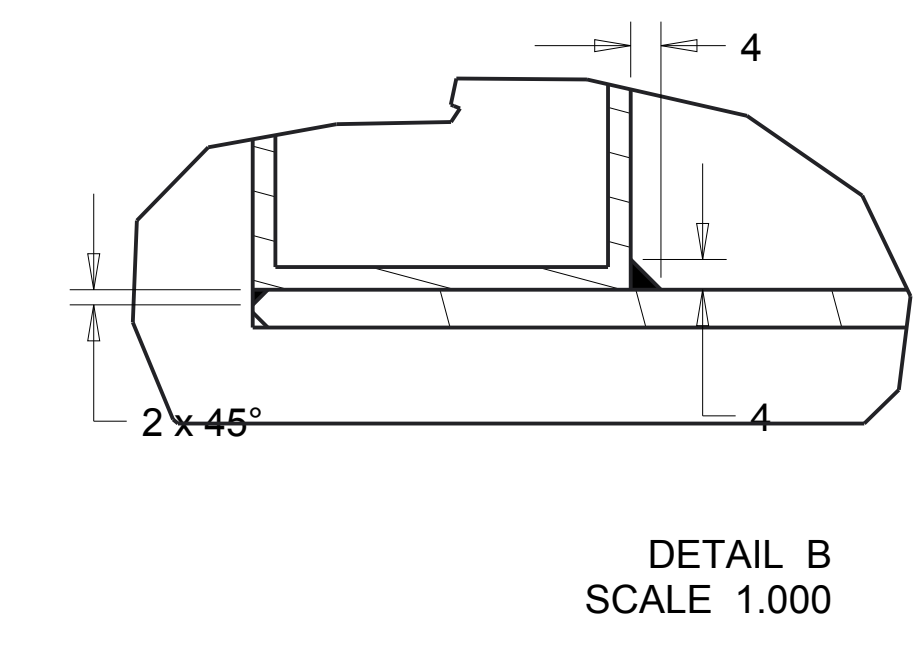
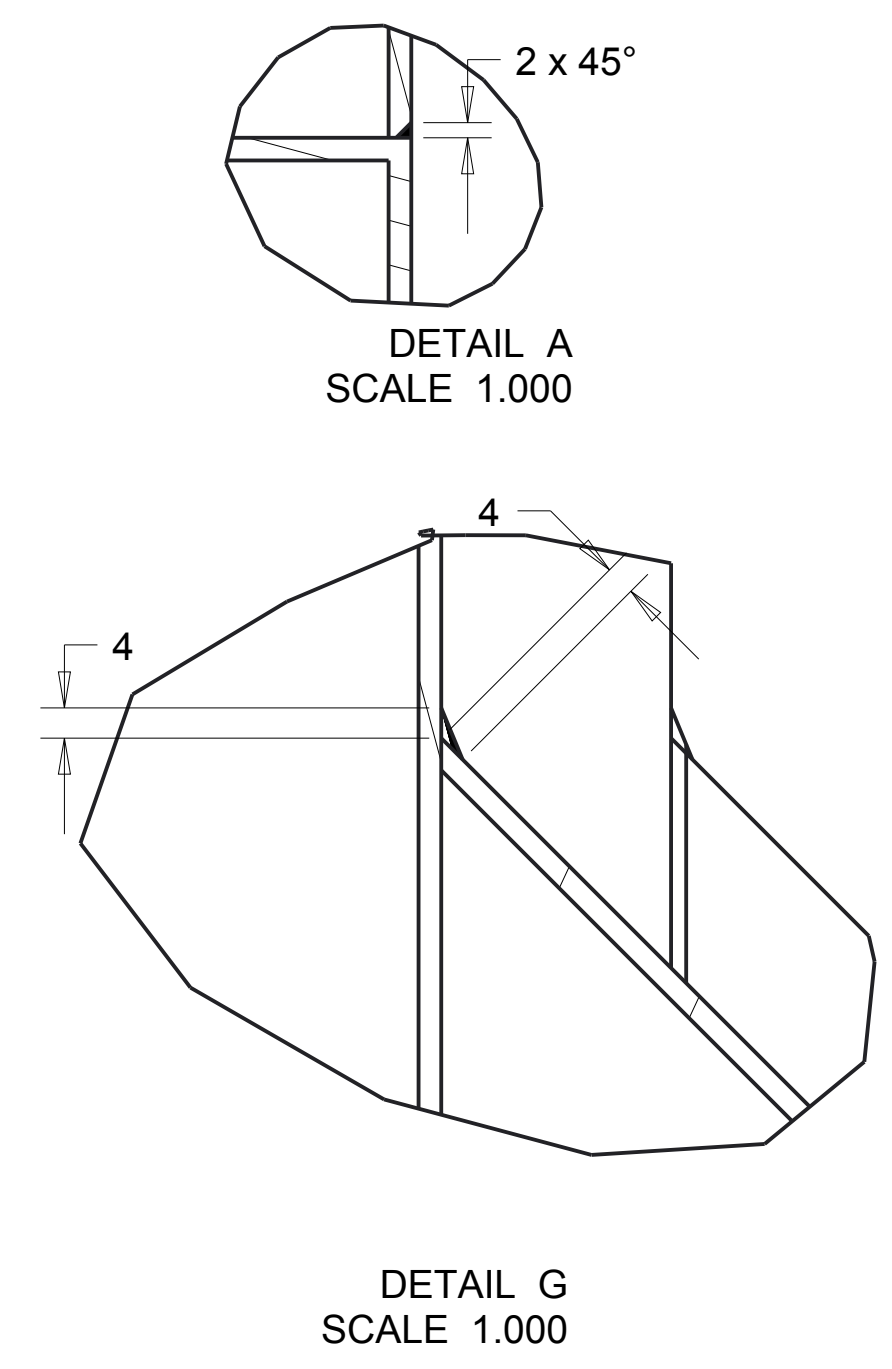
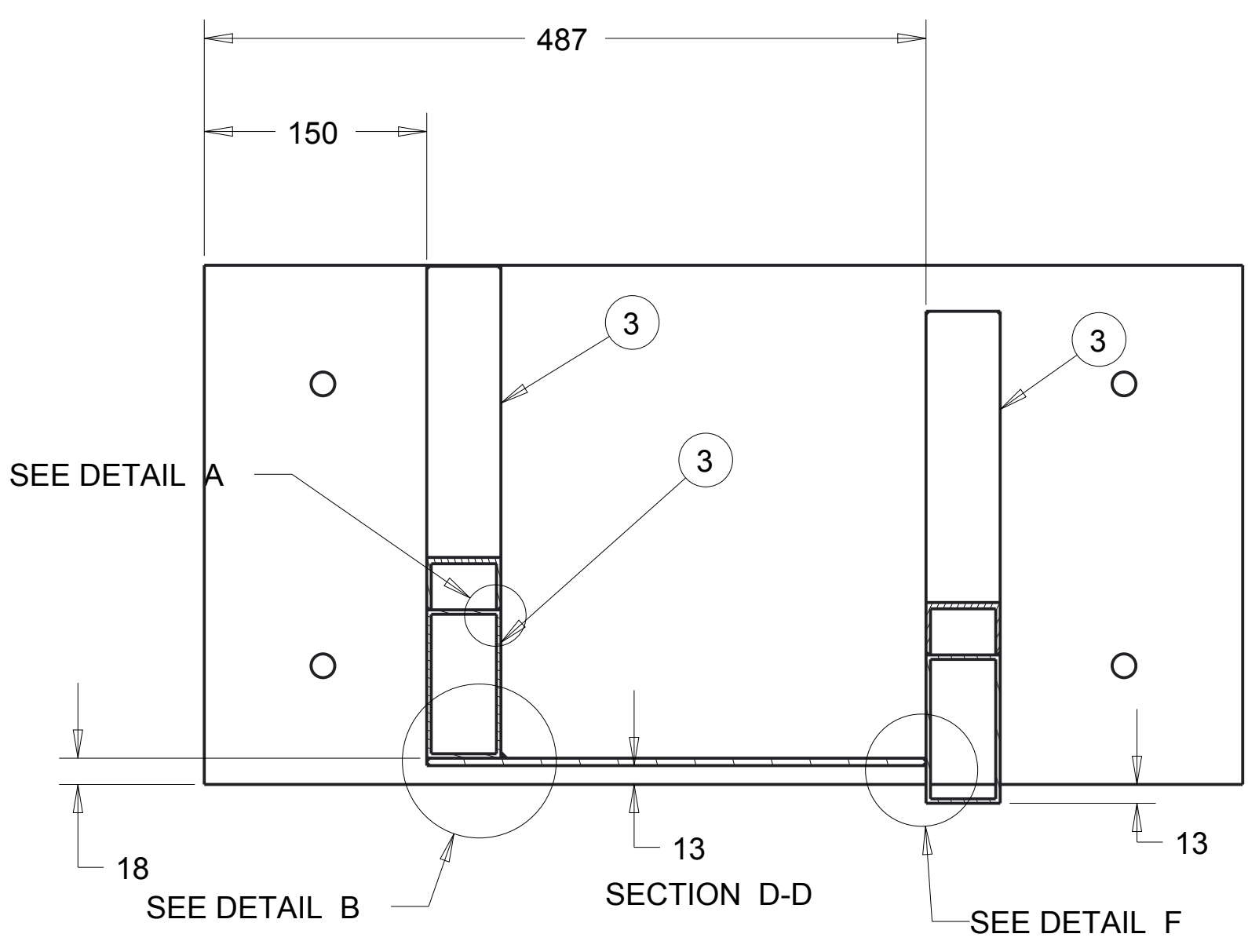
DETAIL D
SCALE 1.000



DETAIL E
SCALE 1.000

REV.	DATE	DATE AND MODIFY DESCRIPTION	DRAW	CHECKED	PROJECT E.

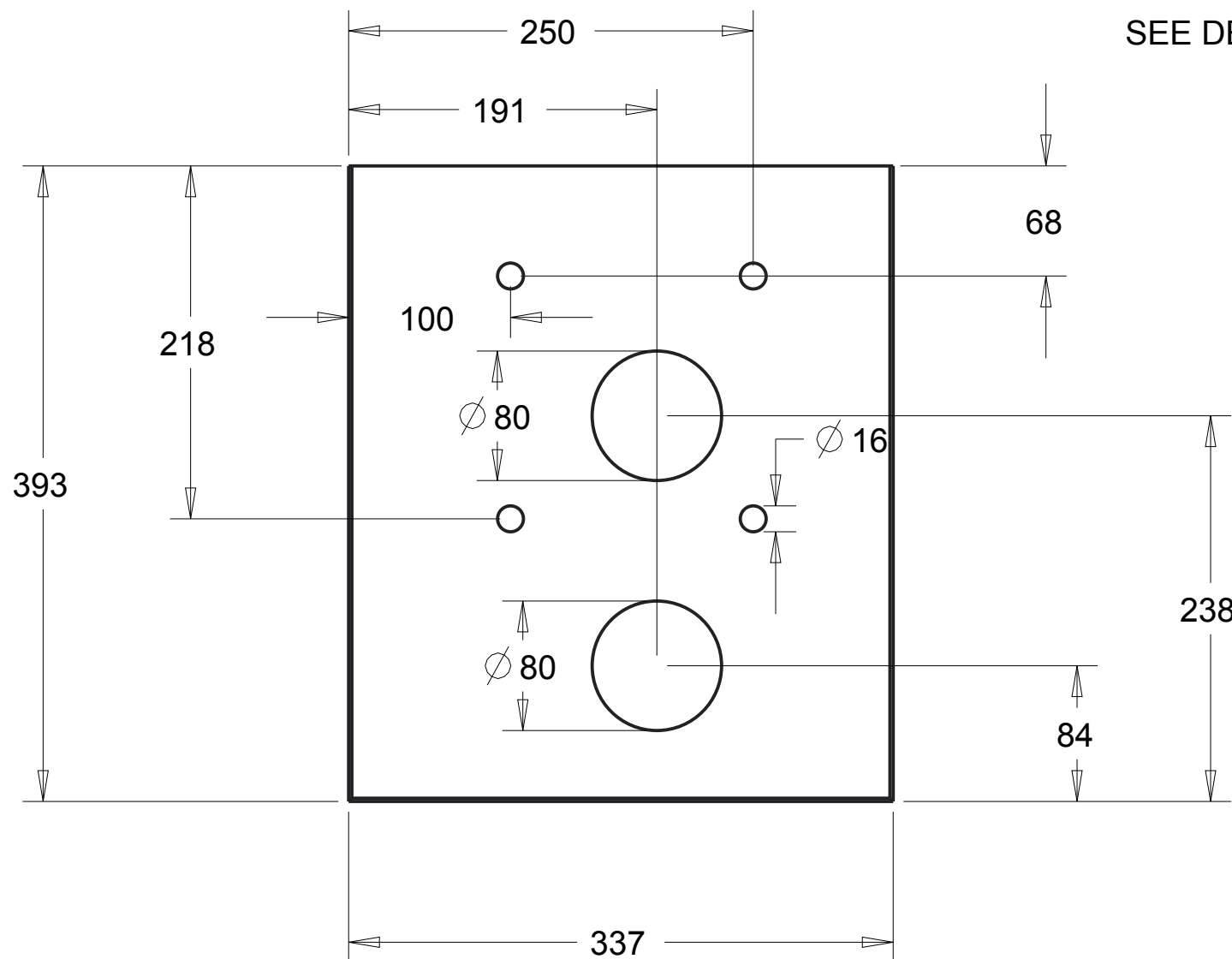
DO NOT SURVEY DIMENSIONS FROM THE DRAWING						
<p>Mechanical and Aerospace Engineering Level 4 Lord Hope Building 141 ST James Road G4 0LT Glasgow UK</p> <p>TEL 01415484851 maeATstrath.ac.uk aldo.iannettiATstrath.ac.uk</p>	DRAW	Aldo Iannetti	CHECKED	PROJECT E. M.Stickland		
	QUANTITY	MASS 5.08		SCALE 0.250		
	MATERIAL	Standard			GENERAL TOLERANCES EN ISO 13920-AE	
	TYPE	BLANK			SIZE	TOLERANCES
TECHNICAL DEPART. WARC	HEAT TREATMENT		None		<input type="checkbox"/> > <input type="checkbox"/> <= <input type="checkbox"/> <	
FORMAT A3	SUPERFICIAL COVERING		None		2 30 ±1 ±20' 30 120 ±1 ±20' 120 400 ±1 ±20' 400 1000 ±2 ±15' 1000 2000 ±3 ±10' 2000 4000 ±4 ±10' 4000 8000 ±5 ±10'	
SHEET 2	DATE 25/06/2013	DENOMINAT. Pump support vertical plate				
N° DRAWING 004-02						



N°	Assembly/Detail	Drawing	Q.
1	Pump support base plate	005-03	1
2	Pump support vertical plate with window	005-02	1
3	Rectangular section hollow beam 100x50		4

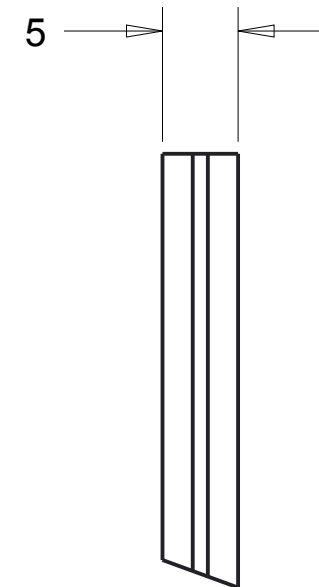
DO NOT SURVEY DIMENSIONS FROM THE DRAWING

		DRAW: Aldo Iannetti CHECKED: [] PROJECT: M. Stickland
QUANTITY: 1 MASS: 22.62 SCALE: 0.250	MATERIAL: Standard HEAT TREATMENT: None SUPERFICIAL COVERING: paint	GENERAL TOLERANCES EN ISO 12000-A1 SIZE TOLERANCE TYPE: GREZZO / BLANK HEAT TREATMENT: None SUPERFICIAL COVERING: paint DIMENSIONS: Pump Support 1
TECHNICAL DEPART: [] FORMAT: A1 SHEET: 1 DATE: 25/06/2013 N° DRAWING: 005-01	TEL: 0145484851 STRATHCLYDE@GMAIL.COM ALDO.IANNETTI@STRATH.AC.UK	SIZE TOLERANCE TYPE: GREZZO / BLANK HEAT TREATMENT: None SUPERFICIAL COVERING: paint DIMENSIONS: Pump Support 1

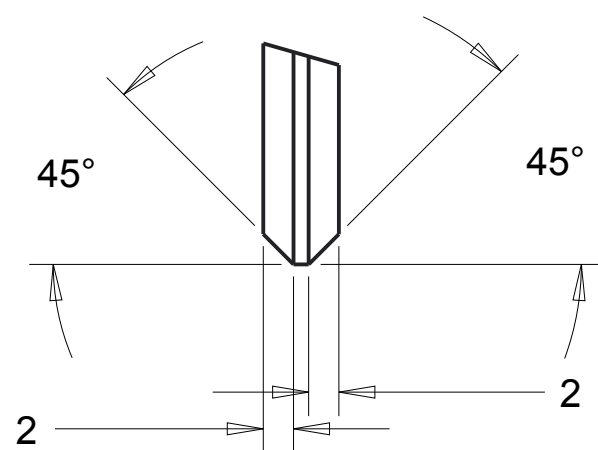


SEE DETAIL D

SEE DETAIL C



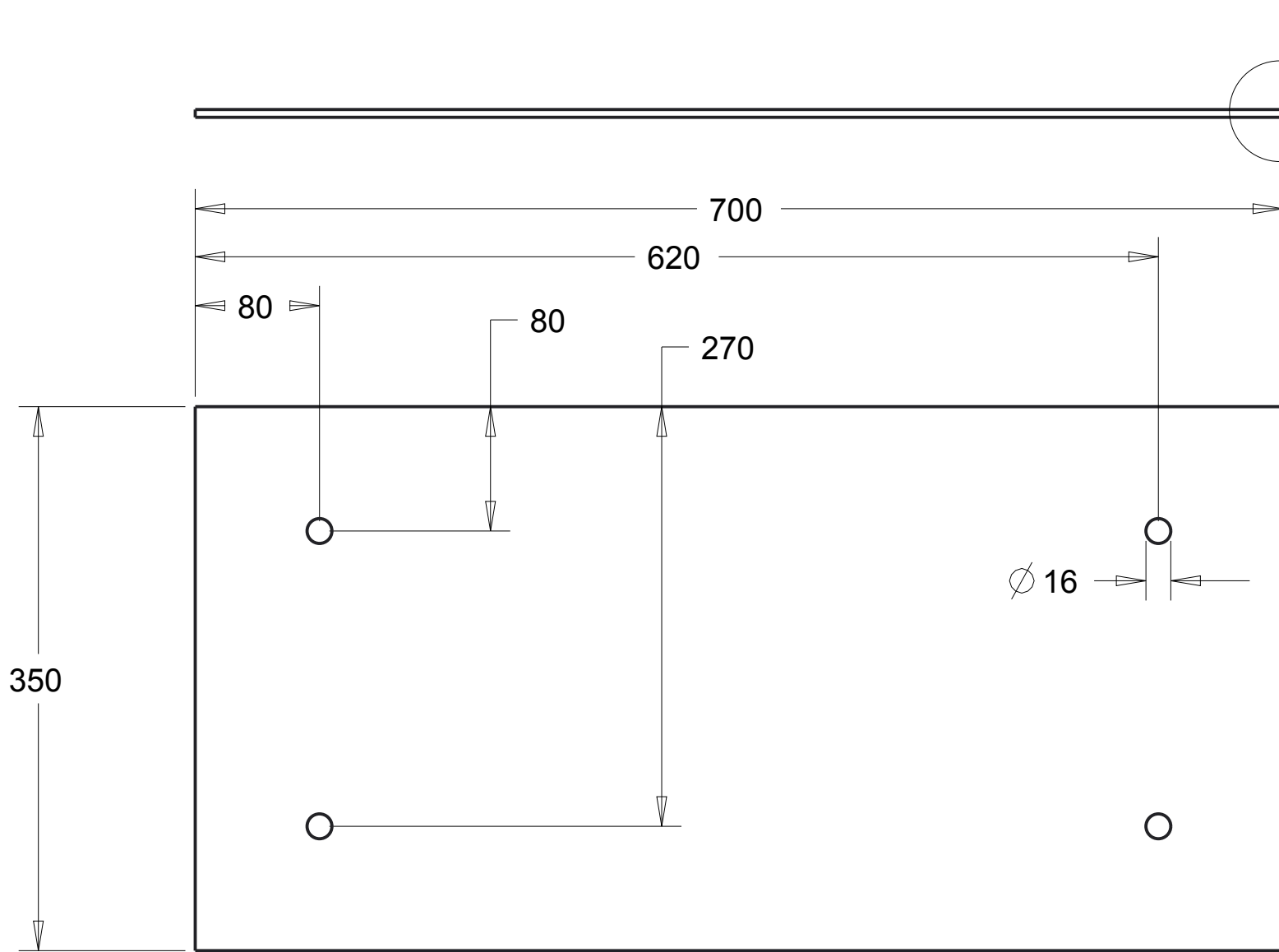
DETAIL D
SCALE 2.000



DETAIL C
SCALE 2.000

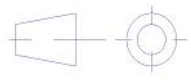
REV.	DATE	DATE AND MODIFY DESCRIPTION	DRAW	CHECKED	PROJECT E.

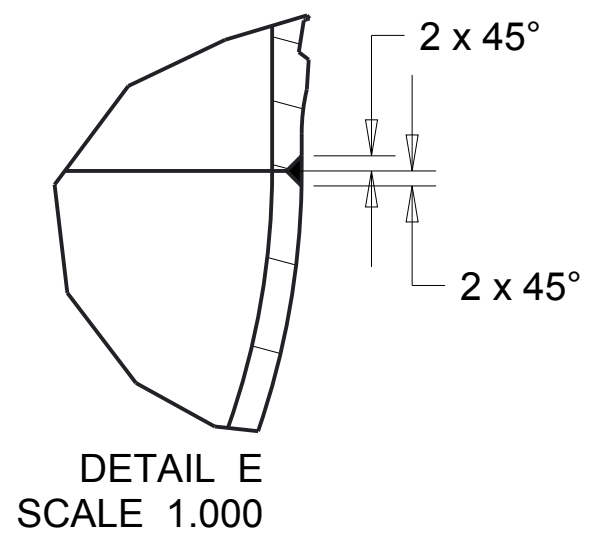
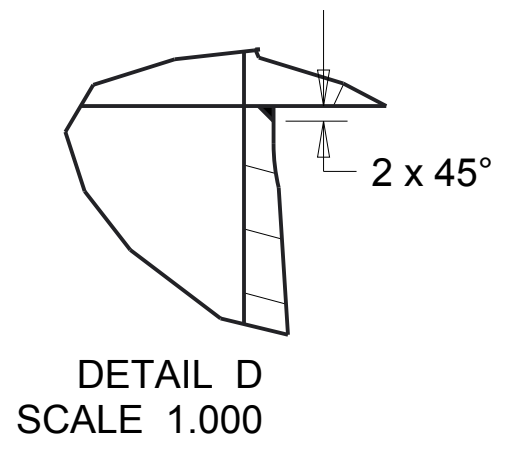
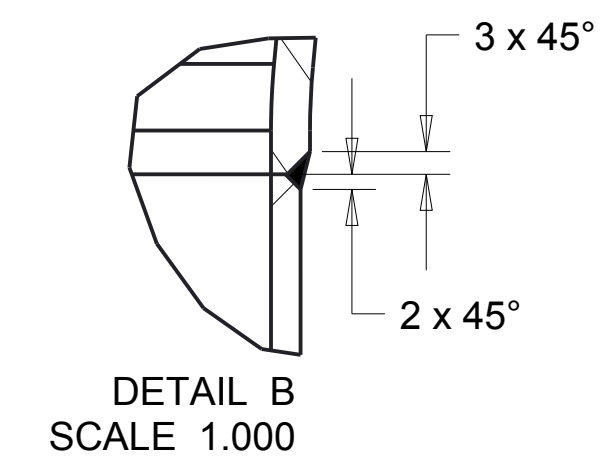
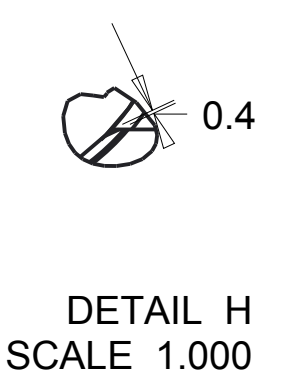
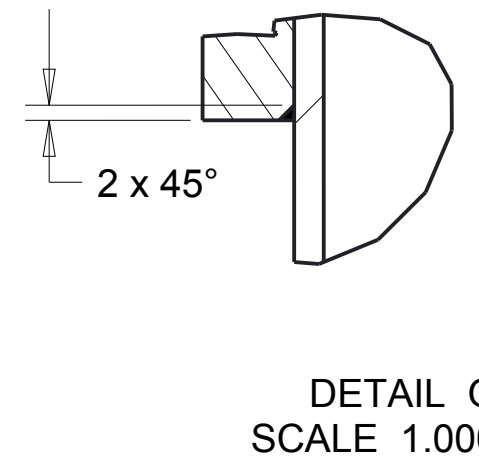
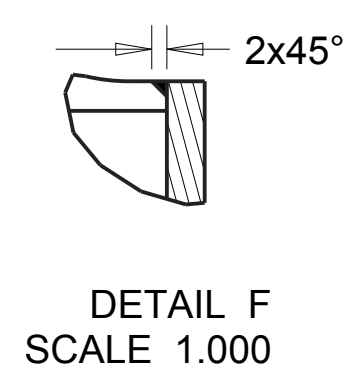
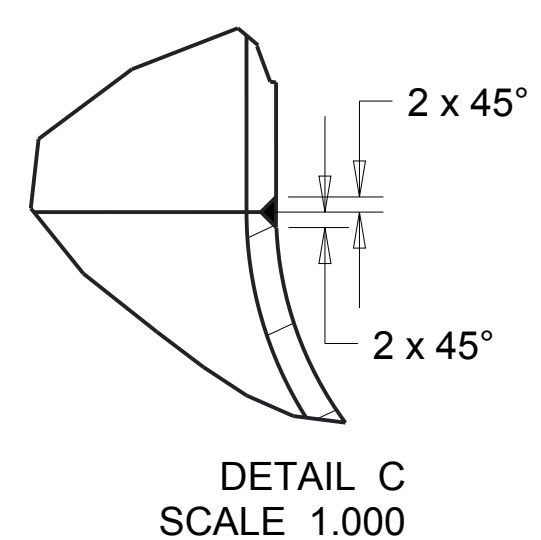
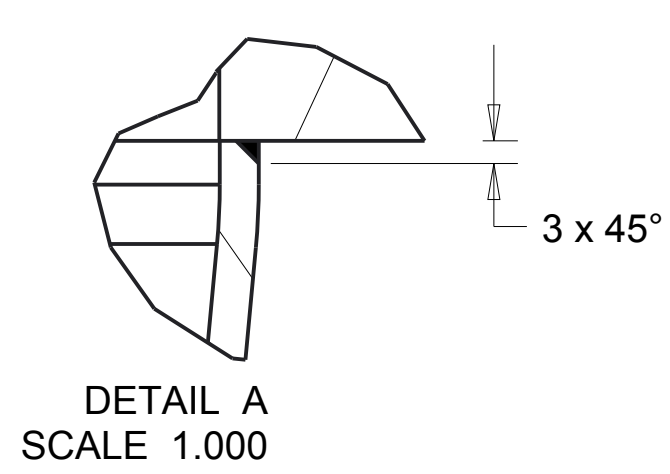
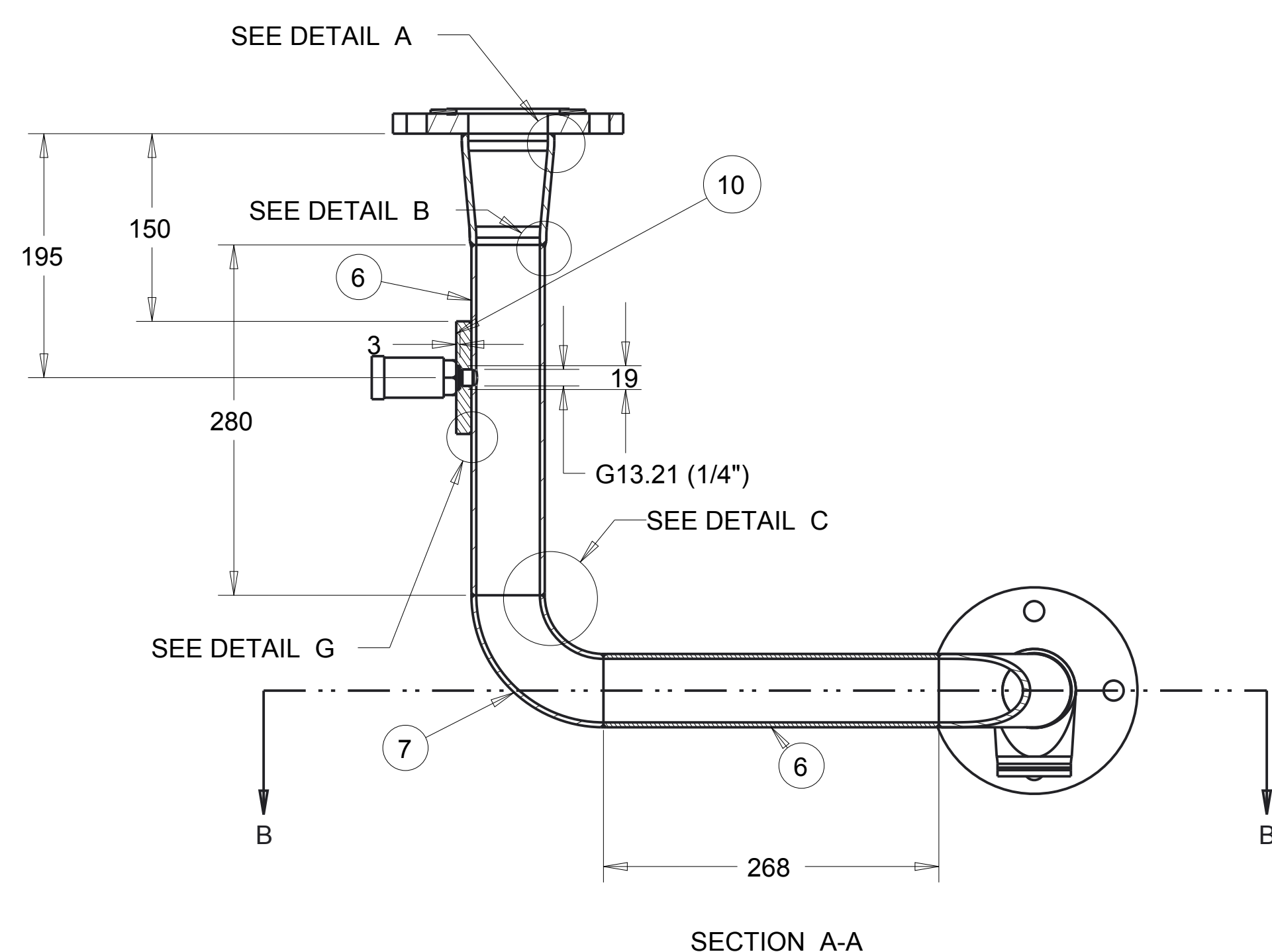
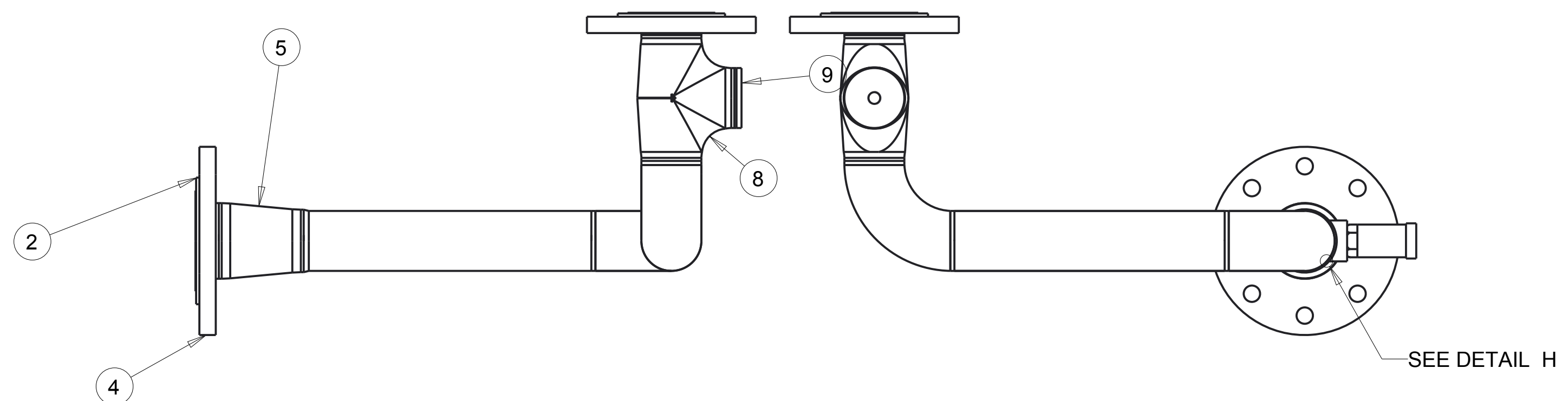
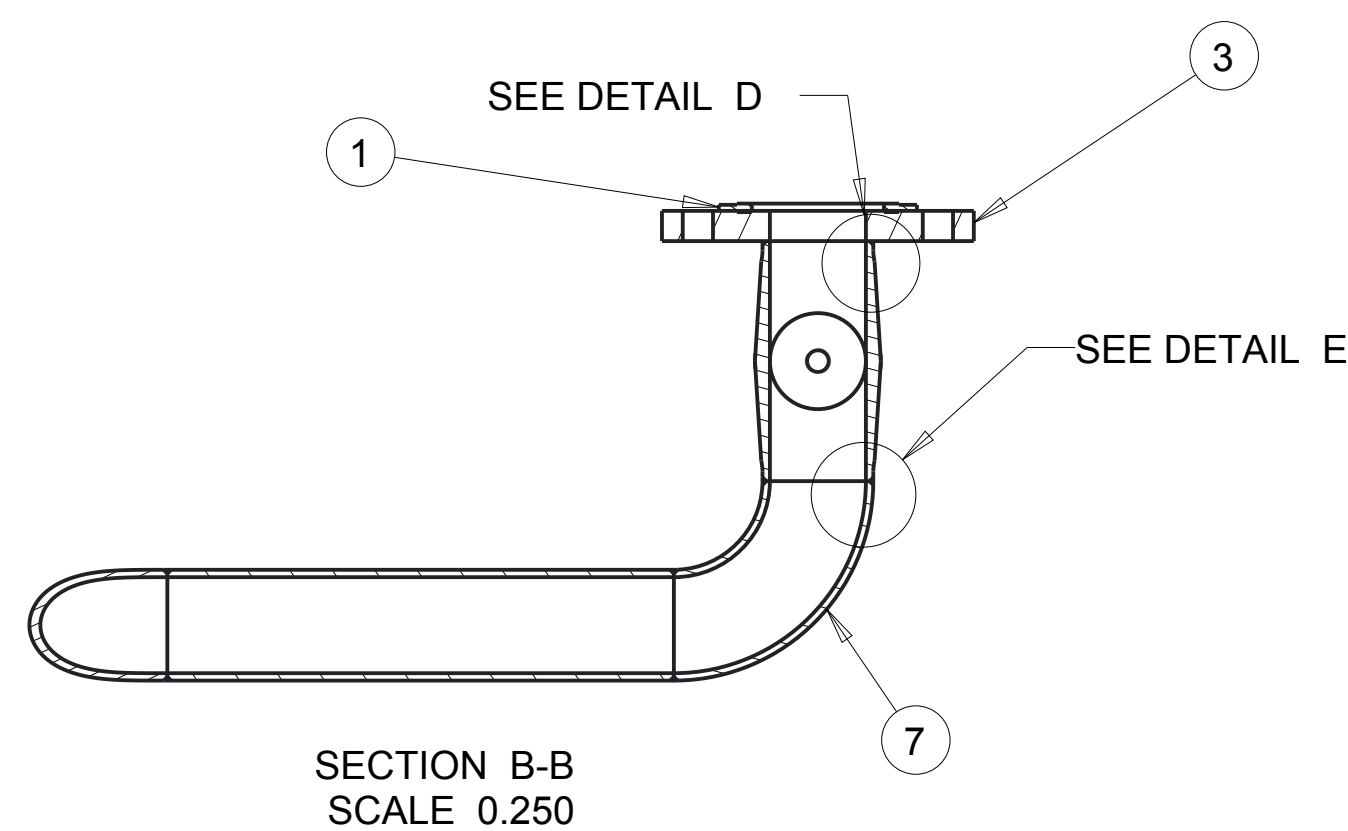
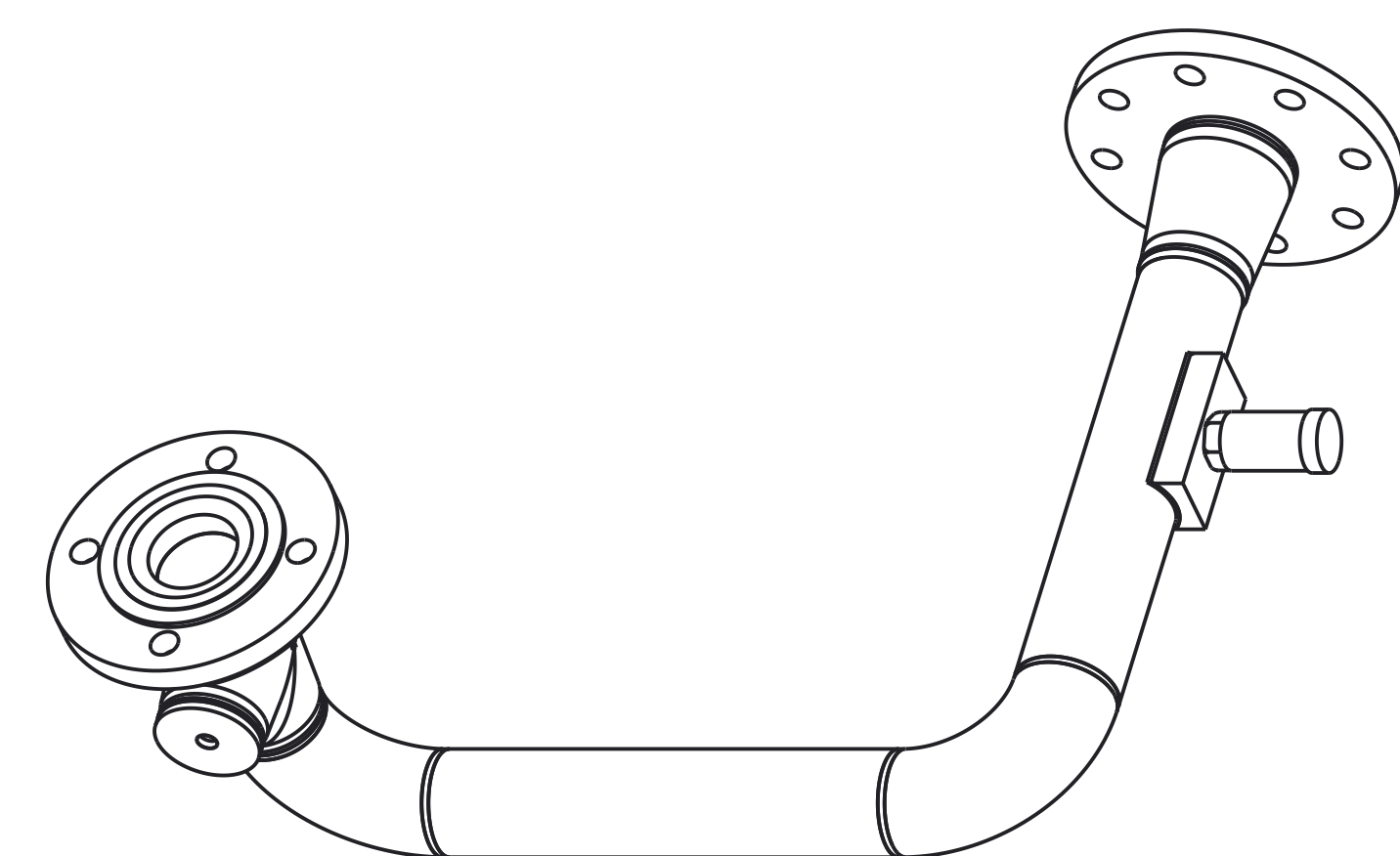
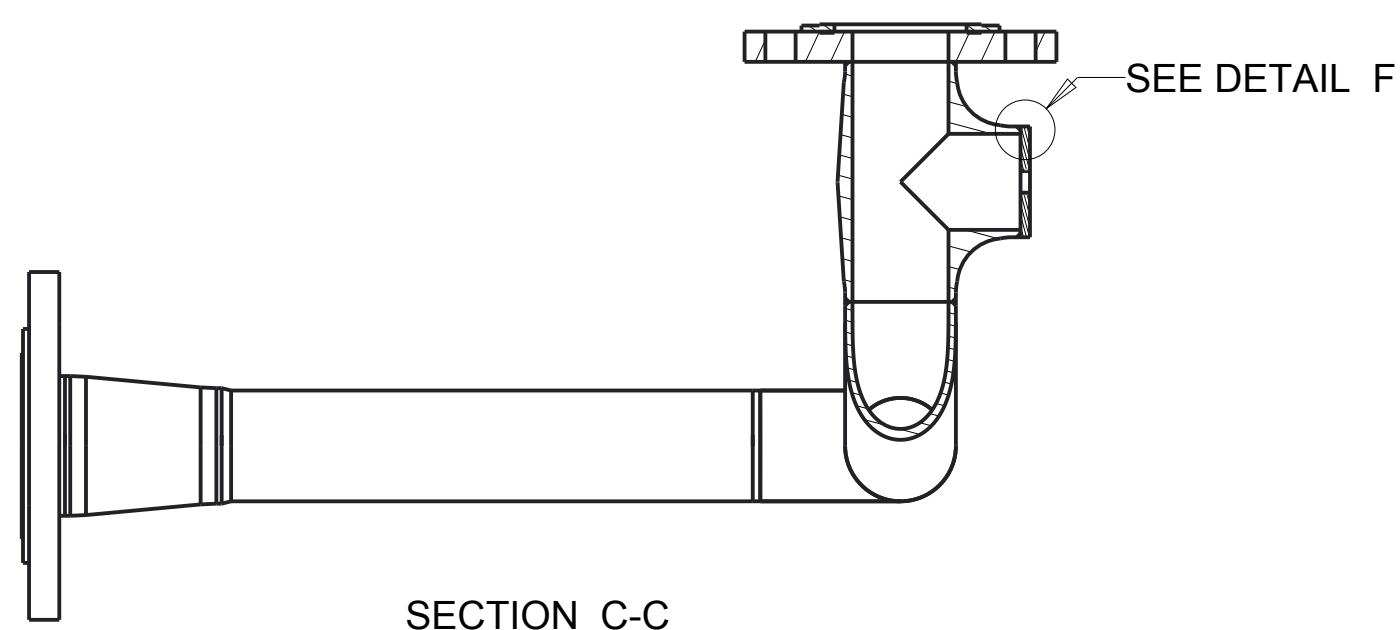
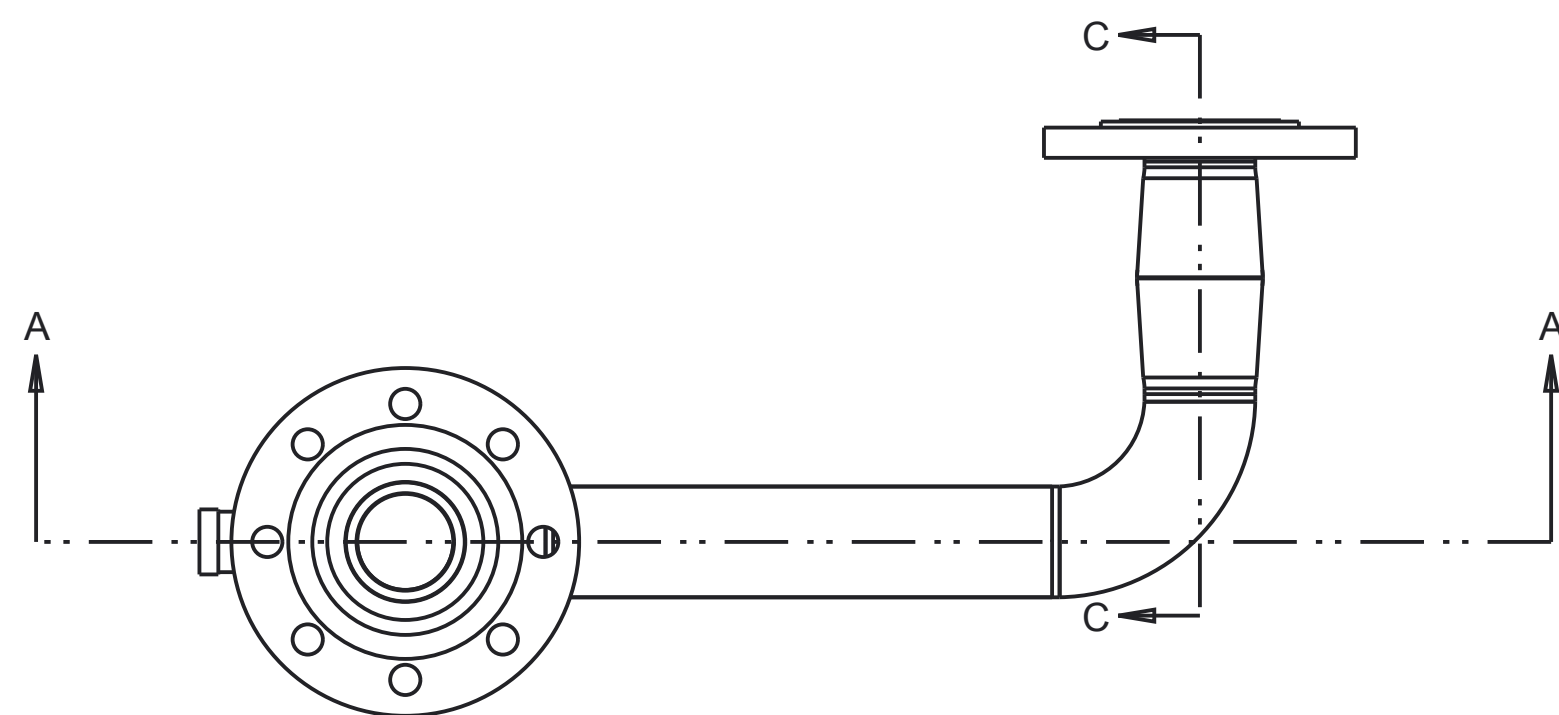
DO NOT SURVEY DIMENSIONS FROM THE DRAWING					
	DRAW	Aldo Iannetti	CHECKED	PROJECT E. M.Stickland	
	QUANTITY	1	MASS	4.68	SCALE
MATERIAL			carbon steel		
TYPE			BLANK		
HEAT TREATMENT			None		
SUPERFICIAL COVERING			Paint		
N° DRAWING			005-02		
SHEET			2		
DATE			25/06/2013		
DENOMINAT.			Pump support vertical plate with window		
GENERAL TOLERANCES EN ISO 13920-AE			SIZE TOLERANCES		
2			30 ±1 ±20'		
30			120 ±1 ±20'		
120			400 ±1 ±20'		
400			1000 ±2 ±15'		
1000			2000 ±3 ±10'		
2000			4000 ±4 ±10'		
4000			8000 ±5 ±10'		



DETAIL E
SCALE 2.000

REV.	DATE	DATE AND MODIFY DESCRIPTION	DRAW	CHECKED	PROJECT E.

DO NOT SURVEY DIMENSIONS FROM THE DRAWING						
 Mechanical and Aerospace Engineering Level 4 Lord Hope Building 141 ST James Road G4 0LT Glasgow UK TEL. 01415484851 maeATstrath.ac.uk aldo.iannettiATstrath.ac.uk	DRAW Aldo Iannetti	CHECKED	PROJECT E. M.Stickland	GENERAL TOLERANCES EN ISO 13920-AE		
	QUANTITY 2	MASS 9.52	SCALE 0.250	TOLERANCES		
	MATERIAL carbon steel			SIZE	TOLERANCES	
	TYPE BLANK			<input type="checkbox"/> > <input type="checkbox"/> <= <input type="checkbox"/> <	± 20'	
TECHNICAL DEPART. WARC			HEAT TREATMENT None			
FORMAT A3	SHEET 3 DATE 25/06/2013		SUPERFICIAL COVERING None			
N° DRAWING 005-03			DENOMINAT. Pump support base plate			
SIZE			2 30 ±1 ±20'	400 1000 ±2 ±15'		
TOLERANCES			30 120 ±1 ±20'	1000 2000 ±3 ±10'		
TOLERANCES			120 400 ±1 ±20'	2000 4000 ±4 ±10'		
TOLERANCES			400 1000 ±2 ±15'	4000 8000 ±5 ±10'		



N°	Assembly/Detail	Drawing	Q.
1	Spiral wound Gasket CG 2"		1
2	Spiral wound Gasket CG 2 1/2"		1
3	Flat flange BS10 Tab F 2"		1
4	Flat flange BS10 tab F 2" 1/2		1
5	concentric reducer BS 1640 Std 2"x2" 1/2		1
6	Pipe 2" BS 1387 Std		2
7	90 elbow long radius BS 1640 Std 2"		2
8	Equal tee BS 1640 Std 2"		1
9	Tee cap 2"	006-02	1
10	plate base 2" pipe	006-03	1

DO NOT SURVEY DIMENSIONS FROM THE DRAWING

		DRAW: Aldo Iannetti CHECKED: _____ PROJECT E: M. Stickland
QUANTITY: 1 MASS: 11.43 SCALE: 0.250	MATERIAL: Standard TYPE: _____ GREZZO: _____ BLANK: _____	GENERAL TOLERANCES EN ISO 12789:AF SIZE TOLERANCE HEAT TREATMENT: None SUPERFICIAL COVERING: paint FINISH: _____ OUTLET PIPE: _____
TECHNICAL DEPART: _____ FORMAT: A1 SHEET: 1 N° DRAWING: 006-01	DATA: _____ DATE: 25/06/2013	GENERAL TOLERANCES EN ISO 12789:AF SIZE TOLERANCE HEAT TREATMENT: None SUPERFICIAL COVERING: paint FINISH: _____ OUTLET PIPE: _____

3

2

1

D

D

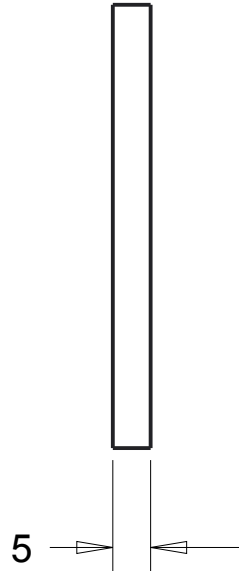
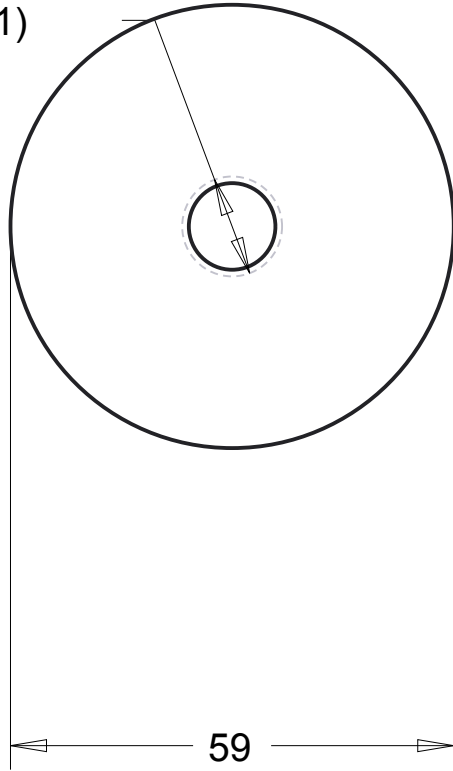
C

C

B

B

G1/4" (∅ 13.21)



					VISTO PROJECTE.
					CONTROLLATO CHECKED
					DISEGNATO DRAW
					DATA E DESCRIZIONE MODIFICA DATE AND MODIFY DESCRIPTION
					DATA DATE
					REV.

DO NOT SURVEY DIMENSIONS FROM THE DRAWING

		DRAW	Aldo Iannetti		CHECKED			PROJECT E.	M.Stickland																																	
		QUANTITY	1		MASS	0.105		SCALE	1.000																																	
Mechanical and Aerospace Engineering Level 4 Lord Hope Building 141 ST James Road G4 0LT Glasgow UK TEL.01415484851 maeATstrath.ac.uk aldo.iannettiATstrath.ac.uk		MATERIAL	Carbon steel						GENERAL TOLERANCES EN ISO 13920-AE																																	
TECHNICAL DEPART. WARC		TYPE	BLANK		HEAT TREATMENT		None		<table border="1"> <tr> <td><input type="checkbox"/></td> <td><input type="checkbox"/></td> <td><input type="checkbox"/></td> <td><input type="checkbox"/></td> </tr> <tr> <td>2</td> <td>30</td> <td>±1</td> <td>±20'</td> </tr> <tr> <td>30</td> <td>120</td> <td>±1</td> <td>±20'</td> </tr> <tr> <td>120</td> <td>400</td> <td>±1</td> <td>±20'</td> </tr> <tr> <td>400</td> <td>1000</td> <td>±2</td> <td>±15'</td> </tr> <tr> <td>1000</td> <td>2000</td> <td>±3</td> <td>±10'</td> </tr> <tr> <td>2000</td> <td>4000</td> <td>±4</td> <td>±10'</td> </tr> <tr> <td>4000</td> <td>8000</td> <td>±5</td> <td>±10'</td> </tr> </table>		<input type="checkbox"/>	<input type="checkbox"/>	<input type="checkbox"/>	<input type="checkbox"/>	2	30	±1	±20'	30	120	±1	±20'	120	400	±1	±20'	400	1000	±2	±15'	1000	2000	±3	±10'	2000	4000	±4	±10'	4000	8000	±5	±10'
<input type="checkbox"/>	<input type="checkbox"/>	<input type="checkbox"/>	<input type="checkbox"/>																																							
2	30	±1	±20'																																							
30	120	±1	±20'																																							
120	400	±1	±20'																																							
400	1000	±2	±15'																																							
1000	2000	±3	±10'																																							
2000	4000	±4	±10'																																							
4000	8000	±5	±10'																																							
FORMAT	A4	SUPERFICIAL COVERING		None		SHEET		2																																		
DATE		25/06/2013		DENOMINAT.		Tee Cap 2		N° DRAWING																																		
006-02																																										

3

2

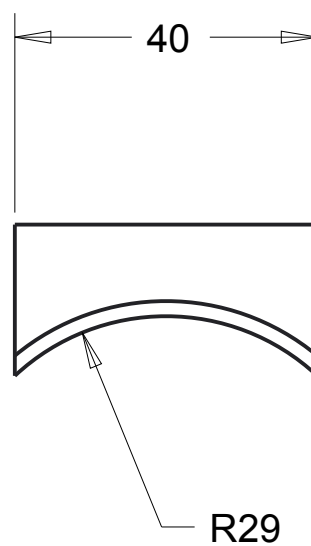
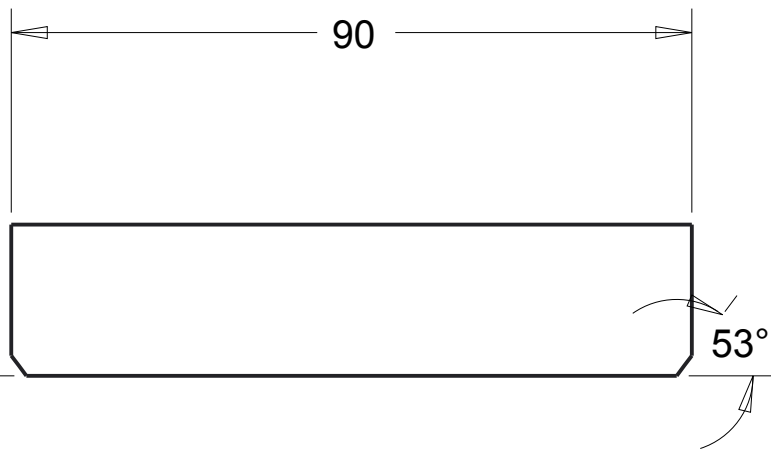
1

3

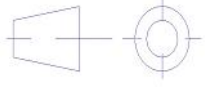
2

1

					VISTO PROJECTE.
					CONTROLLATO CHECKED
					DISEGNATO DRAW
					DATA DESCRIZIONE MODIFICA DATE AND MODIFY DESCRIPTION
					DATA DATE
					REV.



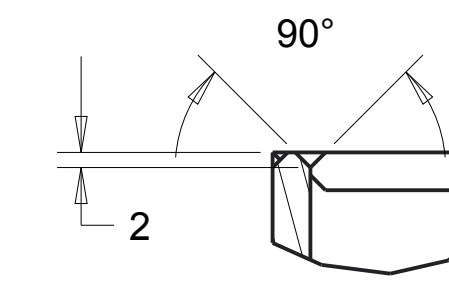
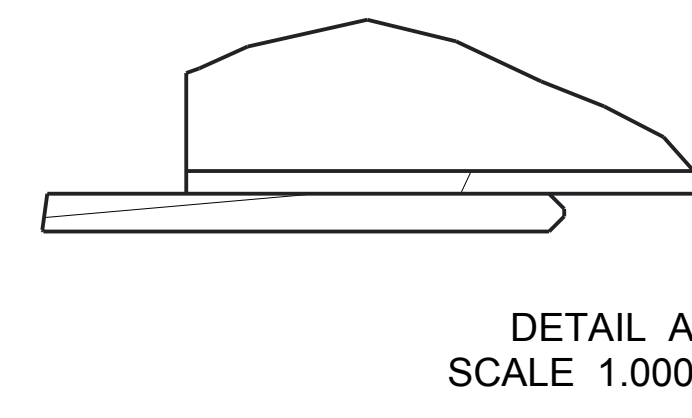
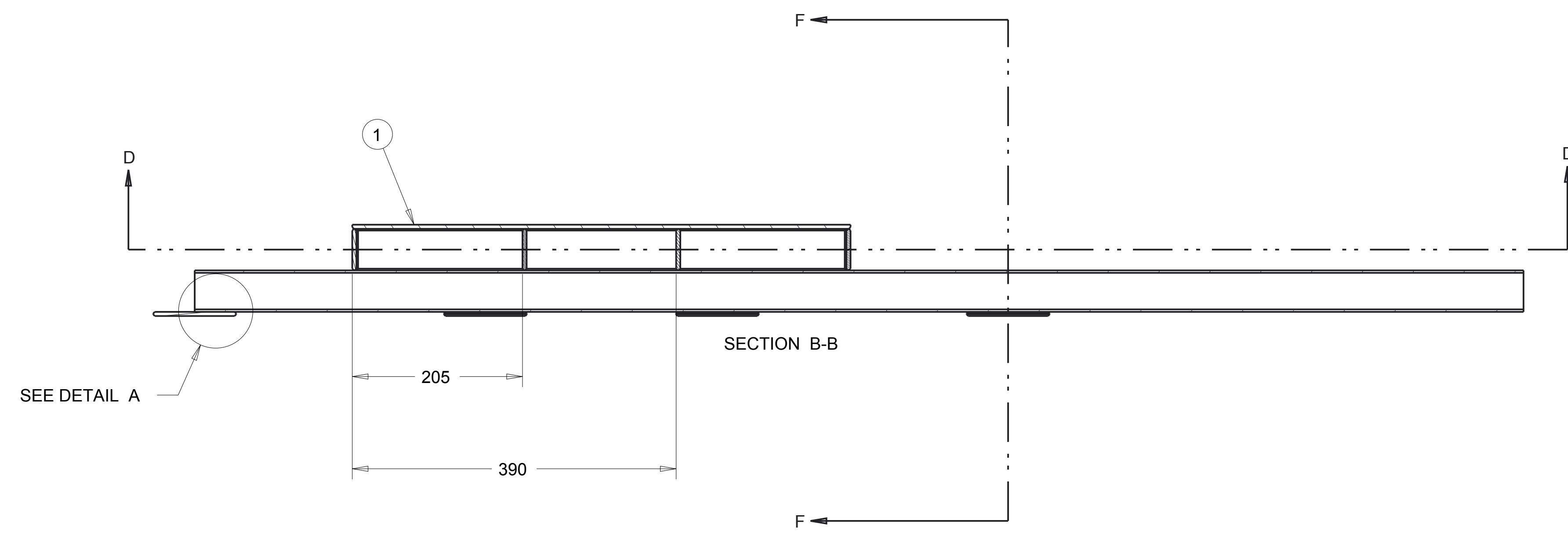
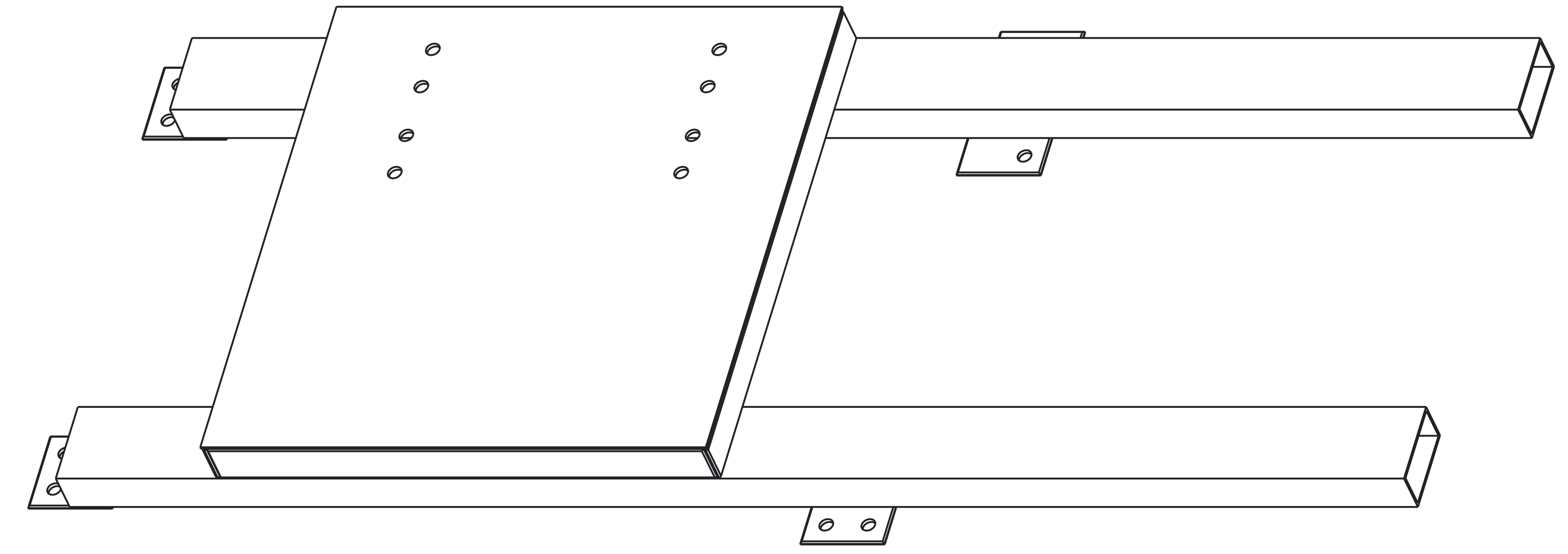
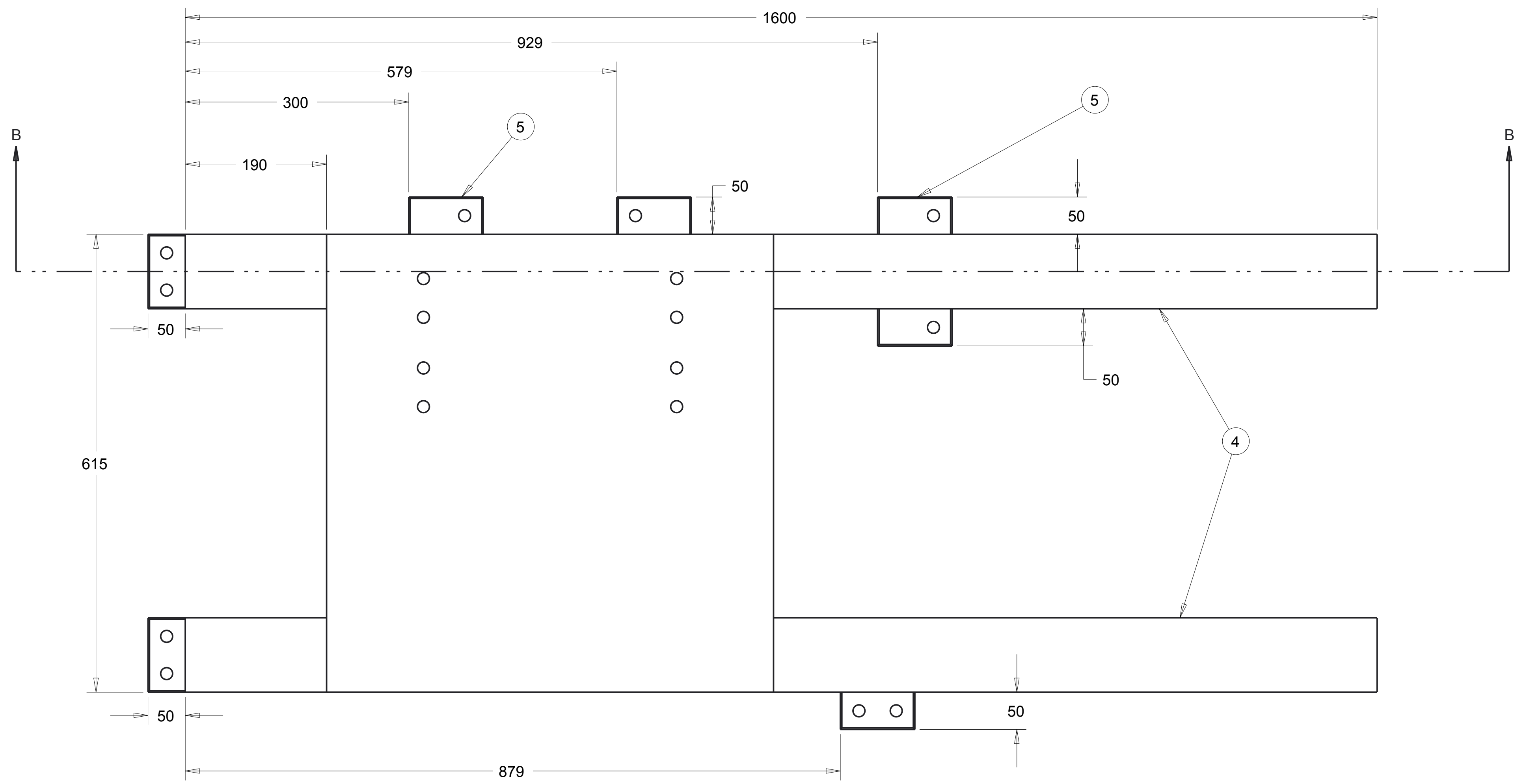
DO NOT SURVEY DIMENSIONS FROM THE DRAWING

	DRAW	Aldo Iannetti	CHECKED		PROJECT E.	M.Stickland																																
	QUANTITY	1	MASS	0.3	SCALE	1.000																																
MATERIAL			Carbon steel			GENERAL TOLERANCES EN ISO 13920-AE																																
Mechanical and Aerospace Engineering Level 4 Lord Hope Building 141 ST James Road G4 0LT Glasgow UK		TEL.01415484851 maeATstrath.ac.uk aldo.iannettiATstrath.ac.uk		TYPE	BLANK																																	
TECHNICAL DEPART. WARC			HEAT TREATMENT			<table border="1"> <tr> <td><input type="checkbox"/></td> <td><input type="checkbox"/></td> <td><input type="checkbox"/></td> <td><input type="checkbox"/></td> </tr> <tr> <td>2</td> <td>30</td> <td>±1</td> <td>±20'</td> </tr> <tr> <td>30</td> <td>120</td> <td>±1</td> <td>±20'</td> </tr> <tr> <td>120</td> <td>400</td> <td>±1</td> <td>±20'</td> </tr> <tr> <td>400</td> <td>1000</td> <td>±2</td> <td>±15'</td> </tr> <tr> <td>1000</td> <td>2000</td> <td>±3</td> <td>±10'</td> </tr> <tr> <td>2000</td> <td>4000</td> <td>±4</td> <td>±10'</td> </tr> <tr> <td>4000</td> <td>8000</td> <td>±5</td> <td>±10'</td> </tr> </table>	<input type="checkbox"/>	<input type="checkbox"/>	<input type="checkbox"/>	<input type="checkbox"/>	2	30	±1	±20'	30	120	±1	±20'	120	400	±1	±20'	400	1000	±2	±15'	1000	2000	±3	±10'	2000	4000	±4	±10'	4000	8000	±5	±10'
<input type="checkbox"/>	<input type="checkbox"/>	<input type="checkbox"/>	<input type="checkbox"/>																																			
2	30	±1	±20'																																			
30	120	±1	±20'																																			
120	400	±1	±20'																																			
400	1000	±2	±15'																																			
1000	2000	±3	±10'																																			
2000	4000	±4	±10'																																			
4000	8000	±5	±10'																																			
FORMAT	A4	SUPERFICIAL COVERING			None																																	
SHEET	3	DATE	25/06/2013																																			
N° DRAWING	006-03		DENOMINAT.			Plate base for pipe 2"																																

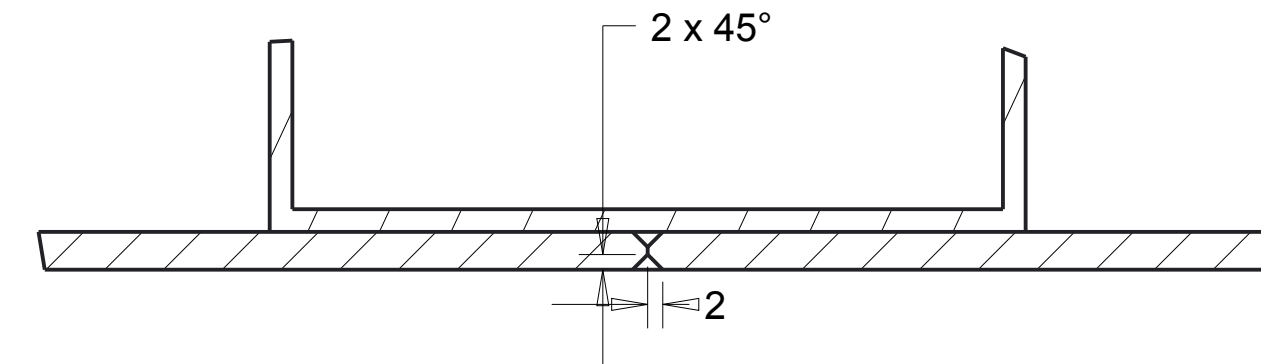
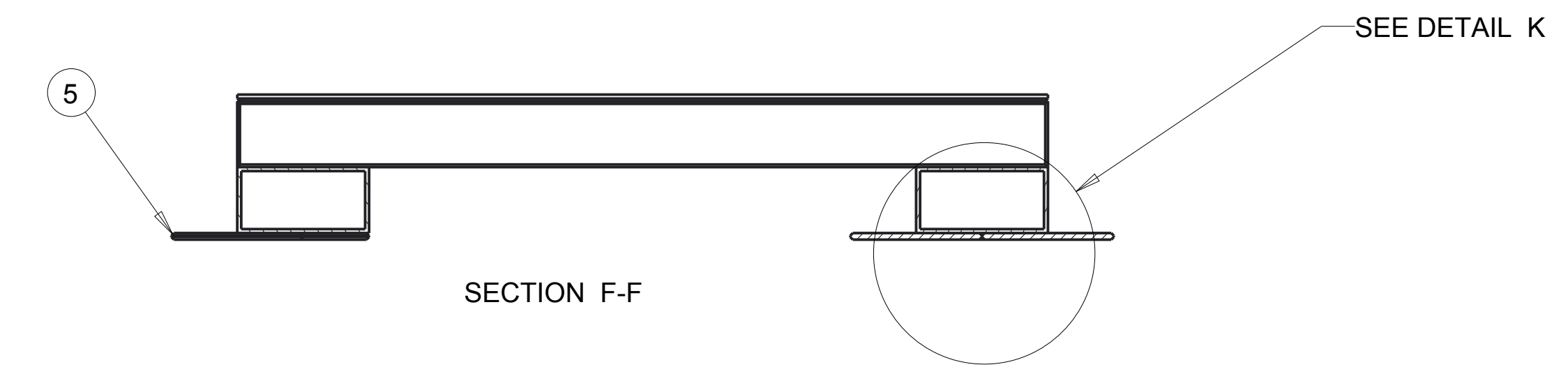
3

2

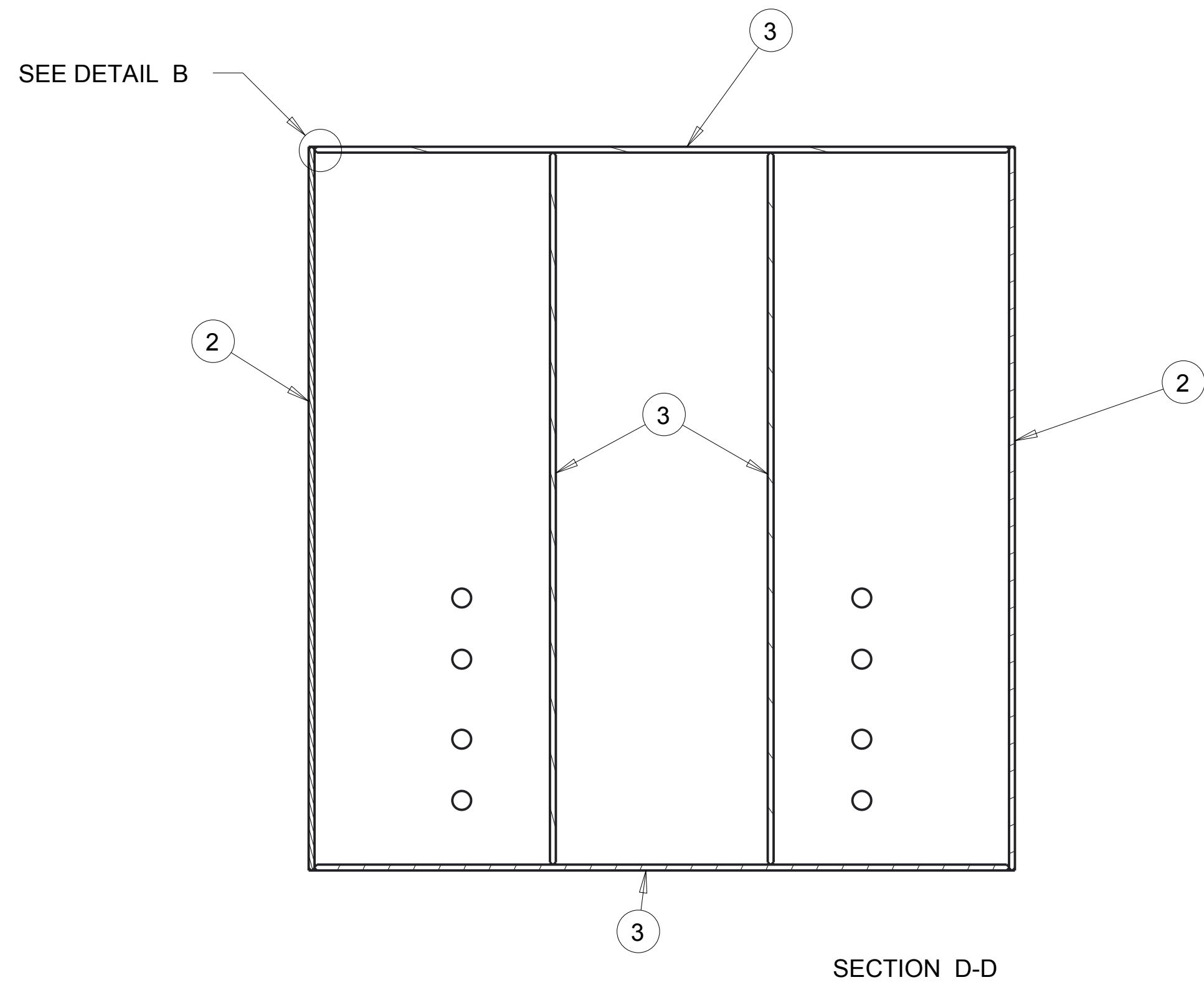
1



DETAIL B
SCALE 1.000



DETAIL K
SCALE 1.000

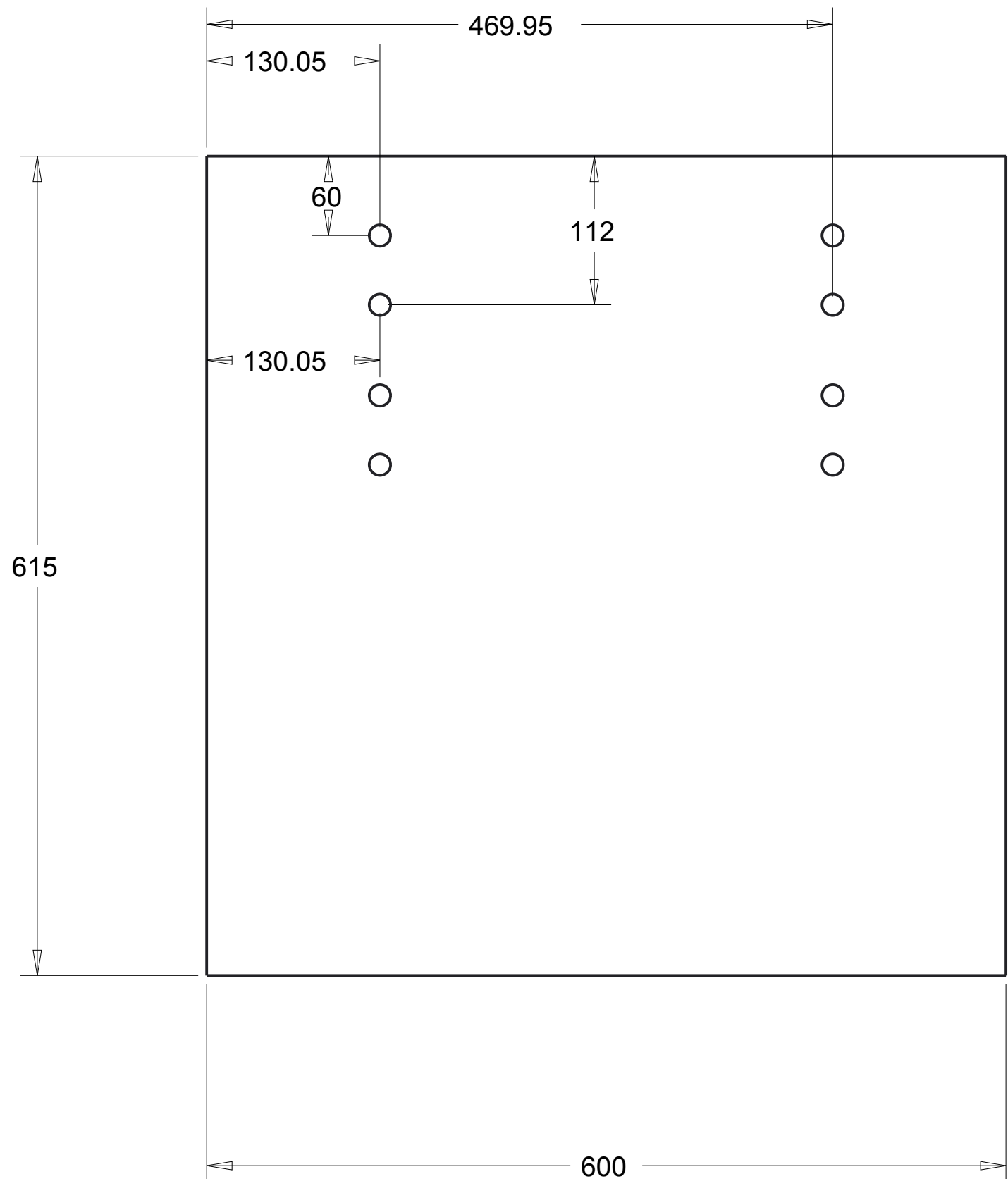


SECTION D-D

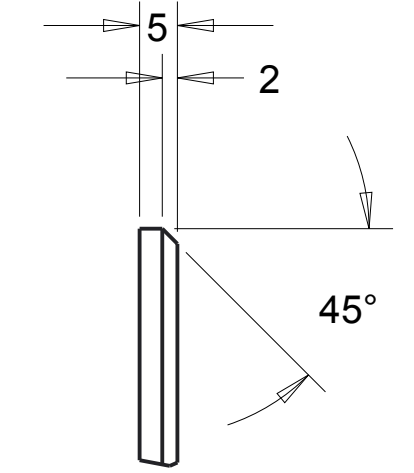
N°	Assembly/Detail	Drawing	Q.
1	Plate 600x600x5	007-02	1
2	Plate 600x50x5	007-03	2
3	Plate 590x50x5	007-04	4
4	rectangular section hollow beam 100x50x3		2
5	connection plate 100x100x5	009-03	7

DO NOT SURVEY DIMENSIONS FROM THE DRAWING

UNIVERSITY OF STRATHCLYDE Strathclyde Glasgow	DESIGNER: Aldo Iannetti	PROJECT: M. Stickland
QUANTITY: 1	SCALE: 45	SCALE: 0.250
SYSTEM: standard	TYPE: none	HEAT TREATMENT: None
FORM: A0	DATE: 25/06/2013	SUPERFICIAL COATING: paint
SHEET: 1	DATE: 25/06/2013	PROJECT: Linear motor framework
DRAWING: 007-01		



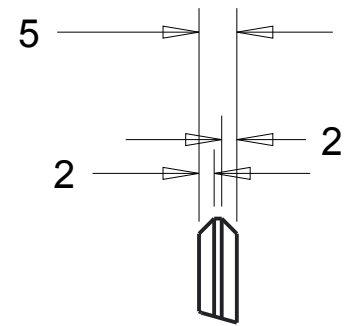
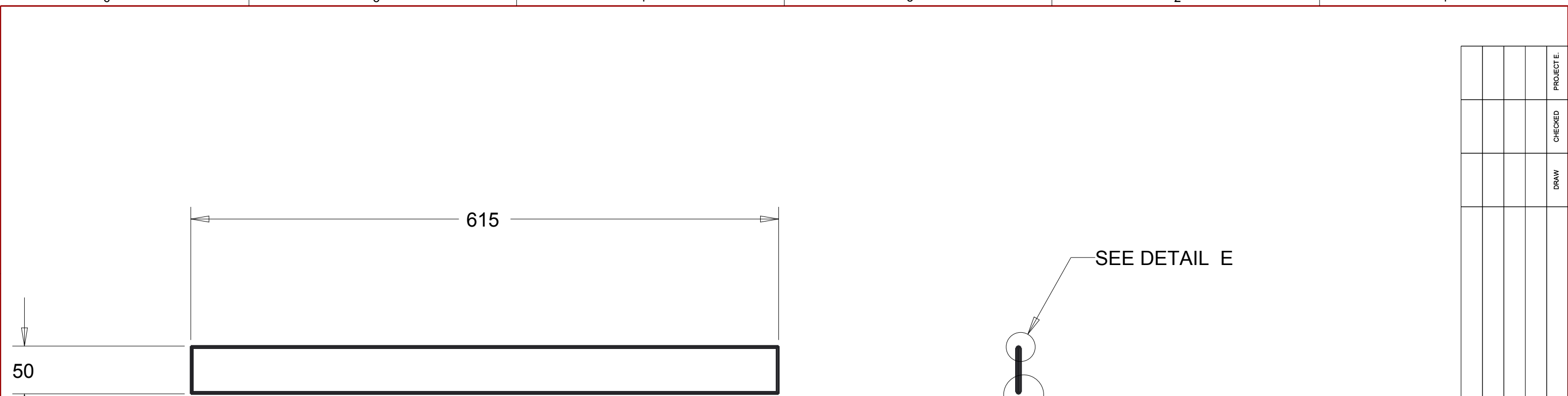
SEE DETAIL D



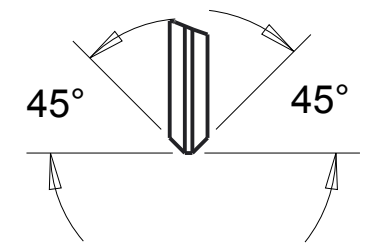
DETAIL D
SCALE 1.000

				PROJECT E.
				CHECKED
				DRAW
				DATE
				REV.

DO NOT SURVEY DIMENSIONS FROM THE DRAWING									
		DRAW Aldo Iannetti		CHECKED		PROJECT E. M.Stickland			
		QUANTITY 1		MASS 13.9		SCALE 0.250			
Mechanical and Aerospace Engineering Level 4 Lord Hope Building 141 ST James Road G4 0LT Glasgow UK TEL. 01415484851 mae@strath.ac.uk aldo.iannetti@strath.ac.uk		MATERIAL carbon steel				GENERAL TOLERANCES EN ISO 13920-AE			
TECHNICAL DEPART. WARC		TYPE BLANK		HEAT TREATMENT None		SIZE		TOLERANCES	
FORMAT A3		DATE 25/06/2013		SUPERFICIAL COVERING None		2 30 ±1 ±20'		30 120 ±1 ±20'	
SHEET 2		N° DRAWING 007-02		DENOMINAT. Plate 600x600		120 400 ±1 ±20'		400 1000 ±2 ±15'	
						1000 2000 ±3 ±10'		2000 4000 ±4 ±10'	
						4000 8000 ±5 ±10'			



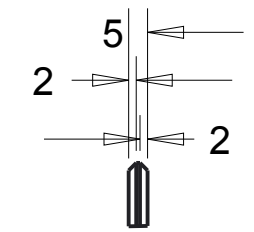
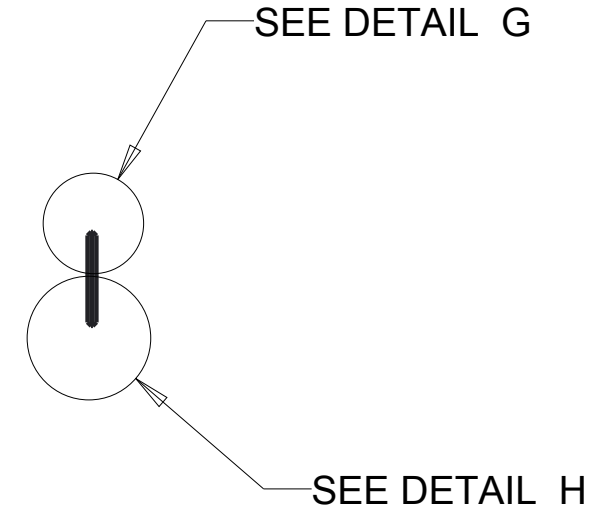
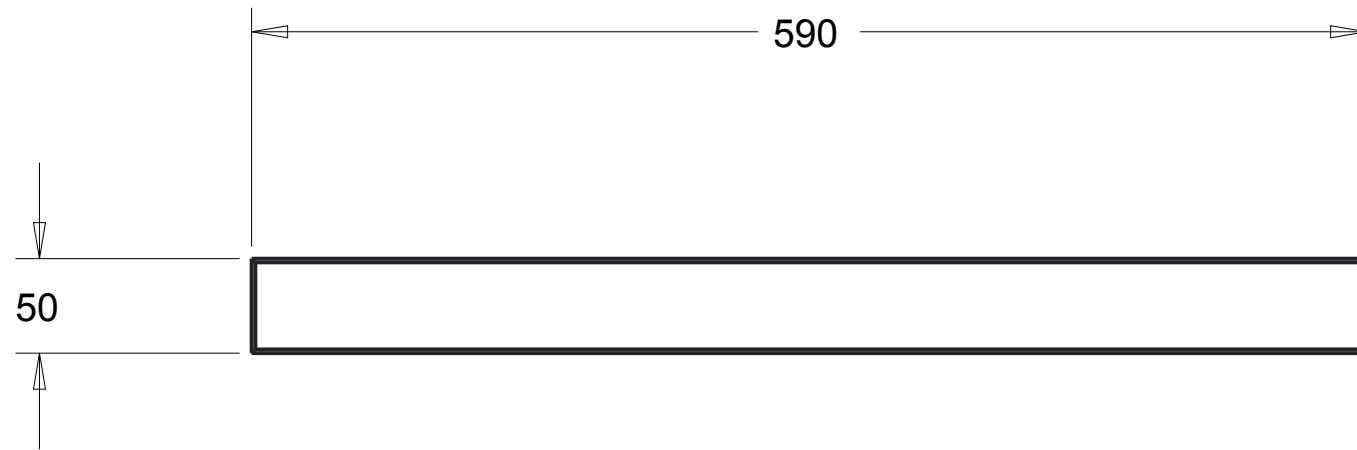
DETAIL E
SCALE 1.000



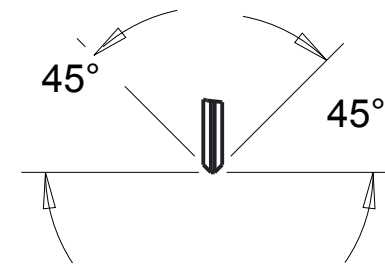
DETAIL F
SCALE 1.000

REV.	DATE	DATE AND MODIFY DESCRIPTION	DRAW	CHECKED	PROJECT E.

DO NOT SURVEY DIMENSIONS FROM THE DRAWING					
<p>Mechanical and Aerospace Engineering Level 4 Lord Hope Building 141 ST James Road G4 0LT Glasgow UK</p> <p>TEL. 01415484851 mae@strath.ac.uk aldo.iannetti@strath.ac.uk</p>	DRAW Aldo Iannetti	CHECKED	PROJECT E. M.Stickland	GENERAL TOLERANCES EN ISO 13920-AE	
	QUANTITY 2	MASS 1.13	SCALE 0.250	TYPE	BLANK
	MATERIAL Carbon steel			SIZE	TOLERANCES
	TECHNICAL DEPART. WARC		HEAT TREATMENT None	<input type="checkbox"/> >	<input type="checkbox"/> <=
FORMAT A3	SHEET 3	DATE 25/06/2013	SUPERFICIAL COVERING None	2 30 ±1 ±20'	30 120 ±1 ±20'
N° DRAWING 007-03		DENOMINAT. Plate 600x50		120 400 ±1 ±20'	400 1000 ±2 ±15'
				1000 2000 ±3 ±10'	2000 4000 ±4 ±10'
				4000 8000 ±5 ±10'	



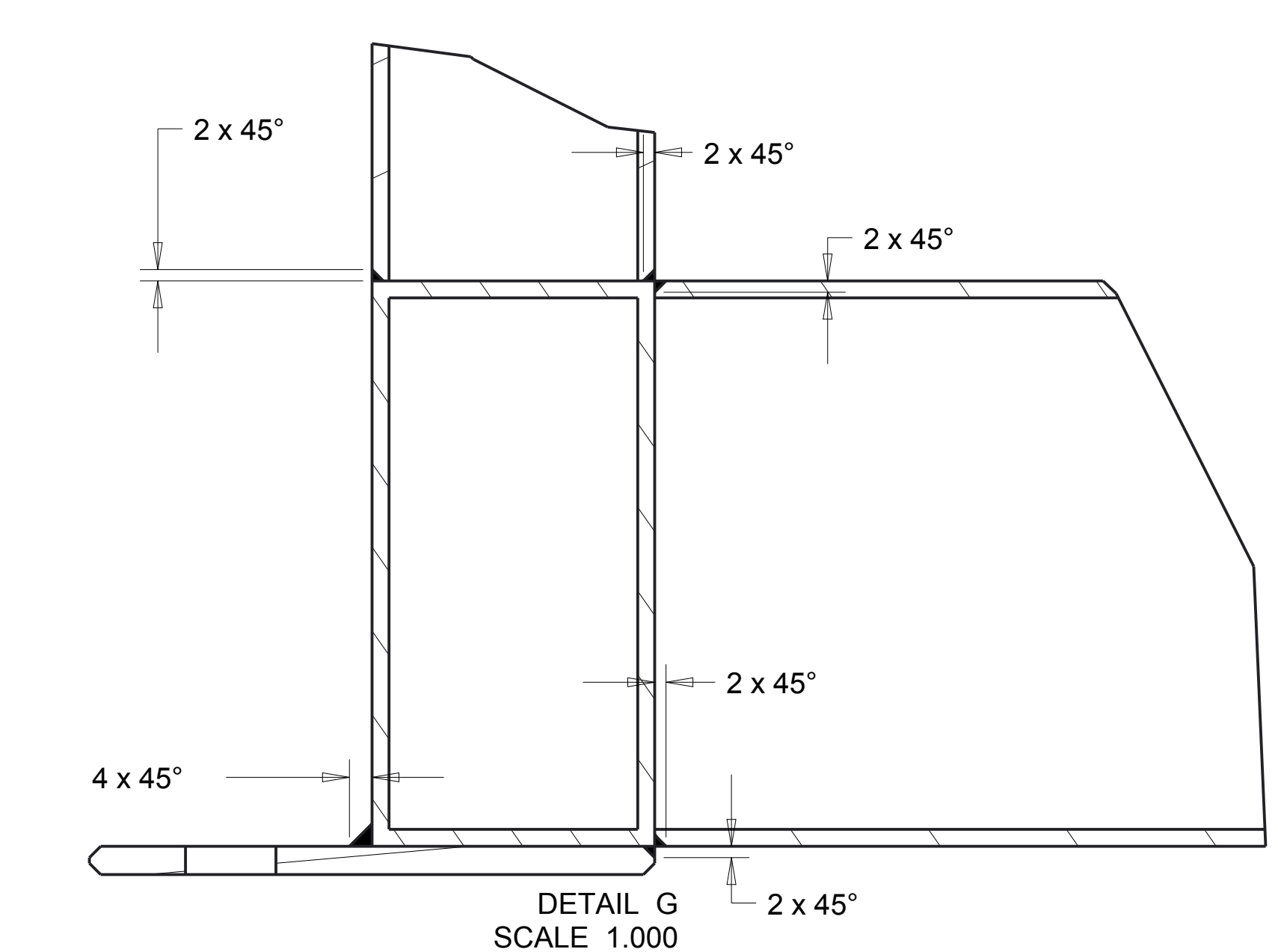
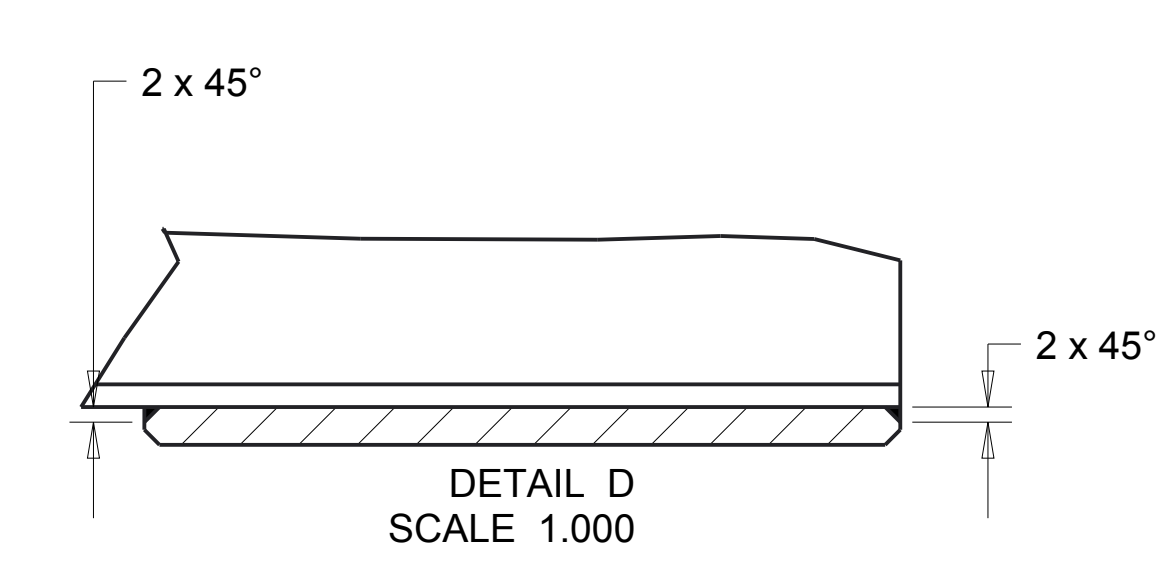
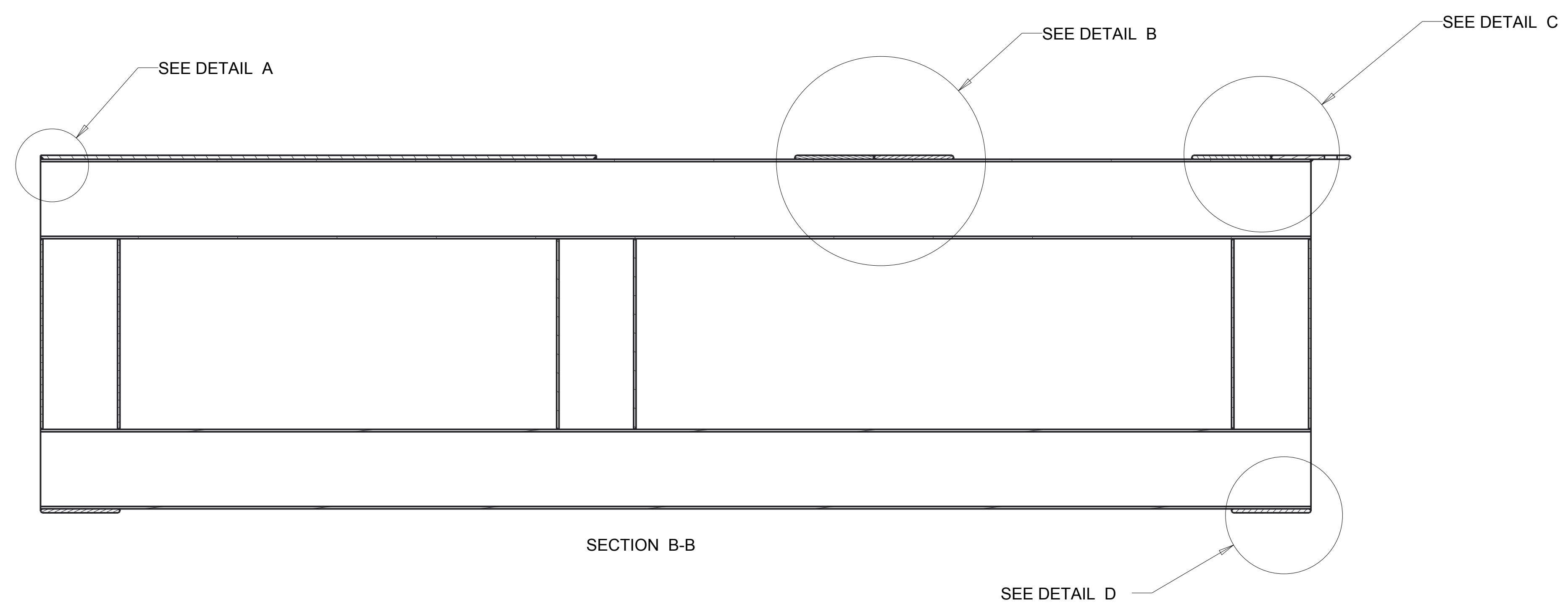
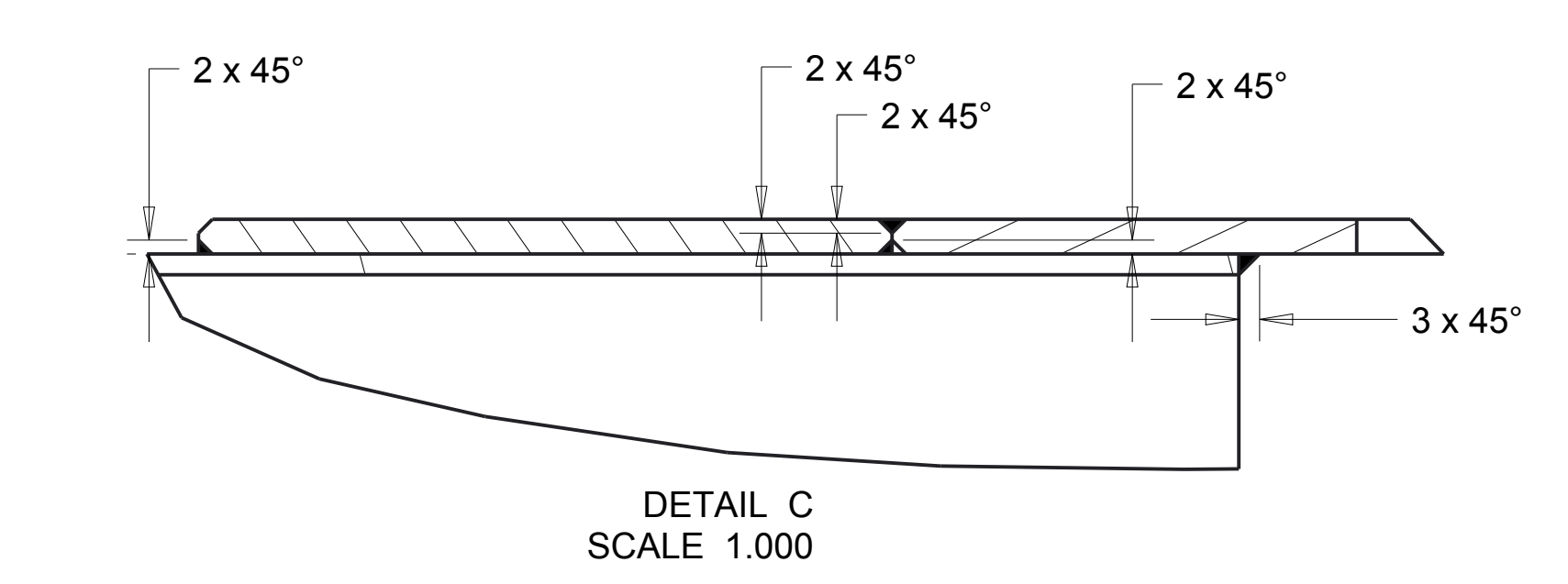
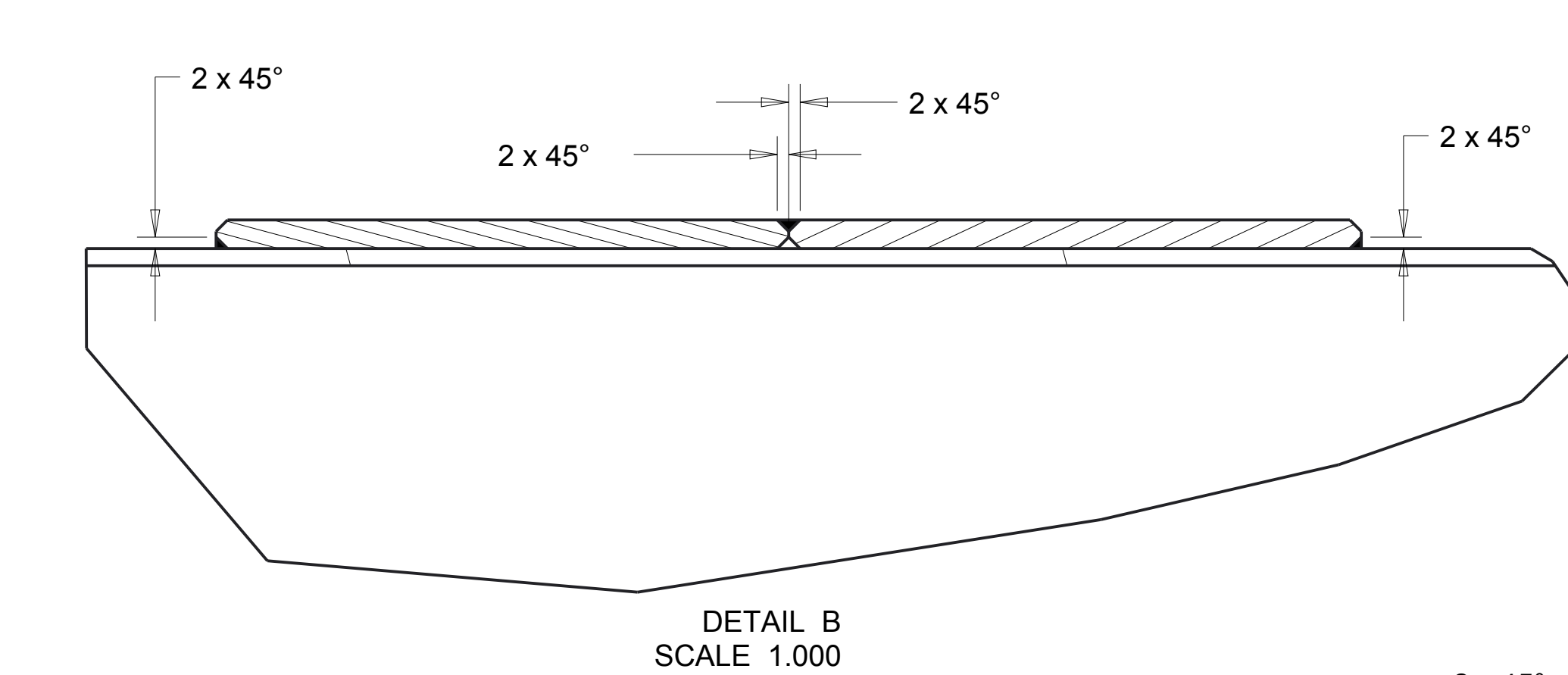
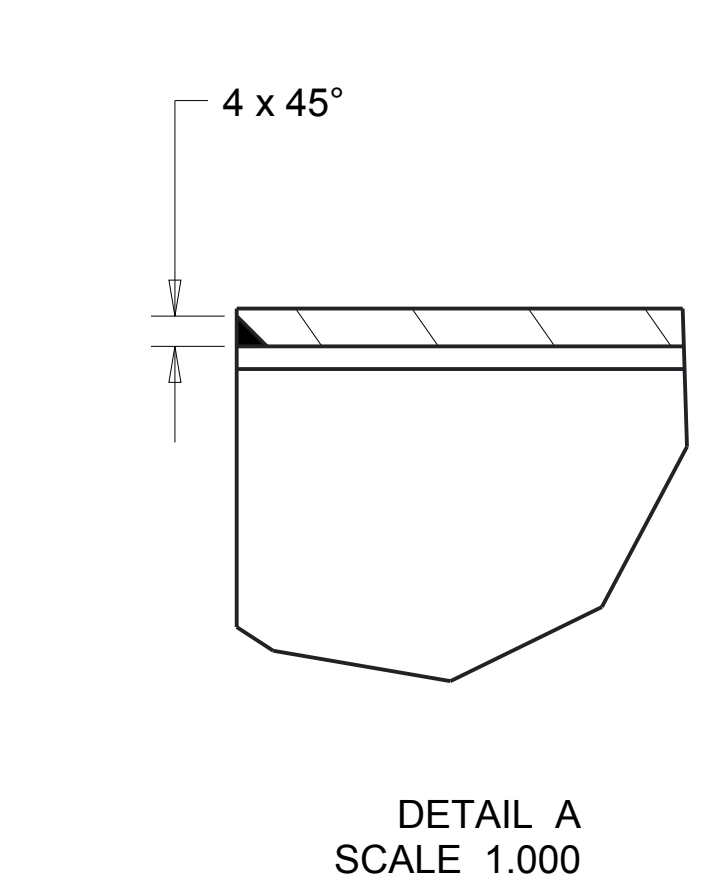
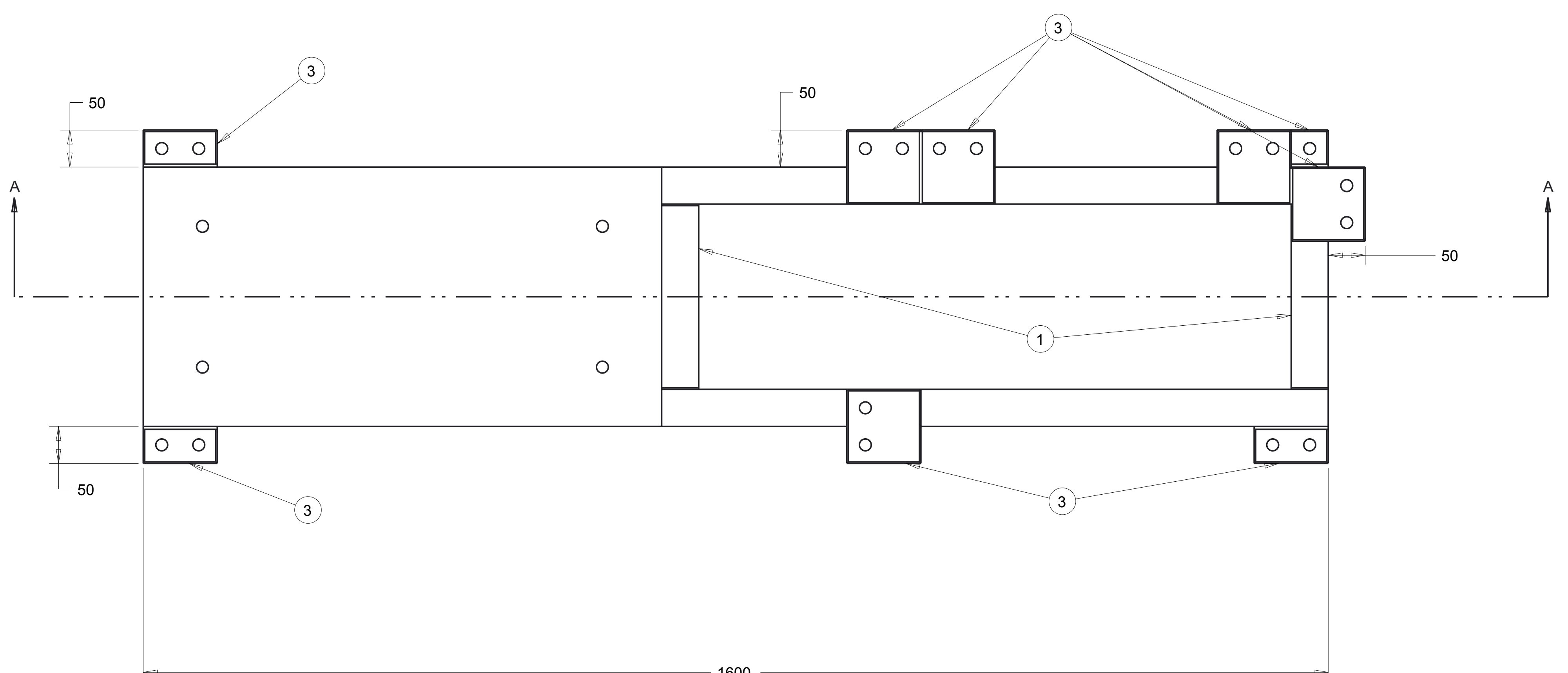
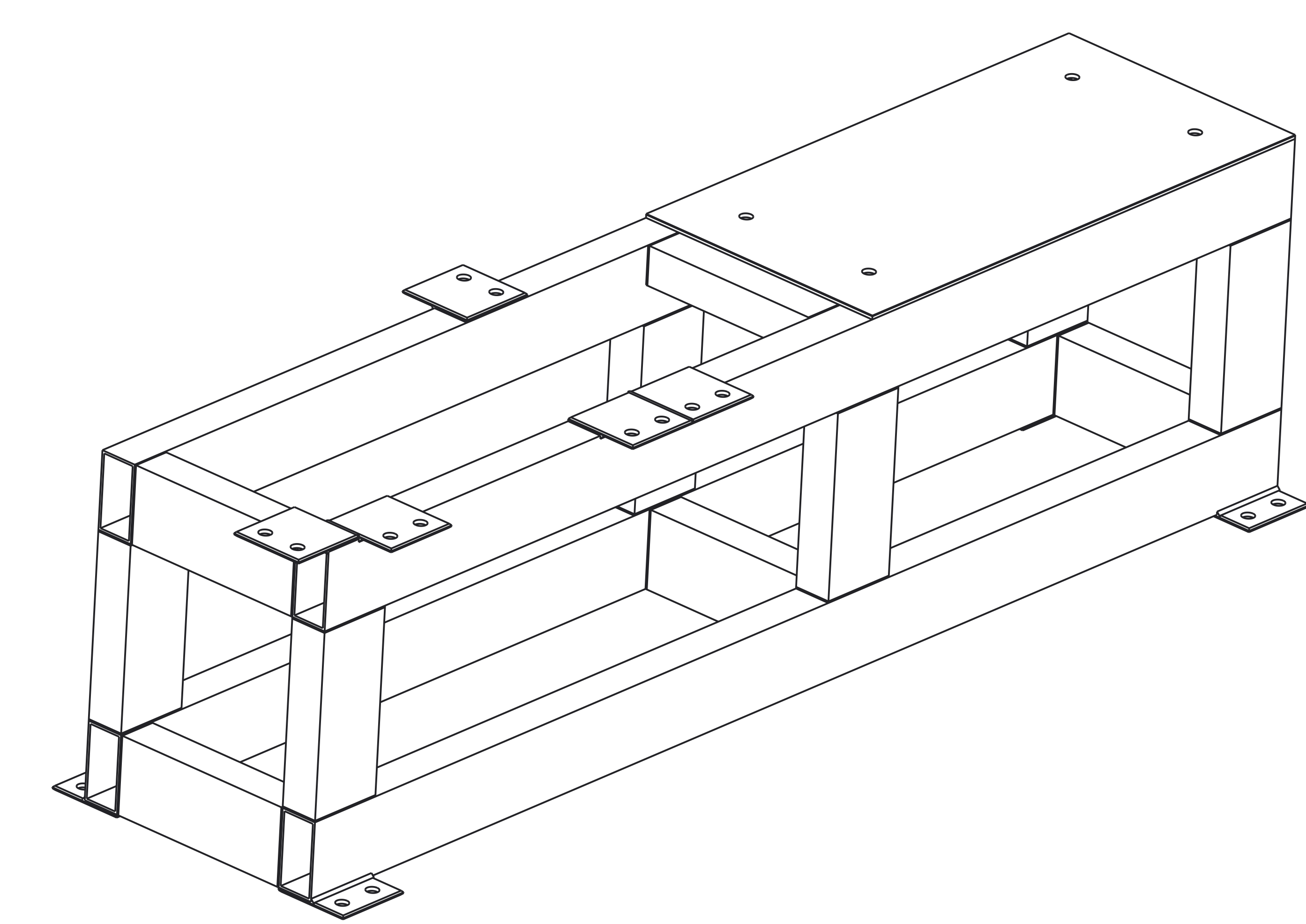
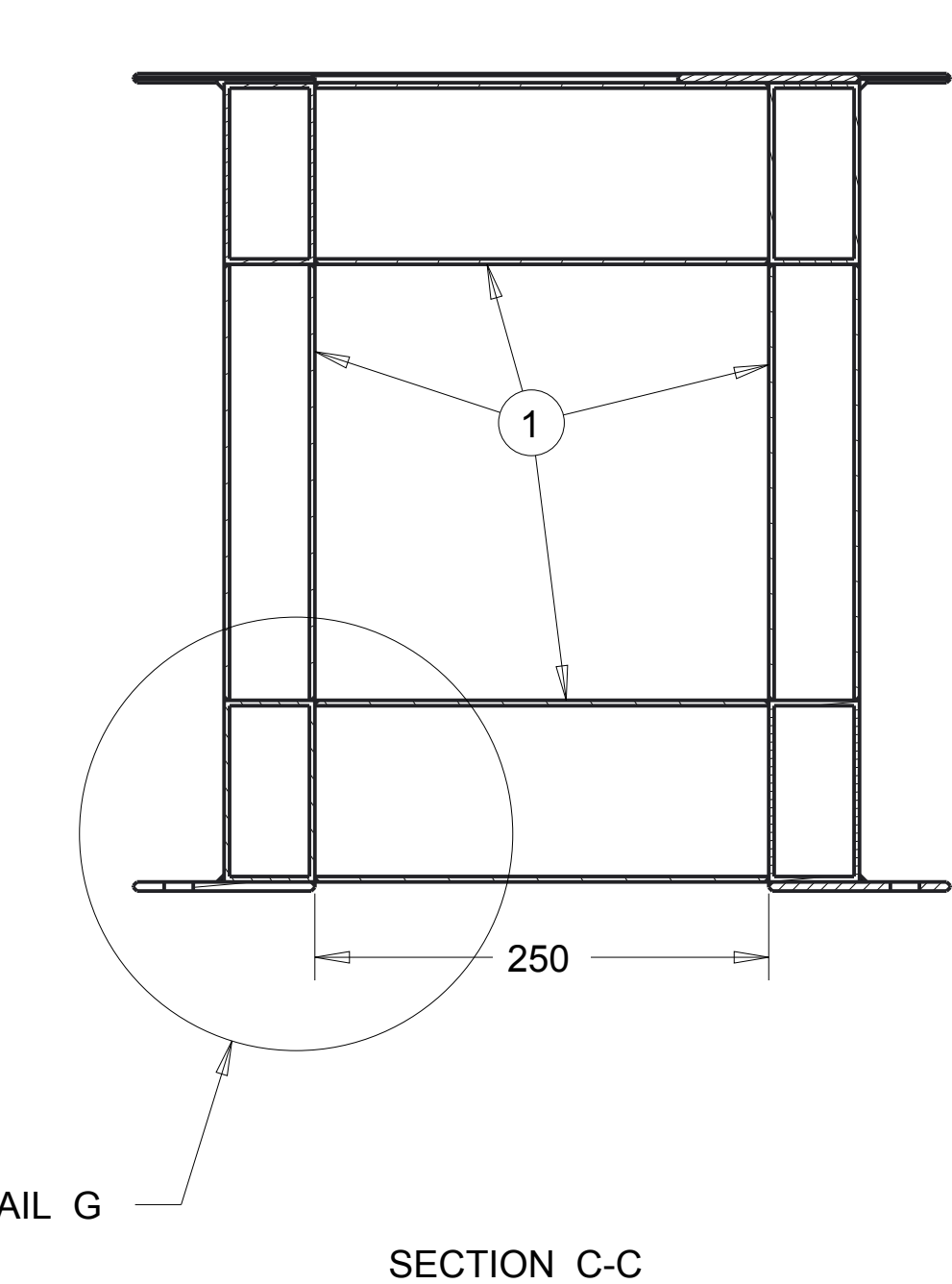
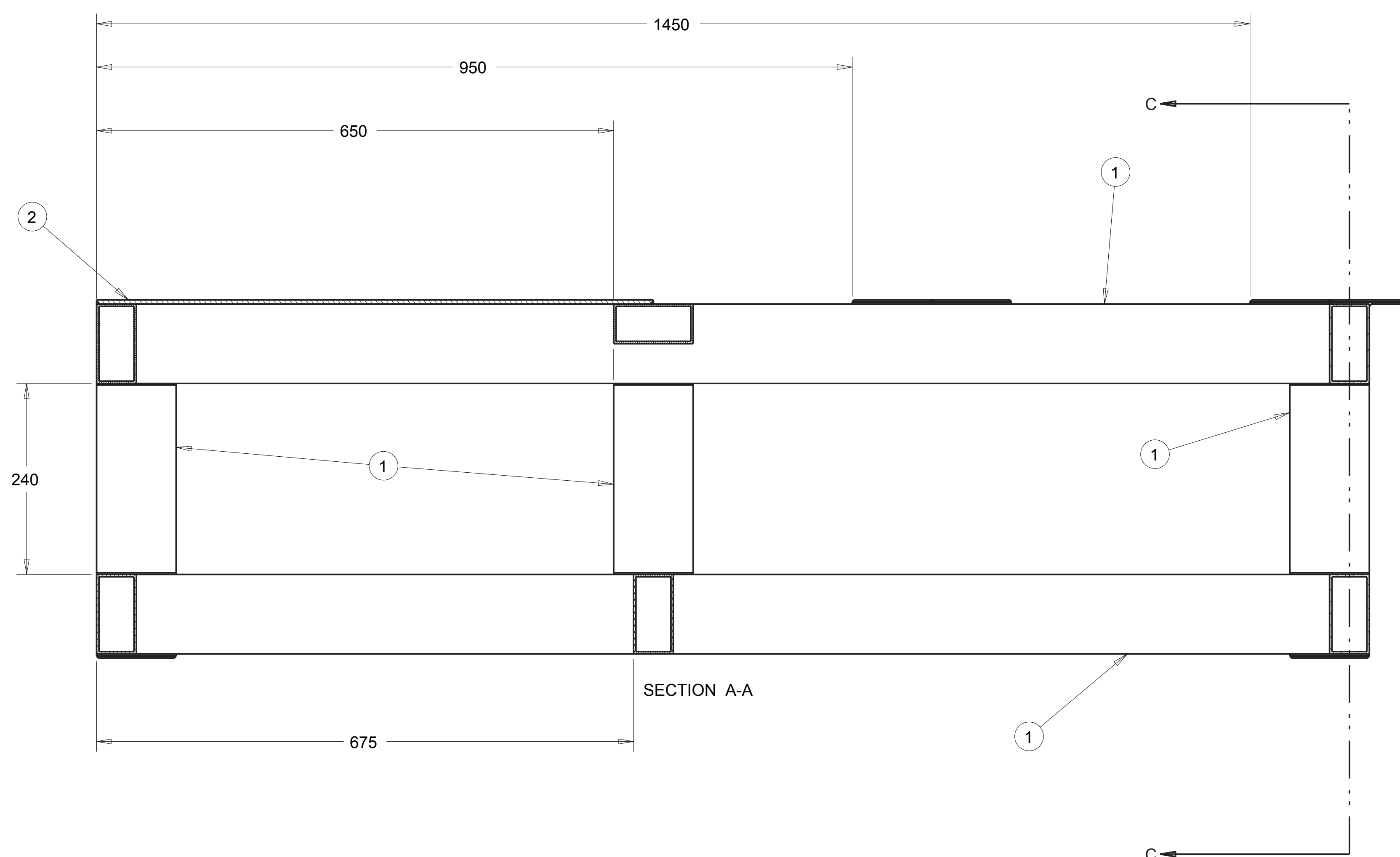
DETAIL G
SCALE 0.500



DETAIL H
SCALE 0.500

REV.	DATE	DATE AND MODIFY DESCRIPTION	DRAW	CHECKED	PROJECT E.

DO NOT SURVEY DIMENSIONS FROM THE DRAWING					
<p>Mechanical and Aerospace Engineering Level 4 Lord Hope Building 141 ST James Road G4 0LT Glasgow UK</p> <p>TEL. 01415484851 mae@strath.ac.uk aldo.iannetti@strath.ac.uk</p>	DRAW Aldo Iannetti	CHECKED	PROJECT E. M.Stickland	GENERAL TOLERANCES EN ISO 13920-AE	
	QUANTITY 4	MASS 1.11	SCALE 0.250	SIZE	TOLERANCES
	MATERIAL Carbon steel			TYPE BLANK	<input type="checkbox"/> > <input type="checkbox"/> <= <input type="checkbox"/> <
	TECHNICAL DEPART. WARC	HEAT TREATMENT None	SUPERFICIAL COVERING None		2 30 ±1 ±20' 30 120 ±1 ±20' 120 400 ±1 ±20' 400 1000 ±2 ±15' 1000 2000 ±3 ±10' 2000 4000 ±4 ±10' 4000 8000 ±5 ±10'
FORMAT A3	SHEET 4	DATE 25/06/2013	DENOMINAT. Plate 590x50		
N° DRAWING 007-04					



N°	Assembly/Detail	Drawing	Q.
1	Rectangular section Hollow beam 100x50	009-02	16
2	Rectangular plate 700x350	009-02	1
3	100x100 connection plate	009-03	9

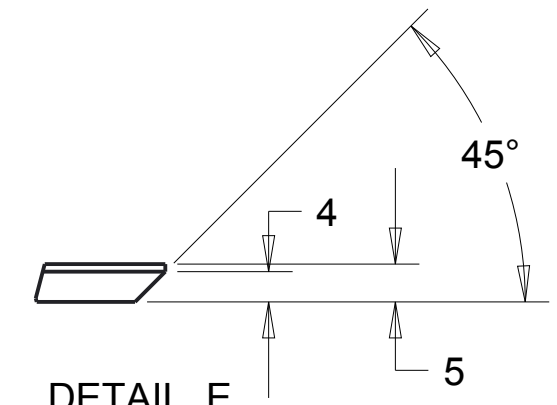
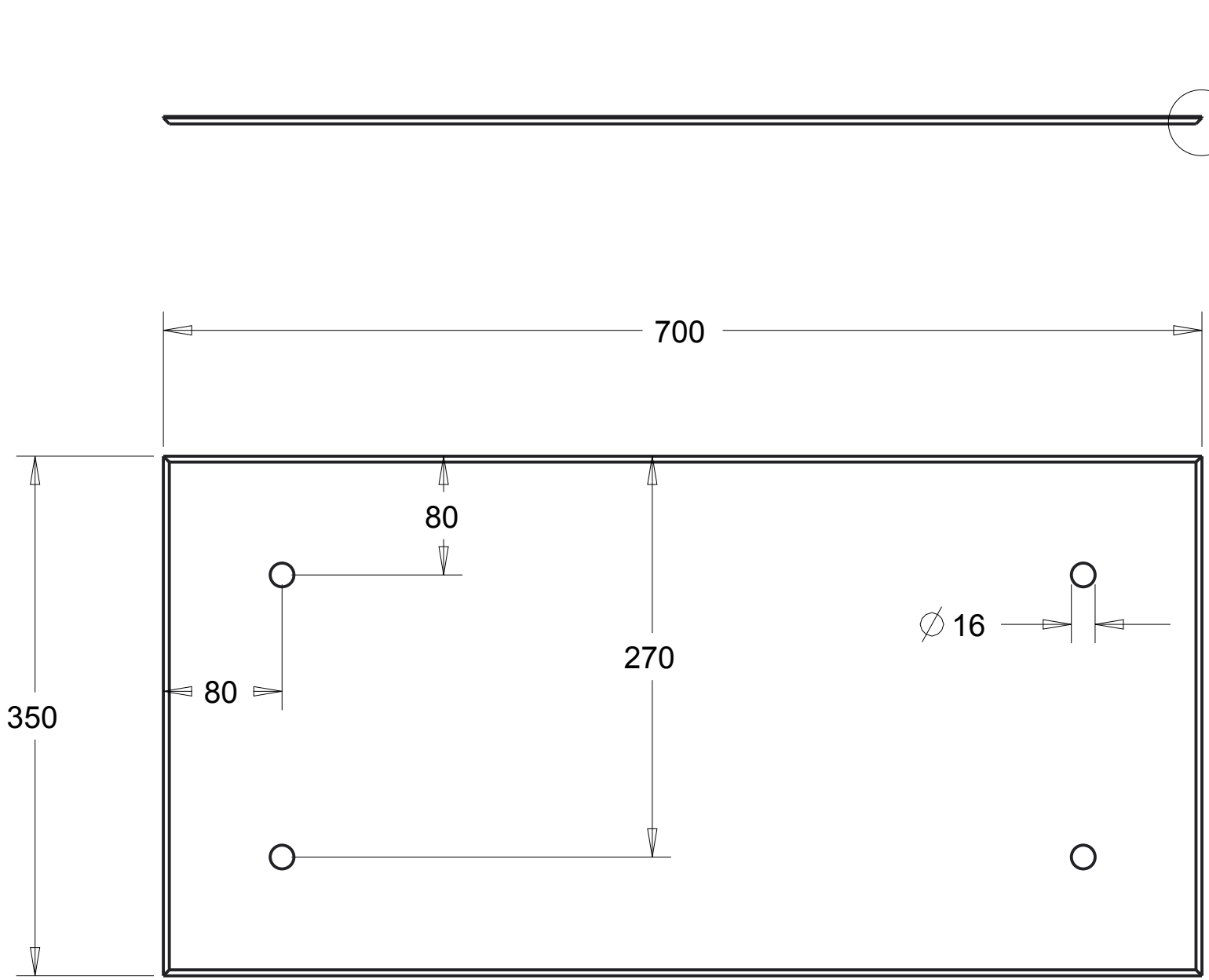
UNIVERSITY OF STRATHCLYDE
Strathclyde
 Glasgow

DO NOT SURVEY DIMENSIONS FROM THE DRAWING

DESIGNER: Aldo Iannetti
 CHECKED: M. Stickland
 QUANTITY: 1
 WEIGHT: 75.8
 SCALE: 0.250

TECHNICAL DEPARTMENT: A0
 DATE: 25/06/2013
 DRAWING: 009-01

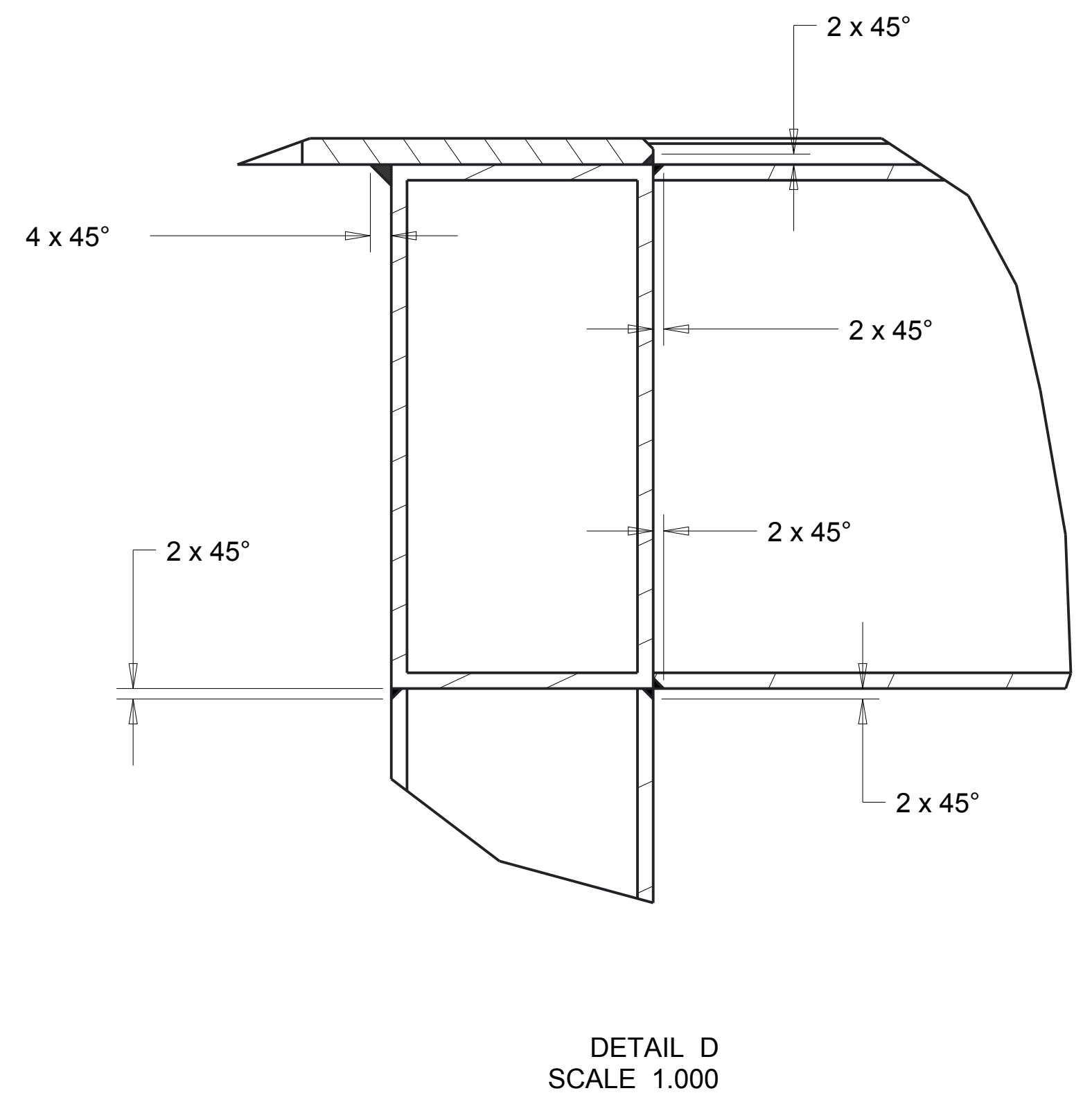
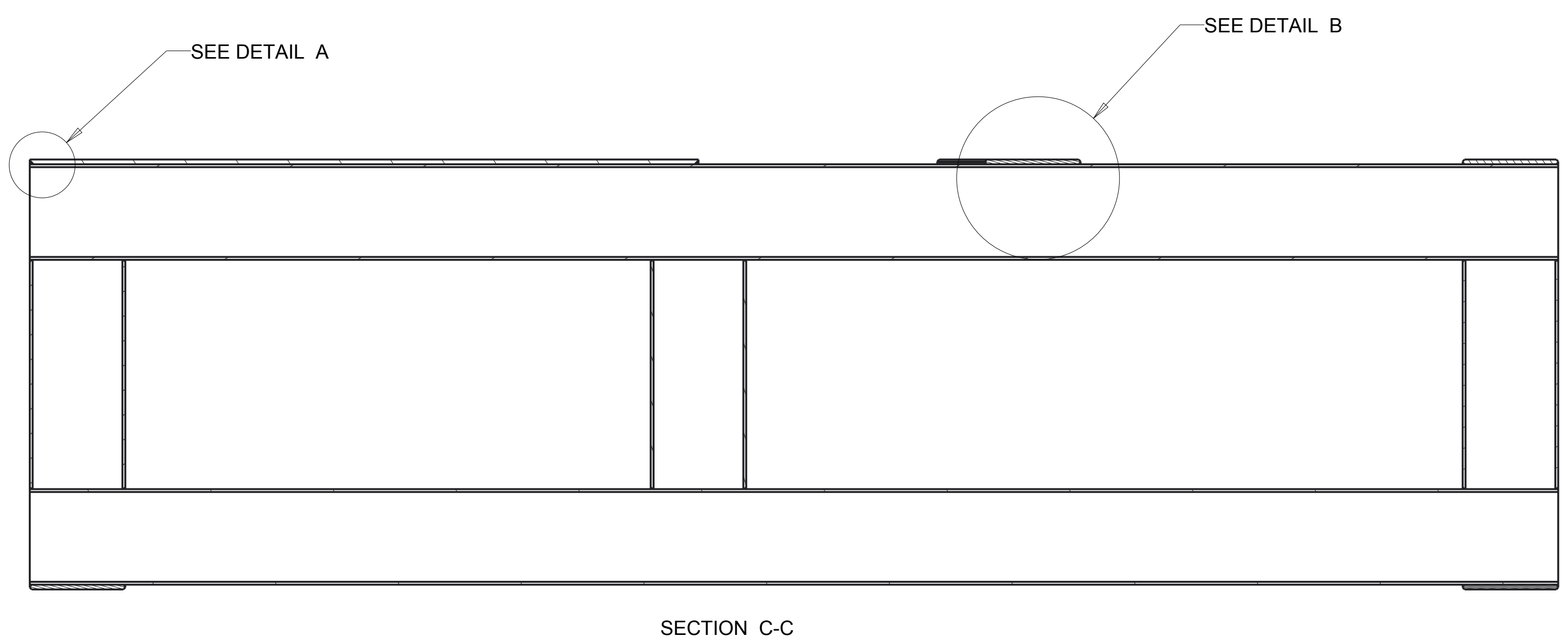
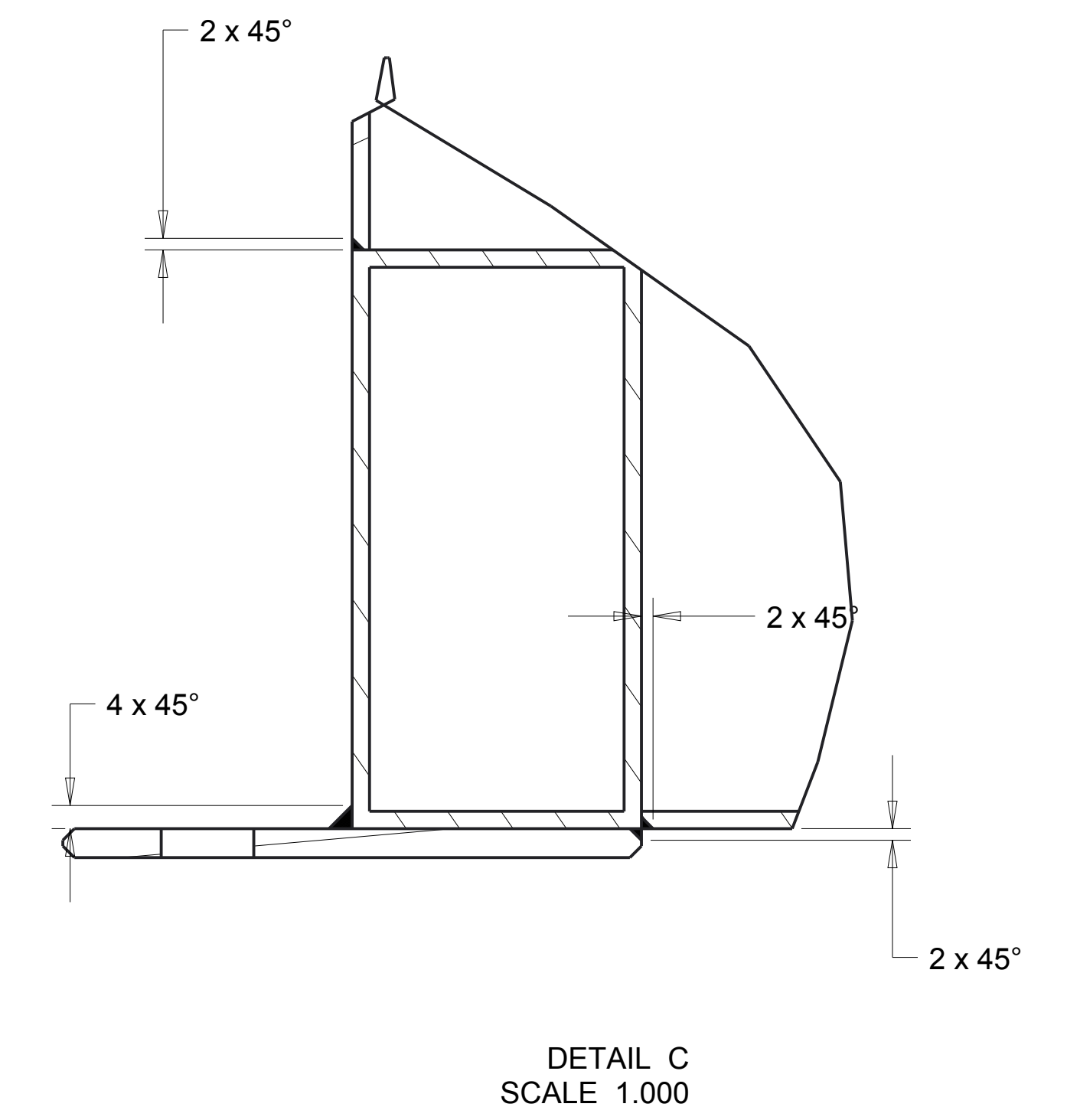
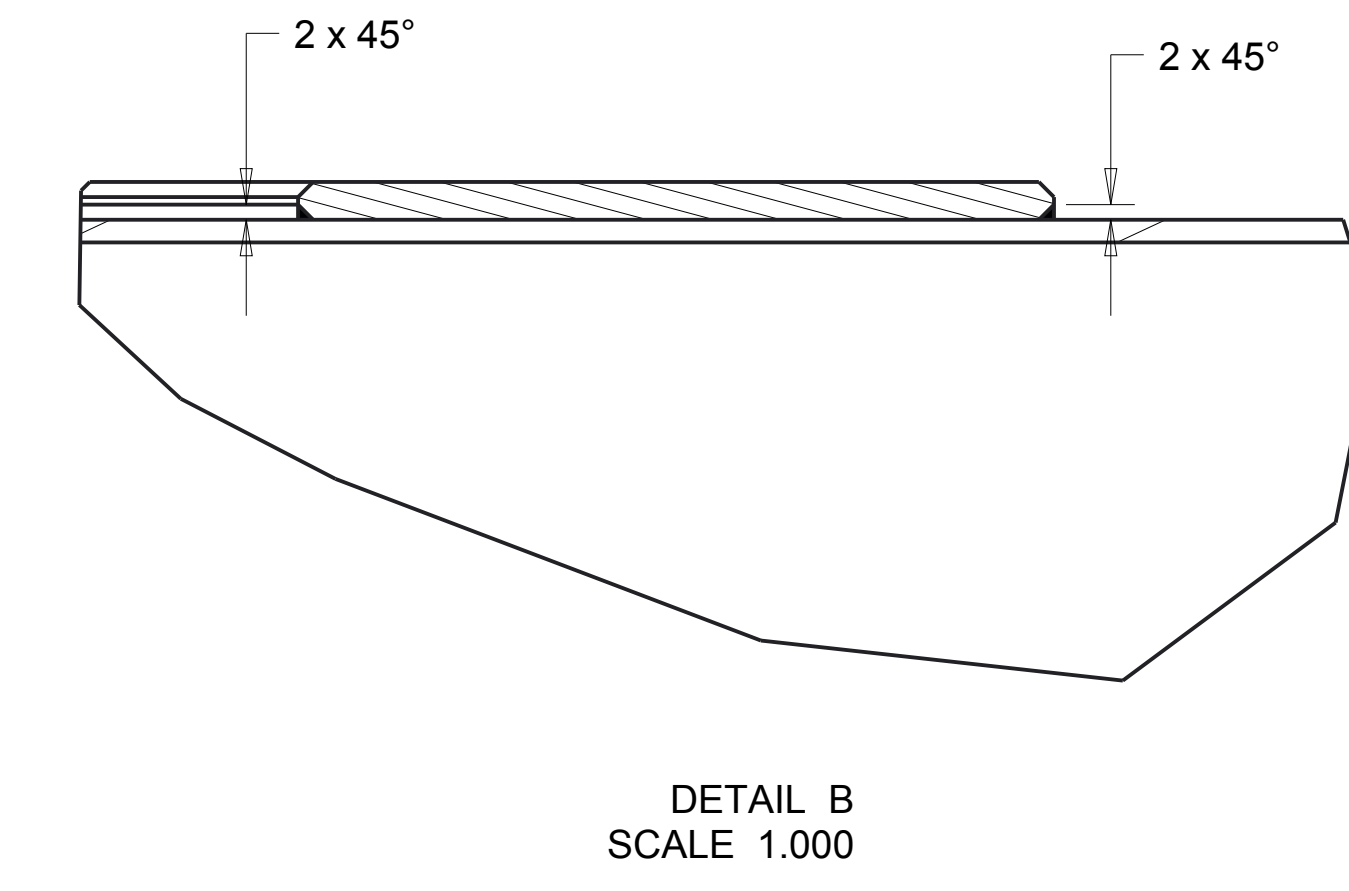
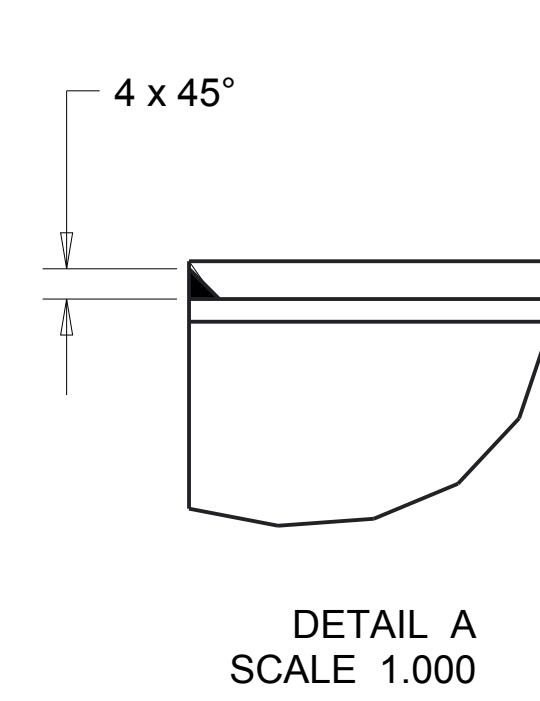
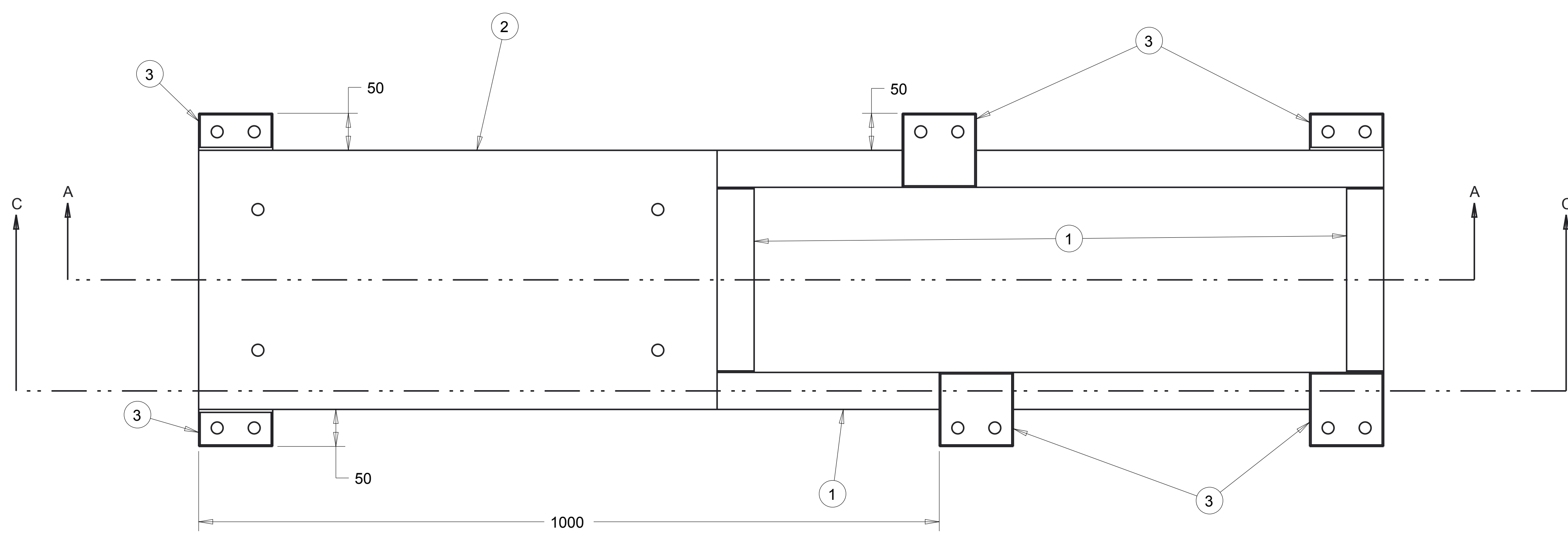
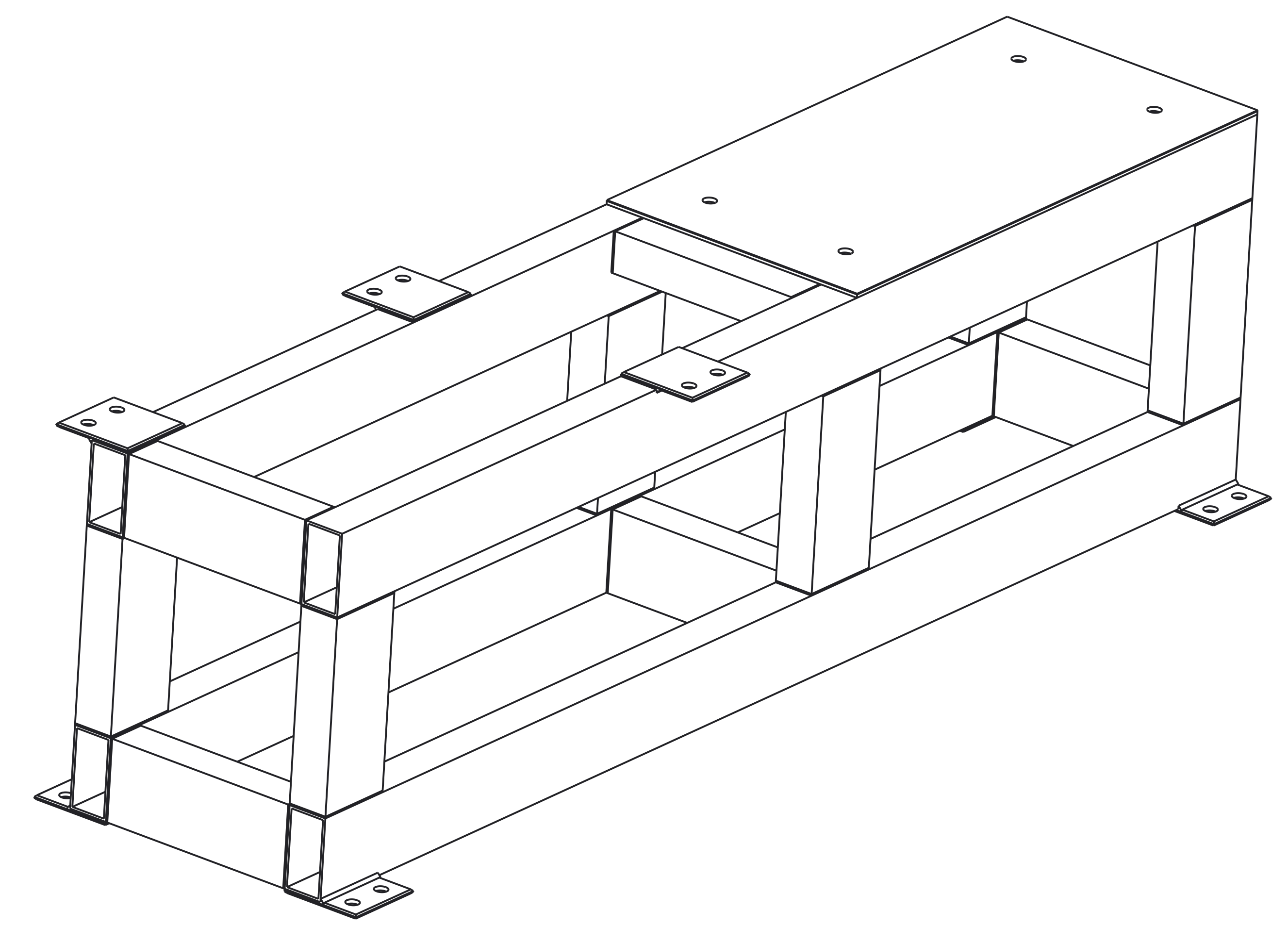
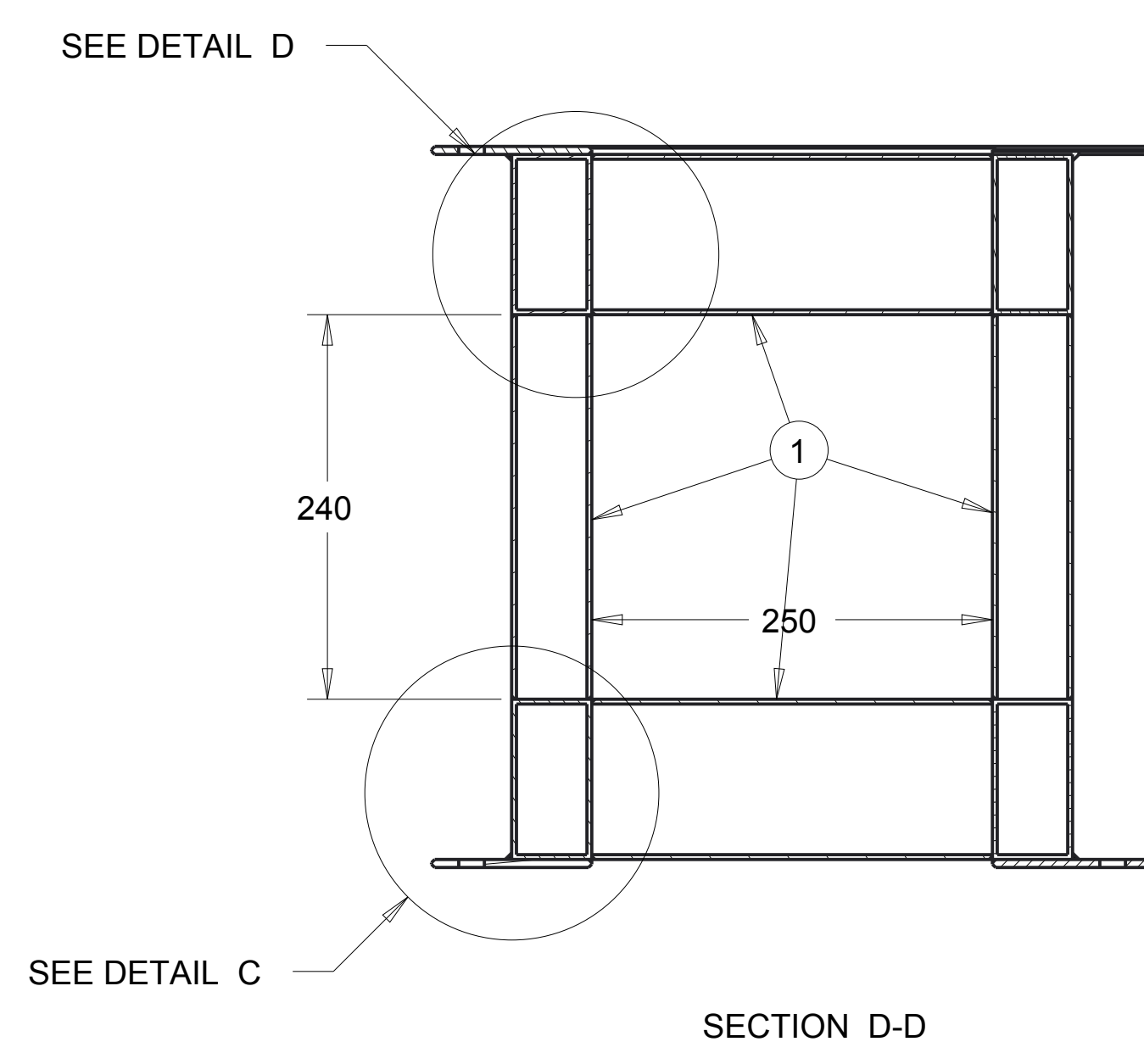
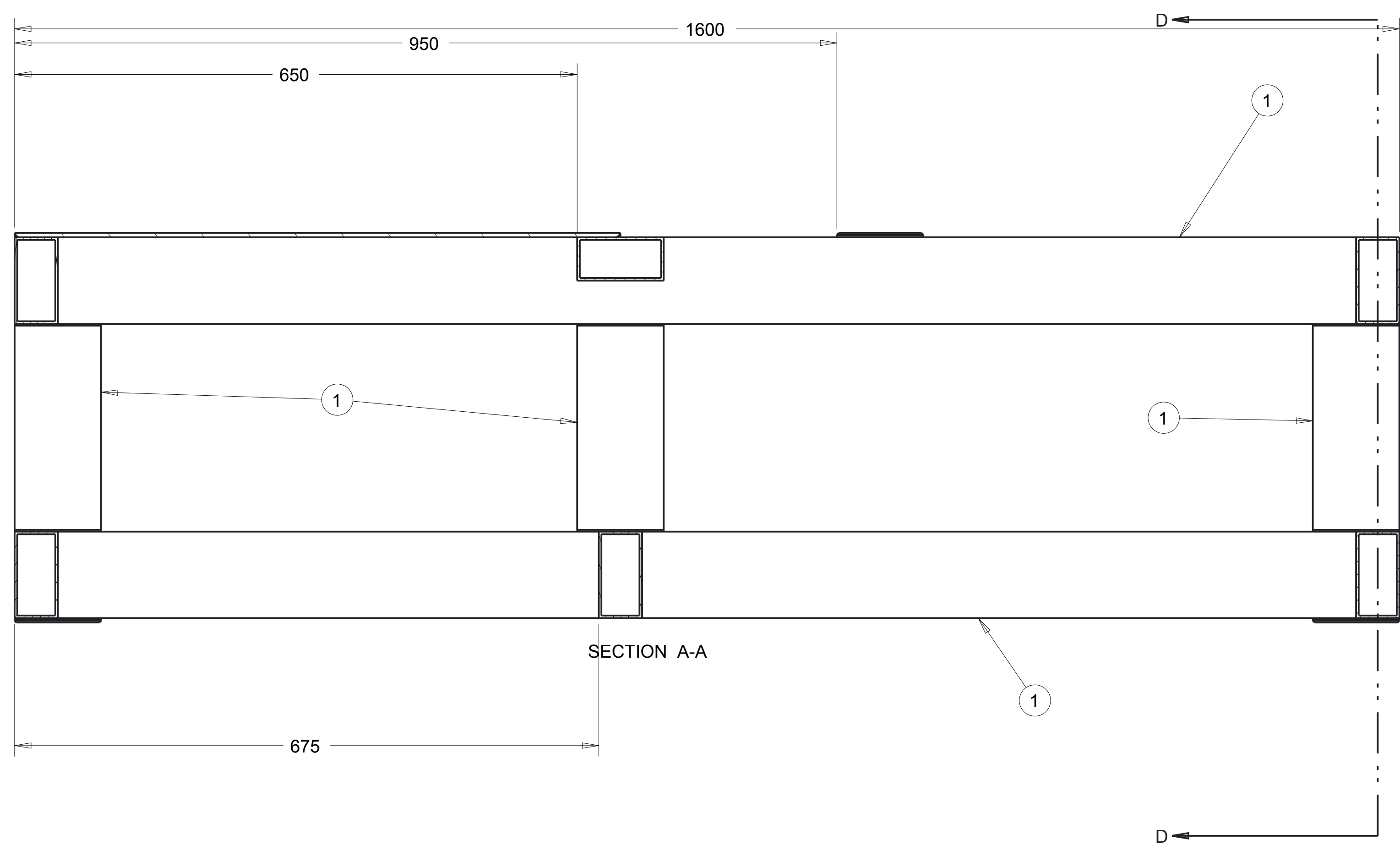
HEAT TREATMENT: None
 SUPERFICIAL COATING: Paint
 FINISH: Framework right side



DETAIL E
SCALE 1.000

REV.	DATE	DATE AND MODIFY DESCRIPTION	DRAW	CHECKED	PROJECT E.

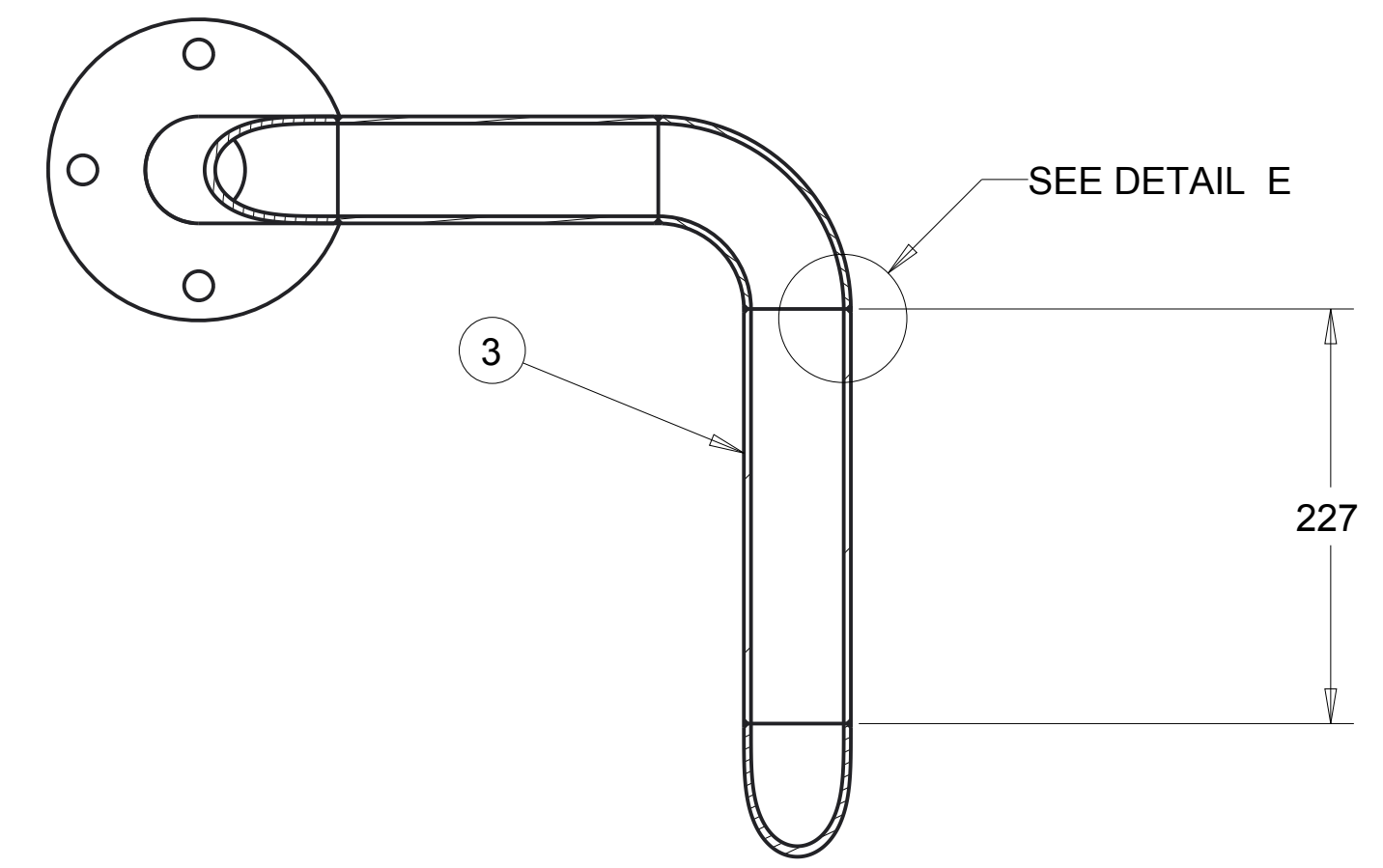
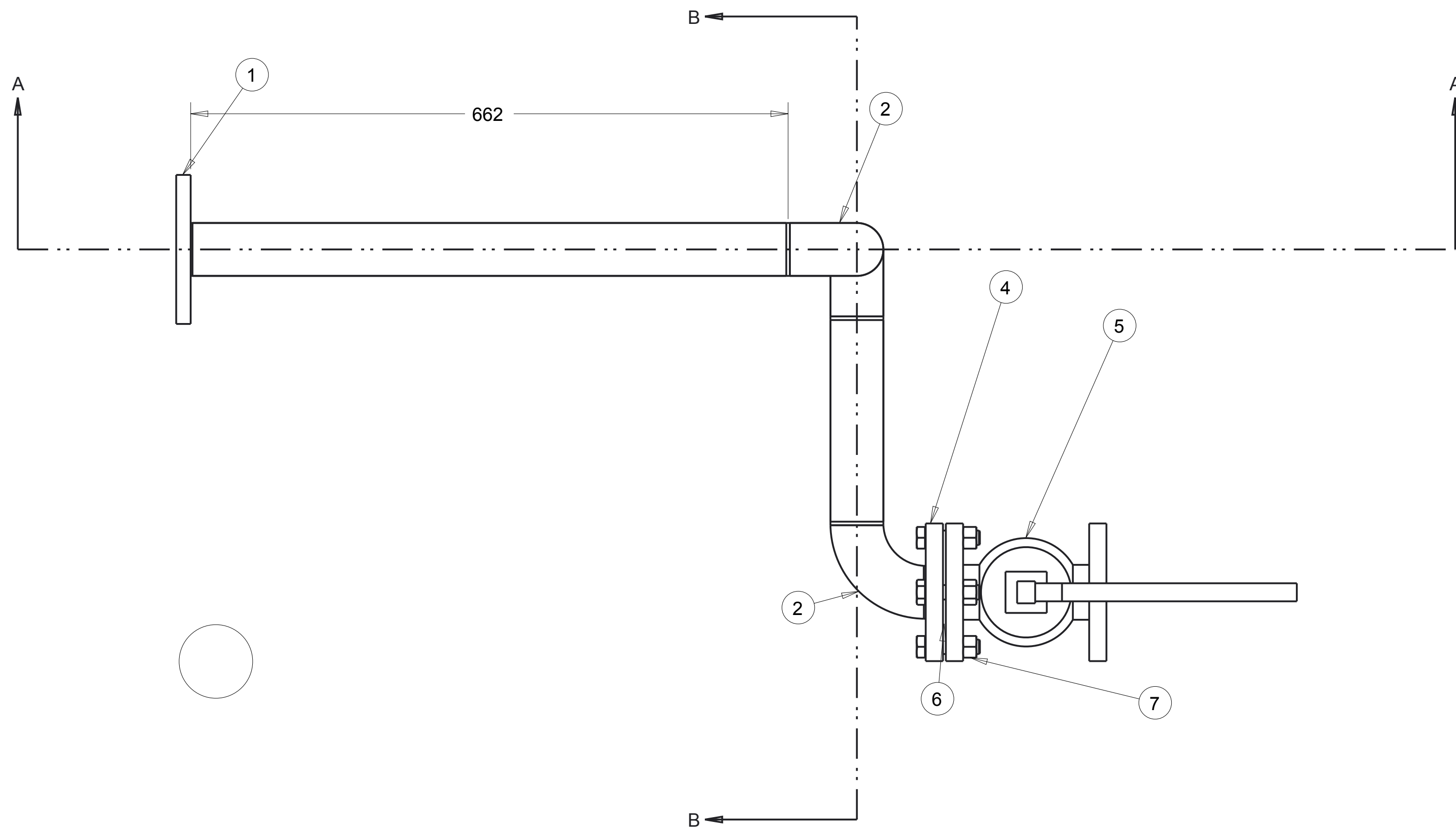
DO NOT SURVEY DIMENSIONS FROM THE DRAWING																													
<p>Mechanical and Aerospace Engineering Level 4 Lord Hope Building 141 ST James Road G4 0LT Glasgow UK</p> <p>TEL. 01415484851 mae@strath.ac.uk aldo.iannetti@strath.ac.uk</p>	DRAW	Aldo Iannetti	CHECKED	PROJECT E. M.Stickland																									
	QUANTITY	2	MASS	9.39	SCALE	0.250																							
	MATERIAL	Carbon steel			GENERAL TOLERANCES EN ISO 13920-AE																								
	TYPE	BLANK			SIZE	TOLERANCES																							
TECHNICAL DEPART. WARC			HEAT TREATMENT		None																								
FORMAT	A3		SUPERFICIAL COVERING		None																								
SHEET	2		DATE	25/06/2013																									
N° DRAWING	009-02		DENOMINAT.		Rectangular Plate 700x350																								
					<table border="1"> <tr> <td>></td> <td><=</td> <td><</td> </tr> <tr> <td>2</td> <td>30</td> <td>±1</td> </tr> <tr> <td>30</td> <td>120</td> <td>±1</td> </tr> <tr> <td>120</td> <td>400</td> <td>±1</td> </tr> <tr> <td>400</td> <td>1000</td> <td>±2</td> </tr> <tr> <td>1000</td> <td>2000</td> <td>±3</td> </tr> <tr> <td>2000</td> <td>4000</td> <td>±4</td> </tr> <tr> <td>4000</td> <td>8000</td> <td>±5</td> </tr> </table>	>	<=	<	2	30	±1	30	120	±1	120	400	±1	400	1000	±2	1000	2000	±3	2000	4000	±4	4000	8000	±5
>	<=	<																											
2	30	±1																											
30	120	±1																											
120	400	±1																											
400	1000	±2																											
1000	2000	±3																											
2000	4000	±4																											
4000	8000	±5																											



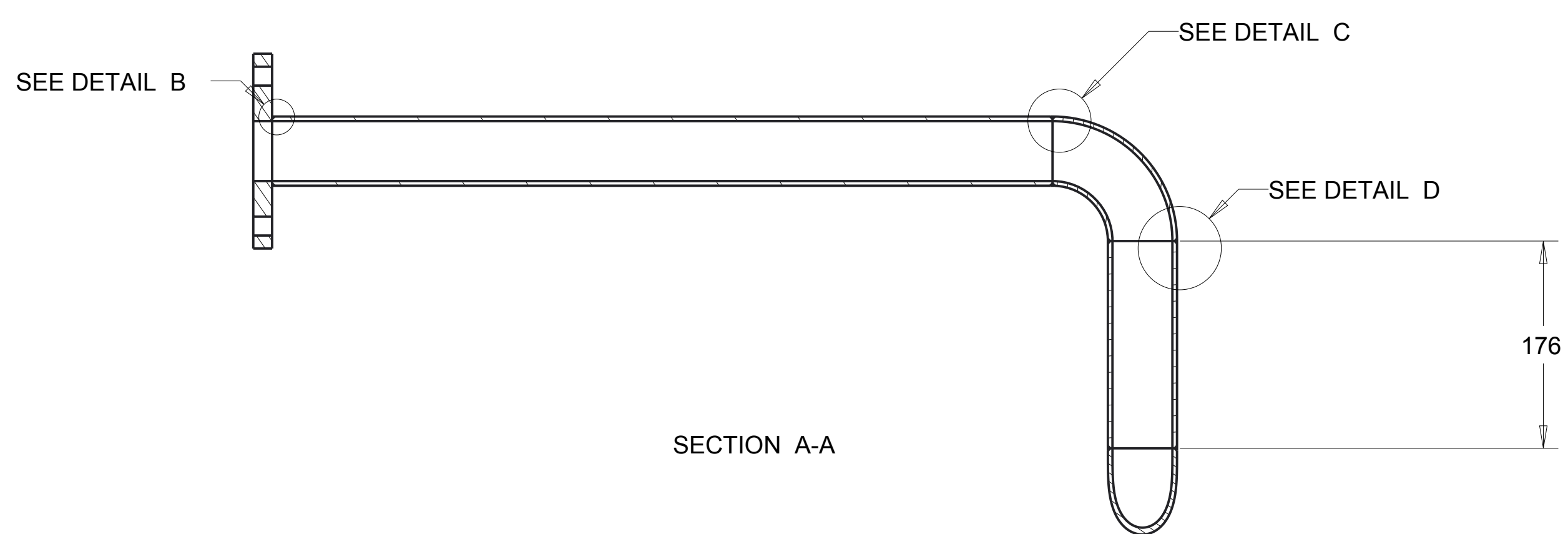
N°	Assembly/Detail	Drawing	Q.
1	Rectangular section hollow beam 100x50	16	16
2	rectangular plate	009-02	1
3	rectangular connection plate 100x100	009-03	7

DO NOT SURVEY DIMENSIONS FROM THE DRAWING

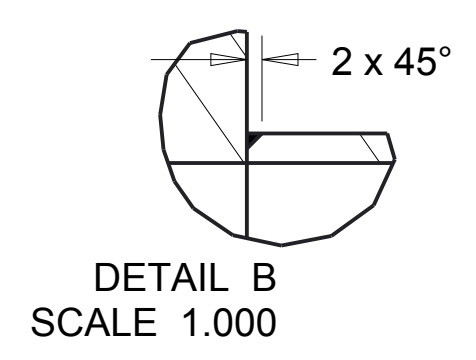
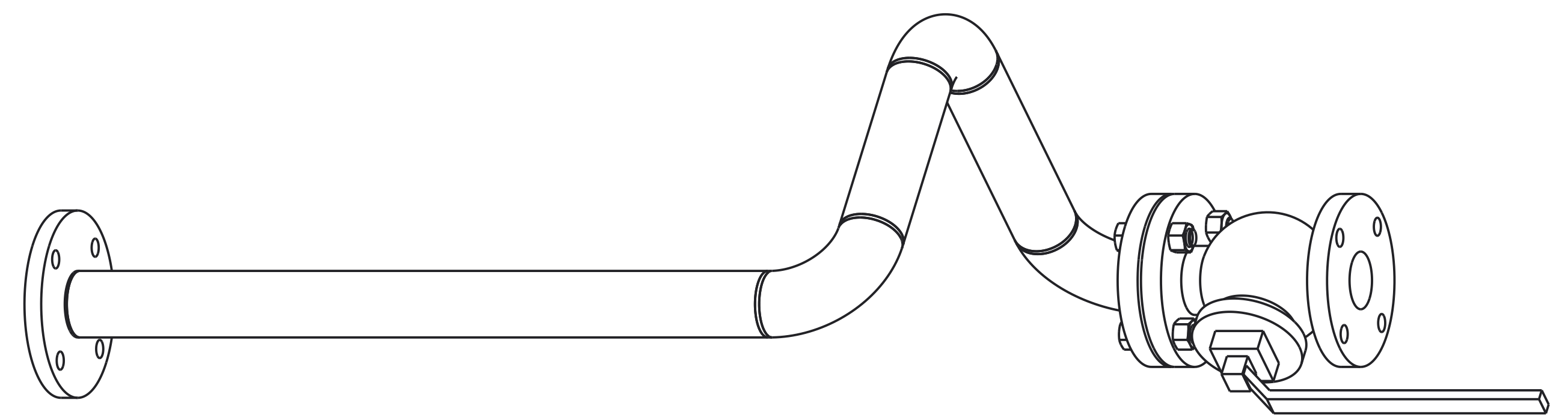
DESIGNER: Aldo Iannetti
 PROJECT: M. Stickland
 QUANTITY: 1
 WEIGHT: 75.06
 SCALE: 0.250
 MATERIAL: Standard
 TYPE: SLAB
 HEAT TREATMENT: None
 SUPERFICIAL COATING: Paint
 FORM: A0
 DATE: 25/06/2013
 DRAWING: 010-01
 FRAMEWORK left part



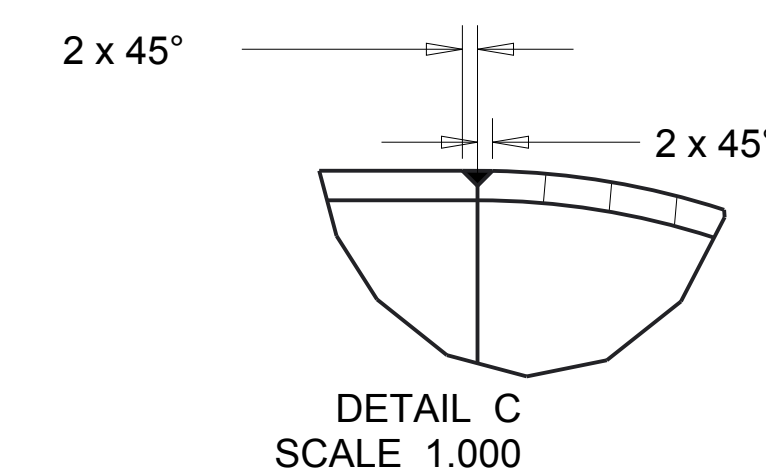
SECTION B-B



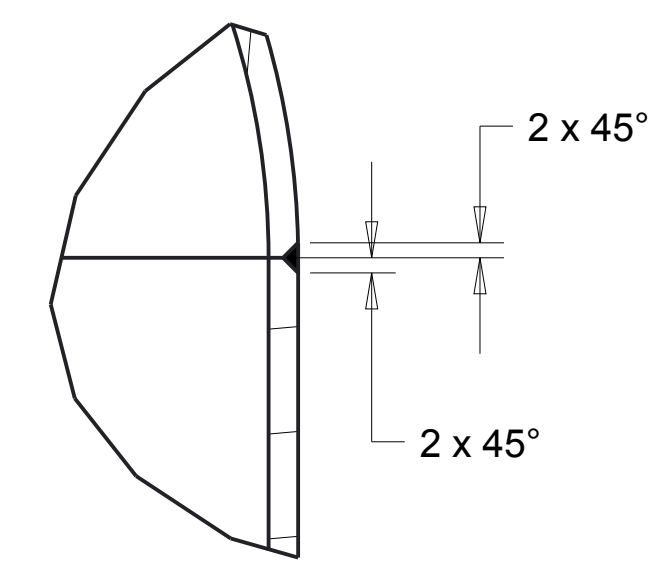
SECTION A-A



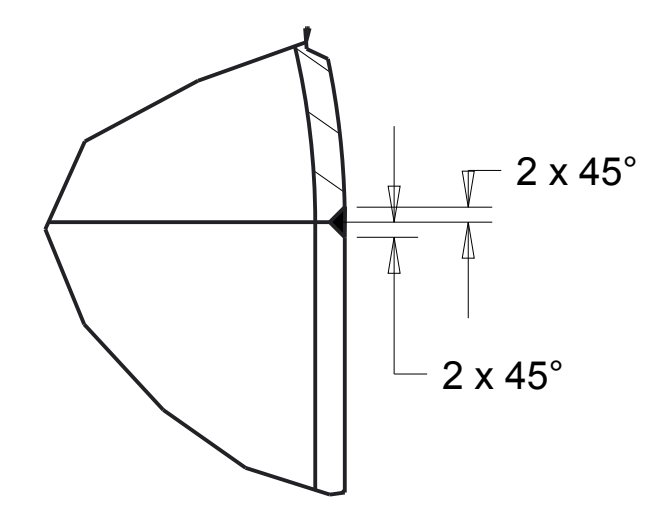
DETAIL B
SCALE 1.000



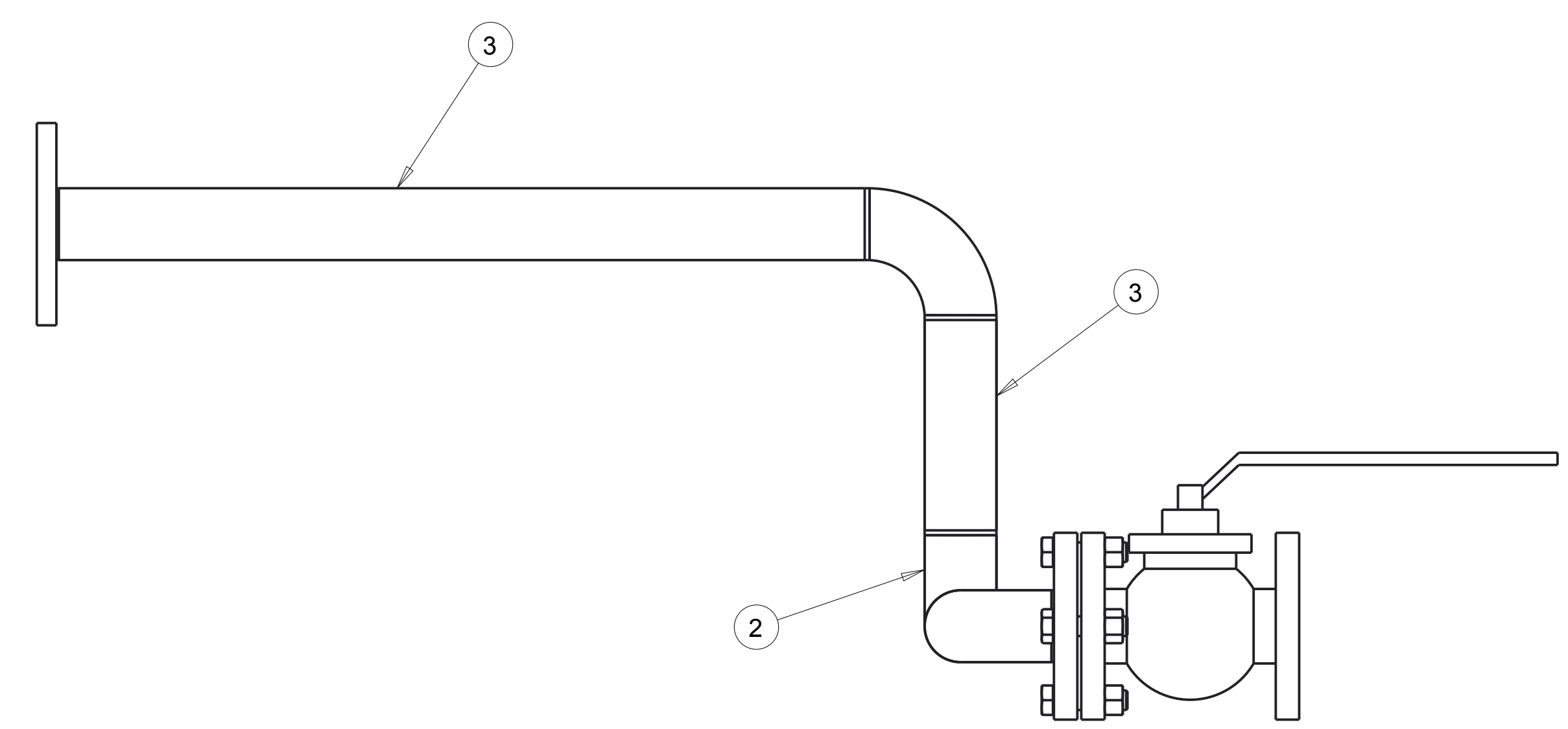
DETAIL C
SCALE 1.000



DETAIL D
SCALE 1.000



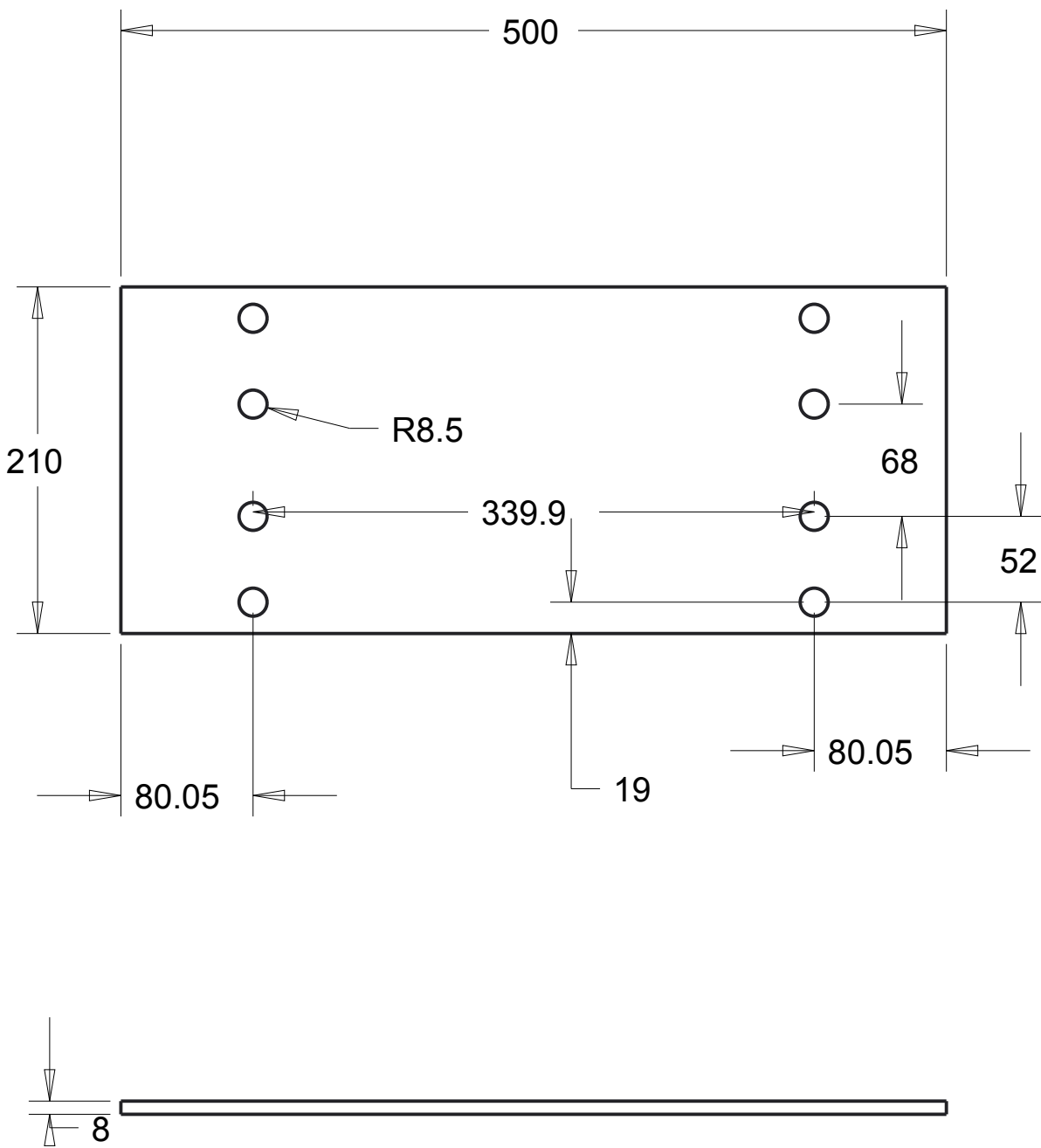
DETAIL E
SCALE 1.000



N°	Assembly/Detail	Drawing	Q.
1	Flat flange BS10 Tab F 2"		1
2	90 elbow long radius BS 1640 Std 2"		3
3	Pipe 2" BS 1387 Std		3
4	Flat flange ANSI 16.5 ASA 150 LB 2"		1
5	KVCfull bore valve class 150 2"		1
6	Spiral wound Gasket CG 2"		1
7	Bolt M16x60		4

DO NOT SURVEY DIMENSIONS FROM THE DRAWING

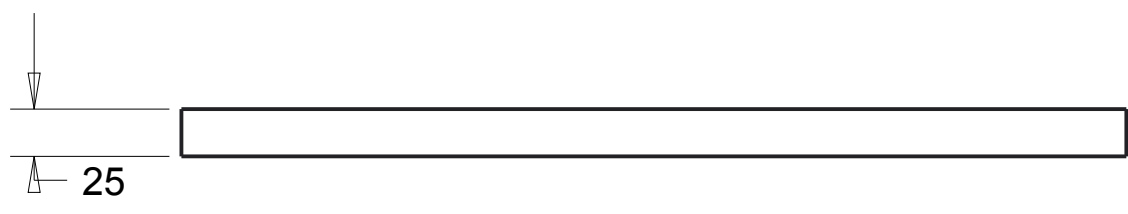
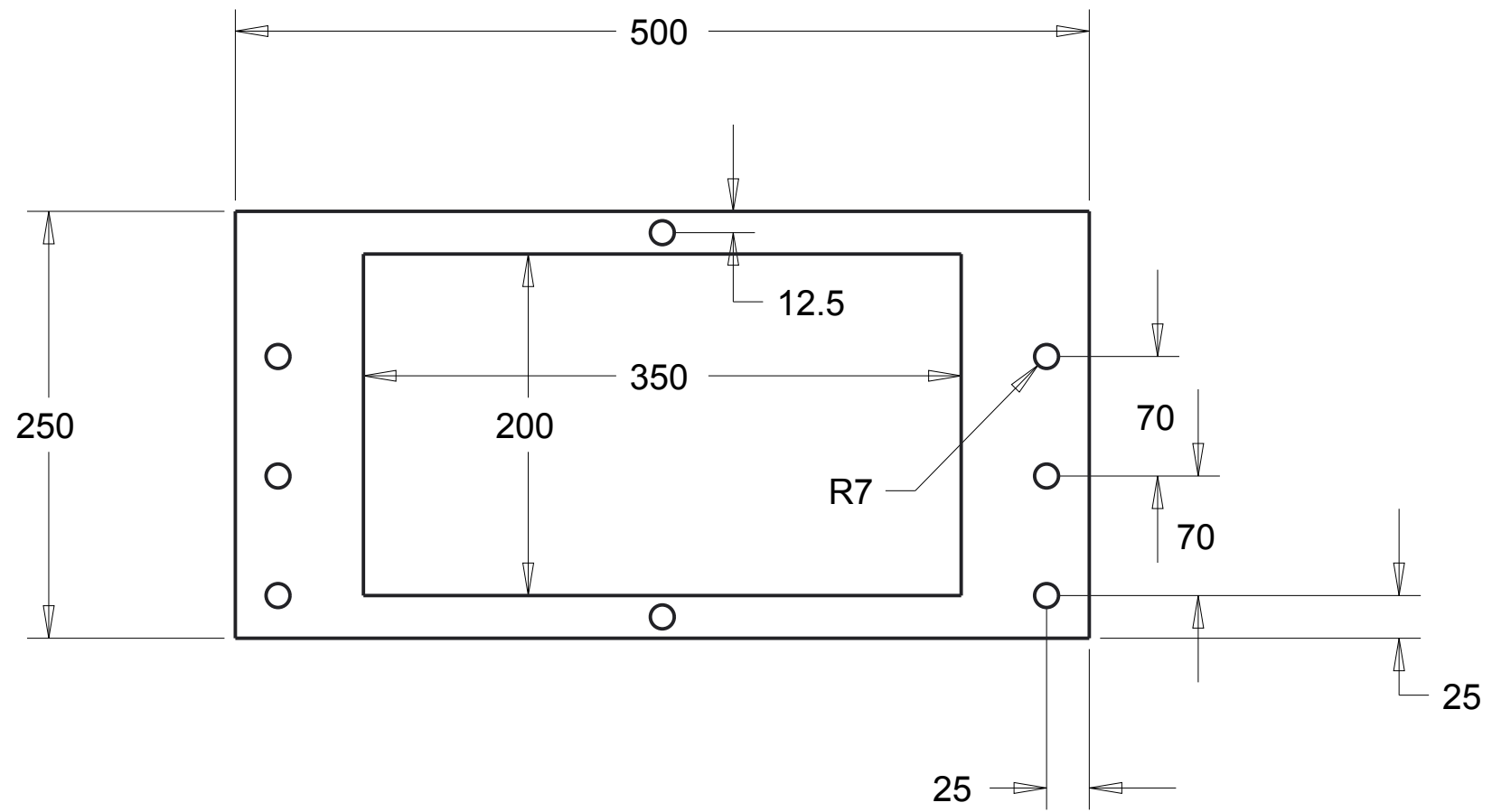
		DRAW: Aldo Iannetti CHECKED: _____ PROJECT: M. Stickland
QUANTITY: 1 MASS: 24.96 SCALE: 0.250	MATERIAL: Standard TYPE: _____ GREZZO: _____ BLANK: _____	GENERAL TOLERANCES EN ISO 12801:
TECHNICAL DEPART: _____ FORMAT: A1 SHEET: 1 DATE: 25/06/2013	HEAT TREATMENT: None SUPERFICIAL COVERING: Paint DELIVERY LINE: Delivery line	SIZE TOLERANCES:
N° DRAWING: 011-01	SHEET: 1	TOLERANCES:



					PROGETTO
					CONTROLLATO
					DISSEGNIATO
					PROGETTO
					DATA
					DATE
					REV.
					DATE
					DATE

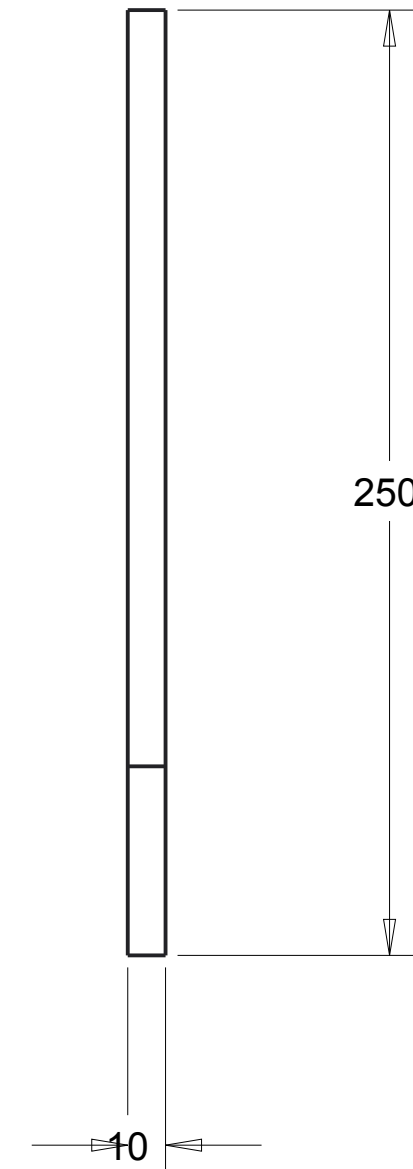
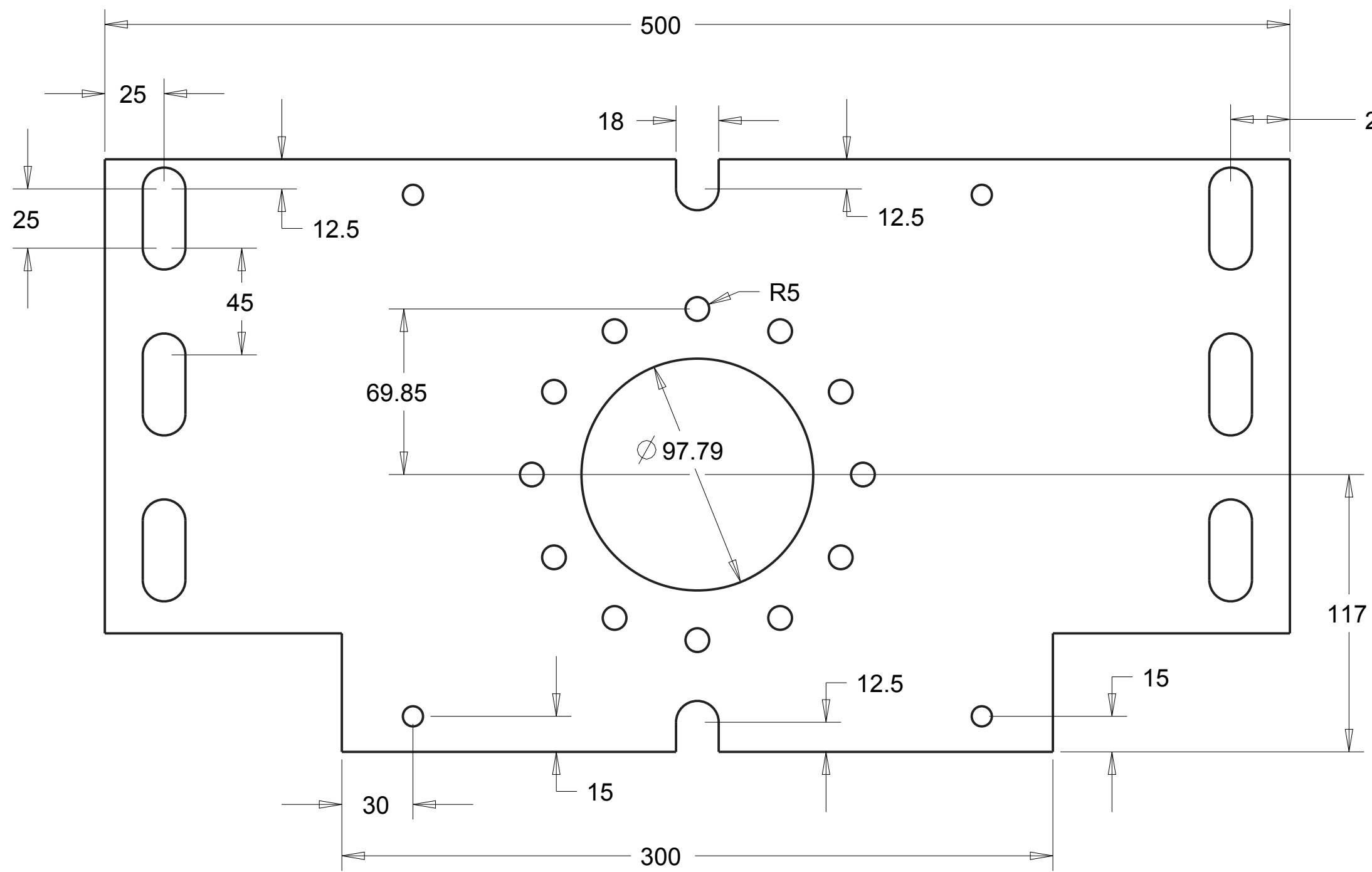
DO NOT SURVEY DIMENSIONS FROM THE DRAWING

		DRAW	Aldo Iannetti	CHECKED		PROJECT E.	M.Stickland	
		QUANTITY	2	MASS	1.72	SCALE	0.250	
Mechanical and Aerospace Engineering Level 4 Lord Hope Building 141 ST James Road G4 0LT Glasgow UK TEL.01415484851 maeATstrath.ac.uk aldo.iannettiATstrath.ac.uk		MATERIAL				Carbon steel		GENERAL TOLERANCES EN ISO 13920-AE
		TYPE		BLANK		SIZE	TOLERANCES	
TECHNICAL DEPART. WARC		HEAT TREATMENT				None		<input type="checkbox"/> > <input type="checkbox"/> <= <input type="checkbox"/> - <input type="checkbox"/> <
FORMAT		SUPERFICIAL COVERING				None		2 30 ±1 ±20' 30 120 ±1 ±20' 120 400 ±1 ±20' 400 1000 ±2 ±15' 1000 2000 ±3 ±10' 2000 4000 ±4 ±10' 4000 8000 ±5 ±10'
SHEET	2	DATE	25/06/2013		DENOMINAT.			Plate 500x218
N° DRAWING		013-02						



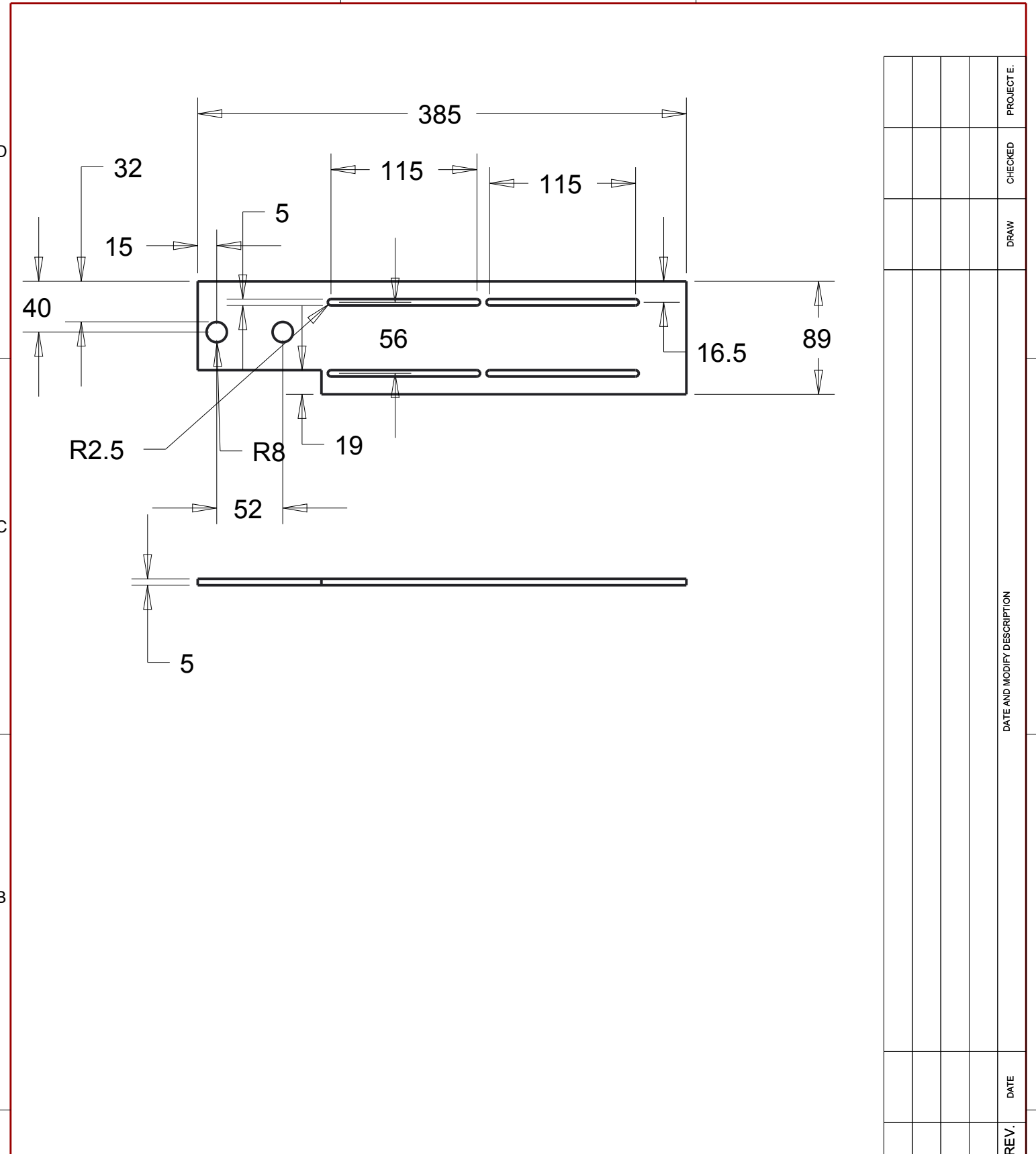
REV.	DATE	DATE AND MODIFY DESCRIPTION	DRAW	CHECKED	PROJECT E.

DO NOT SURVEY DIMENSIONS FROM THE DRAWING						
<p>Mechanical and Aerospace Engineering Level 4 Lord Hope Building 141 ST James Road G4 0LT Glasgow UK</p> <p>TEL. 01415484851 mae@strath.ac.uk aldo.iannetti@strath.ac.uk</p>	DRAW Aldo Iannetti	CHECKED	PROJECT E. M.Stickland			
	QUANTITY 2	MASS 2.5	SCALE 0.250			
	MATERIAL Carbon steel				GENERAL TOLERANCES EN ISO 13920-AE	
	TECHNICAL DEPART. WARC	TYPE BLANK	HEAT TREATMENT None		SIZE	TOLERANCES
FORMAT A3	DATE 25/06/2013	SUPERFICIAL COVERING None		<input type="checkbox"/> > <input type="checkbox"/> <= <input type="checkbox"/> <	<input type="checkbox"/> ± 20' <input type="checkbox"/> ± 15' <input type="checkbox"/> ± 10' <input type="checkbox"/> ± 5'	
SHEET 3	DENOMINAT. Plate 540x250 x25		2000 4000 ±4 ±10'	400 1000 ±2 ±15'	120 400 ±1 ±20'	
N° DRAWING 013-03	4000 8000 ±5 ±10'		30 120 ±1 ±20'			



REV.	DATE	DATE AND MODIFY DESCRIPTION	DRAW	CHECKED	PROJECT E.

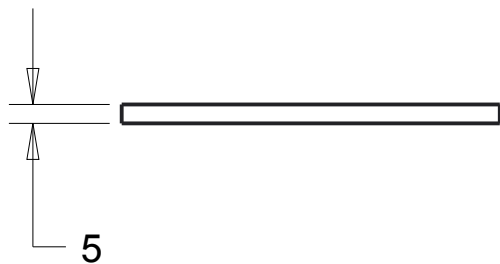
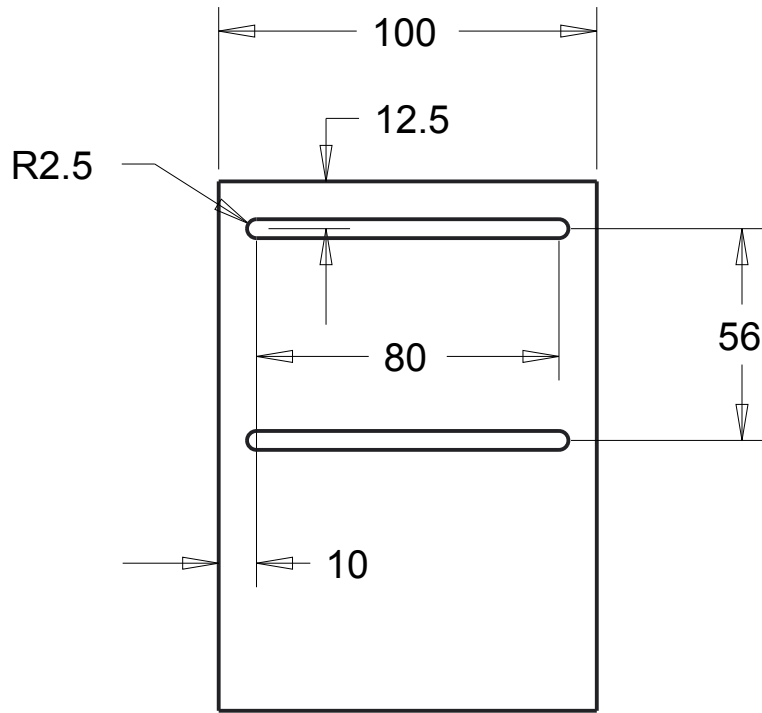
DO NOT SURVEY DIMENSIONS FROM THE DRAWING						
 <p>Mechanical and Aerospace Engineering Level 4 Lord Hope Building 141 ST James Road G4 0LT Glasgow UK</p> <p>TEL: 01415484851 maeATstrath.ac.uk aldo.iannettiATstrath.ac.uk</p>	DRAW A. Iannetti	CHECKED M. Stickland	PROJECT E.			
	QUANTITY 1	MASS 2.65	SCALE 1: 0.5			
	MATERIAL mild Steel					GENERAL TOLERANCES EN ISO 13920-AE
	TECHNICAL DEPART. WARC	TYPE BLANK		HEAT TREATMENT None		SIZE TOLERANCES
FORMAT A3	DATE 11/11/2014		SUPERFICIAL COVERING None		<input type="checkbox"/> > <input type="checkbox"/> <= <input type="checkbox"/> <	
SHEET 4	N° DRAWING 013-04		DENOMINAT. Adjustable Plate		2 30 ±1 ±20' 30 120 ±1 ±20' 120 400 ±1 ±20' 400 1000 ±2 ±15' 1000 2000 ±3 ±10' 2000 4000 ±4 ±10' 4000 8000 ±5 ±10'	



REV.	DATE	DATE AND MODIFY DESCRIPTION	DRAW	CHECKED	PROJECTE.

DO NOT SURVEY DIMENSIONS FROM THE DRAWING

	DRAW A. Iannetti	CHECKED	PROJECT E.
	QUANTITY 2	MASS 1.18	SCALE 0.250
MATERIAL mild steel			GENERAL TOLERANCES EN ISO 13920-AE
Mechanical and Aerospace Engineering Level 4 Lord Hope Building 141 ST James Road G4 0LT Glasgow UK TEL 01415484851 maeATstrath.ac.uk aldo.iannettiATstrath.ac.uk	TYPE BLANK	SIZE TOLERANCES	
TECHNICAL DEPART. WARC		HEAT TREATMENT None	<input type="checkbox"/> > <input type="checkbox"/> <= <input type="checkbox"/> - <input type="checkbox"/> <
FORMAT A3	SHEET 5	DATE 02/12/2014	2 30 ±1 ±20' 30 120 ±1 ±20' 120 400 ±1 ±20' 400 1000 ±2 ±15' 1000 2000 ±3 ±10' 2000 4000 ±4 ±10' 4000 8000 ±5 ±10'
N° DRAWING 013-05	DENOMINAT. limit-switch plate 1		



REV.	DATE	DATE AND MODIFY DESCRIPTION	DRAW	CHECKED	PROJECTE.

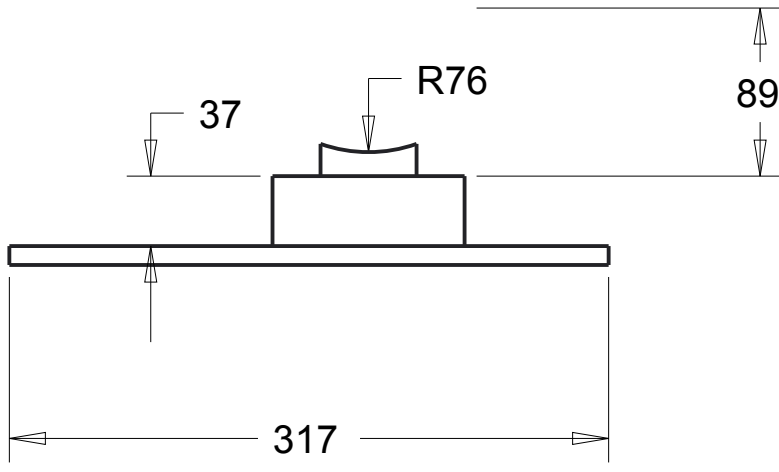
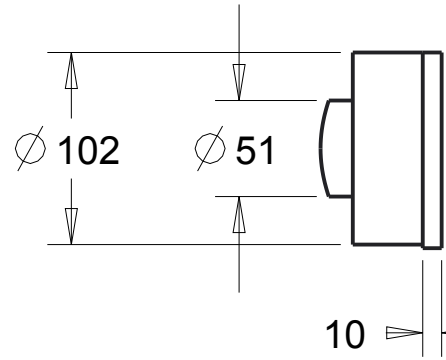
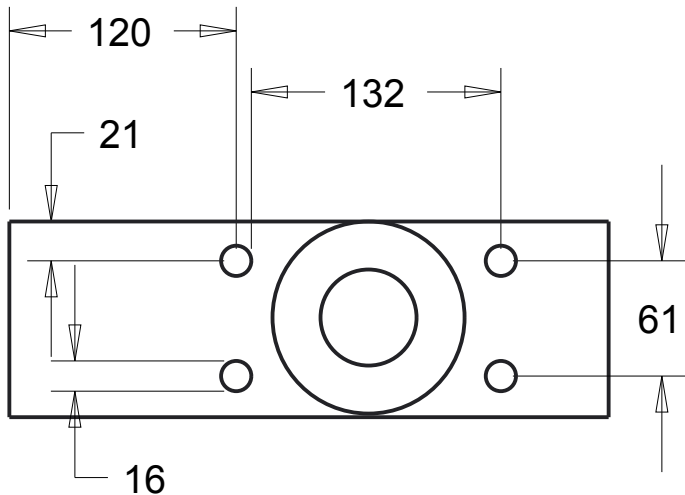
DO NOT SURVEY DIMENSIONS FROM THE DRAWING

	DRAW A. Iannetti	CHECKED	PROJECT E.
	QUANTITY 2	MASS 0.51	SCALE 0.5
MATERIAL mild steel	GENERAL TOLERANCES EN ISO 13920-AE		TYPE BLANK
TECHNICAL DEPART. WARC	HEAT TREATMENT None	SIZE	TOLERANCES
FORMAT A4	SUPERFICIAL COVERING None	2 30 ±1 ±20'	30 120 ±1 ±20'
SHEET 06	DATE 02/12/2014	120 400 ±1 ±20'	400 1000 ±2 ±15'
N° DRAWING 013-06	DENOMINAT. limit switch plate 2	1000 2000 ±3 ±10'	2000 4000 ±4 ±10'
		4000 8000 ±5 ±10'	

3

2

1



					VISTO PROJECTE.
					CONTROLLATO CHECKED
					DISIGNATO DRAW
					DATA E DESCRIZIONE MODIFICA DATE AND MODIFY DESCRIPTION
					DATA DATE
					REV.

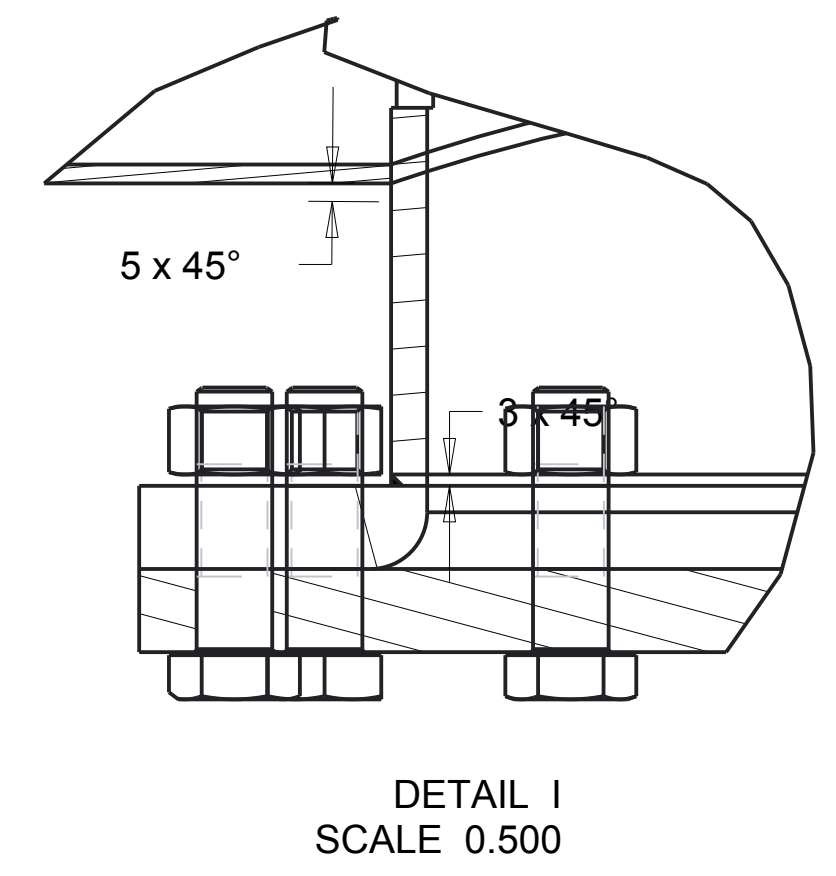
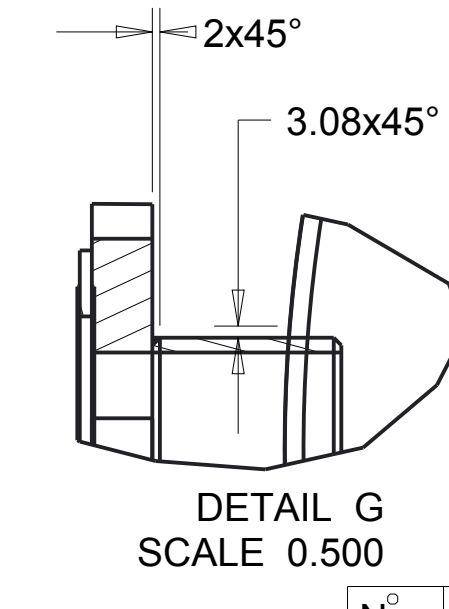
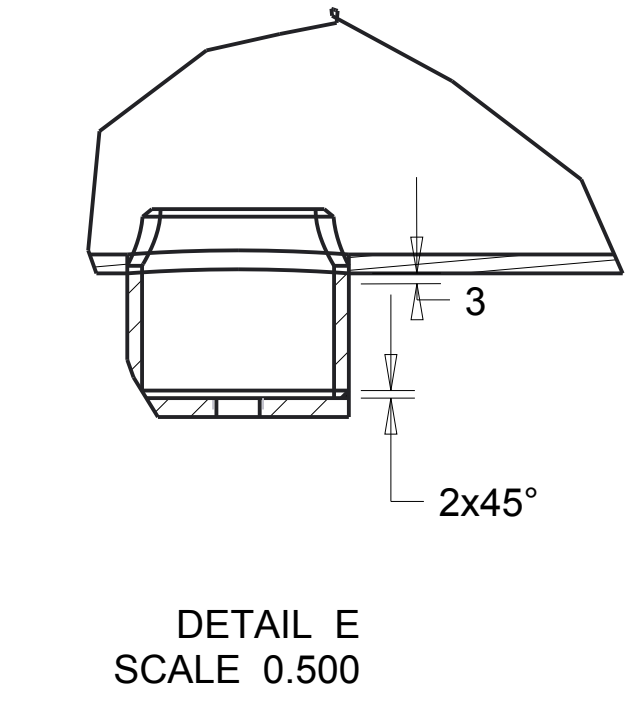
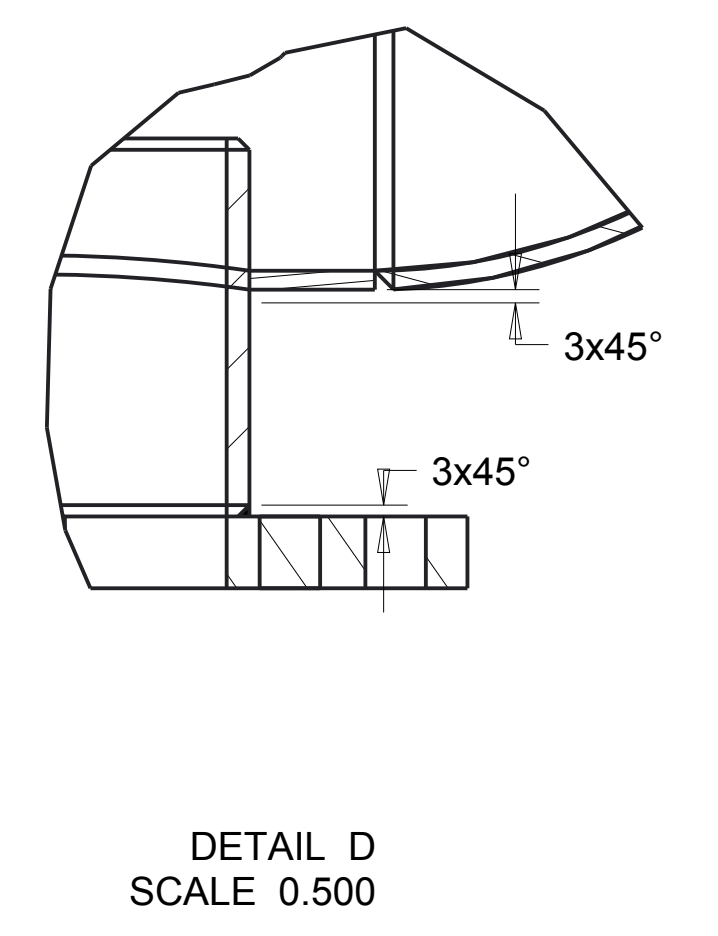
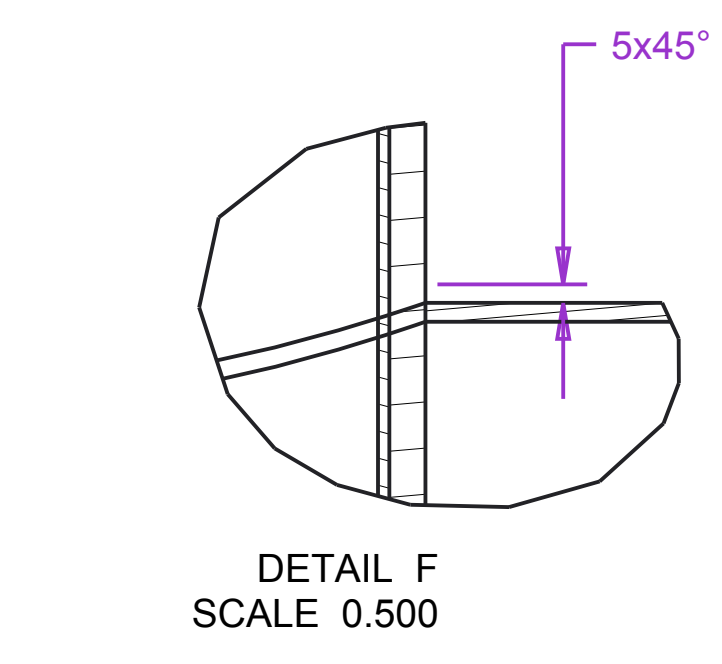
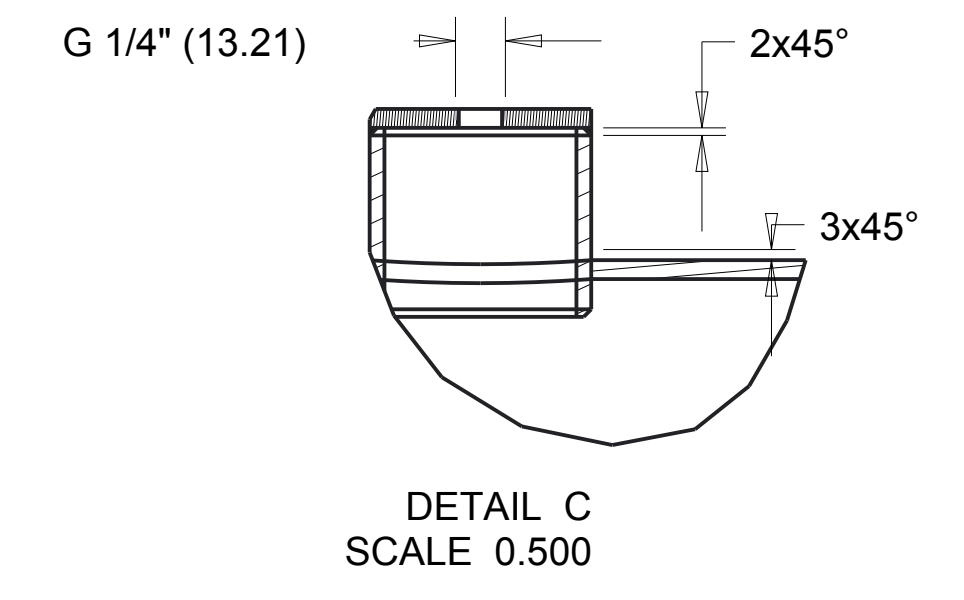
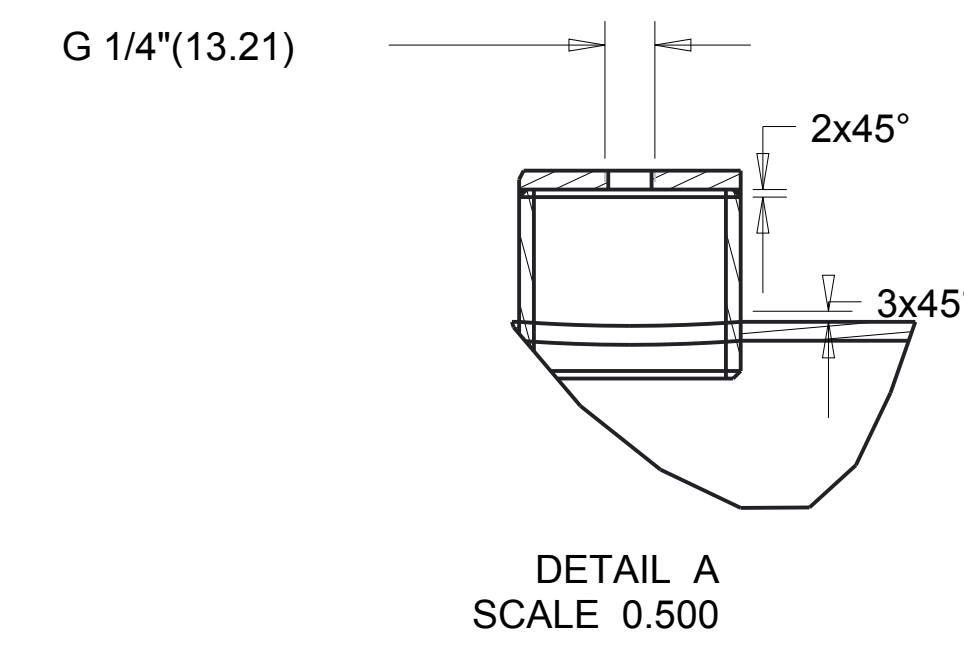
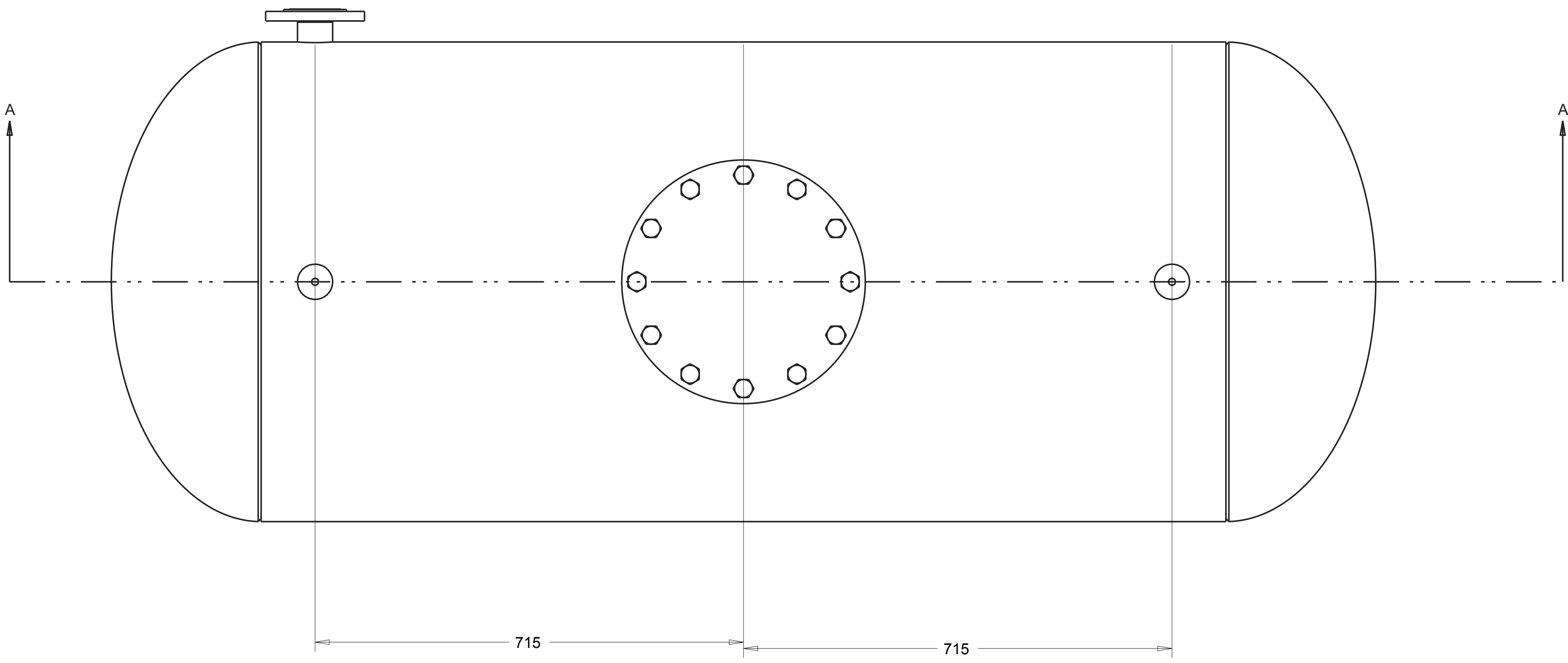
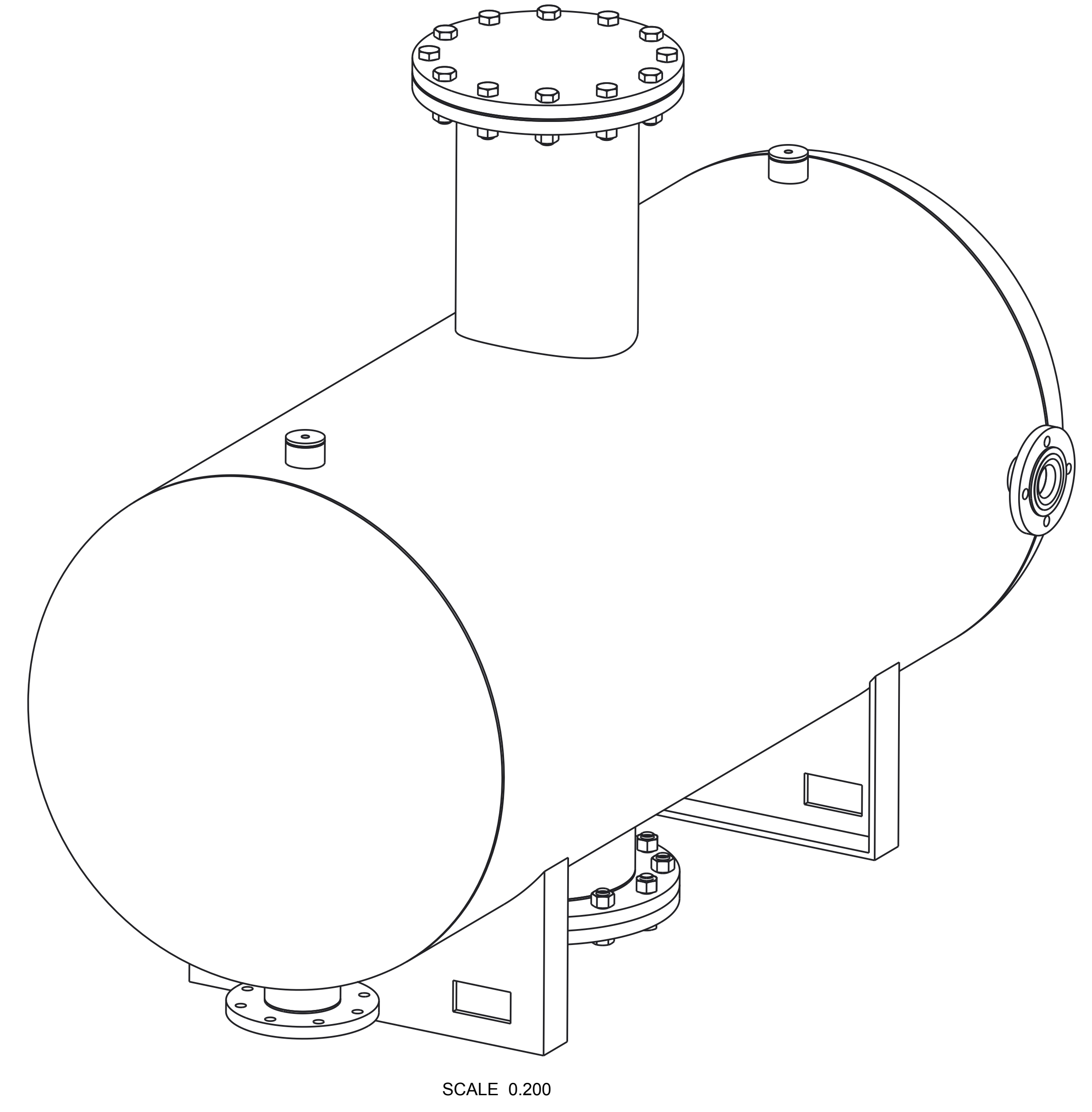
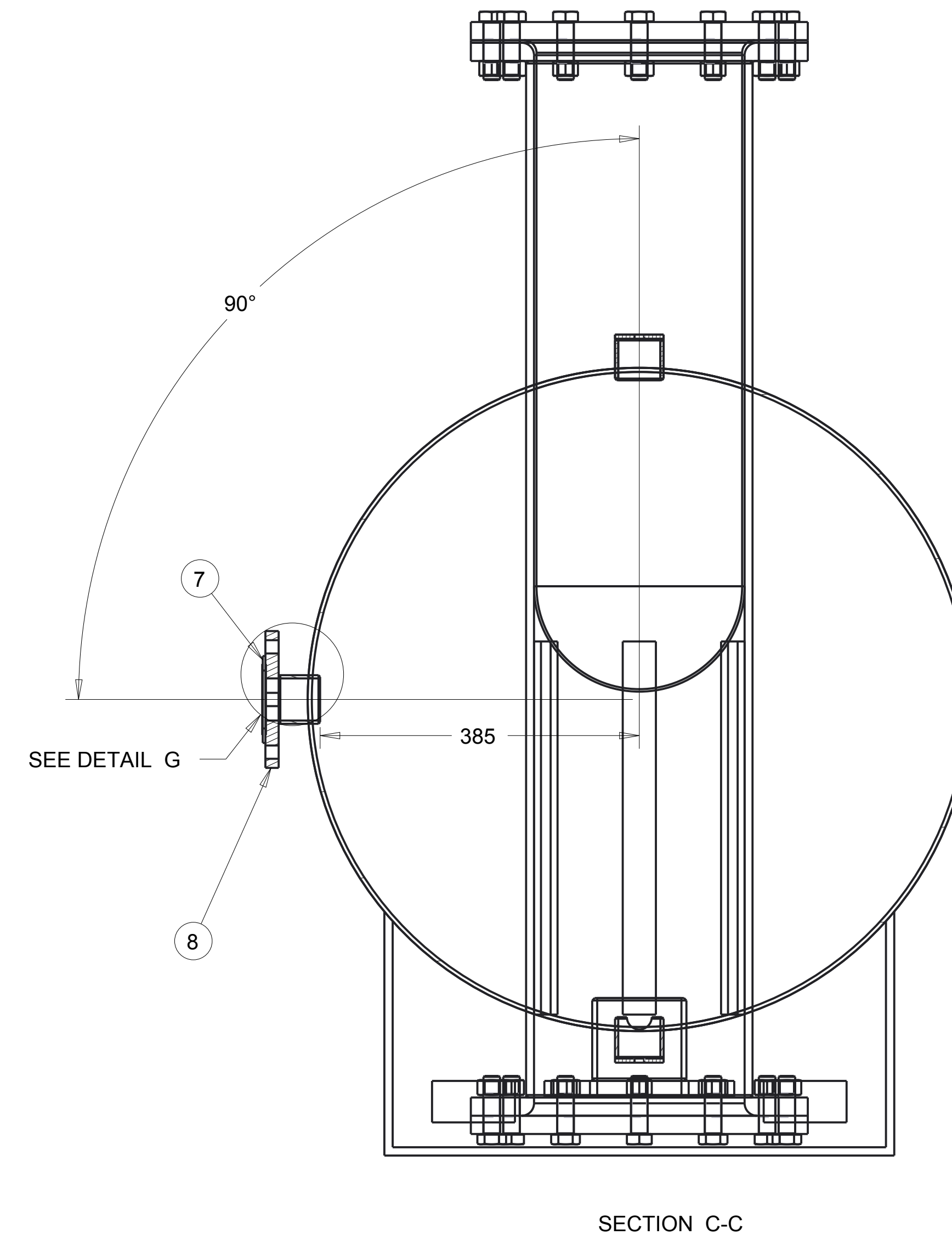
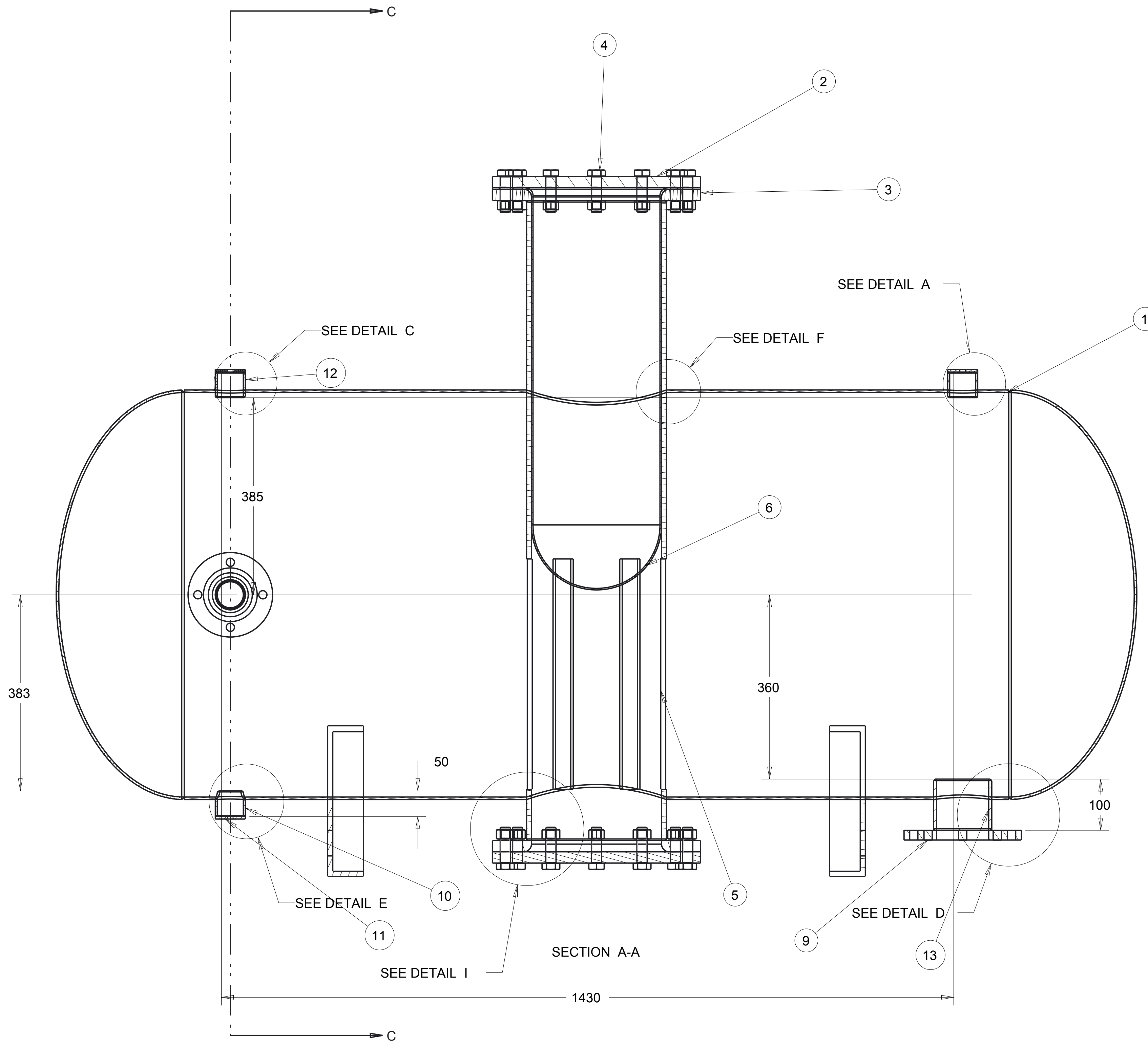
DO NOT SURVEY DIMENSIONS FROM THE DRAWING

	DRAW Aldo Iannetti	CHECKED	PROJECT E. M.Stickland
	QUANTITY 1	MASS 5.05	SCALE 0.250
	MATERIAL Carbon Steel		
Mechanical and Aerospace Engineering Level 4 Lord Hope Building 141 ST James Road G4 0LT Glasgow UK TEL 01415484851 maeATstrath.ac.uk aldo.iannettiATstrath.ac.uk	TYPE BLANK	HEAT TREATMENT None	SIZE TOLERANCES
TECHNICAL DEPART. WARC	SUPERFICIAL COVERING Paint	DENOMINAT. Window-cover2-blind	<input type="checkbox"/> > <input type="checkbox"/> <= <input type="checkbox"/> - <input type="checkbox"/> <
FORMAT A4	DATE 25/06/2013		2 30 ±1 ±20' 30 120 ±1 ±20' 120 400 ±1 ±20' 400 1000 ±2 ±15' 1000 2000 ±3 ±10' 2000 4000 ±4 ±10' 4000 8000 ±5 ±10'
SHEET 1			
N° DRAWING 016-01			

3

2

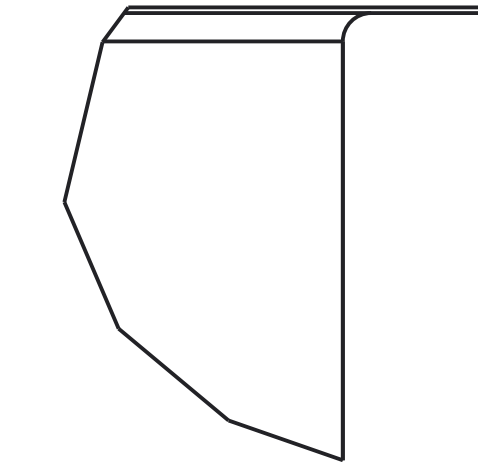
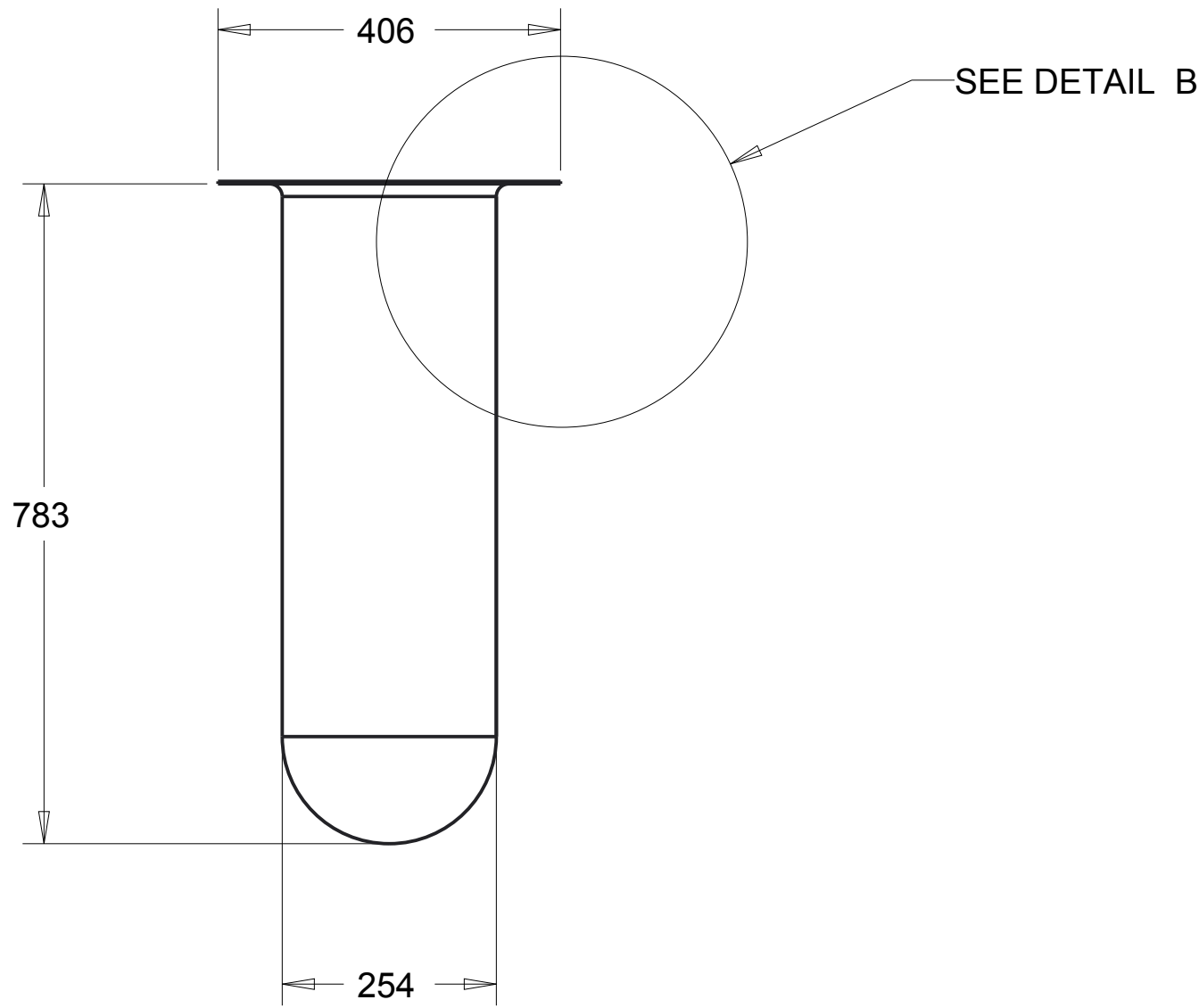
1



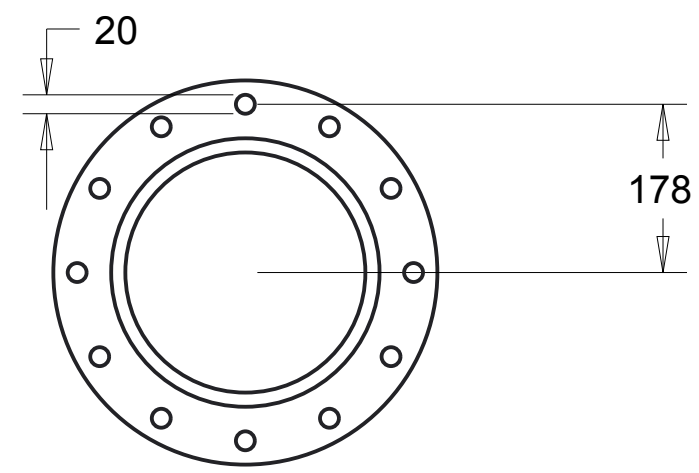
N°	Assembly/Detail	Drawing	Q.
1	Fiorini Water Storage Tank 1000 l		1
2	Flat Flange BS10 Tab E for pipe 10" Blind		2
3	Flat Flange BS10 Tab E for pipe 10"	017-05	2
4	Bolt M20x70		12
5	Pipe 10" BS 1640 Std	017-04	1
6	Indico Rubber Bladder	017-02	1
7	Spiral wound Gasket GC 2"		1
8	Flat flange BS10 Tab F for pipe 2"		1
9	Flat flange BS10 Tab F for pipe 4"		1
10	Pipe 2" BS 1640 Drilled	017-03	1
11	Tee cap2	006-02	3
12	Pipe 2" BS 1640 Std		3
13	Pipe 4" BS 1640 Std		1

DO NOT SURVEY DIMENSIONS FROM THE DRAWING

UNIVERSITY OF STRATHCLYDE Strathclyde Glasgow	PROJECT: 017-01	SCALE: 0.200
QUANTITY: 1	MATERIAL: Carbon steel	
FORM: A0	HEAT TREATMENT: None	
DATE: 25/06/2013	SUPERFICIAL COATING: Paint	
DESCRIPTION: 017-01	Water storage tank	

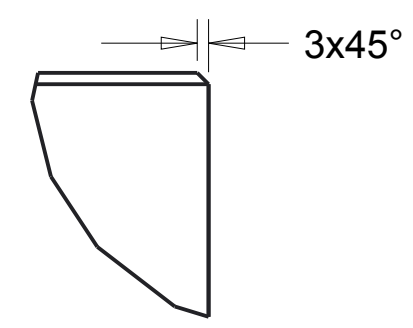
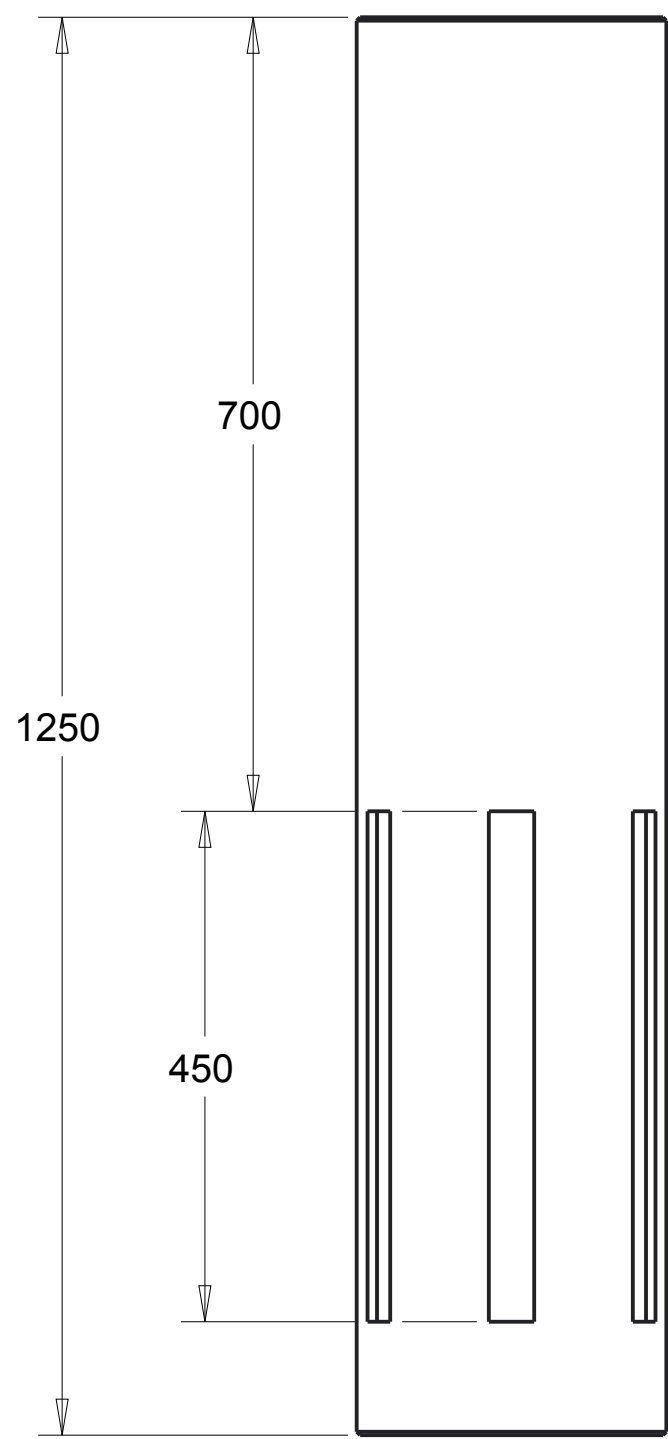
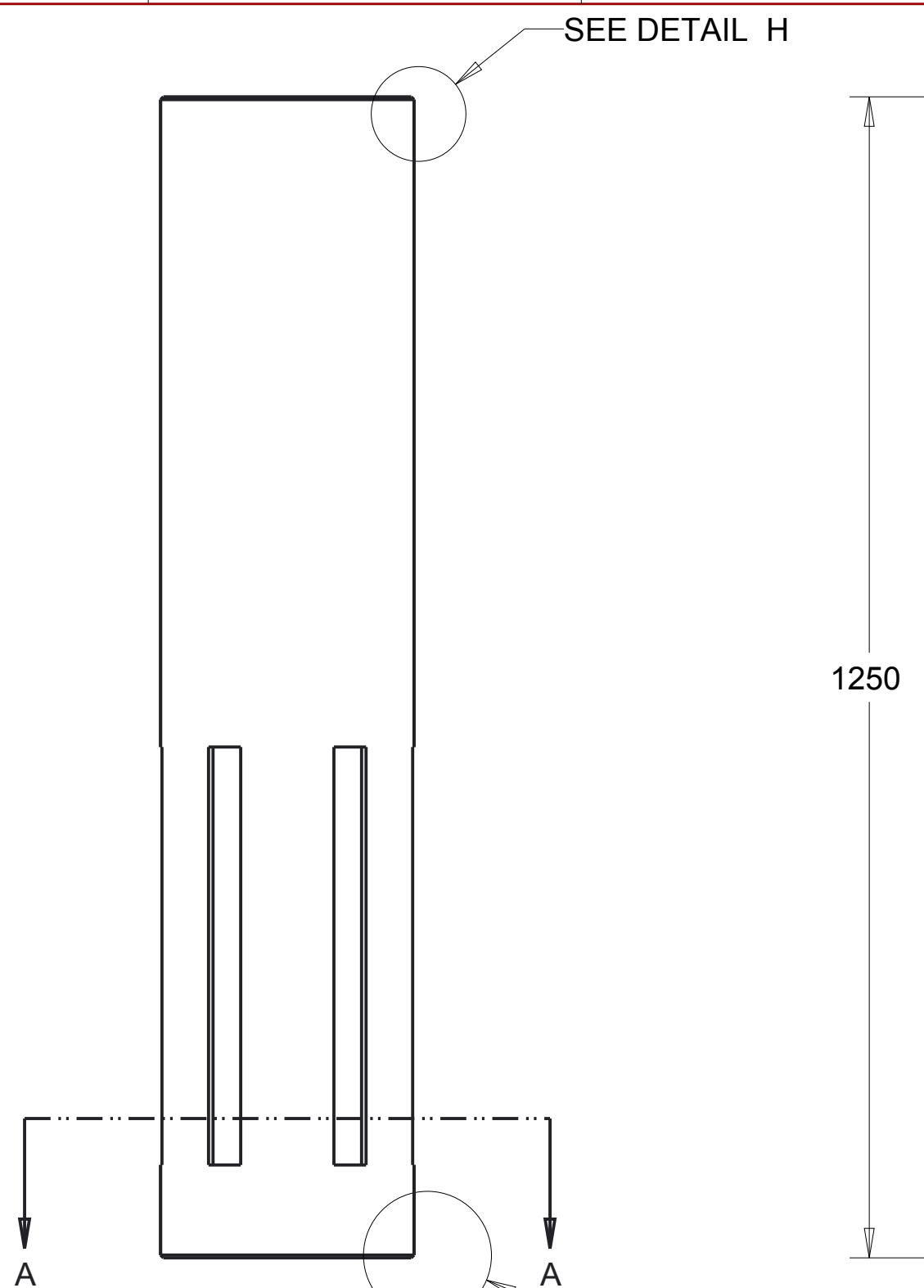


DETAIL B
SCALE 0.250

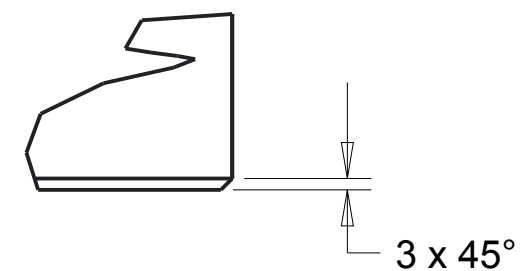


REV.	DATE	DATE AND MODIFY DESCRIPTION	DRAW	CHECKED	PROJECT E.

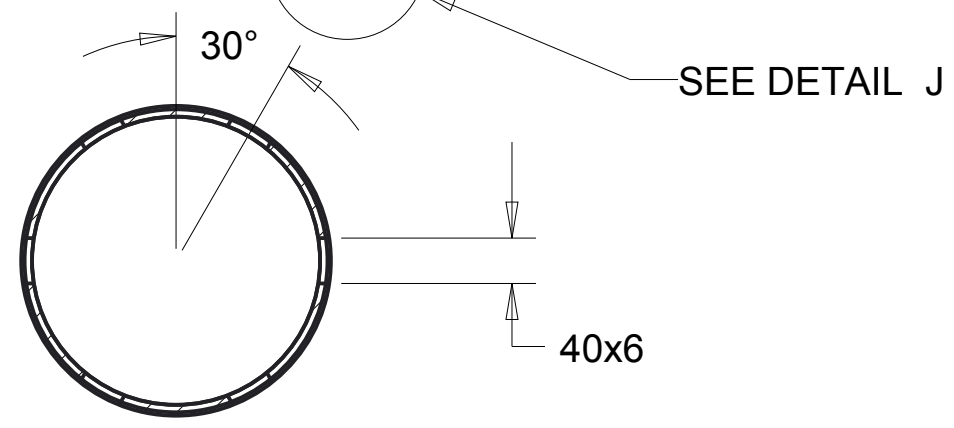
DO NOT SURVEY DIMENSIONS FROM THE DRAWING						
<p>Mechanical and Aerospace Engineering Level 4 Lord Hope Building 141 ST James Road G4 0LT Glasgow UK</p> <p>TEL. 01415484851 mae@strath.ac.uk aldo.iannetti@strath.ac.uk</p>	DRAW Aldo Iannetti	CHECKED	PROJECT E. M.Stickland			
	QUANTITY 1	MASS	SCALE 0.095			
	MATERIAL Rubber				GENERAL TOLERANCES EN ISO 13920-AE	
	TYPE BLANK	HEAT TREATMENT None				SIZE TOLERANCES
TECHNICAL DEPART. WARC			SUPERFICIAL COVERING None			<input type="checkbox"/> > <input type="checkbox"/> <= <input type="checkbox"/> <
FORMAT A3	SHEET 2	DATE 25/06/2013	DENOMINAT. Indico Rubber Bladder			2 30 ±1 ±20' 30 120 ±1 ±20' 120 400 ±1 ±20' 400 1000 ±2 ±15' 1000 2000 ±3 ±10' 2000 4000 ±4 ±10' 4000 8000 ±5 ±10'
N° DRAWING 017-02		GENERAL TOLERANCES EN ISO 13920-AE				DATE



DETAIL H
SCALE 0.500



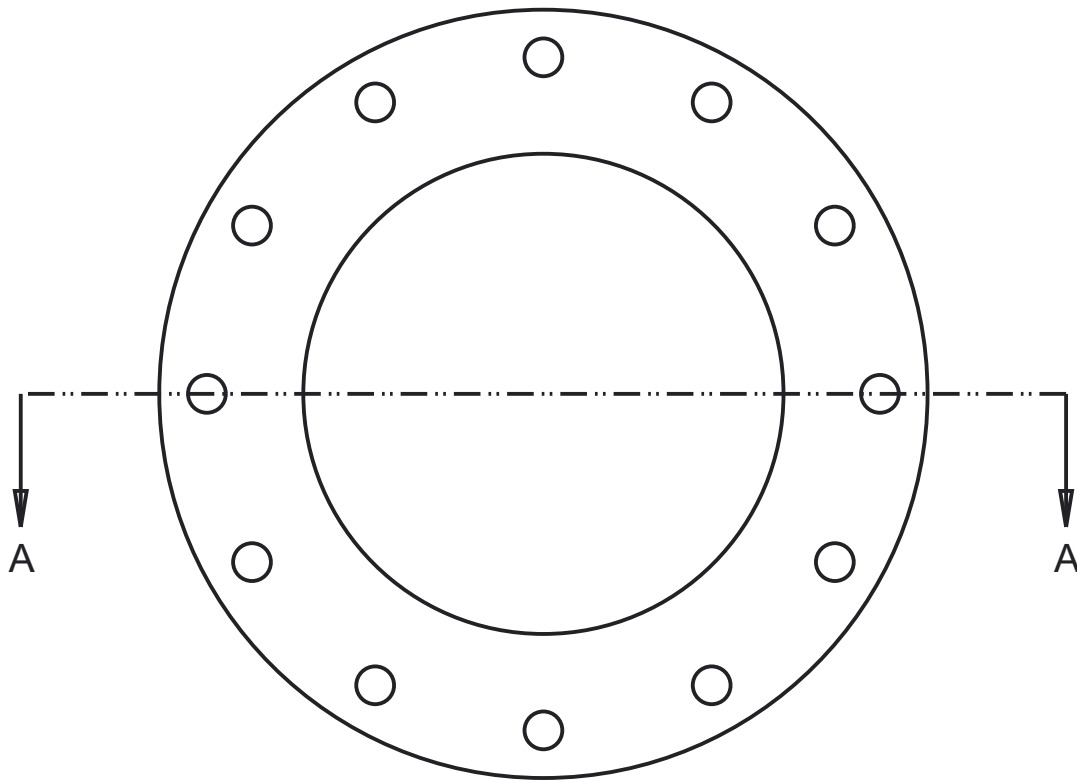
DETAIL J
SCALE 0.500



SECTION A-A

REV.	DATE	DATE AND MODIFY DESCRIPTION	DRAW	CHECKED	PROJECT E.

DO NOT SURVEY DIMENSIONS FROM THE DRAWING						
<p>Mechanical and Aerospace Engineering Level 4 Lord Hope Building 141 ST James Road G4 0LT Glasgow UK</p> <p>TEL. 01415484851 maeATstrath.ac.uk aldo.iannettiATstrath.ac.uk</p>	DRAW Aldo Iannetti	CHECKED	PROJECT E. M.Stickland	GENERAL TOLERANCES EN ISO 13920-AE		
	QUANTITY 1	MASS 65.9	SCALE 0.150	SIZE	TOLERANCES	
	MATERIAL Carbon Steel			<input type="checkbox"/> >	<input type="checkbox"/> <=	<input type="checkbox"/> <
	TYPE BLANK	HEAT TREATMENT None		<input type="checkbox"/> 2	<input type="checkbox"/> 30	<input type="checkbox"/> ±1
TECHNICAL DEPART. WARC		SUPERFICIAL COVERING None		<input type="checkbox"/> 30	<input type="checkbox"/> 120	
FORMAT A3	SHEET 4	DATE 25/06/2013	DENOMINAT. Pipe 10" BS 1640 Std		<input type="checkbox"/> ±1	
N° DRAWING 017-04				<input type="checkbox"/> 120	<input type="checkbox"/> 400	
				<input type="checkbox"/> 400	<input type="checkbox"/> 1000	
				<input type="checkbox"/> 1000	<input type="checkbox"/> 2000	
				<input type="checkbox"/> 2000	<input type="checkbox"/> 4000	
				<input type="checkbox"/> 4000	<input type="checkbox"/> 8000	



SECTION A-A

REV.	DATE	DESCRIPTION	DESIGNATED DRAW	CONTROLLED CHECKED	VISTO PROJECTE

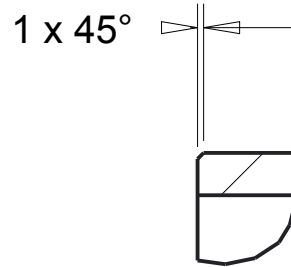
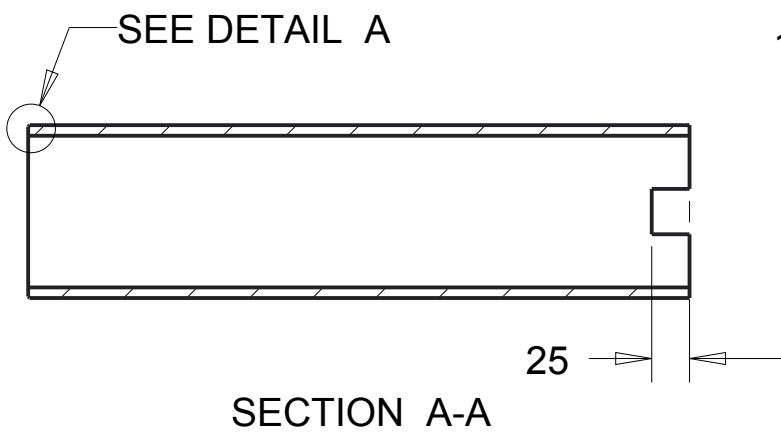
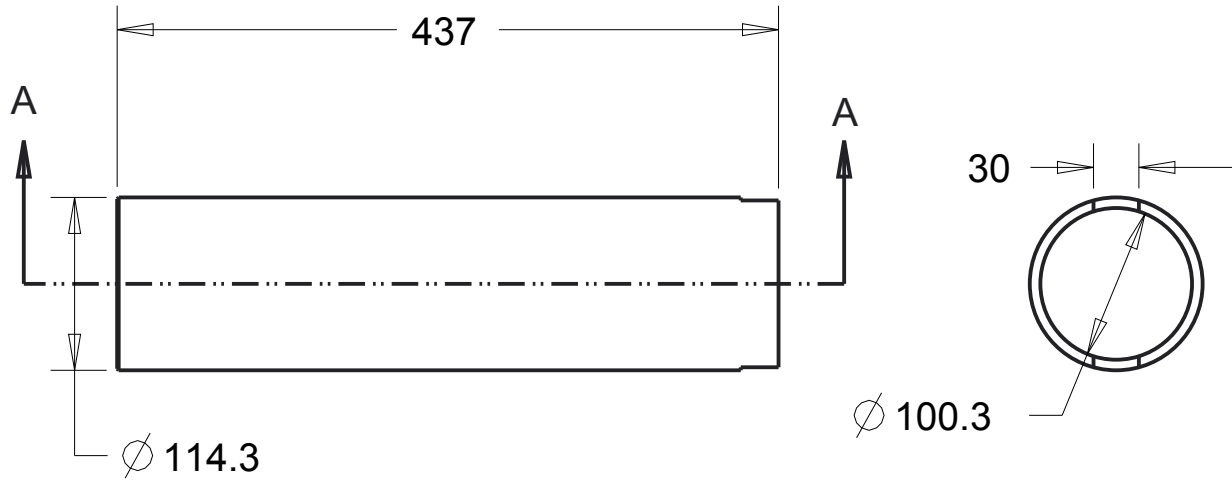
DO NOT SURVEY DIMENSIONS FROM THE DRAWING

	DRAW Aldo Iannetti	CHECKED	PROJECT E. M.Stickland
	QUANTITY 1	MASS 12.6	SCALE 0.250
MATERIAL Carbon Steel	TYPE BLANK		GENERAL TOLERANCES EN ISO 13920-AE
TECHNICAL DEPART. WARC	HEAT TREATMENT None	SIZE	TOLERANCES
FORMAT A4	SUPERFICIAL COVERING None	<input type="checkbox"/> > <input type="checkbox"/> <= <input type="checkbox"/> - <input type="checkbox"/> <	2 30 ±1 ±20'
SHEET 5	DATE 25/06/2013	30 120 ±1 ±20'	120 400 ±1 ±20'
N° DRAWING 017-05	DENOMINAT. Flat Flange BS10 Tab E for pipe 10"	400 1000 ±2 ±15'	400 2000 ±3 ±10'
		2000 4000 ±4 ±10'	4000 8000 ±5 ±10'

3

2

1



DETAIL A
SCALE 0.800

REV.	DATE	DATE AND MODIFY DESCRIPTION	DRAW	CHECKED	PROJECTE.

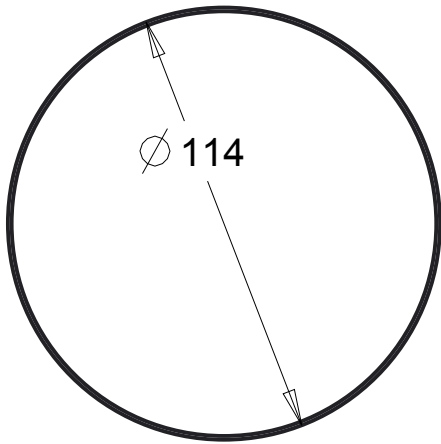
DO NOT SURVEY DIMENSIONS FROM THE DRAWING

	DRAW A. Iannetti	CHECKED	PROJECT E. M. Stickland
	QUANTITY 1	MASS 7.96	SCALE 0.2
	MATERIAL Stainless steel		GENERAL TOLERANCES EN ISO 13920-AE
Mechanical and Aerospace Engineering Level 4 Lord Hope Building 141 ST James Road G4 0LT Glasgow UK TEL 01415484851 maeATstrath.ac.uk aldo.iannettiATstrath.ac.uk	TYPE BLANK	SIZE	TOLERANCES
TECHNICAL DEPART. WARC	HEAT TREATMENT None	<input type="checkbox"/> > <input type="checkbox"/> = <input type="checkbox"/> - <input type="checkbox"/> <	2 30 ±1 ±20'
FORMAT A4	SUPERFICIAL COVERING None		30 120 ±1 ±20'
SHEET 02	DATE 24/05/2014	DENOMINAT. Plunger cylindre	120 400 ±1 ±20'
N° DRAWING 018-02			400 1000 ±2 ±15'
			1000 2000 ±3 ±10'
			2000 4000 ±4 ±10'
			4000 8000 ±5 ±10'

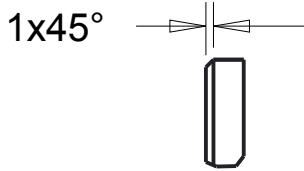
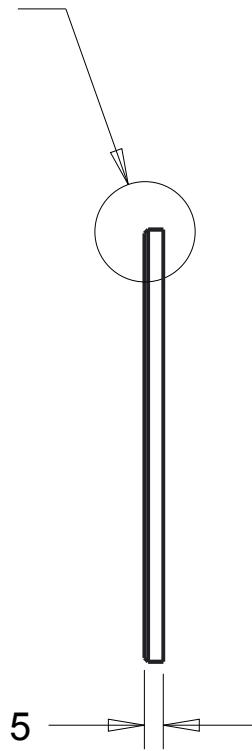
3

2

1



SEE DETAIL C

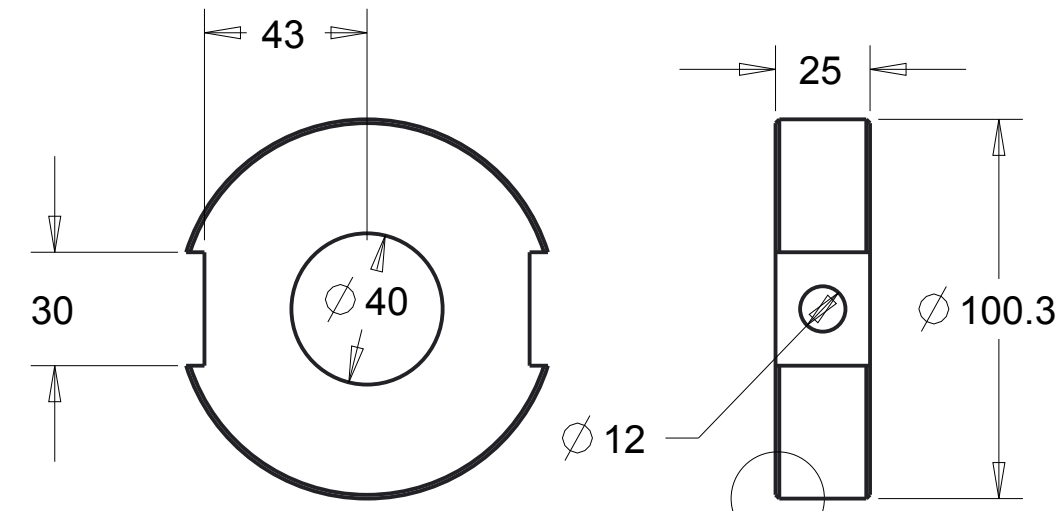


DETAIL C
SCALE 1.000

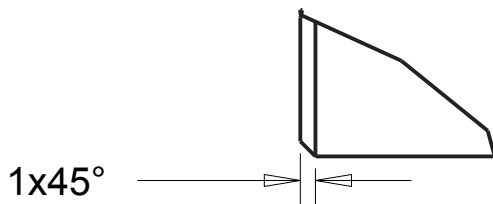
REV.	DATE	DATE AND MODIFY DESCRIPTION	DRAW	CHECKED	PROJECTE.

DO NOT SURVEY DIMENSIONS FROM THE DRAWING

	DRAW A.Iannetti	CHECKED	PROJECT E. M. Stickland
	QUANTITY 1	MASS 0.388	SCALE 0.5
	MATERIAL Mild Steel		GENERAL TOLERANCES EN ISO 13920-AE
Mechanical and Aerospace Engineering Level 4 Lord Hope Building 141 ST James Road G4 0LT Glasgow UK TEL 01415484851 maeATstrath.ac.uk aldo.iannettiATstrath.ac.uk	TYPE BLANK	SIZE	TOLERANCES
TECHNICAL DEPART. WARC	HEAT TREATMENT None	<input type="checkbox"/> > <input type="checkbox"/> <= <input type="checkbox"/> - <input type="checkbox"/> <	2 30 ±1 ±20'
FORMAT A4	SUPERFICIAL COVERING None		30 120 ±1 ±20'
SHEET 04	DATE 24/05/2014		120 400 ±1 ±20'
N° DRAWING 018-04	DENOMINAT. Plunger front cap		400 1000 ±2 ±15'
			1000 2000 ±3 ±10'
			2000 4000 ±4 ±10'
			4000 8000 ±5 ±10'



SEE DETAIL B

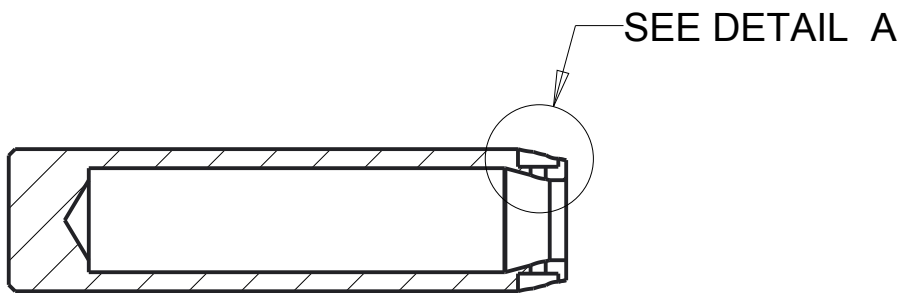
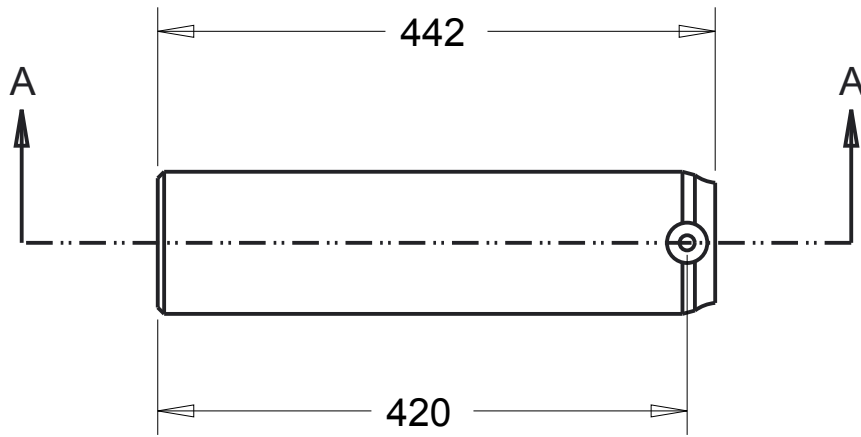


DETAIL B
SCALE 2.000

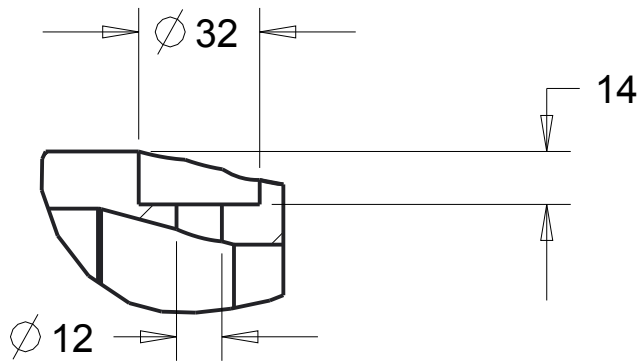
REV.	DATE	DATE AND MODIFY DESCRIPTION	DRAW	CHECKED	PROJECTE.

DO NOT SURVEY DIMENSIONS FROM THE DRAWING

	DRAW A. Iannetti	CHECKED	PROJECT E. M. Stickland																																
	QUANTITY 1	MASS 1.17	SCALE 0.5																																
	MATERIAL Stainless steel			GENERAL TOLERANCES EN ISO 13920-AE																															
Mechanical and Aerospace Engineering Level 4 Lord Hope Building 141 ST James Road G4 0LT Glasgow UK TEL 01415484851 maeATstrath.ac.uk aldo.iannettiATstrath.ac.uk	TYPE BLANK	HEAT TREATMENT None	SIZE TOLERANCES																																
TECHNICAL DEPART. WARC		SUPERFICIAL COVERING None	<table border="1"> <thead> <tr> <th>□ ></th> <th>≤</th> <th>—</th> <th><</th> </tr> </thead> <tbody> <tr> <td>2</td> <td>30</td> <td>±1</td> <td>±20'</td> </tr> <tr> <td>30</td> <td>120</td> <td>±1</td> <td>±20'</td> </tr> <tr> <td>120</td> <td>400</td> <td>±1</td> <td>±20'</td> </tr> <tr> <td>400</td> <td>1000</td> <td>±2</td> <td>±15'</td> </tr> <tr> <td>1000</td> <td>2000</td> <td>±3</td> <td>±10'</td> </tr> <tr> <td>2000</td> <td>4000</td> <td>±4</td> <td>±10'</td> </tr> <tr> <td>4000</td> <td>8000</td> <td>±5</td> <td>±10'</td> </tr> </tbody> </table>	□ >	≤	—	<	2	30	±1	±20'	30	120	±1	±20'	120	400	±1	±20'	400	1000	±2	±15'	1000	2000	±3	±10'	2000	4000	±4	±10'	4000	8000	±5	±10'
□ >	≤	—	<																																
2	30	±1	±20'																																
30	120	±1	±20'																																
120	400	±1	±20'																																
400	1000	±2	±15'																																
1000	2000	±3	±10'																																
2000	4000	±4	±10'																																
4000	8000	±5	±10'																																
FORMAT A4	SHEET 05	DATE 30/05/2014	DENOMINAT. Plunger Rear cap																																
N° DRAWING 018-03																																			



SECTION A-A

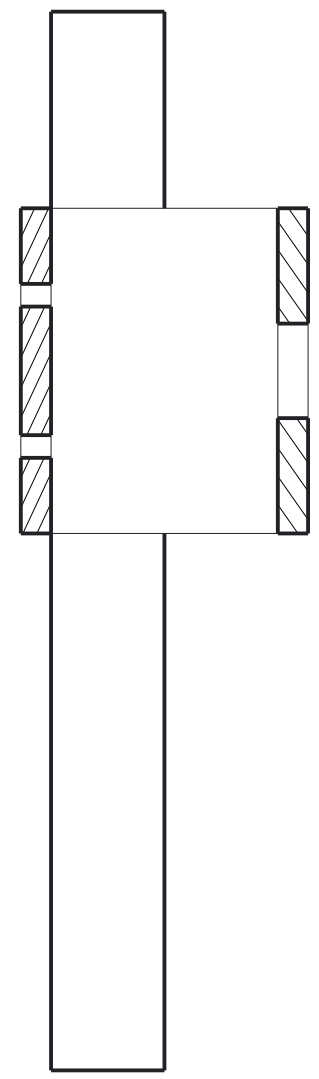
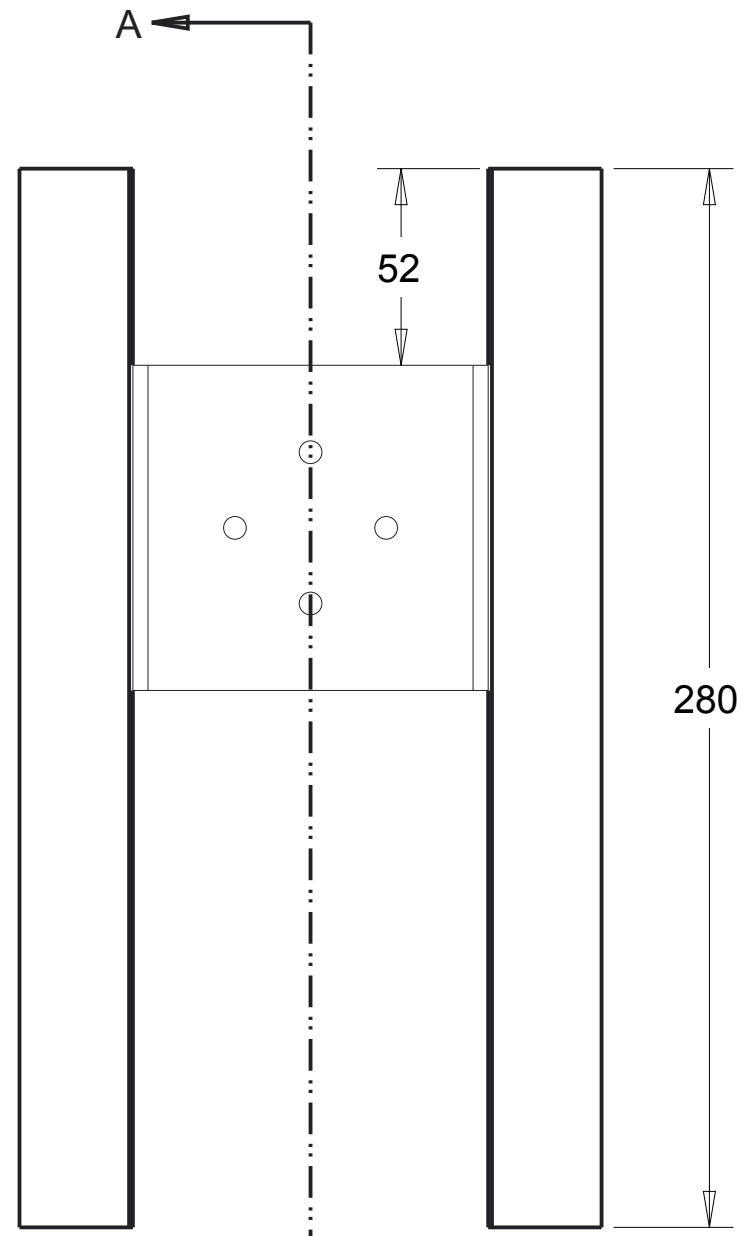


DETAIL A
SCALE 0.500

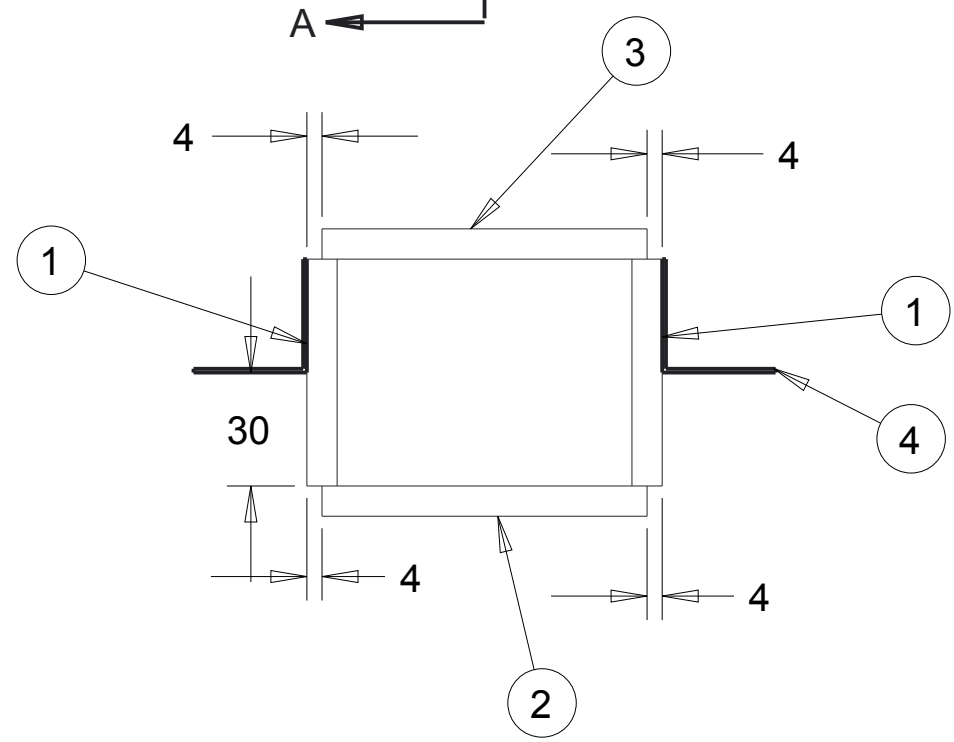
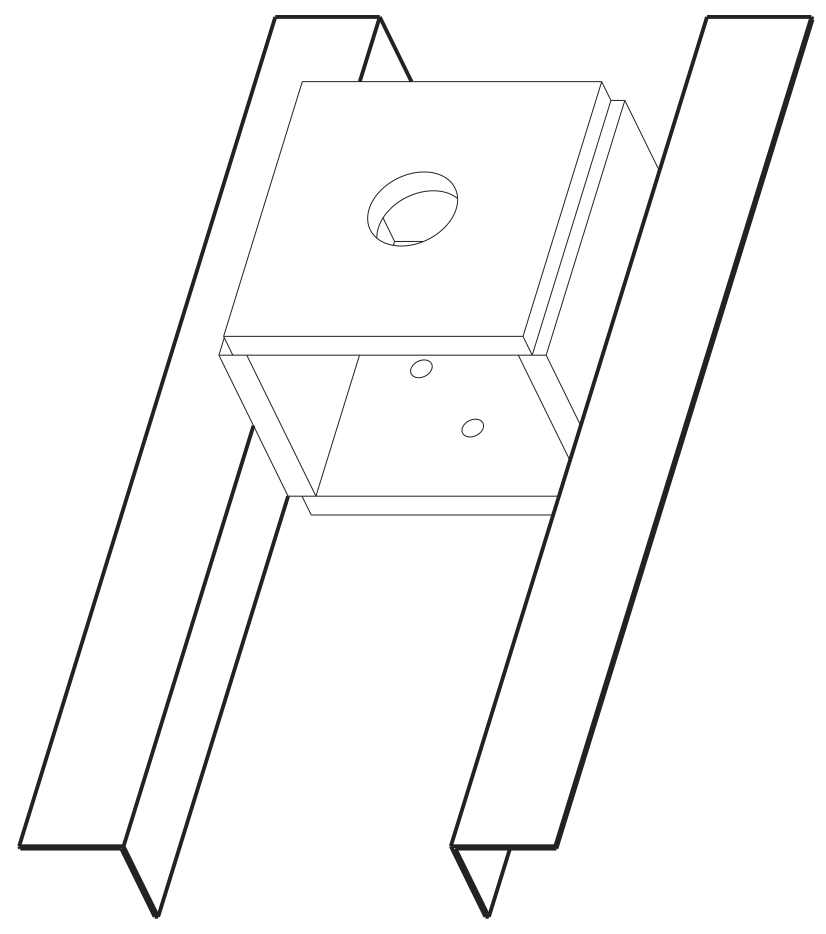
					PROJECTE.
					CHECKED
					DRAW
					DATE AND MODIFY DESCRIPTION
					DATE
					REV.

DO NOT SURVEY DIMENSIONS FROM THE DRAWING

	DRAW A.Iannetti	CHECKED	PROJECT E. M. Stickland																																
	QUANTITY 1	MASS 20	SCALE 0.5																																
	MATERIAL SPM Original		GENERAL TOLERANCES EN ISO 13920-AE																																
Mechanical and Aerospace Engineering Level 4 Lord Hope Building 141 ST James Road G4 0LT Glasgow UK TEL 01415484851 maeATstrath.ac.uk aldo.iannettiATstrath.ac.uk	TYPE BLANK	HEAT TREATMENT None	SIZE TOLERANCES																																
TECHNICAL DEPART. WARC		SUPERFICIAL COVERING	<table border="1"> <tr> <td>$\square >$</td> <td>\leq</td> <td>$-$</td> <td>$<$</td> </tr> <tr> <td>2</td> <td>30</td> <td>± 1</td> <td>$\pm 20'$</td> </tr> <tr> <td>30</td> <td>120</td> <td>± 1</td> <td>$\pm 20'$</td> </tr> <tr> <td>120</td> <td>400</td> <td>± 1</td> <td>$\pm 20'$</td> </tr> <tr> <td>400</td> <td>1000</td> <td>± 2</td> <td>$\pm 15'$</td> </tr> <tr> <td>1000</td> <td>2000</td> <td>± 3</td> <td>$\pm 10'$</td> </tr> <tr> <td>2000</td> <td>4000</td> <td>± 4</td> <td>$\pm 10'$</td> </tr> <tr> <td>4000</td> <td>8000</td> <td>± 5</td> <td>$\pm 10'$</td> </tr> </table>	$\square >$	\leq	$-$	$<$	2	30	± 1	$\pm 20'$	30	120	± 1	$\pm 20'$	120	400	± 1	$\pm 20'$	400	1000	± 2	$\pm 15'$	1000	2000	± 3	$\pm 10'$	2000	4000	± 4	$\pm 10'$	4000	8000	± 5	$\pm 10'$
$\square >$	\leq	$-$	$<$																																
2	30	± 1	$\pm 20'$																																
30	120	± 1	$\pm 20'$																																
120	400	± 1	$\pm 20'$																																
400	1000	± 2	$\pm 15'$																																
1000	2000	± 3	$\pm 10'$																																
2000	4000	± 4	$\pm 10'$																																
4000	8000	± 5	$\pm 10'$																																
FORMAT A4	SHEET 01	DATE 06/08/2014	DENOMINAT. Plunger modifications																																
N° DRAWING 020-01																																			



SECTION A-A

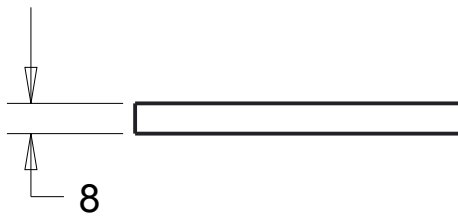
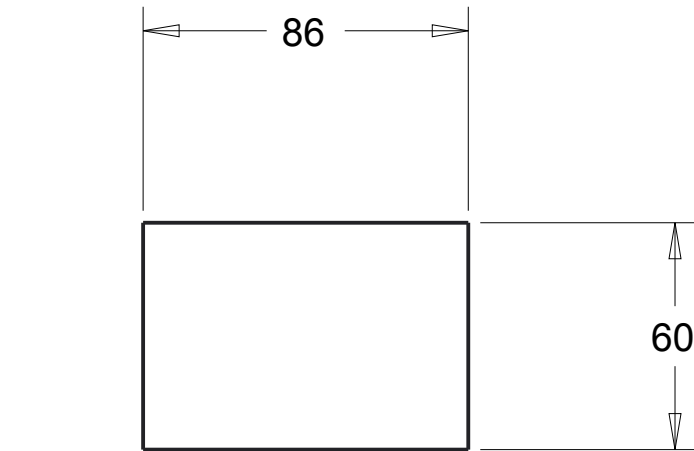


N°	Name Assembly/Detail	Drawing	Q.
1	Plate 60x86x8	021-02	2
2	Plate plunger side	021-03	1
3	Plate motor side	021-04	1
4	limit-stitches-actuator-bar	021-05	2

DO NOT SURVEY DIMENSIONS FROM THE DRAWING

<p>Mechanical and Aerospace Engineering Level 4 Lord Hope Building 141 ST James Road G4 0LT Glasgow UK</p> <p>TEL. 01415484851 mae@strath.ac.uk aldo.iannetti@strath.ac.uk</p>	DRAW A. Iannetti	CHECKED	PROJECT E. M. Stickland	
	QUANTITY 1	MASS 1.53	SCALE 0.5	
	MATERIAL Carbon steel			GENERAL TOLERANCES EN ISO 13920-AE
	TYPE BLANK	SIZE TOLERANCES		
TECHNICAL DEPART. WARC		HEAT TREATMENT None	> <= <	
FORMAT A3	DATE 06/08/2014	SUPERFICIAL COVERING Paint	2 30 ±1 ±20' 30 120 ±1 ±20' 120 400 ±1 ±20' 400 1000 ±2 ±15' 1000 2000 ±3 ±10' 2000 4000 ±4 ±10' 4000 8000 ±5 ±10'	
SHEET 01	DENOMINAT. plunger-motor connection			
N° DRAWING 021-01	PROJECT E.			

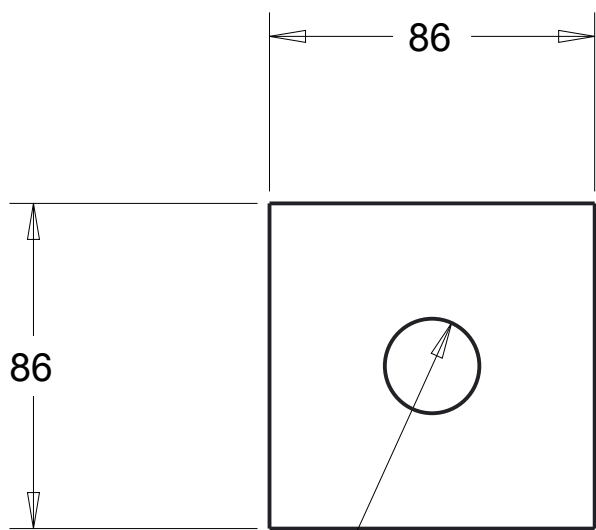
DATE	REVISION	DATE AND MODIFY DESCRIPTION	DRAW	CHECKED	PROJECT E.



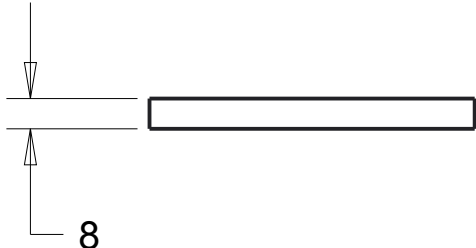
REV.	DATE	DATE AND MODIFY DESCRIPTION	DRAW	CHECKED	PROJECTE.

DO NOT SURVEY DIMENSIONS FROM THE DRAWING

	DRAW A. Iannetti	CHECKED	PROJECT E.	
	QUANTITY 2	MASS	SCALE 0.5	
MATERIAL steel			GENERAL TOLERANCES EN ISO 13920-AE	
Mechanical and Aerospace Engineering Level 4 Lord Hope Building 141 ST James Road G4 0LT Glasgow UK TEL.01415484851 maeATstrath.ac.uk aldo.iannettiATstrath.ac.uk		TYPE BLANK	SIZE	TOLERANCES
TECHNICAL DEPART. WARC		HEAT TREATMENT None		<input type="checkbox"/> > <input type="checkbox"/> <= <input type="checkbox"/> - <input type="checkbox"/> <
FORMAT A4	DATE 04/12/2014	SUPERFICIAL COVERING		2 30 ±1 ±20' 30 120 ±1 ±20' 120 400 ±1 ±20' 400 1000 ±2 ±15' 1000 2000 ±3 ±10' 2000 4000 ±4 ±10' 4000 8000 ±5 ±10'
SHEET 02		DENOMINAT. Plate 60x86x8		
N° DRAWING 021-02				



R12.5

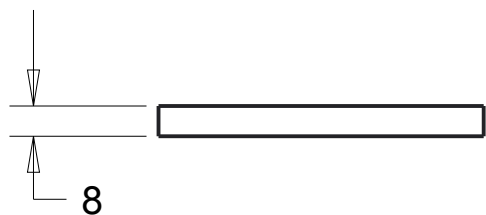
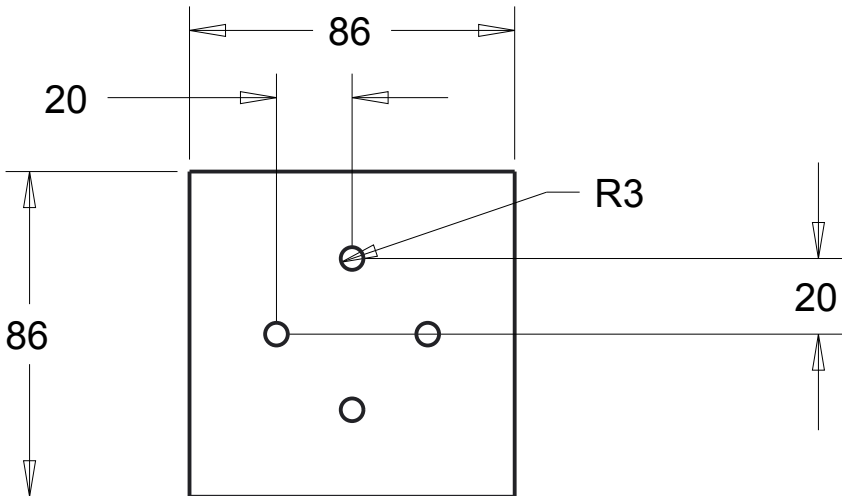


8

REV.	DATE	DATE AND MODIFY DESCRIPTION	DRAW	CHECKED	PROJECTE.

DO NOT SURVEY DIMENSIONS FROM THE DRAWING

		DRAW	A. Iannetti		CHECKED	PROJECT E.			
		QUANTITY	1		MASS	SCALE 0.5			
Mechanical and Aerospace Engineering Level 4 Lord Hope Building 141 ST James Road G4 0LT Glasgow UK TEL 01415484851 maeATstrath.ac.uk aldo.iannettiATstrath.ac.uk		MATERIAL				GENERAL TOLERANCES EN ISO 13920-AE			
TECHNICAL DEPART. WARC		TYPE		BLANK		SIZE		TOLERANCES	
FORMAT A4		HEAT TREATMENT		None		<input type="checkbox"/> > <input type="checkbox"/> <= <input type="checkbox"/> - <input type="checkbox"/> <		<input type="checkbox"/> > <input type="checkbox"/> <= <input type="checkbox"/> - <input type="checkbox"/> <	
SHEET 03 DATE 04/12/2014		SUPERFICIAL COVERING		None		2 30 ±1 ±20' 30 120 ±1 ±20' 120 400 ±1 ±20' 400 1000 ±2 ±15' 1000 2000 ±3 ±10' 2000 4000 ±4 ±10' 4000 8000 ±5 ±10'		DENOMINAT. Plate plunger side	
N° DRAWING 021-03		N° DRAWING 021-03							



REV.	DATE	DATE AND MODIFY DESCRIPTION	DRAW	CHECKED	PROJECTE.

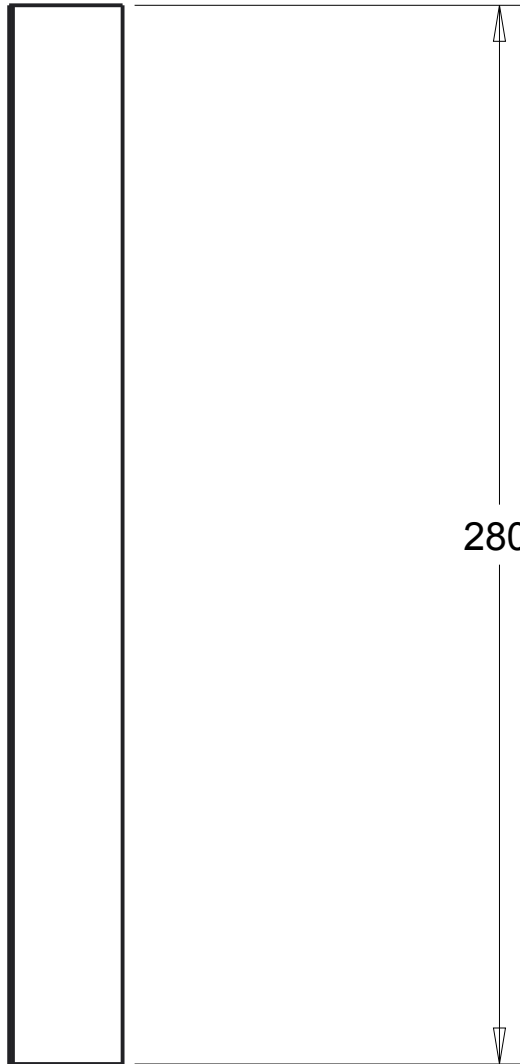
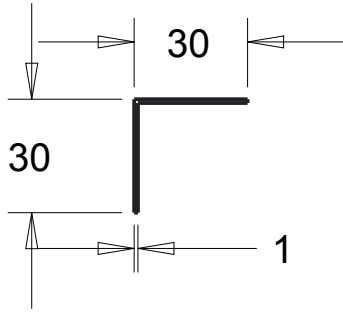
DO NOT SURVEY DIMENSIONS FROM THE DRAWING

		DRAW	CHECKED	PROJECT E.																	
		QUANTITY	1	MASS	SCALE	0.5															
Mechanical and Aerospace Engineering Level 4 Lord Hope Building 141 ST James Road G4 0LT Glasgow UK TEL 01415484851 maeATstrath.ac.uk aldo.iannettiATstrath.ac.uk		MATERIAL			GENERAL TOLERANCES																
TECHNICAL DEPART. WARC		Steel			EN ISO 13920-AE																
FORMAT	A4	TYPE	BLANK	<table border="1"> <thead> <tr> <th>SIZE</th> <th>TOLERANCES</th> </tr> </thead> <tbody> <tr> <td>2</td> <td>30 ±1 ±20'</td> </tr> <tr> <td>30</td> <td>120 ±1 ±20'</td> </tr> <tr> <td>120</td> <td>400 ±1 ±20'</td> </tr> <tr> <td>400</td> <td>1000 ±2 ±15'</td> </tr> <tr> <td>1000</td> <td>2000 ±3 ±10'</td> </tr> <tr> <td>2000</td> <td>4000 ±4 ±10'</td> </tr> <tr> <td>4000</td> <td>8000 ±5 ±10'</td> </tr> </tbody> </table>		SIZE	TOLERANCES	2	30 ±1 ±20'	30	120 ±1 ±20'	120	400 ±1 ±20'	400	1000 ±2 ±15'	1000	2000 ±3 ±10'	2000	4000 ±4 ±10'	4000	8000 ±5 ±10'
SIZE	TOLERANCES																				
2	30 ±1 ±20'																				
30	120 ±1 ±20'																				
120	400 ±1 ±20'																				
400	1000 ±2 ±15'																				
1000	2000 ±3 ±10'																				
2000	4000 ±4 ±10'																				
4000	8000 ±5 ±10'																				
SHEET	04	HEAT TREATMENT	None																		
N° DRAWING	021-04	SUPERFICIAL COVERING	None																		
DATE	04/12/2014	DENOMINAT. Plate motor side																			

3

2

1



					PROJECTE.
					CHECKED
					DRAW
					DATE AND MODIFY DESCRIPTION
					DATE
					REV.

DO NOT SURVEY DIMENSIONS FROM THE DRAWING

	DRAW A.Iannetti	CHECKED	PROJECT E.																	
	QUANTITY 2	MASS	SCALE 0.5																	
MATERIAL Steel			GENERAL TOLERANCES EN ISO 13920-AE																	
Mechanical and Aerospace Engineering Level 4 Lord Hope Building 141 ST James Road G4 0LT Glasgow UK TEL 01415484851 maeATstrath.ac.uk aldo.iannettiATstrath.ac.uk		TYPE BLANK	SIZE	TOLERANCES																
TECHNICAL DEPART. WARC	HEAT TREATMENT None		<input type="checkbox"/> >	<input type="checkbox"/> <=																
FORMAT A4	SUPERFICIAL COVERING None		<input type="checkbox"/> -	<input type="checkbox"/> <																
SHEET 05	DATE 04/12/20104	DENOMINAT. limit-stitches-actuator-bar																		
N° DRAWING 021-05		<table border="1"> <tr> <td>400</td> <td>1000</td> <td>±2</td> <td>±15'</td> </tr> <tr> <td>1000</td> <td>2000</td> <td>±3</td> <td>±10'</td> </tr> <tr> <td>2000</td> <td>4000</td> <td>±4</td> <td>±10'</td> </tr> <tr> <td>4000</td> <td>8000</td> <td>±5</td> <td>±10'</td> </tr> </table>			400	1000	±2	±15'	1000	2000	±3	±10'	2000	4000	±4	±10'	4000	8000	±5	±10'
400	1000	±2	±15'																	
1000	2000	±3	±10'																	
2000	4000	±4	±10'																	
4000	8000	±5	±10'																	

3

2

1

3

2

1

D

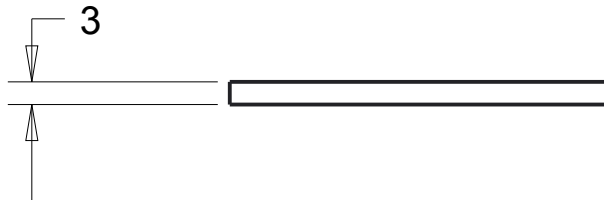
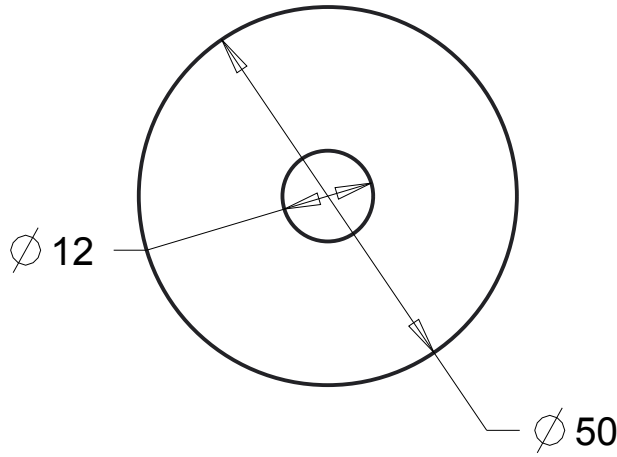
D

C

C

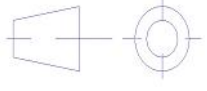
B

B



REV.	DATE	DATE AND MODIFY DESCRIPTION	DRAW	CHECKED	PROJECTE.

DO NOT SURVEY DIMENSIONS FROM THE DRAWING

	DRAW A. Iannetti	CHECKED	PROJECT E. M. Stickland																																
	QUANTITY 2	MASS	SCALE 1																																
MATERIAL Carbon steel			GENERAL TOLERANCES EN ISO 13920-AE																																
Mechanical and Aerospace Engineering Level 4 Lord Hope Building 141 ST James Road G4 0LT Glasgow UK TEL 01415484851 maeATstrath.ac.uk aldo.iannettiATstrath.ac.uk	TYPE BLANK	SIZE	TOLERANCES																																
TECHNICAL DEPART. WARC		HEAT TREATMENT None	<table border="1"> <tr> <td><input type="checkbox"/></td> <td><input type="checkbox"/></td> <td><input type="checkbox"/></td> <td><input type="checkbox"/></td> </tr> <tr> <td>2</td> <td>30</td> <td>±1</td> <td>±20'</td> </tr> <tr> <td>30</td> <td>120</td> <td>±1</td> <td>±20'</td> </tr> <tr> <td>120</td> <td>400</td> <td>±1</td> <td>±20'</td> </tr> <tr> <td>400</td> <td>1000</td> <td>±2</td> <td>±15'</td> </tr> <tr> <td>1000</td> <td>2000</td> <td>±3</td> <td>±10'</td> </tr> <tr> <td>2000</td> <td>4000</td> <td>±4</td> <td>±10'</td> </tr> <tr> <td>4000</td> <td>8000</td> <td>±5</td> <td>±10'</td> </tr> </table>	<input type="checkbox"/>	<input type="checkbox"/>	<input type="checkbox"/>	<input type="checkbox"/>	2	30	±1	±20'	30	120	±1	±20'	120	400	±1	±20'	400	1000	±2	±15'	1000	2000	±3	±10'	2000	4000	±4	±10'	4000	8000	±5	±10'
<input type="checkbox"/>	<input type="checkbox"/>	<input type="checkbox"/>	<input type="checkbox"/>																																
2	30	±1	±20'																																
30	120	±1	±20'																																
120	400	±1	±20'																																
400	1000	±2	±15'																																
1000	2000	±3	±10'																																
2000	4000	±4	±10'																																
4000	8000	±5	±10'																																
FORMAT A4	SHEET 01	DATE	SUPERFICIAL COVERING Paint																																
N° DRAWING 022-01	DENOMINAT. Motor-plunger-connection disk																																		

3

2

1